Proceedings of the 18ᵗʰ International Conference on Soil Mechanics and Geotechnical Engineering

CHALLENGES AND INNOVATIONS IN GEOTECHNICS

Actes du 18ᵉ Congrès International de Mécanique des sols et de Géotechnique

DÉFIS ET INNOVATIONS EN GÉOTECHNIQUE

Paris 2013

Edited by / Sous la direction de
Pierre Delage, Jacques Desrues, Roger Frank, Alain Puech, François Schlosser

VOLUME 1

Presses des Ponts

Technical Committee 208

Slope Stability in Engineering Practice

Comité technique 208

Stabilité des pentes pour la pratique de l'ingénieur

General Report of TC 208
Slope Stability in Engineering Practice

Rapport général du TC 208
La stabilité des talus dans la pratique de l'ingénieur

Bowman E.T.
University of Sheffield

Fannin R.J.
University of British Columbia

ABSTRACT: This General Report reviews 37 papers from 21 countries or provinces that were submitted to the conference on the topic of slope stability in engineering practice. These papers serve either to advance the state-of-the-art, else to inform the state-of-practice. Further, by developing new knowledge, else refining existing knowledge, the observations reported in the papers and the conclusions that are drawn from them provide for improved decision-making in the face of risk and uncertainty.

RÉSUMÉ : Le présent rapport général passe en revue les 37 communications provenant de 21 pays et provinces qui ont été soumis au Congrès sur le sujet traitant de la stabilité des talus dans la pratique de l'ingénieur. Les communications ont comme objectif soit de faire évoluer l'état des connaissances, soit de rendre compte de la pratique actuelle. Par le développement de nouvelles connaissances ou par l'affinement de connaissances existantes, les observations relatées dans ces communications et les conclusions qui en sont tirées permettent d'améliorer les processus décisionnels face aux risques et aux incertitudes.

KEYWORDS: Slope stability, landslide, debris flow

1 INTRODUCTION

Slope stability in engineering practice is considered by many to be a broad-ranging subject, and this viewpoint is perhaps supported by the diversity of papers submitted to the conference. Yet, in reality, studies of slope stability in engineering practice are unified by the common objective of a better understanding of (i) the spatial and temporal variation of demand and capacity at the point of origin and (ii) the magnitude and travel distance of the event along its path of movement downslope. All of the papers submitted to the conference address these objectives in one form or another. In this regard, the findings of the papers serve either to advance the state-of-the-art, else to inform the state-of-practice. More importantly, by developing new knowledge, else refining existing knowledge, the observations reported in the papers and the conclusions that are drawn from them provide for improved decision-making in the face of risk and uncertainty.

This General Report reviews 37 papers from 21 countries or provinces that were submitted to the conference on the topic of slope stability in engineering practice.

1.1 *Focus / approach of papers*

Table 1 indicates that there is overlap in the focus of many of the papers, with 24 of them sharing two or more approaches or topics. This is particularly evident for papers that have a case study element with 14 of these linking to a numerical model, detailed field study and/or risk assessment. It is encouraging to see that such case studies are being increasingly presented with a critical and quantitative assessment of the factors that may have contributed to a slope failure occurring. A further 4 of the case study papers directly link to implementation of mitigation measures (*Şengör et al.; Coutinho and da Silva; Bozo and Allkja; Chang and Huang*), although with the exception of the paper by *Şengör et al*, other than qualitatively showing the utility of such measures, the outcomes are neither analysed nor presented in detail.

Table 1. Number of papers by approach or focus.

Approach / focus	Papers
Case study	21
Numerical - deterministic	9
Numerical - probablistic	6
Field study / instrumentation	6
Experimental / physical model	6
Risk assessment	6
Mitigation measures	6

In contrast, it is interesting to note that 4 of the 9 papers that use deterministic numerical models do not attempt to validate against any particular field situation. In these cases, the models in question may be still at the development stage (*Saha; Nonoyama et al.; Law et al.)* else the authors intend to illustrate a potentially general mechanism of failure (*Dey et al*.).

A total of 6 papers present a detailed study of a particular area via field instrumentation or discuss the development of instrumentation for monitoring of slope instability, while a further 6 papers present an experimental analysis of soil behavior or a detailed physical model of a particular scenario. These approaches are important to enable an understanding of fundamental mechanisms of slope instability and can be very important to determining the details of complex interactions between, for example, groundwater and precipitation on rainfall-induced landslides, or sediment supply and frequency of debris flows.

Six papers take a risk assessment approach – either for a defined area for site-specific purposes related to risk assesement or for a more regional approach that is more appropriate to concern of risk management.

1.2 *Type of instability investigated*

Table 2 shows the types of landslide failures that are discussed in the papers. Approximately 30% of the papers are on rainfall-induced landslides, 8% on earthquake-induced landslides (solely) and nearly 30% on debris flows or flow-

slides, with multi-hazard landslides (mostly earthquake coupled with debris flow) accounting for 10%. The remaining papers address progressive slides (4%) or the triggering / landslide type is unspecified (19%).

The fact that there are 10 papers on debris flows or flow slides is a marked increase on previous years. For the 16th International Conference on Soil Mechanics and Geotechnical Engineering, Chau (2005) noted that only two papers dealt with debris flows. While as Chau (2005) has pointed out, there are dedicated conferences on debris flows elsewhere, the inclusion of these papers in a broader geotechnical forum is promising in terms of applying geotechnical rigor to a problematic subject of global concern.

The recognition of landslides within a multi-hazard causal framework is also extremely important, although the number of papers presented is still relatively small. As determined by Lin et al. (2004), amongst others, earthquakes can lead to worsening conditions for landslides and debris flows, while landslides can be the precursor of debris flows particularly where the landslide meets a body of water or ice. A thorough understanding of the complexity of such scenarios is believed warranted, because the state-of-the-art must continue to inform the state-of-practice and, on occasion, the cutting-edge of practice is challenged to address some very challenging realities of risk management.

Table 2. Number of papers by instability type

Type of failure	Papers
Rainfall / pore pressure induced	11 (14)
Earthquake induced	3 (7)
Debris flow / flow slide	10 (11)
Multi-hazard	4
Progressive	2
Unspecified	7

(Parentheses indicate numbers that include multi-hazard papers)

1.3 *Breakdown of research papers by country*

Table 3 presents the number of papers from different countries and indicates an important reality with respect to where research activity is currently concentrated by region. As has been previously noted by Petley (2012), much of the work on landslides is carried out by researchers in developed economies, where the focus has moved from life impacts (which have been reduced over time due to the development of a relatively good understanding of catastrophic landslide behavior in these countries) to economic impacts (which may be more influenced by slower movements and low-magnitude, albeit high-frequency events). However, in emerging and developing economies, which have large numbers of landslides per annum, there is relatively little research on-going, the threat to life remains unacceptably large.

Table 1. Number of papers in session by country / province

Country	Papers	Country	Papers
Norway	6	India	1
Japan	4	Korea	1
Taiwan / Chinese Taipei	4	Lebanon	1
USA	4	New Zealand	1
Hong Kong, China	3	Russia	1
Albania	2	Sweden	1
Brazil	1	Turkey	1
Canada	1	United Kingdom	1
Mainland China	1	Vietnam	1
Greece	1		

To illustrate this, Figure 1 after Petley (2012) presents the total number of publications on landslides found in ISI journals for each country (taken from provenance of the lead author's

institution) against the recorded number of fatalities in those countries in the period from 2004 to 2010. He has divided the figure into three zones – termed research intensive, research active, and research inactive. The results clearly show that many countries which are least research active have some of the highest incidences of landslide fatalities.
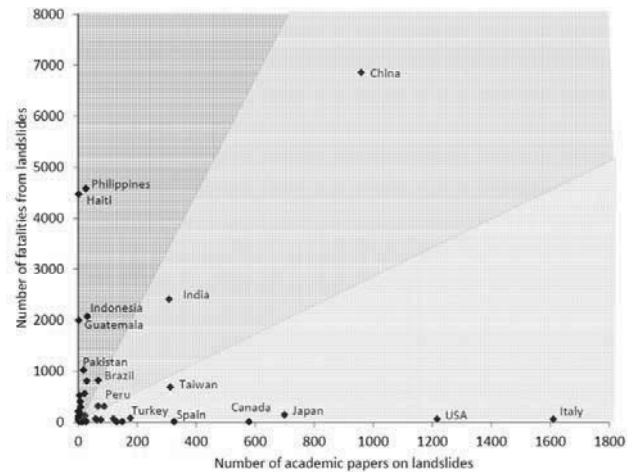

Figure 1. Total number of publications on landslides / slope stability by country in ISI journals from 2006-2010, reproduced from Petley (2012).

Using China as an example, Petley (2012) also showed that increasing the research intensity within a country prone to landslide activity can reduce the rate of fatalities experienced. Two decades of data from 1990 to 2013 are reproduced in Figure 2.
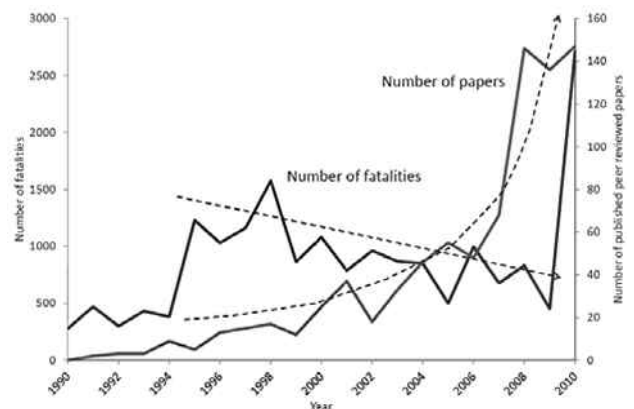

Figure 2. Example of the effect of increasing annual research on landslides on the rate of fatalities in China over 20 years, after Petley (2012). Note that a single landslide that occurred in 2010 in Gansu province killed over 1700 people, which distorts the overall dataset.

In the following section, papers are grouped by type of instability (Table 2).

2 RAINFALL / PORE PRESSURE INDUCED SLOPE INSTABILITY

This section discusses the major findings of the 11 papers on rainfall or elevated pore pressure induced landslides.

Two papers by *Wang et al.* and *Uchimura et al.* discuss the use of a tilt-sensor to detect the onset of instability in slopes that are experiencing creep movements. *Wang et al.* covers details of innovative sensor development and field installation. *Uchimura et al.* elaborates further on the use of the device coupled with volumetric water sensors within an experimental arrangement of artificial rainfall on natural ground. The experiments show that instability can be detected by an increase in the rate of change of the tilt angle, while the volumetric water content is related to

the deformation, and is independent of the rainfall period. Some interesting observations are made regarding the influence of the soil water characteristic curve (SWCC) on the deformation behavior of an unsaturated slope undergoing infiltration – in particular, that a temporary reduction in deformation rate may not be indicative of increased stabilization, but rather an effect of the reduced rate of change of suction loss with infiltration. The finding is an excellent illustration of the potential for the state-of-the-art to influence the state-of-the-practice.

Nakata et al. examines the influence of pore pressure cycles on the collapse behavior of a slope in a study combining element testing of a standard sand with field monitoring of a natural slope. Plane strain compression tests carried out on Toyoura sand showed that cycles of pore pressure always led to soil hardening rather than increasing the likelihood of failure. In the field, it was found that the slope's behavior was a function of both the recent and antecedent rainfall, yielding a recommendation to monitor the groundwater level as well as the use of rainfall data to understand the fundamentals of collapse behavior.

Rahhal et al. presents a study on two landslides that occurred in Lebanon for which geotechnical parameters were obtained via laboratory testing. Slope stability analysis of one slide showed that a loss of cohesion in the clay, at the interface of the clay and underlying stiffer material, due to seasonal moisture infiltration, resulted in the instabilities that were reported. For the second study area, weakening and loss of cohesion in clay schist due to prolonged water contact was thought to be largely responsible for the instabilities recorded, with a minor contribution from cracks that were opened allowing water infiltration.

Jeng et al. present a study on the effects of heavy rainfall on a slope in northeastern Taiwan that is covered with a 10-20m depth of colluvium and instrumented with a surface monitoring system. The results from 295 locations of settlement and displacement monitoring locations are evaluated, together with the significance of rainfall on initiating ground movements. Figure 3 shows annual surface settlements of up to 20mm in the study area. From the analysis of the influence of typhoon rainfall on the ground displacements in different parts of the site, a threshold value curve of risk for rainfall was proposed for the area and a slope stabilization programme subsequently recommended by the authors. Once again, a careful series of field observations serve to influence the state-of-the-practice.

Kavvadas et al. presents the management of a mine site in Greece in which significant ground displacements are seen to occur with rainfall. Figure 4 shows a generally good correlation between surface velocities as determined at monitoring prisms (top) and rainfall records taken approximately 6km away (bottom). The data indicates a stick – slip mechanism and a regressive movement in which the velocity does not increase or decrease at a constant rate but undergoes abrupt changes. The authors posit that, during and after heavy precipitation, the water-filled tension cracks provide an increasing driving force. As displacement continues, the width of the cracks increases and the water level drops with a resulting dissipation of water pressure. This is a different mechanism to that of tertiary creep in which an increase in velocity of slope movement may be the precursor to imminent failure (Rose and Hungr, 2007).
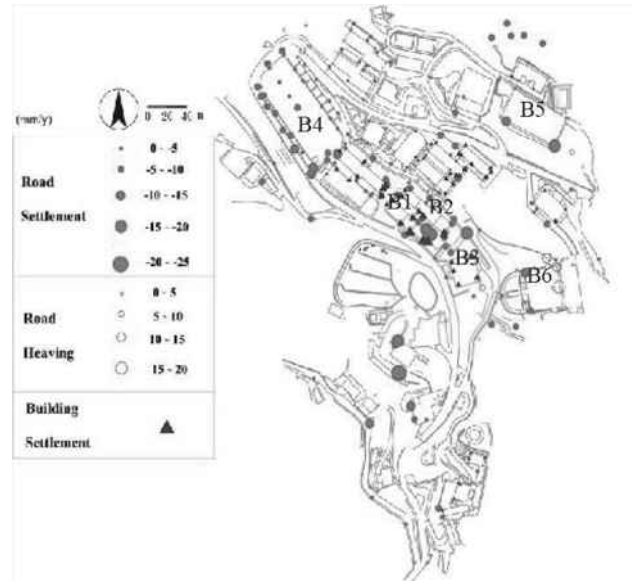

Figure 3. Jeng et al. Annual surface settlement distribution

Kavvadas et al. highlights the importance of understanding the underlying mechanism of slope deformation and, in doing so, shows that high mine slopes can operate under large rates of displacement, as long as the type of sliding mechanism is identified and continuously monitored. Finally, the paper shows that remedial measures can be incorporated in a mine plan in order to reduce movements, if not to arrest them entirely.
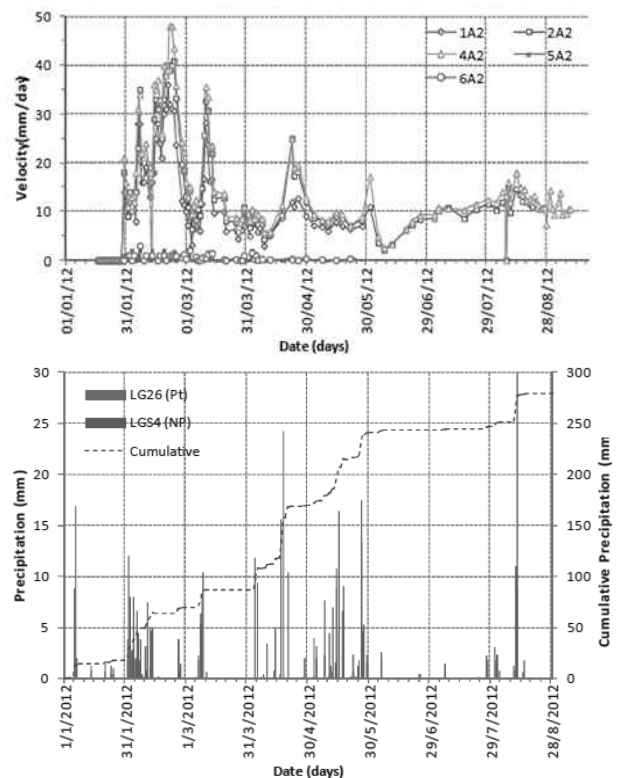

Figure 4. Kavvadas et al. Correspondence of slope velocity change with precipitation.

Coutinho and da Silva present a paper on the characterization, analysis and stabilization of a landslide located in a township in Brazil. The soil formation is characterised as sandy clay to silty sand (Barreiras formation) and residual granitic soil. The landslide was analysed as a two-part process during a precipitation event (Figure 5). The analysis suggested that the upper part of the slide zone failed first, due to a lower

permeability zone, leading to elevated pore pressures in that zone during heavy rainfall. The upper slope failure then resulted in an additional surcharge loading and failure in the lower slide mass. This paper highlights the importance of local geological conditions on the triggering of slope instability and that localized heterogeneity can play a major role in the distribution of groundwater flow.
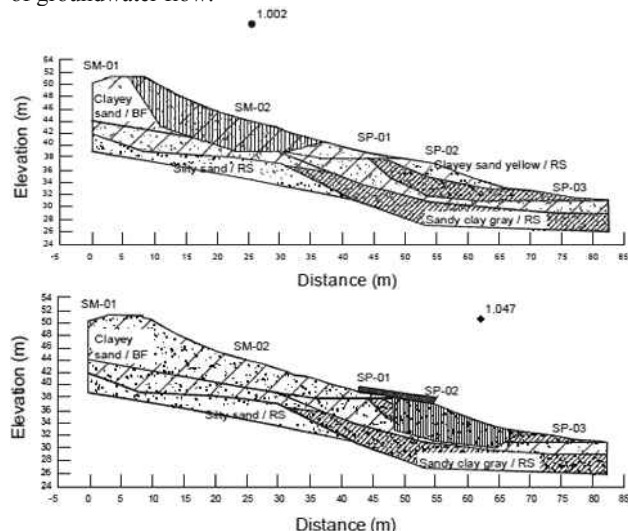

Figure 5. Coutinho and da Silva. Upper and lower slope failure models.

Son et al. present a study on landslide susceptibility zonation for an area in the south central coast of Vietnam developed using a Bayesian conditional probability model. Surveyed landslides from one year's rainy season were used as inputs to the model which was examined to develop suitable weighting factors on elements such as elevation, slope angle, drainage distance, geology etc. and was integrated with GIS analytical tools to produce the map. The reliability of the model can be improved as new landslide occurrences are updated annually in the landslide inventory.

Tremblay et al. discuss the influence of climate change on the risk of landslides and its assessment for a valley in Sweden. Notable effects of climate change are increases in annual precipitation and temperature and potential reduction in water levels in the river through dry summer periods (although controlled by the authorities) and increased river flows in winter (Figure 6). Each of these scenarios may lead to a decrease in slope stability around the river valley. Readers are referred to detailed risk assessment and reports available from SGI.

Li et al. discusses the detailed instrumentation and full-scale field monitoring programme for a study on the mechanisms of rainfall-induced sliding slope, through a study conducted for a new development in Hainan, China. Large variations of volumetric water content and matric suction at shallow depth in decomposed granitic soils, during the rainy season, may explain why so many slope failures have occurred in this region at times of heavy rainstorm activity. The paper also highlights the inherent difficulties associated with the protection of delicate monitoring instruments on an active construction site.

Harris et al. describes the implementation of an early warning system (EWS) for a highway embankment subject to rainfall induced landsliding. Volumetric water content sensors were installed at a cross section of the site. A 2D finite element model was then used to replicate the response of the sensors to rainfall, using monitored rainfall events as an input. Next, a limit equilibrium analysis was carried out and an artificial neural network was trained to predict the factor of safety obtained using the sensor readings as inputs. Data from rainfall forecasts are then used to establish a predicted factor of safety for the slope in real time, allowing road-users to be advised accordingly.
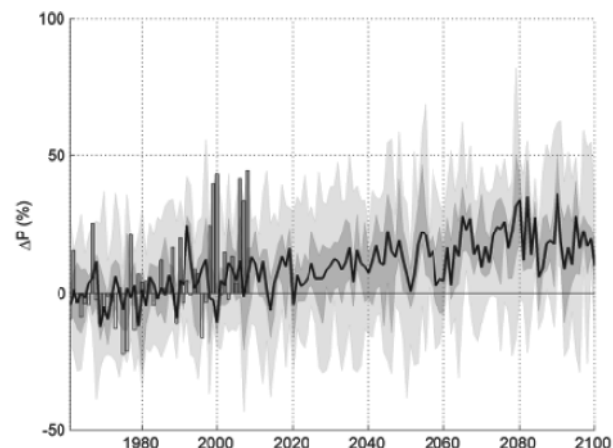

Figure 6. Tremblay et al. Percentage increase in precipitation with year from 16 climate scenarios after Bergstrom et al. (2011)

3 DEBRIS FLOWS AND FLOW SLIDES

In total 10 papers are presented on debris flow or flow slide initiation, and aspects of runout or travel distance if the specifics of entrainment of debris along the path of movement as taken into account (see Fannin and Bowman, 2010)

Several studies are presented that use statistical data to derive debris flow hazard potential in particular areas based on local topography and associated hydro-geological behavior. Some of these studies follow statistical-empirical methodologies that do not require precipitation inputs, and may be used for a general assessment of debris flow potential, while other studies include a temporal element by taking account of precipitation records. *Yune et al.* present a paper on debris flows that occurred in the Umyeon Mountain area of Seoul, Korea during the rainy season of 2011, determining that most were initiated from small slope failures induced by high-intensity rainfall. The paper discusses the application of a statistical landslide hazard map which has been developed on parameters such as slope angle and direction, strength of soil, hazard record, rainfall condition and plantation type. This map has demonstrated the ability to highlight areas that are vulnerable to heavy-rainfall-induced slope failure and resulting debris flow disasters.

Lin and Lin present a study on the analysis of debris flow torrents in Nantou County, Taiwan, using discriminant analysis based on 199 known debris flow torrents and 175 non-debris flow torrents. The influence factors included: watershed area, stream length, form factor, hypsometric integral, stream mean slope, slope distribution, slope aspect, and geological formation. In order to examine the feasibility of the model, the data sets of debris flow torrents and non-debris flow torrents not used in developing the estimation models were used for validation and prediction.

Cepeda et al. presents a probabilistic procedure based on a Monte Carlo simulation for run-out modeling of debris flows, in order to analyse the effect of uncertainties in the input parameters. The framework is based on a dynamic model, which is combined with an explicit representation of the different parameter uncertainties. The main goal is to present a framework to obtain potentially expected run-outs and intensities in areas where it is not possible to determine the rheological parameters on the basis of back analyses.

Two papers are presented that use experimental techniques to examine debris flow behavior. *Katzenbach and Bergmann* present a paper to understand some fundamental flow properties of saturated soil in a large-scale experimental apparatus. The study is designed to examine the influence of parameters such as grain size, grain shape and grain size distribution, water content and pressures on the flow behaviour. This paper focuses on coarse grained water-saturated soils, which excludes the

complexities of cohesive internal forces. Initial results indicate the importance of particle size on the flow velocity of the granular mixture. Results are intended to supplement numerical work that is on-going.

Choi et al. present a paper on a series of flume tests that examine the influence of baffle row number on reduction of debris frontal velocity. The average frontal velocity of the debris flow downstream of the array of baffles was measured. Results show one row to be ineffective in reducing the debris frontal velocity, however, two to three rows of baffles exhibit notable frontal velocity reduction.

Law et al. present a related paper to that of *Choi et al.* on the dynamic interaction between a granular surge flow and baffles. In contrast however, Law et al. use the three-dimensional discrete element method with the granular flow medium modeled as spherical discrete elements and the baffles as rigid square objects. The location, velocity and forces acting on the individual elements during the impact and interaction process are presented. Assessment of the numerical results indicates that a single row of baffles is effective in reducing the kinetic energy and discharge of the granular flow. Interestingly, this actually runs counter to the findings of *Choi et al.* One possibility for this may be a difference in the relative size of largest particles to the baffle spacing used in the experiments by *Law et al.* and *Choi et al.* although data on this are not available from *Choi et al.*
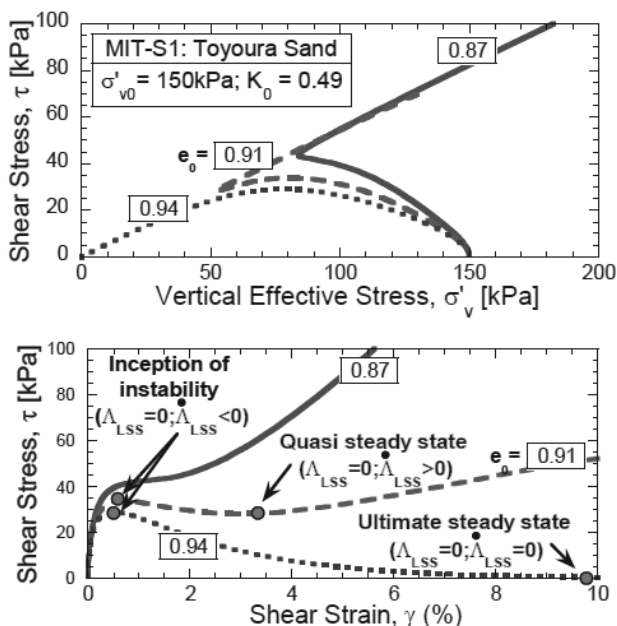

Figure 7. Buscarnera and Whittle. MIT-S1 constitutive model predictions for a sand in undrained shear at different initial void ratios.

Buscarnera and Whittle present a framework for evaluating the triggering of flow slides in infinite slopes using the anisotropic MIT-S1 model. The selected soil model is able to simulate realistic transitions in the contractive/dilative response of sands and enables the prediction of the shear perturbations able to induce instability (Figure 7), as well as the location of potentially unstable zones within the soil mass. In order to show the capabilities of the proposed approach, the methodology has been applied to the well-known case of slope failures in the Nerlerk berm: results suggest that static liquefaction is likely to have contributed to the failures. The analyses illustrate a unified methodology that combines the theory of material stability, the critical state framework for sands and data from in situ tests. The authors state that the methodology offers a simple, consistent and complete geomechanical framework for interpreting and predicting the triggering of flow slides that can be easily applied to other similar engineering cases.

Thakur et al. propose a new approach to assess the potential for flow slides via a new laboratory test procedure referred to as the quickness test. The test focuses on remoulded behaviour of sensitive clays in terms of a numerical value referred as quickness (Q). Based on their study, it is found that a Q < 15 % or remoulded undrained shear strength $c_{ur} > 1$ kPa seems to be the threshold limit above which the extent of retrogression of a landslide is limited to the initial slide. This criterion has been supported using data available from several Norwegian landslides in sensitive clays.

Winter et al. present fragility curves as a means of describing the vulnerability of elements at risk to impact by a debris flow. The specific category of element considered in the paper is a road. Expert engineering judgment was used to develop preliminary fragility curves, from a compilation of responses to a questionnaire. Analysis and interpretation of the collected data is made with reference to two events, in an attempt to relate event volume to the probability of a state of damage.

4 EARTHQUAKE INDUCED SLOPE INSTABILITY

Consideration of seismic slope stability occurs in several papers, two of which are considered here and five of which are more rationally addressed within the context of multi-hazard considerations in the section that follows this one.

Strenk and Wartmen present the findings of a sensitivity analysis conducted on an idealized slope, to examine uncertainty in seismic deformations established using the Newmark rigid-block method, given variability in ground motion. The effect was found to be most pronounced at low acceleration ratios, and little influence of frequency content and waveform was observed. The findings suggest that use of spectral matching to create variability in both intensity and frequency may be "of limited utility".

Paçi et al. presents a study on the stability of a new road located in a very disturbed tectonic zone where the rock quality is extremely poor. Active surface slides are very unstable due to water ingress especially during seismic events. Geotechnical parameters of the intact flysch / clay and limestone rock are determined from laboratory tests and empirical methods, while for residual parameters, a back-analysis is carried out using Plaxis 2D software. Hence, slope stability problems resulting from seismic loading are examined in two stages. The first model determines a critical sliding plane (if any) under an artificial accelerogram that takes account of near-source effects and then the second uses residual parameters for the soil strength mobilized within the sliding plane. The second model is used to define and design the engineering measures (walls, piles, anchored wires, nails, etc.). This two-step process, is a pragmatic approach for designing mitigation measures for prefailed slopes, and may also be used for pore-pressure induced instabilities (e.g. Tatarniuk and Bowman, 2012).

5 MULTI-HAZARD INSTABILITY OF SLOPES

Nadim and Liu present on the use of Bayesian networks to inform reasoning when there is uncertainty and reliance on expert judgment, such as is done in many branches of civil engineering (for example, avalanche risk assessment, dam risk analysis etc.). They built a network for consideration of earthquake-triggered landslides using the open-source MATLAB package BNT, and used it to conduct a sensitivity analysis. The method is believed to have merit in deciding where to take no action, versus installing a warning system, else opting for active countermeasures.

Chang and Huang present an interesting case study on the influence of the Chi-Chi earthquake in 1999 on a road above slope that had been stable. Although no obvious damages to the road were observed at the time of shaking, during Typhoon Nari in 2001, several parallel cracks developed along the road alignment – suggestive of underlying instability. Remedial work

was initiated. Nonetheless, a loss of road base during the monsoon season the next year imposed a stop on the work. The remedial plan was revised and implemented, but failed again due to typhoons in 2005. The current repair works have been completed and generally show no major signs of slope distress. However, data from subsurface exploration and in-situ monitoring have shown signs of slope instability.

Figure 8 indicates potential slip surfaces in the upslope that would have impact on the road section. The downhill side slope also was not improved during the remedial works and its surface was bared with remains of previous slides. The upslope mitigation works are not useful for the stability of the downslope area and do not remove the concerns regarding the long-term stability of the road section and slopes at the site. Discussion addresses the potential for further remedial works, but it is pointed out that the cost of these may make a rerouting of the road desirable in the long term.
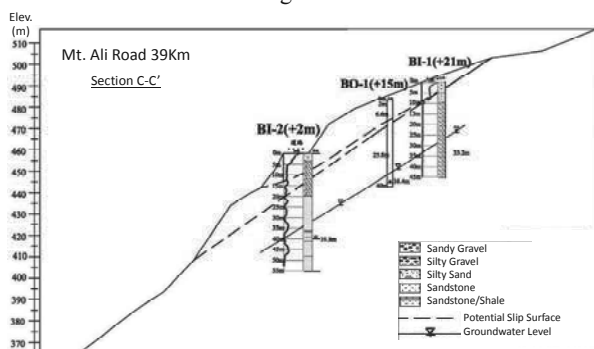

Figure 8. Chang and Huang. Instabilities detected by borehole investigation

Long and Tjok present a paper on submarine slope instability due to earthquake excitation leading to mass gravity flow which may pose risk for the integrity of offshore structures along the flow path. This paper demonstrates the ability of using a fully coupled nonlinear effective stress analysis to simulate the development of liquefaction and the instability of a liquefied slope. A prediction of run-out distance of subsequent debris flows is also made. The authors use a 1D model and parameters correlated with liquidity index in the absence of other data, although they also point out that estimation of run-out distance should be tested and calibrated to the case in question.

Quan Luna et al. present a study on the effects of earthquakes on subsequent slope stability, undertaken in an explicitly multi-hazard framework. The developed model is designed to give a rough spatial and temporal prediction of expected change in landslide hazard in an area following an earthquake. The model is able to describe the reduced impact of earthquakes with distance from the epicenter as well as how the soil looses strength due to shaking and gradually regains it with time. These reductions are then applied to an equilibrium stability analysis in order to compute new factors of safety on stability. The model is demonstrated by using a virtual region, and while further work is required to calibrate and validate the model with respect to real situations, it provides a mechanism whereby prospective outcomes from future hazards can be investigated in a conceptual manner.

Cohen-Waeber et al. presents data from a project combining GPS and InSAR time series analyses for the detailed characterization of spatial and temporal landslide deformation as a result of static and dynamic forces. A review of three independent InSAR time series analyses of the Berkeley Hills from 1992-2011 shows remarkable consistency. They reveal accelerated landslide surface deformation as a consequence of precipitation, though not in relation to seismic activity. Further, after a mild wet season in early 2012, the GPS instrumentation of several landslides in the Berkeley Hills has recorded well-defined precipitation triggered slope movement. In contrast, the occurrence of a nearby Mw = 4 earthquake did not appear to

have produced a measurable effect (Figure 9). Both InSAR and GPS studies confirm strong correlation and sensitivity to periods of precipitation, and downslope sliding velocities of around 30 mm/year. These observations, taken over longer time periods will enable important insight on the triggering mechanisms and internal landslide behavior of this area.
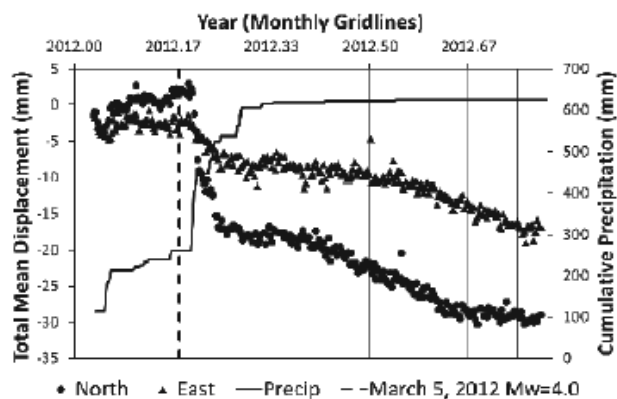

Figure 9. Cohen-Waeber et al. North (circles) and east (triangles) components of relative displacement with respect to reference site P224 shown together with cumulative precipitation (solid line) and time of Mw = 4 earthquake (dashed line).

6 PROGRESSIVE FAILURE OF SLOPES

Two contrasting papers on progressive failure are included – the first presents retrogressive failures in tuff over an existing landslide area, and the second investigates the strain softening behavior of sensitive clays leading to river bank erosion.

Şengör et al. present a paper on a landslide that occurred during foundation excavation of an industrial plant in Turkey. The instability occurred in a natural slope with a slope angle of 9°-13°. The sliding mass grew progressively backward into the slope as multistage rupture surfaces from the toe of the landslide developed. Back-analyses and laboratory tests were performed for the determination of shear strength parameters at the sliding surface. Mitigation measures included: two rows of stabilizing piles which were analyzed by FE independently for geotechnical and structural performance, permanent ground anchors, and surface drainage. The deformations of the system were measured by 12 inclinometers (8 in the soil, 4 in the piles) at each stage of the construction works and there have been no displacements in three years since completion.

Dey et al. present a study on upward progressive failure due to river bank erosion in sensitive Canadian clay which is numerically modeled using nonlinear post-peak strain softening behavior. Three cases are analyzed. In Case-I, the ground surface is horizontal and there is a 15m thick layer of sensitive clay below a 5m crust. The Case-II is same as Case-I but the ground surface is inclined upward at 4°. In Case-III only a 1.0 m thick sensitive clay layer parallel to the horizontal ground surface from the toe of the slope is assumed, with the crust same as for Case I.. In Cases I and II global failure was found to occur. However, for Case-III, although global failure did not occur, the shear band propagation reduced the shear strength in the potential failure plane significantly over a large distance and the slope might be marginally stable for further loading. Hence it is shown that the pattern of propagation of shear band varies with soil type and slope geometry.

7 UNCLASSIFIED

This last group of papers includes some highly theoretical contributions and some highly pragmatic ones – both ends of which help to advance the state of knowledge or practice within the profession.

Saha develops a global population-based search procedure (APMA) and applies this to a classic slope-stability problem as originally defined by Spencer (1967). It does not require problem-specific knowledge in searching the critical slip-surface of a soil slope but rather is a heuristic technique based on the 'generate-and-test' strategy. The results show that a lower factor of safety may be obtained with this technique than is found by Methods-of-Slices that are commonly used.

Bogomolov et al. suggest a method for calculating the stability of a loaded slope, based on the combined use of the finite element method, complex function theory and the principle of virtual displacements, as formalized in a computer program by the authors. The method ensures that a minimal condition of the factor of safety K value at each point is obtained without simplifying assumptions.

Nonoyama et al. apply the SPH (Smoothed Particle Hydrodynamics) method to a series of slope stability problems. This numerical method, in which continuum-based constitutive relations are input, can handle large deformation problems because it is based on a free mesh system. This means it has the potential to describe the deformation of geomaterials from the initial state to subsequent large deformation and can be used to estimate deformation and failure conditions simultaneously. Using two example constitutive models, the authors present analysis of both simple slopes and those with countermeasures (piles) included and compare results to those obtained by the Fellenius method.

In their extremely practical contribution, *Yeh et al.* introduce the currently most adopted ground anchoring inspection system used in Taiwan for anchoring slopes. The paper also proposes a new method of ground anchoring assessment, in order to establish a standardized quantitative analysis procedure for professional reference. They find that four categories of assessment should be made: inspecting the exterior of the anchor, the anchor head, an endoscopy inspection and conducting lift-off tests. They also examine the most common shortcomings of anchor installation and suggest remedies.

Bozo and Allkja present a study on the cuttings constructed for the Vlora road in Albania. A description of the geological setting of the site and of the rock and soil profiles is provided. Using in situ and laboratory tests they have determined the type of cuts and their geometrical forms in a manner designed to protect both the environment and the stability of slopes. Correlations between in situ test results and soil types are given as well as classification data and strength data for the soils encountered. They have also carried out some classifications of cuts for the road taking into account the conditions of the terrain.

The paper by *Lo and Lam* highlights some key lessons learnt and observations made from selected landslide investigations by the Geotechnical Engineering Office (GEO) of the of the Civil Engineering and Development Department (CEDD) of Hong Kong. On average, about 300 landslides are reported to GEO in Hong Kong each year. The paper discusses the use of robust stabilization measures for cut slopes, improved rock slope engineering practices, enhanced practices in the monitoring and maintenance of water-carrying services affecting slopes and improvement to drainage detailing.

Du et al. propose a quantitative model for estimating the vulnerability of elements at risk from impact by a slope failure, where vulnerability is defined as a function of landslide intensity and of susceptibility of the element. A conceptual framework is described for the model, and commentary provided on parametric inputs to it, together with suggested values for those parameters. The authors acknowledge the limitations of the model in its current form, which arise from a need to calibrate some of the input parameters.

Lacasse et al. summarize the findings of a European Commission project, SafeLand and its related 'toolbox' that is web-based, which includes nearly 75 mitigation measures for different types of landslide. Features of the toolbox are

described, which extend to estimates of cost-benefit factors and likely effectiveness, all of which are predicated on a ranking of the most appropriate mitigation measures. In this regard, the toolbox takes the form of a decision-support tool.

8 SUMMARY REMARKS

In engineering, like many other subjects of professional practice, it is important that the state-of-the-art continue to inform the state-of-the-practice. In reality, the state-of-the-practice involves risk management, whether it is done implicitly or explicitly. It is by developing new knowledge, else refining existing knowledge, that the findings of research enable improved decision-making in the face of risk and uncertainty. A total of 37 papers were submitted to the conference on the topic of slope stability in engineering practice.

Although they are broad-ranging in subject matter, they are unified by a common thematic objective of better understanding the spatial and temporal variation of demand and capacity at the point of slope instability, together with the magnitude and likely run-out or travel distance of the ensuing event. In many respects the findings of these studies are a timely reminder of the observations of Karl Terzaghi that "In soil mechanics the accuracy of computed results never exceeds that of a crude estimate, and the principal function of theory consists in teaching us what and how to observe in the field" (Goodman, 1999).

9 REFERENCES (TNR 8)

Chau K.T. 2005. General Report for Technical Session 4a: Slope stability and landslides. *Proceedings of 16th International Conference on Soil Mechanics and Geotechnical Engineering*, Osaka, Japan.

Fannin R.J. and Bowman E.T. 2010. Debris flows—entrainment, deposition and travel distance. *Proceedings of 11th IAEG Congress: Geologically Active*, 5-8 Sept 2010, Auckland, New Zealand

Goodman, R.E. (1999). Karl Terzaghi: the engineer as artist. ASCE Press, Reston, VA, USA, 340p.

Lin C.W., Shieh C. L., Yuan B. D., Shieh Y. C., Liu S. H. and Lee S. Y. 2004. Impact of Chi-Chi earthquake on the occurrence of landslides and debris flows: example from the Chenyulan River watershed, Nantou, Taiwan. *Engineering Geology*, 71, 49-61

Petley D. 2012. Landslides and engineered slopes: Protecting society through improved understanding. *Proceedings of 11th International & 2nd North American Symposium on Landslides*, 3-8 June 2012, Banff, Canada.

Rose N.D and Hungr O. 2007. Forecasting potential rock slope failure in open pit mines using the inverse-velocity method. *International Journal of Rock Mechanics & Mining Sciences*, Vol. 44, 308-320.

Tatarniuk, C.M. and Bowman, E.T. (2012) Case Study of a Road Embankment Failure Mitigated Using Deep Soil Mixing. *4th International Conference on Grouting and Deep Mixing (ICOG)*, 16-18 Feb 2012.New Orleans, LA, USA:

10 PAPERS IN THE TECHNICAL SESSION

.Bogomolov A.N., Ushakov A.N. and Bogomolova O.A. Calculation of slopes stability based on the energy approach.

Bozo L. and Allkja S. Preservation of slope stability along the bypass Vlora.

Buscarnera G. and Whittle A.J. Model prediction of flow slide triggering in shallow sandy slopes.

Cepeda J., Quan Luna B. and Nadim F. Assessment of landslide run-out by Monte Carlo simulations.

Chang M. and Huang R. The challenge of the slope failure problem and its remedial considerations at Mileage 39Km, Mt. Ali Road, Taiwan.

Choi C.E., Ng C.W.W., Kwan J.S.H., Shiu H.Y.K., Ho K.K.S. and Koo R.C.H. Downstream frontal velocity reduction resulting from baffles.

Cohen-Waeber J., Sitar N. and Bürgmann R. GPS instrumentation and remote sensing study of slow moving landslides in the eastern San Francisco Bay hills, California, USA.

Coutinho R.Q. and da Silva M.M. Geotechnical characterization, stability analysis, and the stabilization process for a landslide in a area of Barreiras Formation and granite residual soils, Pernambuco.

Dey R., Hawlader B., Philips R. and Soga K. Progressive Failure of Slopes with Sensitive Clay Layers.

Du Y, Yin K., Nadim F. and Lacasse S. Quantitative vulnerability estimation for landslides.

Harris S., Orense R. and Itoh K. A site specific early warning system for rainfall induced landslides.

Jeng C.J. and Sue D.Z. Characteristics of ground motion on colluviums slope induced by natural disasters.

Katzenbach R. and Bergmann C. Investigation on mass flow of saturated soil by large scale experiments.

Kavvadas M., Agioutantis Z., Schilizzi P. and Steiakakis C. Stability of open-pit lignite mines in Northern Greece.

Lacasse S., Kalsnes B., Vaciago G., Choi Y.G. and Lam A. A web-based tool for ranking landslide mitigation measures.

Law R.P.H., Lam A.Y.T. and Choi K.Y. A numerical study of granular surge flow through a row of baffles.

Li A.G., Qiu, J.J., Mo J.F., Gao W., Tham L.G. and Yan R.W.M. Full-scale field monitoring of a rainfall-induced sliding slope in Hainan, China.

Lin M.L. and Lin Y.S. Estimation and prediction of debris flow potential using discrimination analysis.

Lo D.O.K. and Lam H.W.K. Value of landslide investigation to geotechnical engineering practice in Hong Kong.

Long X. and Tjok K-M. Analyses of seismic slope stability and subsequent debris flow modeling.

Nadim F. and Liu Z.Q. Quantitative risk assessment for earthquake-triggered landslides using Bayesian network.

Nakata Y., Kajiwara T. and Yoshimoto N. Collapse behavior of slope due to change in pore water pressure.

Nonoyama H., Yashima A. and Moriguchi S. Future evolution of slope stability analysis created by SPH method.

Paçi E., Cullufi H. and Dervishaj A. Slope stability along a new road "Drisht-Drisht castle".

Quan Luna B., Vangelsten B.V., Liu Z.Q., Eidsvig U. and Nadim F. Landslides induced by the interaction of an earthquake and subsequent rainfall. A spatial and temporal model.

Rahhal M.E., Hajal M., Seoud J.P. and Rafie E. Analyse des glissements de terrains en région urbanisée.

Saha A. A smart adaptive multivariable search algorithm applied to slope stability in locating the global optima.

Şengör M.Y., Ergun M.U. and Huvaj N. Landslide stabilization by piles: A case history.

Son N.T., Ha P.T.S. and Son L.M. Landslide susceptibility mapping using Bayesian conditional probability model at An Linh Commune, Tuy An District, Phu Yen Province, Vietnam.

Strenk P.M. and Wartman J. Influence of ground motion variability on seismic displacement uncertainty.

Thakur V., Degago S.A., Oset F., Dolva B.K. and Aabøe R. A new approach to assess the potential for flow slide in sensitive clays.

Tremblay M., Svahn V. and Lundström K. Landslide risk assessment in the Göta river valley: effect of climate changes.

Uchimura T., Gizachew G., Wang L., Nishi S. and Seko, I.Deformation and water seepage observed in a natural slope during failure process by artificial heavy rainfall.

Wang L., Nishie S., Seko I. and Uchimura, T. Study on field detection and monitoring of slope instability by measuring tilting motion on the slope surface.

Winter M.G., Smith J.T., Fotopoulou S. & Pitilakis K., Mavrouli O. and Corominas J. The physical vulnerability of roads to debris flow.

Yeh H-S., Wang C-S., Wei C-Y., Lee S-M., Ho T-Y., Hsiao C-A. and Tsai L-S. Inspection and capacity assessment of anchored slopes.

Yune C-Y., Kim G., Lee S.W. and Paik J. 2011 Seoul debris flow and risk analysis.

Calculation of slopes stability based on the energy approach

Calcul de la stabilité des pentes sur la base de l'approche énergétique

Bogomolov A.N., Ushakov A.N., Bogomolova O.A.
Volgograd State University of Architecture and Civil Engineering, Volgograd, Russia

ABSTRACT: For quantitative evaluation of slope's stability value safety factor coefficient K is used, defined by various known methods. However, the results ensued in this way for identical objects may substantially differ. The reason for this are numerous assumptions and simplifications adopted in the calculations. Approach based on the analysis of the stress fields and displacement of soil mass points and principle of virtual displacements allows to get adequate results while solving the corresponding task. The used method of sliding surface constructing ensures realization of minimal condition of K value at each point. Analysis of the stress-strain state of homogeneous and heterogeneous slopes is accomplished by using finite element method (FEM), and the boundary conditions imposed on the design scheme FEM are processed based on the analytical solutions of the first basic boundary value problem of elasticity theory for homogeneous weight simply connected domain, get by the authors.

RÉSUMÉ : Pour l'évaluation quantitative de la stabilité des pentes on utilise la valeur du facteur de sécurité K, définie par diverses méthodes connues. Cependant, les résultats obtenus de cette manière pour des objets identiques peuvent différer substantiellement. Les raisons de cette situation sont de nombreuses hypothèses et simplifications adoptées dans les calculs. Obtenir des résultats satisfaisants lors de la résolution du problème correspondant devient possible grace à l'aproche basée sur l'analyse des champs de tensions et de déplacements des points du massif de sol et aussi sur le principe des déplacements virtuels. La méthode utilisée de la construction de la surface de glissement assure l'accomplissement d'une condition de minimalité pour la valeur K dans chaque son point. L'analyse de l'état précontraint et déformé des pentes homogènes et hétérogènes est realisée en utilisant la méthode des éléments finis (FEM), tandis que les conditions aux limites, imposées au schema de calcul FEM, sont traitées sur la base des solutions analytiques du premier problème aux limites faisant partie de la théorie de l'élasticité pour une domaine homogène simplement connexe, obtenues par les auteurs.

KEYWORDS: slope, safety factor, stresses, displacements, work, restraining and moving forces

1. QUESTION STASUS

Principle of virtual displacements - one of the basic principles of mechanics, evaluating general condition of equilibrium of the mechanical system. It is widely used in static studies of material systems, with the effect imposed on the system connections, considered by adding appropriate reactions. This principle has been used previously in the stability of slopes calculation (Goldstein 1969, Dorfman 1975, Magdeev 1973, etc.), however, movements of the points lied on the most probable slip surface, are not appointed on the basis of the stress-strain state analysis of near the slope area and arbitrarily vary in magnitude until the condition K=Kmin is achieved.

In addition the following quite not correct assumptions can be provided:

– sliding prism splits into separate blocks, the interaction force and the friction between them is rarely taken into account; orientation of this forces and the position of the points of their application does not settle, and set arbitrarily to make a statically indeterminate task about equilibrium of blocks, statically determinate;

– the form and position of the fracture surface are taken in advance, in the process of problem solving their direct link with physical and mechanical properties of soils, slope geometry, surface loads is not established;

– almost always only one (and approximately in the form of bay weight) vertical σz component of the stress at near the slope area is taken into account;

– semi-infinite slope is considered (the fact of stress concentration in the transition region of the slope into the base is left out of the account); well-known calculation methods

doesn't allow to take into account mutual influence of embankment's slopes and excavations on their stability, as in the design scheme base of the slope is not considered, and the daily surface of the slope is infinite, etc. and so on;

– in stability calculation such important value as the coefficient of lateral earth pressure ξo is not considered and etc.

All this makes it necessary to look for new solutions of the slope's stability problem, in particular, based on the analysis of the stress-strain state.

Known method (Potapova 2001), when the value of K is defined as algebraic sum of work of restraining and shearing forces acting at the points of most likely slip line

$$K = \frac{\Sigma A_{i\,y\partial}}{\Sigma A_{i\,c\partial}} = \frac{\Sigma(F_{i\,y\partial}\delta_i \cos\alpha_{i\,y\partial})}{\Sigma(F_{i\,c\partial}\delta_i \cos\alpha_{i\,c\partial})}, \tag{1}$$

where $F_{i\,y\partial}$; $F_{i\,c\partial}$ - restraining and shearing forces agreeably;

δ_i - complete movement; $\alpha_{i\,y\partial}$; $\alpha_{i\,c\partial}$ - angles between positive directions of the restraining and shearing forces and direction of the total displacement vector, respectively, in the i-th point of the sliding surface. Equation (1), in our opinion, is not quite correct, because in this equation full displacements of the points made of movements of the external load and dead weight of the soil are taken into account. Movements from dead weight of soil are formed during all period of the soil mass existence, and therefore their true values cannot be reliably

determined using the theory of elasticity, which may affect the validity of the getting result. Ignoring of this fact can lead to getting while calculation overstated or, conversely, understated safety factors that may result in additional costs of material resources, or emergency initiation.

2. PROPOSED APPROACH

The following algorithm for calculating the value of the slope safety factor K of loaded soil slope, based on the joint application of the finite element method (FEM) and methods of complex function theory (Kolosov 1934, Muskhelishvili, 1966):

a) design scheme of FEM is made up provided with maximum possible degree of homogeneity of the finite element mesh observance, which provides the minimum width of the stiffness matrix of the system;

b) based on an analytical solution of the first fundamental boundary value problem of elasticity theory for a homogeneous isotropic half-plane with a curvilinear boundary (Bogomolov 1996) data handling of boundary conditions applied to uniform FEM scheme so that the stress values $\sigma_x; \sigma_z; \tau_{zx}$ at the corresponding points of the investigating region, found by FEM and analytical solution, coincided with the maximum degree of accuracy;

c) in the case of heterogeneous geological structure of the slope, therein geological elements endowing with corresponding physical and mechanical properties (solid weight γ, specific cohesion C; angle of internal friction φ, coefficient of elasticity E; coefficient of lateral pressure ξ_o (Poisson's ratio μ)) are extracted;

d) to the study area n external loads are applied, which according to all parameters coincide with loads specified in problem specification, but the values of their intensities qn→0. If in the near the slope area plastic deformation regions are absent, the construction of most likely slip surface is performed by the method (Tsvetkov 1979), ensuring fulfillment of the condition of minimum value of K at each point. At the same time the safety factor value K_i in the i-th point of the soil mass is determined by the following expression

$$K_i = \frac{[0,5(\sigma_{iz} - \sigma_{ix})\cos 2\alpha_i + 0,5(\sigma_{ix} - \sigma_{iz})]tg\varphi}{0,5(\sigma_{ix} - \sigma_{iz})\sin \alpha_i + \tau_{ixz}\cos 2\alpha_i} + \rightarrow$$
$$\rightarrow + \frac{[\tau_{ixz}\sin 2\alpha_i + 2\sigma_{cB}]tg\varphi}{0,5(\sigma_{ix} - \sigma_{iz})\sin \alpha_i + \tau_{ixz}\cos 2\alpha_i} \quad (2)$$

where: $\sigma_{cB}=C/tg\varphi$ - cohesion pressure, numerator and denominator of the formula (2) determine, respectively, the numerical values of restraining $F_{y\partial i}$ and shearing $F_{c\partial i}$ forces acting in the i-th point of the slip surface along the most likely site of shift. Analysis of formula (2) shows that the value of K_i depends on the components of the stress and angle α_i most likely site shift at each point of sliding surface, as well as physical properties of soil.

The value of α_i is defined by formulas (4), which arise from the boundary condition (3)

$$\left.\begin{array}{l} \frac{\partial K}{\partial \alpha}=0; \\ \frac{\partial^2 K}{\partial \alpha^2}>0. \end{array}\right\} \quad (3)$$

$$\sin 2\alpha_i = 2N\tau_{ixy} + (\sigma_{iy} - \sigma_{ix})\sqrt{\frac{1}{L} - N^2} \quad (4)$$

where:

$$L = (\sigma_{ix} - \sigma_{iy})^2 + 4\tau_{ixy}^2; \quad N = (\sigma_{iy} + \sigma_{ix} + 2\sigma_{cB})^{-1}$$

If the plastic deformation regions have been developed, but their sizes are small, then the construction of the most probable slip surface is carried out by a method built on the basis of approximate solutions of the mixed problem of elasticity theory and plasticity theory of soil (Bogomolov 1996). In this case, the stress at the plastic region (marked by a prime) are given by

$$\left.\begin{array}{l} \sigma'_{iz} = \sigma_{iz}; \\[4pt] \sigma'_{ix} = \frac{\sigma_{iz}(l - \sin\varphi) - 2\sigma_{cB}\sin\varphi}{l + \sin\varphi}; \\[4pt] \tau'_{ixz} = \frac{(\sigma_{iz} + \sigma_{cB})b\sin\varphi}{l + \sin\varphi}, \end{array}\right\} \quad (5)$$

where $b = tg2\alpha_i^*; l = (1 + b^2)^{0,5}; \alpha_i^* = \alpha_i - (\pi/4 + \varphi/2)$.

The value of the safety factor coefficient K_i' at the point of the slope, which is in the plastic area (obviously $K_i' = 1$) is given by

$$K_i' = \frac{(\sigma_{iz} + \sigma_{cB})\sin\varphi(\cos 2\alpha_i^* + b\sin 2\alpha_i^*) + \sigma_{iz}l + \sigma_{cB}b}{(\sigma_{iz} + \sigma_{c\varepsilon})(b\cos 2\alpha_i^* - 2)\cos\varphi} .(6)$$

The numerator and denominator of formula (6) determine values of appropriate restraining and shearing forces. In m points of sliding surface with the help of FEM total displacements from the gravity forces and the external load are calculated. Note that construction of the most probable slip surface is carried out with such a step, that the difference between the horizontal coordinates of neighboring points on it is $x_{k+1} - x_k = ...x_{m+1} - x_m = 0,01H$ (where H - the height of the slope).

e) the value of the intensity of the external load is increased to the calculated value. Once again we construct the most probable slip surface and the calculation of the total displacements in its m points.

f) the principle of virtual displacements is used, at the same time the role of the possible movements is carried out by *differences* of movements in corresponding m points of the sliding surface, obtained under the use of two previous steps of the algorithm. The role of active forces is played by restraining and shearing forces acting at the same m points of slip surface. The formula for calculating the safety factor value of the slope, provided that the plastic deformation is absent, has the form

$$K = \frac{\Sigma A_{iy\partial}}{\Sigma A_{ic\partial}} = \frac{\Sigma(F_{iy\partial}(\Delta_i - \delta_i)\cos\alpha_{iy\partial})}{\Sigma(F_{ic\partial}(\Delta_i - \delta_i)\cos\alpha_{ic\partial})}, \quad (7)$$

where: δ_i and Δ_i - respectively the total displacement of *i*-th point of the most probable slip surface, calculated from the action of its own weight of soil, provided that $q_n \rightarrow 0$, and taking into account dead weight of soil, provided that the value of the intensity of the external loads are equal to calculated values, i.e. $q_n = q_p$.

The value of the safety factor coefficient of the slope in the case of plastic regions in the near the slope area is determined by the formula

$$K = \frac{S'_{y\partial} + S_{y\partial}}{S'_{c\partial} + S_{c\partial}} \qquad (8)$$

where: $S'_{y\partial}$ and $S'_{c\partial}$ – squares of restraining and shearing force's diagrams, built along a section of the most probable slip surface that is in the region of plastic deformation, $S_{y\partial}$ and $S_{c\partial}$ - squares of restraining and shearing force's diagrams, built for the area most likely slip surface, which is outside the boundaries of the plastic deformation regions. In that way, if in a soil mass there are no plastic deformation regions or their sizes are small, then the proposed procedure excludes from examination of displacement from dead weight of the soil, which, as noted above, it is impossible to determine exactly what increases the reliability of the getting results.

3. PROCEDURE FORMALIZATION

Described above procedure is formalized in a computer program (Bogomolov and others, 2010), which allows to calculate stability of homogeneous slopes and slopes of complex geological structure with any configuration of the outer boundary. At the same time all strength and deformation characteristics of the soil are taken into account, to the surface of the slope can be applied almost any number of point and distributed loads of any orientation, length and intensity. It is possible inside the design schemes automatically generate fields of various shapes, endowed with certain properties, including the voids. Figures 1 and 2 show the most probable slip surfaces in the absence of the plastic deformation areas and while their development. Here
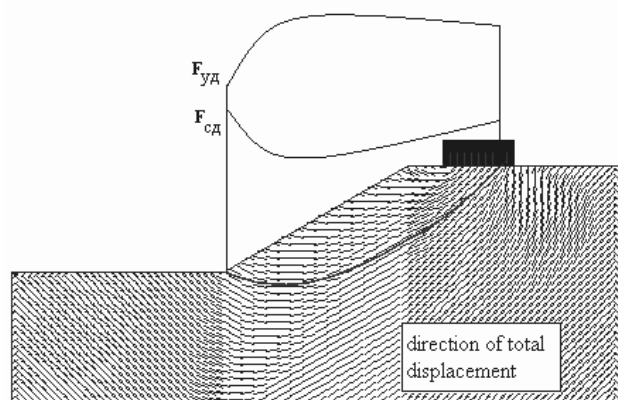

Figure 1. Fragment of a design scheme and work diagrams of restraining and shearing forces (plastic deformation areas are not presented)
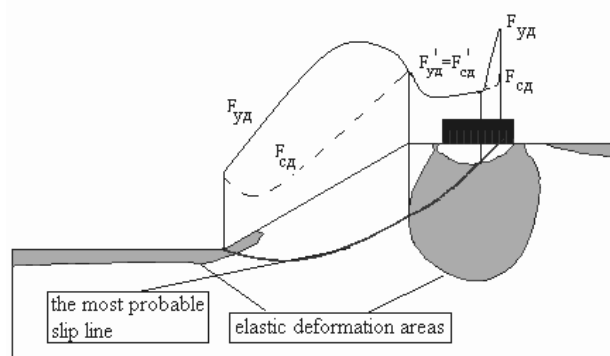

Figure 2. Work diagrams of restraining and shearing forces provided formation of plastic deformation areas

built in the computer program shell developed by the authors work diagrams of restraining and shearing forces acting at the points of the sliding surfaces are showed. Areas of diagrams are calculated automatically and are used in calculations of the safety factor value (see equation (8)).

Note one more circumstance. If the slope is uniform, then safety factor value calculated by the proposed method is independent from the value of deformation modulus of soil E_o, as in this case, displacements linearly depend on the numerical value. If the slope is not uniform, then the stresses at the points of soil mass will depend on size of the deformation modules and coefficient of lateral earth pressure of the nearby geological engineering elements. Consequently, the safety factor value will also be a function of these variables. This fact cannot be accounted by any of these methods, during the implementation of which analysis of the stress-strain state of the soil mass is not conducted.

4. COMPARISON OF NUMERICAL RESULTS WITH EXPERIMENTAL DATA AND FIELD OBSERVATIONS

We (Bogomolov & Vereshchagin, 1990) conducted experiments on the destruction of loaded slopes, made on the models from equivalent materials, as a basis for which were used: a) a mixture of river sand (97%) and motor oil (3%) having the following physical properties: $\gamma=1,55$ t/m^3; C=0,49 MPa; $\varphi=24°$; b) gelatinegel XC having the following characteristics: mass concentration of gelatine 30% - $\gamma=1,15$ t/m^3; C=72 MPa; $\varphi=25,5°$, and at 15% - $\gamma=1,078$ t/m^3; C=34,8 MPa; $\varphi=13,5°$. Value ξ_o for sand-oil mixture is set by pulling steel strips in a tray filled with the material which is under study (Terzaghi 1961), equal $\xi_o=0,75$.

Models from sand and oil mixture have height $H=0,3$ m, width $L=0,6$ m, $\beta=75°$. They were loaded with uniformly distributed load over the stamp which has the following dimensions in plan $0,6\times0,5$ m, consistently placed at a distance $b=0;0,25H;0,5H$ from the edge of the escarpment. When $b=0$ the average value (based on 10 experiments) of the intensity of the breaking load $q_p=1,84$ *kPa*, when $b=0,25H$ - $q_p=0,78$ *kPa*, and when $b=0,5H$ - $q_p=1,39$ *kPa*. Calculated safety factor values for each of the three variants were found to be $K_1=1,11$; $K_2=0,99$; $K_3=1,02$. Evidently these values differs from limit value K=1 for no more than 11%.

Models from gelatingel *XC* formed in dismountable container made of organic glass, in the same forms loading of models up to failure was conducted, and at this moment loading size was fixed. Safety factor values, calculated on the basis of our proposals for the moment of destruction, were found to be $K_{30\%}=1,08$ and $K_{15\%}=1,1$, i.e. differ from the limiting value of $K=1$, on 8% and 10%.

Figure 3 show the most probable surface of failure obtained theoretically (1 and 2) and in experiments (1 'and 2'), which are almost identical to the corresponding models.
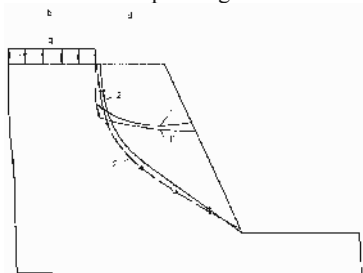

Figure 3. Theoretical and experimental slip lines in model made of equivalent materials

A case (Mochak 1964) of landslides formation in the quarry in Tsinzendorf (Germany) in the excavator ledge with the angle β=36° was described. Soils - ribbon clay with the following content 42,9-58,5 of silt and 30,6-43,5% of clay, consistency – flexibly soft, with φ=21°, C=17,2 kPa. The intensity of the load created by the excavator, which was at the edge of the slope (d=0), q=4,4 kPa, its width b=7 m.

Author (Mochak 1964) calculated the slope stability by the method of K. Tercagi, resulting in safety factor value determined to be KT=1,19. The calculation by the proposed method results in K=0,97, which is only 3% different from the limit.

5   CONCLUSIONS

Method for calculating of loaded slope's stability, based on the combined use of the finite element method, complex function theory and the principle of virtual displacements, which is formalized in a computer program was suggested. The results of calculations with the help of the program that was announced with sufficient accuracy for engineering practice with the experimental data and behavior of landslide danger objects specifically.

6   REFERENCES

Goldstein M.N. 1969. About calculus of variations application to the stability of foundations and slopes. Bases, foundations and soil mechanics 1, 2-6.

Dorfman A.G. 1977. The exact analytical solution of new problems in the stability of slopes theory. Geotechnical issues. 26, 53-57.

Magdeev U.H 1972. Investigation of slopes stability by variational method in conditions of the spatial task. Geotechnics questions, 20, 120-129.

Potapova, N.N. 2001. Evaluation of slopes stability and soil bearing capacity of foundations on the basis of distribution of stresses and displacements analysis. Dissertation, 205.

Kolosov G.V. 1934. Application of complex diagrams and complex function theory to the elasticity theory. Scientific and technical information department, Moscow.

Muskhelishvili N.I. 1966. Some basic problems of the mathematical elasticity theory. Science, Moscow.

Bogomolov A.N. 1996. Calculation of carrying capacity of the facility foundations and stability of soil masses in elastoplastic formulation. Perm State Technical University, Perm.

Cvetkov V.K. 1979. Calculation of slopes and scarps stability. Lower Volga Book Publishers, Volgograd.

Bogomolov A.N., Bogomolova O.A., Redin A.V., Nestratov M. Ju., Potapova N.N., Stepanov M.M., Ushakov A.N. Stability. Stress-strain state. Certificate of state registration of computer programs № 2009613499 from 30.06.2009.

Bogomolov A.N. & Vereshchagin V.P. 1990. Modelling of the loaded slopes destruction. Foundations in the geological conditions of Urals. PPI, Perm, 112-114.

Tercagi K. 1961. Theory of soil mechanics. Gosstroyizdat, Moscow, 507.

Mochak G. 1964. Landslides as a result of the existing sliding surfaces and contact layers in glacial deposits. Meeting materials of studying landslides and strife with them measures. Kiev, 53-57.

Preservation of slope stability along the by-pass Vlora

Maintien de la stabilité des pentes dans le contournement de « vlora »

Bozo L.
POLIS University

Allkja S.
ALTEA& GEOSTODIO 2000 Shpk

ABSTRACT:The development of the tourism in Albania is a very profitable branch of the economy. For this reason we have request to construct much new roads. One of them is the road to Jonian sea side which is with rarely beautiful nature. In this zone has constructed much restaurants, hotels, touristic resorts, but the access to them is difficult because the low quality of the existing roads. In these conditions is decided construction of the by-pass Vlora, and we have accomplished the geological and geotechnical study along the track of the new road. By this study we have in evidence : a) all dangerous phenomena's which can appear during the construction of the road, b) the sites where the road will passes by viaducts and bridges, c) the zones where the road will passes by cuts, d) the zones where the road will passes by embankments. In this paper we would like to present our study about the road's section which passes by cuts in hills terrain. By in situ tests and laboratory tests we have determined the kind of cuts, their geometrical forms in manner to protect environment and stability of slopes. Also we have take some classifications of cuts in this road regarding real conditions of the terrain.

RESUME: Le tourisme en Albanie est l'une des activités les plus profitable pour l'économie du pays. Afin d'en accélérer le développement, le pays à souhaiter construire un grand nombre de nouvelles routes. L'une d'entre elle est la route qui conduit au littoral de Jonian, site naturel d'une grande beauté. Dans cette zone ont été construits beaucoup d'hôtels, de restaurants et des stations touristiques. Malheureusement, l'accès au site de Jonian est difficile à cause des routes de qualité médiocres. Aussi, a été décidé la construction du coutournement de "Vlora" et à cette occasion, de nombreuses études géologique et géotechnique ont été effectué. Grace à ces études in-situ, nous avons pu a) détecter les phénomènes dangereux qui sont susceptibles d'apparaitre pendant de la construction de la route, b) identifier les sites où la construction de la route Allait induire la construction de viaducs et de ponts, c) les zones des excavations seraient nécessaires, d) les zones où des remblais devraient être édifier. Dans cet article, nous souhaitons présenter notre étude sur la portion de route pour laquelle des excavations ont été réalisées. Par le biais d'essais in-situ et d'essais de laboratoire, nous avons pu dimensionner les excavations à effectuer en tenant compte de la problématique de la stabilité des talus.

KEYWORDS: cutting, slope, stability, geological study, geotechnical study, environment, classification.

1. INTRODUCTION

The new road "By-pass Vlora" passes in the hill's and mountain's zones, which intersects several small streams and rivers. In the 29 km of their length 80% of the road passes in cutting and 20% in embankment. The hills of east part of the city Vlora are longitudinal of the direction of the Vlora By-pass. These hills are built from sedimentary rocks and they form steep rocky slopes. The soft slopes of these hills are transformed into agricultural lands, while the deep slopes are covertures with small trees. The intention of the study is the determination of the physical and mechanical properties of the soils and rocks encountered in the area where will passes the new road. The data taken from field and laboratory works will be useful to made the detailed road project for embankments, cutting, new bridges, or viaducts etc. Also from geological and geotechnical study can judge for the dangerous phenomena's which can appear during the construction and exploitation of road and for the selection of the construction material. These properties are determined by specimens from bore-holes, trial pits, refraction seismic tests, field tests, and laboratory tests. We wont to present in our study the following problems:
The evidence of the dangerous phenomena's for the road and environment.
Determination of the physical and mechanical properties of the soils and rocks in this zone.

The evidence of the zones where the road passes in cutting and their calculation.
Classification of the different cutting's types.
Engineering measures for the protection of the equilibrium of the slopes and environment in the zone of the new road.

2. PHYSICALGEOLOGICALAND GEODYNAMICAL PHENOMENA'S

By Albanian geological map, existing investigations and new information from our study, in the zone where will passes the new road, we have evidenced or observed the following geological phenomena's:[1]

2.1. *Erosion Phenomenon*

This phenomenon is visible in all hilly part of the road's axis. The heavy rainfall, the current of the surface water, the inclination of the slopes, the type of the soils and weathered part of core formation are causes of this phenomenon. The body of road is at the middle part of the valley and it is exposed to this phenomenon and negative action of the erosion. For this we recommended not only remove the water by means of ditches, but during excavation, the road must protected in the upper and bottom part, to not allow erode of the slope's material, small surface slides and detaching of the mass rock.

2.2. Weathering Phenomenon

This phenomenon is visible at the rock formation that are composed by sedimentary rocks(mudstone, sandstone, conglomerates), which are new deposits with weak clay cementation. Under the action of the atmospheric agents they are transformed from weak rock to soils. When the road passes in cutting in the zone with clay rocks we will be attention and we will take the engineering measures to protect the stability of the environment.

2.3. The movement and sliding of the weathered mass rocks

From the beginning of the new road we have identified some zones with limited area landslide. The kind of the instability are:
Slide of the colluviums
Slide of the upper part of the weathered rocks
 Rock landslides
Debris flow
We thing that , the design of this road to show maximal care for the stability of the slopes during and after the construction of the road and a special attention must to paid for the protection of the foundations of the bridges that are on the slopes prone to slide.

2.4. Activity of the tectonic movements(tectonic faults)

In Albania there are a developed regional tectonics, which is mainly horizontal with a
,low angle over thrust and others secondary tectonic movement.[5] The eastern areas have moved with a low angle over thrust towards west. This phenomenon has caused a total destruction of the rock mass in 7 km length of the road, and it is associated with a lot of other local tectonics. These zones are founded in the contact between different rocks, or inside the same rock. As result of this phenomenon in the hills side many rocky mass have moved toward the relieve fall and have created a rocky bent relieve. We must be very attention to not destruct the existing brittle, or frail equilibrium.
2.5 Seismic Hazard
After Albanian Seismic Code [4] the zone to be studied is classify (by MKS-64) with intensity 8 ball and the soils in the second category [   ]. For calculation of the slope stability, by [2] we can use $a_{max} = 0,2g$, and the deep of epicentrum 25-30 km. For these conditions some of the observed slides can to reactivate caused the destruction of the road.

3. GEOLOGY AND HYDROGEOLOGY

The geological structure of the studied area[1] is composed by sedimentary deposits,   limestone rocks, and granular rocks as below:

3.1 Limestone rock (Pg$_2$, Cr$_2$, Cr$_1$, J$_1$, J$_{2-3}$ up T$_3$).

 They have white to grey color, little cracks, in some part karst phenomenon, very resistible against atmospheric agents, very good characteristics for the foundations of the bridges, stabilized slopes and for the embankment.

3.2 Paleogene's deposits (Pg$_1$, Pg$_3^I$).

 They are flysch deposits, brown to beige color, medium to weak cementation, in superficial part weathered, they form unstable slopes and at Radhima   is very active sliding zone.

3.3. Neogene's deposits (N$_I^{2h}$, N$_I^{2t}$, N$_I^3$).

They are composed by mudstone, sandstone and rare conglomerates, conglobreccias, brown to beige color, good to weak cementation with superficial part weathered. In the mudstone layer and colluviums drposits can observed landslide.

3.4. Quaternary deposits (Q$_4$),

Are alluvial, torrent and colluviums deposits. Alluviums of the Dukati and Shushica rivers are consolidated gravel, sands, silty- sands, silty- clay, with 20-25m thickness. Elluviums or torrent deposits are moderate consolidate silty- clay, silty- sands with 8-15 m thickness. Colluviums are presented by silty- clays and gravely-silty-clays, moderate consolidated, unstable and with 2-4,5m thickness.
The level of the underground water is deep and the water is not aggressive to concrete and steel.

4. FIELD AND LABORATORY INVESTIGATIONS

 For the part of the road that passes in cutting or over embankments, we have made trial pits   which passes by viaducts and bridges, we have made bore-holes until 10-40m depth. At the same time we have realized SPT-tests and laboratory tests in ALTEA laboratory from samples taken by BH. From laboratory test[1] we have determined physical and mechanical properties for the soils, some characteristics for the rocks, and LA, soundnes, Proctor, CBR etc for the disturbed soils and rocks which will be serve as building material for the road and embankment.

4.1. Results of the site investigations.

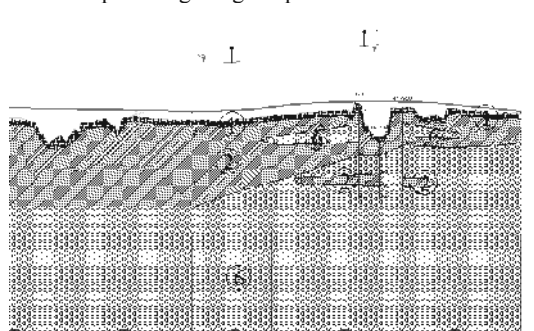From BH we have discover some different layers and we have compile the geotecical profile.

Fig. 1 Geological Profile

4.1.1 *By description of layers and SPT-tests we have evidence six layers (Table 1)*

Table 1. Description of the different layers

Nr.of layer	Description	Thickness(m)	Classification	N$_{SP}$
1	soft brown silty-clay	3-4	CL	9-12
2	medium dense silty-clay-gravel	3,5-4	GC	24-28
3	clayey's elluvium	6-8	ML-CL	60-80
4	sand's elluvium	4-6	SM	50-60
5	gravel and sandy-silty-gravel	7-14	GM	35-50
6	moderately weak mudstone and sandston	7-30	- 80-12	

4.2. Results of laboratory investigations

From laboratory tests we have determined the following parameters :
Grain size distribution

Moisture content   W = (5-29)% mean   15%
Specific gravity γ_0 = (26-27,2) kN/m^3 mean 26,5 kN/m^3
Bulk density γ = (18,8-23) kN/m^3 mean 19,5 KN/m^3
Limits of plasticity (liquid)   LL= (18-50)% (plastic)
PL = (13-28)% mean 34% and 25%
Void ratio   e = 0,355-0,743 mean 0,62
Resistive parameters of soils by direct shear test :
C = 22-25 kPa mean 23 kPa ϕ = 22°-24° mean23^o
Bearing capacity R = 150-300 Kpa   mean 200kpa
Modulus of deformation   E = (0,4-0,7).10^4 kPa mean 0,55.10^4 kPa etc.

4.3. Correlation between different soil parameters.

After elaboration of the results from laboratory tests and in situ tests we have take the following correlations :
Correlation between bearing capacity of each layer "R" and percentage of gravel.
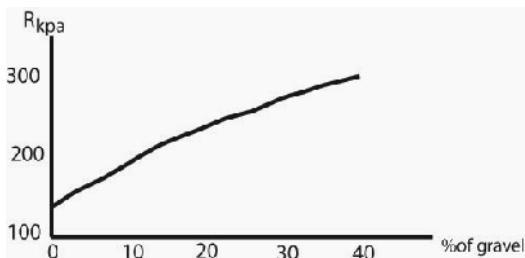
Fig.2 Correlation between R and percentage of gravel

Correlation between bearing capacity "R" and percentage of silty grains
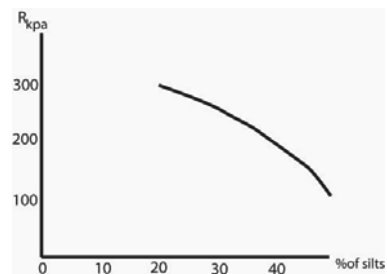
Fig.3 Correlation between R and percentage of silty grains

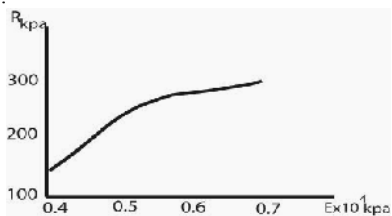Correlation between bearing capacity "R" and modulus of deformation "E"(fig.4)

Fig.4   Correlation between R and E

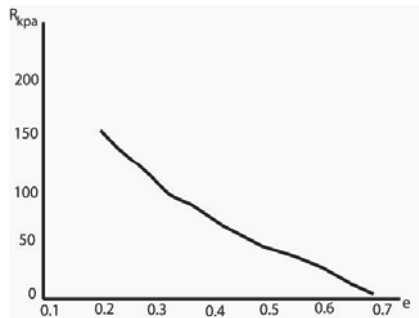Correlation between N_{SPT} and void ratio "e"

Fig.5   Correlation N_{SPT}-e

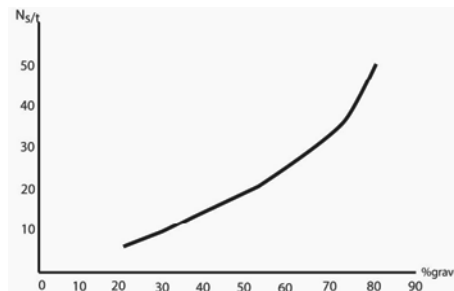Correlation between N_{SPT} and percentage of gravel grains

Fig.6   Correlation N_{SPT} and percentage of gravel grains

By the results of the test in direct shear apparatus we have the following values :
In the upper layers (3-5 m depth), which are "UCS" classification are silty-clay, maximum shear strength is 0,88, that to say the soils are with low sensibility.
The "pic" value and the "residual" value of the resistive parameters of this layer are : ϕ_p = 23°-24° ϕ_{res}= 20°; C_p = 20-25KPa, C_{res} = 10KPa
From static loading test, for the upper layer (3m depth) they are suitable for the construction of the road because they have R>150KPa and E> 40MPa.

5. THE CHOICE OF THE CUTTING'S TYPE

The choice we base in our calculations about the stability of the cohesive slopes that have :
γ = 19-20 KN/m^3, ϕ = 23°-24°,   C = 20-25 KPa. In the zones where are visible slides we have determined the depth of the sliding surface (4-5)m and residual resistive parameters of the soil ϕ = 20°, C = 10 Kpa. For the seismic zone with magnitude M = 5,5, depth of epicentrum of the earthquake   25- 30 km, second category of soils and a_{max} = 0,2g, by [3] we have take the coefficient K_s = 0,07 for the calculation of the supplement earth inertial force. The factor of safety "FS", in general, is FS = 1,5-1,8 but we have the cases when   FS,1,3. The types of cutting choice by us satisfied three conditions:
Preservation of existing equilibrium of natural slopes
Unloading of the part of the slopes when they are in limit state (FS,1,3).
Harmonization of the cuttings with environment to create beautiful landscape.
5.1Classification of the cuttings
For the road with length 29 km, where 80% passes in cutting, by our study we have made some classification:
5.1.1Classification by relief

The hills when passes the new road have the slopes with inclination 10°-35° and more.

Regarding this relief we have use four categories of cuttings

Table 2 Classification by relief

Category	Slope inclination	Nr.of escalations	Schema H_1 H_2
1	(8-14)°	1 and 2	3-8 2-4
2	(15-22)°	2 and 3	8-15 1,5-3
3	(23-30)°	2 and 3 in	8-14 3-14
4	(31-35)°	5 and 6	18-24 10-28

5.1.2 *Classification by geological conditions*

In the unstable slopes we have choice two categories of cuttings:

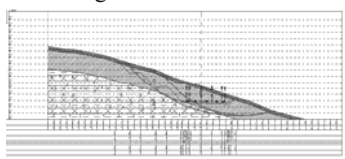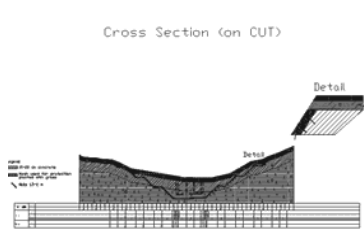Construction of the cuttings by excavation of the part of the sliding mass

Fig7 Cutting by exavation in the sliding mass

Construction of the cuttings based in the stable rock mass and preservation of slopes by nails protection mesh and concrete slab.

5.1.3 *Classification by geotechnical properties of the slope's soils*

Regarding the resistive soils parameters of the slopes and characteristics of the rock mass of the slopes also the inclination and fault direction of the layers in slopes, we have design three categories of slopes (Table 3)

5.1.4. *Classification by geotechnical properties*

Table 3

Geotechnical characteristics)	High(H),width(b),inclination(α
Rock mas $R_c = (50-60)$Mpa	H = (3-6) b = (2-3)m $\alpha = 60^0-65^0$ m=2:1
Medium cemented soils $\phi = 25°$ C = 50KPa	$\alpha = (60-65)°$ m = 2:1 H = (3-5)m b= (2-3)m$\alpha = 45°$ m = 1:1
Silty-clay soils $\phi = (20-23)°$ C = 20KPa	H = (3-5)m b = (2-3)m $\alpha = (33-35)°$ m = 1:1,5

5.1.5. *Classification by dangerous phenomena's.*

Regarding the more dangerous phenomena's which can appear during the construction and exploitation period of the new road, we have made the following classification. In the colluviums zones ,which are in limit state of equilibrium, we can predict the protective geotechnical structures as piles, sheet piles and retaining walls

In more weathering zones we have predict protective geo-synthetic covertures combined with different vegetable

In the rock zones with intensive erosion phenomena's or weathering phenomena's we can use protective metallic mesh combined with metallic construction

6. CONCLUSIONS

For the new road "By-pass Vlora"that passes in cutting we have take the following conclusions:

By geometry we have classify three types of cuttings:

With big cut in left side

With big cut in right side

With two big cuts in both sides

By cutting's height we have three classifications:

Shallow cutting   H = 5m - 6m

Middle cutting   H = 6m – 15m

Deep cutting   H > 15m

By intersect layers the cuttings are classify:

Cutting which intersects 1 layer

Cutting which intersects two or more layers

Regarding the dangerous zones we have classify:

Cutting without the sliding plane

Cutting with presence of the sliding plane

Regarding the base of the road in cutting we have classify:

Cutting based completely in the same layer

Cutting based in two layers

Cutting based in core formation

partially in embankment

Escalations we have made regarding the inclination of the terrain to secure esthetical harmonization with environment, not damage of the environment and security for the road.

In the sliding zones we must undertake (predict) the following engineering measures:

Excavation of the soils over sliding surface to unload the slope

Construction of the retaining walls, anchorage walls etc

Enforcement of the slopes by piles, micro-piles etc

In the zones that have evidence the rolling rock mass must take the following engineering measures:

Horizontal drainage

Enforcement by metallic nyle mesh combined with metallic profiles

Use vegetable revetment

Enforcement by geo-synthetics, concrete revetment etc

7. REFERENCES

Altea & Geostudio 2000 Shpk   2011 Report on the geological and geotechnical conditions of "*Vlora by-pass*" Tirana

Bozo L. *1989 Behaviour of the basements and foundations under seismic action-*

Ph.D. Thesis Tirana

Bozo L. 2004 *Soil Dynamics – Vol. 1,2,3 Press "Natyra" Tirana*

KTP-Antisizmic (Albanian Seismic Code for construction design) 1989 Tirana

Landslide and Geo-environment   2011 Proceedings of the International Symposium Press "Natyra" Tirana

A Methodology for Evaluating Liquefaction Susceptibility in Shallow Sandy Slopes

Une méthodologie pour l'évaluation de susceptibilité à la liquéfaction dans les pentes sableuses

Buscarnera G.
Northwestern University

Whittle A.J.
Massachusetts Institute of Technology

ABSTRACT: The paper illustrates a modeling approach for evaluating the liquefaction susceptibility of shallow sandy slopes. The proposed methodology consists of two main components: (i) a theoretical framework for undrained stability and (ii) the MIT-S1 constitutive model for simulating the response of sands. In the first part of the paper, the use of a stability index able to capture the onset of undrained failure in infinite slopes is illustrated. In the second part, the practical significance of the method is discussed by back-analyzing the series of flow failures in an underwater berm at the Nerlerk site. The reinterpretation of these events in the light of the theory of material stability confirmed that liquefaction was a plausible mechanism for the failures. In addition, the analyses have provided a prediction of the spatial distribution of the unstable masses which is compatible with what was observed through bathimetric surveys conducted after the events. This particular application of the theory supports the idea that realistic constitutive modeling is crucial for achieving consistent predictions of liquefaction potential under field conditions.

RÉSUMÉ: L'article illustre une approche de modélisation pour évaluer la susceptibilité à la liquéfaction des pentes sablonneuses peu profondes. La méthodologie proposée se compose de deux éléments principaux: (i) un cadre théorique pour la stabilité non drainée et (ii) MIT-S1, le modèle de comportement pour la simulation de la réponse des sables. La première partie du document illustre l'utilisation d'un indice de stabilité capable de saisir le début de la rupture dans des pentes infinies dans des conditions non drainées. Dans la deuxième partie, les implications pratiques de la méthode sont évaluées par rétro-analyse d'une série de ruptures par écoulement dans une risberme sous-marine sur le site de Nerlerk. La réinterprétation de ces événements, à la lumière de la théorie de la stabilité des matériaux, a confirmé que la liquéfaction est un mécanisme plausible pour expliquer ces défaillances. En outre, les analyses ont fourni une prédiction de la distribution spatiale des masses instables, qui est compatible avec ce qui a été observé par des mesures bathimétriques menées après les défaillances. Cette application de la théorie soutient l'idée qu'une modélisation réaliste du comportement est essentielle pour faire des prédictions cohérentes de potentiel de liquéfaction dans des conditions de terrain réalistes.

KEYWORDS: sands, static liquefaction, flow slides, material stability, theoretical analyses, constitutive modeling.

1 INTRODUCTION.

Landslides and slope failures are widely recognized as one of the major natural hazards affecting both the development of densely populated areas in rugged terrain and the design of artificial earthworks [Terzaghi 1957, Sladen et al. 1985b]. Within the general class of slope failures, runaway instabilities or flow slides represent impressive phenomena that still raise several open questions.

Even though various studies have been carried out on the subject [Sladen et al. 1985a, Lade 1993], there is still need for advanced tools of analysis that can explain catastrophic failures, evaluate hazard levels in landslide prone areas and define geotechnical design criteria. The purpose of this work is to propose a predictive modeling methodology to study flow slide phenomena. The proposed methodology aims to evaluate (i) the shear perturbations that can trigger a flow slide, (ii) the spatial distribution of soil masses prone to liquefaction and (iii) the characteristics of the post-failure response of the slope.

2 MODELING FLOW SLIDE TRIGGERING.

The evaluation of liquefaction conditions based on geotechnical criteria typically relies on the combined use of the critical state theory and empirical observations from laboratory experiments and in situ tests [Poulos et al. 1985]. Although these methods provide guidance to assist engineering judgement, they lack appropriate geomechanical foundations that can be applied to general cases.

Indeed, the application of stability criteria to field conditions requires accurate consideration of the realistic static-kinematic characteristics of the problem at stake. An important example is represented by shallow slopes, in which initial stress conditions and kinematics are highly anisotropic and cannot be appropriately represented through classical triaxial testing. One of the first approaches to consider the role of soil behavior through a comprehensive constitutive model was suggested by di Prisco et al. (1995). In order to study the onset of a flow slide, these authors considered the geometry of an infinite slope (Figure 1) and modeled sand behavior through simple shear simulations.
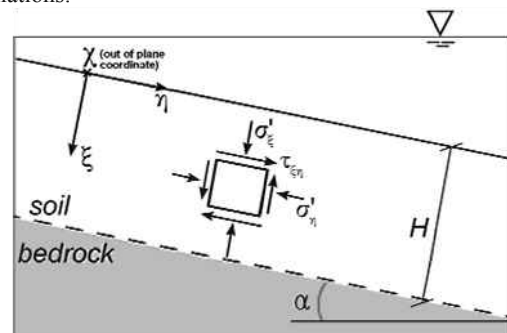

Figure 1. Reference system for a submerged infinite slope and initial stress conditions.

The present paper discusses a methodology which is inspired by this original idea, but tries to link it directly to the critical

state of sands and in situ observations. The key contribution is the incorporation of a constitutive model with predictive capabilities for describing transitions from contractive to dilative volumetric behavior upon shearing. As a result, the approach is able to distinguish among different types of sand response induced by an undrained perturbation (e.g., complete liquefaction, partial liquefaction, etc.), which is an essential aspect to define the expected post-failure behavior of a sliding mass.

In order to define in appropriate mathematical terms the onset of failure in a shallow infinite slope, our methodology frames static liquefaction within the theory of material stability [Hill, 1958, Buscarnera et al. 2011, Buscarnera and Whittle 2013]. In particular, we introduce an index for undrained simple shear failure:

$$\Lambda_{LSS} = H - H_{LSS} \qquad (1)$$

where H is the hardening modulus of the sand considered as an elastoplastic medium, while H_{LSS} is a kinematic correction factor that depends on the mode of deformation. Vanishing values of (1) indicate the onset of unstable conditions. In other words, H_{LSS} represents a critical value of the hardening modulus at which undrained simple shear perturbations are no longer admissible. More details about the derivation of the index (1) are given by Buscarnera and Whittle (2012). For the purpose of the current paper, it is sufficient to note that positive values of (1) at a given state of stress and density reflect a stable undrained response of the infinite slope, while vanishing/negative values indicate the loss of undrained strength capacity. In this way, the values of Λ_{LSS} (as well as its increment, $\dot{\Lambda}_{LSS}$) can be used to assess both the initial stability conditions prior to shearing and the critical triggering perturbations. More specifically, the simple shear response predicted by a constitutive model can be interpreted by means of (1), identifying the stresses at the initiation of a flow failure and the residual margin of safety. For example, Figure 2 illustrates two MIT-S1 simulations of undrained simple shear response at the same level of initial vertical effective stress but with different values of initial shear stresses (representing different slope angles).
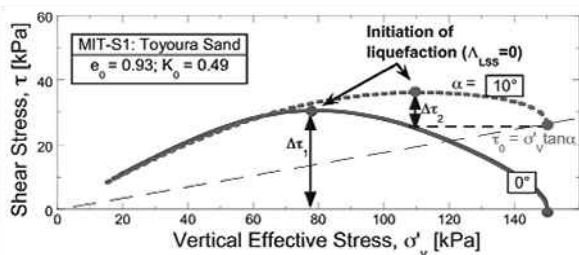

Figure 2. Example of simple shear simulations (loose Toyoura Sand simulated with the MIT-S1 model).

The results illustrate that the initial state of stress affects the magnitude of the shear perturbation required to induce instability ($\otimes|_1$ vs $\otimes|_2$). The onset of an instability coincides with the peak in the shear stress, and can be readily interpreted through the stability index (1).

As is well known, the undrained behavior of sands is also influenced by changes in the effective stress and density. For example, even very loose sands can exhibit a tendency to dilate at low effective stress levels, but will collapse for undrained shearing at high levels of effective stress. Hence, the prediction of liquefaction potential requires a constitutive framework that can simulate realistically the stress-strain properties as functions of stress level and density. To illustrate this aspect, Figure 3 shows MIT-S1 simulations for a pre-shear void ratio ranging from 0.87 to 0.94, with the model predicting a sharp transition from a stable behavior to complete collapse.
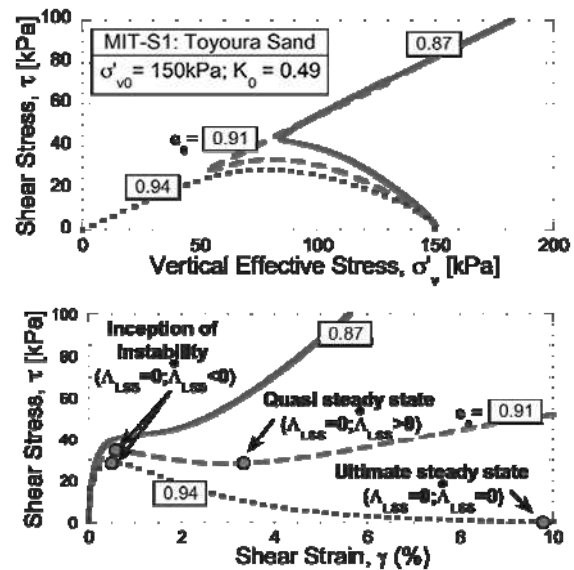

Figure 3. MIT-S1 predictions: effect of void ratio on undrained simple shear response of Toyoura Sand: a) stress path; b) stress-strain behavior.

The effect of confining pressure and density on the undrained response of sands implies that the perturbation shear stress ratio, $\otimes|/\Gamma'_{v0}$, associated with the initiation of liquefaction is not only a function of the slope angle, but must be evaluated at the depth of interest. This information can be encapsulated in appropriate stability charts of the triggering perturbations. Figure 4 gives an example of such charts, and uses MIT-S1 simulations for a constant value of the initial void ratio to show the effect of the stress level on the predicted triggering perturbations.

In general, such charts should be evaluated at any depth of interest, being they a function of the values of density and stress state at that specific location. Once the stability charts expressing the shear resistance potential have been obtained, it is possible to define the variation of the triggering perturbation at any depth. These capabilities are illustrated in the next section by applying the theory for a case study involving flow failures in a sandy deposit.
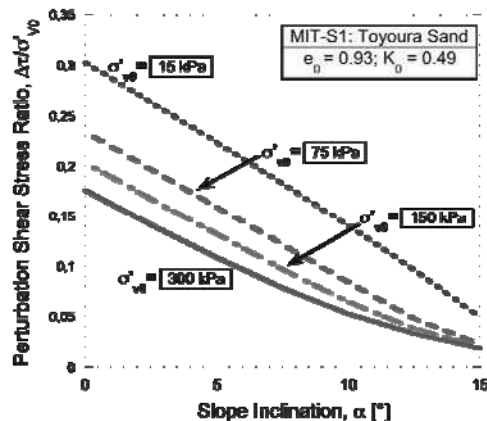

Figure 4. Effect of effective stress level on the stability charts (all points in the chart are characterized by $\Lambda_{LSS}=0$).

3 EXAMPLE OF APPLICATION: THE NERLERK CASE.

The Nerlerk berm case history refers to an impressive series of slope failures that took place in 1983 during construction of an artificial island in the Canadian Beaufort Sea (Sladen et al., 1985b). We have used the MIT-S1 model to investigate potential static liquefaction mechanisms in the Nerlek berm. In order to apply the theory to the Nerlerk case, it is assumed that

the local behavior of the sides of the berm can be approximated by considering stress conditions in an infinite slope. Although this choice represents an important simplification of the real geometry, this assumption allows an immediate mechanical evaluation of possible incipient instabilities within the fill and provides an insight on the type of expected undrained phenomena.

The application of the methodology is based on the calibration of the MIT-S1 model parameters for the site-specific properties of the Nerlerk sands. Given the lack of data, the calibration procedure required a number of approximations. Here only some key aspects of the calibration process are described, while more details are available in Buscarnera and Whittle (2012). First, the parameters governing the critical state of the Nerlerk sands have been evaluated on the basis of the available literature data (Sladen et al., 1985a). Then, the critical state properties of the Nerlerk sands have been compared with those of similar Arctic sands (Figure 5), for which one-dimensional compression data were available.
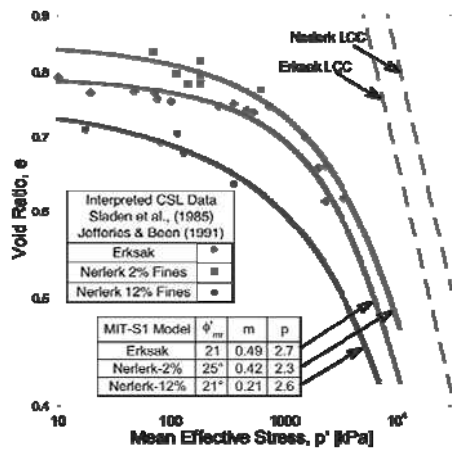

Figure 5. Comparison of Critical State Lines (CSL) and Limit Compression Curves (LCC; dotted lines) for Erksak and Nerlerk sands (while fines content affects the CSL of Nerlerk sand, no influence on the LCC is assumed given the lack of data).
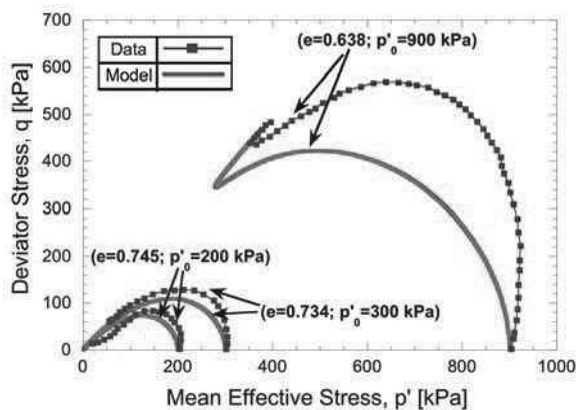

Figure 6. Comparison of computed and measured undrained shear behavior for Nerlerk Sand with 12% fines.

Such comparisons, together with empirical considerations compiled for a broad set of sands (Pestana and Whittle, 1995), allowed the definition of a set of parameters for the compression response of Nerlerk sands. The remaining model constants were calibrated using data on the undrained response (Figure 6).

In order to use the calibrated MIT-S1 model for the Nerlerk berms it is finally necessary to define the in situ void ratios along the slope profile and evaluate the stability charts of the Nerlerk berm for several depths within the slope. The first step

is largely dependent on a reliable interpretation of the available in situ tests. Several CPT tests were performed on the hydraulic fills at Nerlerk, with the aim of estimating the in situ density. For consistency with prior studies (Sladen et al. 1985b; Lade 1993), the current analyses assume that relative density (D_r) can be estimated using the CPT correlation proposed by Baldi et al. (1982). It is clear that the choice of a specific interpretation method for CPT test results will affect the estimation of relative density (and, in turn, the model predictions). This uncertainty, however, is probably unavoidable in any method of interpretation. Figure 7 shows that the estimated values for D_r range from 30 to 55 %, while Figure 8 illustrates the distribution of these initial states relative to the CSL of Nerlerk sands with 12% fines content.
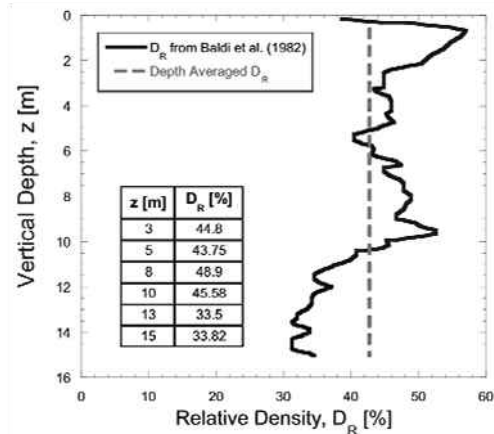

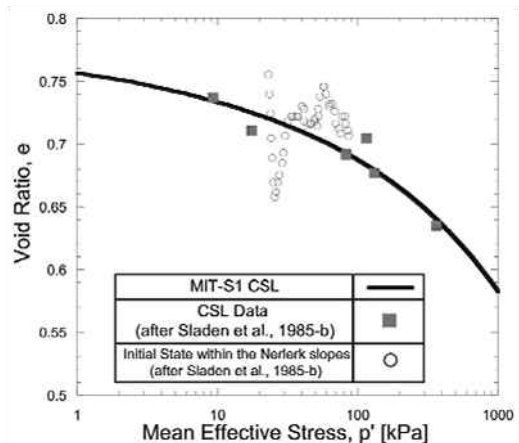Figure 7. In situ relative density from CPT tests (Baldi et al. 1982)

Figure 8. Relative location of in situ and critical states for Nerlerk sands

Figure 9 shows the computed stability charts at selected depths for infinite slopes in Nerlerk sand, while Figure 10 illustrates the undrained response predicted by the MIT-S1 model at various depths for a slope made of the same material and characterized by a slope angle ⟨=13°.

The results show that the magnitude of the shear perturbation needed to cause instability can be significantly affected by the selected depth within the slope profile. More specifically, the analyses define the initial state of stability within the Nerlerk berm slopes in a proper mechanical sense, allowing a prediction of the critical inclination for incipient instability. Since the Nerlerk berm was constructed at slope angles in the range ⟨=10°-13°, these results suggest that the Nerlerk slopes were likely not in an incipient state of instability, and additional shear stresses were required to trigger flow failures. In other locations where steeper slopes were recorded, however, only very small perturbations in shear stress could have triggered failure. This result suggests that an undrained collapse triggered by rapid

deposition can be considered as a mechanically feasible failure mechanism for the berm.
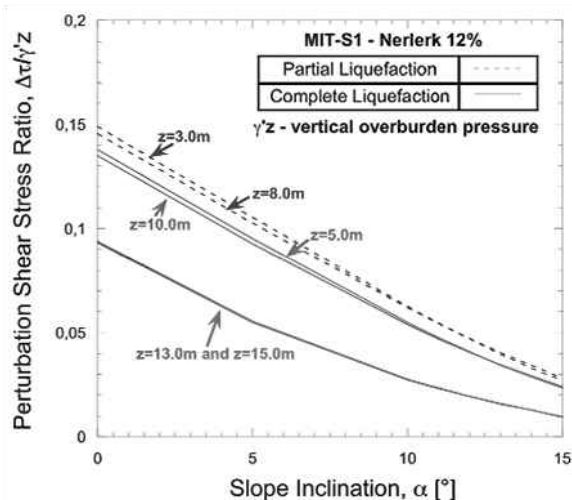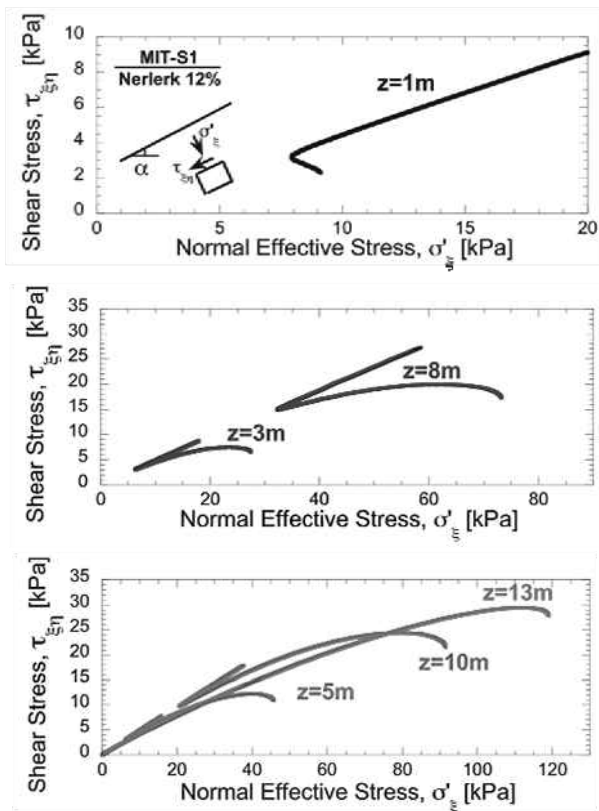

Figure 9. Stability charts for the Nerlerk berm.

Figure 10. Predictions of undrained response across the Nerlerk berm section (⟨=13°): a) no potential for liquefaction; b) limited potential for liquefaction; c) high potential for liquefaction.

4 CONCLUSIONS

This paper has presented a framework for evaluating the triggering of flow slides in infinite slopes by modeling the undrained shear behavior using the anisotropic MIT-S1 model. The selected soil model is able to simulate realistic transitions in the contractive/dilative response of sands and enables the prediction of the shear perturbations able to induce instability, as well as the location of potentially unstable zones within the soil mass. In this paper, these features have been used to derive stability charts of triggering perturbations for different combinations of initial density and stress state.

In practice the model needs to be calibrated for the site specific properties of the soil, and requires reliable data on in situ density in order to make predictions of liquefaction potential. In order to show the capabilities of the proposed approach, the methodology has been applied to the well-known case of slope failures in the Nerlerk berm. A general picture of the distribution of liquefaction susceptibility on the Nerlerk slope profile has been obtained. The analyses have been based on the calibration of model input parameters against published laboratory test results, while empirical correlations for CPT data have been used to define the initial density conditions prior to shearing. The results show that there were two zones within the slope that were vulnerable to flow failure. Although some sections of the berm were oversteepened, most were deposited with a slope angle ⟨=10°-13°. For these slope angles, the current analyses show that instability could have been triggered by the undrained perturbations possibly induced by the rapid deposition of hydraulic fill. Thus, static liquefaction is likely to have contributed to the observed failures, confirming earlier hypotheses by Sladen et al. (1985b).

The analyses presented in this work illustrate a unified methodology that combines the theory of material stability, the critical state framework for sands and data from in situ tests. As a result, the proposed methodology offers a simple, consistent and complete geomechanical framework for interpreting and predicting the triggering of flow slides that can be easily applied to other similar engineering cases.

5 REFERENCES.

Baldi G., Bellotti R., Ghionna V., Jamiolkowski M., Pasqualini E. (1982). Design parameters for sands from CPT. Proceedings of the Second European Symposium on Penetration Testing, ESOPT 11, Amsterdam, Holland, pp. 425-432.

Buscarnera, G., Whittle, A.J. (2012). "Constitutive modeling approach for evaluating the triggering of flow slides". Can. Geotech. J. 49(5): 499-511.

Buscarnera, G., Whittle, A.J. (2013). Model prediction of static liquefaction: the influence of the initial state on potential instabilities. To appear on J. Geotech. Geoenviron. Eng. ASCE.

Buscarnera G., Dattola G., di Prisco, C. (2011). Controllability, uniqueness and existence of the incremental response: a mathematical criterion for elastoplastic constitutive laws. Int. J. Solids Struct., 48 (13), 1867-1878.

di Prisco C, Matiotti R, Nova R. (1995). Theoretical investigation of the undrained stability of shallow submerged slopes, Géotechnique , 45, 479-496.

Hicks M. A., Boughrarou R. (1998). Finite element analysis of the Nerlerk underwater berm failures. Géotechnique 48, No. 2, 169–185.

Jefferies M.G., Been K. (1991). Implications for critical state theory from isotropic compression of sand. Géotechnique 50:44, 419-429.

Hill, R. (1958). A general theory of uniqueness and stability in elastic-plastic solids. J. of the Mech. and Phys. of Solids 6, pp. 239–249.

Lade P. V. (1993). Initiation of static instability in the submarine Nerlerk berm. Can. Geotech. J. 30, 895-904.

Pestana J.M., Whittle A.J. (1995). Compression model for cohessionless soils, Géotechnique, 45 (4), 611-631.

Pestana J.M., Whittle, A.J. (1999). Formulation of a unified constitutive model for clays and sands, Int. J. Numer. Anal. Meth. Geomech., 23, 1215-1243.

Poulos, S.J., Castro, G. and France, J. (1985). Liquefaction evaluation procedure. Journal of the Geotechnical Engineering Division, ASCE. 111(6): 772-792

Sladen, J. A., D'Hollander, R. D. & Krahn, J. (1985a). The liquefaction of sands, a collapse surface approach. Can. Geotech. J. 22, 564-578.

Sladen, J. A., D'Hollander, R. D., Krahn, J. & Mitchell D. E. (1985b). Back analysis of the Nerlerk berm Liquefaction slides. Can. Geotech. J. 22, 579-588.

Terzaghi K. (1957). Varieties of submarine slope failures. NGI Publication N. 25, 1-16.

Assessment of landslide run-out by Monte Carlo simulations

Évaluation de la dynamique des glissements de terrain par des simulations de Monte-Carlo

Cepeda J., Quan Luna B., Nadim F.
Norwegian Geotechnical Institute – NGI and International Centre for Geohazards - ICG, Oslo, Norway.

ABSTRACT: Landslides run-out models are based on theoretical descriptions of mass motion which attempt to model the complex behaviour of the actual flow phenomenon. To reproduce the general features of the mass motion, these models simplify the problem by using parameters that account for complex aspects, which are not explicitly included. This simplification results in model parameters that cannot be related to a specific physical process, and therefore cannot be directly measured. In order to analyse the effect of uncertainties in the input parameters, a probabilistic procedure based on a Monte Carlo simulation for run-out modelling was considered. The framework is based on a dynamic model (MassMov2D), which is combined with an explicit representation of the different parameter uncertainties. The main goal with the proposed methodology is to present a framework to obtain potentially expected run-out extents and intensities in areas where it is not possible to determine the rheological parameters on the basis of back-analyses. The outlined procedure provides a useful approach for experts to produce hazard or risk maps in cases where historical records are either poorly documented or completely lacking, as well as to derive confidence limits on the proposed zoning.

RÉSUMÉ : Les modèles de la dynamique des glissements de terrain sont basés sur des formulations mathématiques qui tentent de théorétiser les phénomènes d'écoulement réels, par nature très complexes. Afin de simuler les caractéristiques générales du mouvement, ces modèles utilisent des paramètres qui représentent et simplifient les aspects complexes du problème, sans pour autant les prendre en compte explicitement. Il en résulte une simplification des paramètres du modèle: ceux-ci ne sont donc plus liés à un processus physique réel, et ne peuvent par conséquent pas être mesurés directement. Afin d'analyser l'effet des incertitudes entourant ces paramètres, une approche probabiliste, basée sur la méthode de Monte Carlo, a été employée. Celle-ci se base sur un modèle dynamique (MassMov2D) ainsi que sur une représentation explicite des incertitudes des différents paramètres. L'objectif principal de cette méthode est de proposer une approche générale dans le but de prédire la taille et l'amplitude des glissements de terrain dans des zones où il n'est normalement pas possible de déterminer les paramètres rhéologiques par méthode arrière. La méthode décrite ici propose une approche pratique afin d'établir des cartes de risque dans les cas où la documentation est limitée, voire inexistante, ainsi que pour estimer les limites de confiance des zonages proposés.

KEYWORDS: Landslides, run-out, Monte Carlo, Bingham rheology, Voellmy rheology, quantitative risk assessment.

1 INTRODUCTION

Dynamic run-out models for landslides are able to simulate the spatial distribution of depth and velocity of the moving mass, which is essential for a quantitative evaluation of hazard and risk at a specific site. Another advantage of the application of dynamic models is that they can simulate the effect of variations in the release volume as well as in the rheological parameters for different scenarios including ones that have no historical evidences.

In practice, a substantial degree of uncertainty characterizes the definition of the deterministic model parameters. This is due to the lack of experimental data and the poor knowledge of the mechanical behaviour of the moving flows. Consequently all models, either those widely used in practical applications or those more recently developed, are based on simplified theoretical descriptions of mass motion which try to capture the complex rheology of the flow phenomenon. This results in a generalization of all models to attempt to reproduce the general features of the moving mass through the use of parameters (mostly for evaluating base shear) which account for aspects not explicitly described or oversimplified. The outcome is that the model parameters cannot be related to a specific physical process, and therefore directly measured, but need to be calibrated. At the moment, a relatively complete and well-established calibration for most of the run-out models is still lacking or not reliable enough to be applied in practical applications. This is connected with one of the basic limitations with the use of dynamic run-out models, which are significantly sensitive to the parameters controlling the base shear (Revellino et al. 2004, Hurlimann et al. 2007, Hungr & McDougall 2009). Inherent uncertainties in the specification of the input data for models are well acknowledged but usually not explicitly incorporated into the analyses. Such uncertainties are normally addressed through conservative estimate of parameters, or in some cases, by a sensitivity analysis. These approaches do not integrate objectively the estimation of uncertainties, and thus may be impractical and lead to either conservative or underestimated hazard levels.

In order to analyze the effect of the uncertainty of input parameters, a probabilistic framework based on a Monte Carlo simulation for run-out modelling is considered as an alternative approach. Monte Carlo analysis is a method that uses statistical sampling techniques of input parameters to derive the probability distributions of solutions for mathematical equations or models. The Monte Carlo analysis was initially developed in the 1940's and it has been applied to a wide variety of problems for addressing the uncertainty of data and models (Metropolis 1987).

2 METHODOLOGY

The dynamic model used in this study was MassMov2D (Beguería et al. 2009), which solves the equations of conservation of mass and momentum averaged over the depth of the landslide mass using an Eulerian scheme scripted in PCRaster, a GIS modelling environment (Karssenberg et al. 2001). In the equation of conservation of momentum, the shear stress at the bed contact (base of the analysed differential column) is calculated using a rheological model (a relation coupling stresses and strain rates) that should be physically consistent with the overall behaviour of the landslide. In this particular case, two models are used for describing frictional and cohesive-like dominated behaviours, namely the Voellmy and the Bingham models. Simplified formulations of these models are presented in Equations (1) and (2), respectively:

$$\tau = \sigma \tan \phi_{app} + \frac{\rho g v^2}{\xi} \qquad (1)$$

$$\tau = \tau_y + \mu \dot{\gamma} \qquad (2)$$

where, τ is the shear stress at the base of a differential column of landslide mass, σ is the normal stress at the base, ϕ_{app} is an apparent friction angle, ρ is the bulk density of the landslide mass, g is the acceleration of gravity, v is the velocity, ξ is the turbulent coefficient, τ_y is the yield strength, μ is the viscosity, and $\dot{\gamma}$ is the shear strain rate. The apparent friction angle and the turbulent coefficient are material parameters of the Voellmy rheology. The yield strength and the viscosity are the corresponding parameters for the Bingham model.

The main objective of the present application of the Monte Carlo analysis is to examine the effect of uncertainty associated to the variability of the rheological parameters of the Voellmy and Bingham models on the estimation of debris flow run-out. This method allows evaluating the probability distribution of the relevant output parameters (intensity parameters) for a hazard assessment once the proper probability distributions for the parameters of both rheologies have been defined. In other words, it is possible to account explicitly and objectively for the effect of uncertainties in the model. For the application of the Monte Carlo analysis, each of the input parameters was assigned a distribution. The output from the model is calculated several times for a set of randomly selected input parameters. This produces a probability distribution for the output values, such that the uncertainty for the exceedance of any particular value can be estimated. Figure 1 presents a simplified flowchart of this procedure.
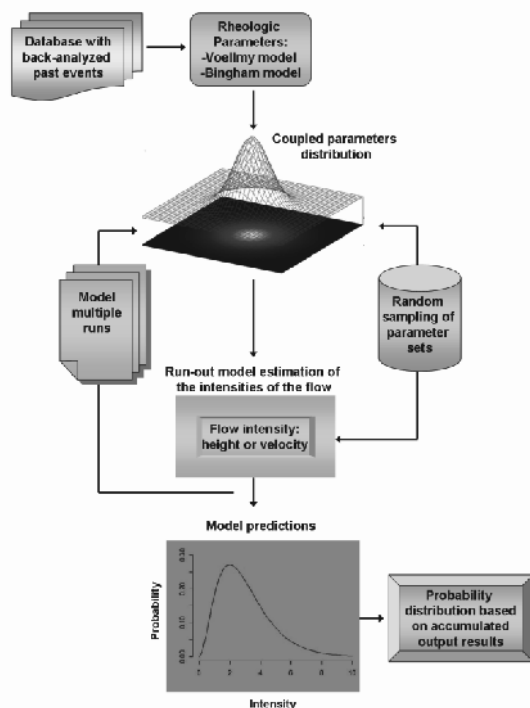

Figure 1. Flow chart of the application of a Monte Carlo method for a probabilistic assessment of landslide run-out.

The uncertainty resulting from the physical process (variability inherent to the phenomenon) is expressed inside the probability density functions of the parameters characterizing the base shear. An extensive literature study was carried out for collecting a database of past back-analyzed landslides, including the calibrated rheological parameters for each event. The relationships between the parameters of the Voellmy and Bingham rheologies were modelled as a "Gaussian Copula" to define the probability density function for both rheological models (Fig. 2)
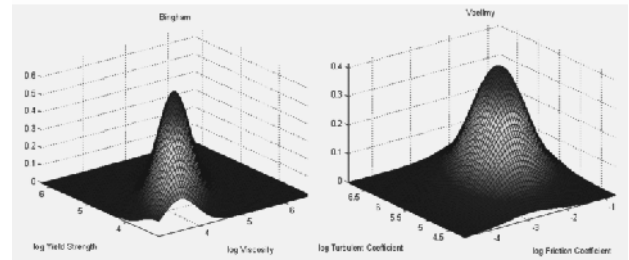

Figure 2. Fitted "Gaussian copula" distribution function to the Bingham rheology (left) and Voellmy rhoelogy (right).

Each distribution was randomly sampled to obtain a set of 5000 pairs of rheological parameters. In the next step, a routine was coded to repeatedly run the simulations for each pair of parameters. At the end of each simulation, the output values of peak intensity parameters (maximum depth and velocity) were saved for selected points on the area of interest. Finally, the output values were fitted to a theoretical probability density function. The parameters for each probability distribution were reported. In addition, the probability that the output exceeds a particular value or will fall within a certain range was calculated.

The dynamic run-out model MassMov2D (Begueria et al. 2009) was selected because it allows the use of scripts which can be modified to include output reports in the form of maps or text files. A batch file was built-in and incorporated inside MassMov2D which selects the randomly generated sets of parameters to produce multiple simulations. The results of each simulation regarding the maximum flow depth and maximum velocity at each control point were reported in a text file form for being fitted to a theoretical probability density function.

3 STUDY CASES

3.1 The Faucon catchment in the Barcelonnette Basin

Inside the Barcelonnette Basin, the Faucon torrent was selected as a test site. The Faucon catchment is a steep forested watershed with an area of approximately 10.5 km^2 which rises to 2984 m a.s.l. Most slopes are steeper than 25°, reaching 80° at the highest elevations. Many of the slopes in the Faucon catchment are covered by various types of Quaternary deposits: thick taluses of poorly sorted debris; moraine deposits; screes and landslide debris. These deposits have a sandy-silty matrix, may include boulders up to 1–2 m in size and are between 3 and 15 m thick (Remaître 2006). The main incised channel has an average slope of about 20°, ranging from 80° in the headwater basin to 4° on the alluvial fan, and is approximately 5500 m in length. Channel morphology is characterized by a V-shaped profile with a steep channel in the upper part, and a flat-floored cross-profile between steep slopes. The Faucon torrent has formed a 2 km^2 debris-fan that spreads across the Ubaye valley floor. It has a slope gradient ranging from 4 to 9°. The fan consists mostly of cohesionless and highly permeable debris (debris-flows strata and/or torrent deposits) (Remaître et al 2005). Two points within the area of interest (in terms of exposed elements) were selected on the accumulation area to calculate the maximum flow height and the maximum velocity (Fig. 3).

3.2 Tresenda village in the Valtellina Valley

Valtellina is an important Italian alpine valley located in Central Italian Alps (Northern Italy, Sondrio Province). The valley starts near Bormio (1,225 m a.s.l.) and it runs for about 100 km to Colico (218 m a.s.l.) near Como Lake. The axis of the valley is formed by the Adda River, originating from small lakes in the Rhaetian Alps at 2,335 m a.s.l. The Adda River flows through the entire valley in a flat alluvial plain up to 3 km wide and it joins the Po River in the Lombardy Plain. Valtellina has a U-shaped valley profile derived from Quaternary glacial activity. The lower part of the valley flanks are covered with glacial, fluvio-glacial, and colluvial deposits of variable thickness (Crosta et al. 2003) The Tresenda village is located in the Valtellina area and is located in the municipality of Teglio in the Valtellina Valley. Spatial information of past damage derived from historical records, local chronicles, and interviews with local people confirmed that the village of Tresenda was affected by debris flows events which caused significant losses in 1983, 2000 and 2002. Soil slips, resulting in debris flows were triggered on the steep slopes above Tresenda, where the soil thickness varies from 0.7 to 2.5 m.
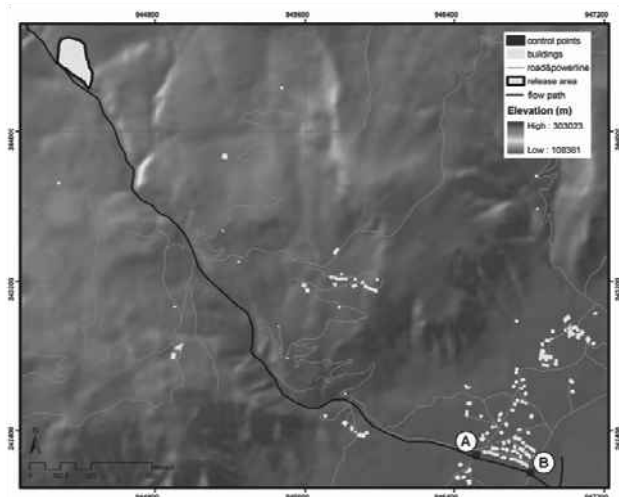

Figure 3. Digital elevation model of the Faucon catchemnt with the location of the two points used for reporting the results (A and B).

The documented past events crossed minor roads and impacted buildings in the Tresenda village, while running along main drainage lines (Cancelli & Nova 1985, Guzzetti et al. 1992). Major events in future may produce casualties and serious property damages as well as the obstruction of a main road. In the Tresenda case study two location points were also located within the area having the highest concentration of exposed elements.

4 RESULTS

4.1 Application of the methodology to the Faucon catchemnt

The release volume chosen in the Faucon study was 50,000 m^3 and was set as constant in the simulations. Past events in the Faucon area have had final volumes between 55,000 m^3 – 80,000 m^3. The unit weight of the debris flow was set to a constant value of 19 kN/m^3. The time step was set at 1 s and the total duration of each simulation was 500 s. The Monte Carlo method applied in the Faucon catchment was modelled with the Bingham model. This model was selected because of the geo-environmental setting of the area where past events are described to have viscoplastic behaviour (Remaître et al. 2005). In total, 5,000 runs were completed corresponding to the input parameters obtained from randomly sampling the fitted Gaussian copula. For each of the 5,000 runs, the maximum flow

heights and maximum velocities were reported for each of the two points. The results of each point were used to populate a probability density function of each intensity parameter. A Gamma distribution was the distribution that best fitted the maximum flow height and velocities measured in points A and B (Fig. 5 & 6).
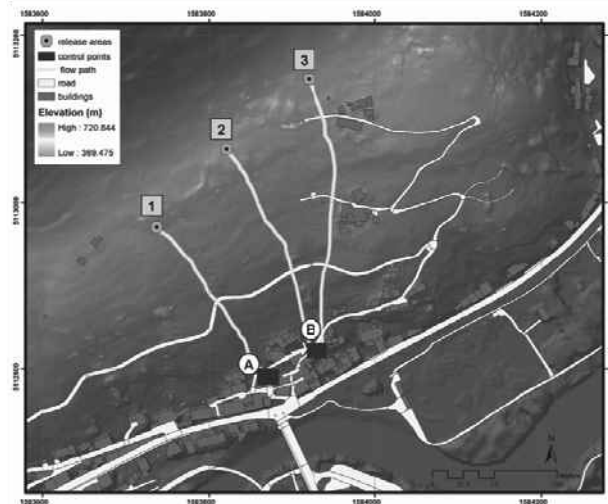

Figure 4. Digital elevation model of the Tresenda village with the location of the two points used for reporting the results (A and B) and three different release areas (1, 2 and 3).
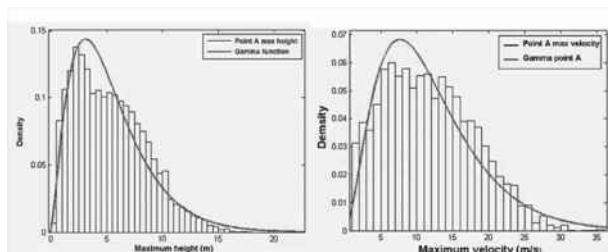

Figure 5. Gamma distribution fitted to the maximum height (left) and velocities (right) values obtained in point A.
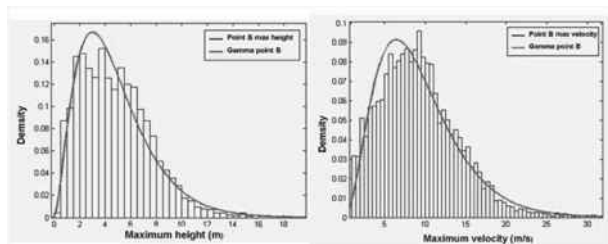

Figure 6. Gamma distribution fitted to the maximum height (left) and velocities (right) values obtained in point B

The obtained results of the mean values of height and velocity computed with the Monte Carlo method were compared with the events that took place in 1996 and 2003 (Remaître et al. 2008, Remaître et al. 2009). In both cases, the mean value of the distribution overestimates the flow height and the flow velocities. In the results, point A which is located higher up in the catchment than point B (apex of the fan) reports higher values for both intensity parameters (height and velocity).

4.2 Application of the methodology to the Tresenda village

In the Tresenda case, the main purpose of the study was to observe the response of the model when using more than one release area. In the Tresenda case, three simultaneous release

areas with different volumes were considered (Table 1). The initiation of the debris flow is assumed to be caused by soil slips and the flows are unchanneled along most of the path. The unit weight of debris flow was set to the same value as in the case of Faucon. The total duration for each simulation was 500 s. The Voellmy model was used in the run-out analysis.

In total, 5,000 simulations were carried out associated to the corresponding set of input parameters sampled from the Gaussian copula. For each simulation

Table 1 Release volume used for the Monte Carlo simulation for the three different release areas in the Tresenda village

	Release Volume (m^3)
Release area 1	1424
Release area 2	1410
Release area 3	1518
Total released volume	4352

the maximum flow heights and maximum velocities were reported for each point. Also in the Tresenda case, a Gamma distribution had the best fit to the output parameters. Figures 7 and .8 show the results for the maximum flow height and velocities calculated in points A and B.
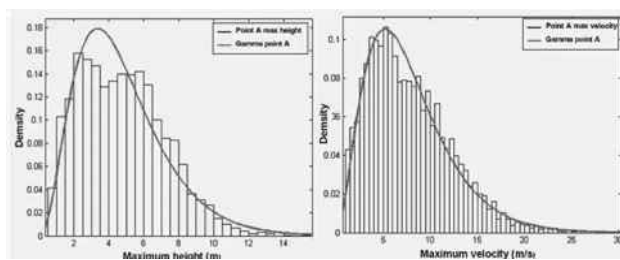

Figure 7. Gamma distribution fitted to the maximum height (left) and velocities (right) values obtained in point A.
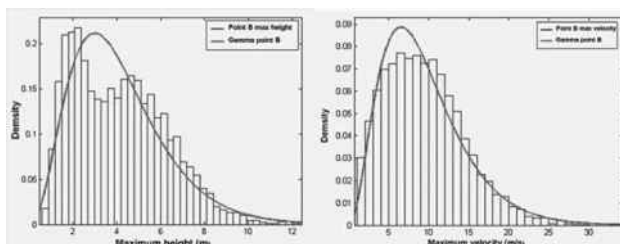

Figure 8. Gamma distribution fitted to the maximum height (left) and velocities (right) values obtained in point B.

The results for the Tresenda case study were compared with events in 1983 and 2002. In these incidents, only information regarding the flow heights was available (no velocities were estimated for these events). In the Tresenda case, the mean value of the flow height in point A is overestimated compared to the actual event while point B has a lower mean value than the observed event. In the Tresenda case the simulated values are closer to the actual events than in the Faucon case. This can be possibly attributed to the potential of the Voellmy rheology to model consistently these types of events.

5 CONCLUSIONS

The Monte Carlo method offers the advantage of modelling the probability distributions of the intensity parameters from run-out simulations. Of course, the reliability of the fitted probability density functions for the input parameters strongly depends on the completeness and accuracy of the original back-analyses included in the collected database. Another limitation of this study is that the estimated probabilities do not explicitly

account for the temporality of the phenomena. For future assessments it is recommended that run-out simulations using a stochastic approach become a routine practice in order to produce adequate future hazard scenarios and quantify the uncertainty due to the input parameters. This will result in intensity maps that are easier to interpret for end users, especially within a probabilistic framework for landslide mitigation.

6 ACKNOWLEDGEMNETS

7 REFERENCES

Begueria S., van Asch Th.W.J., Malet J.-P., Grondahl S. 2009. A GIS-based numerical model for simulating the kinematics of mud and debris flows over complex terrain. *Nat. Hazards and Earth Syst. Sci.*, 9, pp. 1897-1909.

Cancelli A. and Nova R.. 1985. Landslides in soil debris cover triggered by rainstorms in Valtellina (Central Alps – Italy). In: Proceedings of 4th International Conference and Field Workshop on Landslides. The Japan Geological Society, Tokyo, pp. 267–272.

Crosta G.B., Dal Negro P., Frattini P. 2003. Soil slips and debris flows on terraced slopes. *Nat. Hazards and Earth Syst. Sci.*, 3, 31- 42.

Guzzetti F., Crosta G., Marchetti M., Reichenbach P. 1992. Debris flows triggered by the July, 17–19, 1987 storm in the Valtellina area (Northern Italy). International Symposium Interpraevent 1992, Bern, Switzerland, pp. 193-203

Hungr O. and McDougall S. 2009. Two numerical models for landslide dynamic analysis. *Computers & Geosciences* 35, pp. 978–992.

Hürlimann M., Medina V., Bateman A., Copons R., Altimir J. 2007. Comparison of different techniques to analyse the mobility of debris flows during hazard assessment-Case study in La Comella catchment, Andorra. In Chen & Majors (eds.) Debris-Flow Hazard Mitigation :Mechanics, Prediction and Assessment. Millpress, Netherlands, pp. 411-422.

Karssenberg, D., Burrough, P. A., Sluiter, R., De Jong, K. 2001. The PCRaster software and course materials for teaching numerical modelling in the environmental sciences. *Transactions in GIS*, 5(2), pp. 99-110.

Metropolis N. 1987. "The beginning of the Monte Carlo method". Los Alamos Science (1987 Special Issue dedicated to Stanisław Ulam): 125–130.

Remaître A., Malet J.-P., Maquaire O. 2005. Morphology and sedimentology of a complex debris flow in a clay-shale basin. *Earth Surf. Process. Landforms* 30 pp.339-348.

Remaître A. 2006. Morphologie et dynamique des laves torrentielles: Applications aux torrents des Terres Noires du bassin de Barcelonnette (Alpes du Sud). Ph.D. thesis.

Remaître A., van Asch Th.W.J., Malet J.-P., Maquaire O. 2008. Influence of check dams on debris flow run-out intensity. *Nat. Hazards Earth Syst. Sci.* 8, pp. 1403-1416.

Remaître A., Malet J.-P., Maquaire O. 2009. Sediment budget and morphology of the 2003 Faucon debris flow (South French Alps): scouring and channel-shaping processes.Proc. Landslide Processes: from geomorphological mapping to dynamic modelling, pp. 75-80.

The Challenge of the Slope Failure Problem and Its Remedial Considerations at Mileage 39km, Mt. Ali Road, Taiwan

Le défi du problème du glissement de pente et des dispositions correctives apportées, au kilomètre 39, de la route Mt. Ali Road, àTaïwan

Chang M., Huang R.
National Yunlin University of Sci. & Tech., Taiwan

ABSTRACT: Mt. Ali Road is a main scenic route to Alishan National Scenic Area and Yushan National Park in the middle of Taiwan. At Mileage 39Km, the downslope side of the road consists of a 200m deep 60° angle bare cliff with a creek passing around the slope's toe. Despite complex geologic conditions, the underlying slope materials appeared competent for about 20 years after the road opening. In 1999, however, a severe earthquake (Chi-Chi, M_w = 7.6) hit central Taiwan and caused numerous landslips in the mountain range of the island. Although no obvious damages to the road were observed after the time of shaking, the geologic setting of the site was deteriorating. During the attack of Typhoon Nari in 2001, the first serious effect on the road appeared and caused several parallel cracks along the alignment. Remedial work was initiated. Nonetheless, a loss of road base during the monsoon season next year had called for a stop of the work. The remedial plan was revised and implemented, but failed again due to Typhoons Talim and Longwang in 2005. The current repair works have been completed and generally show no major signs of slope distress. In view of repair histories and the geologic setting, this paper discusses the concerns and challenges for long-term stability of slopes at the site.

RÉSUMÉ : Mt. Ali Road est une route principale pittoresque qui mène à l'Alishan National Scenic Area et au parc national de Yushan, au centre de Taiwan. Au kilomètre 39, le côté aval de la route est formé d'une falaise nue de 200m de haut, inclinée à 60° avec un ruisseau la bordant en pied de pente. En dépit des conditions géologiques complexes, les matériaux de la pente se sont bien comportés au cours des 20 années l'ouverture de la route. Cependant, un violent tremblement de terre (Chi-Chi, *Mw* = 7,6) a frappé le centre de Taiwan en 1999, et a causé de nombreux glissements de terrain dans la partie montagneuse de l'île. Bien qu'aucun dommage apparent n'ait été détecté après la secousse, la situation géologique du site s'est détériorée. Les premiers effets conséquents ont pu être observés lors du typhon Nari en 2001, plusieurs fissures parallèles étant apparues le long du tracé. Un projet de confortement fut entrepris. Malgré cela, une rupture de la couche de fondation, de la route l'année suivante pendant la saison des moussons a necesssité un arrêt temporaire des travaux. Le projet fut révisé et remis en œuvre, mais a du être à nouveau arrêté en raison des typhons Talim et Longwang en 2005. Les réparations sont aujourd'hui terminées, et la pente ne montre en général aucun signe de désordre. Compte tenu de l'historique des réparations et de la situation géologique, ce document aborde les préoccupations et les défis concernant la stabilité à long terme des pentes du site.

KEYWORDS: slope failure, repair works, landslip prevention and mitigation, slope stability, case histories, Mt. Ali Road.

1 GENERAL

Mt. Ali Road is a main scenic route to Alishan National Scenic Area and Yushan National Park in the middle of Taiwan. As entering into the hilly terrain of central mountain range of the island, the road starts climbing up along the side of slopes for a distance of about 5Km until it reaches a hill top with an elevation of 460m MSL at the mileage of 39Km, where the road levels off and makes a loop around the hill. The downslope side of the road at this location consists of a 200m deep 60° angle bare cliff with a creek passing around the slope's toe.

Although both regional and local geology generally show a complex geologic structure at the site, the subgrade materials and underlying rock appeared competent for about 20 years since the road's opening. Figure 1 shows the regional geology of the area, and Figure 2 illustrates the geologic profile of the road section and its adjacent slopes.

On September 21, 1999, a severe earthquake (Chi-Chi, M_w=7.6) hit central Taiwan and caused numerous landslips or slope failures in the mountain range of the island, as indicated in Figure 3. Based on studies by National Center for Researches on Earthquake Engineering (NCREE 2000), approximately 1500-2000 landslides were directly induced by the earthquake. Although the shaking did not have immediate impacts at the site, the condition of the road and its adjacent side slopes appears to be deteriorating.
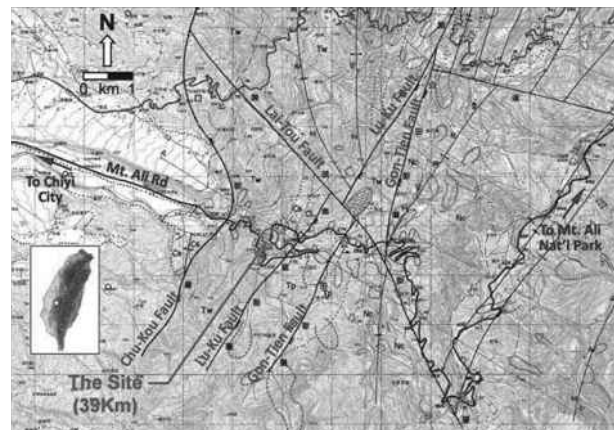
Figure 1. Regional geology of the area (Liu & Tseng 2000).

The monsoon season normally starts from early April to the end of September in the island. Annual precipitation is around 2150mm (Sinica 1999). Figure 4 shows accumulated rainfalls of the site in 2001 & 2005 were 4700mm & 4600mm, respectively. As will be discussed later, the abundance of rainfalls appeared to have contributed to the failures of slopes along the Mileage 39Km in 2001 & 2005.
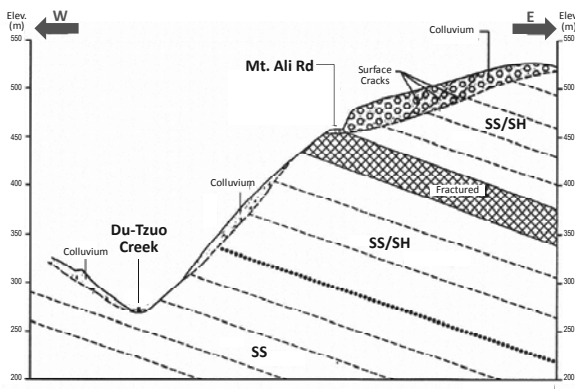
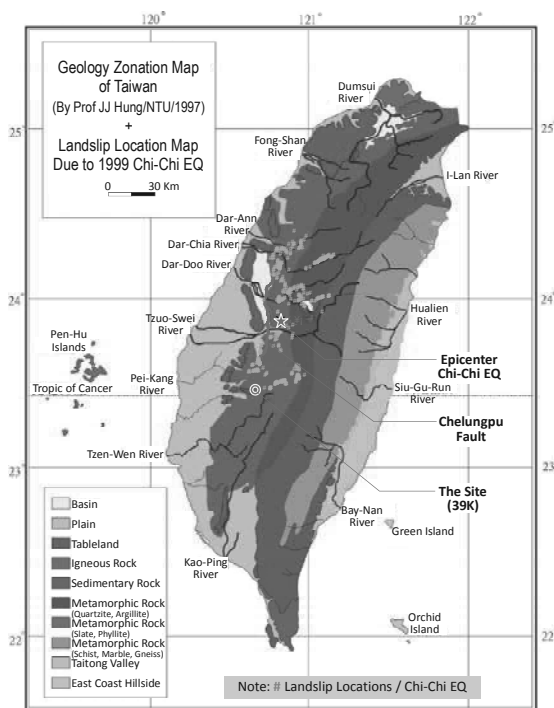Figure 2. Geologic cross-section at the 39Km project site (CECI 2005).

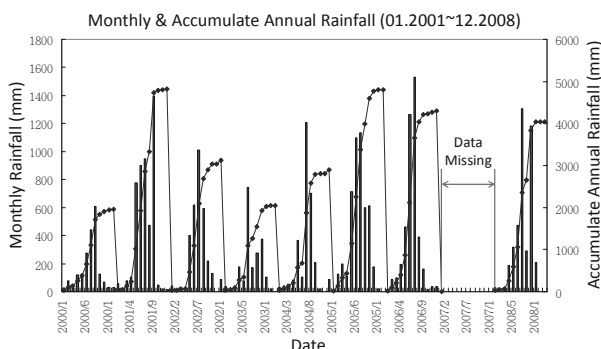Figure 3. Locations of landslides due to Chi-Chi EQ (NCREE 2000).

Figure 4. Monthly and accumulated rainfalls at the site (Peng 2009).

2 SLOPE FAILURE & ROAD REPAIR HISTORIES

Prior to failures of the subject slopes, a sever typhoon (Herb) with a rainfall of about 2000mm attacked Taiwan in 1996 and resulted in significant damages in central region of the island. Based on an official investigation report, the event had caused 91 landslips and 57 losses of road base along the entire length of

Mt. Ali Road (DOT 1996). However, the subject road and its slopes were only experienced very minor effects due to this typhoon and had no influence on the slope stability.

Three years after the severe typhoon incident, a damaging earthquake (Chi-Chi, 1999) occurred. As mentioned previously, the earthquake had resulted in numerous landslips in central Taiwan. Although the site and its adjacent slopes appeared to be competent during the shaking, the in-situ earthen materials were apparently weakened and deteriorating due to the earthquake. In subsequent years, signs of slope distress and movement became obvious, and some key events and associated repair histories are discussed in the following sections.

2.1 *2001 Typhoon Nari*

Typhoon Nari swiped Taiwan in September, 2001, and brought about 1400mm precipitation to the site, 4700mm for the entire year. This had been the largest rainfall event since the attack of Typhoon Herb in 1996. The site had experienced a series of parallel cracks of 10~80cm in width along the road alignment which called for a temporary shutdown for one lane of the road. A remedial action was subsequently taken by District V of Directorate General of Highways (DGH), Taiwan, that included the repair of surface cracks by a new AC paving and a planning on reconstruction of the road section by conventional retaining structure on the downhill side of the road.

2.2 *2002 monsoon rainfalls*

As the reconstruction work for the retaining structure was about to start in 8 months after Typhoon Nari, a failure in downslope of the road occurred (Figure 5). The failure was apparently due to the intense rainfall during the monsoon season. Recorded accumulated precipitation was greater than 1000mm within the two months prior to the failure.

Figure 5. Slope failure at Mileage 39Km due to 2002 monsoon rainfalls.

The original construction work had to be terminated and re-planned. In view of steep downslope and insufficient road width, DGH had once considered remedying the problem by cutting back and flattening the upslope. However, the plan was turned down due to unsuccessful negotiations with local ownerships of lands adjacent to the road.

The remedial plan was finally decided to limit within the extent of the road owned by DGH. Considerations of the road redesign had included a section of box-type concrete structure, as shown in Figure 6, which would provide a design with enough road width, structure rigidity, and relatively light-weight. The box structure was secured to the native ground by two rows of ground anchors, each of which with a total length of 35m, a horizontal spacing of 20m, and an anchor force of 45T. The

base of the box structure was also fixed to the ground by a series of mini piles of 16m in length.

Figure 7 shows the rebuilt road section after completion of the remedial works.
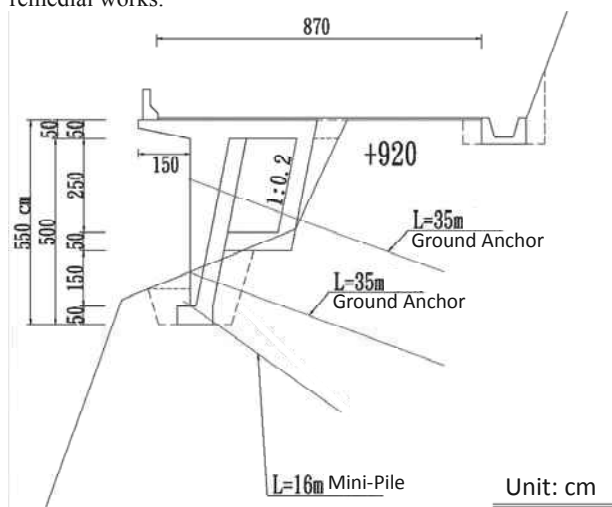

Figure 6. Box-type structure design for road section at Mileage 39Km.

Figure 7. Completion of box-type structure at Mileage 39Km.

2.3 *2005 Typhoons Talim & Longwang*

The new road section appeared to be in good shape for the next 1-1/2 years until mid of 2005 when the precipitation started to reach another historic peak.

Figure 8. Failure of box-structure road section due to Typhoon Talim.

In late August of 2005, a severe Typhoon Talim slammed Taiwan. By considering a series of heavy rainfalls in the previous two months, the accumulated precipitation of the year at the site had exceeded 4000mm. As a result, the box-type structure finally gave up and the entire road section of about 100m in length fell into the valley (Figure 8).

Post-failure investigation had revealed that the loss of entire road section was due to the downslope movement of the uphill slope mass which pushed the box-type structure, tore down the ground anchor tendons, and sheared off the mini piles.

Emergency action was implemented right after the failure by constructing a temporary road to the uphill side and installing I-beams for the downhill support (Figure 9) in order to maintain the local traffic (DGH 2005).

Figure 9. Emergency repair of the road section due to Typhoon Talim.

In late September, 2005, the emergency measure failed again one month after the attack of Typhoon Longwang. The temporary road lost 5m of its road width. Site reconnaissance showed significant tension cracks at the crest of uphill slope.

District V of DGH had to launch another remedial measure to mitigate potential impacts on the road section in the future. The plan had considered mostly the upslope protections that included filling of tension cracks, rechanneling surface drainage, installing subsurface horizontal drains, and surface vegetation, etc. Figure 10 shows the completion of upslope remedial works after Typhoon Longwang.

Figure 10. Completion of upslope remedial works at Mileage 39Km.

3 FIELD MONITORING & STABILITY ANALYSIS

In the following few years after Typhoon Longwang, the annual precipitation of the site was decreasing. To date the road section and its adjacent slopes appear competent for maintaining local traffic. However, data from subsurface exploration and in-situ monitoring during the previous remedial works showed signs of slope instability at the site (LEC 2006). Figure 11 indicates potential sliding masses (slip surfaces) in the upslope that would have impact on the Mileage 39Km road section. The downhill side slope was not improved during the remedial works and its surface was bared with remains of previous slides, as shown in Figure 12.
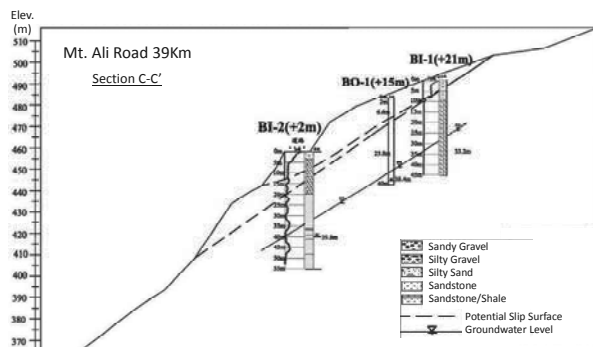

Figure 11. Material strata and potential slip surfaces at Mileage 39Km.

Figure 12. Downhill slope of Mt. Ali road section at Mileage 39Km.

4 CONCLUSIONS

In view of past failure incidents and associated remedial works, the road section at Mileage 39Km and the alongside slopes are still at perceivable risks of a potential slide. The signs of slope instability appeared to be pronounced since the attack of 1999 Chi-Chi Earthquake, which was believed that the shaking had weakened the underlying geologic units and thus accelerated the weathering process of materials at the site.

Conclusions on causes of slope instability and measures of slope mitigation for this site can be drawn and discussed below.

4.1 *Potential & triggering factors*

From a retrospective stand point, the factors that had caused instabilities of slopes at Mileage 39Km road section could be attributed to the following:

- A complex geologic structure at the site (Figure 1) where the underlying geologic units are generally fractured.
- The 1999 earthquake shaking that had weakened underlying geologic structure and enhanced deterioration process of the materials.
- The steep downhill slope geometry (60° angle & 200m deep).

- The potential uphill sliding masses (Figure 11).
- The unprotected downhill slope surface that enhanced rainfall infiltration and surface runoff erosion.
- A long-term erosion of slope toe by Do-Tzuo Creek (Figure 12).
- The abundance of groundwater that was observed seeping out of the surface of downhill slope.
- The prolonged and intense rainfalls that infiltrated, saturated and softened the slope materials, increased the perched water level, and directly triggered the slips.

4.2 *Long-term stability considerations*

The previous remedial works at site after Typhoon Longwang has been successful to date. However, the work details were mainly for improvements on surface protection of the upslope. From the analysis above on causes of slope failure, the current remedial activities would be helpful to mitigate the infiltration of rainfall and possibly prevent the triggering of a slide in the upslope. It would not be useful, however, for the stability of downslope, and would not either remove the concerns (i.e., potential factors) above that could be detrimental to the long-term stability of the road section and slopes at the site.

In accordance, more stability considerations and measures need to be taken to ensure the safety of the road section, and to maintain the transportation function of Mt. Ali Road as well. The considerations might include:

- Removal of potential sliding masses or reducing slope angle in the uphill.
- Downhill slope protection including vegetation and drainage installations.
- Road base and adjacent slopes strengthening by piling and anchoring.
- Subsurface drainage installations in uphill & downhill slopes.
- In-situ monitoring and warning system installation.

The above measures appear to be sound from an engineering standpoint. However, the total cost and time for all of the above works would be extremely high, in view of difficulties in access for construction and generally incompetent subsurface materials at the site. Another option would appear more favorable as to reroute the Mt. Ali Road away from this difficult section.

5 ACKNOWLEDGEMENTS

6 REFERENCES

China Engineering Consultants, Inc. (CECI). 2005. *Engineering planning and budget estimate for slope mitigation at Mileage 39Km, Mt. Ali Road, Taiwan*. The 5th District, DGH/DOT, Taiwan.

Department of Transportation (DOC). 1996. Taiwan Province Government. 1996. *Documentary of Typhoon Herb*.

Directorate General of Highway (DGH). Taiwan. 2005. *Emergency plan for mitigation of slope failure at Mileage 39Km, Mt. Ali Road due to Typhoon Talim*.

Land Engineering Consultants, Co. (LEC). 2006. *Report on land survey, subsurface exploration, and in-situ monitoring for slope failure at Mileage 39Km, Mt. Ali Road, Taiwan*.

Liu S.D. and Tseng J.J. 2000. *Investigation report on geology and landslides along Mt. Ali Road, Taiwan*. Central Geology Survey, MOE, Taiwan.

National Center for Researches on Earthquake Engineering (NCREE). 2000. *Investigation report on geotechnical engineering damages due to September 21, 1999, Chi-Chi Earthquake*. Taipei, Taiwan.

Peng K.Y. 2009. *A study on groundwater fluctuation and geology structure through rainfall and well pumping*. MS thesis, NYUST, Taiwan.

Sinica, Taiwan, ROC. 1999. http://webgis.sinica.edu.tw/epa/epa.html.

Downstream Frontal Velocity Reduction Resulting from Baffles

Effets des déflecteurs dans la réduction des vitesses frontales dans un écoulement descendant.

Choi C.E., Ng C.W.W.
Department of Civil and Environmental Engineering, Hong Kong University of Science and Technology

Kwan J.S.H., Shiu H.Y.K., Ho K.K.S., Koo R.C.H.
Geotechnical Engineering Office, Civil Engineering and Development Department, HKSAR

ABSTRACT: Debris flows occur in mountainous regions during rainfall and can result in disastrous consequences to downstream facilities if appropriate mitigation measures are not taken. Common mitigation measures include flow impeding structures within the flow path. An array of baffles is a type of flow impeding structure used primarily to reduce the mobility of landslide debris. However, they are usually designed on an empirical and prescriptive basis and the degree of impedance resulting from an array of debris flow baffles is not well understood. This paper presents a series of systematic flume tests examining the influence of baffle row number on reduction of debris frontal velocity. Photoconductive sensors installed at the base of the flume channel have been used to measure the average frontal velocity of the debris flow downstream of the array of baffles. Results show that one row is ineffective in reducing the debris frontal velocity. Two to three rows of baffles exhibit notable frontal velocity reduction.

RÉSUMÉ : Les coulées de granulaires représentent un risque majeur en régions montagneuses en période de fortes pluies et peuvent avoir des conséquences désastreuses pour les installations en aval si des mesures appropriées ne sont prises. De telles mesures comprennent la construction de déflecteurs à matériaux sur le parcours des coulées avec pour objectif principal est de réduire la mobilité de la masse granulaire en mouvement. Cependant, la construction de ces déflecteurs repose sur des hypothèses empiriques. La contribution exacte des déflecteur est mal comprise à l'heure actuelle et elle est difficile à évaluer précisément. Cet article présente une série de tests expérimentaux ayant pour objectif d'évaluer l'influence de l'augmentation du nombre de déflecteurs sur la réduction de la vitesse frontale de la coulée granulaire. Des capteurs photoconducteurs placés dans le fond du canal de test ont été utilisés pour mesurer la vitesse frontale moyenne des grains en aval des déflecteurs installées. Les résultats révèlent qu'au moins deux à trois rangées de déflecteurs sont nécessaires pour avoir une réduction significative de la vitesse frontale de l'écoulement.

KEYWORDS: physical modelling; flume; debris flow; baffles; landslide mitigation measures

1 INTRODUCTION

Ground mass detached from landslide source travels down hillside under gravitational actions. Landslide debris can have high mobility and can result in serious consequences to downstream facilities. Velocity of debris fronts can reach up to 30 m/s (Costa 1984; Rickenmann 1999) with peak discharges several times greater than floods occurring in the same catchment (Hungr et al. 1984). In order to mitigate this hazardous phenomenon, debris-resisting structures are often used as defence measures to retain landslide debris and impede debris mobility (Mizuyama 2008). Defence measures may include the rigid and flexible barriers (Wendeler et al. 2007), levees, slit dams (Watanabe et al. 1980), and arrays of baffles.

The primary function of baffles is to impede the flow pattern such that flow slows down after it passes through the baffles (USFHA 2006). Baffles can be installed upstream of barriers to reduce the impact resistance required by the barriers and to promote lateral dispersion of flow in deposition basins (Cosenza et al. 2006). Figure 1 shows rectangular gabion baffles installed in front of a rigid barrier in Lantau Island, Hong Kong. Baffles are usually designed by empirical and prescriptive methods and their fundamental impedance capacity is not well understood.

Similar studies on snow avalanche impeding obstacles report that an individual row of obstacles can dissipate energy by 20% and an additional row contributes to 10% extra energy dissipation (Hakanordottir et al. 2001). Salm (1987) reports that the degree of impedance can be estimated based on the consideration of the cross-sectional blockage over the channel area. However, the above criteria are applicable only for snow avalanches because the flow regimes characterising avalanche and debris flow are quite different (see Sect. 2.1 for further details). This study aims to examine the reduction of downstream debris frontal velocity resulting from an array of baffles. The influence of the number of staggered rows of baffles on downstream debris frontal velocity is investigated.

Figure 1. Array of baffles installed in front of a rigid barrier in Lantau Island, Hong Kong

2 METHODOLOGY

2.1 Scaling

Three types of similitude are required for modelling debris flow-baffle interaction; they are (i) geometric similarity, (ii) kinematic similarity, and (iii) dynamic similarity. For simplicity, geometric similarity is achieved by normalising

model dimension by the flume channel width and debris flow depth (more details presented in Sect. 3). Kinematic similarity describes the impedance resulting from baffle interaction which is unknown and constitutes the objective of this study. Dynamic similarity is attained by adopting the Froude number, F_r, which governs the behaviour of gravity-driven flows in open channels. The F_r number is the ratio of inertial forces to the gravitational forces and is given as follows:

$$F_r = \frac{v}{\sqrt{gh}}$$

$$(1)$$

where v = frontal velocity (m/s), g = gravitational acceleration (m/s^2), and h = debris flow depth (m).

Debris flow can be characterised with approaching F_r which ranges from 0 to 4.5 (Arrattano et al. 1997, Hubl et al. 2009) based on field observations. An $F_r \approx 3$ is adopted for characterising the approaching flow in this study. This corresponds to debris flow event with an approaching velocity of about 10 m/s and flow depth of about 1 m. Details of the scaling process and control test are discussed by Ng et al. (2012).

2.2 Flume model

Further to flume experimental studies of debris flow mechanisms (Law et al. 2008, Zhou et al. 2009) at the Hong Kong University of Science and Technology (HKUST), a new five metre long rectangular flume (see Figure 2) with a channel base width of 0.2 m and height of side walls of 0.5 m was developed for this study. Based on calibration exercises, an inclination angle of 26° is used (Ng et al. 2012) to match an $F_r \approx 3$. Instrumentation and lighting are mounted on the external frame surrounding the flume. Debris material is contained in a storage container located at the most upstream end of the flume. The storage container has a maximum storage volume of 0.08 m^3 and is equipped with a spring-loaded door secured by a magnetic lock. At the most downstream end of the flume is a deposition container for collecting debris materials.

2.3 Instrumentation

Ten photoconductive sensors are installed throughout the base of the flume at intervals of 0.5 m. When debris passes over the sensor, a signal is sent to the data logger at that particular instant. With the known spacing and difference in time at which signals are received between two sensors, the average debris frontal velocity can be deduced along the entire transportation zone. The uncertainty of photoconductive sensors is estimated to be ± 0.05 m/s.

Laser sensors are mounted over the top of the channel to capture centreline flow depths at specific locations along the flume. Furthermore, high speed cameras are installed above and at the side of the flume to capture the flow dynamics during interaction with the array of baffles. The full resolution capacity of the cameras is 1024 × 1024 pixels and with a potential frequency of 759 frames per second.

3 TEST PROGRAMME

A series of four flume experiments are presented in this paper. The details of experiments are given in Table 1. The four experiments consist of one control experiment without baffles in the channel to serve as reference and the three baffle configurations which vary in number of staggered rows (one to three rows). All experiments have been repeated to ensure repeatability. For simplicity, a single baffle height of 0.75 times the approach debris flow depth (h = 80 mm) is adopted for all configurations. Details on the approach debris flow depth are discussed by Ng et al. (2012). The degree of transverse

blockage is selected as 30% in this study. The degree of transverse blockage is defined as the sum of obstruction in the transverse direction divided by the width of the flume channel. According to Ikeya and Uehara (1980) and Watanabe et al. (1980), slit dams function primarily to retain flow material through the mechanism of arching, while baffles primarily impeded the flow mobility. Slit dams entail an equivalent degree of transverse blockage of greater than 40%, therefore the degree of transverse blockage selected in this study (i.e. 30%) is appropriate for modelling debris flow baffles.
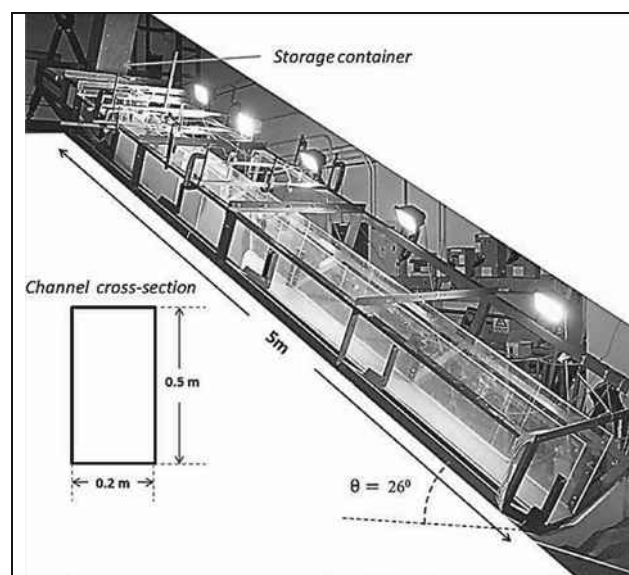

Figure 2. Flume model setup

Table 1. Test programme

Test ID	Baffle height (h)	Transverse blockage (%)	Number of rows
H0_R1	0	0	0
H075_R1	0.75h	30	1
H075_R2	0.75h	30	2
H075_R3	0.75h	30	3

h: approach flow depth (80 mm)

The arrangement of full and half sized baffles used to create a staggered formation as shown in Fig. 3. The dimensions of full baffles are 20 mm × 20 mm × 60 mm, and the dimensions of half baffles are 20 mm × 10 mm × 60 mm. The spacing between successive rows is selected to be 50 mm or 0.25 times the width of the flume channel. This spacing is selected based on recommendations by Hakonardottir et al. (2001) that baffles should be placed as close together as possible to promote the deflection and interception of discharge from the slits of the previous row.

4 EXPERIMENTAL RESULTS

5.1 Flow dynamics

As a flow front impacts an array of baffles, streams of debris material discharge through the slits and part of debris also runs up along the upstream vertical face of the baffles simultaneously. The debris run up eventually exceeds the baffle height and some materials become airborne. Synchronously, material is deposited upstream of the baffles. The upstream flow eventually rides over the deposited material and cascades over the array of baffles. There are essentially two components of downstream discharge, namely discharge through and overtop of the baffles, both of which combine and propagate downslope after the landing of overflow trajectory.
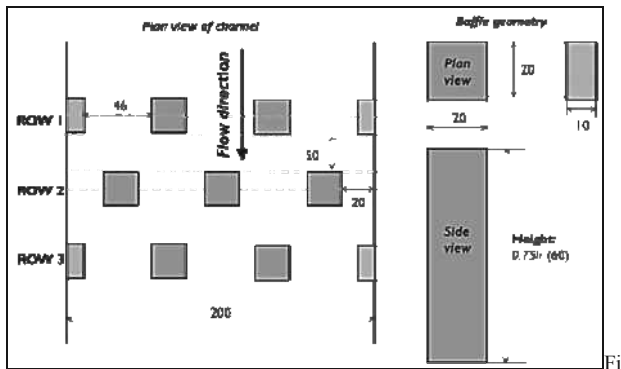
Figure 3. Baffle arrangement and dimensions (all dimensions in mm)

5.2 Frontal velocity

The measured debris frontal velocity profiles of different tests are compared and shown in Fig. 4. The measured debris frontal velocity is plotted against normalised distance travelled along the transportation zone (N_d), which is the ratio of distance travelled by the debris front along the 5 meter flume. The debris flow direction is from left to right on x-axis and the location of the baffles along the transportation zone is shown as a vertical dashed line.

The frontal debris velocity profile of the control test (H0_R0) is shown as a reference for comparison purposes. The debris frontal velocity of the control test rapidly increases upon release from the storage container. At $N_d = 0.2$, a steady debris flow profile develops, beyond $N_d = 0.6$, the debris frontal velocity begins to decrease. A similar debris velocity profile is observed in the experiment of one-row baffle test (H075_R1). However, for the two-row and three-row baffle tests, a prominent debris velocity reduction at the immediate downstream of the baffle groups was observed. The velocity profile rapidly decreases to less than 2 m/s after which it gradually increases beyond $N_d = 0.3$.

Results show that one row of baffles (H075_R1) exhibits negligible reduction in frontal debris velocity and the propagation of the front is similar to unobstructed flow (H0_R0). Obvious reduction in debris frontal velocity is observed in the test with two rows of baffles (H075_R2) at the location immediately downstream of the baffle group. This may be attributed to the second row of staggered baffles intercepting the discharge from the slits of the first row which dissipates energy by disrupting streamlines of the flow (USFHA 2006). The provision of an additional row of baffles (i.e. the third row; test H075_R3 refers) exhibits a frontal debris velocity reduction of 47% at $N_d = 0.3$ relative to the control experiment, whereas two rows of baffles (H075_R2) only exhibits 30% reduction of frontal debris velocity relative to the control experiment at $N_d = 0.3$. Moreover, the higher frontal velocity reduction may be attributed to an additional third row of baffles which intercepts discharge from the second row and disrupts streamlines. Beyond $N_d = 0.4$, two rows (H075_R2) and three rows (H075_R3) baffle groups exhibit a similar gradual increase in frontal debris velocities. An increase in frontal debris velocities may be attributed to subsequent excessive overflow of material due to the use of shorter baffles (0.75 times the approach flow depth) in this study. Overflow of debris in test H075_R1 is captured from high speed imagery at the side of the flume model and is shown in Fig. 5. Overflow does not experience impedance and launches downstream (Barbolini et al. 2009) to increase the momentum and thus the frontal velocity of the flow. Overflow is hazardous particularly in situations where its trajectory is not easily predicted. Johannesson (2001) surveyed a torrent which had been deflected by a dam at Flateyri in north-western Iceland and observed that the deflected stream came to rest 100 m further downslope than the un-deflected part. The mechanism of overflow appears to be significant and results from this study require further interpretation.
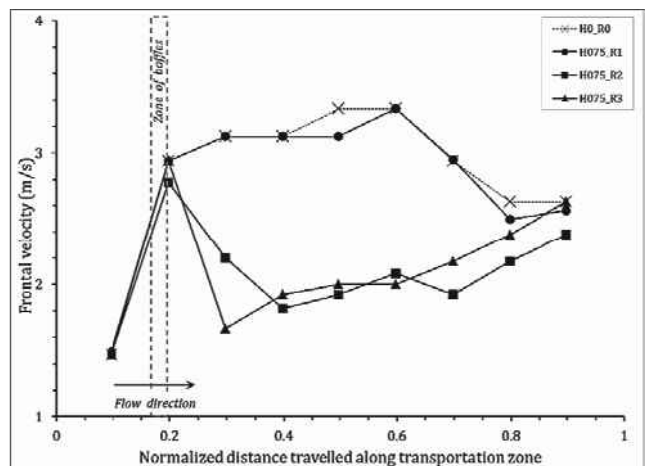

Figure 4. Comparison of measured frontal velocity
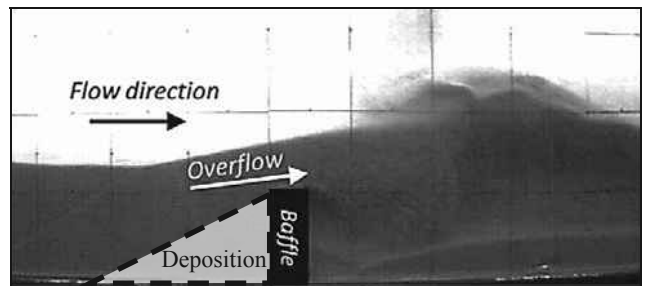
Figure 5. Observed overflow dynamics (test H075_R1)

5.3 Preliminary Particle Image Velocimetry (PIV) analysis

A preliminary Particle Image Velocimetry (PIV) analysis has been carried out to investigate the flow dynamics and quantify the flow velocity by interpreting the results of the flume test using the Particle Image Velocimetry package (geoPIV) developed by White et al (2003). This package is developed based on close-range photogrammetry techniques capable of tracing movements of soil grains captured in high-resolution images. It produces displacement and velocity vectors of the soil grains.

Typical flume test results for three rows of baffles produced by geoPIV are presented in Figure 6. It shows the flow dynamics of the debris upon hitting the baffles. Details of debris run-up against baffles, deposition behind baffles and filling up of the baffle zone and the subsequent overflowing from the crest of baffles were captured. In general, the preliminary results of the calculated velocity vectors by PIV method are consistent with the measured debris frontal velocity by the instrumented photo-sensors. Further PIV analysis will be carried out in the next stage of interpretation of the experimental study.

2167

Figure 6. Preliminary results using PIV method

5 CONCLUSIONS

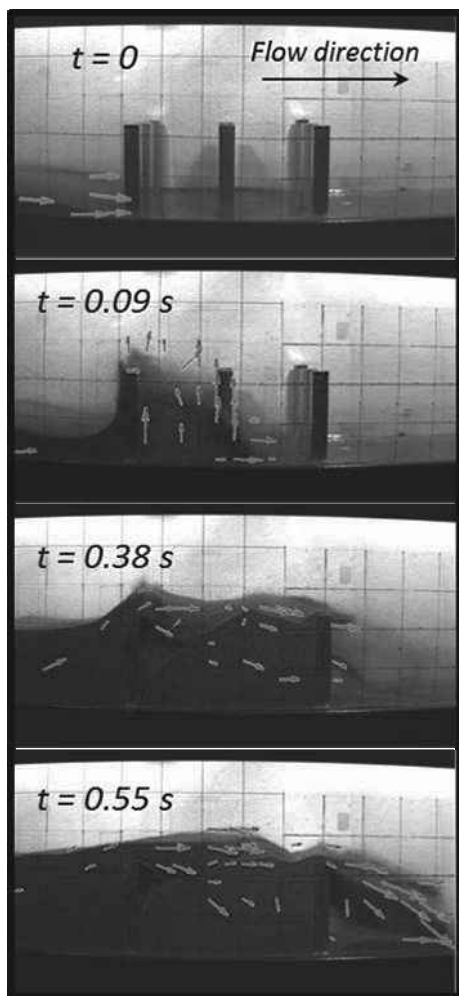A series of systematic flume experiments modelling debris-baffle interaction has been conducted. The influence of increasing the row number on frontal debris velocity is presented and some preliminary conclusions are drawn as follows:

1. One row of baffles exhibits negligible reduction of frontal debris velocity compared to unobstructed channelised flow.
2. Two and three rows of baffles result in reduction of frontal debris velocities immediately at the downstream from the array of baffles. Increasing the number of staggered rows of baffles disrupts streamlines and intercepts discharge from slits of the previous row of baffles which dissipates energy and reduces the frontal debris velocity.
3. Overflow resulting from the use of baffles may result in subsequent increase in frontal velocity downstream and warrants further studies.

6 ACKNOWLEDGEMENTS

7 REFERENCES

Arattano, M., Deganutti, A. M. and Marchi, L. 1997. Debris flow monitoring activities in an instrumented watershed on the Italian Alps. *Proceedings of the 1st ASCE International Conference on Debris-Flow Hazards Mitigation: Mechanics, Prediction and Assessment*, San Francisco, California, 506-515.

Barbolini, M, Domaas, U., Faug, T., Gauer, P., Hakonardottir, K.M., Harbitz, C.B., Issler, D., Johannesson, T., Lied, K., Naaim, M., Naaim Bouvet, F. and Rammer, L. 2009. *The design of avalanche protection dams recent practical and theoretical developments*. European Commission, Luxembourg. 212 p.

Cosenza, E., Cozzolino, L., Pianese, D., Fabbrocino, G., and Acanfora, M. 2006. Concrete structures for mitigation of debris-flow hazard in the Montoro Inferiore Area, Southern Italy. *Proceedings of 2nd International Congress,* Naples, Italy, 12 p.

Costa, J.E., 1984. Physical geomorphology of debris flows. *Costa. J.E.; Fleischer. P.J. (eds.): Developments and Applications of Geomorphology*. Berlin: Springer, 268-317.

Hákonardóttir, K. M., Jóhannesson, T., Tiefenbacher, F. and Kern, M. 2001. *A laboratory Study of the Retarding Effect of Braking Mounds in 3, 6 and 9m Long Chutes*, Reykjavík, Veðurstofa Íslands, Report No. 01007.

Hubl, J., Suda, J., Proske, D., Kaitna, R. and Scheidl, C. 2009. Debris flow impact estimation. *Proceedings of International Symposium on Water Management and Hydraulic Engineering*, Ohrid, Macedonia, 137-148.

Hungr, O., Morgan, G.C. and Kellerhals. 1984. Quantitative analysis of debris flow torrent hazards for design of remedial measures. *Can. Geotechnical Journal,* 21, 663-677.

Ikeya, H. and Uehara, S. 1980. Experimental study about the sediment control of slit sabo dams. *Journal of the Japan Erosion Control Engineering Society,* 114, 37-44 (in Japanese).

Johannesson, T. 2001. Run-up of two avalanches on the deflecting dams at Flateyri, northwestern Iceland. *Annals of Glaciology,* 32(1), 350-354.

Law, R.P.H., Zhou, G.D., Chan, Y.M. and Ng, C.W.W. 2007. Investigations of fundamental mechnisms of dry granular debris flow. *Proceedings of the 16th Southeast Asia Geotechnical Conference*, Malaysia.

Law, P.H. 2008. *Investigations of Mobility and Impact Behaviour of Granular Fows*. MPhil Thesis, The Hong Kong University of Science and Technology, Hong Kong.

Mizuyama, T. 2008. Structural countermeasures for debris flow disasters. *International Journal of Erosion Control Engineering* 1(2), 38-43.

Ng, C.W.W., Choi, C.E., Kwan, J.H.S, Ho, K.S.S and Koo, R.C.H. 2012. Flume modelling of debris resisting baffles. *Proceedings of AGS Seminar on Natural Terrain Hazard Mitigation Measures 2012*, Hong Kong, 16-21.

Rickenmann. D. 1999. Empirical relationships for debris flows. *Natural Hazards,* 19(1), 47-77.

Salm, B. 1987. Schnee, Lawinen und Lawinenschutz. Vorlesungsskript, 273 p. ETH Zurich

Teufelsbauer, H., Wang, Y., Pudasaini, S.P., Borja, R.I. and Wu, W. 2011. DEM simulation of impact force exerted by granular flow on rigid structures. *Acta Geotechnica*: 10.1007/s11440-011-0140-9.

United States Federal Highway Administration. 2006. *Hydraulic Design of Energy Dissipaters for Culverts and Channels*, Hydraulic Engineering Circular No. 14. Publication No. FHWA-NHI-06-086, 286 p.

Watanbe, M., Mizuyama, T, and Uehara, S. 1980. Review of debris flow countermeasure facilities. *Journal of the Japan Erosion Control Engineering Society,* 115, 40-45 (in Japanese).

Wendeler, C., Volkwein. A., Denk. M., Roth A. and Wartmann S. 2007. Field measurements used for numerical modeling of flexible debris flow barriers. *4th DFHM Conference*. Chengdu.

White, D.J., Take, W.A. & Bolton, M.D. (2003). Soil Deformation Measurement using Particle Image Velocimetry (PIV) and Photogrammetry. *Geotechnique*, 53, 619-631.

Zhou, G.D., Law, R.P.H. and Ng, C.W.W. 2009. The mechanisms of debris flow: a preliminary study. *Proceedings of the 17th ICSMGE*, Alexandria, Egypt. 2, 1570-1573.

GPS instrumentation and remote sensing study of slow moving landslides in the eastern San Francisco Bay hills, California, USA

Instrumentation GPS et télédétection de glissements de terrains lents dans les collines est de la Baie de San Francisco, Californie, USA

Cohen-Waeber J., Sitar N.
University of California Berkeley, Civil and Environmental Engineering

Bürgmann R.
University of California Berkeley, Earth and Planetary Science

ABSTRACT: Active slow moving landslides in the East Bay Hills, San Francisco, California, have been the object of many investigations over recent decades, though their mechanisms are still poorly understood. Contemporary geodetic technologies, such as continuous Global Positioning Systems (GPS) and Interferometric Synthetic Aperture Radar (InSAR), allow for remote detection and characterization of ground surface displacements with sub-centimeter precision and accuracy. This project combines GPS and InSAR time series analyses for the characterization of spatial and temporal landslide deformation as a result of static and dynamic forces. Several independent InSAR time series analyses show accelerated landslide surface deformation as an effect of precipitation, though not in relation to recent seismic activity. Additionally, recent advances in InSAR analysis methods allow the observation of intra-slide deformation patterns. Since the implementation of a comprehensive continuous GPS network in January 2012, landslide related surface displacements have also been recorded in response to precipitation. Both InSAR and GPS studies not only confirm strong correlation and sensitivity to periods of precipitation but downslope sliding velocities of around 30 mm/year as well.

RÉSUMÉ : Bien que leurs mécanismes soient encore mal compris, des glissements de terrains lents dans les collines Est de la baie de San Francisco, Californie, font depuis plusieurs décennies l'objet de nombreuses recherches. Les technologies géodésiques d'aujourd'hui comme le GPS continu et l'InSAR, permettent la télédétection et la caractérisation de déplacements de la surface terrestre avec précision et exactitude millimétrique. Ce projet a donc pour but de caractériser les déformations spatio-temporelles de la surface terrestre, liés aux glissements de terrains sous effets statiques et dynamiques, par l'application de ces outils géodésiques. Plusieurs analyses indépendantes de séries chronologiques InSAR montrent une accélération superficielle de ces glissements sous l'effet de précipitation mais pas sous l'effet d'activité sismique. D'avantage, de récents progrès des méthodes analytiques d'InSAR permettent l'étude des modes de déformation intra-glissements. La mise en place d'un réseau GPS en Janvier 2012, montre aussi une accélération des glissements sous l'effet de précipitation. Ces deux méthodes confirment non seulement une sensibilité aux périodes de précipitation, mais aussi une vitesse approximative de 30 mm/an.

KEYWORDS: Landslides, creep, GPS, InSAR.

1 INTRODUCTION

Recent advances in geodetic technologies allow for remote data collection and the analysis of spatial and temporal ground surface deformation at a scale that was previously not possible. Technologies such as continuous GPS and Interferometric Synthetic Aperture Radar (InSAR) are capable of measuring active surface displacement with as much as sub-centimeter precision and accuracy. This clearly lends itself to the characterization of active slow moving landslides. Furthermore, the urgency for improved efficiency of primary geologic and geotechnical site investigations stresses that these methods be incorporated in the current state of practice.

Active landsliding across the Lawrence Berkeley National Laboratory (LBNL) site and the East Bay Hills, California, has been the object of many investigations over recent decades. Though studies suggest a trend in landslide mobility is associated with regional climate and active tectonic conditions in addition to the local geologic setting, the mechanisms of these currently slow moving slides are still poorly understood. Thus, the objective of this study is to characterize slope deformation as a result of static and dynamic forces by a careful observational program using the most current geodetic technologies. The intent is to help develop a method for the remote determination and evaluation of landslide hazards and their eventual risk assessment.

This monitoring program includes the instrumentation of individual landslides with a comprehensive network of permanent, continuously streaming GPS stations, and regional monitoring of slope surface deformation by InSAR time series analysis. To date, historical InSAR and recent GPS observations confirm similar downslope sliding velocities as an effect of precipitation, though not in relation to seismic activity. A closer review of InSAR time series also reveals a pattern of intra-slide surface deformation and important insight on internal slide mechanisms. This is a presentation of preliminary GPS findings and an observation of InSAR time series analyses.

2 GEOLOGIC SETTING

The study area for this project is located along the western flank of the Berkeley Hills, east of the San Francisco Bay, California. The local geology is the product of an approximately 360 million year old accretionary process during which the North American Plate margin transitioned from subduction of the Farallon Plate to a transform boundary against the Pacific Plate. Hence, several orogenies and accreted terranes are responsible for a wide variety of metamorphic, volcanic and sedimentary formations in this relatively small area known as the California Coast Range geomorphic province, characterized by a northwest trending and low lying mountain range.

As part of the California Coast Range geomorphic province, the Berkeley Hills are an uplifted block of Jurassic to Tertiary sedimentary, volcanic and metamorphic rocks bound by the Hayward and Calaveras faults and folded in a northwest trending synclinal form during regional transpression related to the active plate margin 1-2 million years ago. Now largely

overlain by Quaternary colluvial and alluvial deposits, this highly fractured, intensely weathered, moderately soft rock is prone to landsliding.

In addition to the geologic setting, studies suggest that Berkeley Hills landslide mobility is driven by precipitation and regional active tectonic conditions (Alan Kropp and Associates 2002, Hilley et al. 2004, Quigley et al. 2010). Local orographic precipitation forms a wet microclimate and the close proximity to active fault traces within the San Andreas Fault zone brings strong seismicity. Today, several hundred landslide-related geologic and geotechnical investigation reports are available for LBNL and the Berkeley Hills alone, and form a solid background to this project.

3 METHODOLOGY

Two state of the art geodetic sensing technologies form the primary modes of data acquisition in this project: high rate, continuously streaming, GPS and InSAR. While these methods have individually been shown capable of measuring active ground surface displacement at scales that were previously not possible; the appropriate characterization of landslide related slope movement benefits from the application of both.

Where continuous GPS provides three dimensional ground surface displacement measurements with millimeter scale accuracy and precision at full temporal resolution, the spatial distribution of measurement points is sparse. On the other hand, InSAR time series analysis produces improved spatial averages at decameter resolution with sub-centimeter precision, and the inclusion of datasets spanning several decades of observations. These methods are complimentary using deformation detected across a GPS network to calibrate that measured using InSAR.

The objective is thus to accurately measure landslide slope deformation over time. Combining these methods allows for spatial and temporal analysis of ground surface displacements due to landsliding in relation to local precipitation and ground shaking events. By incorporating these surface observations with previous investigations and monitoring, the landslide mechanisms can then be modeled.

3.1 GPS Data Acquisition

The first phase of this project has been to establish a network of continuously streaming GPS stations to track landslide related ground surface displacement over time. This involves the instrumentation of individual landslides with autonomous, continuously streaming GPS stations, as well as several permanent reference stations. Each landslide station has been specifically designed for permanent, stand-alone installation and built to capture landslide displacement at depth. Anchored on a deep seated reinforced concrete foundation to limit the effects of surficial disturbance, the stations are solar powered and equipped with a wireless antenna for remote access. Reference station locations are chosen on the basis of proximity to the "mobile" devices and being seated on immobile ground.

Since January 2012, 5 such "mobile" stations have been successfully installed at LBNL and one at the University of California Blake Garden on the Blakemont Landslide. One reference station has been established at the Lawrence Hall of Science above LBNL. Average daily solutions are being obtained for each station based on a 1Hz data set, and a 25Hz buffer is held for displacement-time histories in the case of seismic activity. Three additional sites are in the process of being developed.

3.2 InSAR Time Series

InSAR time series are a record of change in radar signal return phase over time, reflecting the change in distance between the ground surface and a satellite based radar platform (or range-change). The strength of the return signal for each radar pulse is dependent of the physical properties of the target (or scatterer). Where distinct structures will return a persistent strong signal, less prominent surfaces will return lower intensity distributed signals and noise. Among others, two types of InSAR time series analyses are thus known as Permanent or Distributed Scatterer methods (respectively).

With the concurrent development of the GPS network, analysis of InSAR time series has also begun, though is not presented here in detail. Rather, a brief review of prior results is described with observations based on TerraSAR-X satellite data processed with the Tele-Rilevamento Europa (TRE) SqueeSAR^{TM} algorithm (Ferretti et al. 2011, Giannico et al. 2011).

4 PRIOR GEODETIC RESULTS

The use of InSAR time series analysis has been shown to successfully track landslide related ground surface displacement in the Berkeley Hills area using data sets from different satellites over several time periods between 1992 and 2011 (Hilley et al. 2004, Quigley et al. 2010, Giannico et al. 2011). In each case, analysis of Permanent and/or Distributed Scatterers over the period of interest clearly exhibit accelerated rates of displacement related to periods of high precipitation. Though no such relationship could be established with local seismicity, it is considered to be likely that large earthquakes can accelerate landslide motion. Furthermore, one attempt at the use of Continuous GPS to track landslide motion was also of no avail (Quigley et al. 2010).

4.1 1992-2007 Time Series of ERS and RADARSAT

In the InSAR time series analysis of Permanent Scatterers performed by Hilley et al. (2004), known landslides across the Berkeley Hills were successfully detected and tracked from 1992 to 2001 using ERS-1 and ERS-2 data acquisitions. Over this period, these data indicate landslide related surface displacement rates varied between 5 to 7 mm/year range-change in the radar line of sight direction. Based on local average slope inclinations, this implies equivalent downslope velocities of 27 to 38 mm/year and has been verified in the field by subsurface inclinometer displacement measurements of approximately 33 mm/year (Allan Kropp and Associates 2002). Hilley et al. (2004) also observed that periods of landslide acceleration were closely related to seasonal precipitation, though non-linear in that precipitation related displacement did not occur immediately, with lag times of up to 3 months, and did not predictably increase with larger events. Additionally, Hilley et al. (2004) suggest the potential for seismic related landslide displacement given a $M_w \approx 3.9$ Hayward fault event on December 4, 1998. Though the temporal resolution of the time series could not directly document seismically triggered deformation, unexpectedly high InSAR displacement measurements were observed relative to the amount of precipitation during the same period.

Similarly, Quigley et al. (2010) examine seasonal precipitation-related displacement, supplementing the same ERS data set with RADARSAT-1 acquisitions from 2001 to 2006. Landslide displacement was shown not only to be of same magnitude, but clearly seasonal and sensitive to variations in rainfall patterns. Detrended and stacked (by month) observations plotted against average monthly precipitation exhibited a clear 1 to 3 month displacement response lag time and a positive correlation to the intensity of precipitation.

4.2 2007-2009 Continuous GPS Tracking.

Quigley et al. (2010) used Continuous GPS at one known active landslide location to track surficial displacements between 2007 and 2009. Though InSAR time series (Hilley et

al. 2004) and local inclinometer data (Quigley et al. 2010) clearly illustrated slide activity in the years before the station's installation, the GPS monitoring did not. This was likely due to a particularly dry period and the station was disassembled before an adequate data set could be collected to observe long term landslide behaviors.

5   RECENT INSAR TIME SERIES OBSERVATIONS

While the Permanent Scatterer InSAR method uses stable coherent targets as shown in the examples above, it is also limited by their presence. To increase the number of observed scatterers and improve time series resolution, the new proprietary algorithm (SqueeSAR™) developed by TRE (Ferreti et al. 2011), utilizes both the Permanent and Distributed Scatterer methods. Thus, a third InSAR time series analysis was performed over the Berkeley Hills by Giannico et al. (2011) applying the SqueeSAR[TM] method to TerraSAR-X data acquisitions from 2009-2011.

As observed in the 1992-2007 InSAR time series analyses (Hilley et al. 2004, Quigley et al. 2010), landslide related displacements were clearly identifiable with velocities averaging between 6 and 8 mm/year range-change and with periods of precipitation-related acceleration. Figures 1 and 2 show the location and average displacement time histories for different areas (top, middle and bottom) within the Blakemont Landslide (respectively), plotted against cumulative precipitation over the period of observation.

Located at the northern-most end of the study area, field investigations have described the Blakemont Landslide as an approximately 915-m-long, 215-m-wide translational soil and rock landslide with nested rotational failures, and an active sliding depth of 8 to 20 m (Alan Kropp and Associates 2002). While the entire slide appears to be moving coherently downslope (increasing range-change displacement from the descending orbit acquisition), clear accelerations occur in early 2010 and early 2011, some 3 months after the onset of each wet season. Furthermore, the landslide exhibits a positive correlation between displacement and intensity of precipitation with smooth variations during a more gradual 2009-2010 wet season, in comparison to abrupt accelerations during a higher intensity 2010-2011 season.

An important advantage of the higher spatial resolution afforded by the TRE SqueeSAR[TM] method is a better understanding of landslide mechanisms as expressed at the ground surface. A closer look at the downslope displacements of different areas within the Blakemont Landslide (Figure 2) reveals that it is in fact not moving as one coherent mass, rather with what physicists would call an "accordion effect". Differencing the average downslope displacements of each of the highlighted areas from top to bottom of the landslide, a pattern of apparent landslide shortening (positive) and extension (negative) becomes evident (Figure 3). Here the largest differential displacement variations are observed between the top and bottom areas of the landslide. During wet seasons, the difference in displacement between top and bottom of the landslide increases as the lower portions of the slide accelerate earlier than the upper portions. The same can be said for the opposite case during dry periods, when the difference in displacement between the top and bottom of the landslide decreases as the lower portions of the landslide slow and the upper portions catch up. Naturally, as this currently short dataset is augmented, it is the authors' hope to observe similar trends over longer time periods.
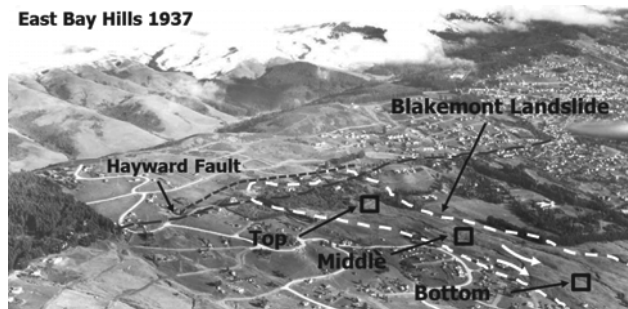

Figure 1. 1937 Oblique view of Blakemont landslide showing location of approximate highlighted areas in TerraSAR-X InSAR study.
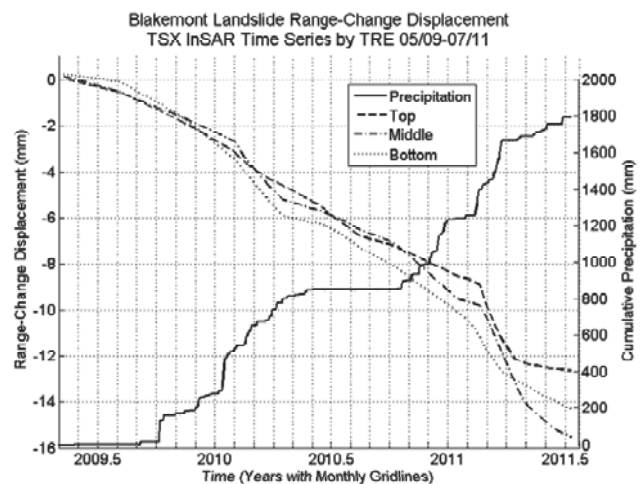
Figure 2. TRE SqueeSAR[TM] analysis of TerraSAR-X data acquisitions (2009-2011), illustrating average downslope (negative) range-change displacement (left axis) in top, middle and bottom areas of Blakemont Landslide versus cumulative precipitation (right axis).
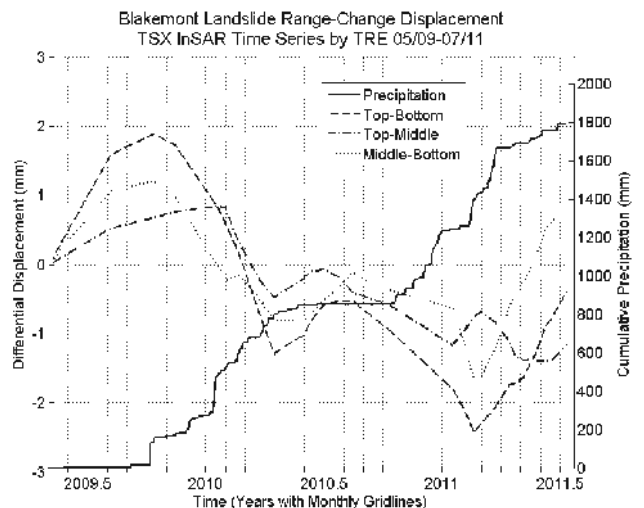
Figure 3.   Differential of average downslope displacements (left axis) from TRE SqueeSAR[TM] analysis of TerraSAR-X acquisitions (2009-2011) between highlighted areas of the Blakemont Landslide, from top to bottom, plotted against cumulative precipitation (right axis).

6   PRELIMINARY GPS RESULTS

Daily solutions from the first 6 continuously streaming GPS stations have been recorded since their installation in January 2012. Highlighted here are stations "LRA 1-3" located on the same landslide in Chicken Canyon at LBNL, as depicted in the 1935 air photo (Figure 4). While historical ground surface displacement related to this landslide has yet to be characterized and quantified, extensive field investigations have described it

as an approximately 230-m-long, 75-m-wide and 24-m-deep translational soil and rock landslide with nested rotational failures (Alan Kropp and Associates 2009).

Already, a clear signal at each of these 3 stations is apparent, showing down-slope displacements of up to 3 cm which occurred directly related to local precipitation. As an example, Figure 5 illustrates the time history of daily solutions for station LRA 2 from January through October 2012, plotted against cumulative rainfall. To remove tectonic related displacements and measure actual displacement of the station, daily solutions for the station's North and East baselines are taken with respect to a fixed station (P224) several kilometers to the South. As such, LRA-2 clearly exhibits long term down-slope displacement to the southwest, accelerating during large rainfall events. Also indicated in Figure 5 is the time of the March 5, 2012 M_w = 4.0 Hayward fault earthquake with epicenter in El Cerrito, CA, approximately 10 km north of the site. While no clear seismically driven permanent slope displacements can be discerned, this may be due to the "dry" state of the landslide as well as the event's size and distance.
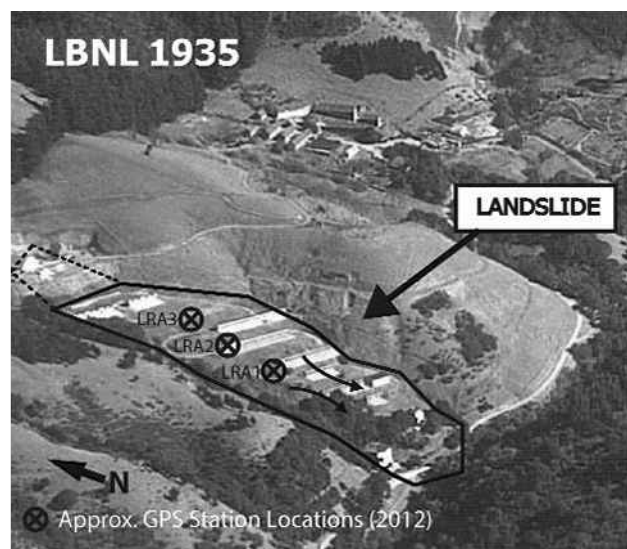

Figure 4. 1935 Oblique view of LBNL landslide with current GPS station locations.
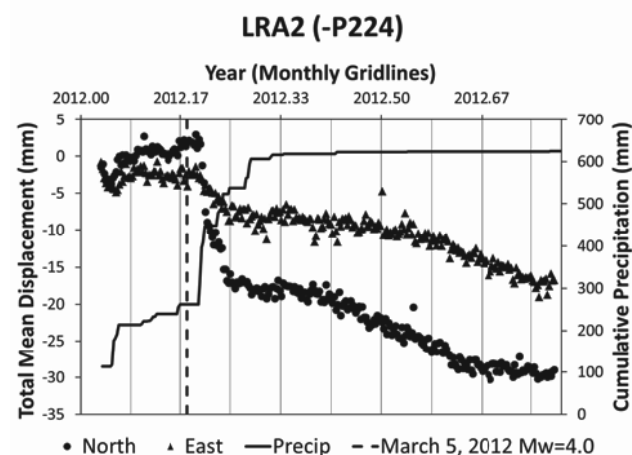

Figure 5. GPS position time series of station LRA 2 with respect to reference station P224. North (circles) and east (triangles) components of relative displacement with respect to reference site P224 are show together with cumulative precipitation (solid line) and time of M_w = 4 earthquake (dashed line).

7 CONCLUSION

A review of three independent InSAR time series analyses of the Berkeley Hills, from separate satellite acquisitions and over different time intervals from 1992-2011 shows remarkable consistency. In each case, similar mean landslide velocities were estimated, and precipitation dependent displacement behavior was observed. Though we were not able to document any motions induced by recent moderate earthquakes in the region, improved spatial resolution has allowed us to draw preliminary conclusions on the mechanics of displacement within one landslide. Further insight is expected as the quality of analysis improves and larger datasets are acquired.

After a mild wet season, the GPS instrumentation of several landslides in the Berkeley Hills, has recorded well-defined precipitation triggered slope movement. In contrast, the occurrence of a nearby M_w = 4 earthquake did not appear to have produced a measurable effect. Overall, the system has already demonstrated its capability to record landslide motions that otherwise would not have been observed with such level of detail and it continues to function and collect new data.

While both methods of observation presented here have not yet been directly compared, they do exhibit similar trends. In both cases, records of landslide related surface displacement have comparable down-slope velocities, increased with periods of precipitation and varied with its intensity. Observations over longer periods will provide important insight on the triggering mechanisms and internal landslide behavior we have described.

8 ACKNOWLEDGEMENTS

9 REFERENCES

Alan Kropp and Associates 2002. Blakemont Area Geologic Study, El Cerrito and Kensington CA. *Report*. Berkeley. CA.

Alan Kropp and Associates 2009. Geologic and Geotechnical Investigation Report, Helios Energy Research Facility, University of California Berkeley, Berkeley CA. *Report*. Berkeley. CA.

Ferretti A., Fumagalli A., Novali F., Prati C., Rocca F., Rucci A. 2011. A New Algorithm for Processing Interferometric Data-Stacks: SqueeSAR. *IEEE Geoscience and Remote Sensing* 49(9), 3460-3470.

Giannico C. and Ferretti A. 2011. SqueeSAR™ Analysis Area: Berkeley. *Processing Report*. Tele-Rilevamento Europa, Milano, IT.

Hilley G.E., Bürgmann R., Ferretti A., Novali F. and Rocca F. 2004. Dynamics of Slow Moving Landslides From Permanent Scatterer Analysis. *Science* 304, 1952-1955.

Quigley K. C., Bürgmann R., Giannico C. and Novali F. 2010. Seasonal Acceleration and Structure of Slow Moving Landslides in the Berkeley Hills. Proceedings of the Third Conference on Earthquake Hazards in the Eastern San Francisco Bay Area; edited by Keith Knudsen. *California Geological Survey Special Report 219*, 169-178.

Geotechnical Characterization, Stability Analysis, and the Stabilization Process for a Landslide in a area of Barreiras Formation and Granite Residual Soils, Pernambuco

Caractérisation géotechnique, analyse de la stabilité et procédés de stabilisation pour un glissement de terrain dans des matériaux du type « Barreiras Formation » et sols de granite résiduel, Pernambuco

Coutinho R.Q.
Federal University of Pernambuco, Brazil

Silva da M.M.
Federal Educational Institute of Pernambuco, Brazil

ABSTRACT: A large number of Brazilians live in conditions that involve elevated risk for landslides. Both technical and social problems are involved. This study presents results of a research project involving technical support for the Municipal administration of the City of Camaragibe - PE. An important landslide occurred in an occupied area after a period of intense rainfall, causing considerable losses for the local population. Three years later, another period of intense rainfall exacerbated the problem, causing cracks to develop in the walls and foundations of many houses, and broadening the area initially affected. An important program involving investigation that included field and laboratory activities, instrumentation, and stability and flow analysis was carried out. The results produced were considered to be very satisfactory, and they were able to point out the main causal factors, along with the mechanisms involving the landslide, which could then be better understood, and thoroughly studied. Afterwards, a proposal for stabilization for the entire area was elaborated, aiming to significantly reduce the risk levels by means of superficial and sub-superficial drainage, geometric modifications, placement of structures for stabilization of the land, and other activities.

RÉSUMÉ : Un grand nombre de brésiliens vivent dans des zones à risque d'un point de vue des glissements de terrain. Cela engendre des problèmes aussi bien techniques que sociétaux. Les travaux présentés dans cet article découlent d'un projet de recherche financé par l'administration municipale de la ville de Camaragibe – PE. Suite à un épisode pluvieux très important, un glissement de terrain s'est produit et a causé des dégâts considérables pour la population locale. Trois années plus tard, un nouvel épisode pluvieux a aggravé la situation et de nombreux ouvrages furent endommagés (murs de soutènement, fondations de maisons, …). Un programme d'investigation important fût alors mis en place : instrumentation sur site, analyses de stabilité et d'écoulement. On présente dans cet article une synthèse des résultats obtenus ainsi que les mécanismes aux origines des instabilités. Pour finir, une solution de stabilisation du site est proposé, avec pour but de réduire significativement le niveau de risque (drainage, modification géométrique de la pente et mise en œuvre d'ouvrages de stabilisation).

KEYWORDS: geotechnical characterization, slope stability, stabilization process.

1 INTRODUCTION

This paper presents study results from a research project, including details involving technical support supplied to the Municipal administration of the City of Camaragibe – PE, Brazil. The area investigated is located in the Township of Camaragibe, belonging to the western portion of the Recife Metropolitan Region. The landslide that occurred was classified as a multiple rotational landslide, characterized by the appearance of various steps along its slope. Geological characteristics of the area studied define an unsaturated granite residual soil that is partially covered by the Barreiras Formation. The residual soil of granite is found throughout the entire city. In some places, the granite rock mass is exposed.

In the Recife Metropolitan Region, it is common to find crystalline based rocks (Granite-Gneissic complex) covered by granite residual soils that originate from a crystalline structure; and by sediments from the Barreiras Formation. The crystalline base is formed by ancient intrusive rocks (1.5 to 21 billion years) belonging to the Pernambuco – Alagoas Massif.   It presents at least four phases of deformation, the latter of which, associated to the faults deformed, resulted in the formation of the "Pernambuco Lineamento".

The results presented here refer to a synthesis of the program of geotechnical characterization (field and laboratory testing, along with instrumentation), flow and stability analysis, and proposals for stabilization of the area in an attempt to significantly reduce the level of risk. This study aims to give continuity to a research project by the GEGEP – DEC / UFPE, with support from the CNPq/FACEPE, designed to comprehend and elaborate mechanisms involving instability of slopes, and providing manners in which stabilization can be achieved.

2 GEOTECHNICAL CHARACTERIZATION

In the studies, an extensive effort involving *in situ* and laboratory investigation was carried out. For basic geotechnical characterization, laboratory analysis consisted of physical, chemical, and mineralogical characterization tests, strength tests (including direct shear tests, and direct shear tests utilizing controlled suction), and oedometric tests.

The *in situ* investigation carried out in the area was performed by using topographic profiles of the region, cross sections, geological engineering mapping, subsurface exploration (soil / rock mass – SPT / RQD measurements), soil moisture content profiles, sampling of soils (Block and Denison), and field permeability tests (Guelf). Field instrumentation utilized piezometer, water table level, inclinometer, and rainfall measurement equipment. More information can be found in Silva (2007) and Silva *et al.* (2009).

2.1 Field Investigation Results

For the subsurface exploration, twelve boreholes were utilized in the area investigated. Ten were carried out in soil (SPT), and

two more in soil and rocky mass (SPT / Core boring–RQD). All boreholes the SPT was measured for each 0.5 m, in general with a depth of 10 to 15 m, but some went down to 20 m (SM-01, SM-02 and SP-02). Geological characteristics were identified together with soil / material descriptions.

In general, for all borehole tests performed, the SPT values ranged from 2 to 17 down to a depth of 7 m from the level of the natural ground surface, within the limits of the two geological formations. From this point on, the SPT values increase markedly, up to an order of 30, until becoming impenetrable to the SPT borehole. In the vertical profile, soil types vary from clayey sand, to sandy clay, silty sand, and sandy silt, with the layers varying in thickness, and showing the presence of increased amounts of sandy materials. The greatest alterations in SPT values were found very close to the Barreiras Formation contact with the granite residual soil. An exception involved the SP-02 borehole, found to be basically granite residual soil (Figure 1). Due to high sand content, the Barreiras Formation in the area is identified as an alluvial plain facie. Based on technical interpretation, the failure surface was shown to be near to the geological formation contact point, later confirmed by instrumentation (inclinometer results).

The presence of granite residual soil from the ground level in the SP-02 region demonstrated a profound influence on the landslide process, as evidenced later on in the study.

Soil profile cross-sections were detailed from the subsurface exploration, along with results from geological engineering mapping. Typical soil profile information is shown in Figure 1.
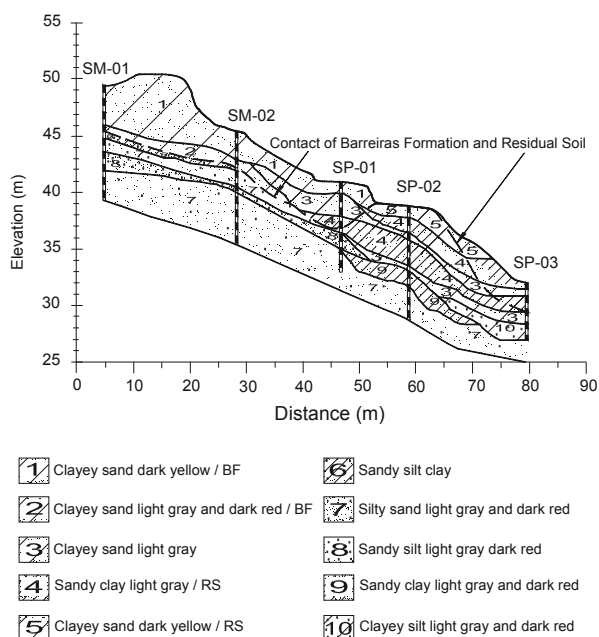

Figure 1. Typical Soil profile-cross section – post failure.

The climate in the area is classified by Koppen, as ´As´, described as humid tropical, with rainy periods during the autumn – winter seasons, and a dry period during the summer.

Rainfall precipitation in the Camaragibe township region was measured by instruments installed in two places, initially in a location within the city (during 2000 to 2004), and then later via instrumentation installed in the landslide area (2004 to 2006).

The rainy season is concentrated in the months from March to August, with the precipitation approximating average monthly maximum levels ranging from 150 mm to 600 mm. From January to March the average maximum monthly precipitation is around 150 mm, with April, May, July and August showing 250 mm. The month of June presented

precipitation above 500 mm, being considered the critical period for landslides. During the period from September to December, precipitation levels were lower, averaging around 50 mm. The period from September to February normally presents less precipitation; however, in some years (examples being 2000, 2002, 2004 and 2010) significant rainfall occurs in the months of January and February. During 2000, the annual rainfall level was above the general average, with increased precipitation during most of the calendar months. This occurrence coincided with the first appearance of signals of a non-stabilization condition in the area. Landslides occurred in June of 2002, after a period of intense rainfall.

Hydraulic conductivity of the soils was determined through field testing using a Guelph permeameter, an in-hole constant head permeameter employing the Mariotte Principle. It delivers essentially a "point" measurement. The tests were made along of the slide, close for the SPT boreholes, and was performed for each 0.5 m to a depth of 2.5 m. In the Barreiras Formation soils, permeability results varied from 2 to 6 x 10-6 m/s, with higher values from the materials containing a higher percentage of sand. In the SP-02 region (Figure 1), granite residual soils are present in the surface levels, presenting permeability results in the order of 2 x 10-7 m/s, and demonstrating values 10 times lower than the corresponding Barreiras Formation. This difference influenced flow conditions in the slide area.

The field instrumentation program in the landslide area was based on 25 Casagrande type piezometers (with 18 Casagrande piezometers having the ability to register maximum levels during a rainy period), 6 water level instruments, 5 vertical inclinometers, and 1 rainfall registration instrument.

In general the period of highest elevation of the piezometric level coincides with the period of high rainfall, in the months from March to August (with water managing to emerge from the surface level of the ground near borehole SP-01). Starting during the month of September, piezometric levels show a reduction, tending to remain constant until March, coinciding with the dry season. Similar behavior can be observed regarding the water levels encountered. Even in periods of low rainfall intensity, piezometric levels are observed to be quite high, demonstrating hydraulic influence on slope stability.

Results obtained in the vertical inclinometer analysis relating to borehole SP-02 showed maximum horizontal displacement of 130 mm as a block mass. It should be noted that horizontal displacements measured refer to the stage of reactivation, featuring movements along the existing failure surface, given that instrumentation was implemented in November 2004, after the occurrence of the failure. The influence rainwater had in the acceleration of horizontal movements was clear in observations regarding the slope studied. It appears that during a period of reduced rainfall (November 2004 to March 2005) the displacements observed were virtually nil, without significance.

Results of the vertical readings from inclinometers confirmed the information obtained from the SPTs boreholes, showing that the failure surface seems to be very close to the contact between the Barreiras Formation, and the granite residual soils, measured to be located at a depth just over 7 m from the surface of the ground, the exception being the region around SP-02, where only residual soils are found.

2.2 Laboratory Investigation Results

The mature residual granite soil studied presents a fine texture, with a liquid limit of 54%, plasticity limit of 32% (PI=22%), grain size distribution of 39% clay, 26% silt, 23% fine sand, and 12% a mixture of medium and thick sand. The soil is classified as CL in the Unified Classification System.

Grain-size distribution test without the use of deflocculates was also performed. Grain size distribution was designated as

5% clay; 33% silt; 50% fine sand, and 12% medium and thick sand; showing a strong reduction in the portions of clay, and increases in the fine sand portions. Results indicate that the particles of clay in this soil are aggregated in their natural state.

The soil-water characteristic curve obtained through the paper filter method, Haines funnel and Richard´s chamber, is presented in Figure 2. The format of the curve displays a saddle aspect, allowing it to be divided into three distinct stretches. The curves indicate an initial air entry suction of 1 kPa, where de-saturation begins. After that, a region approximating horizontal is observed, where suction varies from 20 to 200 kPa. In the last stretch, a second air entry value is depicted, where the water content starts to diminish with the increase in suction due to the removal of water from the soil micro pores (see more information in Silva and Coutinho, 2009).
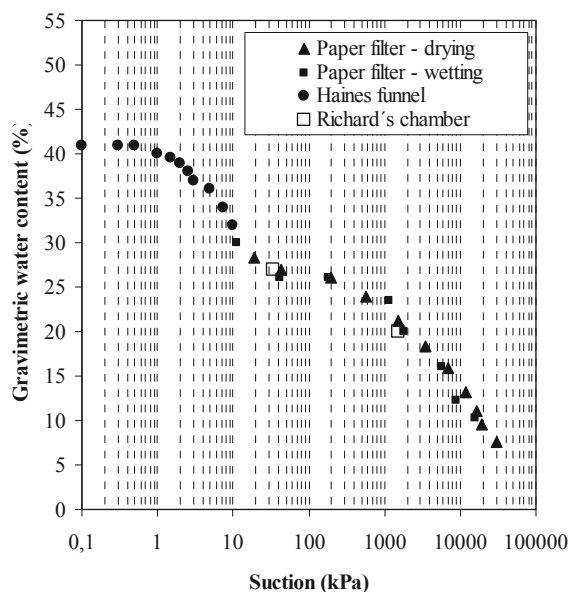

Figure 2. Soil-water characteristic curve from mature residual soil from Camaragibe-PE - Silva and Coutinho (2009)

The shear strength was determined using conventional and controlled suction direct shear tests. The equipment used consisted of a conventional press, adapted for use with a cell that allowed the imposition and control of suction through the principle of translation of axes.

The suction is imposed on the soil by the difference between air pressure supplied by hydrogen applied through an air valve, and the water column maintained in the reservoir fixed on top of the press. The tension is applied through a system of hanging weights, identical to the conventional direct shear tests. The air pressure was applied only under the weight of a charge transference plate, and it was maintained during 10 days. The horizontal force was determined through a load ring. The suctions employed were 25, 100, 300 and 500 kPa. After this period (of suction equilibrium), specific normal stress values were applied, accompanying the deformations up to stabilization. The normal stresses adopted were 50, 100, 150 and 200 kPa, and they were maintained for a minimum of 24 hours. Square samples were used that measured 50 mm or 100 mm the side, and 22 mm or 44 mm in height.

The shear strength envelopes in the plain (σ_v, τ) for the suction values of 25, 100, 300 and 500 kPa are represented in Figure 3. Envelopes considering suction of 0 kPa, obtained through conventional direct shear tests in the submerged condition, are also presented in this figure. It can be observed that the friction angle, in general, is close to 31°. The results indicate that the envelopes are near to linear in the stress range.
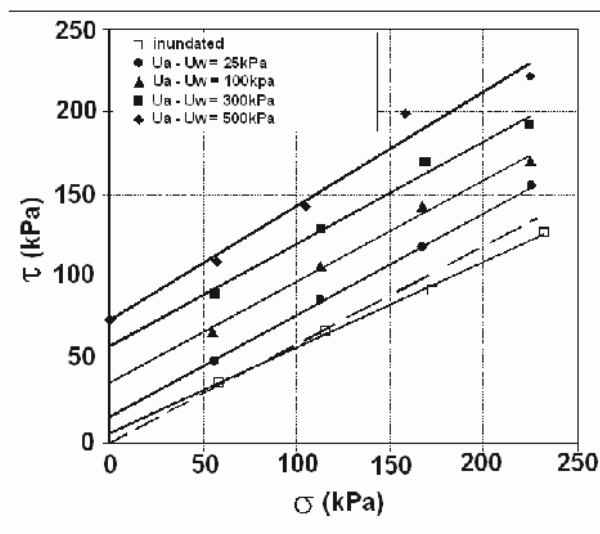
(Ua–Uw)= 0kPa	c = 9,7kpa	ϕ = 26,3°	R^2= 0,996
(Ua–Uw)= 0kPa	c = 0,0kpa	ϕ = 31,0°	estimated
(Ua–Uw)= 25kPa	c = 15,4kpa	ϕ = 31,6°	R^2= 0,999
(Ua–Uw)= 100kPa	c = 36,5kpa	ϕ = 31,3°	R^2= 0,991
(Ua–Uw)= 300kPa	c = 58,7kpa	ϕ = 31,5°	R^2= 0,987
(Ua–Uw)= 500kPa	c = 74,7kpa	ϕ = 34,4°	R^2= 0,956

Figure 3. Shear strength envelopes for different values of suction – mature residual soil from Camaragibe.

3   STABILITY ANALYSIS

Through the field investigation, together with flow and stability studies (failure and post failure conditions), a clear perception and understanding of the landslide mechanism was made possible. In this paper, only results corresponding to the failure state are presented. The slope stability evaluation was performed using Spencer method with consideration given to the original topography for the main cross section, as a two-dimensional saturated stability analysis, and considering the "actual" failure surface, along with the pore pressure distribution obtained from the flow analysis, and the geotechnical parameters obtained from laboratory testing (conventional direct shear tests in the submerged condition). Due to the intense rainfall during the failure period, the water level was considered at the surface position from the results produced through instrumentation and field observation, with the materials being in a saturated condition (Silva et al. 2009).

Flow analysis was performed for the failure condition, considering all the information from the studies, including the geotechnical profile, the geotechnical parameters of hydraulic conductivity for the materials composing the Barreiras Formation and residual soils, along with the rainfall and water level conditions. A summary of pore pressure distribution results is shown in Figure 4. Higher positive pore pressure values in the SP-01 and SP-02 regions were obtained showing ascends flow. These results are due to the variability of the soil profile and differences among the hydraulic conductivity values occurring for the materials. This condition is in conformity with water flow observed in this area during the period of intense rainfall.

With the flow analysis results that were provided, stability evaluation for global failure was initially performed (one-step failure) for the complete slope cross-section. The safety factor result was 1.278, showed not to be a condition for failure. Stability analysis was then performed considering the possibility of two-step failure, taking into account the concentrated high pore pressure values around the SP-01 region.
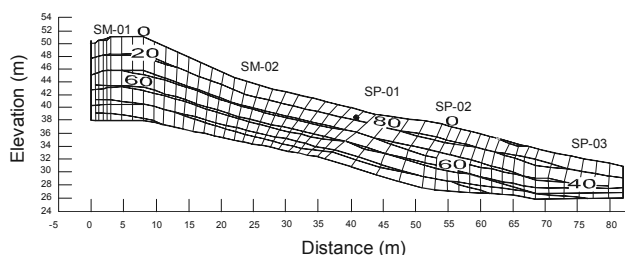
Figure 4. Flow Analysis – Pore Pressure Distribution.

The first landslide occurred between the positions SM 02 and SP-01. For this case, the safety factor value was 1.002, for practical purposes, considered to be a condition of failure, and initiating the landslide mechanism in the area (Figure 5).
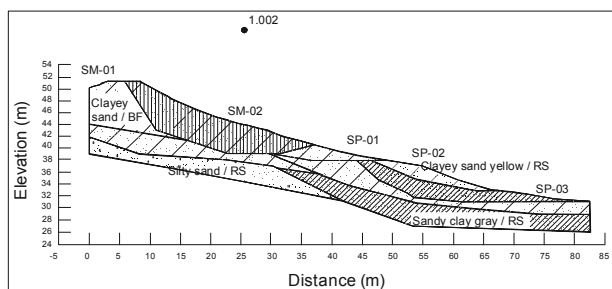

Figure 5. Back-analysis of the first slope failure – from SM-01 to SP01

The mass that moved in this area (from the first failure) caused a surcharge estimated at 30KN/m between positions SP-01 and SP-02, which associated with pore pressure conditions, provoked the second step of the landslide. With this understanding, stability analysis was performed (back-analysis) using geotechnical information from the field and laboratory investigations. Figure 6 presents the minimum safety factor value obtained (1.047), confirming the displacements, and the failure mechanism considered to be the cause of the landslide that occurred in the area.
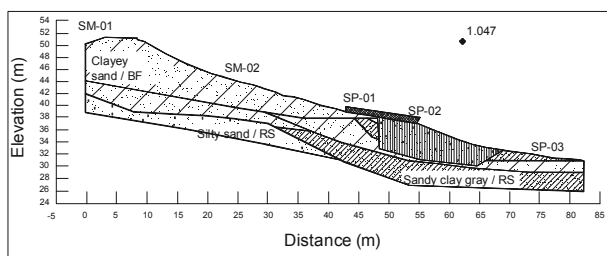

Figure 6. Back-analysis of the second slope failure – SP-01 to SP-03

After three years, another intense rainfall period amplified the problem, with cracks forming in many other houses, and extending the area initially showing damage. See the right side of the two upper-center squares of Figure 7.

4 MITIGATION AND REHABILITATION MEASURES

The mitigation and rehabilitation measures consisted of reducing damage and losses through control of the processes, and protection of the exposed elements in order to reduce their vulnerability. During the investigation and studies, it became possible to understand the processes involved, and to identify the causal factors and triggering mechanisms in the area. The general plan was to propose a risk management program that included both structural and non-structural mitigating actions, considering the social conditions of the area (Coutinho, 2011).

The stabilization measures proposed for all damaged areas (initial and extended areas) included: surface and subsurface drainage (sub-horizontal drains), surface protection, placement of access stairs with surface drainage, modification of slope shape, installation of retaining walls, definition of areas where occupation was to be prohibited, definition of houses to be relocated, dissemination of information to the public, and raising overall awareness of the conditions, along with community consciousness. Figure 7 shows some of the mitigation and control measures proposed.
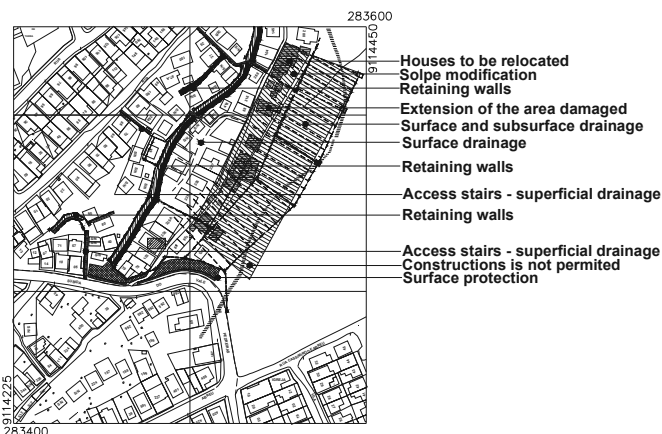
Figure 7. Measures Proposed for Mitigation and Control

5 CONCLUSION

The geotechnical characterization, along with flow and stability analyses / back-analysis results, were considered to be very satisfactory, and in accordance with the literature, permitting that the principal causal factors, and the mechanisms of the landslide could be comprehended and studied. It was understood that due to the heavy rainfall, the water level became elevated, saturating the soil, and producing a concentrated flow. The strength parameters used in the analysis were derived from direct shear laboratory tests in the corresponding condition. Considering all of the information available, mitigation and rehabilitation measures were then proposed, generating a risk management program that included structural and non-structural stabilization actions, considering the social conditions of the area.

6 ACKNOWLEDGEMENTS

7 REFERENCES

Coutinho, R. Q.; Silva, M. M. and Lafayeete, K. P. V. 2011. Geotechnical characterization of two unsaturated mature granite residual soils from Pernambuco, Brazil. *PCSMGE*. CD-ROM Proceedings, p.7. Toronto, Canada.

Coutinho, R. Q. 2011. Projeto de Estabilização de Encostas no Município de Camaragibe – PE. Relatório Técnico ("Technical Report"). Prefeitura de Camaragibe – PE, Brazil.

Silva, M. M.; Coutinho, R. Q. and Lacerda, W. A. 2009. Estudo de um movimento de massa ocorrido numa encosta em Camaragibe, Pernambuco. *V COBRAE*. CD-ROM, p. 10. São Paulo, Brazil.

Silva, M. M. and Coutinho, R. Q. 2009. Geotechnical characterization of an unsaturated residual soil of granite from Pernambuco, Brazil. *17th. ICSMGE*. v. 5, 3417-3420. Alexandria, Egypt.

Silva, M. M. 2007. Estudo geológico – geotécnico de uma encosta com problemas de instabilidade no Município de Camaragibe – PE. Tese de Doutorado (DSc.). UFPE. Engenharia Civil, Recife-PE, Brazil.

Progressive failure of slopes with sensitive clay layers

Rupture progressive de pentes comportant des couches d'argile sensible

Dey R., Hawlader B.
Memorial University of Newfoundland, St. John's, Canada.

Phillips R.
C-CORE, St. John's, Canada.

Soga K.
University of Cambridge, Cambridge, UK.

ABSTRACT: Progressive failure of slopes can trigger large scale landslides. The presence of sensitive clay layers is one of the main reasons for progressive failure of a slope. The whole soil mass involved in a potential landslide might be of sensitive clay, while in some cases there exist only thin layers of sensitive clay interbedded with relatively strong soils. The movement of a slope might be initiated due to the presence of a weak soil layer, where the shear stress is increased or soil strength is reduced by various triggering factors. Once the failure/movement is initiated in a small zone, the imbalanced force is transferred to the surrounding soil in which slip surface might propagate in the form of a shear band through the sensitive clay layer even though the sensitive clay layer is relatively thin. The propagation of shear band in sensitive clay is also associated with post-peak strain softening behaviour of soil. In this study, upward progressive failure due to river bank erosion has been modelled using nonlinear post-peak strain softening behaviour. It is shown that the pattern of propagation of shear band varies with soil type and slope geometry.

RÉSUMÉ : La rupture progressive de pentes peut déclencher des glissements de terrain de grande envergure. La présence de couches d'argile sensible est l'une des principales raisons de la rupture progressive d'une pente. La masse de sol impliquée dans un glissement de terrain potentiel pourrait être totalement constituée d'argile sensible, alors que dans certains cas, il existe seulement des couches minces d'argile sensible intercalées entre des sols relativement résistants. Le mouvement d'une pente peut être initié en raison de la présence d'une couche de sol peu résistant, dans laquelle le taux de cisaillement augmente ou sa résistance diminue en raison de divers facteurs de déclenchement. Lorsque la rupture / le mouvement sont initiés dans une petite zone, le déséquilibre de force se développe vers le sol environnant, dans lequel la surface de glissement peut se propager sous forme d'une bande de cisaillement à travers la couche d'argile sensible, même si la couche d'argile sensible est relativement mince. La propagation des bandes de cisaillement dans l'argile sensible est également associée au ramollissement post-pic du comportement du sol. Dans cette étude, la rupture progressive amont due à l'érosion des berges a été modélisée par le ramollissement non-linéaire post-pic du comportement. Il est montré que le faciès de propagation des bandes de cisaillement varie en fonction du type de sol et de la géométrie de la pente.

KEYWORDS: Sensitive clay, progressive failure, spread, shear band propagation, strain softening.

1. INTRODUCTION

Large landslides in soft sensitive clays are common in Eastern Canada and Scandinavia. Most of the onshore slides which occurred in soft sensitive clay have been reported as progressive in nature (Bernander 2000, Locat et al. 2008, Quinn 2009, Locat et al. 2011). The presence of strain-softening clay layers is one of the main reasons for progressive failure of a slope.These slides could be in the form of multiple retrogressive, translational progressive or spreads (Tavenas 1984, Karlsrud et al. 1984). Failure might be initiated in a fully stable and/or marginally stable slope depending on the nature of triggering factors. Failure could propagate either in upward or downward direction and the movement of the slope might be initiated due to the presence of a weak soil layer, where the shear stress is increased or soil strength is reduced by various triggering factors. Large landslides in sensitive clays classified as spread (Cruden and Varnes 1996) might be triggered by erosion near the toe of the river bank slope (Quinn et al. 2007, Locat et al. 2008). Numerous spread failures such as Sköttorp landslide in Sweden (Odenstad 1951) and the landslides occurred in Quebec including 1989 Saint-Liguori landslide (Grondin and Demers 1996), Saint-Ambroise-de-Kildare landslide (Carson 1979), Saint-Barnabé-Nord slide (Locat et al. 2008) have been reported to be triggered by erosion at the toe of the slope (Bernander 2000, Locat et al. 2008, Quinn et al. 2007, Locat et al. 2011), although it is very difficult to identify the true disturbing agents which caused these spread failures.

Progressive failure might occur in drained as well as undrained conditions. Bjerrum (1967) explained upward progressive failure initiation in an intact slope containing overconsolidated plastic clays and clay shales and considered the failure as drained. Sensitive clays from Eastern Canada and Scandinavia show strain softening behavior under undrained loading which has been considered as one of the main reasons for developing progressive failure (Bernander 2000, Locat et al 2008, Quinn 2009, Locat et al 2011). Hence undrained condition is considered in this study for analyzing spread failure.

During Ormen Lange field development, numerical simulations have been carried out by Norwegian Geotechnical Institute (NGI) using PLAXIS software to analyze the potential of retrogressive sliding due to strain softening effect in mild clay slopes (NGI 2001). Anderson and Jostad (2007) conducted numerical analyses of progressive failure of slope by modeling the shear band as an interface element using the NGI finite element (FE) code BIFURC. Quinn (2009) also demonstrates the use of linear elastic fracture mechanics concept in progressive failure of slopes.

This paper describes a numerical technique which can be used to analyze the spread or upward progressive failure of a slope typically occurs in river banks due to toe erosion.

2. PROBLEM DEFINITION

The geometry of the slope modeled in this study is shown in Fig. 1. The river bank has a slope of 30° to the horizontal. A thick crust of overconsolidated clay near the face of the slope and below the ground surface is assumed. For simplicity the

groundwater table is assumed at the crest of the slope and the river is full. A block of soil near the toe of the slope shown by the hatched zone is removed, which could be caused by erosion or by excavation in the field. This block will be referred as "excavated/eroded soil block." It is also assumed that the erosion or excavation is occurred relatively fast such that the deformation/failure of remaining soil is in undrained condition.

Three cases are simulated in this study. In Case-I, the ground surface is horizontal and there is a 15 m thick layer of sensitive clay below the 5 m crust. The Case-II is same as Case-I but the ground surface is inclined upward at 4°. Sometimes in the field there may not be a thick sensitive clay layer. To investigate the effect of thickness of the sensitive clay layer, in Case-III only 1.0 m thick sensitive clay layer parallel to the horizontal ground surface from the toe of the slope is assumed. The soil above this layer has the same geotechnical properties of the crust used in Cases I & II. In all three cases, the base layer below the toe of the slope is very stiff and therefore the failure is occurred in the soil above the base layer. The length of the soil domain in the present FE model is 500 m and therefore no significant effects on the results are expected from the right boundary.
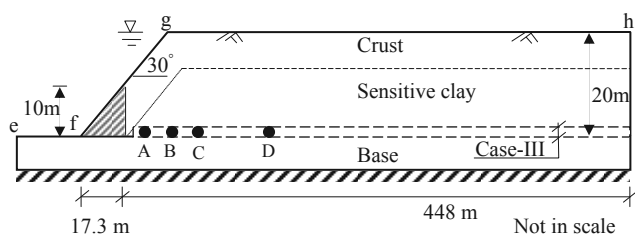

Figure 1. Geometry of the slope used in numerical analysis

3. FINITE ELEMENT MODELING

3.1 Numerical technique

ABAQUS 6.10 EF-1 is used in this study. The progressive slope failure is fundamentally a large deformation problem as very large plastic shear strain is developed in a thin layer of soil through which the failure of the slope is occurred. Conventional finite element techniques developed in Lagrangian framework cannot model such large strain problems because significant mesh distortion occurs. In order to overcome these issues, Coupled Eulerian-Lagrangian (CEL) technique currently available in ABAQUS FE software is used. The finite element model consists of three parts: (i) soil, (ii) excavated/eroded soil block, and (iii) void space to accommodate displaced soil mass. The soil is modeled as Eulerian material using EC3D8R elements, which are 8-noded linear brick, multi-material, reduced integration with hourglass control elements. In ABAQUS CEL, the Eulerian material (soil) can flow through the fixed mesh. Therefore, there is no numerical issue of mesh distortion or mesh tangling even at large strain in the zone around the failure plane.

The excavated/eroded soil block is modeled in Lagrangian framework as a rigid body, which makes the model computationally efficient. A void space is created above the model shown in Fig. 1 using the "volume fraction" tool. Soil and void spaces are created in Eulerian domain using Eulerian Volume Fraction (EVF). For void space EVF is zero (i.e. no soil). On the other hand, EVF is unity in clay layers shown in Fig. 1, which means these elements are filled with Eulerian material (soil).

Zero velocity boundary conditions are applied at all faces of the Eulerian domain (Fig.1) to make sure that Eulerian materials are within the domain and cannot move outside. That means, the bottom of the model shown in Fig. 1 is restrained from any movement, while all the vertical faces are restrained from any lateral movement. No boundary condition is applied at the soil-

void interface (efgh in Fig. 1) so that the soil can move into the void space when displaced.

Only a three-dimensional model can be generated in ABAQUS CEL. In the present study the model is only one element thick, which represents the plane strain condition.

The numerical analysis consists of two steps of loading. In the first step geostatic load is applied to bring the soil in in-situ condition. Note that under geostatic step the slope is stable with some shear stress especially near the river bank. In the second step, the rigid block of excavated/eroded soil is moved horizontally 2 m to the left using displacement boundary condition.

3.2 Soil parameters

Table 1 shows the geotechnical parameters used in this study. The crust has an average undrained shear strength of 60 kPa, and a modulus of elasticity of 10 MPa (=167s_u). The soil in the base layer is assumed to be very strong and s_u=250 kPa and E_u=100 MPa is used.

Table 1. Parameters for finite element modelling.

Crust	
Undrained modulus of elasticity, E_u (kPa)	10,000
Undrained shear strength, s_u (kPa)	60
Submerged unit weight of soil, ©2 (kN/m^3)	9.0
Poisson's ratio, $\int_u$	0.495
Sensitive clay	
Undrained modulus of elasticity, E_u (kPa)	7,500
Poisson's ratio, $\int_u$	0.495
Peak undrained shear strength, s_{up} (kPa)	50
Residual undrained shear strength, s_{ur} (kPa)	10
Submerged unit weight of soil, ©2 (kN/m^3)	8.0
Plastic shear strain for 95% degradation of soil strength, γ^p_{95} (%)	33

Proper modeling of stress-strain behavior of sensitive clay layer is the key component of progressive failure analyses in sensitive clays. When sensitive clay is subjected to undrained loading it shows post-peak softening behavior. Various authors (e.g. Tavenas et al. 1983, Quinn 2009) showed that the post-peak softening behavior is related to post-peak displacement or plastic shear strain. The following exponential relationship of shear strength degradation as a function of plastic shear strain is used in the present study.

$$s_u = [1+(S_t-1)\exp(-3\delta/\delta_{95})]s_{ur} \qquad (1)$$

where s_u is the strain-softened undrained shear strength at δ; S_t is sensitivity of the soil; ™=™$_{total}$-™$_p$ where ™$_p$ is the displacement required to attain the peak undrained shear strength (s_{up}); and δ_{95} is the value of δ at which the undrained shear strength of the soil is reduced by 95% of (s_{up}-s_{ur}). Equation 1 is a modified form of strength degradation equation proposed by Einav and Randolph (2005) and was used by the authors (Dey et al. 2012) to model submarine landslides. If the thickness of shear band (t) is known, the corresponding plastic shear strain (γ^p) can be calculated as, $\gamma^p=\delta/t$ assuming simple shear condition. Therefore, Eq.1 in terms of γ^p can be written as

$$s_u = [1+(S_t-1)\exp(-3\gamma^p/\gamma^p_{95})]s_{ur} \qquad (2)$$

where γ^p_{95} is the value of γ^p at 95% strength reduction (i.e. $\gamma^p_{95}=\delta_{95}/t$). Note that, it is very difficult to determine the thickness of the shear band in the field. Similar to some previous studies (e.g. Quinn 2009) t=0.375 m is used which is same as the mesh height used in the present FE analysis. In ABAQUS the degradation of shear strength of sensitive clay is varied as a function of plastic strain. The parameters used to

model the sensitive clay using Eq. 2 are also shown in Table 1. These parameters are estimated based on the laboratory tests conducted on sensitive clays (e.g. Tavenas et al., 1983) and the interpretation of test data and constitutive model development by other researchers (e.g. Bernander 2000, Leroueil 2001, Locat et al. 2008, Quinn 2009, Locat et al. 2011).

4. FINITE ELEMENT RESULTS

4.1   Propagation of shear band

Figure 2 shows the variation of equivalent plastic shear strain for three cases. In Cases-I & II the shear band initially propagates horizontally and then curved upward resulting in global failure. The failed soil mass follows the excavated/eroded soil block. Figures 2(a) & 2(b) show the equivalent plastic shear strain when the plastic shear strain in the entire failure plane is greater than $\gamma^p{}_{95}$. Global failure does not occur in Case-III (Fig. 2c). There is an approximately 1.4 m gap between the vertical face of the block and soil mass at the right. The shear band propagates horizontally and finally ended at certain length. Figure 2(c) also shows the plastic shear strain when the shear band propagation is ended. Whether the shear
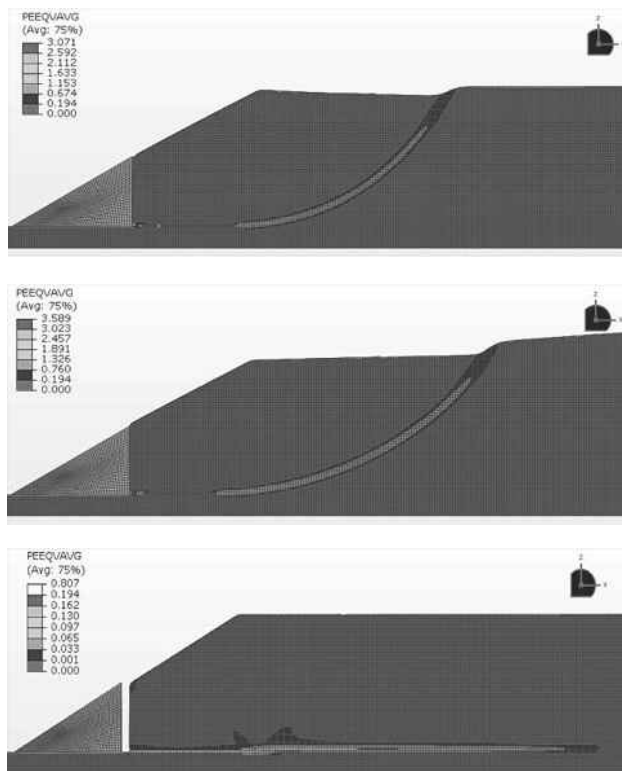

Figure 2. Developed equivalent plastic strain in the softening layer in case I, II and III respectively

band will propagate upward and cause the global failure or not, depends on the shear strength of the upper soil layer and mobilized shear strength along the shear band. For the soil properties and geometry used in the present study the failure pattern is almost same for Cases-I and II. However, the released energy from the excavated/eroded soil block is not sufficient to move the shear band upward in Case-III to cause the failure of the slope.

The equivalent plastic shear strain, denoted by the symbol PEEQVAVG in Fig. 2, is related to γ^p as PEEQVAVG= $\gamma^p/$. According to Eq. (2), when $\gamma^p \varepsilon \gamma^p{}_{95}$ (=33%), that means PEEQVAVG=0.194, the undrained shear strength is less than

12 kPa (=50-0.95(50-10)). Figure 2(c) shows that the equivalent plastic shear strain greater than 0.194 is developed in the shear band only near the vertical face of excavated/eroded block in Case-III. However, the equivalent plastic shear strain greater than 0.194 is developed in the entire length of the failure plane in Case-I & Case-II. Therefore, the failure of the slope is occurred in both cases at residual shear strength on the failure plane as large strain is developed.

4.2   Shear stress and mobilized shear strength

The Case-III is considered for further examination of the development of shear stress and mobilized shear strength along the potential failure plane. Figure 3 shows the variation of shear stress along the failure plane with movement of excavated/eroded block. Shear stress for four displacements (115 mm, 245 mm, 380 mm and 500 mm) are shown. In order to explain the process, consider the shear stress on the potential failure plane for the block displacement of 115 mm. The maximum shear stress (50 kPa) is developed at 12.5 m from the vertical face of the cut. The shear stress between 0 to 12.5 m is less than 50 kPa (i.e. s_{up}) and greater than 10 kPa (i.e. s_{ur}). That means, 0-12.5 m of the shear band represents the post-peak softening zone where the reduction of shear strength is occurred because of plastic strain as Eq. 2, and the mobilized shear strength is in between the peak and residual shear strength of the soil. In the right side of the peak (i.e. distance greater than 12.5 m) the shear stress is again reduced with distance. For this displacement of the block (115 mm), the shear stress in the
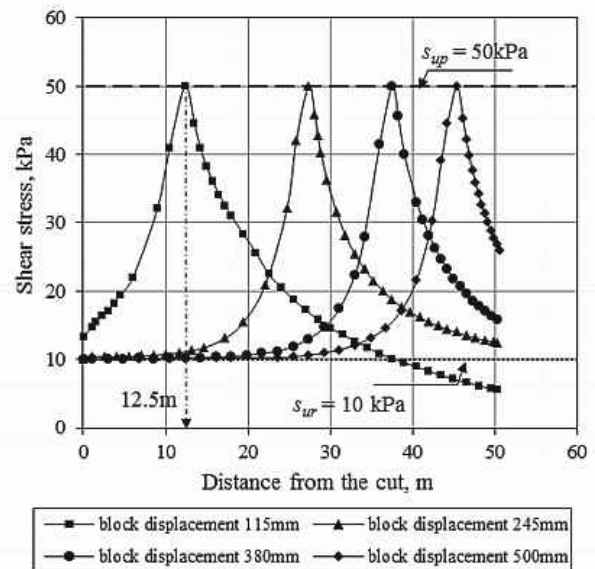
Figure 3. Shear stress along the potential failure plane

potential failure plane at a distance greater than 12.5 m is not increased to the peak, and therefore it represents the pre-peak behavior. At a very large distance, the shear stress is reduced to zero in Case-III as the ground surface is horizontal. The pattern of shear stress development for any other displacement of the block is similar as shown in Fig. 3. The location of the peak shear stress shifts to the right with increase in block displacement; that means a greater length of the potential failure plane is in post-peak stress-strain condition. For example, for 500 mm block movement the peak is occurred at 45.5 m and therefore 0-45.5 m is in post-peak condition with approximately 30 m in residual shear strength level. This process will be continued until the shear band propagation is ended for stable slopes as in Case-III. However, if the failure is occurred, as in Case-I and II, the large plastic shear strain will reduce the shear

strength of soil in the entire failure plane to the residual shear strength and global failure will occur.

Figure 4 shows the variation of shear stress at 4 different locations A, B, C and D (Fig. 1) which are located from the vertical face of the excavated/eroded block at horizontal distance of 3 m, 12.5 m, 25 m and 35 m, respectively. Consider the soil element B at 12.5 m distance. The shear stress in this element is increasing with movement of the excavated/eroded soil block. When the block is displaced by an amount of 115 mm, the shear stress in this element is reached to the peak shear strength of the soil (50 kPa). However, at this displacement of the block, the element A is almost at the residual shear strength. On the other hand, the elements C and D are still in the pre-peak state. That means the shear stress is gradually transferred to the soil elements in the right with displacement of the excavated/eroded soil block. For the soil element under the slope of the river bank there is an initial shear stress. With movement of the block the shear stress is increased from that initial value. However, the initial shear stress is less in the elements far from the river bank. Similar variation in shear stress and mobilized shear strength are obtained for Case-I and II.
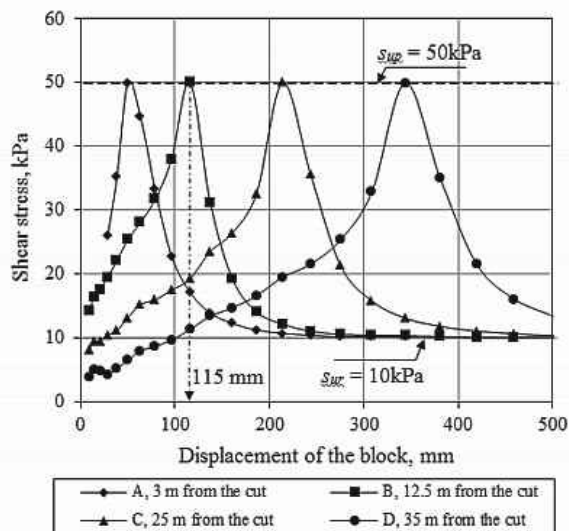

Figure 4. Variation of shear stress at four different locations from the cut

5. CONCLUSION

This paper presents a new numerical approach to model the initiation and propagation of shear band in upward progressive failure as encountered near the river banks. Toe erosion is considered as the triggering factor. Coupled Eulerian-Lagrangian (CEL) approach currently available in ABAQUS FE software is used for numerical analysis. Nonlinear strain softening behavior of sensitive clay is incorporated in this large deformation finite element analysis. Three cases are analyzed in this study. In Cases I and II global failure is occurred. However, in Case-III, although global failure is not occurred, the shear band propagation reduced the shear strength in the potential failure plane significantly over a large distance and the slope might be marginally stable for further loading.

6. ACKNOWLEDGEMENTS

7. REFERENCES

Anderson L. and Jostad H.P. 2007. Numerical modeling of failure mechanisms in sensitive soft clays — application to offshore geohazards. Offshore Tech. Conf., Texas. Paper OTC 18650.

Bernander S. 2000. Progressive failure in long natural slopes: formation, potential extension and configuration of finished slides in strain-softening soils. Licentiate Thesis, Luleå University of Technology.

Bjerrum L. 1967. Progressive failure in slopes in overconsolidated plastic clay and clay shales. Terzaghi Lecture. J. of the Soil Mech. and Found. Div., ASCE 93(5), 3-49.

Carson M.A. 1979. On the retrogression of landslides in sensitive muddy sediments: Reply. Can. Geotech. J. 16(2), 431-444.

Cruden D.M. and Varnes D.J. 1996. Landslides types and processes. In Landslides investigation and mitigation. Special Report 247. Transportation Research Board, NRC. Edited by A.K. Turner and R.L. Schuster. National Academy Press, Washington, D.C., 37-75.

Dey R., Hawlader B., Phillips R. and Soga K. 2012. Effects of shear band propagation on submarine landslide. Proc. of the 22nd Int. Offshore and Polar Engineering Conf., Rhodes, Greece,766- 773.

Einav I. and Randolph M.F. 2005. Combining upper bound and strain path methods for evaluating penetration resistance. Int. J. Num. Methods Engineering63(14), 1991-2016.

Grondin G. and Demers D. 1996. The Saint-Liguori flakeslide: Characterization and remedial works. In Proc. of the 7th Int. Symposium on Landslides, Trondheim, Norway, 2, 743-748.

Gregersen O. 1981. The quick clay landslide in Rissa, Norway. In Proc. of the 10th Int. Conf. on Soil Mech. and Foundation Engineering, Stockholm, Sweden. NGI, Publication No. 135, 421-426.

Karlsrud K., Aas G. and Gregersen O. 1984. Can we predict landslide hazards in soft sensitive clays? Summary of Norwegian practice and experiences. In Proc. of the 4th Int. Symposium on Landslides, Toronto, Ont., 1, 107-130.

Leroueil S. 2001. Natural slopes and cuts: movement and failure mechanisms. Géotechnique 51 (3), 197-243.

Locat A., Leroueil S., Bernander S., Demers D., Locat J. and Ouehb L. 2008. Study of a lateral spread failure in an eastern Canada clay deposit in relation with progressive failure: the Saint-Barnabé-Nord slide. In Proc. of the 4th Canadian Conf. on Geohazards: From Causes to Management, Québec, Que., 89-96.

Locat A., Leroueil S., Bernander S., Demers D., Jostad H.P. and Ouehb L. 2011. Progressive failures in eastern Canadian and Scandinavian sensitive clays. Can. Geotech. J. 48 (11), 1696-1712.

NGI Report 2001. Effect of strain softening on stability analysis. Analysis of retrogressive sliding due to strain softening-Ormen Lange case study, Report No 521001 (10).

Odenstad S. 1951. The landslide at Sköttorp on the Lidan River, February 2, 1946. Royal Swedish Institute Proceedings 4, 1-38.

Quinn P., Diederichs M.S., Hutchinson D.J. and Rowe R.K. 2007. An exploration of the mechanics of retrogressive landslides in sensitive clay. In Proc. of the 60th Canadian Geotechnical Conf., Ottawa, Ontario, 721-727.

Quinn P. 2009. Large Landslides in Sensitive Clay in Eastern Canada and the Associated Hazard and Risk to Linear Infrastructure. Doctoral thesis, Queen's University.

Tavenas F., Flon P., Leroueil S. and Lebuis J. 1983. Remolding energy and risk of slide retrogression in sensitive clays. Proc. of the Symposium on Slopes on Soft Clays, Linköping, Sweden, SGI Report No. 17, 423-454.

Tavenas F. 1984. Landslides in Canadian sensitive clays — a state-of-the-art. In Proc. of the 4th Int. Symposium on Landslides, Toronto, Ont., 1, 141-153.

Quantitative vulnerability estimation for individual landslides

Estimation quantitative de la vulnérabilité aux glissements de terrain

Du J., Yin K.
China University of Geosciences (Wuhan), China

Nadim F., Lacasse S.
International Centre for Geohazards / Norwegian Geotechnical Institute (NGI), Norway

ABSTRACT: Vulnerability has not been systematically considered for landslides until recently, but is a fundamental component in the evaluation of risk. Vulnerability depends on the landslide intensity, the characteristics of the elements at risk, and the impact of landslide. A quantitative model is proposed to estimate the vulnerability of the exposed structures and individuals. The model accounts for landslide intensity, different classes of vulnerable elements and the impact of both slow and rapid moving slides.

RÉSUMÉ : La vulnérabilité est un facteur important du risque associé aux glissements et n'a pas été considérée jusqu'à tout récemment. Elle dépend de l'intensité et de l'impact du glissement et des propriétés des éléments exposés. L'article propose un modèle calculant la vulnérabilité de structures et d'individus. Ses paramètres caractérisent l'intensité du glissement, tiennent compte de différentes classes de vulnérabilité et distingue l'impact de glissements évoluant lentement et rapidement.

KEYWORDS: Landslide, Quantitative vulnerability evaluation, Intensity, Susceptibility

1 INTRODUCTION

The ISSMGE glossary of risk assessment terms defines vulnerability as the degree of loss to an element within the area affected by the landslide hazard. It is expressed on a scale of 0 (no loss) to 1 (total loss). In contrast to flooding and earthquakes, it is not straightforward to define or assess, the vulnerability to landslides, due to the complexity and range of the landslide process (Leroi 1996). However vulnerability can influence the losses to a greater degree than the hazard (Einstein 1988; Alexander 2004). Despite this, it is an economic and political necessity to quantify vulnerability (Varnes 1984; Alexander 1984).

Two different perspectives exist for the vulnerability estimation: that based on the natural sciences and that based on the social sciences (Crozier 2004). Most often, the assessments of landslide risk are based on the natural science approaches. Some apply damage matrices (Leone 1996) based on qualitative (Cardinali 2002) and quantitative approaches (Fell, 1994). Conceptual frameworks for quantitative vulnerability estimation have been presented (Düzgün and Lacasse 2005, Uzielli *et al* 2008).

2 PROPOSED MODEL

Following Uzielli *et al* (2008) and Li (2010), the proposed model defines vulnerability as a function of landslide intensity and susceptibility of element at risk. The parameters are established on the basis of the landslide impact mechanism and categories of vulnerable elements. The proposed vulnerability model is defined by Eq. 1 and represented graphically in Fig. 1:

For $I \leq 1\text{-}S$ $\qquad V = \frac{1}{2}[I/(1\text{-}S)]^2$

For $I > 1\text{-}S$ $\qquad V = 1\text{-}\frac{1}{2}[(1\text{-}I)/S]^2$ $\qquad$ (1)

$V \in [0, 1]$ is the vulnerability of elements exposed to the threat. For structures, 1 means that the structure is completely destroyed, while values less than one represent the degree of damage and 0 describing no damage. For individuals, 1 means loss of life, while a value < 1 is the probability of loss of life. $I \in [0, 1]$ is the intensity of landslide. An intensity of 1 means that the landslide has the potential of destroying all elements in its path.
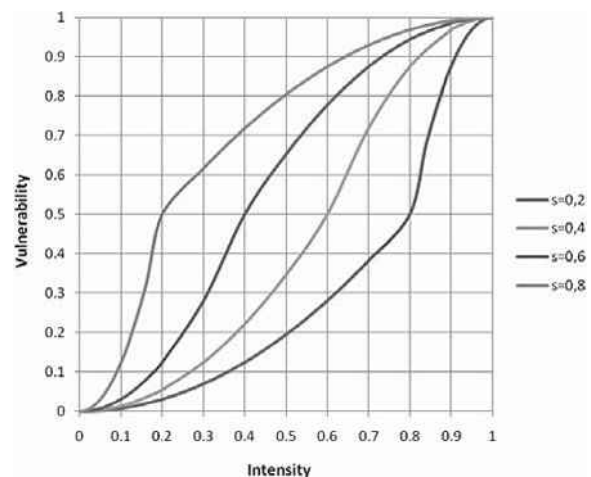
Fig. 1 Vulnerability (*V*) from susceptibility (*S*) and landslide intensity (*I*).

$S \in [0, 1]$ is the element susceptibility: S=0 means that the vulnerable element has high inherent resistance under impact. The terms *V*, *I* and *S* are non-dimensional and the values of 1 and 0 indicate the highest and lowest boundaries for the three parameters. To account for the landslide impact in the vulnerability estimation, two stages of deformation are considered: 1) a slow deformation stage and 2) the failure (rapid movement) stage.

3 LANDSLIDE INTENSITY

The definition of vulnerability requires information on landslide intensity (Guzzetti *et al* 1996), which should include information on the landslide severity degree and spatial dimensions.

3.1 *Slow deformation stage*

Under slow deformation, cracks and tilting may occur in structures located on the landslide, due to displacement and velocity of the ground surface and foundation substrata. The intensity parameters include landslide velocity and local deformation,

which describe the severity degree, and landslide depth, which reflects the spatial dimensions. The model is defined as:

$$I_{def} = 1 - (1 - I_{d-def})(1 - I_{d-vel})(1 - I_{d-dep}) \quad (2)$$

where I_{d-def}, I_{d-vel} and I_{d-dep} are the parameters for deformation, velocity and landslide depth at the location of the structure. The deformations include settlement, horizontal movement and inclination (Bell 1978; Peng 1992; Zheng 2007). A basic relationship (Eq. 3) seems to provide a good approximation:

$$W_s = aW_g + bW_s \quad (3)$$

where W_s and W_g are the deformations of structure and ground, a is the slope and b is the intercept. Table 1 gives the range of a and b vs movement and structure types (Peng 1992; Zheng 2007). The deformation intensity depends on the ratio of deformation to allowable threshold value as shown in Table 2.

Table 1. a and b as function of ground deformation and structure type

Structure	Brick masonry, concrete structures		Reinforced (RC) concrete structures	
	a	b	a	b
Settlement (mm)	0.87-0.99	0.50-1.27	0.96-1.03	1.19-3.57
Tension (mm/m)	0.74-0.89	—	0.68-0.71	—
Compression (mm/m)	0.28-0.32	—	0.24-0.27	—
Inclination (mm/m)	0.99-1.06	0.80-0.90	0.69-0.97	0.03-0.2

Table 2. Proposed value of intensity parameters for deformation

Ratio of deformation to allowable threshold	I_{d-def}
<0.2	0.1
0.2-0.4	0.2
0.4-0.6	0.4
0.6-0.8	0.6
0.8-1.0	0.8
1.0-1.2	0.9
≥1.2	1.0

According to the landside movement scale and response of structures (Cruden and Varnes 1996), the intensity of the landslide velocity can be obtained by the model described in Eq. 4 (Li 2010). v is the velocity of landslide (mm/s).

For $v \leq 5 \times 10^{-7}$ $I_{d-vel} = 0$
For $5 \times 10^{-7} < v \leq 5 \times 10^{-1}$ $I_{d-vel} = 1/36[\log_{10}v + 6.30]^2$ (4)
For $v \geq 5 \times 10^{-1}$ $I_{d-vel} = 1$

For structures on a moving landslide, the degree of damage depends mainly on the relative depth of the structure foundation to the sliding surface. Ragozin (2000) quantified the vulnerability of structures as a function of the foundation depth h (m) depending on the depth of predicted landslide d (m). The model described by Eq. 5 is proposed used.

For $d/h < 0.8$ $I_{d-dep} = (1.25 \cdot d/h)^{1/3}$
For $0.8 < d/h \leq 1.2$ $I_{d-dep} = 1$ (5)
For $d/h > 1.2$ $I_{d-dep} = 1.44 \cdot (d/h)^{-2}$

3.2 Failure stage

3.2.1 Landslide intensity for structures

The structures located within the release zone of a rapidly moving landslide are completely destroyed and have a vulnerability of 1.0. For the structures within the run-out distance, the impact mechanisms can be divided into two main categories: burial and impact pressure. For structures, the intensity of the landslide is defined as a function of its depth and impact pressure, where I_{pre} and I_{f-dep} are impact pressure and landslide depth parameters:

$$I_{fai-s} = 1 - (1 - I_{pre})(1 - I_{f-dep}) \quad (6)$$

(1) Impact pressure
After the landslide fails, the horizontal impact pressure is the main cause of damage to structures (Glade 2004; Ulusay 2007). Petrazzuoli (2004) analyzed the collapse limit load of regular and irregular RC structures to horizontal pressure with the strong beams and weak columns structural models. The proposed vulnerability model uses the average value of each typology to estimate the horizontal pressure limit P vs the number of

stories n, in which the values of coefficient α and β for each structure type are listed in Table 3.

$$P = \alpha\ln(n) + \beta \quad (7)$$

Table 3. Coefficients α and β in Eq. 7 for different structure types.

Structure	Strongly aseismic	Weakly aseismic	Strongly non-aseismic	Weakly non-aseismic
Regular structure				
A	-4.384	-2.717	-2.157	-1.276
B	19.125	13.164	10.568	7.693
Irregular structure				
A	-3.779	-2.467	-1.821	-1.343
B	14.553	10.288	8.068	6.066

The ratio of landslide impact pressure on the building to horizontal pressure limit is defined as the intensity parameter I_{pre} (Table 4). The horizontal pressure limit of RC frame can be obtained according to Eq. 7, while the limit pressure of terracotta panels in Table 5 can be used for masonry structure.

Table 4. Proposed values of impact pressure intensity parameter.

Landslide impact pressure/Structure horizontal pressure limit	I_{pre}
<0.1	0.05
0.1-0.2	0.20
0.2-0.4	0.40
0.4-0.7	0.70
0.7-1.0	0.90
≥1.0	1.00

Table 5. Estimated resistances of buildings and elements (Spence 2004)

Building elements	Failure pressure(kPa)
Terracotta tile infill panel with openings	7.6-8.9
Terracotta tile infill panel without openings	5.5
Tuff infill panel (length 4 m, thickness 40 cm)	6.8-9
Tuff infill panel (length 4 m, thickness 60 cm)	10-13
Weak non-aseismic RC buildings (1 to 3 storeys)	4.5-8
Strong non-aseismic RC buildings (4 to 7 storeys)	5-9
Weak aseismic RC buildings (multi-storeys)	5-10
Strong aseismic RC buildings (multi-storeys)	6-14

(2) Landslide depth
As inferred from the structural damage, the intensity parameter for landslide depth should be defined as the ratio of landslide depth to height of structure. When landslide depth is equal to or greater than the structure, the structure loses completely lose its functionality. The proposed values of I_{f-dep} are found in Table 6.

Table 6. Proposed values of landslide depth intensity parameter

Ratio of landslide depth to height of structure	I_{f-dep}
<0.2	0.10
0.2-0.4	0.30
0.4-0.6	0.50
0.6-0.8	0.70
0.8-1.0	0.90
≥1.0	1.00

Depending on location, the persons within the affected area can be divided into two categories: indoors and outdoors. Landslide velocity, depth and width become the intensity parameters:

$$I_{fai-p} = I - (I - I_{f-vel})(I - I'_{f-dep})(I - I_{wid}) \quad (8)$$

where I_{f-vel}, I'_{f-dep} and I_{wid} are the parameters of landslide velocity, depth and width, respectively. A moving slide depth greater than knee-height makes it difficult to escape. Using 1.6 m and 0.482 (Swami 2006) as average height and leg ratio, a threshold value of 0.8m for critical landslide depth is obtained. The values of I'_{f-dep} in Table 7 are proposed:

For landslide width, five degrees are identified to allow for change in landslide activity conditions (Table 8). The landslide velocity scale defined by Eq. 9 is identical to that proposed by Li (2010). The value v is the velocity of the landslide (mm/s).

For $v \leq 5 \times 10^{-1}$ $I_{d-vel} = 0$
For $5 \times 10^{-1} < v \leq 5 \times 10^{3}$ $I_{d-vel} = 1/16[\log_{10}v + 0.3]^2$ (9)
For $v \geq 5 \times 10^{3}$ $I_{d-vel} = 1$

Table 7. Proposed values of landslide depth intensity parameter

Landslide depth (m)	$I'_{f\text{-}dep}$
<0.1	0.10
0.1-0.3	0.30
0.3-0.6	0.70
0.6-0.8	0.90
≥0.8	1.00

Table 8. Proposed values of landslide width intensity parameter

Landslide width (m)	I_{wid}
< 50	0.10
50-200	0.30
200-400	0.50
400-700	0.80
≥ 700	1.00

4 SUSCEPTIBILITY
4.1 *Susceptibility of structures*

The capacity of a structure to withstand the landslide hazard depends on the morphological characteristics and utilization conditions (Amatruda 2004; Coburn 2002). Four parameters were considered, including structure type s_{str}, maintenance state s_{mai}, ratio of service years to design service life s_{ser} and the difference in the directionality of landslide movement and the principal longitudinal direction of the structure s_{dir}, with the model given in Eq. 10. Together, these parameters describe the susceptibility of the structures to be damaged by a landslide (Table 9 for s_{str}, Table 10 for s_{mai}, Table 11 for s_{ser}, Table 12 for s_{dir}).

$$S_s = 1 - (1 - s_{str})(1 - s_{mai})(1 - s_{ser})(1 - s_{dir}) \quad (10)$$

Table 9 Structure susceptibility parameter (Heinimann 1999)

Structural typology	Resistance	s_{str}
Lightest, simple structures	Very high	1.00
Light structures	High	0.90
Rock masonry and concrete	Medium	0.70
Brick masonry, concrete structures	Low	0.50
Reinforced concrete structures	Very low	0.30
Reinforced structures	Extremely low	0.10

Table 10 Proposed values of maintenance state susceptibility parameter

State of maintenance	s_{mai}
Extremely good	0.00
Good	0.05
Slight deformation	0.25
Medium deformation	0.50
Serious deformation	0.75
Extremely Serious deformation	1.00

The damage would be most serious when the angle between the two directions is 0° and be lightest when the angle gets close to 45° (Table 12).

Table 11 Proposed values of service year susceptibility parameter

Ratio of service year to design service life	s_{ser}
≤ 0.1	0.05
0.1 - 0.4	0.10
0.4 - 0.6	0.30
0.6 - 0.8	0.50
0.8 - 1.0	0.70
1.0 - 1.2	0.80
> 1.2	1.00

Table 12. Values of directionality difference susceptibility parameter.

Directionality of landslide movement (°)	s_{dir}
0-5	1.0-0.6
5-15	0.6-0.4
15-30	0.4-0.2
30-45	0.2-0.0

4.2 *Human susceptibility*

The susceptibility of persons to be hurt or killed by the landslide depends strongly on the cognitive and reaction capacity upon the occurrence of a landslide and the protection measures at the site, e.g. escape routes or early warning system. The following model was proposed to describe the landslide susceptibility for persons:

$$S_p = 1 - (1 - s_{hel})(1 - s_{age})(1 - s_{war}) \quad (11)$$

where s_{hel}, s_{age} and s_{war} are the susceptibility parameters, health condition, age and existence of a warning system, respectively.

A person's health condition, i.e. evacuation capacity, can be divided into three classes: 1) healthy, 2) weak physical condition, e.g. chronic disease slowing down movement, and 3) complete incapacitation with inability to evacuate. The susceptibility parameter values listed in Table 13 are proposed.

On the basis of fatality rate-age distribution data from earthquakes, Li (2010) proposed a quadratic polynomial function (Eq. 12) in terms of age a, which was adopted in this paper:

$$s_{age} = 0.95 - 0.00486 \, [\text{INT}(a/5) - 5]^2 \quad (12)$$

where INT() is the downward rounded integer function.

Table 13. Proposed values of health condition susceptibility parameter.

Health condition	s_{hel}
Healthy	0-0.1
Weak physical condition	0.1-0.8
Complete incapacitation	0.8-1.0

"Early warning" refers to all the measures that can be taken before the occurrence of a catastrophic event reducing the risk or contributing to avoid it (Table 14). Completeness level in the table refers to the efficiency of early warning or other mitigation measures in place to reduce or avoid risk.

5 VULNERABILITY OF PERSONS IN STRUCTURES

When a landslide occurs, the vulnerability of persons in the structures is directly correlated with the structure damage.

To estimate the casualty level in a building, one needs to assess the proportion of people trapped in the debris of a collapsed building and the casualty level for different degrees of damage.

When buildings collapse, not all the occupants are trapped inside. The number of people trapped in a collapsed building depends on the size and type of building, the collapse itself, the time of collapse and the escape options during and after the col-

Table 14. Proposed values of "generic" early warning system susceptibility parameter

Completeness level	S_{war}	Description of risk reduction or risk avoidance measure
None	1.0	Investigate the geological background and deformation of the landslide, without any monitoring measures.
Simple	0.6-1.0	Simple manual monitoring measurements with low precision and measurements at long interval (one month), e.g. manual measurement of extension velocity of crack and subsidence velocity of head of landslide.
Moderate	0.2-0.6	Accurate monitoring equipment with moderate precision, long interval readings (one month) and low distribution density of monitoring points; monitoring involves only geological parameters); investigation of population exposed to landslide risk; simple emergency plan includes warning transmission and evacuation paths.
Comprehensive	0.0-0.2	Accurate monitoring equipment with high precision and close interval readings (one day/one week); density of monitoring points high enough to sense deformation of entire landslide; monitoring involves geophysical, atmospheric, hydrodynamic and soil quantities; decision procedures in place based on experience with time prediction, triggering threshold and evacuation successes/failures with landslide; overview of population and public facilities exposed; overall emergency plan includes warning transmission, evacuation paths, logistics, medical assistance and so on.

lapse. Masonry and reinforced concrete, have different collapse mechanisms and rubble characteristics. The total collapse of masonry buildings provides smaller cavities than the collapse of frame structures. Li (2010) proposed an exponential description of the vulnerability of persons inside structures. Coburn (2002) estimated the average percentage of occupants trapped in a collapsed building to range between 30% and 70%, and estimated the injured proportion of occupants at collapse (Table 15).

The four levels of casualty, i.e. fatalities, seriously injured, moderately injured and lightly injured or uninjured, were denoted by vulnerability values of 1, 0.8, 0.5 and 0.2. The vulnerability of persons (V_p) in different structures is listed in Table 16 ($V_s = 1$ or collapse). Equation 13 quantifies the vulnerability of persons V_p (index α for different structures is listed in Table 16).

$$V_p = 0.001 \exp(\alpha\, V_s) \qquad (13)$$

Table 15. Casualty distribution, collapsed buildings (Coburn 2002)

Class	Fatalities	Seriously injured	Moderately injured	Lightly injured or uninjured
Masonry	17.5	10	17.5	55
RC frame	21	0.8	9.2	70
RC shear wall	10	0.7	9.3	80
Steel	16	0.6	9.4	75
Timber	0.6	0.2	10.2	89

Table 16. Vulnerability of persons and value of index α

Structure type	Masonry	RC frame	Steel	RC shear wall	Timber
V_p (when $V_s = 1$)	0.45	0.40	0.36	0.31	0.24
α	6.1	6	5.9	5.75	5.5

6 CONCLUSIONS

A model for the quantitative estimate of landslide vulnerability is proposed with two parameters: landslide intensity and susceptibility of the elements at risk. A reliable estimate of landslide intensity should consider the relationship between landslide severity and spatial dimensions. For the slow-moving landslides, the quantitative relationships for three categories of ground deformation and structure response are considered in the assessment of the landslide intensity. Based on empirical data, a function describing the ratio of landslide depth to foundation depth can be used to estimate the effect of geometric intensity.

In the landslide failing stage, intensity models were established for stationary and non-stationary vulnerable elements. Impact pressure and landslide depth were included in the vulnerability assessment of structures. For persons in open space, the parameters include landslide velocity, depth and width.

Functions of horizontal limit pressure versus the number of storeys of different structures were proposed to quantify the landslide impact intensity parameter of the moving mass. For the human susceptibility, generic mitigation measures were proposed to include a component of risk prevention and emergency awareness. Further, collapse mechanisms and construction characteristics of different construction types, the vulnerability functions for persons in different structure categories were proposed.

The model has limitations and needs further research. Some of the subjective and empirical parameters in the model should be calibrated and gradually documented with the addition of objective data, experience, observations and expert judgment.

7 ACKNOWLEDGEMENTS

8 REFERENCES

Alexander, D.E. 1984. Building damage by landslide: the case of Ancona, Italy. *Ekistics-The Problems and Science of Human Settlements*, 51:452-462.

Alexander, D.E. 2004. *Vulnerability to landslide. Landslide Hazard and Risk*. John Wiley & Sons, Ltd. pp. 175-198.

Amatruda, G., Bonnard, C., Castelli, M. *et al.* 2004. A key approach: the IMIRILAND project method. Identification and mitigation of large landslide risks in Europe - advances in risk assessment. In: Bonnard *et al* (Eds.), *European Commission, Fifth Framework Program*. Balkema. 13–44.

Bell, S.E. 1978. *Successful design for mining subsidence. Large movements and structures. New York: Acad. Press* 562-578.

Crozier, M.J., Glade, T. 2004. Landslide hazard and risk: issues, concepts and approach. *Landslide hazard and Risk* .John Wiley&Sons, Ltd. 1-40.

Coburn, A., Spence, R. 2002. *Earthquake protection*. John Wiley & Sons Ltd, The Atrium, Southern Gate, Chichester, West Sussex PO19 8SQ, England.

Cruden, D.M., Varnes, D.J. 1996. Landslide types and processes. In: *Landslide investigation and mitigation*. National Academy Press, Washington 36–75.

Cardinali, M., Reichenbach, P., Guzetti, F. *et al.* 2002. A geomorphological approach to the estimation of landslide hazards and risks in Umbria, Central Italy. *Natural Hazards and Earth System Sciences* 2:57-72

Düzgün, HSB, Lacasse, S. 2005. Vulnerability and acceptable risk in integrated risk assessment framework. Hungr *et al* (eds) *Landslide risk management*. Balkema, NL. 505–515.

Einstein, H.H. 1988. Special lecture - landslide risk assessment procedure. In: *5th International Symposium on Landslides*. Landslides 2:1075-1090.

Fell, R. 1994. Landslide risk assessment and acceptable risk. *Canadian Geotechnical Journal* 31:261-272

Glade, T. 2003. Vulnerability assessment in landslide risk analysis. *Erde* 134(2):123–146.

Glade, T., Crozier, M.J. 2004. The Natural of Landslide Hazard Impact. *Landslide Hazard and Risk*. England: John Wiley&Sons, Ltd, 44-74.

Guzzetti, F., Carrara, A., Cardinali, M., Reichenbach, P. 1996. Landslide hazard evaluation: an aid to a sustainable development. *Geomorphol* 31:181–216

Heinimann, H.R. 1999. Risikoanalyse bei gravitativen Naturgefahren-Fallbeispiele & Daten. *Umwelt-Materialen* 107/I, Bern.

Leroi, E. 1996. Landslide hazard-risk maps at different scales: objectives, tools and development. *Proc. of 7th international symposium on landslides*, June 17–21, Trondheim, 35–51.

Leone, F., Ast´e, J.P., Leroi, E. 1996. Vulnerability assessment of elements exposed to mass moving: working towards a better risk perception. In: Senneset K (ed) *Landslides*. Balkema, Rotterdam, 263–269.

Li, Z, Nadim, F, Huang, HW, Uzielli, M, Lacasse, S. 2010. Quantitative vulnerability estimation for scenario-based landslide hazards, *Landslides* 7:125–134.

Peng, S.S. 1992. *Surface subsidence engineering*. Colorado: Society for Mining, Metallurgy and Exploration 77-90.

Swami, V., Einon, D., Furnham, A. 2006. The leg-to-body ratio as a human aesthetic criterion, *Body Image* 3:317–323.

Ulusay, R., Aydan, Ö., Kılıc, R. 2007. Geotechnical assessment of the 2005 Kuzulu landslide *Engin. Geology* 89:112–128.

Uzielli, M., Nadim, F., Lacasse, S., Kaynia, A.M. 2008. A conceptual framework for quantitative estimation of physical vulnerability to landslides. *Engin. Geology* 102:251–256.

Varnes, D.J. 1984. *Landslide hazard zonation: a review of principles and practice*. UNESCO, France, 1–63.

Zheng, K.Z., Guo, G.L., Tan, Z.X. 2001. Analysis of Movement and Deformation Characteristics of Buildings Above Mining Subsidence Areas. *Journal of China University of Mining & Technology* 30(4):354-358.

A site specific early warning system for rainfall induced landslides

Utilisation d'un site spécifique pour l'élaboration d'un système d'alerte rapide pour les instabilités de pente induites par les pluies.

Harris S., Orense R.
Department of Civil and Environmental Engineering, The University of Auckland, Auckland, New Zealand
Itoh K.
National Institute of Occupational Safety and Health, Tokyo, Japan

ABSTRACT: An early warning system (EWS) to warn users of imminent landsliding caused by rainfall has been developed. The EWS is deterministic, based on a pre-determined failure mechanism present at a specific site. A prototype of the EWS was developed for a roadway embankment located in Silverdale, New Zealand. Prolonged rainfall caused a landslide at the site in 2008. Soil debris from this landslide event almost obstructed a major highway, which could have been potentially dangerous to motorists as well as causing major delays to the Auckland roading network. Volumetric water content sensors were installed at various depths and locations along the same cross section of the site. A 2D finite element model was used to replicate the response of the sensors to rainfall, using monitored rainfall events as an influx in the model. Next, a limit equilibrium analysis was used to obtain the factor of safety against slope failure for each time step in the finite element model. An artificial neural network was then trained to predict this factor of safety using the sensor readings as inputs. Thus, the factor of safety of the slope can be predicted in real time. This predicted factor of safety forms the basis of the EWS.

RÉSUMÉ : Un système d'alerte précoce (SAP) pour avertir les utilisateurs de glissements de terrain provoqués par des pluies imminentes a été développé. Le SAP est déterministe, basée sur les mécanismes de rupture pré-déterminés présents sur un site spécifique. Un prototype du SAP a été développé pour un remblai de la chaussée située à Silverdale en Nouvelle-Zélande. Des pluies prolongées ont causé un glissement de terrain sur le site en 2008. Les coulés de sol engendrées par ce glissement de terrain ont presque obstrué une route importante, ce qui aurait pu être potentiellement dangereux pour les automobilistes ainsi qu'être à l'origine de retards importants sur le réseau routiers d'Aucklande. Des capteurs volumétriques de teneur en eau ont été installés à des profondeurs différentes et à des emplacements variés le long de la section transversale du site. Un modèle par éléments finis 2D a été utilisé pour reproduire la réponse des capteurs aux précipitations, en utilisant les données expérimentales de comme données d'entrée. Ensuite, une analyse d'équilibre limite a été utilisée pour obtenir le facteur de sécurité pour la stabilité de la pente pour chaque pas de temps. Un réseau neuronal artificiel a ensuite été formé pour prédire ce facteur de sécurité en utilisant les relevés du capteur comme modèle. Ainsi, le facteur de sécurité de la pente peut être prédite en temps réel. Ce facteur de sécurité prévu est à la base du SAP.

KEYWORDS: rainfall, landslide, artificial neural network, early warning system

1 INTRODUCTION

As a means to mitigate the risk of rainfall induced landslides which cause millions of dollars' worth of damage each year in New Zealand (NIWA & GNS Science, 2010), an early warning system (EWS) has been developed. A prototype of this EWS was installed at a site in Silverdale, Northland, New Zealand. Much of the damage which incurs from rainfall induced landslides occurs in this region of New Zealand (NIWA & GNS Science, 2009).

EWSs for rainfall induced landslides started as empirical relationships which related the number of landslides in a given region to the intensity and duration of rainfall events. Examples can be seen in Dhakal & Sidle (2004), Keefer et al (1987) and Caine (1980). As technologies have developed, focus on EWSs has become more site specific. Current EWSs rely on measuring parameters such as pore pressure and displacement at a given site. Such EWSs are based on issuing an alarm when a predetermined level of these parameters has been reached (Chae & Kim, 2012; Intrieri et al., 2012). The EWS developed in this research was required to return to the user a number related to the possibility of failure, and also a timeframe for failure to occur. To achieve this, volumetric water content (VWC) sensors were installed at a variety of depths at the toe, mid-point and top of the slope. A tipping bucket rain gauge was used to monitor the intensity and duration of rainfall events. The fluctuations in VWC recorded by the sensors were replicated in a finite element model (FEM), using the recorded rainfall events as an influx into the slope. Next, a limit equilibrium analysis was used to determine the factor of safety (FOS) at each time step in the FEM. Thus, a database was created which contained values of the VWC as measured by the sensors at the site, and the corresponding FOS. This database was then used to train an artificial neural network (ANN). The ANN can thus predict the FOS of the slope in real time, using sensor readings as an input. The ANN can also predict the future FOS of the slope, using rainfall forecasts for the site as an input. The trend of the predicted FOS using the sensor data, and the future FOS obtained according to the rainfall forecast, form the basis of the EWS. Based on this information the user of the EWS can take the required action; in this case, lowering speed limits and putting detours in place.

1.1 *Site and Soil Description*

The site consists of a roadway embankment created from a cut operation during the construction of State Highway One, which runs parallel to the toe of the embankment. State Highway One is a major arterial which services Auckland city. The slope angle of the embankment is approximately 15°. A concrete dish drain is located on a bench at mid-height of the slope. The site is grassed, with some low height trees present. Debris from a landslide which occurred at the site in 2008 following prolonged rainfall almost crossed into the traffic lanes of State

Highway One, which could be potentially dangerous to motorists and cause significant disruption to the Auckland road network.

The soil at the site consists of weathered soil from the Northland Allochthon formation, which is renowned for its montmorillonite content (Power, 2005). This formation is susceptible to landsliding due to seasonal pore-pressure changes (Lentfer, 2007; O'Sullivan, 2009). The site consists of 3 strata; the underlying parent rock, a transition zone and a completely weathered residual soil. The transition zone consists of unweathered rock fragments in a silty clayey matrix. This transition zone has many slickensided shear surfaces present, and is thought to be one of the underlying factors that give rise to the susceptibility of the formation to landslides. The residual soil is a silty clay, susceptible to shrink swell movement. In general, sites in the Northland Allochthon have high ground water tables even in dry periods (O'Sullivan, 2009).

For a more detailed description of the site and soil properties, the reader is referred to Harris et al. (2012).

2 METHODOLOGY

A total of 13 VWC sensors were installed along the same cross section of the slope; at the toe, mid-height and crest. The sensors consisted of MP406s and ECH_2O probes (ICT International Pty Ltd, 2012), which were installed at approximately 0.25m depth intervals. A tipping bucket rain-gauge was used to record rainfall events. Recordings were made via a data logger at an hourly interval.

SEEP/W (GEO-SLOPE International Ltd, 2009a) was used for the FEM. The hourly rainfall captured at the site was input as an influx into the slope. A general evaporation pattern was applied to the model as a negative influx between rainfall events. This generalised evaporation pattern was based on a trial and error method to get the best agreement between the FEM results and the field monitoring results. The level of evaporation applied following a rainfall event was determined by the cumulative rainfall amount of the event. This FEM was coupled with the limit equilibrium analysis (LEA) program *SLOPE/W* (GEO-SLOPE International Ltd, 2009b). Thus at each hourly time step in the FEM, the FOS was obtained.

The soil properties used in these models are given in Table 1. The soil water characteristic curve was described using the Van Genuchten (1980) method, the parameters of which were obtained using the pressure plate apparatus. The permeability was determined using the falling head method. A variety of triaxial tests, including constant shear drained tests, were used to determine the shear strength parameters. The shear strength values used for the top soil layer were reasonably high to force the slip surface obtained in the LEA to a reasonable depth. φ^b represents the angle of shearing resistance due to matric suctions, as described by Fredlund et al. (1978)

Table 1. Soil parameters used in the models.

	Van Genuchten (1980) Parameter					Shear Strength		
	k	a	n	m	θ_r	φ	φ^b	c
	m/hr 10^{-3}	kPa^{-1}			%	°	°	kPa
Top Soil	36	608	3.27	0.69	38.5	40	20	10
Residual Soil	0.36	608	3.27	0.69	38.5	36	20	0
Transition Zone	0.036	297	5.23	0.81	37.2	21	20	3
Underlying Rock	0.0036	29	5.23	0.81	37.2	35	20	5

The ANN was developed using the software *Matlab* (The MathWorks Inc, 2012). For more information regarding ANNs and their use in geotechnical engineering, the reader is referred to Khanlari et al. (2012). The ANN was trained to predict the LEA-obtained FOS using the sensor readings from the field monitoring as inputs. The ANN was developed as a closed-loop recurrent dynamic network, where the FOS predicted by the ANN for the previous time-step was used as an input for the prediction of the FOS for the current time-step. The Levenberg-Marquardt method (Mathworks, 2010) was used to optimize the ANN, which had 10 hidden layers. The accuracy of the ANN improved when cumulative rainfall amounts were included as inputs into the ANN. Thus, cumulative rainfall amounts ranging from 2 to 200 hours were included as inputs into the ANN.

A second ANN was developed which predicts the LEA obtained FOS based solely on rainfall data. Thus the future FOS could be predicted at the site using rainfall forecasts obtained from the Meteorological Service of New Zealand (2012).

3 RESULTS

A reasonable agreement was obtained between the field measured and FEM obtained VWC. The permeability of the top soil layer had to be increased in the FEM in comparison to the underlying soil layers to obtain the required infiltration amount. Presumably this reflects the discontinuities such as surface cracks and vegetation of the soil. In some locations the agreement was very good, in others the agreement quite poor The reason for this is thought to be due to natural variability within the soil, as described by Dai et al. (2002).

To confirm this modelling process, the rainfall record obtained from the Meteorological Service of New Zealand (2012) leading up to the 2008 landslide was input into the models. As a FOS of just above unity was obtained at approximately the same time as the landslide occurred, it is assumed that the models used in the development of this EWS were reasonably accurate.

Because few extreme rainfall events occurred during the field monitoring period, artificial rainfall events were input into the rainfall record. Such artificial rainfall events can be seen in the upper graph of Figure 1, at an elapsed time of 1500 hours and 2200 hours. The comparison between the FOS obtained from the LEA, that obtained from the ANN using sensor data, and that obtained from the ANN using just rainfall data is shown in the lower graph of Figure 1. As observed, at each significant rainfall event there is a large decrease in the FOS. This FOS recovers rapidly following the rainfall event.

The ANNs are reasonably accurate at predicting the LEA obtained FOS. The mean squared error of the ANN using sensor was 0.41. Using just rainfall data, the mean squared error increased to 1.16. The FOS predicted by the ANNs is susceptible to large fluctuations, particularly during times of evaporation. This is seen at elapsed times of approximately 1600 hours and 2600 hours. Because these fluctuations occur during times of evaporation, they are not critical to the accuracy of the EWS; however they do indicate that some discrepancies occur due to the generalised evaporation pattern which was used. If a deterministic approach was used to measure evaporation, such as that described by Penman (1948), it is thought that such discrepancies will be minimised. The improvement in accuracy from the ANN which uses just rainfall data as an input, compared to the ANN which uses sensor data also, indicates that the use of the sensors provides an indication as to the actual amount of rainfall infiltration in the slope.

To provide an example of the EWS in use, the data corresponding to the point shown in Figure 1 was input into the EWS. The resulting plot is shown in Figure 2. Elapsed time = 0 corresponds to the point in time when the data was obtained from the site. The upper graph in Figure 2 shows the rainfall record obtained from the site (from an elapsed time of -24 to an elapsed time of 0). The rainfall is constant as it is obtained during an artificial rainfall event, as shown in Figure 1 (a). The rainfall record in Figure 2 from an elapsed time of 0 to and elapsed time of 5 hours is that obtained from the forecast.

The solid line in the lower graph of Figure 2 is the ANN – predicted FOS of the last 24 hours, using the sensor data as inputs. The dotted line is the predicted FOS over the next 5

hours, using the rainfall forecast data as an input. Because the ANN using the sensor data is more accurate than that using just rainfall data, this predicted FOS using rainfall forecasts loses accuracy over time. Thus, the predicted future FOS using rainfall forecast data is set to equal the FOS predicted using sensor data each time the sensor data is downloaded.
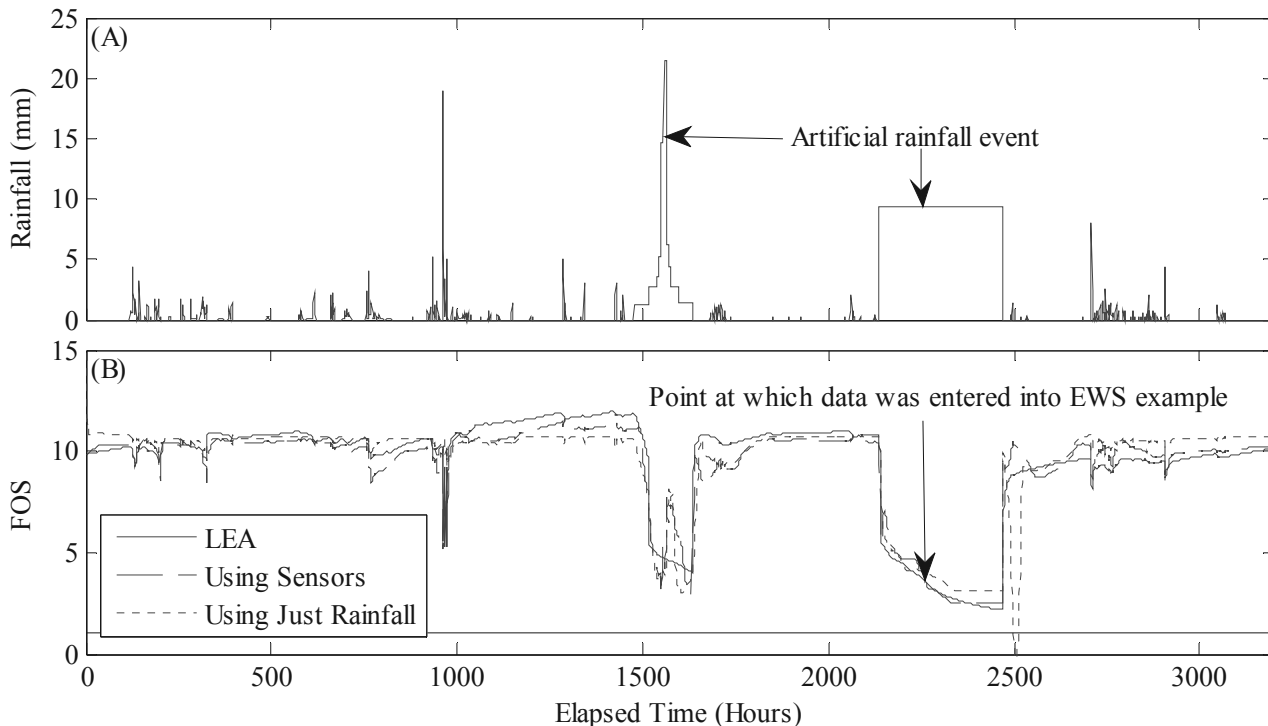

Figure 1. (A) Rainfall events input into the FEM and (B) corresponding FOS obtained from LEA, the ANN using field measured data, and the ANN using only rainfall events. The black line shows a FOS of unity (i.e. when failure will occur).
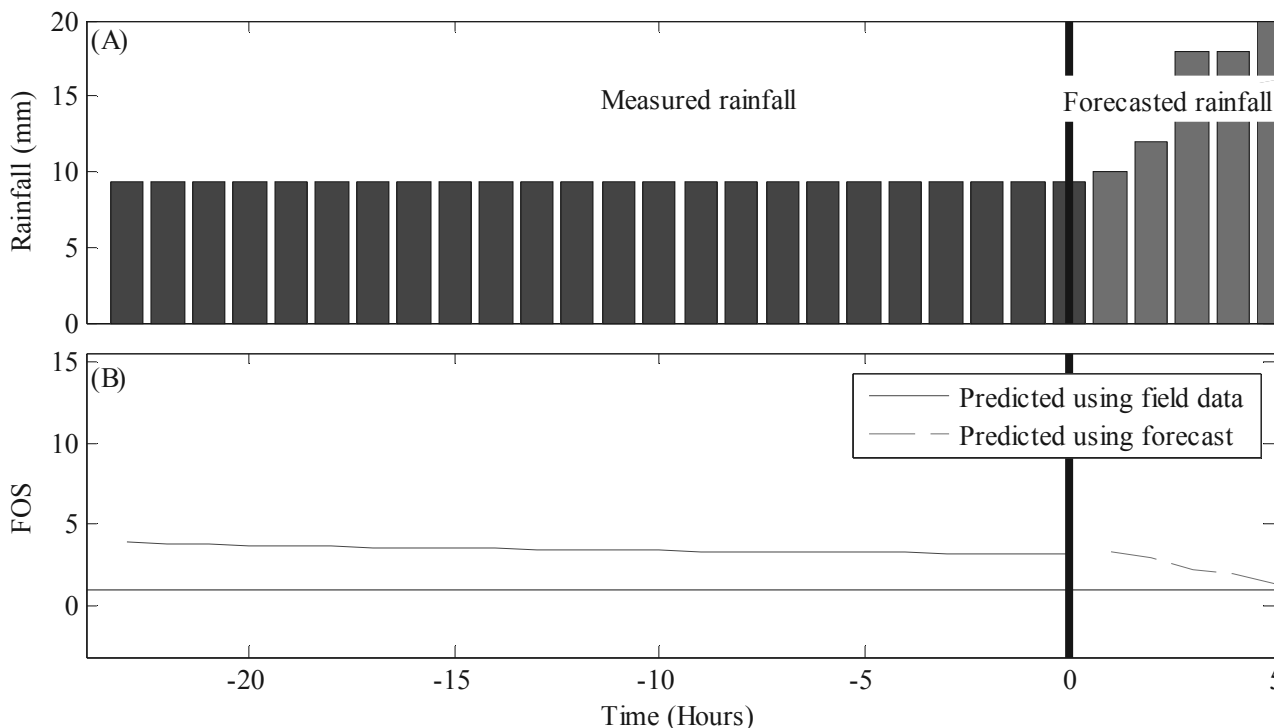

Figure 2. Example of the EWS in use. Elapsed time = 0 corresponds to the point in time at which the data was downloaded from the site (shown in Figure 1). The upper graph (A) shows the rainfall recorded at the site, and the forecasted rainfall at the site. The lower graph (B) shows the predicted FOS using the field data, and the predicted future FOS using the rainfall forecast. A FOS of unity is shown by thing black line.

4 APPLICATION OF THE EWS

The use of the EWS is summarised as follows. During a heavy rainfall event the field data is downloaded from the site in real time via the internet. This field data is then uploaded into the EWS. The FOS of the previous 24 hours, using the field data, is then obtained using the ANN. Based on the rate of change of this predicted FOS, the time until the FOS will reach a FOS of unity is returned to the user.

Next, the rainfall forecast for the next 5 hours for the site is obtained from the Meteorological Service of New Zealand (2012) via the internet. This forecast can be freely obtained by the public. This forecast is based on the Weather Research and Forecasting model, using data obtained from automatic weather stations, weather radar facilities, upper air sites and marine observation stations (Bridges, 2011). The predicted FOS over the next 5 hours is obtained using this rainfall forecast as an input into the ANN. The starting FOS for this predicted FOS is the last FOS obtained using the actual sensor data. Because of the difficulty in verifying forecasts at a local scale (Hodson, 2009), both the predicted FOS according to this forecast, and the rate of change of the FOS obtained from the field monitoring data, are used to estimate when failure may occur.

If failure is predicted to occur within five hours, then a stage one warning is issued. This involves warning motorists to lower speed limits around the landslide site. If failure is to occur within one hour, then a stage two warning is issued. This puts a detour in place, so motorists avoid the site altogether. Two warnings were used because the detour route adds approximately 25 minutes to the journey. Thus this detour route is put in place as late as possible to avoid frustration with the EWS due to false alarms. Warning motorists to lower speeds around the possible landslide site in advance is intended provide a balance between minimising the cost should the landslide occur, and avoiding frustration at the delay to motorists. During periods of heavy rainfall, the EWS should be updated on an hourly basis.

5 CONCLUSIONS

A site specific EWS for rainfall induced landslides has been developed. The EWS is based on the ability to predict the current FOS of the site using ANNs, rainfall forecast data and real time field measurements. The EWS proves to be useful at predicting when failure might occur, and also returns to the user a parameter related to the possibility of failure (the current FOS).

A FEM was used to replicate the field response of the site to rainfall events. This FEM was coupled with a LEA to predict the FOS at each time-step. The results of this modelling process were reasonably accurate, considering discrepancies caused by natural variation within the soil and the generalised evaporation pattern which was applied within the model.

The ANN which uses field measured data could predict the LEA obtained FOS with good accuracy; a mean squared error of 0.41 was obtained. To predict the future FOS, an ANN using just rainfall forecast data was developed. This ANN was less accurate, with a mean squared error of 1.16 obtained.

It is envisioned that the methodology used to develop this EWS can be replicated at a variety of sites as a means of risk reduction for rainfall induced landslides.

6 ACKNOWLEDGEMENTS

The Authors would like to thank the Auckland Motorways Alliance, Babbage Consultants, Beca Consultants and Hiway Geotechnical for their assistance throughout the project.

7 REFERENCES

Bridges, J. (2011). MetService's Investment in Forecasting. Retrieved 10 December, 2012, from http://blog.metservice.com/2011/04/metservice%E2%80%99s-investment-in-forecasting/

Caine, N. (1980). The rainfall intensity-duration control of shallow landslides and debris flows. *Geografiska Annaler Series A, 62*(1-2), 23-27.

Chae, B.-G., & Kim, M.-I. (2012). Suggestion of a method for landslide early warning using the change in the volumetric water content gradient due to rainfall infiltration. *Environmental Earth Sciences, 66*(7), 1973-1986.

Dai, F. C., Lee, C. F., & Ngai, Y. Y. (2002). Landslide risk assessment and management: an overview. *Engineering Geology, 64*, 65-87.

Dhakal, A. S., & Sidle, R. C. (2004). Distributed simulations of landslides for different rainfall conditions. *Hydrological Processes, 18*(4), 757-776.

Fredlund, D. G., Morgenstern, N. R., & Widger, R. A. (1978). The shear strength of unsaturated soils. *Canadian Geotechnical Journal, 15*(3), 313-321.

GEO-SLOPE International Ltd. (2009a). *Seepage Modeling with SEEP/W 2007, An Engineering Methodology, Fourth Edition* (4 ed.). Calgary, Alberta, Canada: GEO-SLOPE International Ltd.

GEO-SLOPE International Ltd. (2009b). *Stability Modeling with SLOPE/W 2007 Version, An Engineering Methodology, Fourth Edition* (4 ed.). Calgary, Alberta, Canada: GEO-SLOPE International Ltd.

Harris, S. J., Orense, R. P., & Itoh, K. (2012). Back analyses of rainfall-induced slope failure in Northland Allochthon formation. *Landslides, 9*(3), 349-356.

Hodson, A. (2009). Weather Forecast Accuracy: Part 1 Rainfall. Retrieved 17 December, 2012, from http://www.hortplus.com/main/article/weathersense/ws0903.pdf

ICT International Pty Ltd. (2012). Solutions for Soil, Plant and Environmental monitoring. Retrieved 31 August, 2012, from http://www.ictinternational.com.au/

Intrieri, E., Gigli, G., Mugnai, F., Fanti, R., & Casagli, N. (2012). Design and impementation of a landslide early warning system. *Engineering Geology, 147-148*, 124-136.

Keefer, D. K., Wilson, R. C., Mark, R. K., Brabb, E. E., Brown, W. M., Ellen, S. D., et al. (1987). Real-time landslide warning during heavy rainfall. *Science, 238*(4829), 921-925.

Khanlari, G. R., Heidari, M., Momeni, A. A., & Abdilor, Y. (2012). Prediction of shear strength parameters of soils using artificial neural networks and multivariate regression methods. *Engineering Geology, 131-132*, 11-18.

Lentfer, K. (2007). *Engineering geology of the Northland Allochthon, Silverdale, North Auckland, New Zealand.* Unpublished Master Thesis, The University Of Auckland, Auckland.

Mathworks. (2010). NARX Network (narxnet, closeloop), *Matlab Users Guide*.

Meteorological Service of New Zealand Ltd. (2012). MetService.com - your website for New Zealand Weather Forecasts. Retrieved 20 September, 2012, from http://www.metservice.com/national/index

NIWA, & GNS Science. (2009). *Natural Hazards 2008*.

NIWA, & GNS Science. (2010). *Natural Hazards 2009*.

O'Sullivan, A. S. (2009). *Suitability of Advanced Soil Models for Stability Analysis of Slopes in Northland Soils.* Masters Thesis, The University of Auckland, Auckland.

Penman, H. L. (1948). Natural Evaporation from Open Water, Bare Soil and Grass. *Proceedings of the Royal Society of London. Series A, Mathematical and Physical Sciences, 193*(1032), 120-145.

Power, J. (2005). *Engineering Geological Properties and Slope Movements in the Pakiri Formation and Northland Allochthon, Mahunrangi, North Auckland, New Zealand.* The University of Auckland, Auckland.

The MathWorks Inc. (2012). Matlab The Language of Technical Computing. Retrieved 4 September, 2012, from http://www.mathworks.nl/products/matlab/

Van Genuchten, M. T. (1980). A closed-form equation for predicting the hydraulic conductivity of unsaturated soils *Soil Science Society of America Journal, 44*(5), 892-898.

Characteristics of Ground Motion on Colluviums Slope Induced by Heavy Rainfall

Caractéristiques du déplacement du sol sur la pente de colluvions induit par la pluie violente

Jeng C.J., Sue D.Z.
Huafan University, Taiwan

ABSTRACT: In this study, a slope covered with various depths of colluvium soil and set up with monitoring system has been studied. The results from hundreds of settlement and displacement observation marks were taken into account. It was found that the maximum settlement and displacement were concentrated around the buildings of Hui-tsui, Zhian and Wu-Ming, and coincided with rainfall records for the area. The direction and distribution of displacement and surface cracks supports previous findings of a sliding block. The slope stability analysis for this study was carried out with the STABL program. A drainage system with additional stability measures was proposed to prevent an unstable slope caused by the rising up of the ground water table during rainfall. Finally, a curve showing the relationship between rainfall and slope stability is established and presented.

RÉSUMÉ : Dans cette étude, une pente couverte de colluvions de différentes profondeurs et équipée d'un système de surveillance a été étudiée, ayant recours aux remarques tirées des observations sur les affaissements et les déplacements de la pente. Nous avons découvert que les plus grands affaissements et déplacements de pente, coïncidant avec les précipitations dans la région, avaient lieu autour des bâtiments Hui-tsui, Zhian et Wu-Ming. La direction et la répartition des déplacements de pente ont confirmés nos recherches précédentes sur un bloc coulissant. Cette recherche a été faite avec le programme STABL. Un système d'évacuation des eaux avec des mesures de stabilité a été proposé pour protéger une pente instable contre les eaux souterraines qui montaient lors des averses. À la fin de cette étude, une courbe a été présentée pour expliciter la relation entre les précipitations et la stabilité de pente.

KEYWORDS: colluviums slope, ground monitoring, settlement and displacement, slope stability analysis, threshold value of rainfall.

1 INTRODUCTION

Rainstorms frequently trigger colluvium landslides. For example, in November 1993, more than 800 landslides were triggered by rainstorms on Lantau Island, Hong Kong (Dai & Lee 2002). In Taiwan, colluvium slope disasters related to rainfall are very common (Jeng et al, 2007; Jeng and Lin, 2011; Pan et al, 2008). The threshold values of typhoon disasters were studied extensively by Wang and Yeh(2011) and Hu and Liao (2010). This paper focuses on the effects of heavy rainfall on the colluvium slopes in northeastern Taiwan. The results from 295 points of settlement and displacement monitoring marks and their significance to ground motion were evaluated. Finally, a threshold value curve for typhoon rainfall is proposed.

2 BASIC INFORMATION OF THE FIELD CASE

The field case discussed in this research is the campus of Huafan University in northeastern Taiwan. The University was constructed on the slope. For risk management and research on slope stability, a monitoring system was set up and data was collected for over ten years. The monitoring system includes the inclinometer, building tilt measurement, tiltmeters, crack gauges, water level observation wells, settlement and displacement monitoring marks, rebar strain gauges, concrete strain gauges and rain gauges. According to the records obtained from the rain gauges from 2003 to 2010, the average annual rainfall is about 4000mm, most of which is attributed to torrential rainfall concentrated in the period of typhoon season. The maximum monthly rainfall record is in October 2010 with 1208mm.

2.1 Geological Condition

The base stratum of the site consists of the Miocene Mushan Formation. On the ground surface is 10 to 20 meters of colluvium comprised of a bottom layer of sandstone (SS) and thin alternating layers of sandstone and shale (SS-SH). The attitude of the bedrock is strike in the east-west direction with the dip-anchor 10° to 20° toward south.

2.2 Ground Motion Monitoring Results

2.2.1. Settlement and Displacement Monitoring

Since 2001, hundreds of settlement and displacement monitoring marks were set up and recorded every six months. Some additional marks were gradually included over the years. Data was recorded until January 2011, and after ten years of monitoring, a total of 295 marks were collected. The accuracy of the investigation was controlled to within 1/5000 by the plane triangulatuin method with GPS (TRIMBLE 4800) for six fixed station points. Four traverse points were then laid within the survey area and double-checked for accuracy to be within 1/10000. The coordinates and elevation of each observation mark were then surveyed based on those traverse points. The displacement and settlement values were obtained by comparing the coordinates and elevation results of each survey to the initial results from the first survey. The data marks were then divided into two categories for buildings, and for roads and land.

2.2.2 Settlement and Displacement Distribution

Figure 1 shows the results of the settlement distribution. The settlement marks around buildings are shown in solid triangle and the settlement marks for roads and other land are shown in solid circles, while the heaving points are shown in hollow circles. The values of settlement or heaving are discriminated into five levels from 5 to 25mm and are represented by different size circles. As indicated in Fig. 1, the maximum annual settlement is more than 20mm, distributed around the Hui-tsui building(B1), Chih-an building(B2) and Wu-Ming

building(B3). Although these values did not reach a dangerous level per the general management criteria, for some areas, the cumulated settlements reached over 10cm in the 10 years data. Moreover, when comparing the settlement distribution in Fig. 1 to the distribution of thickness of filled land, in the greater thickness of the filled land areas such as the Sport Ground(B4), the Basketball Court(B5) and Asoka Square(B6), the settlement is apparent. It is speculated that these higher settlement areas have something to do with the thicker fill. On the other hand, for the few heaving points like the upper slope of the Asoka Square, it is the result of the surface concrete pavement heaving caused by extrusion of the slope slide, not the ground surface condition.

Fig. 1 The settlement distribution diagram

Figure 2 shows the displacement tracks of each observation mark on the plan map. The scale of displacement has been enlarged to 200 times to highlight its tendency. It is shown in Fig. 2 that the main displacement direction is downward to the slope in the southwest or south direction. Meanwhile, the larger displacement is distributed, same as the aforementioned settlement distribution, around the areas of Hui-tsui building, Chih-an building and Wu-ming building. However, the upper slope of the Asoka Square shows movement in the upward direction to the slope. This also can be attributed to the aforementioned heaving phenomenon caused by extrusion of the slope slide, such that an overturning condition occurred in that area. The cracks created in the crown can also confirm this situation. Additionally, the direction of movement for the Sport court is different from the upper slope Dormitory building. That is because they are departing into different sliding blocks.

2.3 Correlation WITH rainfall

According to the results of the aforementioned settlement and displacement distribution, the most critical areas are concentrated in the Hui-tsui building, Chih-an building and Wu-ming building. As expected, the most significant contributing factor is rainfall. The correlation between settlement, displacement and, rainfall for the Hui-tsui building is discussed below.

The tendency of displacement with respect to time shown in Fig. 3 is generally similar to that of settlement vs. time shown in Fig. 4. Based on the increment tendency, both can be separated into four distinct time segments: (1) May 2001 to March 2002, (2) September 2004 to June 2006, (3) June 2007 to April 2009; (4) April 2010 to January 2011.
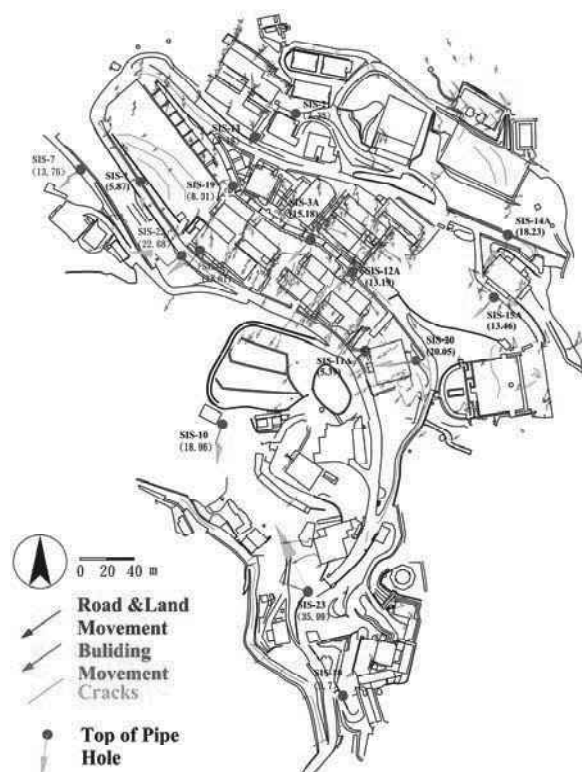

Fig. 2 displacement tracks and ground surface crakes distribution

When comparing the displacement and settlement time in Fig. 3 and Fig. 4 with the rainfall record, the displacement and settlement of the slope have a strong correlation with the rainfall record. In addition to the rainfall, another important influence factor to the displacement and settlement of the slope is the construction. For instance, within the third time segment, a new Library and Information Building were built with the excavation for the foundation at the toe of the slope. This may be the cause for the increased amount of displacement and settlement in the third time segment, despite the greater total accumulated rainfall in the second time segment (8973.5mm) versus the third (7241.5mm).

Aside from accumulated amounts, rainfall rate and duration also contribute to the threshold value that triggers displacement and settlement of the slope. Jeng and Sue (2008) illustrated that a rainfall threshold value of 800mm/month is able to trigger the displacement and settlement of the slope.

3 THE INCLINOMETER MONITORING

Many inclinometers have been installed starting the year 2000. Since then they have gradually settled in the test field, with some being damaged due to deformation. At present, 32 holes remain functional and are recording measurements. The results shows a sliding layer that deforms in depth from 14 to 15m. As seen from the core box the sliding occurs along the fracture layer.

4 COMPARISON THE RESULTS BETWEEN DISPLACEMENT MONITORING MARKS AND THE INCLINOMETER

The displacement monitoring marks are able to characterize the ground surface deformation and the inclinometer pipes can describe the ground deformation for the entire depth. To investigate the deformation of the slope, efforts were made by comparing the deformation of the top of the inclinometer pipes to the displacement monitoring marks. The comparison results shown in Fig. 2 indicated that the tendency of slope surface deformation obtained from both of these two data sets is

generally consistent. The primary slope deformation is toward the southwest and south direction, similar to the slope surface direction, which means the slope soil is generally moving downward along the slope.
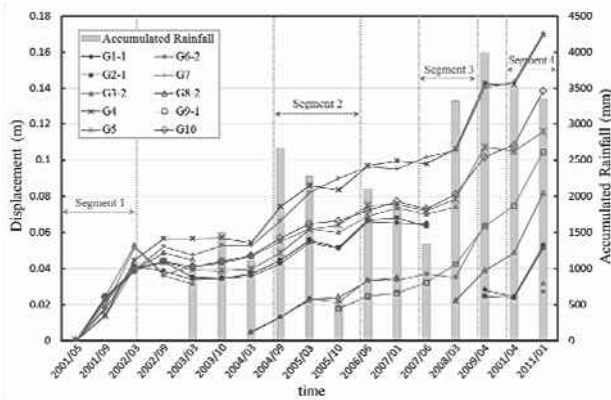

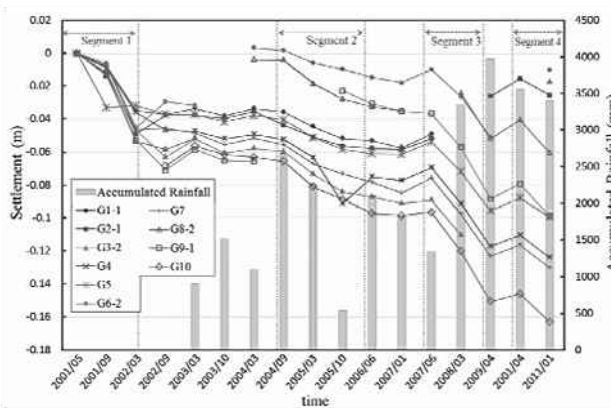Fig. 3 Relation curves of displacement and rainfall for Hui-tsui building

Fig. 4 Relation curves of settlement and rainfall for Hui-tsui building

5   SLOPE STABILITY ANALYSIS

After learning of the significant amount of slope deformation, there was concern for the integrity of the slope and any potentially hazardous contributing factors. To determine the slope stability, the limite equilibrium program - STABL was adopted and used for analysis. A simplified Bishop method with circular failure type was selected for the study. The input soil parameters were based on previous study (Jeng, 2003; Jeng and Li, 2009), as shown in Table 1. Areas with similar ground water variation and rainfall conditions were compared, and the crack distribution on the slope were used to assess potential failure areas.

Table 1 soils and rocks parameters

soils and rocks type	Cohesion (kPa)	Friction angle (°)	Unite weight (kN/m³)
Colluviums	18.45	29.92	19.31
sandstone and shale alternation	41.52	32.24	25.52
Sandstone	41.85	34.60	23.86

Figure 5 shows the slope stability analysis results for normal conditions. The safety factor is 2.17, which higher than the suggested value 1.5, remains within a stable state. However for rainfall conditions, when the ground water rises 3m, the safety factor decreases to 0.86. An unstable condition can then happen. Thus, it is concluded that the slope stability is significantly influenced by the rise in ground water during rainfall events.
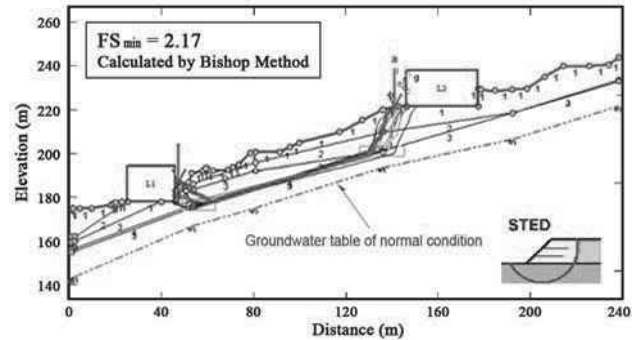

Fig. 5 Slope stability for normal condition (FS=2.17)

6   SLIDING BLOCKS DETERMINATION FROM SETTLEMENT AND DISPLACEMENT RESULTS

According to the inclinometer monitoring results provided by Jeng and Hsieh (2010), there are six sliding blocks within the slope. In that study, the sliding rate, depth and area of each block were presented. In addition to that information, this study evaluates the result of ground surface movement, including displacement direction and settlement, trend of ground water flow, and the distribution of ground surface cracks. A comprehensive evaluation was made to exam the previous sliding blocks study results. Fig.6 shows the finding which supports the presence of two sliding blocks. Among them, block No. A-1 is located in the area around Wu-Ming building, Asoca Square and the Chea-chau building; block No. A-2 is located in the area around Sport ground where there is 20m of fill. These two sliding blocks coincide with blocks R1 and L1 of the previous study (Jeng and Hsieh, 2010).   Both blocks show movement in the shallow layer and are located in the active sliding areas. Numerous cracks can be found along the ground surface in these areas.

7   STABILIZE MEASURES AND THRESHOLD VALUE OF RAINFALL

According to aforementioned stability analysis results, it was learned that the rise of ground water in rainstorm conditions significantly impacts slope stability. Consequently, slope stability will be improved with the addition of drainage and drawdown systems and retaining structures. With budget and effectiveness in mind, the first step should focus on the area around the Wu-Ming building where the ground water and geological condition is least favorable. A detailed description of improvement steps includes :
  1. Improvement of the ground surface drainage system for water runoff.
  2. Installation of six catchpits with the horizontal drainage pipes, shown in Fig.7, to draw down the ground water level.
  3. Filling of ground surface cracks to prevent seepage of water runoff into cracks.
  4. Construction of bore piles and tiebacks with ground anchors behind the Wu-Ming building to strengthen the retaining structure for the toe of the slope.
    Finally, for the safety management of the slope, threshold curves were established to illustrate the relationship between rainfall intensity and accumulation, and the observed slope deformation (Fig. 8). Looking ahead, these curves can be used for predicting slope stability before typhoons as it often brings significant amount of rainfal. The information correlating rainfall and slope stability improves slope management and risk assessment. To minimize the slop disaster from occurring, the proposed approaches are believed to be beneficial to the community.
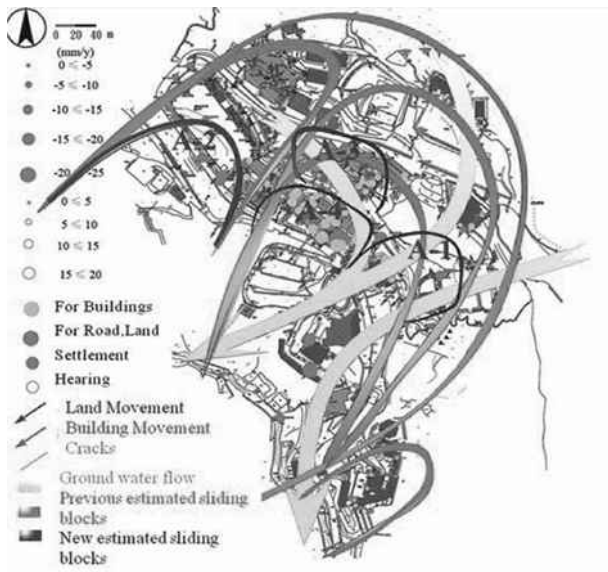
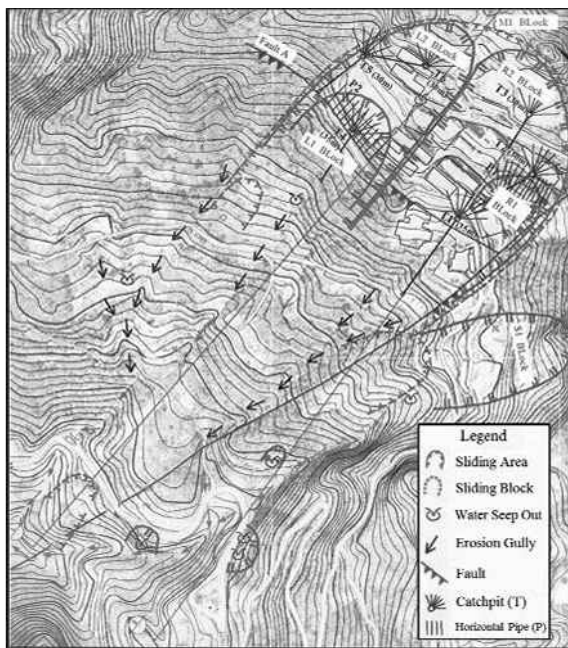Fig. 6 Sliding blocks and movement distribution plane

Fig. 7 Plan for catchpits location

8   CONCLUSIONS AND DISSCUSSION

This paper discusses the displacement and settlement of the slope, evaluates the sliding block theory, and analyzes slope stability. After summarizing the results, stabilization measures
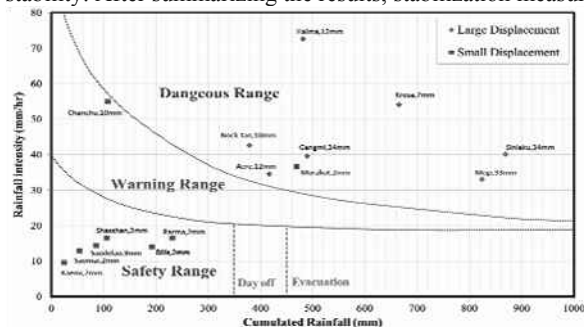

Fig. 8 Threshold value curves correlate with displacement

and rainfall threshold values were established. Based on the results, the following conclusions can be made:

1. The areas with the most significant settlement and displacement are located around the buildings of Hui-tsui, Zhian and Wu-Ming Building. Due to lack of slope stability, surface cracks appeared and several sliding surfaces have been observed.
2. The deformation of the top of the inclinometer pipes is consistent with the displacement monitoring marks. Findings indicate the primary slope deformation to be toward the southwest and south direction. In addition, rainfall was found to be the most significant factor for slope deformation and slope stability.
3. The results of the slope stability analysis show that an increase in ground water level is the most critical factor for slope stability.
4. The distribution of potential sliding blocks was examined by using slope displacement and settlement data, and the location of surface cracks. The sliding direction is strongly correlated to the direction of ground water flow. Depth or thickness of fill also contributes to slope sliding.
5. Several stabilization measures including catchpits with horizontal drainage pipes, bore piles and tieback ground anchors, and threshold value of rainfall are recommended to improve the slope stability. It was believed that the information presented is very important for slope disaster prevention.

9   REFERENCES

Dai F.C. & Lee C.F. 2002. Landslides on natural terrain— physical characteristics and susceptibility mapping in Hong Kong. *Mountain Research and Development*, 22(1), 40-46.

Hu I-Chou and Liao H. J. 2010. A Model of Slope Mitigation Priority for Alishan Mountain Road in Taiwan. *Journal of Performance for Constructed Facilities*, *ASCE*, 24(4), 373-381.

Jeng C.J. 2003. Study on Slope Stability Mechanism of Huafan University by Using of Inclinometer Displacement and Limiting Equilibrium Stability Analysis. *Hua Fan Annual Journal*. 9, 115-127.

Jeng C.J. Chu B.L. Tsao S.P. Lin T.A. 2007. Matrix Suction of Unsaturated Colluvium Slope Influenced by Rainfall and Plant Condition : A case of Taiwan Huafan University. *Wuhan University Journal of Natural Sciences*, 12(4), 689-694.

Jeng C.J. Su D.Z. 2008. Case study on the settlement and displacement monitoring results on a slope induced by natural hazards. *Proceedings of 3rd Taiwan-Japan Joint Workshop on Geotechnical Hazards from Large Earthquakes and Heavy Rainfall*. 119-130.

Jeng C.J. Li C.T. 2009. Case Study on the Numerical Analysis of the Building Foundation Excavation on the Dip-Slope. *Journal of Architecture*, (68), 147-162.

Jeng C.J. Hsieh T.Y. 2010. Case study on the sliding surface judgment for the monitoring slope. *Journal of Huafan art and design*. 6, 1-14.

Jeng C.J. and Lin T.A. 2011. A Case Study on the In-situ Matrix Suction Monitoring and Undistubed-sample Laboratory Test for the Unsaturated Colluvium Slope. *Soils and Foundations*. 51(2),321-331.

Wang H.M. and Yeh T.C. 2011. An Analysis on the Characteristics of Extreme Hourly Rainfall of Typhoon over Taiwan. *Meteorological Bulletin*, 48(3) September, 1-14.

Stability and movements of open-pit lignite mines in Northern Greece

Stabilité et mouvements de terrain dans les mines de lignite à ciel ouvert en Grèce du Nord

Kavvadas M.
National Technical University of Athens, Greece

Agioutantis Z.
Technical University of Crete, Greece

P. Schilizzi P.
Public Power Cooperation, Greece

Steiakakis C.
General Consulting Ltd "ISTRIA", Greece

ABSTRACT: This paper presents a case of a lignite mine in Northern Greece with excavated slopes exceeding 100-120m in depth in which substantial movement is occurring, with an average rate 10-20mm/day. The Mavropigi mine is very important for the power supply of Greece and uninterrupted operation is often critical, meaning that excavation is taking place on moving soil masses. The stability of the moving southeast slope is investigated and the information developed from an extensive monitoring campaign, with survey prisms, inclinometers and piezometers is presented. The use of the investigation data to evaluate the type of movement, the geometry of sliding surface and the effectiveness of remediation measures are analyzed in detail. The procedure of assessing the stability and safe slope operation during production, even with high rates of movement and the effect of precipitation are presented. It is shown that there are situations that mine slopes can move several meters laterally and still be operational without catastrophic failures.

RÉSUMÉ : On présente dans cet article une étude des mouvements de terrain dans une mine de lignite du nord de la Grèce. Dans cette mine à ciel ouvert de 100 à 120 m de profondeur, des glissements de pente (lents) sont observés : 10-20 mm/jour. L'exploitation de cette mine (Mavropigi) de lignite, primordiale pour la production d'énergie en Grèce, s'effectue sans interruption dans des pentes en mouvement permanent. Les problèmes de stabilité de la pente sud-est de la mine sont étudiés et les mesures effectués in situ à l'aide de différents appareillages (mesures topographiques, inclinomètres et piézomètres) sont présentés. L'analyse de l'ensemble des mesures est effectuée afin de caractériser le type de mouvement de terrain et la géométrie de la surface de glissement. Par ailleurs, l'efficacité des mesures adoptées pour stabiliser les pentes est analysée via les mesures effectuées sur le site. Une procédure permettant d'évaluer le risque de perte de stabilité pendant les phases d'exploitation (intensive) en tenant compte des effets défavorables des précipitations est proposée. On met ainsi en évidence des cas pour lesquels les pentes peuvent se déplacer latéralement de plusieurs mètres sans pour autant engendrer des ruptures majeures.

KEYWORDS: Slope movement, Coal open pit, Slope monitoring, Slope stability, Landslide.

1 INTRODUCTION

The Public Power Cooperation (PPC) operates a number of large open pit lignite mines in Northern Greece (Amyntaio-Ptolemais Basin). The Mavropigi mine has been mined since 2003 and at present the excavated slopes have reached depths exceeding 100-120m. Since 2011, the southeast slopes have shown persistent large horizontal movements at an average rate of 10-20mm/day, at times reaching more than 40-50mm/day affected by increased precipitation. The moving mass was estimated around 6Mm^3. This paper presents a case of significant movements that occurred at the southeast slope (Fig. 1), and details the monitoring, evaluation and mitigation measures taken to safeguard mining operations which had to be uninterrupted for production management purposes.

Figure 1. Southeast slopes of Mavropigi lignite mine.

2 GEOLOGICAL AND GEOTECHNICAL CONDITIONS

The Mavropigi mine is in the sedimentary fill of the Ptolemais basin which includes terrestrial and lacustrine deposits of Miocene up to Pleistocene age, with abundant lignite horizons (Diamantopoulos, 2006). Near horizontal intercalations of Marls, Lignites, Stiff Clays and Sands are the predominant materials; from a geotechnical point of view they can be described as "Hard Soils – Soft Rocks". The main intercalations are Marl and Lignite. The Marl material is mostly classified as Elastic SILT or Organic SILT (MH-OH) per USCS (ASTM D2487). Locally in the Marl – Lignite intercalations, thin (few centimeters thick) beds of High Plasticity CLAY (CH) are found. These almost horizontal thin beds have very low residual shear strength and often act as slip surfaces. The mechanical properties of the different materials encountered in the area of Mavropigi are presented in Table 1. These parameters are assessed from triaxial, direct shear and ring shear tests performed on selected core samples and are used for the slope stability calculations of the Mine.

Table 1. Range of Geotechnical Properties of Mavropigi Mine Materials.

Parameters / Materials	Marl	Lignite	Clay (CH)
Unit weight γ (kN/m^3)	16-18	11-13	16-18
Effective Cohesion c' (kPa)	50-150	150-200	5-50
Effective friction φ' (deg)	28-35	34-36	26-30
Residual Friction φ_r' (deg)	-	-	5-10

3 MONITORING OF SLOPE MOVEMENTS

At the end of 2010, tension cracks were observed at the crest of the Southeast mine slopes and visually observed horizontal transverse movements at the toe under prisms 5A3 and 6A4. Although this is usual in large and deep open pit mines, nevertheless, 20 prism monitoring stations, two inclinometers (KL-10, 11) and two piezometers (PM-10, 11) were installed on the slopes. The locations of the instruments are shown in Figure 2 together with the limits of the moving mass.

Prism measurement records were made available between January 2012 and up to the writing of this paper (Sept. 2012).
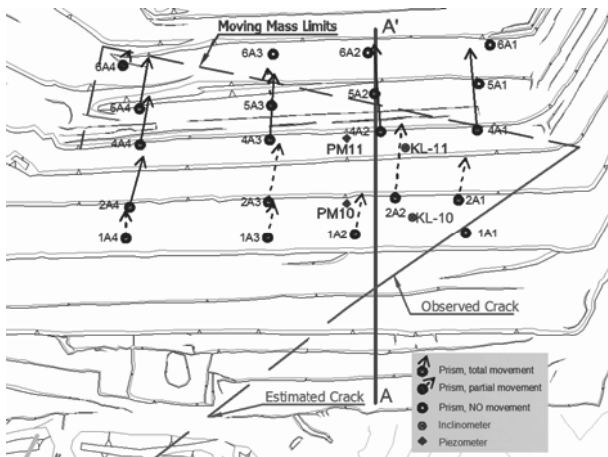

Figure 2. Monitoring equipment and trends on Southeast slopes

Initially the measurements were executed with a lower accuracy total station and only the "sloping distance" between the prism and the measurement base was evaluated. Due to the complexity and criticality of the situation, a new robotic total station of high accuracy (0.5cc) replaced the old one. With the new total station the movement vectors could easily be measured and evaluated. The use of the robotic total station eliminated the surveyor operation error and the high accuracy significantly reduced the horizontal and vertical angular measurement error.

Due to the high rate of movement, few measurements were taken from the inclinometers before they were sheared off. From inclinometer KL-10, six measurements were obtained in a period of one month which recorded a total displacement 100mm at 27m depth from ground surface. Inclinometer KL-11 recorded only three measurements in a period of 11 days, with maximum displacement 150mm at 9m depth. The two piezometers could only be measured twice due to operational reasons and recorded water table elevation at 18.4m in PM-10 and 9.9m in PM-11. A precise water table could not be estimated based on the piezometer measurements because of the number of measurements and since the faces of the slopes were found dry. Piezometric conditions and water pressures are very difficult to model with a high degree of accuracy in mines (Sullivan, 2007) mainly due to the presence of multiple perched aquifers. Figure 3 shows a geological cross section with the monitoring equipment and the failure surface location (white line). Dark zones indicate the lignite beds.
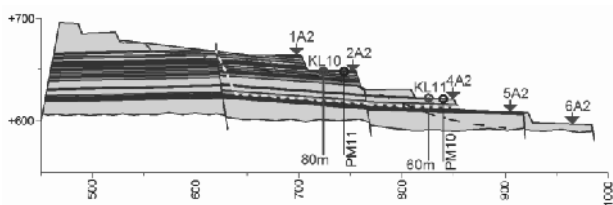

Figure 3. A-A' cross section with monitoring locations

4 EVALUATION OF SLOPE MOVEMENTS

The operation of Mavropigi mine is very important for the power supply of Greece and uninterrupted operation is often critical. Mining operations may take place even in moving slopes, as long as safety of personnel and equipment is satisfied. Zavodni (2000) states that "*mining operations can proceed safely with minimum interruption if failure mechanisms are understood and slopes are properly monitored*" even in moving slopes. The way to assess if a "moving slope" can be mined safely is to determine if the slope movement is regressive or progressive. A regressive movement is cyclic decelerated while a progressive movement exhibits overall acceleration without appreciable deceleration intervals (Zavondi, 2000). In regressive movements, mining operation can continue after incorporating a monitoring system. If monitoring data indicate a progressive type of movement the operations are in danger of imminent collapse. The question posed to the Geotechnical Engineer is to determine the type of movement that characterizes each particular slope. The failure mechanism needs to be understood and a sufficient quantity of qualitative measurements is required. In the literature, most case studies are analyzed after an incident and with adequate monitoring data and the type of movement is identified (Ryan & Call 1992). At the Mavropigi mine, decisions had to be made based on the day to day data becoming available without a priori having a large amount of data that could be used to determine the type of movement.

Initially, based on the geological model of the area, the visual observations of the cracks in the crest and the translational surface located by the inclinometers, a limit equilibrium model was analyzed to evaluate if the movement was possible and to back calculate the material properties of the shear surface. Based on back analysis (Figure 4) it was found that a sliding surface was possible with residual friction angle of $\varphi_r = 7^o$ for the near horizontal surface and $\varphi' = 24^o$ for the back scarp. These values were considered to be the lower bounds since no water pressures were introduced and were in good agreement with the laboratory ones provided in Table 1 for the area.
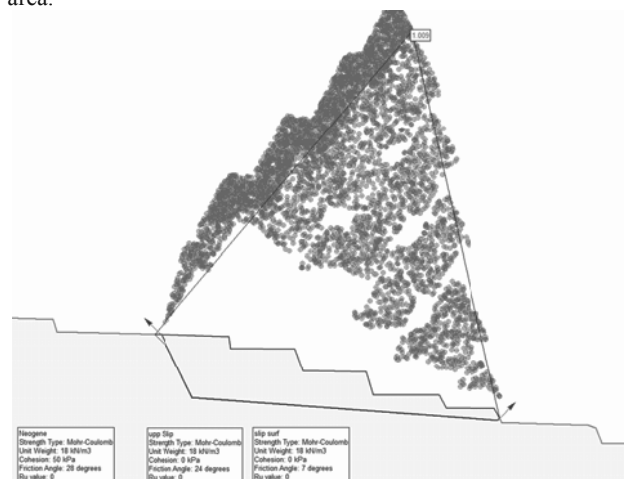

Figure 4. Back analysis of the sliding surface

From the geological model, the inclinometer readings and the back analysis it was found that the movement is taking place in a failure shear zone (thin high plasticity clay interlayer) with an inclination of about 4-5°. Based on this information an initial estimate was made that the movement could be of the regressive type based on the recommendations by (Zavodi and Broadbent, 1980), by which movements are deemed regressive when taking place on a surface with a lower angle in relation to the slope face inclination and the shear resistance (friction angle) of the material. Initial remediation measures consisting of excavating part of the top two benches were analyzed with the same data. Analysis showed that the FS became 1.06 which was considered

positive for reducing the rate of movement. The slope stability analysis was considered only indicative due to the complex nature of the sliding mass (fig 2) and greater emphasis was placed on slope monitoring.

The data were further analyzed to verify the regressive type of movement and to identify a possible onset of a progressive type of movement, leading to failure. One method to evaluate monitoring data is the inverse velocity measurement versus time. Based on this method, as described by (Rose and Hungr, 2007), when the inverse velocity of slope movement is plotted against time, failure is imminent as the trend line approaches zero values (velocity increases asymptotically). In Figure 5 the inverse velocity versus time is presented for prism 2A4.
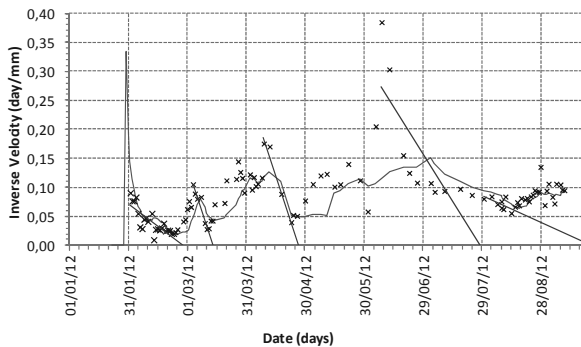

Figure 5. Inverse velocity versus time for prism 2A4

Figure 5 suggests that if this method is to be followed, at numerous times the mine slopes could be at imminent collapse. This is evaluated based on the extrapolation to zero of the regression lines for different time intervals (straight lines). For example the first imminent collapse could have been evaluated to have occurred on 01/03/12, which did not happen.
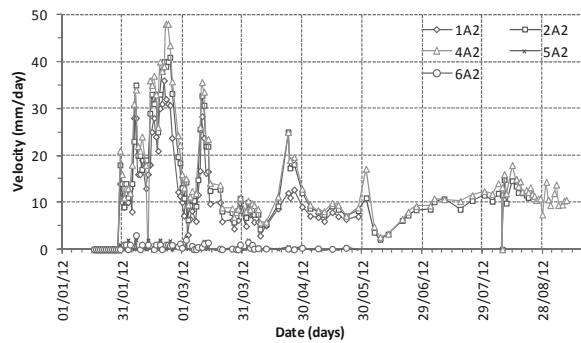

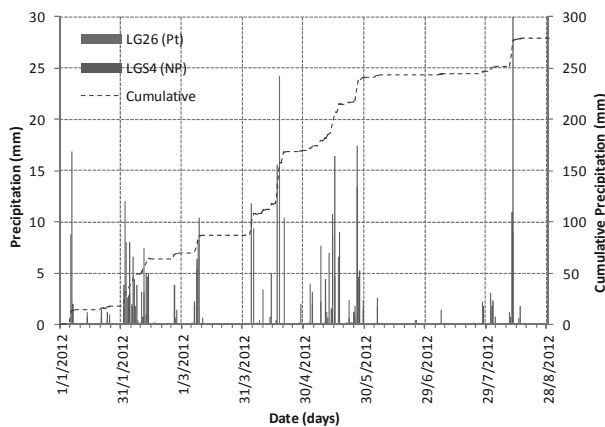Figure 6. Velocity versus time for prisms of bench 2

Figure 7. Precipitation versus time from two stations

Subsequently regression analysis presented times that failure could take place. This graph presents a situation where the

method could not work properly without evaluating other critical factors such as precipitation or excavation unloading.

Figure 6 presents velocity versus time for all prisms of bench 2 while figure 7 shows the daily and cumulative precipitation for two weather stations. The mine is located in between these stations with a distance of about 7km. No precipitation data at the mine were available.

From the evaluation of figures 6 and 7, a strong correlation between the precipitation and the increase of velocity is observed. Further observation of figure 6 provides information of a stick – slip mechanism and a regressive type of movement in which the velocity does not increase or decrease at a constant rate but undergoes abrupt changes. During and after heavy precipitation the water filled tension cracks provide an increasing driving force. As displacement continues, the width of the cracks increase and the water level drops with a dissipation of water pressure. This is a repetitive situation which modifies the velocity of the sliding mass. Beginning of February 2012 limited (day shift) remedial excavation was executed on bench 1 and above to reduce the weight of the sliding mass. Such excavation increased after March 2012 being conducted on 24hour shifts. As a result movement velocities were reduced after that date.

In retrospect the movement was of the regression type (or behaved in this respect due to the excavation at the top of the slope) as can be seen from the displacement measurements at bench 4 presented in Figure 8. In this graph the displacement at the bench is plotted versus time for four different prisms in different locations transversally placed on the slope (Figure 2).
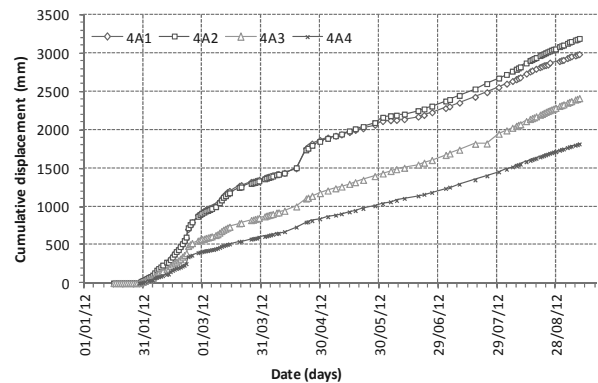

Figure 8. Cumulative displacement of prisms on bench 4

When the cumulative displacement becomes convex, movement acceleration is evident and a progressive type of movement can be inferred. When the cumulative displacement becomes concave then deceleration takes place. As can be seen from Figure 8 displacements "cyclically" change from convex to concave and back to convex meaning that this is of a mixed condition where the regressive type of movement prevails. Although the cumulative displacement of this slope for a period of 7 months is over 3m, the slope is still in a regressive type of movement and therefore mine operations continue.

5 GEOMETRICAL MOVEMENT INFORMATION

The dense grid of monitoring prisms together with the high accuracy of the robotic total station produced additional invaluable data for the moving mass. As can be seen from Figure 2 the vectors of motion are presented with arrows. The continuous arrows present monitoring information until the writing of this paper. The dashed arrows present monitoring data that were discontinued for operational reasons at different times. As can be seen from the arrows and the displacements at bench 4 (figure 8) the slope moves more to the east than to the west while both translation and rotation occurs at the same time. The reason for this complex movement can be explained taking

into account the sloping surface geometry and the kinematic conditions of the adjacent southwest slopes.

The southwest slopes can be considered in a regressive moving condition as well. The movement there occurs at a very deep seated slip surface which is, partly formed on the schist bedrock probably on top of an old "inactive" fault and partly on the Neogene formation. The movement of that deeper slide may be generating lateral forces that are applied on the moving mass at the southeast mine slopes.

The complex movement of the southeast slope is also affected by the inclination of the sliding surface where the southeast slopes are moving on. As was shown previously in section A-A' the shear surface was found to have an unfavorable inclination of about 4-5°. This unfavorable situation is not continuous transversely across the slope. This can be safely stipulated after careful evaluation of the vertical – horizontal displacement of different prisms in the same bench (figure 9). In this plot the abrupt change of measurements is due to maintenance of the prisms.
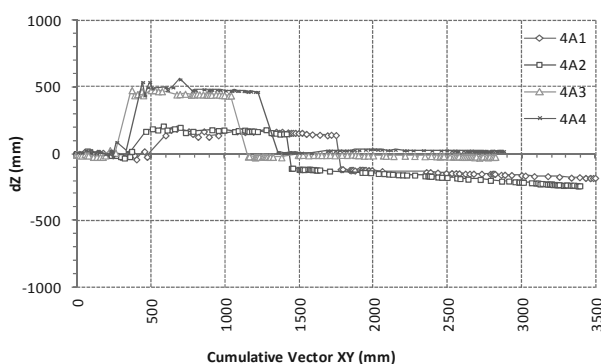

Figure 9. Vertical versus horizontal displacement

As can be seen from figure 9 and especially after about 1500mm of horizontal displacement, when no abrupt changes are recorded, the prisms at the east (4A1, 4A2) produce a downward movement with an angle of about 4-5°. The 4A2 prism which is located at cross section A-A' produces the same shear surface inclination as determined by the inclinometers. Further to the west the sliding surface becomes horizontal or even with slight favorable inclination. This sliding surface geometry is responsible for the increased movement to the east and the rotation of the moving mass.

This detailed evaluation of the moving mass could not be possible without the dense grid of measuring points and the high accuracy of the robotic total station. It is evident that with accurate monitoring data shear surface inclinations can be evaluated from surface measurements.

6   CONCLUSIONS

A case study of high horizontal movements recorded on operational surface mine slopes has been presented. The slopes have been moving with an average velocity of about 10-20mm/day and until today they have moved more than 3m.

The sliding mechanism was investigated and, based on back-analysis, it was determined that the southeast slopes of the mine are moving on top of a near horizontal shear surface with a residual friction angle of about 7°. As no water pore pressure was used in the analysis, this value is considered a lower bound, and coincides with values determined through lab experiments for similar material in the mine area. The slope stability analysis is considered only indicative due to the complex geometry of the moving mass. It is not possible to exactly model this mass with plain strain limit equilibrium methods.

Great emphasis was given in the monitoring program in which twenty prisms, two inclinometers and two piezometers were used. The surface monitoring of the prisms was greatly

enhanced when a high accuracy robotic total station was used. With the high accuracy of the robotic total station, movement vectors could easily and accurately be measured.

The measurements presented a complex type of movement of the slopes which most of the time was of the regressive type. The slope movement has been found to be greatly affected by the periodic precipitation and the infilling of the tension cracks.

Based on the regressive type of movement, the mining operation could continue and at the same time remedial measures taken with excavation of the top benches for unloading. This remediation decreased but did not stop slope movements. Although the slopes have moved more than 3m horizontally, they are still in operation without significant problems. Movements were found to be very sensitive to external conditions such as precipitation.

The increased accuracy of the prism measurements allowed the identification of the sliding surface inclination along the mine slopes. It was found that the sliding surface changed inclination transversely.

High mine slopes can be in operation even if they produce high rates of movement, as long as the sliding mechanism type is identified and continuously monitored. Remedial measures can be incorporated in the mine plan in order to reduce movements.

REFERENCES

ASTM D2487-98. *Standard Practice for Classification of Soils for Engineering Purposes (Unified Soil Classification System).* American Society for Testing and Materials.

Diamantopoulos, A., 2006. *Plio-Quaternary Geometry and Kinematics of Ptolemais Basin (Northern Greece): Implications for the Intral-Plate Tectonics in Western Macedonia.* Geologia Croatica, 59/1, Zagreb.

Rose, N.D, Hungr, O., 2007. *Forecasting potential rock slope failure in open pit mines using the inverse-velocity method.* International Journal of Rock Mechanics & Mining Sciences, Vol. 44, pp. 308-320.

Ryan, T. M. & Call, R. D., 1992. *Applications of rock mass monitoring for stability assessment of pit slope failures.* Rock Mechanics, Tillerson & Wawersik (eds), Balkema, Rotterdam.

Sullivan, T. D., 2007. *Hydromechanical Coupling and Pit Slope Movements.* Slope Stability 2007, Potvin (ed), Australian Center for Geomechanics, Perth

Zavodni, Z. M. and Broadbent, C. D., 1980. *Slope failure kinematics.* CIM Bulleting, Vol. 73, No. 816.

Zavodni, Z. M., 2000. *Time-Dependent Movement of Open-Pit Slopes.* Chapter 8, Slope stability in surface mining, Hustrulid, McCarter, VanZyl (eds), Society for Mining, Metallurgy and Exploration.

A web-based tool for ranking landslide mitigation measures

Un outil internet pour classer les techniques visant à diminuer le risque de glissements de terrain

Lacasse S., Kalsnes B.
International Centre for Geohazards / Norwegian Geotechnical Institute (NGI), Norway

Vaciago G.[1], Choi Y.J.[2], Lam A.[3]
[1]*Studio Geotecnico Italiano, Milano, Italy;* [2]*NGI Inc., Houston, TX USA;* [3]*GEO Civil Engineering Development Dept, Hong Kong, HKSAR*

ABSTRACT: As part of the European project SafeLand, a compendium of structural and non-structural mitigation measures for different landslide types in Europe was prepared, and the measures were assembled into a web-based "toolbox". The purpose of web-based toolbox is to assist decision-making and to guide the user in the choice of the most appropriate mitigation measures. The paper presents an overview of the toolbox features, mitigation measures considered and an example of the report for one application of the toolbox.

RÉSUMÉ : Parti intégrante du projet européen « SafeLand », un recueil des mesures d'atténuation structurelles et non structurelles pour les différents types de glissements de terrain en Europe a été établi. Les mesures d'atténuation ont été assemblées dans une "boîte à outils" utilisable via internet. Le but de la boîte à outils est d'aider la prise de décision et de guider l'utilisateur dans le choix des mesures de diminution des risques les plus appropriées. Le document présente un aperçu des fonctionnalités de la boîte à outils, des mesures de diminution des risques envisagées et un exemple de rapport pour une utilisation spécifique de la boîte à outils.

KEYWORDS: Landslide, Quantitative vulnerability evaluation, Intensity, Susceptibility

1 INTRODUCTION

As part of the research done in the European project SafeLand "Living with landslide risk in Europe: assessment, effects of global change, and risk management strategies", a compendium of structural and non-structural mitigation measures for different landslide types in Europe was prepared, and the measures were assembled into a web-based "toolbox". Emphasis was placed on providing a rational and flexible framework applicable to existing and future mitigation measures.

The purpose of web-based toolbox is to assist decision-making and to guide the user in the choice of the most appropriate mitigation measures.

The mitigation measures were classified into three categories, describing whether the mitigation measures addressed the landslide hazard, the vulnerability or the elements at risk themselves. The measures considered include structural measures reducing hazard and non-structural mitigation measures, reducing either the hazard, the vulnerability or the exposure of the elements at risk. The structural measures include surface protection and control of surface erosion; measures modifying the slope geometry and/or mass distribution; measures modifying surface water regime - surface drainage; measures modifying groundwater regime - deep drainage; measured modifying the mechanical characteristics of unstable mass; transfer of loads to more competent strata; retaining structures (to modify slope geometry and/or to transfer stress to competent layer); deviating the path of landslide debris; dissipating the energy of debris flows; and arresting and containing landslide debris or rock fall.

The non-structural mitigation measures, reducing either the hazard or the consequences: early warning systems; restricting or discouraging construction activities; increasing resistance or coping capacity of elements at risk; relocation of elements at risk; sharing of risk through insurance. The measures are described in the toolbox with fact sheets providing a brief description, guidance on design, schematic details, practical examples and references for each mitigation measure. Each of the measures was given a score on its ability and applicability for differ-

ent types of landslides and boundary conditions, and a decision support matrix was established.

The web-based toolbox organizes the information in the compendium and provides an algorithm to rank the measures on the basis of the decision support matrix, and on the basis of the risk level estimated at the site. The toolbox includes a description of the case under study and offers a simplified option for estimating the hazard and risk levels of the slide at hand. The user selects the mitigation measures to be included in the assessment. The toolbox then ranks, with built-in assessment factors and weights and/or with user-defined ranking values and criteria, the mitigation measures included in the analysis. The toolbox includes data management, e.g. saving data half-way in an analysis, returning to an earlier case, looking up prepared examples or looking up information on mitigation measures. The toolbox also generates a report and has user-forum and help features.

The paper presents an overview of the toolbox features, mitigation measures considered and an example of the report for one application of the toolbox. The reports in the reference list can be found on the SafeLand project website, www.safeland-fp7.eu. Much more details and the descriptions of each mitigation measure along with references for each can be found in the reports in the list of reference.

2 TOOLBOX FEATURES

The toolbox is organized to guide the user in ranking different mitigation measures and to assist in the decision-making about the most appropriate mitigation measures to select for a site. The toolbox suggests the ranking of mitigation measures for a given landslide situation. The toolbox offers an extensive menu of different mitigation measures, and the user selects those that he wishes to consider in the study at hand.

The toolbox documents "do's and don'ts" and "how to". It estimates relative costs, benefits, hazards, effectiveness and vulnerability of each measure to mitigate hazard and/or risk.

The toolbox offers a simplified option for estimating the hazard and risk levels of the slide at hand. The user selects the mitigation measures to be included in the assessment. The toolbox then ranks, with built-in assessment factors and weights and/or with user-defined ranking values and criteria, the mitigation measures included in the analysis.

The web-based toolbox does data management, generates a report and provides help to the user, as well as a user forum.
The web-based toolbox has the following features:

- Algorithm to describe a case study, estimate the expected hazard and risk level and to rank, on an engineering judgment basis, the mitigation measures included in an analysis.

- Data management (e.g. save data half-way in analysis, return to an earlier case, look up prepared examples or look up in database for information on mitigation measures).

- Report generation function.

- User forum.

- Help function.

- User management, with password-protected user login.

The toolbox will probably always be in evolution, even after the SafeLand project is completed, as it has "dynamic" technical contents that need to be updated as experience grows and new information becomes available. At all times, the user has access to the toolbox with options to Create a new case, Open a saves case, View a case study, Save a current case, Save as, Delete a current case , and Print.

Several modern technologies were implemented in developing the toolbox. One of them includes desktop toolbar that can automatically be enabled, disabled or hovered to improve user-interface. These toolbar icons of 64 x 64 pixels were designed using graphic software.

3 DECISIONS IN TOOLBOX

3.1 Risk classes and need for mitigation

The risk classes used in the toolbox are shown in Figure 1. Depending on a combination of levels of consequence and hazard selected by the user, three risk classes can be assigned by the toolbox: Low, Medium and High. In this simplified model, "High risk" represents an unacceptable risk that requires new site investigations, stability calculations and mitigation measures, "Medium risk" is a risk level that requires considering doing new site investigations and analyses. For "Low risk" situation, further risk reducing measures are not necessary.

Hazard \ Consequence	Low	Medium	High
High	Medium Risk	High Risk	High Risk
Medium	Low Risk	Medium Risk	High Risk
Low	Low Risk	Low Risk	Medium Risk

Figure 1. Risk classes in Toolbox of Mitigation measures.

3.2 Ranking of measures

The selection of the most appropriate mitigation measures to be adopted in specific situations take into account the following:

(1) the factors that affect the hazard, in terms of the type, rate, depth and the probability of occurrence of the movement or landslide, such as, for example:

– the physical characteristics of the geo-system, including the stratigraphy and the mechanical characteristics of the materials, the hydrological (surface water) and the hydro-geological (groundwater) regime;

– the morphology of the area;

– the actual or potential causative processes affecting the geo-system, which can determine the occurrence of movement or landslides;

(2) the factors that affect the nature and the quantification of risk for a given hazard, such as the presence and vulnerability of elements at risk, both in the potentially unstable area and in the run-out area; and (3) the factors that affect the feasibility of specific mitigation measures, such as, for example:

- the phase and rate of movement at the time of implementation;

- the morphology of the area, accessibility and safety of workers and the public;

- environmental constraints, e.g. archeological, historical and visual values;

- pre-existing structures and infrastructure that may be affected directly or indirectly;

- capital and operating cost, including maintenance.

The user selects in the toolbox the mitigation measures to be considered. To rank the selected mitigation measures, a simple additive algorithm with weighted scoring factors for both default criteria and user-defined criteria in the toolbox was developed. The ranking (R_i) is therefore done on the basis of the summation of weighted (w_i) contributing factors (F_i) for each evaluation criterion:

$$R_i = \sum w_i \cdot F_i \qquad (1)$$

Where i are the mitigation measures selected by the user for analysis, from 1 to *n*; *w* is the weighting factor proposed by the toolbox; the default value for all w_i at start is 1.0 and can be changed by the user; and *F* is the scoring factor proposed by the toolbox and which can be changed by the user

Values for *F* and *w* are proposed by the toolbox, based on a decision support matrix. The user can change the values of *F* and *w* according to his/her experience and/or engineering judgment. The user can also add additional factors F_i that will then be automatically included in the analysis.

The scoring factors (F_i) for each mitigation measure offered as default in the toolbox are for the user to consider, adopt or modify during his/her assessment of the problem at hand. The scoring for all ranking parameters is on a scale of 1 to 10, where 1 describes the least favourable attribute (worst, lowest, poorest, most expensive), and 10 the most favourable attribute (best, highest, strongest, least expensive or not expensive). The scoring of 0 is used when the mitigation measure is inapplicable or inappropriate.

The weighting factor (w_i) reflecting the relative importance of criteria or corresponding scoring factors is in the range of 0 (least) to 1 (most). The default value is set to zero, and the toolbox assigns a values of unity (1) as a function of the input provided by the user in the following technological criteria categories: type of movement, type of sliding material, depth of movement, rate of movement, groundwater, and surface water.

3.3 Priority setting

At the end of the ranking process, the toolbox lists the ranking of the selected mitigation measures in the order of most appropriate to least appropriate measures. The calculated value for R_i

is also given as well as which factor(s) F_i has the most significance on the result. The user can compare the ranking order and can go back to the previous steps and change the weighting and scoring factors, especially those with high effect on the ranking R_i, if necessary.

4 CLASSIFICATION OF MITIGATION MEASURES

The Safeland partner Studio Geotechnico Italiano S.r.l. (SGI) prepared a "Compendium of tested and innovative structural, non-structural and risk-transfer mitigation measures for different landslide types" (SafeLand 1). This review was used a basis for the selection and evaluation of the different mitigation measures included in the toolbox for landslide hazard and risk mitigation measures.

The classification of the mitigation measures was done in terms of the components of a risk assessment (hazard, vulnerability and elements at risk). Table 1 presents this classification. The classification system addresses three components of risk: hazard, vulnerability and elements at risk, where risk R can be expressed as:

$$R = H \cdot C = H \cdot V \cdot E$$

where H is the hazard or the probability of occurrence of an adverse event (landslide); C is the consequence(s); V is the vulnerability or the degree of loss of an element at risk for a given hazard; and E are the elements at risk.

To reduce (or mitigate) the risk, one can reduce the hazard or reduce the consequences (reduce the vulnerability or reduce the exposure of the elements at risk).

Table 2. Classification of mitigation measures (structural measures on top, non-structural measures on bottom)

Class	Component of risk addressed	Brief description	Notes and other terms used
Stabilization	Hazard (H)	Eng'g works to reduce the landslide probability of occurrence	Preventive, remedial, hard, soft, active stabilization.
Control	Vulnerability(V) (consequence)	Eng'g works to protect, reinforce, isolate the elements at risk from the landslide area	Preventive, hard, soft, passive stabilization.
Avoidance	Elements (E) (consequence)	Temporary or permanent reduction of exposure w/ warning systems, evacuation/-relocation, sheltering, land-use planning.	Reduction of the exposure of the elements at risk. Monitoring, early warning systems and civil protection procedures, often temporary, selective avoidance measures.
Tolerance	Elements(E) (consequence)	Awareness, acceptance and/or sharing of risk	Indirect reduction of the exposure of the elements at risk.

Within the general domain of the structural mitigation measures classified above as "stabilization", i.e. reduction of hazard, it is possible to consider a further subdivision in relation to the triggering factors and mechanisms that each measure addresses.

5 MITIGATION MEASURES CONSIDERED

The toolbox includes near 70 structural mitigation measures and six non-structural mitigation measures. The structural measures are divided into ten categories and belong to the class of measures either reducing hazard or reducing consequences. The structural mitigation measures included are:

A Structural measures reducing hazard
1 Surface protection and control of surface erosion
1.1 Hydro-seeding, turfing and trees/bushes
1.2 Fascines/brush
1.3 Geosynthetics
1.4 Substitution - drainage blanket
1.5 Beach replenishment, rip rap
1.6 Dentition
2 Modifying the slope geometry and/or mass distribution
2.1 Removal of (actual or potentially) unstable soil/rock mass
2.2 Removal of loose or potentially unstable blocks/boulders
2.3 Removal of material from driving area
2.4 Substitution in driving area with lightweight fill
2.5 Addition of material to the area maintaining stability
3 Modifying surface water regime - surface drainage
3.1 Surface drainage works (ditches, channels, pipe works)
3.2 Local re-grading to facilitate run-off
3.3 Sealing tension cracks
3.4 Impermeabilization (geo-membranes, impervious facing)
3.5 Vegetation - hydrological effect
3.6 Hydraulic control works (channel lining and check dams)
3.7 Diversion channels
4 Modifying groundwater regime - deep drainage
4.1 Shallow trenches filled with free-draining material
4.2 Deep trenches filled with free-draining material
4.3 Sub-horizontal drains (conventional drilling)
4.4 Sub-horizontal drains (directional drilling)
4.5 Wells
  4.5.1 Small and medium dia. vertical wells (<800 mm)
    4.5.1.1 Relief of artesian pressure
    4.5.1.2 Under-drainage of perched aquifer
    4.5.1.3 Pumps
    4.5.1.4 Siphons
  4.5.2 Medium diameter vertical wells (1200-1500 mm)
  4.5.3 Large diameter vertical wells (>2000 mm)
  4.5.4 Caissons (>5-6 m) with gravity drainage
4.6 Drainage tunnels, adits, galleries, with secondary drains
5 Modifying mechanical characteristics of unstable mass
  5.1 Vegetation - mechanical effects
  5.2 Substitution
  5.3 Compaction from surface
  5.4 Deep compaction (e.g. vibro-compaction)
  5.5 Mechanical deep mixing with lime and/or cement
  5.6 Low pressure grouting with chemical binder
  5.7 Jet grouting
  5.8 Modification of ground water chemistry
6 Transfer of loads to more competent strata
  6.1 Counterfort drains (trench drains)
  6.2 Piles
  6.3 Barrettes (diaphragm walls)
  6.4 Caissons - mechanical effects
  6.5 Soil nailing
  6.6 Dowels and harnessing
  6.7 Rock bolting
  6.8 Strand anchors
7 Retaining structures (to modify slope geometry and/or to transfer stress to competent layer)
7.1 Reinforced soil structure
7.2 Gabion walls
7.3 Crib walls
7.4 Dry stack masonry walls
7.5 Mass concrete or masonry walls
7.6 Reinforced concrete stem walls

B Structural measures reducing consequences
8 Deviating the path of landslide debris
8.1 Deflection structure
8.2 Debris flow/rockfall shed
9 Dissipating the energy of debris flows
9.1 Drop structure
9.2 Debris-restraining structure
9.3 Debris flow impediments

10   Arresting and containing landslide debris or rockfall
10.1 Debris-resisting barrier
10.2 Rock fall barrier
10.3 Rock fall net
10.4 Debris retention basin

The following non-structural mitigation measures, reducing either the hazard or the consequences (or vulnerability and exposure of elements at risk) or in some cases both hazard and consequence, are included in the toolbox:
a   Early warning systems
b   Restricting construction activities
c   Discouraging construction activities
d   Increasing resistance/coping capacity of elements at risk
e   Relocation of elements at risk
f   Sharing of risk through insurance

6   RANKING CRITERIA

Six criteria categories were implemented to rank the appropriateness of each mitigation measure: type of movement, type of sliding material, depth of movement, rate of movement, groundwater, and surface water. Table 3 lists the criteria used in the toolbox.

Table 3.   Ranking criteria used for each mitigation measure

Ranking criterion	Descriptor
Type of movement	Falls
	Topples
	Slides
	Spreads
	Flows
Material type	Earth
	Debris
	Rock
Depth of movement	Superficial (< 0.5 m)
	Shallow (0.5 to 3 m)
	Medium (3 to 8 m)
	Deep (8 to 15 m)
	Very deep (> 15 m)
Rate of movement	Moderate to fast
	Slow
	Very slow
	Extremely slow
Groundwater	Artesian
	High
	Low
	Absent
Surface water	Rain
	Snowmelt
	Localized
	Stream
	Torrent
	River
Maturity of technology	
Reliability of performance	
Reliability in terms of uncertainty in design	
Reliability in terms of uncertainty in implementation	
Safety during construction	
Service life required (durability)	
Aesthetics	
Typical cost	

7   EXAMPLE RESULT

Table 4 presents a typical result of the ranking algorithm for a potential instability in a soft clay slope.

Table 4. Typical report from toolbox.

Rank	Category	Measure	Score	Most significant parameters *
1	Surface protection	Vegetated cover	66	Material/debris Type of movement/-flow
2	Surface protection	Surface drainage	65	Depth of movement Surface water/-stream
3	Surface protection	Infilling of cracks	62	Surface water/stream Rate of movement/-slow
4	Reducing consequence	Early warning system	36	Depth of movement/-superficial Material/rock

* With respect to measure appropriateness

8   SUMMARY

The paper provides only a glimpse in the toolbox. One has to use it to actually see how it functions. The toolbox will be available at the Safeland web site in 2013.

The purpose of web-based toolbox is to assist decision-making and to guide the user in the choice of the most appropriate mitigation measures. The mitigation measures are classified into three categories, describing whether the mitigation measures addressed the landslide hazard, the vulnerability or the elements at risk themselves. The measures are described in the toolbox with fact sheets providing a brief description, guidance on design, schematic details, practical examples and references for each mitigation measure. Each of the measures was given a score on its ability and applicability for different types of landslides and boundary conditions, and a decision support matrix was established.

The web-based toolbox organizes the and provides an algorithm to rank the measures on the basis of a decision support matrix, and on the basis of the risk level estimated at the site.

9   ACKNOWLEDGMENTS

10   REFERENCES

SafeLand (2012). Deliverable D5.1. "Compendium of tested and innovative structural, non-structural and risk-transfer mitigation measures for different landslide types" (rev 1-Final dated 2011-03-31) prepared by Studio Geotechnico Italiano S.r.l. (SGI).
SafeLand (2012). Deliverable D5.2. " Toolbox of landslide mitigation measures" (rev 1-Final dated 2012-05-11) prepared by the Norwegian Geotechnical Institute (NGI).
SafeLand website. www.safeland-fp7.eu .

A Numerical Study of Granular Surge Flow through a Row of Baffles

Une étude numérique des écoulements granulaires à travers une rangée de chicanes

Law R.P.H., Lam A.Y.T., Choi K.Y.
Geotechnical Engineering Office, Civil Engineering and Development Department, The Government of the Hong Kong Special Administrative Region, Hong Kong, China

ABSTRACT: A numerical study that utilizes three-dimensional discrete element method was undertaken to investigate the impact process and the dynamic interaction between granular surge flow and baffles. In the numerical analyses, the granular flow medium and the baffles were modelled as frictional spherical discrete elements and rigid square objects respectively. The location, velocity and forces acting on the individual discrete elements during the impact and interaction process were captured and recorded in the analyses. A detailed assessment of the numerical output data indicates that a single row of baffles is effective in reducing the kinetic energy and discharge of the granular surge flow.

RÉSUMÉ : Une étude numérique utilisant une approche par éléments discrets en 3D a été mise en oeuvre pour étudier le processus d'impact et l'interaction dynamique entre un écoulement granulaire et des chicanes. Dans cette étude, le milieu granulaire a été modélisé par des objets sphériques et les chicanes par les objets carrés. Les grains comme les chicanes sont considérées comme parfaitement rigides. L'emplacement, la vitesse et les forces agissant sur les éléments discrets au cours du processus d'impact et l'interaction ont été ainsi calculés. Une évaluation détaillée des données de sortie indique qu'une seule rangée de chicanes est efficace pour la réduction de l'énergie cinétique et l'évacuation de l'écoulement granulaire.

KEYWORDS: baffles, granular flow, discrete element method, energy dissipation, impact pulse, discharge.

1 INTRODUCTION

Granular surge flows such as debris flows and snow avalanches are dangerous natural hazards. Baffles have been employed to dissipate the kinetic energy of such flows and reduce the entrainment of channel bed deposits. Rows of baffles could be constructed across the flow path in order to reduce the flow velocity, the entrainment potential and dynamic impact force on downstream structures. Baffles constructed across the debris flow path are potentially more advantageous than the conventional rigid debris-resisting barriers because baffles are generally easier to construct without the need for extensive site formation works. However, the dynamic interaction of granular surge flow with baffles is still an emerging area of research to both the academics and the practitioners.

Discrete element method was introduced in geomechanics by Cundall and Strack in 1979 and was later adopted as a research tool by other researchers (e.g. Muir et al., 2008; Sibille et al., 2008; Thompson et al., 2009). The discrete element method is an appropriate and useful tool for modelling debris flow and snow avalanche because of the granular flow nature (Zwinger 2000; Nicot 2004; Hutter et al, 2005; Pudasaini & Hutter 2007) of these phenomena. In a previous study by Law 2008, a series of flume model tests and three dimensional discrete element analyses were conducted to investigate the impact behaviour of granular surge flow on a rigid barrier. The study has been extended to investigate granular surge flow through a row of baffles. This paper focuses on the numerical study of the impact process and the dynamic interaction between baffles and granular surge flow using the discrete element method.

2 NUMERICAL STUDY

2.1 Introduction

The granular medium was modelled as incompressible frictional discrete elements and the planar rigid surfaces were used to model the baffles and the ground surface. In the analyses, the location and velocity of the individual discrete elements together with the forces acting on each element were captured and recorded in order to study the impact process and the dynamic interaction between baffles and granular surge flow. The displacement of individual discrete elements is independent of one another, and they only interacted when coming into contact with each other or with the baffles and other rigid boundaries. The motion of each discrete element was calculated on the basis of the forces acting on it by the Newton's laws of motion. The displacements and rotations of the discrete elements were computed in the numerical analyses.

2.2 Numerical model setup and test procedure

Figure 1 shows the geometry of the flow path and the baffles. The granular medium comprises a total of 30,000 spherical discrete elements and all the discrete elements have a uniform diameter of 0.05m. The material density of each discrete element is 2,650 kg/m^3. The discrete elements were not intended to simulate motion of individual particles in the granular medium. Instead, the macroscopic behaviour of the granular medium was represented by the contact behaviour between the discrete elements. Planar rigid surfaces were used to model the baffles and the ground surface.
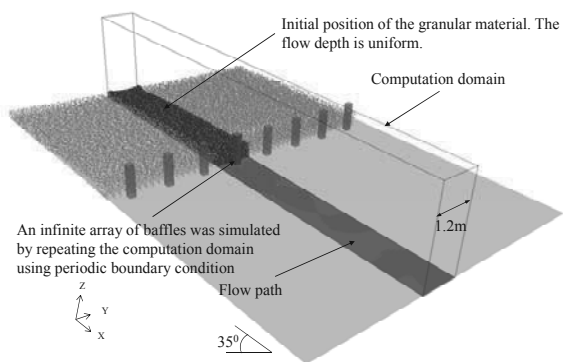
Figure 1. Numerical model setup

The length and width of the computation domain were 15m and 1.2m respectively. The slope gradient was chosen to be 35^0. The plan area and the height of the individual baffle were 0.2m x 0.2m and 1m respectively. The baffle was located in the middle of the flow path. The periodic boundary condition (PBC) was applied along the y-direction (Figure 1) of the computation domain. With the PBC, discrete elements leaving one side of the computation domain in the y-axis will emerge on the opposite side with the same dynamic properties, such as velocity, force, etc. This boundary condition helps to reduce the computation time since the impact of granular flow medium on an array of baffles could be simulated using a single baffle and a reduced number of discrete elements (i.e. only the dark particles shown in Figure 1 need to be modelled). With reference to Chen 2009, a baffle spacing of 1m and the ratio of baffle spacing to element diameter of 20 were adopted in the analysis to prevent clogging of the discrete elements between the baffles.

Each numerical analysis is divided into two stages, namely the initial stage and the impact stage. At the initial stage, the granular medium comprising an assembly of discrete elements with random packing was placed on a rigid surface inclined at 35^0 as shown in Figure 1. The individual discrete elements stabilized itself under the action a body force, which was equivalent to gravity and acting perpendicularly downwards at the ground surface. The body force acting on the individual discrete elements was rotated to the vertical direction in the next stage to enable the granular medium to flow downslope under the action of gravity and impact the baffles. The initial thickness of the granular medium was uniform and chosen to be 0.5m before impacting on the baffles. At the impact stage, the granular medium was given an initial velocity of 8 m/s. The corresponding Froude number of the initial flow condition is close to 4 which fall within the range of Froude number of debris flow events reported by Hubl et al 2009.

2.3 *Contact law applied in numerical model*

The local rheology of the flow material was simulated by applying the contact law in the numerical model. The linear Hookean stiffness model was adopted for the discrete elements and the rigid planar surfaces in the numerical analyses. According to Crosta et al. 2001, the contact stiffness of the discrete element has negligible influence on the computed mobility of granular material. Given that the chosen stiffness value have only minimal influence on the computed result, the discrete element and wall stiffness used were both chosen to be 1×10^8 (N/m) such that the elements almost behave like a rigid body.

The relative translational and rotational motions between the discrete elements are mainly resisted by contact friction. The macroscopic friction angle of dry sand was measured to be 35^0 (Teufelsbauer et al. 2011, Chiou 2005, Pudasaini et al 2005 and 2007, Pudasaini and Hutter 2007). Based on field and laboratory tests conducted by Chau et al. 2002, Azzoni and Freitas 1995 and Robotham et al. 1995, the coefficient of restitution was chosen to be 0.5.

According to Calvetti and Nova 2004, the macroscopic friction angle of the granular medium is typically much less than 30^0 irrespective of the value of the contact friction angle adopted on spherical discrete elements without rolling resistance. Calvetti et al 2003 and Tamagnini et al 2005 emphasized the need to inhibit particle rotations and calibrate the particle contact friction angle based on the desired value of the macroscopic friction angle of the granular medium.

In the numerical analyses, a rolling resistance term was added in the calculation of rolling motion of discrete elements. The rolling resistance was calculated using a directional constant torque model elaborated by Ai et al 2011. The model applies a constant torque on a particle to represent the rolling friction. The direction of the torque was always against the relative rotation between the two contact entities. The torque between two in-contact spheres i and j can be expressed as:

$$M_r = -(\omega_{rel} / |\omega_{rel}|) \mu_r R_r F_n \qquad (1)$$
$$\omega_{rel} = \omega_i - \omega_j \qquad (2)$$

where
ω_i = the angular velocities of sphere i;
ω_{rel} = the relative angular velocity between two elements;
μ_r = the rolling friction coefficient;
F_n = the normal contact force; and
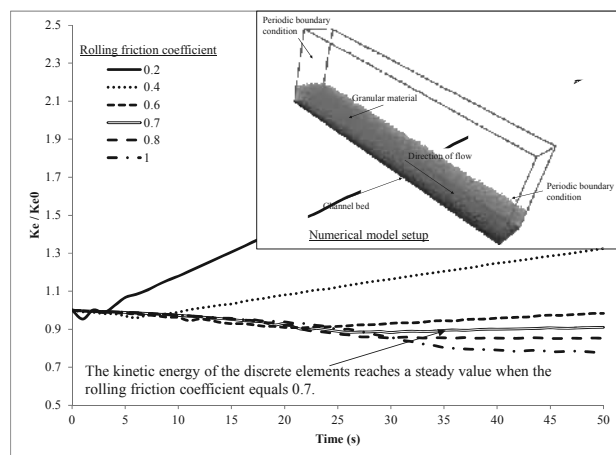R_r = the radius of the discrete element

Figure 2. The effects of the rolling friction coefficient on the time history of the computed kinetic energy

A calibration exercise was carried out to identify the appropriate rolling friction coefficient for the numerical study. Figure 2 shows the numerical setup for the calibration work. The simulation box boundary was periodic in nature in order to allow the granular material to transport on the incline indefinitely. The granular material was given an initial velocity of 8m/s. By adopting a macroscopic friction angle of 35^0 (i.e. same as the channel inclination), a coefficient of restitution of 0.5 and trying different rolling friction coefficients (i.e. μ_r = 0.2, 0.4, 0.6, 0.7, 0.8 and 1) in the calibration exercise, the granular flow would eventually reach a steady kinetic energy.

Figure 2 shows the time history of the kinetic energy (k_e) of all discrete elements relative to the computed k_e at time zero (k_{e0}). The k_e is the sum of kinetic energy of all discrete elements. Based on the results of the calibration exercise, the granular flow could attain a steady velocity when the rolling friction coefficient reached a value of 0.7, which was chosen to be the appropriate rolling friction coefficient for the numerical study. The input parameters adopted is summarized in Table 1.

Table 1. Parameters adopted in the numerical study

Parameter	Magnitude
Slope angle	35^0
Baffle dimension	0.2m x 0.2m x 1m
Particle diameter	0.05m
Density of each particle	$2650kg/m^3$
Particle and wall stiffness	1×10^8 (unit)
Contact friction angle	35^0
Coefficient of restitution	0.5
Rolling friction coefficient	0.7
Approaching velocity	8m/s

3   COMPUTED RESULTS

3.1   *Flow Profile*

Figure 3 shows the plan and side view of a number of snapshots recorded in the numerical analyses.   The time difference between each snapshot is 0.012 second. The darker the particle colour, the lower was its velocity. A velocity reduction of the discrete elements immediately behind the baffles was observed on plane and Section A-A as shown in Figure 3.

In Figure 3a, at time = 0s, the particles at the front of the flow were just in contact with the baffle. In Figure 3b, at time = 0.012s, the dark region signified the slowing down of the discrete elements behind the baffle after impacting it. The boundary of the dark region where the momentum of the discrete elements was reduced by the baffle is marked by a white dashed line.
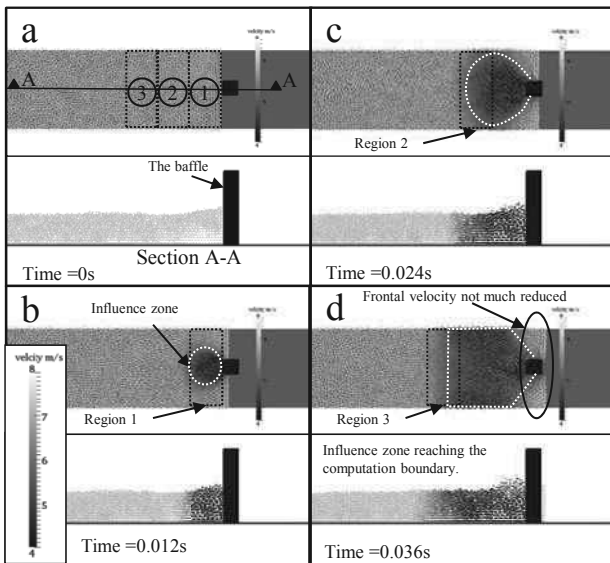

Figure 3. The snapshots showing the change of particle velocity during impact. The time difference between each snapshot is 0.012 second.

In Figure 3c, at time = 0.024s, the size of the dark region increased in size, and the dark region reached the computation boundary in Figure 3d. This indicates that the reduction of the momentum of the discrete elements behind each baffle was no longer localized, but a continuous zone of momentum reduction behind the row of the baffles.   The presence of such a momentum reduction zone suggests that most discrete elements passing through the baffles will be decelerated by the flow resistance provided by the baffles. The only exception was the frontal discrete elements located between the baffles.   As highlighted in Figure 3d, the velocity of the frontal discrete elements between the baffles was not reduced by the baffles. It is noted from the side view snapshots that the flow depth right behind the baffle increases at the time of frontal impact. The

deceleration of the discrete elements was observed to be uniform over the flow depth.

In order to capture and record the dynamic behaviour of the discrete elements behind the baffles, three measurement regions (i.e. region 1, 2 and 3) as shown in Figure 3a were established. Each measurement region was 0.4m in length in the longitudinal direction. The unbalanced force, kinetic energy and discharge rate of the discrete elements within the measurement regions in the first 0.14 seconds of the impact process were recorded and presented as follows.
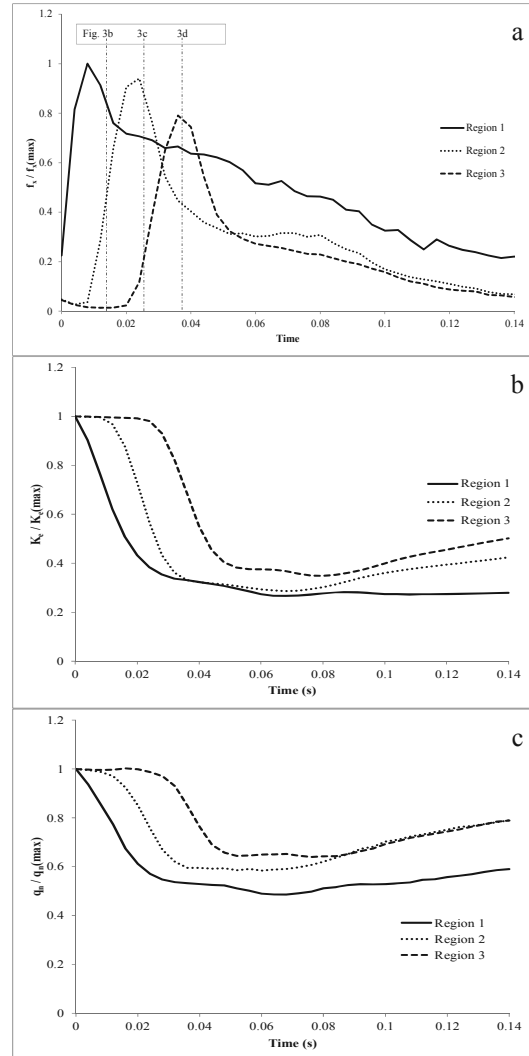

Figure 4. The computed f_x, k_e and q_n of discrete elements located in region 1, 2 and 3 (please refer to Figure 3a for the location of the regions).

3.2   *Unbalanced force on discrete element close to the baffle*

The unbalanced force (f_x) is the sum of the unbalanced force of all discrete elements in the flow direction. When the granular flow approaches the baffles, a change in the normalized unbalanced force ($f_x / f_{x(max)}$) with time is an indication of the internal stress experienced by the discrete elements due to the dynamic impact on the baffles.   Figure 4a shows the relationship of ($f_x / f_{x(max)}$) with time in region 1, 2 and 3. The built up and decline of f_x were recorded in the three measurement regions 1, 2 and 3 and presented in Figure 4a.

From Figure 4a, the duration of the peak f_x acting on the baffle was less than 0.01s, and the sequential peak f_x observed in all the three measurement regions had indicated the propagation of impact pulses in the opposite direction of the flow during frontal impact of granular flow on the baffles. By comparing Figure 3 and Figure 4a, it is observed that the

discrete elements located close to the edge of the dark region had the peak f_x. The impact pulse is therefore correlated to the propagation of the dark region where the discrete elements reduced their momentum notably. As the f_x decreased steadily with time after impact, the post-peak f_x was found to be less than 30% of the peak f_x after about 0.14s. This finding suggests the highly transient nature of the impact.

3.3 *Energy dissipation and discharge*

Figure 4b shows the relationship of the normalized kinetic energy ($k_e/k_{e(max)}$) of the discrete elements with time in region 1, 2 and 3. The solid line, dotted line and dashed line represent the computed $k_e/k_{e(max)}$ in region 1, 2 and 3 respectively. The k_e is the sum of the kinetic energy of all the discrete elements in a region. From Figure 4a and Figure 4b, it can be observed that k_e decreased much more rapidly with time than f_x. In region 1, k_e reduced to 30% of the peak k_e after less than 0.02s while f_x requires about 0.14s to reduce to 30% of its peak f_x. The magnitude of k_e rose gently following the rapid reduction.

Figure 4c shows the mean discharge rate (q_n) of the discrete elements relative to the maximum computed q_n ($q_{n(max)}$) in region 1, 2 and 3. Similar to the trend of k_e, the normalized discharge rate reduced with time. The reduction of the discharge rate was less rapid in comparison with the reduction of k_e shown in Figure 4b. A rising trend of q_n is observed following the reduction. It is interesting to note that both the k_e and q_n rose following the sharp reduction of their values. It is inferred that the deceleration effect caused by the baffles are more significant during the first impact (i.e. time before 0.04 second for regions 1 to 3) at which the impact pulse propagated along these regions. The trend of kinetic energy of these regions beyond 0.14 second is likely to be affected by the presence of various deposition mechanisms, such as runup, reflected wave, jet and hydraulic jump, etc (Armanini and Scotton 1993; Armanini 1997; Sun and Law 2012). Further research will be carried out to study the influence of these mechanisms on the computed kinetic energy and discharge. Based on the above observations of the first impact process, the baffles reduced the kinetic energy and the discharge of the discrete elements behind them effectively.

4 CONCLUSIONS

In this study, the three-dimensional discrete element method was used to analyse a granular surge flow through a row of baffles. The analysis focused on the short moment at which the first impact of the discrete elements on the baffles took place. The propagation of impact pulses in the upstream direction was observed at the moment of impact. The magnitude of the impact pulse decreased with the distance upstream from a row of baffles. The deceleration of the discrete elements was uniform over the flow depth at the moment of impact. More than half of the kinetic energy of the discrete element right behind the row of baffles was dissipated in less than 0.02s. The kinetic energy of the granular medium behind the row of baffles decreases more rapidly with time than the unbalanced force. Based on the findings of the analysis, a single row of baffles is effective in reducing the kinetic energy and discharge of the granular surge flow at the moment of impact.

5 ACKNOWLEDGEMENTS

6 REFERENCES

Ai J., Chen J.F., Rotter J.M. and Ooi J.Y. 2011. Assessment of rolling resistance models in discrete element simulations. *Powder Technology* 206 (2011) 269–282

Armanini A., 1997, On the dynamic impact of debris flows, Recent developments on debris flows. Lecture Notes in Earth Science (Armanini and Michiue, Ed.). Berlin: *Springer*, 1997, vol. 64, p. 208-224.

Armanini A., Scotton P., 1993, On the dynamic impact of a debris flow on structures, *Proceed. of XXV IAHR Congress, Tokyo Technical session B., debris flows and Landslides* 3:203-210

Azzoni, A., and de Freitas, M. H. (1995). Experimentally gained parameters, decisive for rock fall analysis. *Rock Mechanics and Rock Engineering*, 28(2), 111-124.

Calvetti F., Nova R. 2004. Micromechanical approach to slope stability analysis. In: Darve, F., Vardoulakis, I. (Eds.), Degradation and Instabilities in Geomaterials, *CISM Courses and Lectures No. 461. Springer*, Wien, pp. 235-254.

Calvetti F., Viggiani G., Tamagnini C. 2003. A numerical investigation of the incremental behavior of granular soils. *Rivista Italiana di Geotecnica* 37 (3), 11-29.

Chau K.T., Wong R.H.C. and Wu J.J. 2002. Coefficient of restitution and rotational motions of rockfall impacts. *International Journal of Rock Mechanics and Mining Sciences*, 39(1), 69-77.

Chen F. 2009. Coupled Flow Discrete Element Method Application in Granular Porous Media using Open Source Codes. Doctoral Dissertations. University of Tennessee – Knoxville.

Chiou M.C. 2005. Modelling dry granular avalanches past different obstructs: numerical simulations and laboratory analyses. *Dissertation, Technical University Darmstadt, Germany*

Crosta G.B., Calvetti F., Imposimato S., Roddeman D., Frattin P. and Agliardi F. 2001. Granular flows and numerical modelling of landslides

Cundall P.A. and Strack O.D.L. 1979. A distinct element model for granular assemblies. *Geotechnique* No 29, pp 47–65.

Hubl J., Suda J., Proske D., Kaitna R. and Scheidl C. 2009. Debris flow impact estimation. *Proc. of the 11th Int. Sym. on Water Management and Hydraulic Engineering*, Macedonia, pp 139-148.

Hutter K., Wang Y. and Pudasaini S.P. 2005. The Savage-Hutter avalanche model: how far can it be pushed? *Philos Transact A Math Phys Eng Sci.* No. 363, pp1507–1528.

Law R.P.H. 2008. Investigations of Mobility and Impact Behaviour of Granular Flows. *MPhil. Thesis. Hong Kong University of Science and Technology*, 378 p. Hong Kong.

Muir W.D. and Maeda K. 2008. Changing grading of soil: effect on critical states. *Acta Geotech* 3:3–14

Nicot F. 2004. Constitutive modelling of snow as a cohesive granular material. *Granular Matter.* No 6, pp47–60.

Pudasaini S.P., Hsiau S., Wang Y. and Hutter K. 2005. Velocity measurements in dry granular avalanches using particle image velocimetry-technique and comparison with theoretical predictions. *Phys Fluids* 17(9)

Pudasaini S.P. and Hutter K. 2007. Avalanche dynamics: dynamics of rapid flows of dense granular avalanches. *Springer*, Berlin.

Robotham M.E., Wang H. and Walton G. 1995. Assessment of risk from rockfall from active and abandoned quarry slopes. *Transactions - Institution of Mining & Metallurgy*, Section A, 104.

Sibille L., Donze F.V., Nicot F., Chareyre B. & Darve F. 2008. From bifurcation to failure in a granular material: a DEM analysis. *Acta Geotech* 3:15–24

Sun H.W. and Law R.P.H. 2012. A Preliminary Study on Impact of Landslide Debris on Flexible Barriers. *Technical Note No. TN 1/2012. Geotechnical Engineering Office*, Hong Kong, 42 p.

Tamagnini C., Calvetti F., Viggiani G. 2005. An assessment of plasticity theories for modeling the incrementally nonlinear behavior of granular soils. *Journal of Engineering Mathematics* 52, 265-291.

Teufelsbauer H., Wang Y., Pudasaini S.P., Borja R.I., Wu W. 2011. DEM simulation of impact force exerted by granular flow on rigid structures. *Acta Geotechnica* 6:119–133

Thompson N., Bennett M.R. and Petford, N. 2009. Analyses on granular mass movement mechanics and deformation with distinct element numerical modelling: implications for large-scale rock and debris avalanches. *Acta Geotech* No 4, pp233–247.

Zwinger T. 2000. Dynamik einer Trockenschneelawine auf beliebig geformten Berghängen. PhD Thesis, *Vienna University of Technology*. Austria.

Full-Scale Field Monitoring of a Rainfall-Induced Sliding Slope in Hainan, China

Étude en vraie grandeur d'un talus glissant soumis à des précipitations à Hainan en Chine

Li A.G., Qiu J.J., Mo J.F., Gao W.
Shenzhen Geotechnical Investigation & Surveying Institute Co. Ltd., Shenzhen, China

Tham L.G., Yan R.W.M.
Department of Civil Engineering, The University of Hong Kong, Hong Kong, China

ABSTRACT: This paper investigates the mechanism of rainfall-induced sliding slope through a study based on a full-scale field monitoring conducted in a sliding slope in Shimei Bay, Wanning City, Hainan, China, where some premium hotels and residential buildings are being built along a natural hillside slope. Due to the heavy rainfall in October, 2011, it was found that the hillside slope was sliding during the heavy rainfall. A number of instruments, including soil moisture probes, tensiometers, open standpipes and piezometers, inclinometers, and a rain gauge were installed in the slope. Field monitoring of the sliding slope was conducted during one dry and one wet seasons before the stabilization of the sliding slope. The paper mainly introduced the instrumentation system of field monitoring of the sliding slope. It also introduced the preliminary analysis of the variations of rainfall intensity, soil moisture content, matric suction, ground water level, slope deformation during the dry season of 2011 and the wet season of 2012 before the stabilization of the sliding slope.

RÉSUMÉ : Cet article étudie le rôle des précipitations sur une pente glissante via une étude basée sur un suivi sur le terrain à grande échelle, menée dans une pente glissante dans Shimei Bay, ville de Wanning, Hainan, en Chine, où certains hôtels de luxe et des bâtiments résidentiels sont en cours de construction, le long d'une la pente naturelle. En raison des fortes pluies en Octobre 2011, il a été constaté que la pente (colline) glissait pendant les fortes pluies. Un certain nombre d'instruments, y compris les sondes d'humidité, tensiomètres, bornes-fontaines, des piézomètres ouverts, inclinomètres, et une jauge de pluie ont été installés dans la pente. Le contrôle du glissement a été effectué pendant une saison sèche et une saison humide, avant la stabilisation de la pente. Cet article présente le système d'instrumentation mise en place sur le site. On présente également dans cet article l'analyse préliminaire sur des variations de l'intensité des précipitations, l'humidité du sol, succion matricielle, le niveau de la nappe phréatique et la déformation de la pente pendant la saison sèche de 2011 et la saison des pluies de 2012, avant la mise en place des renforcements du site.

KEYWORDS: field-monitoring ; sliding slope ; rainfall-induced ; strumentation.

1 INTRODUCTION

Rainfall-induced landslides are common in the tropical areas in China, especially in Southen China. Each year hundreds of landslides, occur during the rainy season. Many of these landslides have caused heavy damage and numerous fatalities. The majority of these landslides are associated with heavy rainfall. Hence, rainfall-induced slope failure becomes one of the most common types of landslides in Hong Kong (Lumb, 1962a, 1962b, 1975; Brand, et al. 1984; Au, 1998; Franks, 1999, Dai, et al. 1999, 2001; Li , et al. 2002, 2003, 2005a, 2005b, 2006).

Due to the new policy that China aims to build the southern island of Hainan into a top international tourism destination by 2020, the Hainan local government promises to boost development not only by expanding oil and gas exploration, offering more duty free services, developing logistics, reducing pollution, but also by improving transportation networks and infrastructure. Thus, more premium hotels, resorts, family-run hotels and residential buildings are being built along the east coast of the island.

In area of our study site, a lot of landslides were reported. A total of 4 landslides were recognized within the site. Site investigation was also carried out, which found that there was even a big landslide with a scar volume of 500000 m^3 just one kilometer away from the site. There was even a heavy debris flow, which almost damaged the newly built east fast train for Haikou to Sanya, which is just 5 kilometers away. As little research work was carried out in Hainan for the landslides, there

are even few documents for the landslides, only occasionally in the local newspapers.

In order to investigate the mechanism of rainfall-induced slope failure, a study is being carried out based on a full-scale field monitoring conducted in a sliding slope in Shimei Bay, Wanning City, Hainan, China, where some premium hotels and residential buildings are being built along a natural hillside slope.

Due to the heavy rainfall in October, 2011, it was found that the hillside slope was sliding during the heavy rainfall. The sliding slope was a gentle hillside, which was cut to accommodate a temporary road construction, and consisted mainly of residual soil, CDG and HDG. To characterize the soil properties of the sliding slope, a detailed site investigation was carried out prior to the instrumentation.

A number of instruments, including soil moisture probes, tensiometers, open standpipes and piezometers, inclinometers, and a rain gauge were installed in the slope. Site investigation included borehole drilling, soil sampling, field and laboratory tests was carried out. Field monitoring of the sliding slope was conducted during one dry and one wet seasons before the stabilization of the sliding slope. The pre-stabilized slope was monitored during the dry season of 2011 and the wet season of 2012. The stabilization of the sliding slope started before the end of the wet season in 2012.

Anti-sliding piles plus pre-stressed anchors were designed to stabilize the sliding slope. Other instruments including load cells and strain gauges were suggested to be installed in the

anchors and piles during the stabilization of the sliding slope. It was suggested that the post-stabilized slope should also be monitored for another dry season of 2012 and another wet season of 2013.

The paper mainly introduced the instrumentation system of fielding monitoring of the sliding slope. It also introduced the preliminary analysis of the variations of rainfall intensity, soil moisture content, matric suction, ground water level, slope deformation during the dry season of 2011 and the wet season of 2012 before the stabilization of the sliding slope.

2 SITE CONDITIONS

The site is a natural hillside terrain covered by a lot of vegetation. The section was originally a gentle slope and then it was cut to accommodate the footpath for the main road. Ground investigation work was carried out during instrument installation. The site ground as revealed by the ground investigation is mainly residual soil, completely decomposed granite (CDG) and highly decomposed granite (HDG), which are underlain by moderately decomposed granite (MDG) and slightly decomposed granite (SDG).

Laboratory tests were carried out on the soil samples obtained at the sliding slope during the site investigation. The soil, as revealed by site investigation, is completely decomposed medium-grained granite and can be classified as a very weak to weak, light brown to brown, silty/clayey sand. The laboratory program to characterize the soil properties included: (1) Bulk density, (2) Dry density, (3) Specific gravity, (4) Atterberg limits and (5) Particle size distribution.

Part of the laboratory tests results are summarized in Table 1.

Table 1. Soil properties for the sliding slope.

Bulk density (Mg/m3)	*1.76~1.93*
Dry density (Mg/m3)	1.44~1.54
Specific gravity	2.627~2.655
Void ratio	0.7314~0.8443
Porosity	0.42~0.46
Liquid limit (%)	31.5~44.3
Plasticity index (%)	12~23

3 INSTRUMENTATION SYSTEM

The instruments included soil moisture probes to measure volumetric water content, tensiometers to measure matric suction (negative pore water pressure), open standpipes and piezometers to measure ground water level and positive pore water pressure, inclinometers to measure the lateral ground movements, and a rain gauge to measure rainfall intensity.

The philosophy for instrumentation design was as follows: The moisture probes and tensiometers were installed in the shallow depth to monitor volumetric water content and matric suction in the unsaturated zone of the soil. The open standpipes and piezometers were installed in both the shallow depth and greater depth to monitor both perched and deep ground water or positive pore pressure in the saturated zone of the soil. The inclinometers were installed in the soil to monitor horizontal deformation of the sliding slope. The rain gauge was installed to monitor the specific rainfall intensity of the monitored sliding slope. Figure 1 shows instrumentation layout plan.

A total of six moisture probes were used to measure volumetric water contents inside different parts of the sliding slope (Figure 1). Three moisture probes were installed in borehole M1 (M1-1 (1m), M1-2 (2m) and M1-3 (3m)) at depths

of 1 m, 2 m and 3 m, respectively, at the toe of the slope. The other three moisture probes were installed in boreholes M3 (M3-1 (1m), M3-2 (2m) and M3-3 (3m)) at depths of 1 m, 2 m and 3 m, respectively, near the crest of the slope. A total of six tensiometers were used to measure matric suction at different locations of the sliding slope (Figure 1). Three of them were installed in boreholes T1 (T1-1 (1m), T1-2 (2m) and T1-3 (3m)) at depths of 1 m, 2 m, 3 m and 4 m, respectively at the toe of the sliding slope. The other three were installed in boreholes T3 (T3-1 (1m), T3-2 (2m) and T3-3 (3m)) at depths of 1 m, 2 m, 3 m and 4 m, respectively, near the crest of the sliding slope. A total of three open standpipes were used to measure ground water levels at different locations of the sliding slope (Figure 1). A total of three vibrating wire piezometers (P1, P2 and P3) were used to measure positive pore water pressures at different locations of the sliding slope (Figure 1). A total of three inclinometer tubes (IN1, IN2 and IN3) were used to measure the lateral ground movements at different locations of the sliding slope (Figure 1). One 0.5 mm "tipping bucket" rain gauge with internal logger was used to monitor the rainfall intensity of the monitored slope site automatically (Figure 1).

Ground water levels in the open standpipes were monitored manually with the help of a dipmeter. An automatic data acquisition system was set up for the sliding slope to monitor moisture content, matric suction, positive pore water pressure and horizontal deformation continuously. The automatic data acquisition system consists of sensors, cables, data loggers and power supplies. An instrumentation hut was constructed at the top of the sliding slope to house the data loggers and power supplies. The data loggers were configured to collect data at 15/30-min intervals and the data were transmitted to both the office in the site and the office in Shenzhen instantly via wireless data transition system.
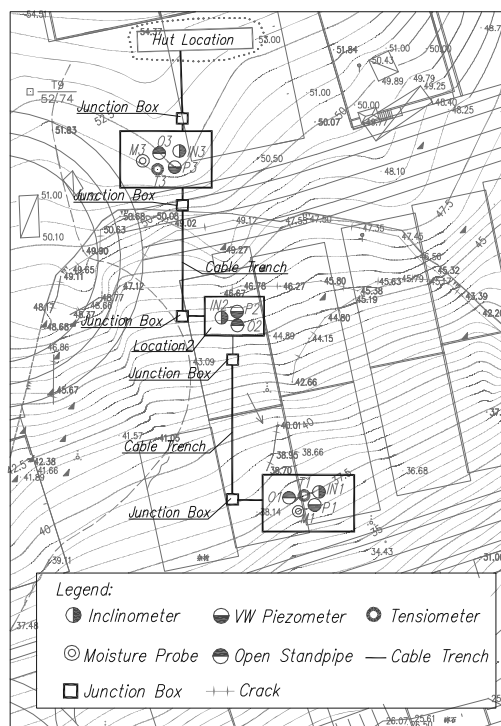

Figure 1. Boreholes and instrumentation layout plan.

4 PRELIMINARY MONITORING RESULTS

4.1 *Moisture Probes and Tensiometers*

Figures 2 and 3 show the variations of the volumetric water content and the matric suction of Borehole M3 at the crest of the sliding slope from November 2011 to June 2012. By examining the volumetric water content and the matric suction records and their comparison with daily rainfall in borehole M3 at the crest of the sliding slope during the above period (Figures 2 and 3), the following observations can be made:

(1) The volumetric water content increased due to rainfall infiltration in the wet season and decreased due to evaporation in the dry season. The matric suction decreased due to rainfall infiltration in the wet season and increased due to evaporation in the dry season.

(2) The volumetric water content at different depths was not uniform. Generally, the volumetric water content at a shallow depth was lower than that at greater depths during the dry season, while the volumetric water content at a shallow depth was higher than that at greater depths during the wet season. The matric suction at different depths was not uniform too. Generally, the matric suction at a shallow depth was higher than that at greater depths during the dry season, while the matric suction at a shallow depth was lower than that at greater depths during the wet season.
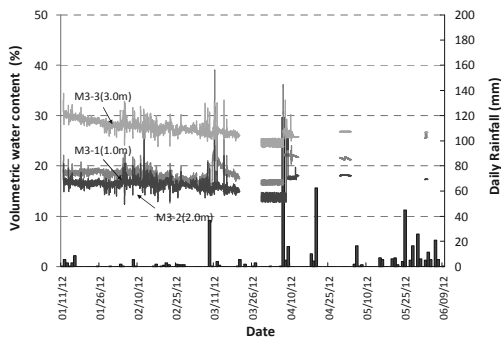

Figure 2. Variations of volumetric water content and daily rainfall from November 2011 to June 2012 in borehole M3 at the crest of the sliding slope.
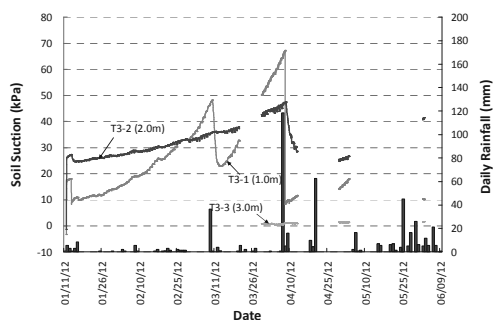

Figure 3. Variations of matric suction and daily rainfall from November 2011 to June 2012 in borehole M3 at the crest of the sliding slope.

4.2 *Open Standpipes and Piezometers*

The monitoring of the three open standpipes was carried out by using a dipmeter. The monitoring of the open standpipes was to check the monitoring data of nearby installed piezometers. Figure 4 shows the variations of the ground water levels in Borehole P1 at the toe of the sliding slope from November 2011 to June 2012. By examining the ground water level records and comparing them with the daily rainfall data during the above period, the following observations can be made:

(1) The pore water pressure at P1-A was higher than that at P1-B. It probably implies that there was a perched water level in

the sliding slope and the permeability of the residual soil is higher than that of CDG.

(2) The groundwater level deceased around 6.0 m at both P1-A and P1-B.

(3) The rise of the groundwater level was sensitive to rainfall, and it was more sensitive at shallow depth. Furthermore, there was a time lag for monitoring the highest ground water level due to rainfall.

(4) The highest groundwater levels monitored in November, 2011 was probably due to the heavy rainfall during the wet season in 2011, which caused the landslide.
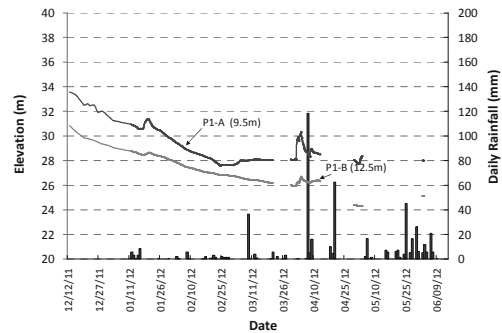

Figure 4. Variations of ground water level and daily rainfall from November 2011 to June 2012 in borehole P1 at the toe of the sliding slope

4.3 *Inclinometers*

Figure 5 shows the monitored horizontal displacements from November 2011 to June 2012 in borehole IN1 at the toe of the sliding slope. By examining the monitored horizontal displacements during the above period, the following observations can be made:

(1) The maximum horizontal displacement from June 2011 to July 2012 in borehole IN1 at the toe of the sliding slope was about 10.0 mm (Figure 25).

(2) The monitored sliding slope was sliding slowly. It is believed that with rainfall infiltration, the matric suction in soils at shallow depth partially disappeared, which decreased the stability of this sliding soil slope.

(3) The decease of groundwater level was up to 6.0 m during the dry season, however, the increase of groundwater level due to the heavy rainfall on April 7 was less than 1.0 m, therefore, the maximum horizontal displacement was insignificant.
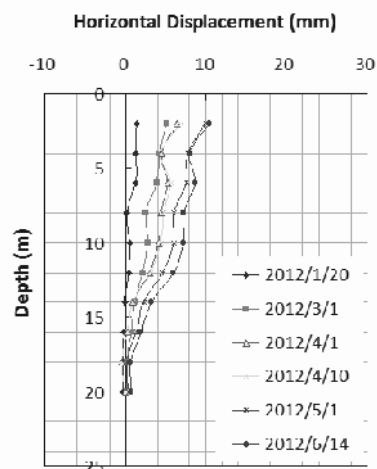

Figure 5. Horizontal displacements from November 2011 to June 2012 in borehole IN1 at the toe of the sliding slope

5 THE FAILURE OF THE MONITORING SLIDING SLOPE

As the client started the stabilization of the sliding slope using man-dug piles and anchors, it was found that it was very difficult to protect the monitored system. Therefore, automatic monitoring system for the sliding slope has to be given up. Instead, the sliding slope was being monitored manually during the stabilization of the sliding slope.

There are several rows of piles needed to be constructed during the stabilization and furthermore, there are a lot of excavations before the stabilization. Though many warning letters had been issued to the Contractor by the Consultant, before the completion of the stabilization works, due to a heavy rainfall on November 4, part of the sliding slope had completely collapsed, which caused the fifth landslide for the site.

The investigation of the fifth landslides was carried out later. It was found that the main reason for the landslide was the improper excavation. Some of the excavation has an angle of 45 º to 50º. As the Contractor believed that the wet season would end and there would be no heavy rainfall in November 2012 just as in November 2011, improper excavation was carried out for the sliding slope.

Another very important reason for the failure of the improper excavated sliding slope may be due to the significant increase of the volumetric water content and the dramatic decrease of the matric suction of the sliding slope. It may be proved that negative pore-water pressure (or matric suction) plays a crucial role in the stability of unsaturated soil slope. With rainfall infiltration, the matric suction in soils at shallow depth would partially or completely disappear. Consequently, a slope failure may occur.

It is a pity that the automatic monitored system has to be abandoned due to the construction.

Figure 5. Failure of the sliding slope during a heavy rainfall on November 4, 2012.

6 CONCLUSIONS

From the study of the field monitoring of a monitoring sliding slope in Hainan, China and the failure of the sliding slope at last, the following conclusions can be made:

(1) The volumetric water content increased in the wet season and decreased in the dry season. Correspondingly, the matric suction decreased in the wet season and increased in the dry season.

(2) The variations of the volumetric water content and matric suction with time at different depths were different. Maximum variations often occurred near the ground surface. The large variations of volumetric water content and matric suction during rainy season at shallow depth may explain the reason why so many slope failures occurred in this region during heavy rainstorms.

(3) The ground water level generally rose during the wet season and fell during the dry season. The rise of the ground water level occurred during heavy rainfall or long after the rainfall. The ground water level also decreased temporarily after the heavy rainfall.

(4) As the volumetric water content increased during the rainfall, the monitored slope was sliding slowly, though insignificantly. Furthermore, the monitored horizontal displacement during the monitored period was not significant, which is probably due to insignificant rise of the groundwater level in the sliding slope.

(5) It is believed that the main reason for the failure of the sliding slope was the improper excavation. It could also be due to the loss of the matric suction, which plays a crucial role in the stability of unsaturated soil slope.

7 ACKNOWLEDGEMENTS

8 REFERENCES

Lumb, P. (1962a). General nature of the soils of Hong Kong, Proc. Symp. Hong Kong Soils. Hong Kong, 19-32.

Lumb, P. (1962b). Effect of rainstorms on slope stability, Proc. Symp. Hong Kong Soils. Hong Kong, 73-87.

Lumb, P. (1975). Slope failures in Hong Kong. Q. J. Engng Geol. 8, 31-65.

Brand, E.W., Premchitt, J. & Phillipson, H.B. (1984). Relationship between rainfall and landslides. Proceedings of the fourth International Symposium on Landslides. Canada, 1, 377-384.

Au, S.W.C. (1998). Rain-induced slope instability in Hong Kong. Engineering Geology. 51, 1-36.

Franks, C.A.M. (1999). Characteristics of some rainfall-induced landslides on natural slopes, Lantau Island, Hong Kong. Quarterly Journal of Engineering Geology. 32 247-259.

Dai, F.C., Lee, C.F., Wang, S.J., & Feng, Y.Y. (1999). Stress-strain behavior of a loosely compacted volcanic-derived soil and its significance to rainfall-induced fill slope failures. Engineering Geology 53, 359-370.

Dai, F.C. & Lee, C.F. (2001). Frequency-volume relation and prediction of rainfall-induced landslides. Engineering Geology 59, No. 3-4, 253-266.

Li, A.G., Yue, Z.Q., Tham, L.G., Lee, C.F. & Law, K.T. (2002). Rainfall Infiltration at an Instrumented Cut Slope. 55th Canadian Geotechnical Conference, October 20-23, 2002, Ontario, Canada, 1159-1167.

Li, A.G., Yue, Z.Q., Tham, L.G., Lee, C.F. & Law, K.T. (2003). Design and Installation of a Comprehensive Instrumentation System for a Slope in Hong Kong. Chinese Journal of Rock Mechanics and Engineering, 22 No. 5, 790-796. (In Chinese)

Li, A.G., Yue, Z.Q., Tham, L.G., Lee, C.F. & Law, K.T. (2005a). Field Monitored Variations of Soil Moisture and Matric Suction in a Saprolite Slope. Canadian Geotechnical Journal. 42 13-26.

Li, A.G., Tham, L.G., Yue, Z.Q., Lee, C.F. & Law, K.T. (2005b). Field Soil-Water Characteristics of Completely Decomposed Granite. Journal of Geotechnical and Geoenvironmental Engineering. 131 No.9 1176-1180.

Li, A.G., Xiong, J.A., Nan, L. and Qiu, J. J. (2006). The Study of Rainfall-Induced Sliding of a Fill Slope in Shenzhen, China, The 10th IAEG Congress, 6-10 September 2006, Nottingham, United Kingdom.

Estimation and Prediction of Debris Flow Potential Using Discrimination Analysis

Estimation et prédiction du potentiel d'écoulement de boue utilisant une analyse discriminante

Lin M.L., Lin Y.S.

Department of Civil Engineering, National Taiwan University, Taiwan

ABSTRACT: Taiwan is situated at the juncture of tectonic plates, which caused complex and fragile geological condition with steep mountain terrain. Being frequently struck by typhoons and earthquakes, the landslide and debris flow hazard occurs frequently. In this research, the estimation model of regional debris flow potential was constructed based on the geo-morphological and hydrological conditions of the research area. For constructing the estimation model of debris flow potential, the Fisher's discrimination analysis was used. A study area of Nantou County in Central Taiwan was selected. Influence factors were identified and a database for both debris flow torrents and non-debris flow torrents were constructed. Estimation model was constructed using the Fisher's analysis by random sampling of the debris flow and non-debris flow torrents. The estimation model is validated and then used for prediction of debris flow potential. The final model can be determined by evaluating the estimation stability and prediction rate with each additional influence factor. The resulting potential estimation of the study area appears to be satisfactory. The influence factor stability of the Fisher's discriminant model and the prediction rate associated with the differences in influence factors were discussed.

RÉSUMÉ : Taiwan est situé à la jonction de plaques tectoniques, ce qui engendre un terrain escarpé avec des situations complexes et des conditions géologiques fragiles. L'île étant régulièrement frappée par des typhons et des tremblements de terre, des glissements de terrain et des écoulements de boue se produisent fréquemment. Pour cette étude, le modèle d'estimation des coulées de boue régionale potentiel a été construit sur la base des conditions géomorphologiques et hydrologiques de la zone de recherche. Pour la construction de celui-ci, l'analyse discriminante de Fisher a été utilisée. Une zone d'étude du comté de Nantou qui se situe au centre de Taïwan a été choisie. Les facteurs d'influence ont été identifiés et des bases de données pour les torrents d'écoulement de boue et torrents d'écoulement de non-boue ont été construites. Le modèle d'estimation a été construit en utilisant une analyse de Fisher par échantillonnage aléatoire des torrents d'écoulement de boue et des torrents d'écoulement de non-boue. Le modèle d'estimation est validé, puis utilisé pour la prédiction de potentiels écoulements de boue. Le modèle final peut être déterminé en évaluant l'estimation de la stabilité et la fréquence prédite avec chaque facteur d'influence additionnel. L'estimation résultante potentielle de la zone d'étude semble être satisfaisante. Le facteur d'influence de stabilité du modèle discriminant de Fisher et la fréquence prédite associée aux différences des facteurs d'influence ont été discutés.

KEYWORDS: debris flow, potential estimation, Fisher's discriminaton analysis, influence factor, prediction model.

1 INTRODUCTION

More than 70 percent of areas in Taiwan are in mountain region and with steep and fragile slopes. The earthquakes and heavy rainfall introduced by typhoons often induced significant landslide and debris flow hazards in Taiwan, which lead to significant loss of properties and lives. For effective mitigation of the debris flow hazards, it is important to evaluate the potential of debris flow torrents, which supports decision on mitigation measures and priority.

This research is based on the data of the 1,420 debris flow torrents published by Soil and Water Conservation Bureau in 2003. The fundamental data of the debris flow torrents for the study area of Nantou County in Central Taiwan were collected, and the basic database along with the related influence factors were established utilizing the geographic information system software, Arcview. The influence factors database included watershed area, stream length, hypsometric integral, stream mean slope, form factor, slope distribution, slope aspect and geology category, were extracted from the fundamental data. The statistic analysis was performed on all influence factors to discuss their significances. The multi-variant discrimination analysis was used to discriminate debris flows and non-debris flows. The analysis model was verified, and accordingly the potential of debris flow torrents in Nantou County was evaluated.

2 STUDY AREA AND FUNDAMENTAL DATABASE

The Nantou County located in central Taiwan is selected as the study area in this research, which has a large area with high mountains and rugged topography. The debris flow hazard in Nantou County came into great concern since 1996, when Typhoon Herb caused severe losses of properties and lives. In addition, severe debris flow hazard struck this area frequently after the Chi-Chi earthquake, 1999. According to the data published by Soil and Water Conservation Bureau (2003), the number of debris flow torrents reaches 199 in Nantou County, which are for the potential analysis. The distribution of the debris flow torrents and the study area are as shown in Figure 1. The fundamental database used for construction of related database for analysis include: the digital elevation model published in 1989 with a resolution of 40m x 40m, 1/500,000 Taiwan geology map produced by the Central Geological Survey in 1986, aerial photographs, topographical map.

The primary geologic formations of the study area include slate, phyllite, sandstone, and shale. According to the engineering geology zonation proposed by Hung in 1997, the research area contents C zone (metamorphic rocks, metamorphic sandstone, shale, slate, phyllite), D zone (sedimentary rocks), E zone (lateritic tableland), and G zone (basin and plain). As shown in Figure 1. Study area and distribution of Debris Flow Torrents and Non-Debris Flow Torrents
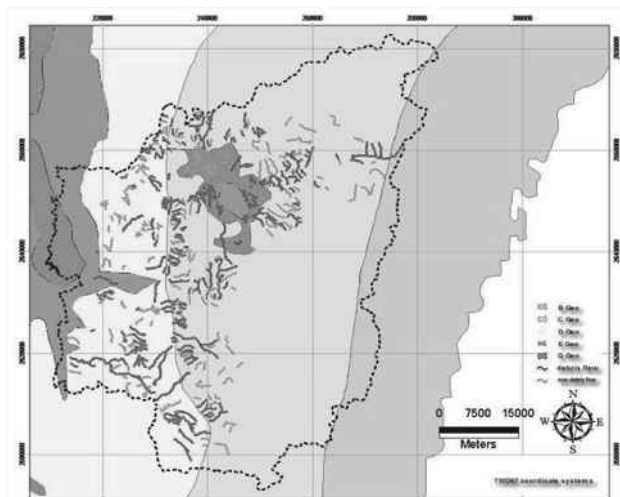
Figure 1, most of the debris flow torrents in Nantou County distribute in C zone and D zone.

In order to perform the discriminant analysis, database for both debris flow torrents and non-debris flow torrents are constructed as discussed in the followings:

a. Debris flow torrents: the debris flow torrents in research area are based on the debris flow torrents published by Soil and Water Conservation Bureau in 2003 in 1/5,000-scale. The total number of debris flow torrents in the research area is 199. The watershed of each debris flow torrent was generated using DEM accordingly.

b. Non-debris flow torrents: The procedures for establishing the non-debris flow torrents are to establish watersheds and streams based on the 1/25,000 topographic map and DEM, and are not debris flow torrents by SWCB (Lin, et al. 2003). The non-debris flow should be in the neighboring area of debris flow torrents and with similar geologic traits and watershed size. Accordingly, a total number of 175 non-debris flow torrents was generated in the research area. Cross examination of these torrents were performed by comparing the torrent distribution to the aerial photograph. The results appeared to be consistent, and the distribution of the non-debris flow torrents is as shown in Figure1.

3 INFLUENCE FACTORS AND THEIR SIGNIFICANCES

The necessary conditions for triggering debris flow include affluent debris materials, sufficient water supply, and appropriate geomorphological conditions. For evaluation of debris flow potential, the influence factors were selected based on the three conditions, and the database were generated. Based on previous researches (Lin, et al. 2003, Lin and Chen, 2005, and Lin and Wen, 2006), eight influence factors are selected as: watershed area, streams length, hypsometric integral, form factor of basin, stream mean slope, slope angle, slope aspect, and geology formation, respectively.

1. Watershed area: BA, in hectare. The watershed with larger area usually contributes more water, which is regarded as a factor related to the water supply.

2. Stream length: SL, in meter. Stream length means the largest length of the stream in the related watershed. The longer the stream length is, the larger the watershed area is. Stream length is also regarded as another factor of sufficient water supply.

3. Hypsometric Integral: HI, dimensionless. The hypsometric integral is determined from the integral of the basin's height versus area percentage curve, which is a characteristic of geomorphic evolution of the watershed. It also stands for terrain ruggedness and is regarded as a factor related to the abundance of debris material.

4. Form factor: Form factor, FF (dimensionless), is proposed by Horton in 1920, and is defined as the basin area divided by the square of stream length. A higher form factor suggests broader basin shape, and different basin shapes affect flow hydrograph of the stream (Robet and Raymond, 1978).

5. Stream mean slope: SMS, in degree. Stream slope is an important factor related to flow velocity; the steeper the slope is, the faster the stream flow. The stream mean slope serves as an indicator of appropriate slope conditions.

6. Slope aspect: N, NE, E, ES, S, SW, W, WN, in percentage of area ratio. Most debris flow disasters were triggered by typhoon or heavy rainfall. According to the landing path of typhoons, rain falls concentrated more on windward side. Strong wind also influences the weathering process. Slope aspect serves as an indicator of geomorphlogical condition.

7. Slope distribution: SD10(0°~10°), SD15(10°~15°), SD20(15°~20°), SD30(20°~30°), SD45(30°~45°), SD90(45°~90°), in percentage of area ratio. Steeper slope has a higher tendency of slope failure and leads to more debris material.

8. Geological formation: E1, E2, EO, Mj, Ml, MS, My, O1, O2, O3, P1, P2, Q2, Q3, Q0, as listed in Table 1, in area ratio percentage. Weak rock quality, complicated geologic structure, highly developed fault and fold, and intensive tectonic activity zone tend to provide abundant debris material. Different geological formation contributes to different material strength, degree of fracture, and soil type.

The influence factors were derived from fundamental data through performing spatial and hydrological analysis using GIS and the related database were established. The distributions and characteristics of the influence factors of debris flow torrents and non-debris flow torrents are compared and discussed.

Table 1. Geological formations of the study area

Category	Symbol	Rock Type
Metamorphic Rock (C Zone)	E1	Slate, interlaminations of slate and sandstone
	E2	Indurate sandstone with carbonaceous slate interbeds
	EO	Slate, phyllite, with sandstone interbeds
	Mj	Sandstone, shale
	Ml	Argillite slate phyllite sandstone interbeds
	MS	Sandstone, shale
	O1	Quartzitic sandstone, slate, graphitic shale
	O2	Argillite, indurate sandstone, slate
	Q2	Gravel, laterite, clay, sand
	Q3	Clay, sand, gravel
Sedimentary Rock (D Zone)	My	Sandstone, shale
	O3	Sandstone, shale
	P1	Shale, sandy shale, mudstone
	P2	Sandstone, mudstone, shale
	Q0	Sandstone, mudstone, shale, conglomerate (limestone)

During the analysis, it was found that the distribution of factors for different engineering geological region had different characteristics with significant effects on triggering of the debris flow; the potential analysis of the study area was conducted on whole area with combined geological zones, Zone C, and Zone D, respectively. The number of debris flow and non-debris flow torrents in Zone C are 99 and 95, and 54 and 54 in Zone D as shown in Figure 1. In order to conduct the statical analysis, the independcy and significance level of each influence factor was checked using analysis of covariances and Pearson Test. A significance level of 0.1 with 90% of confidence was chosen, and it appeared that the influence factors selected were independent of each other. The resulting significant influence factors for the whole area, Zone C, and Zone D are listed in order of level of significance in Table 2. Due to the complexity of the geological characteristics when the whole area was

analyzed, the principal component analysis was performed on slope distribution and aspect distribution. In Table 2, the PS2 factor indicated a resulting principal component of slope for the whole area. As shown in Table 2, the significant factors are quite different for the whole area, Zone C, and Zone D except with the Hypsometric Integral, HI. This justified that the debris flow potential would be better understood if separate analysis were conducted for regions of different geological properties.

Table 2 The significant influence factors for different geological zones

Order of significance	Whole area	Zone C	Zone D
1	HI	HI	HI
2	PS2	E1	Mj
3	Q0	O1	FF
4	NE	WN	Q0
5	ES	Ml	ES
6	My	SD10	O3
7	Ml	-	SD10

4 ESTIMATION MODEL OF DEBRIS FLOW POTENTIAL

In this research the multi-variant variables discrimination analysis is used to establish the differential function for debris flow torrents and non-debris flow torrents. The discrimination analysis is to form a linear combination of variables for each associated group to provide estimation values, where the coefficient of each individual variable represents its contribution to the associated group. The differential function of discrimination analysis defines the line which differentiates two groups, and its coefficients help to discriminate properties of each group. This research uses the commercial statistic software, SPSS, with Fisher's discrimination analysis, and analyses are performed for the whole area, Zone C and Zone D. Random sampling of the debris flow and non-debris flow torrents were used assuming normal distribution of each factor. For each analysis, the contributing influence factor was added following the order of significance, and the improvement of the rate of accuracy was checked with each additional factor. The definition of accuracy rate is expressed as the sum of accurately estimated debris flow torrents and non-debris flow torrents divided by the total number of torrents.

1. Whole area with combined geological zones: The analysis was performed over the whole area using 87 sets randomly sampled out of 199 and 175 debris and non-debris flow torrents. It was found that the HI appeared to be the most significant factor; the additional factors were added following the significant sequence of PS2, Q0, NE, ES, My, and Ml, with accuracy rate of 78.9%, 81%, 82.2%, 82.2%, 83.3%, 84.5%, and 85.1%. The resulting discrimination function, y, is:

$$y=5.108(HI)+0.090(PS2) - 0.020(Q0) - 0.027(NE) - 0.065(ES) - 0.018(My)+0.003 (Ml) - 1.911 \qquad (1)$$

The accuracy rate increases more or less steadily with the additional parameters, but the trend is not significant with addition of NE, and the amount of increase in accuracy was not steady, suggesting different contribution of the parameters compared to their significance level.

2. Zone C: The analysis was performed for the Zone C using 40 sets randomly sampled out of 80 sets debris and non-debris flow torrents. It was found that the HI appeared to be the most significant factor; the additional factors were added following the significant sequence of E1, O1, WN, Ml, SD10, with accuracy rate of 82.5%, 83.8%, 85.0%, 85.0%, 83.8%, and 83.8%. The resulting discrimination function, y, is:

$$y=19.050(HI) + 0.018(E1) - 0.016(O1) +0.009(WN) - 0.025(M1) + 0.082(SD10) - 11.388 \qquad (2)$$

The accuracy rate increases with the additional parameters up till O1, and then remains the same and decreases. Thus, the amount of increase in accuracy does not increase beyond parameter O1. Although the rest of the parameters appear to be significant, they do not contribute to the estimation model

3. Zone D: The analysis was performed for the Zone D using 40 sets randomly sampled out of 54 sets debris and non-debris flow torrents. It was found that the HI appeared to be the most significant factor; the additional factors were added following the significant sequence of Mj, FF, Q0, ES, O3, and SD10, with accuracy rate of 61.3%, 70%, 68.8%, 75%, 80%, 80%, and 80%. The resulting discrimination function, y, is:

$$y= - 5.070(HI) +0.036(Mj) - 1.516(FF) - 0.015(Q0) - 0.083(ES) +0.024(O3) +0.009(SD10) +4.731 \qquad (3)$$

The accuracy rate increases with the additional parameters till ES and then remains the same. It suggests that the addition of O3 and SD10 parameters does not improve the accuracy rate, although both parameters are significant.

Observing the estimation models for the three regional analyses, the accuracy rate has a tendency to increase with the additional factors, and the HI factor appears to be the most effective factor in all three models. For all three models, the coefficient of each parameter indicates the contribution of the parameter, and is consistent with the variation in accuracy rate. However, the effectiveness of the influence factors is not fully in accord with the order of factor significance shown in Table 2. Therefore, the level of significance of the parameter could not be correlated to the contribution of the parameter to the estimation model.

5 VALIDATION AND PREDICTION

In order to verify the feasibilities of the potential estimation model discussed previously, the data sets of debris flow torrents and non-debris flow torrents not used in developing the estimation models were used for validation and prediction. A total of 112 debris flow torrents and 87 non-debris flow torrents were used for the prediction of the whole area using Eq.1. A total of 40 sets of debris flow and non-debris flow torrents were used for the Zone C, and a total of 14 sets of debris flow and non-debris flow torrents were used for prediction using Eqs. 2, and 3, respectively. The prediction accuracy rates were compared to the estimation accuracy rates for whole area with combined geological zones, Zone C, and Zone D, as shown in Figure 2, Figure 3, and Figure 4, respectively.

From Figure 2, it was found that the accuracy rate for prediction increased steadily up to ES but then decreased with additional factor for whole area with combined geological zones compared to the estimation model. Therefore, the factors used for the model are only up to ES, and the model is rectified as:

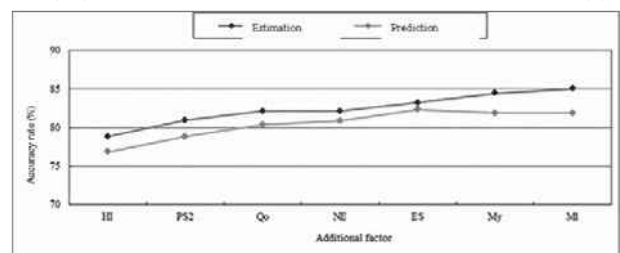$$y=4.955(HI)+0.090(PS2) - 0.0205(Qo) - 0.027(NE) - 0.065(ES) - 1.741 \qquad (4)$$

Figure 2. Accuracy rates of estimation and prediction for whole area
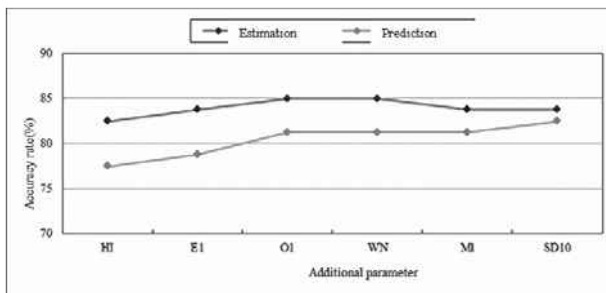
Figure 3. Accuracy rates of estimation and prediction for Zone C

The estimation accuracy rate is 83.3%, and the prediction accuracy rate is 82.4% with a difference of 0.9%.

From Figure 3, it was found that the accuracy rates for both estimation and prediction increased steadily with additional factor up to O1 but then varied for Zone C. It appears that the accuracy rate would become stable only with factors up to O1, and the model is rectified as:

$$y=15.531(HI)+0.019(E1) - 0.007(O1) - 9.255 \qquad (5)$$

The estimation accuracy rate is 85.0%, and prediction accuracy rate is 81.3% with a difference of 3.7%.

From Figure 4, the accuracy rates varied for both estimation and prediction, but the accuracy rates increased steadily with additional factor up to ES for Zone D. It appears that the accuracy rate would become stable with the factors up to ES only, and the model is rectified as:

$$y= - 5.685(HI)+0.032(Mj) - 1.504(FF) -0.015(Qo) -0.085(ES) +5.380 \qquad (6)$$

The estimation accuracy rate is 80.0%, and the prediction accuracy rate is 78.6% with a difference of 1.4%.

For all three analyses, the prediction curves appear to be quite stable and approach the estimation curves with the similar trends. The resulting accuracy rates are satisfactory and the differences between prediction accuracy rate and estimation accuracy rate of all three models are all within 4%. Thus the discrimination functions used is good for differentiating debris flow torrents from non-debris flow torrents with satisfactory results. Comparing the three modified function equations, not all factors contributed effectively to the model for all three models. The prediction accuracy rate actually reduced if all the factors were included, which suggested over-fitting of the estimation models. Observing the number of factors used for the whole area prediction model is higher than the Zone C and Zone D, it may doe to the complexity of multi-geological zones included. The accuracy rate of the Zone D analysis appeared to be lower than the other two analyses, which might due to less samples were available for estimation and prediction compared to number of samples in whole area and Zone C.

Based on the analysis results, the potential of debris flow torrent can be evaluated using distribution of the calculated discriminatio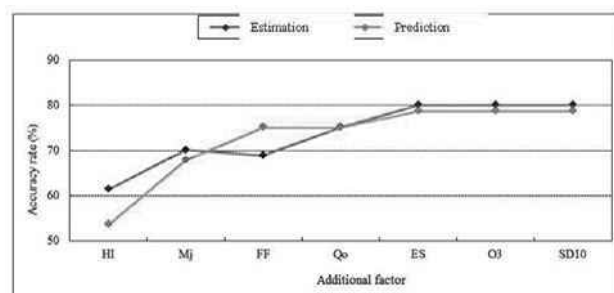n function. The accumulated distribution density of 30% and 70% values are selected as the boundary indicators for low-moderate and moderate-high potential. For the whole area analysis, the discrimination function value for 30% is 0.506 and 3.092 for 70%. Thus the debris flow torrents with discrimination values greater than 3.092 are classified as high potential and moderate potential when discrimination values range within 0.506 to 3.092. The debris flow torrents are considered as low potential when the values are less than 0.506. Similar procedures were applied to Zones C and D. For Zone C the discrimination value for 30% accumulation is 0.765, and 3.143 for 70% accumulation. The discrimination value for 30% accumulation is 0.325 and for 70% is –1.720 for Zone D. Thus the potential of debris flow torrents can be evaluated in all three analysis models.

6   CONCLUSIONS

In this research, the potential analysis of the debris flow torrents in Nantou County was performed using discrimination analysis. The influence factors included: watershed area, stream length, form factor, hypsometric integral, stream mean slope, slope distribution, slope aspect, and geological formation. Base on the previous discussions, most influence factors selected are within significance level. Among the factors used, the hypsometric integral appears to be the most important factor, which is a characteristic of geomorphic evolution of the watershed. The second most important factor is the geological properties of the analysis area. For all three models, the accuracy rates are about 80%, which suggests that the discrimination analysis provide satisfactory results. The accuracy rate for Zone D is slightly smaller than the accuracy rates for both the whole area and Zone C, which might due to smaller sample sizes in both estimation and prediction compared to the sample sizes of the whole area and Zone C. The final model could be determined based on the stability of accuracy rates in both estimation and prediction. However, not all the significant factors are contributing to the model effectively. The final potential of the debris flow torrents can be evaluated based on the values of discrimination function in all three models properly.

7   REFERENCES

Hung J.J. 1997. Engineering Geology Zonation of Taiwan
Lin M.L. and Chen T.C. 2005. Frame in renovation and feedback mechanism of database of potential debris flow torrents. SWBC-94-048 (Chinese)
Lin M.L. and Lien H.P. and Hsieh C.L. 2003. Follow-up investigation and observation in developed tendency of potential debris flow torrents. SWCB-92-107. (Chinese)
Lin M.L. and Wen H.Y. 2006. Field investigation and trend analysis of potential debris-flow rivers. *Sino-geotechnic.* 110, 45-54 (Chinese)
Robet L.S. and Raymond J.K. 1978. *Landslide analysis and control.* Special Report 176, National Academy of Science, Washington, D.C. 17-27
Taiwan Geology Map (1/500,000), 1986, Central Geological Survey

Figure 4. Accuracy rates of estimation and prediction for Zone D

Value of Landslide Investigation to Geotechnical Engineering Practice in Hong Kong

Ingénierie des glissements de terrain à Hong Kong

Lo D.O.K., Lam H.W.K.
Geotechnical Engineering Office, Civil Engineering and Development Department, Government of the Hong Kong SAR

ABSTRACT: On average, about 300 landslides were reported to the Geotechnical Engineering Office (GEO) of the Civil Engineering and Development (CEDD) in Hong Kong each year. Over the years, GEO conducted landslide investigations to advance knowledge on slope performance and improve understanding of the causes and mechanisms of landslides. Landslide investigations have become an integral part of the Government's Slope Safety System in Hong Kong. Studies on notable landslides on man-made slopes have led to the use of more robust stabilisation measures for cut slopes, improved rock slope engineering practices, enhanced practices in the monitoring and maintenance of water-carrying services affecting slopes and improvement to drainage detailing. Studies on natural terrain landslides have allowed better understanding on the modes and mechanisms of failure. This also enables advancement in debris mobility assessment which is critical to natural terrain risk management. This paper highlights some key lessons learnt and observations made from selected landslide investigations and how this knowledge helps advance the geotechnical engineering practice in dealing with man-made slopes and natural terrain landslide hazards in Hong Kong.

RÉSUMÉ: En moyenne, environ 300 glissements de terrain sont signalés au Bureau Géotechnique (GEO) chaque année. Au fil des années, les enquêtes de glissements de terrain sont menées par le GEO et jouent un rôle clé dans l'avancement des connaissances sur la stabilité des pentes et la compréhension des causes et des mécanismes de glissements de terrain et sont devenus une partie intégrante du système de sécurisation des pentes à Hong Kong. Les études sur les glissements de terrain sur les pentes anthropiques ont conduit à l'utilisation de mesures plus robustes pour la stabilisation des pentes artificielles, l'amélioration des pratiques d'ingénieurs pour les pentes dans les matériaux rocheux et l'amélioration des pratiques de suivi. Les études sur les glissements de terrains naturels ont permis de mieux comprendre le mode et les mécanismes de défaillance. Cela permet également l'amélioration de l'évaluation des déplacements des boues, ce qui constitue un point essentiel dans la gestion des risques naturels. Ce document met en lumière certains des principaux enseignements tirés des observations faites à partir des enquêtes de glissements de terrain sélectionnés et comment cette connaissance contribue à l'avancement de la pratique de la géotechnique dans le traitement des pentes artificielles et naturelles à Hong Kong.

KEYWORDS : landslides, investigation, geotechnical engineering practice

1. INTRODUCTION

The rapid population growth in Hong Kong since the 1960s and substantial economic expansion has been accompanied by extensive civil engineering and building works, resulting in the formation of a considerable number of man-made slopes and retaining walls over the hilly territory. However, as there was very limited geotechnical control of slope formation in the old days, the stability of many of these slopes is therefore in doubt. Coupled with severe rainstorms and dense hillside development, Hong Kong is prone to landslide risk.

Following a number of landslide disasters in 1970s, the Hong Kong Government established the Geotechnical Control Office in 1977 (renamed as the Geotechnical Engineering Office (GEO) in 1991) to regulate geotechnical engineering works and slope safety in Hong Kong. This paper gives an overall review of the slope engineering practices that have been enhanced as a result of the landslide investigation (LI) findings.

2. GEOTECHNICAL STANDARDS AND PRACTICE

Setting geotechnical standards has been one of the GEO's functions. To date, some 300 guidance documents have been published covering standards of good practice for the investigation, design, construction and maintenance of slopes.

For public development projects, the prevailing Government policy stipulates that all permanent geotechnical works involving slopes and retaining walls as well as related activities, including investigations, designs and construction should be carried out in accordance with the prevailing standards. Details of the geotechnical works are required to be submitted to the GEO for checking. In general, the standards for public development projects are also adopted for private building and civil engineering works in Hong Kong.

3. LANDSLIDE INVESTIGATION

Figure 1: The Kwun Lung Lau Landslide in July 1994

On average, about 300 landslides are reported to the GEO each year. Most of these occurred at man-made slopes affecting buildings, roads or pedestrian walkways. Many landslides which occurred in remote areas or in natural terrain were not reported. Prior to mid-1990s, the GEO conducted LI on few selected cases of technical interest or having significant consequence. The occurrence of a number of fatal landslides in the mid-1990s has highlighted the need to further enhance the landslide risk management strategy in

Hong Kong. Following the Kwun Lung Lau landslide of 23 July 1994 (Figure 1), which killed five people and seriously injured three others (Morgenstern & GEO 2000), the GEO introduced a number of new enhancement initiatives including a systematic LI programme. The scope of landslide investigations includes examination of all reported landslide incidents and in-depth studies of selected landslides to identify the causes of failure and necessary follow-up actions. The objectives of the systematic LI are to identify those slopes in need of early attention, and undertake forensic investigation of landslides that involve coroner inquests, legal actions or financial disputes. Through landslide investigations, the performance of the Government's slope safety system will be reviewed and areas for improvement identified. Landslide investigations help advance the understanding of causes and mechanisms of landslides and enhance slope engineering practices and the reliability of landslide preventive or remedial works.

The annual expenditure of the LI programme is about US$3 million. Based on observations from LI, new guidelines are promulgated to improve the prevailing geotechnical practice. Some salient LI observations and improvements for soil cut slopes, rock slopes, retaining walls, fill slopes and natural hillside are described below.

4. SOIL CUT SLOPES

Soil cut slopes formed or treated prior to 1990s typically involved trimming back to a less steep gradient without the provision of reinforcement or structural support. They are prone to degradation and vulnerable to the presence of local weaknesses in the groundmass. Large scale landslides involving such unsupported cut slopes are not uncommon. Notable examples are the Ching Cheung Road landslide in 1997 (Figure 2) and Shek Kip Mei failure in 1999 (Figure 3). The 1997 Ching Cheung Road landslide involved a failure volume of over 2,000 m^3, resulting in the trapping of a motor car and temporary closure of a major route connecting east and west Kowloon for two months. The Shek Kip Mei failure involved a distressed volume of 6,000 m^3, resulting in permanent evacuation of three housing blocks. Findings from investigation of such failures highlight the vulnerability of unsupported cut slopes to adverse geological features and hydrogeological conditions, which may be difficult to detect. A pragmatic approach of adopting more robust design solutions, such as the use of soil nailing was called for. A soil nailed slope tends to behave as an integral mass and is less sensitive to local adverse conditions as compared with an unsupported cut. The use of soil nailing has been widely adopted for upgrading of slopes in Hong Kong since mid 1990s.

Figure 2: The Ching Cheung Road Landslide in 1997

So far, there are 40 failures among some 7000 slopes installed with soil nails. None of these are major landslides

(volume ≥ 50 m^3). This indicates that the use of soil nails is effective in averting large scale failure. These minor failures were mostly involved surface erosion or minor local detachment in the groundmass between soil nail heads. Lessons learnt from investigation of soil-nailed slope failures have led to enhanced understanding of the behaviour of soil-nailed slopes (e.g. the importance of soil-nail head), improved detailing of surface drainage provisions (e.g. provision of intersecting drains for long sloping grounds), and enhanced surface protection details. Advances have also been made in the design of soil nails, as promulgated in the Geoguide 7 (GEO 2008).
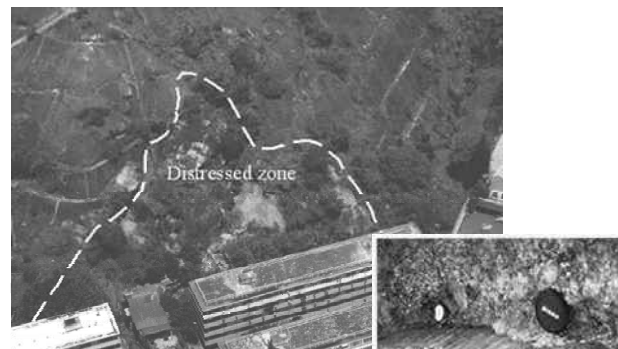

Figure 3: Laterally-persistent discontinuity infilled with slickensided kaolin and manganese oxide deposits at the 1999 Shek Kip Mei failure

5. ROCK SLOPES

Major failures (volume ≥ 50 m^3) involving rock slopes are not very common. Most of the landslides were rain-induced and structurally-controlled, involving build-up of cleft water pressure in rock joints. Other contributory factors such as presence of soft infill along discontinuities, slope deterioration, root wedging effect, etc were also noted. These failures highlight the importance of identifying adversely-orientated jointing system which could have implication to the stability of slopes in the design. With respect to minor rock slope failures such as rockfalls, the primary causes were due to presence of local adverse groundwater regimes and/or loose or unstable blocks. Many of the rockfalls were initiated by tree-root actions. Given the scale of the failure and the consequence of the failure in the urbanized setting in Hong Kong, rockfalls are difficult to guard against in design. A pragmatic approach is to provide suitable protective and mitigation measures such as rock mesh netting, rock fall fence and buffer zone where practicable. LI findings are incorporated in the relevant manuals and guidelines to enhance the rock slope engineering practice (GEO 2009).

6. RETAINING WALLS

A few major landslides involving retaining wall failures had occurred in the past, the most notable one being the 1994 Kwun Lung Lau landslide. The landslide involved the a brittle collapse of a 100-year old masonry wall (Morgenstern & GEO 2000) releasing 1000 m^3 of debris causing 5 fatalities. No tell-tale sign was reported prior to the failure. The failure was triggered by saturation of the soil behind the masonry wall as a result of leakage from nearby defective buried water-carrying services. The incident highlighted the importance of regular inspection and maintenance of water-carrying services affecting slopes. Following the incident, a guidance document entitled "Code of Practice on Inspection and Maintenance of Water Carrying Services Affecting Slopes" was issued by the Government, setting out the recommended good practice for regular inspection and maintenance of water-carrying services affecting slopes.

Furthermore, the landslide investigation findings indicated that the failed wall was 10 m high but only about 0.8 m thick. The wall thickness is much less than that indicated in the record available. This incident highlighted the danger of slender masonry walls that are liable to fail in a brittle manner without any prior signs of distress, and the importance of verifying the wall thickness in stability assessment. This lesson learnt was incorporated in the guideline for stability assessment of old masonry walls (GEO 2004a).

7. FILL SLOPES

Following the disastrous failure of a fill slope at Sau Mau Ping in 1976, the Government appointed an Independent Review Panel to review the landslide problem and make recommendations on the design of fill slopes in Hong Kong. The Panel recommended, amongst others, that the minimum treatment of existing loose fill slopes should consist of removing the loose surface soil by excavating to a vertical depth of not less than 3 m and recompacting to an adequate standard, together with the provision of subsurface drainage behind the recompacted fill layer at the toe of the slope. Technical guidance on the treatment of existing loose fill slopes is given in relevant manual and technical circular (GCO 1984, GEO 2004b).

Up to 2012, about 260 loose fill slopes have been upgraded using the recompaction approach by the GEO. Between 1997 and 2012, a total of 18 landslides occurred on recompacted fill slopes. The primary causes of landslides of these incidents are:

(a) Surface flow concentration
(b) Leakage or bursting of water-carrying services
(c) Inadequate subsurface drainage provisions

Discounting washout failures due to concentrated surface water flow or leakage of water-carrying services, landslides on recompacted fill slopes were generally ductile in nature and did not involve sudden and fast-moving debris as in liquefaction failure.

Enhancement measures have been implemented with reference to the lessons learnt from these landslides. For instance, the Code of Practice on Monitoring and Maintenance of Water Carrying Services Affecting Slopes, which was first issued in 1996, has been updated taking into account lessons learnt from landslides triggered by leakage or bursting of water-carrying services (ETWB 2006).

Detailing of slope drainage provisions has also been improved. Areas for improvement include provision of adequate movement joints for surface drainage channels and provision of filter pipes at upstream end of the subsurface drainage blankets behind the recompacted fill etc. The improvement measures were promulgated in the GEO Report Nos. 210 and 225 (Hui et al. 2007, Fugro 2008)

8. NATURAL HILLSIDE

Hong Kong has a land areas of about 1,100 km^2. About 60% is natural terrain, over 30% of which has a slope gradient over 30°. Natural terrain landslides in Hong Kong are mainly rain-induced. Most of them occurred in remote areas while some affects developments. The GEO has been undertaking technical development works based on the study of natural terrain landslides since the early 1990s.

Based on observed runout distance of landslide debris, a set of simple and suitably conservative guidelines has been developed (Wong 2003) for initial screening purposes to assist planners, land administrators, project managers, etc. to review whether or not a given site is subject to natural terrain

landslide hazards. Where a site is shown to be potentially affected by landslide hazards, more refined criteria are then used to examine whether the proposed development meets the 'in-principle objection' criterion (i.e. relocate the proposed development or amend development layout), or the 'alert criteria' (i.e. carry out natural terrain hazard study and appropriate mitigation measures as part of the development).

In June 2008, Hong Kong was hit by a severe rainstorm. The short-duration rainfall intensity had a return period of about 1,000 years. The rainstorm triggered over 2,400 natural terrain landslides mainly on Lantau Island. Some of them affected developed areas and caused significant social disruption such as evacuation of houses and temporary closure of road sections. The GEO carried out systematic studies on some of these landslides. Detailed field mappings and in-depth landslide investigation provided valuable insights into the characteristics of natural terrain landslides.

Comparing the June 2008 landslides with past landslide records revealed that the 2008 landslides seem to 'cluster' around old ones. Up to 92% of the 2008 landslides occurred within 50 m of at least one past landslide, and 80% within two or more past landslides (Wong 2009). Although further work is needed to interpret this phenomenon, this sheds light on the prediction of regions of natural terrain that is more prone to failure and has implications in the determination of natural hillsides that warrant priority for the mitigation of landslide hazards.

Figure 4: Landslide on the hillside behind the Hong Kong University

Detailed landslide investigations on selected June 2008 landslides showed that past failures could have a significant implication to the scale of the landslides. Past failures could lead to extensive colluvial accumulations on hillside, which are susceptible to give rise to a laterally extensive and a much larger scale failure during heavy rainstorm than those in the past (Figure 4) (Maunsell 2009). If the debris of previous failures deposited along the drainage line, it could become 'entrainable', giving rise to a larger scale of a channelized debris flow (CDF) event (Figure 5) (AECOM 2009). In the 2008 rainstorm, significant entrainment was noted in many of the long runout CDFs with entrainment ratio up to 10 or higher (the entrainment ratio is the volume of additional material that has been entrained by a landslide expressed as a proportion of the source volume). The amount of the pre-existing 'entrainable' materials in a drainage line is dynamic and may change significantly after a rainstorm. This highlights the implications of the deposition of debris from past failures on occurrence of some large-scale failures in natural hillsides.

Figure 5: Yu Tung Road channelized debris flow

In general, the June 2008 landslide debris was found to be more mobile when compared with the previous historical natural terrain landslides in Hong Kong (Figure 6). About 20% of the June 2008 landslides have runout distances over 100 m, as compared with about 10% in past landslides that are observed from old aerial photographs.
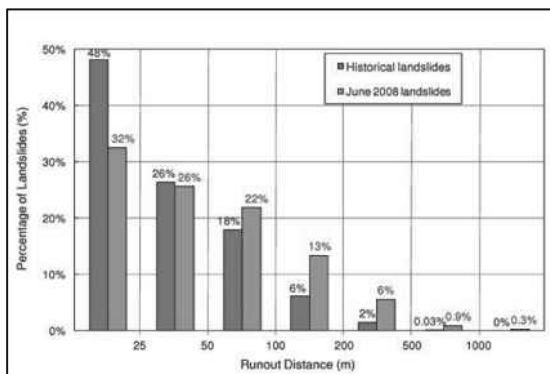

Figure 6: Distribution of landslide runout distance

Detailed studies on selected CDFs revealed that some of the CDFs with long runout generally involved debris with high water content, e.g. the failure near Yu Tung Road (Figure 5). After detaching from the source of failure, the debris mixes with a large amount of water along the drainage line, and results in higher debris mobility. LI revealed that a number of circumstances may lead to such 'watery debris', such as:

(a) debris flows along a major drainage line with a large catchment and a long flow path;
(b) debris flows occurring during heavy rain; and
(c) debris flows along a main drainage line into which many tributaries of drainage lines are feeding.

To facilitate the modeling of debris mobility under such circumstances for natural terrain hazard studies, systematic back analyses were carried out on some selected long runout CDFs that occurred in June 2008 using a 2-D dynamic modelling algorithm, known as 'debris mobility modeller' (2d-DMM) program, as well as 3d-DMM in some cases, to refine the modeling parameters. Improved guidance on debris mobility modeling was promulgated by the GEO (2011).

9. CONCLUSIONS

The landslide investigations have brought insights into the causes, mechanisms and characteristics of landslides. The investigations enhance the understanding of the behaviour of man-made slopes and natural hillside under severe rainstorm and the findings have helped to advance geotechnical engineering practices, and improve standards and design guidelines for enhancing the robustness of slope upgrading and landslide mitigation works.

REFERENCE

AECOM Asia Co. Ltd. (2009) "Detailed Study of the 7 June 2008 Landslides on the Hillside above Yu Tung Road, Tung Chung" (GEO LSR No. 14/2009). GEO, CEDD, Hong Kong.

ETWB (2006). "Code of Practice on Monitoring and Maintenance of Water Carrying Services Affecting Slopes (Second Edition)". Environment, Transport and Works Bureau, Hong Kong.

Fugro Scott Wilson Joint Venture (2008). "Review of Sub-surface Drainage Provisions for Recompacted Fill Slopes" (GEO Report No. 225). GEO, CEDD, Hong Kong.

GCO (1984). "Geotechnical Manual for Slopes" Geotechnical Control Office, Civil Engineering Services Department, Hong Kong.

GEO (2004a). "Guidelines for Assessment of Old Masonry Retaining Walls in Geotechnical Studies and for Action to be Taken on Private Walls" (GEO Circular No. 33). GEO, CEDD, Hong Kong.

GEO (2004b). "Fill Slope Recompaction – Investigation, Design and Construction Considerations" (GEO Technical Guidance Note No. 7). GEO, CEDD, Hong Kong.

GEO (2008). "Guide to Soil Nail Design and Construction" (Geoguide 7). GEO, CEDD, Hong Kong.

GEO (2009). "Enhancement of Rock Slope Engineering Practice Based on Findings of Landslide Studies" (GEO Technical Guidance Note No. 10). GEO, CEDD, Hong Kong.

GEO (2011). "Guidelines on the Assessment of Debris Mobility for Channelised Debris Flows" (GEO Technical Guidance Note No. 29). GEO, CEDD, Hong Kong.

Hui T.H.H., Sun H.W. & Ho K.K.S. (2007). "Review of Slope Surface Drainage with reference to Landslide Studies and Current Practice" (GEO Report No. 210). GEO, CEDD, Hong Kong.

Maunsell Geotechnical Services Limited (2009). "Detailed Study on the 7 June 2008 Landslide on the Natural Hillside behind Chow Yei Ching Building at the University of Hong Kong" (GEO LSR No. 3/2009). GEO, CEDD, Hong Kong.

Morgenstern N.R. & GEO (2000). "Report on the Kwun Lung Lau Landslide of 23 July 1994" (GEO Report No. 103). GEO, CEDD, Hong Kong.

Wong H.N. (2003). "Natural terrain management criteria - Hong Kong practice and experience." *Proceedings of the International Conference on Fast Slope Movements - Prediction and Prevention for Risk Mitigation,* Naples, Italy, vol. 2.

Wong H.N. (2009). "Rising to the challenges of natural terrain landslides." *Proceedings of the HKIE Annual Seminar on Natural Hillsides: Study and Risk Mitigation Measures*, HKIE, Hong Kong, 15-54.

Analyses of Seismic Slope Stability and Subsequent Debris Flow Modeling

Analysis de stabilité de pente sous sollicitation sismique et modélisation des écoulements de boues induits

Long X., Tjok K.-M.
Fugro GeoConsutling Inc., Houston, Tx

ABSTRACT: Earthquake-triggered slope failures and subsequent submarine debris mass flow can cause severe consequences and jeopardize the integrity of offshore structures in the proximity. In this paper, a two-dimensional seismic slope stability analysis for an offshore liquefied slope site located in American Petroleum Institute (API) seismic zone 4 with layered stratigraphy is addressed. A nonlinear dynamic analysis using the stress-strain law of "hysteretic modeling" allowing for soil weakening under large strains was adopted to study flow failure instability. Laboratory tests were performed for the derivation of soil dynamic parameters and calibration of hysteretic soil model. Using "Constant-volume" constraints, the run-out distance of subsequent debris flow was also estimated.

RÉSUMÉ : Lors de séismes, les ruptures de pentes et les écoulements (de boue) sous-marin qui s'en suivent peuvent avoir des conséquences graves et compromettre l'intégrité des structures « offshore » voisines. Dans cet article, on présente une étude (2D) de stabilité d'une pente dans un site « offshore » liquéfiable, dans un zone sismique de niveau 4 (référentiel de l'American Petroleum Institute). Une analyse dynamique non-linéaire utilisant la loi « hysteretic modeling » (loi permettant la modélisation du radoucissement en grande déformation) a été adoptée pour étudier la rupture des pentes et les écoulements induits. Des tests de laboratoire ont été effectués afin d'identifier et de déterminer les paramètres numériques de la loi de comportement. En se plaçant dans le cadre des déformations à volume constant, la modélisation a permis d'estimer la distance parcourue par les écoulements de boues.

KEYWORDS: earthquake slope debris flow non-linear dynamic.

1 INTRODUCTION

Earthquakes are one of the major casuses of submarine slides. Large shear stresses and deformations may be generated due to seismic vibrations and irrecoverable volume changes are accumulated accompanied by the rise of pore water pressure (i.e., decrease of effective stress) and cyclic degradation of shear strength. Liquefaction occurs when the effective stress equals zero and soil behaves as a liquid. The submarine debris mass flow following the onset of liquefaction and instablity of liquefied slope can pose significant impact force and thus jeopardize the integrity of offshore structures in the flow path.

In this paper, a two-dimensional seismic submarine slope stability analysis is performed using commercial computer program FLAC (*F*ast *L*agrangian *A*nalysis of *C*ontinua) (Itasca, FLAC 7.0, an explicit finite difference program operating in the time domain. It simulates the behavior of soils which may subject to plastic flow when their yield limits are reached. The Finn Model- Byrne Formulation is implemented in the analysis to assess dynamic pore pressure generation and liquefaction potential. Based on "constant-volume" constraints, the run-out distance of subsequent debris flow was predicted using the one-dimensional subagqueous debris flow model BING (Imran and Parker, 2001).

2 TWO-DIMENSIONAL NON-LINEAR DYNAMIC ANALYSIS

The slope stability and liquefaction potential for a project site under seismic loading is assessed using FLAC for a two-dimensional non-linear dynamic analysis. The dynamic stress-strain behavior for the soil layers are simulated using a hysteretic model by means of a non-linear stress-strain back bone curve and the associated stress-strain loops that represent the energy dissipated in the soil during seismic loading. Strain-controlled cyclic simple shear tests have been performed to determine dynamic soil parameters and calibration of hysteretic soil model.

2.1 Site Condition

The site is located in International Organization for Standardization (ISO) seismic zone 4 (ISO 2004). Soil stratigraphy consists of soft to firm clay layers overlying dense fine sand. Based on the in situ suspension P (compression wave velocity)-S (shear wave velocity) logging and cone penetration test (CPT) data, the upper 33m (100ft) of the effective seabed is around 160 m/s (525 ft/s) and the site is classified as either American Petroleum Institute (API) criteria Type C or ISO criteria Type E.

Figure 1 below illustrates the soil strategraphy at the study site. The subsurface conditions comprise of 50 m (160 ft) soft to firm clay underlain by a layer of dense to very dense fine sand down to 105 m (350 ft). The mean sea level is 61.0 m (200 ft) above seafloor. Due to soil erosion, a 20˚ slope is formed as detected from the geophysical multibeam bathymetric data. In light of variations of material parameters, three soil Strata, i.e., Stratum I , II and III, respectively, are defined within the clay sediment. For the study of effective stress analysis, four Strata with Stratum I, II and III for cohesive materials and Stratum IV for cohesionless sediment, are used. The soil parameters including submerged unit weight γ, average shear wave velocity V_s, cohesion c, and friction ϕ for each stratum are also provided on the figure. .

The laboratory test data from cyclic direct simple shear (CDSS) along with the generic curves of similar soil types (Seed & Idriss for sand) were used as guidance to develop hysteretic model for the analysis. Figure 2 presents the dynamic

soil characteristics used in the model as defined by the shear modulus degradation (G/Gmax) and damping ratio (D) curves.

Figure 1. Soil stratigraphy for the study site (Not to scale).
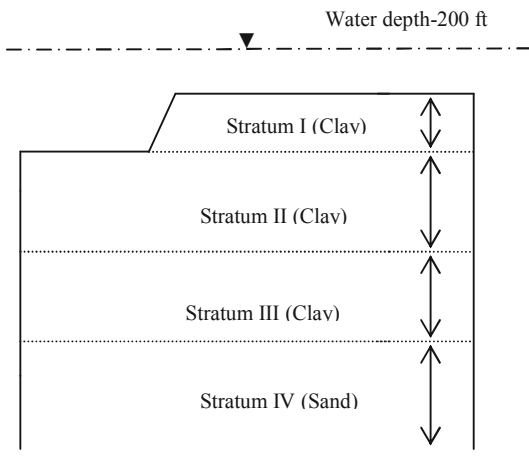
Stratum	Soil Parameters for Effective Stress Analysis
I (4.3m (14ft) thick)	γ=726 kg/m^3, Vs=122 m/s, c=4.8 kPa, ϕ=15°
II (21.3m (70ft) thick)	γ=807 kg/m^3, Vs=186 m/s, c=5.8 kPa, ϕ=20°
III (23.5m (76ft) thick)	γ=888 kg/m^3, Vs=300 m/s, c=5.8 kPa, ϕ=20°
IV (58.0m (190ft) thick)	γ=1000 kg/m^3, Vs=335 m/s, ϕ=35°
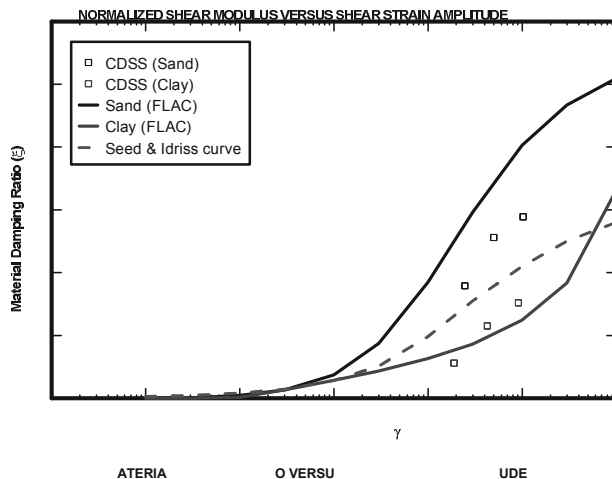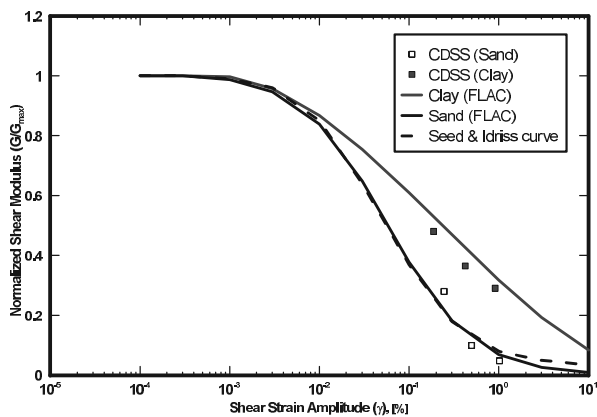
Figure 2. Soil dynamic characteristic curves

2.2 Characteristic of Earthquake Input Motion

The peak ground acceleration (PGA) of the earthquake motion is 0.48 g with a duration time of 40 sec. As indicated from the power spectra of input velocity and input acceleration as shown on Figure 3, the highest frequency component of the input motion is less than 10 Hz with the majority of the frequencies are less than 6 Hz. The input motion is applied at the depth of 105m (350ft).
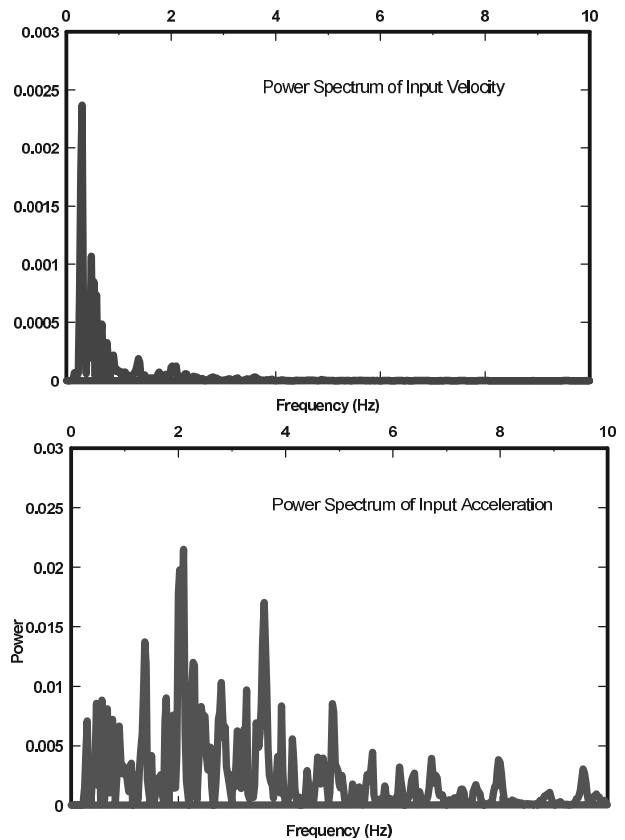
Figure 3. Acceleration time history and power spectrum of input motion.

2.3 Two-Dimensional Numerical Modeling

Kuhlemeyer and Lysmer (1973) state that for accurate representation of wave transmission through a model, the spatial element size, Δl, must be smaller than approximately one-tenth to one-eighth of the wavelength associated with the highest frequency component of the input wave, i.e., $\Delta l \leq \lambda/10$, or f$\leq$Cs/(10Δl), where λ is the wavelength associated with the highest frequency component that contains appreciable energy; and Cs is speed of propagation associated with the mode of oscillation. Since the majority of the frequencies of input motion are less than 6.0 Hz, a 1.83m (6ft) x 1.83m (6ft) mesh size is selected for the modeling. The maximum frequency that can be modeled accurately for this element size is 6.7 Hz. The frequency of Dynamic excitation to the FLAC model was specified using the compliant-base deconvolution procedure (Mejia and Dawson, 2006). The input excitation was specified as a stress time history at the base of the model as a function of mass density ρ, shear wave velocity Vs at the half-space depth (105 m (350 ft) below seafloor) and input shear particle velocity v. Figure 4 demonstrates the FLAC mesh with rectangular and triangle shapes for this two-dimensional analysis. The free-field on vertical sides and quiet boundary conditions at the bottom are applied in the soil domain.
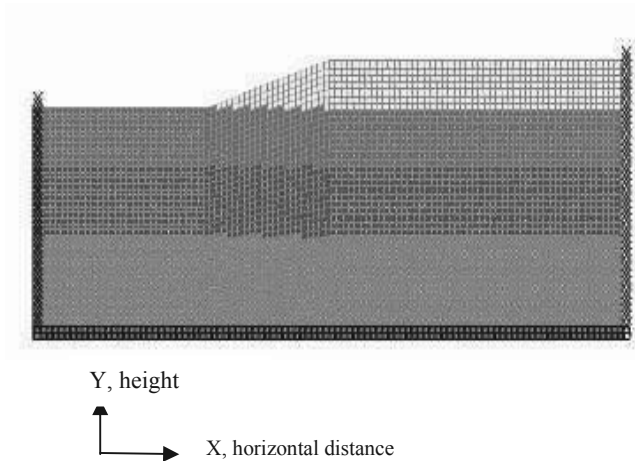
Figure 4. FLAC model for the modeling

The static equilibrium state at the time of the earthquake event is established to obtain the initial shear-stress distribution of the soil mass. The preliminary analysis, assuming undamped elastic-material, was performed to estimate maximum levels of cyclic shear strains and velocity levels throughout the model during the dynamic excitation. The maximum shear strain contour from the preliminary run is shown on Figure 5 indicating that the maximum elastic shear strains are smaller than 0.7 % throughout almost the entire modeled area. This range of shear strains is considered appropriate for inclusion of hysteretic damping based upon the dynamic characteristics of the soils as illustrated on Figure 2. The frequency range for the natural response of the elastic materials is calculated to be relatively uniform throughout the model, with a dominant frequency of approximately 3 Hz.

A fully coupled nonlinear seismic analysis is performed using the Mohr-Coulomb model to represent the soil layers, with additional hysteretic damping applied to simulate the non-linear soil dynamic behavior. Due to the fact that hysteretic damping does not completely damp high frequency component, a small amount of stiffness-proportional Rayleigh damping is also employed in the analysis.

The Finn-Byrne model is used for the liquefaction simulation by considering Strata I and II as liquefiable materials. Based on CPT/SPT correlations from in-situ CPT data and fine contents (Kulhawy and Mayne, 1990), the equivalent normalized SPT blow counts are assigned for the two strata. The automatic rezoning logic is applied in the analysis to correct for severely distorted mesh conditions developed during the simulation of earthquake shaking. The onset of liquefaction is identified by the cyclic pore-pressure ratio, u_e/σ_c', where u_e is the excess pore pressure and σ_c' is the initial in-situ effective confining pressure. After the liquefaction, the soil shear strength is reduced to residual strength which is 30% of the original value.

The numerical analysis indicates the development of liquefaction and failure surface in the slope. Figure 6 displays the contours of maximum shear strain at the end of earthquake excitation (40 seconds). The contour of excess pore pressure ratio equaling 1 (onset of liquefaction) at 40 seconds is also marked in green line on Figure 6. Figure 7 shows the vertical and horizontal displacement histories at the slope crest. The negative sign for X and Y axes indicate the left direction and downward direction, respectively. the slope moves horizontally approximately 8.5m.
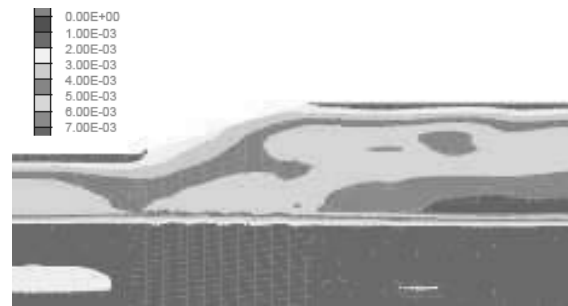

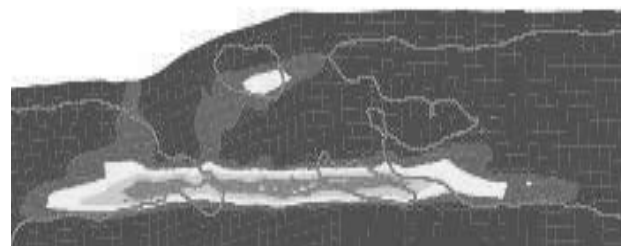Figure 5. Maximum shear strain contours from undamped elastic analysis

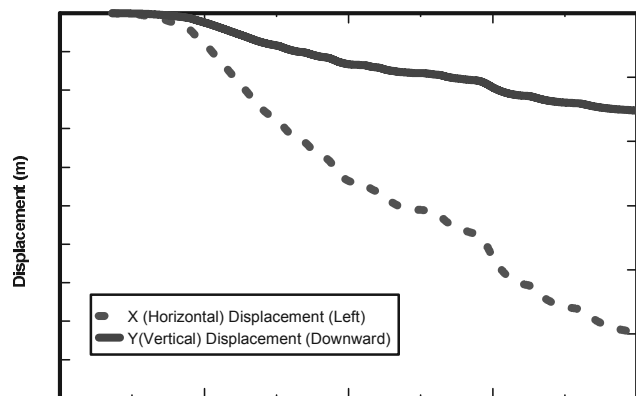Figure 6. Shear strain contours and excess pore pressure ratio=1 contour at 40 seconds

Figure 7. Horizontal (x) and vertical (y) displacement histories at crest of the slope

3   DEBRIS FLOW RUN-OUT DISTANCE

After the development of liquefaction and failure surface in the slope, debris flow can be triggered and the remolded mass during initial failure travels further downslope until the initial stored potential energy is dissipated by friction.

The debris flow run-out distance can be estimated using one- or two- dimensional numerical modeling of sediment-laden submarine flow. For this study, the one-dimensional (1-D) model *BING* assuming one phase flow and "constant volume" constraint. The required input for the simulation includes the bed profile over which the debris mass flow, the initial configuration of the pile of debris slurry, rheological parameters describing the debris slurry and numerical parameters to describe spatial and temporal discretization, run duration and

soil viscosity (Imran and Parker, 2001& 2001). The Herschel-Bulkley rheological model is used for the run-out distance prediction. In the absence of laboratory test data, the yield strength τ_y of 1.5 kPa (30 psf) and reference strain rate γ_r of 1/s were adopted using published relationships as shown on Figure 8 based on soil liquidity index LI (Locat and Lee, 2002).

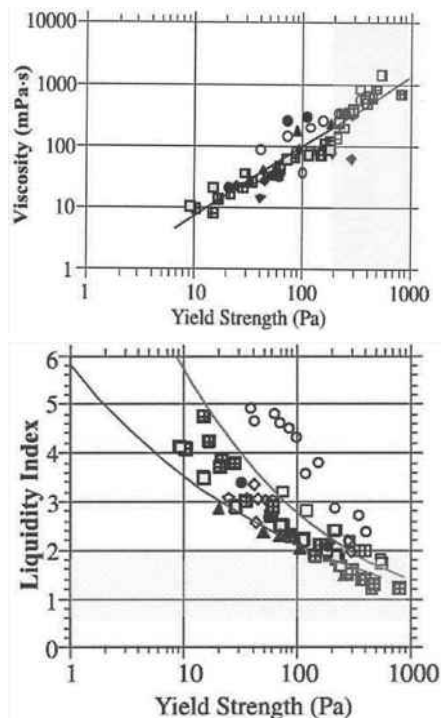Figure 8. Relationship between yield strength, dynamic viscosity, and soil liquidity index (Reproduced from Locat and Lee, 2002)

Considering debris flow originated at the bottom of the slope and the flow origination mass length of around one-half of the sliding mass length, the estimated run-out distance is around 25 m from the toe of the liquefied slope. These mobilized debris flow mass may pose significant impact force against subsea infrastructure in the flow path, even lead to loss of foundation support.

4   CONCLUSIONS

Dynamic slope instability due to earthquake excitation and subsequent submarine slides can cause mass gravity flow which may cause significant impact force or the loss of foundation support and thus pose great risk for the integrity of offshore structure along the flow path.   This paper demonstrated the ability of using a fully coupled nonlinear effective stress analysis to simulate the development of liquefaction and the instability of liquefied slope. The prediction of run-out distance of subsequent debris flow was also discussed here.   For practical application, it should be emphasized that the numerical model for assessing the run-out distance should be tested and calibrated with identified historic mass transport deposits (MTD) and geomorphologic conditions along study site.

5   REFERENCES

American Petroleum Institute : Recommended practice for planning, designing and constructing fixed offshore platforms – working stress design, API RP 2A-WSD, twenty-first edition.2000.

International Organization for Standardizatin : *ISO* 19902- Petroleum and natural gas industries- fixed steel offshore structures, DIS version. 2004.

Imran J. and Parker J. 2001. BING, Subaqueous and subaerial finite source debris flow model.

ITASCA Consulting Group Inc. (2012). FLAC- Fast Lagrangian Analysis of Continua Dynamic Analysis.

Kuhlemeyer, R.L., and J.Lysmer. "Finite Element Method Accuracy for Wave Propagation Problems," J.Soil. Mech. & Foundations, Div., ASCE, 99 (SM5), 421-427, May 1973.

Kulhawy, F.H. and Mayne, P.H. 1990. Manual on estimating soil properties for foundation design. Electric Power Research Institute, EPRI.

Locat, J. and Lee H. 2002. Submarine landslides: advanced and challenges, Canadian Geotechnical Journal, No. 39, 193-212.

Mejia, L.H. and Dawson, E.M. 2006. Earthquake Deconvolution for FLAC. FLAC and numerical modeling in geomechanics Proceedings of the 4th international FLAC symposium, Madrid, Spain.

Quantitative risk assessment for earthquake-triggered landslides using Bayesian network

Évaluation quantitative du risque associé aux glissements de terrain déclenchés par séisme en utilisant un réseau Bayésien

Nadim F., Liu Z.Q.
Norwegian Geotechnical Institute (NGI) / International Centre for Geohazards (ICG), Norway

ABSTRACT: Strong earthquakes in mountainous regions usually trigger many landslides that lead to damage and destruction. Separate investigations of single hazard processes (earthquake and landslide) might lead to a misjudgement of the risks associated with this type of cascading hazards. The assessment and mitigation of the risks require a multi-risk analysis approach that can account for the interactions among the threats and among the vulnerabilities to these threats. In this paper, a quantitative risk assessment model using Bayesian network is proposed to estimate the risk for the buildings exposed to the threat of earthquake-triggered landslides. A sensitivity analysis was done to identify the optimum and appropriate risk reduction strategy in a multi-hazard perspective.

RÉSUMÉ : De forts séismes dans les régions montagneuses déclenchent habituellement des nombreux glissements de terrain qui mènent à dommages et destruction. Si l'on traite les aléas singuliers séparément, par exemple un tremblement de terre et un glissement de terrain, une estimation erronée des risques associés à ce type d'aléas cascadés peut être obtenue. L'évaluation et l'atténuation des risques nécessitent une approche multi-risques qui doit tenir compte des interactions entre les dangers et les vulnérabilités à ces dangers L'article propose un modèle d'évaluation quantitative des risques en utilisant un réseau Bayésien pour estimer le risque aux bâtiments exposés aux glissements de terrain déclenchés par un séisme. Une analyse paramétrique a été réalisée pour identifier une stratégie optimale et appropriée pour réduire le risque dans une perspective multi-aléas.

KEYWORDS: Landslides, Earthquake, Quantitative risk assessment, Bayesian network

1 INTRODUCTION

Earthquake-triggered landslides are one of the most common secondary disasters caused by earthquake in mountainous areas. In the Wenchuan earthquake of May 2008, more than 15 000 landslides of various types were triggered in the steep mountain slopes (Huang 2008). The landslides caused more than 20 000 fatalities (Yin *et al* 2009) and caused extensive damage to housing settlements and irrigation channels (Tang *et al* 2011).

In earthquake-triggered landslide risk assessment, complex interactions are present between the earthquake and landslide threats. The vulnerabilities of the elements at risk are sometimes also correlated to the threats. Amplified risk resulting from hazard and vulnerability interactions has to be considered. Unfortunately, to date, the risk assessment involving multiple hazards is commonly done with independent analyses neglecting possible cascade effects (Marzocchi *et al* 2012) and standard approaches for dealing with the multi-risk situations are not available (Kappes *et al* 2012). In this paper, a quantitative risk assessment model using Bayesian network is proposed to estimate the risk for the buildings exposed to the threat of earthquake-triggered landslides.

2 BAYESIAN NETWORKS

A Bayesian network (BN), also called a belief network, Bayes net or casual network, is an increasingly popular method for reasoning under conditions of uncertainty and modelling uncertain domains. It has been applied to a number of civil and environmental engineering problems, ranging from avalanche risk assessment (Grêt-Regamey and Straub 2006), dam risk analysis (Smith 2006), earthquake risk management (Bayraktarli *et al* 2005; Bensi *et al* 2011), design of early warning system for landslide hazard mitigation (Medina-Cetina *et al* 2007) and environmental modelling and management (Aguilera *et al* 2011).

A BN is a probabilistic model based on directed acyclic graph

$$B_s = G(Z, E) \qquad (1)$$

where B_s represents the structure of the network, Z is the set of random variables (Z_1, Z_2, ... Z_n), and $E \in Z \times Z$ is the set of directed arcs, representing the probabilistically conditional dependency relationships among random variables. Each variable Z_i can be defined in a discrete and finite outcome space (discrete random variable) or as a continuous outcome space (continuous random variable).

One important property of the Bayesian network is that the joint probability function of all random variables in the network can be factorized into conditional and unconditional probabilities implied in the network (Jensen 2007). Thus, the joint distribution can be expressed in the compact form as

$$P(z_1, z_2, ..., z_n) = \prod_{i=1}^{n} P\left(z_i \mid pa\left(Z_i\right)\right) \qquad (2)$$

where $pa(Z_i)$ is the parent set of z_i. It should be noted that if child node z_i has no parents, then the equation reduces to the unconditional probability of $p(z_i)$.

A simple Bayesian network with five nodes and five arcs is illustrated in Fig.1. These nodes are: Magnitude (M), Distance (D), Seismic severity (S), Landslide severity (L), and Building damage (B). These nodes are connected via the arcs: *M-S*, *D-S*, *S-L*, *S-B* and *L-B*. The prior probability of B, $P(B = B_1)$ can be calculated by

$$P(B=B_1) = \sum_{i=1}^{2}\sum_{j=1}^{2}\sum_{k=1}^{2}\sum_{m=1}^{2} P\left(B=B_1, M=M_i, D=D_j, S=S_k, L=L_m\right) \quad (3)$$

where P = probability, B_1 = no damage, M_1 = small magnitude, M_2 = large magnitude, D_1 = small distance, D_2 = large distance, S_1 = low seismic severity, S_2 = high seismic severity, L_1 = low landslide severity, L_2 = high landslide severity.

In this case, as both M and D are the parents of S, S is the parent of L, and both S and L are the parents of B, the joint probability can be derived according to Eq. 2:

$$P(B = B_l, M = M_i, D = D_j, S = S_k, L = L_m)$$
$$= P(M = M_i) \times P(D = D_j) \times P(S = S_k \mid M = M_i, D = D_j)$$
$$\times P(L = L_m \mid S = S_k) \times P(B = B_l \mid S = S_k, L = L_m) \quad (4)$$

where the (conditional) probabilities on the right hand side of the equation are quantified with available information (e.g., statistical data, expert knowledge, and physical approaches).
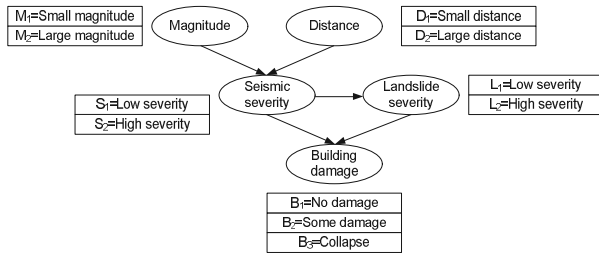
Fig. 1 A simple Bayesian network.

The BN allows one to enter evidence as input, meaning that probabilities in the network are updated when new information is made available, for instance, a case with a small magnitude and large distance. This information will propagate through the network and the posterior probabilities of B, $P(B = B_l)$ can be calculated as:

$$P\left(B = B_l \mid M = M_1, D = D_2\right) = \frac{P\left(B = B_l \mid M = M_1, D = D_2\right)}{P\left(M = M_1, D = D_2\right)} \quad (5)$$

$$= \frac{\sum\limits_{j=1}^{2}\sum\limits_{i=1}^{2} P\left(B = B_l, S = S_j, L = L_i, M = M_1, D = D_2\right)}{\sum\limits_{k=1}^{3}\sum\limits_{j=1}^{2}\sum\limits_{i=1}^{2} P\left(B = B_k, S = S_j, L = L_i, M = M_1, D = D_2\right)}$$

where the joint probabilities in the above equation are calculated with Eq. 3 on the basis of Baye's theorem (Ang and Tang 2007).

3 BAYESIAN NETWORK FOR EARTHQUAKE-TRIGGERED LANDSLIDE RISK ASSESSMENT

According to the ISSMGE Glossary of Risk Assessment Terms, 'Risk' is the measure of the probability and severity of an adverse effect to life, health, property, or the environment. Quantitatively risk is the product of the threat times the potential worth of loss and can be expressed as:

$$Risk = Probability\ of\ Threat \times Worth\ of\ Loss \quad (6)$$

Otherwise expressed (e.g. Einstein 1997):

$$Risk = P(T) \times P(E|T) \times U(E) \quad (7)$$

where $P(T)$ is probability of threat, $P(E|T)$ is conditional probability of damage of the element(s) at risk exposed to threat, i.e. vulnerability, and $U(E)$ is utility of element(s) at risk.

A comprehensive Bayesian network (modified after Einstein et al 2010) for estimating the risk of buildings in an assumed earthquake-triggered landslide case was built with an open-source MATLAB package BNT (Bayes Net Toolbox) (Murphy 2001) as shown in Fig. 2. There are 11 nodes and 16 arcs in the network. Each node is characterized by several discrete states as shown in Table 1.
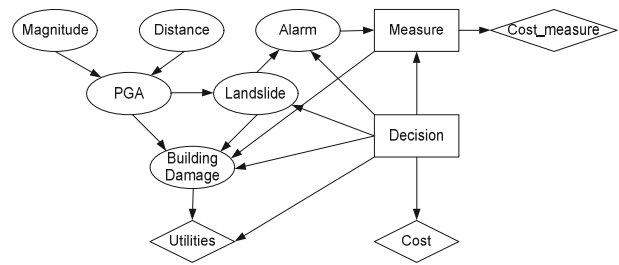

Fig. 2 Bayesian network for earthquake-triggered landslide risk assessment with possible decisions (modified after Einstein et al 2010).

Table 1 Nodes and their states of the Bayesian network in Fig. 2

Nodes	No. of states	States
Magnitude (M_w)	6	4.0-4.5-5.0-5.5-6.0-6.5-7.0
Distance (km)	6	22-25-28-31-34-37-40
PGA (g)	6	0-0.08-0.16-0.24-0.32-0.40-0.48
Landslide	2	Happens; Does not
Building damage	3	No damage; Some damage; Collapse
Alarm	2	Yes; No
Measure	2	Yes; No
Decision	4	Passive; Active; No action; Warning system
Cost_measure	-	
Cost	-	
Utilities	-	

4 QUANTIFYING THE NETWORK

4.1 Seismic hazard

The seismic source is assumed as a line source in this study. Using the geometric characteristics of the source, the distribution of distances can be calculated as shown in Fig. 3.
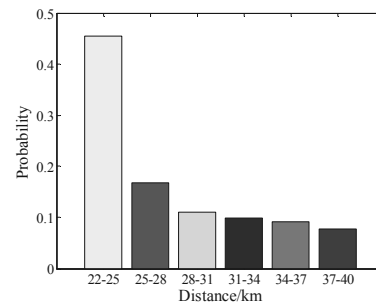

Fig. 3 Specification of the discrete probabilities of distance.

The annual probabilities for each range of Mw are calculated using the Gutenberg-Richter magnitude recurrence relationship (Gutenberg and Richter 1994), as shown in Fig. 4.
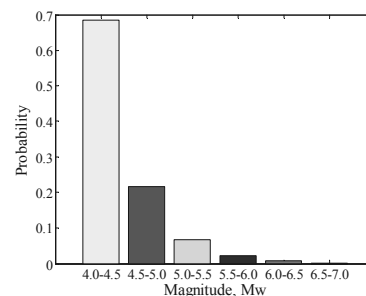

Fig. 4 Specification of the discrete probabilities of magnitude.

The conditional probabilities of PGA given the magnitude and distance to epicenter are calculated with the ground motion equation proposed by Ambraseys et al (2005), using Monte Carlo simulation in Microsoft Excel. The joint probabilities of

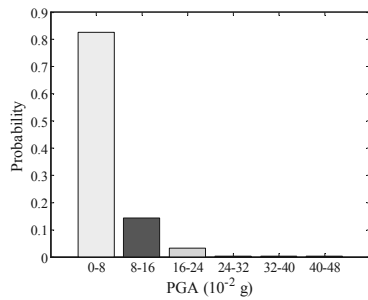PGA are obtained based on inference of Bayesian network, as shown in Fig. 5

Fig. 5 Specification of the discrete probabilities of PGA.

4.2 *Landslide hazard*

Approaches developed to assess the stability of slopes during earthquake fall into three general categories: (1) pseudo-static analysis, (2) stress-deformation analysis, and (3) permanent displacement analysis. In this paper, dynamic performance of slopes is modelled using permanent displacement analysis developed by Newmark (1965). The critical acceleration of a landslide block can be calculated by

$$a_c = (FS-1) \ g \ sin\alpha \tag{8}$$

where *FS* is the static factor of safety; *g* is the acceleration of Earth's gravity; and α is the angle of the sliding surface, which can generally the approximated as the slope angle.

The static factor of safety (*FS*) for an infinite slope is

$$FS = c'/(\gamma z \ sin\alpha \ cos\alpha)+(1-m \ \gamma_w/\gamma)tan\varphi'/tan\alpha \tag{9}$$

where *c'* and φ' are the effective cohesion and friction angle of the soil; *z* is the depth of the failure surface; α is the slope angle; γ is the soil unit weight; and γ_w is the specific weight of water.

In the present study, the Newmark displacement is estimated using Eq. 10 reported by Ambraseys and Menu (1998):

$$Log \ D_n = 0.9+log[(1-a_c/a_{max})^{2.53} \ (a_c/a_{max})^{-1.09}] \tag{10}$$

where D_n is the Newmark displacement in centimeters, a_c and a_{max} are critical acceleration and peak ground acceleration in *g's* respectively.

The probability of slope failure as a function of Newmark displacement, as described by Jibson *et al* (2000) is estimated using the following equation

$$P(f) = 0.335 \times [1-exp \ (-0.048 \times D_n^{1.565})] \tag{11}$$

The soil and slope properties used in this study are shown in Table 2.

Table 2. Soil and slope properties.

Variable	Mean	St. Dev
c' (N/m^2)	10 000	2 000
φ' (degree)	30	2
z (m)	2.5	0
α (degree)	35	0
γ (N/m^3)	27 500	0
γ_w (N/m^3)	10 000	0
m	0.4	0

The probabilities of slope failure computed by Eq. 11 for various ranges of PGA are listed in Table 3. Countermeasures made to landslide could reduce risk. Specifically, active actions can reduce the probability of slope failure, passive actions and warning system can reduce the vulnerability of element(s) at risk. The assumed probability of slope failure when active actions are taken is shown in Table 4.

Table 3. The probability of slope failure

PGA (10^{-2} g)	0-8	8-16	16-24	24-32	32-40	40-48
P(f)	0.124	0.256	0.305	0.328	0.339	0.346

Table 4. The probability of slope failure when active actions are taken

PGA (10^{-2} g)	0-8	8-16	16-24	24-32	32-40	40-48
P(f)	0.025	0.03	0.035	0.04	0.045	0.05

4.3 *Other nodes*

In the case of a building subjected to a multi-hazard situation involving additive load effects (e.g. earthquake + landslide), the damage will be increased. Herein, the conditional probabilities of building damage are modified from Einstein *et al* (2010). For other nodes, we adopt from Einstein *et al* (2010). These probabilities (conditional probabilities) are shown in Tables 5-11.

Table 5. Four combinations of conditional probabilities of Building damage

Parent nodes	PGA	0-0.08			
	Measure	Yes			
	Decision	Passive		Active	
	Landslide	Happens	Does not	Happens	Does not
Build-ing damage	No damage	0.4	0.1	0.52	0.1
	Some damage	0.3	0.1	0.43	0.1
	Collapse	0.3	0.8	0.05	0.8

Table 6. Four combinations of conditional probabilities of Measure

Parent nodes	Alarm	Yes			
	Decision	Passive	Active	No action	Warning system
Measure	Yes	0	0	0	1
	No	1	1	1	0

Table 7. Four combinations of conditional probabilities of Alarm

Parent nodes	Landslide	Happens			
	Decision	Passive	Active	No action	Warning system
Alarm	Yes	0.5	0.5	0.5	0.9
	No	0.5	0.5	0.5	0.1

Table 8. Four combinations of conditional probabilities of Alarm

Parent nodes	Landslide	Happens			
	Decision	Passive	Active	No action	Warning system
Alarm	Yes	0.5	0.5	0.5	0.9
	No	0.5	0.5	0.5	0.1

Table 9. Conditional probabilities of Cost

Parent nodes	Decision	Passive	Active	No action	Warning system
Cost		-1250	-2000	0	-500

Table 10. Conditional probabilities of Utility

Parent nodes	Damage	No damage	Some damage	Collapse
Utilities		0	-10000	-20000

Table 11. Conditional probabilities of Cost_measure

Parent nodes	Measure	Yes	No
Cost_measure		-1000	0

5 RESULTS

The results obtained using the described Bayesian network of the entire risk assessment and decision are shown in Fig. 6. Different mitigation measures result in different utilities. The warning system, showing the lowest (negative) utility is the optimal mitigation measure.
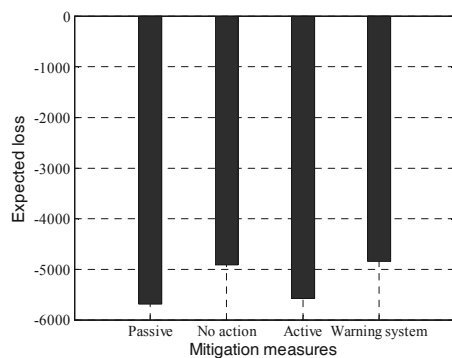
Fig. 6 Comparison of results for Passive countermeasure, No action, Active countermeasure, and Warning system.

This result is based on many parameters that can vary, for instance, the costs; the probability of slope failure or the reliability of the warning system. Therefore, sensitivity analyses were conducted to assess the effects of these variations on the results. Fig. 7 investigates the effect of changing the probability of landslide occurrence against different measures. As expected, for very low failure probabilities, no action is preferred; otherwise a warning system is the best choice, except for very high probabilities where active countermeasures are preferred. It is worth noting that this is only one example, and the sensitivity of the decision to other factors needs to be similarly investigated.
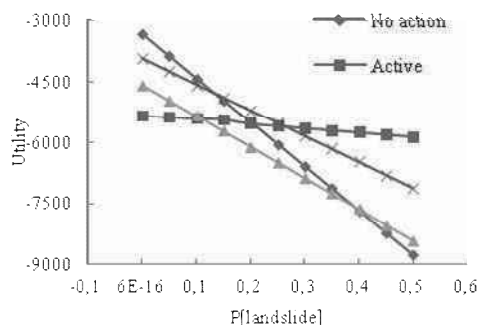
Fig. 7 Sensitivity analysis of the resulting risk arising from varying the probability of slope failure while employing different mitigation actions.

6 CONCLUSIONS

This paper present a new model for evaluating the risks associated with earthquake-triggered landslide using a Bayesian network. The model considered the interactions between different threats in a systematic structure, and accounted for the uncertainties and expert judgments, which are always present in risk analysis. The results obtained in this study are a preliminary step in furthering the earthquake-triggered landslide risk assessment and similar multi-hazard risk assessments. Some of the subjective and empirical parameters in the model need to be further calibrated with the addition of objective data, experience and observations.

7 ACKNOWLEDGEMENTS

8 REFERENCES

Aguilera, P.A., Fernandez, A., Fernandez, R., Rumi, R., Salmeron, A. 2011. Bayesian networks in environmental modeling. *Environmental Modelling & Software* 26(12): 1376-1388.

Ambraseys, N.N., Douglas, J., Sarma, S.K., Smit, P.M. 2005. Equations for the estimation of strong ground motions from crustal earthquakes using data from Europe and the middle east: horizontal peak ground acceleration and spectral acceleration. *Bulletin of earthquake engineering* 3:1-53.

Ambraseys, N.N., Menu, J.M. 1988. Earthquake-induced ground displacements. *Earthq Eng Struct Dyn* 16:985-1006.

Ang, A, H-S. Tang, W.H. 2007. Probability concepts in engineering, with emphasis on applications to civil and environmental engineering. 2nd Ed., John Wiley & Sons, Ltd.

Bayraktarli, Y., Ulfkjaer, J., Yazgan, U., Faber, M. 2005. On the application of bayesian probabilistic networks for earthquake risk management. *9th International Conference on Structural Safety and Reliability (ICOSSAR 05)*, June 20-23, Rome.

Bensi, M.T., Der Kiureghian, A., Straub, D. 2011. A Bayesian network methodology for infrastructure seismic risk assessment and decision support. *PEER Report* 2011/02.

Einstein, H.H. 1997. Landslide risk - systematic approaches to assessment and management. Proc. Int'l Workshop on Landslide Risk Assessment. Landslide Risk Assessment, D. Cruden, R. Fell eds. Balkema.

Einstein, H.H., Sousa, R.L., Karam, K., Manzella, I., Kveldsvik, V. 2010. Rock slopes from mechanics to decision making. *Rock Mechanics in Civil and Environmental Engineering*, Edited by Jian Zhao, Vincent Labiouse, Jean-Paul Dudt and Jean-Francois Mathier. London: CRC Press, 3-13.

Grêt-Regamey, A., Straub, D. 2006. Spatially explicit avalanche risk assessment linking Bayesian networks to a GIS. *Natural Hazards and Earth System Sciences* 6(6):911-926.

Gutenberg, B., Richter, C. F. 1944. Frequency of earthquakes in California. *Bulletin of the Seismological Society of America* 34:185-188.

Huang, R.Q. 2008. Preliminary analysis of the development, distributions, and mechanisms of the geohazards triggered by the Great Wenchuan Earthquake, State Key Laboratory of Geohazards Prevention and Geological Environment Protection, Chengdu University of Technology, Chengdu, China.

Jesen, F.V. 2007. Bayesian networks and decision graphs, Springer, New York.

Jibson, R.E., Harp, E.L., Michael, J.A. 2000. A method for producing digital probabilistic seismic landslide hazard maps. *Eng Geol* 58:271-289.

Kappes, M.S., Keiler, M., von Elverfeldt, K., Glade, T. 2012. Challenges of analyzing multi-hazard risk: a review. *Natural Hazards* 64:1925-1958.

Marzocchi, W., Garcia-Aristizabal, A., Gasparini, P., Mastellone, M.L., Di Ruocco, A. 2012. Basic principles of multi-risk assessment: a case study in Italy. *Natural Hazards* 62:551-573.

Medina-Cetina, Z., Nadim, F. 2008. Stochastic design of an early warning system. *Georisk: Assessment and Management of Risk for Engineered Systems and Geohazards* 2(4): 223-236.

Murphy, K. 2001. The Bayes Net Toolbox for MATLAB. *Computing Science and Statistics* 33:1024-1034.

Newmark , N.M. 1965. Effects of earthquake on dams and embankments. *Geotechnique* 15(2):139-160.

Piteau, D.R., Martin, D.L. 1977. Slope stability analysis and design based probability techniques at Cassiar mine. *Bulletin of the Canadian Institution of Mining and Metalurgy*. 70:139-150.

Smith, M. 2006. Dam risk analysis using Bayesian networks. *Proceedings of the 2006 ECI Conference on Geohazards*, June 18-21, Lillehammer, Norway.

Tang, C., Zhu, J., Qi, X. 2011. Landslide hazard assessment of the 2008 Wenchuan earthquake: a case study in Beichuan area. *Canadian Geotechnical Journal* 48:128-145.

Yin, Y.P., Wang, F.W., Sun, P. 2009. Landslide hazards triggered by the 2008 Wenchuan earthquake, Sichuan, China. *Landslides* 6: 139-152.

Collapse behavior of slope due to change in pore water pressure

Effondrement d'une pente à cause d'une variation de la pression interstitielle

Nakata Y., Kajiwara T., Yoshimoto N.
Yamaguchi University ,Ube, Japan

ABSTRACT: In 2010, a slope failure occurred due to heavy rain following an elevation in ground water level. Although a significant rainfall was experienced at the site in the previous year, there was no deformation with a similar elevation. In the past several collapses were recorded at the site due to heavy rain. Thus tests were performed using a plane strain compression apparatus to understand the deformation behavior of sand subjected to cyclic loadings in pore water pressure which were simulated the observed data on the collapsed slope. Rainfall records and data obtained from the observation well and extensometer were also shown. Finally lessons learned from the data were outlined.

RÉSUMÉ : En 2010, un glissement de terrain eu lieu après une élévation du niveau de la nappe phréatique à cause de fortes pluies. L'année précédente, bien que des précipitations légèrement plus fortes aient été enregistrées sur le site, il n'y eu pas de mouvement de terrain avec un niveau similaire de la nappe. Dans le passé, plusieurs effondrements ont été enregistrés à cause de fortes pluies. Des essais ont été effectués en utilisant un appareil de compression en déformation plane pour comprendre le comportement en déformation d'un sable soumis à des pressions interstitielles cycliques qui expliquent les données observées sur la pente effondrée en 2009-2011. Les relevés pluviométriques et les données obtenues dans un puits d'observation et à partir d'extensomètres sont également indiqués. Enfin on souligne les leçons tirées de l'ensemble de ces données .

KEYWORDS: slope stability, heavy rain, ground water level, pore water pressure, monitoring system, .

1 INTRODUCTION

Slope failures induced by heavy rainfall are one of the most destructive natural hazards and these have claimed untold numbers of lives and millions of dollars in infrastructure losses every year in many parts of the world. The rapid progress of global warming is already leading to changes in climate and related environmental problems. In line with global trends, temperatures in Japan are rising. At the same time active seasonal weather fronts carrying heavy clouds are resulting in increasingly heavy local downpours. As a result of these local downpours of torrential rain there is a national increase in geotechnical failures including slope failure and debris flows. These notable tendencies due to climate change have been increasingly recognized since the beginning of the 21st century.

In 2010, a slope failure due to heavy rain occurred at Hagi city in Yamaguchi Prefecture, which has been known as an unstable landslide area. In 2009, rainfall of significant intensity was experienced at the site, but there was no evident the deformation at that time. Additionally in the past, several collapses occurred at the site due to heavy rain. This means that several cycles of rise-and-fall of the ground water level have occurred at the site. The cycle could be linked to the cyclic changes of pore water pressure.

This paper firstly focuses on the cyclic change of pore water pressure. So far, there has been little research work done on cyclic loading of pore water pressure using triaxial compression apparatus (Ohtsuka & Miyata, 2001, and Orense et al., 2004). Therefore, in order to understand the deformation behavior of soil subjected to cyclic loading of pore water pressure, an experimental research using plane strain compression apparatus was carried out for sand specimens and the results are presented. Subsequently, the observed data on the collapsed slope in 2009-2011 is explained. Especially rainfall records and the data obtained from the observation well and extensometer

are shown. Finally, the lessons learned from the data are described.

2 DEFORMATION BEHAVIOR SUBJECTED TO CYCLIC CHANGE OF PORE WATER PRESSURE

2.1 Plane strain compression test

In order to simulate the cyclic rise-and-fall of ground water level, experimental tests were performed by applying the cyclic change of pore water pressure in the specimen. In past researchers (Ohtsuka & Miyata, 2001, and Orence et al., 2004), tests were carried out using triaxial compression test apparatus applying monotonic loading of the pore water pressure. Thus, plane strain compression tests were adopted to reproduce stress condition closer to the site.

Each specimen was approximately 60mm wide, 160mm high and 80mm deep. Axial loading was applied through an electric motor from the top pedestal of the specimen. Confining and pore water pressures were applied by E/P transducers. All the external forces were controlled by a developed computer program. Grease was painted on the front and back planes of specimen in the direction of zero strain to minimize the friction. Note that the intermediate principal stress could not be measured in this study. Photos of the front plane of the specimen in the direction of zero strain were taken during the shearing process to observe local deformations.

The material used was Toyoura sand which has a higher permeability to propagate the quick change in pore water pressure and to keep the homogeneity of the effective stress condition. The material can be considered to show the relatively small compression deformation component. The specimens were prepared by air pluviation method with a constant falling height of 125mm. The specimen was formed in 5 layers with the falling height kept constant for each layer. As a result, the

initial relative density of specimens produced were 80%±3%. To saturate the specimen, de-aired water was flushed through the specimen and then a back pressure of 50 kN/m² was applied. All specimens were isotropically consolidated for 1 hour and then were sheared to reach maximum and minimum principal stress ratio of about 4.0. The cyclic change in pore water pressure was applied to the anisotropically consolidated specimen with constant amplitude. The principal stress difference was also kept constant by moving the top pedestal with constant axial deformation rate of 0.1%/min. The loading and unloading of the pore water pressure was conducted through a constant pressure increment of 1 kPa/min. After cyclic loading, monotonic loading of pore water pressure was applied to understand the strength of the specimen.

2.2 Cyclic deformation behavior due to pore water pressure
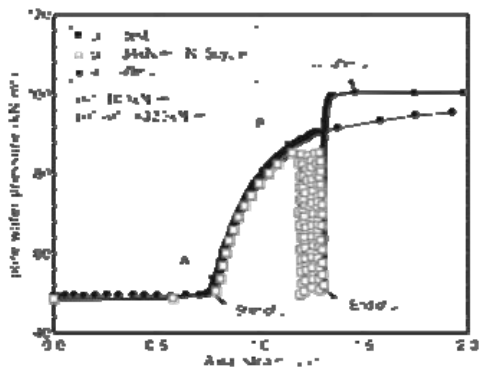
Figure 1 Deformation behavior due to cyclic and monotonic loadings of pore water pressure
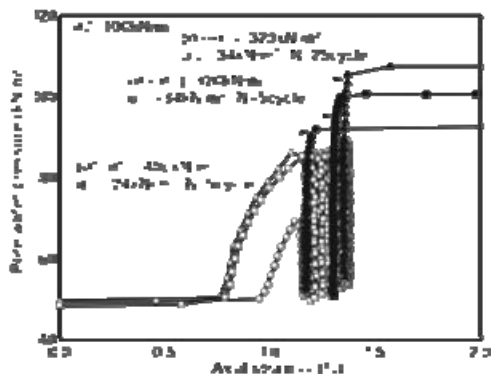
Figure 2 Effect of N and ($\Gamma'_1 \square \Gamma'_3$) on the deformation behavior

Figure 1 shows the pore water pressure and axial strain relationship for the cyclic test under 100 kN/m² of the lateral pressure. The principal stress difference ($\Gamma'_1 - \Gamma'_3$) was kept constant at 320 kN/m². This value corresponded to the residual stress obtained from plane strain compression (PSC) test under 100 kN/m² of lateral pressure. The cyclic change in pore water pressure, u_{cyc} was the amplitude of 34 kN/m². The maximum principal stress ratio reached corresponded to that of PSC test result at 100 kN/m². The sand specimen generated 0.40% of axial distortion from 0.75% (A) to 1.15% (B) during the 1st loading of pore water pressure. After this, the specimen showed 0.15% of axial strain during the rest of the cyclic loading. For comparison, monotonic pore water pressure loading was applied as shown in the figure. The specimen subjected to cyclic pore pressure loading showed rigid-plastic behavior and reached a higher pore water pressure level than the monotonically-loaded specimen without any cyclic loading.

Figure 2 shows the cyclic loading test results with 100 kN/m² of lateral pressure. As the number of cycles increase, the axial deformation becomes larger during the cyclic loading.

Also, as the principal stress difference ($\Gamma'_1 - \Gamma'_3$) is kept higher, the peak pore water pressure during the monotonic loading after the u_{cyc} process becomes lower. This is because the higher stress difference ($\Gamma'_1 - \Gamma'_3$) is closer to the failure stress condition. After first loading, relatively small axial deformations were obtained irrespective of the amount of u_{cyc} and number of cycles N. This indicates that the cyclic loading of pore water pressure never lead to any larger deformation and failure.

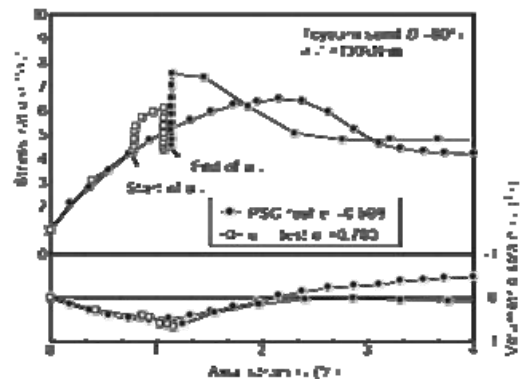### 2.3 Failure after cyclic change of pore water pressure

Figure 3 Stress-strain behavior from monotonic and cyclic loading of pore water pressure

Figure 3 shows the principal stress ratio Γ'_1/Γ'_3 and axial strain relationship for the test results shown in Figure 1. The stress-strain curves before u_{cyc} loading are the same indicating good reproducibility of the specimen. Then, cyclic loading was initiated from the residual stress condition as described earlier. The sand subjected to the loading with $u_{cyc} = 34$ kN/m² reaches a higher maximum stress ratio (Γ'_1/Γ'_3)$_{max}$ = 7.5 compared with (Γ'_1/Γ'_3)$_{max}$ = 6.0 for the conventional PSC test. The volume change during the cyclic loading is relatively small.
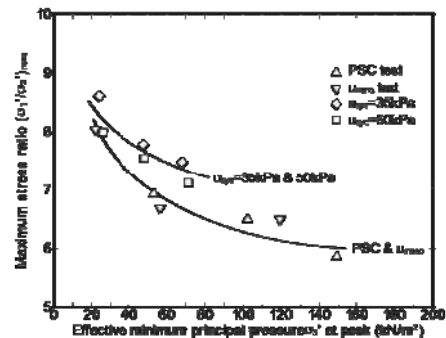

Figure 4 Stress dependency on peak stress ratio

Figure 4 shows the maximum stress ratio (Γ'_1/Γ'_3)$_{max}$ plotted against the minimum principal stress at the peak stress condition. It can be seen that the value of (Γ'_1/Γ'_3)$_{max}$ decreases as Γ_3 at peak increases. As generally well known the stress dependency on the peak stress has been observed. In addition, the results of the cyclic loading of pore water pressure shows a higher (Γ'_1/Γ'_3)$_{max}$ than PSC tests. The results of the monotonic tests were similar with those of PSC test results. It can be recognized that the cyclic loading may induce the hardening and strengthening of the soil.

3 COLLAPSE BEHAVIOR OF SLOPE DUE TO GWL

The Kiyo District of Hagi City, Yamaguchi Prefecture has been known to be an unstable landslide area. The slope has geologic profile consisting of rhyolite and granite with a lower

permeability. Previous failures have occurred at the site in 1973, 1981, 1991 and 1994. In 2000, a landslide occurred as far as the lower debris flow barrier. In 2002 ground surface movements were observed without any apparent flow of soil mass. In order to monitor the stability of the slope, a monitoring system was installed since 1988 as shown in Figures 5 and 6. The main parameters measured were rainfall, ground water level (GWL) and slope movements using extensometers. The data were recorded remotely at the National Highways Bureau in Hagi. The system was upgraded in 2004 by installing inclinometers in the slope and debris barrier. In addition, a strain-gauged tell-tale system was installed across a crack in the barrier. The data logging and communications system was updated with wireless technology. The data has been automatically updated on a website. Moreover a mailing notification system has been installed in case of unusual conditions developing at the site.
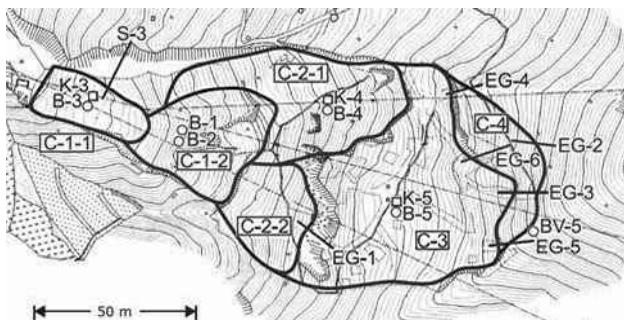
Figure 5 Plane view with failure blocks and measurement points ("C" represenrts failure block, "S" and "EG" are extensometers, "B" and "BV" are observation wells and "K" are for inclinometers)
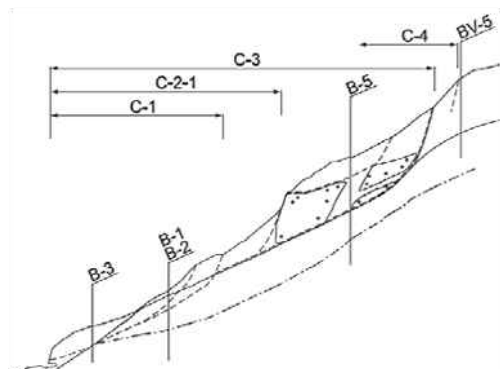

Figure 6 Cross section with failure block and measurement points

Three types of countermeasures were implemented to mitigate slope failure. Firstly the top third of the slope was covered with rubber sheeting to prevent inflow of rainwater. Secondly, water head relief tubes were installed below the area covered by the rubber sheets. And thirdly, a debris flow protection gallery was built over the road in front of the collapsed slope. This gallery was designed to resist an overburden of 4m thick of debris.

4   RAINFALL RECORD AND FAILURE PROCESS

As shown in Figure 7, the rainfall commenced at 22.00 on 10/7/10 with a maximum recorded intensity of 25 mm/hr. At the time of failure, i.e. 5:00 on 10/7/14, the rainfall rate of 18 mm/hr on 7/12 led to a cumulative rainfall of 269mm. By 10:00 on 7/15 the accumulated rainfall was 351mm. The first failure occurred at 5:00 on 7/14 at the lower slope area C-1-2 over a slope length of 80m, width of 50m and depth of 2m. The total volume of the slip was 1600m^3. The second failure occurred between 15:00 on 7/14 and 10.00 on 7/15 at Block C-2-1 over a slope length of 30m, width of 35m and depth of 2m. With these failures, the lower part of the slope was covered by a 2m to 3m

thick layer of debris. This layer was unstable and was liable to flow failure under future heavy rainfall. The upper part of the debris deposit had a vertical slope face. Also a visible continuous crack on the topside of block C-3 was discovered. This means higher potential for further movement of this block under the next heavy rainfall. So the stability of blocks C-2-2 and C-3 was worsened by the rainfall in July 2010.
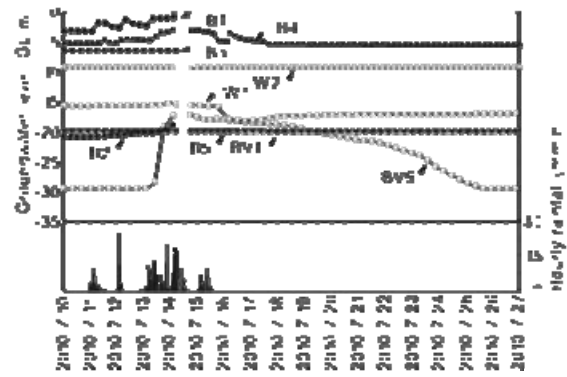

Figure 7 Variation of ground water level in July 2010

5   GROUND WATER LEVEL RECORD

B1 and B2 were located in Block C-1-2. The elevation of GWL firstly occurred in B1 following the rainfall as shown in Figure 7. The GWL rose to within 0.51m below ground level (BGL). In the case of B2 the GWL rose to 18.54m BGL before the first failure, which represented a rise of 3m from the dry period. In previous failures in 1991 and 1994 similar GWL observations were made. It is therefore thought that the GWL was the trigger for the series of failures. The GWL in C3 had not apparently risen above normal levels.

BV-5 was located at the top of the slope and recorded a significant rise in GWL which correlated to the failure of C-3. During the dry period the GWL was at a depth of 29m. The GWL rose from 12:00 on 7/13 reaching a depth of 17.35m BGL at the initiation of failure and started to fall slowly again after 17:00 on 7/14. From 7/14 to 7/21 the rate of decrease was between 0.3m and 0.8m/day and from 7/22 to 7/25 the rate was 1.85m/day, finally reaching 29m BGL on 7/25. The movement of the extensometers stabilised when the ground water level dropped to 20m BGL. B4 was located at the top of the C-2-1 block. The GWL rose to 2.03m BGL which was a 3.5m rise. The rate of decrease was more than BV5 and on 7/17 it fell to 5m BGL. The major movement of Block C3 was considered to be the result of the earlier failure of C1-2 and C2-1 which effectively unloaded the toe of C3.

6   GROUND MOVEMENT

Before the rainfall there were no indications of movement from the monitoring system located in Block C-3. However after the second failure, movement of the C-3 block was observed with rising GWL. After the first failure the monitoring system failed to work for a temporary period of time and was reinstated at 15.00 on 7/14. At this time it was noted that Block C-3 was moving at a rate of 30 mm/hr. This movement was monitored by the inclinometers at K-3. According to the inclinometer data, the slip surface was located at a depth of 20m. The movement at the surface was the same as that at depth, indicating that Block C-3 was moving as a single mass. From 7/15 the rate of movement decreased from 15 mm/hr to 1 mm/hr on 7/19, coming to a virtual halt on 7/22. This decrease correlated with the decrease in GWL. The S-3 extensometer became inactive due to the failure. No movement was observed by the extensometers EG1 and EG2 as shown in Figure 8. Movement was measured by EG3, EG4, EG5 and EG6 after 17.00 on 7/14 with greater than full-scale readings.

From 7/14 to 7/15 the rate of deformation was 5 mm/hr to 15 mm/hr and on 7/16 to 7/18 it reduced to 1 to 5 mm/hr. From 7/18 it gradually decreased. From 7/19 it reduced to 1mm/hr ceasing on the 7/22. The S-4 extensometer was set up on 7/17 because of the failure of C-2-1 and the enhanced risk of failure of the RHS of the slope. During the time the ground water level was going up, progression of displacement was not seen at all. Moreover, displacement between -17m and -20 m of the groundwater level was very remarkable. Furthermore, if the groundwater level falls lower than -23m, it can be considered that the movement of the block stopped in general.
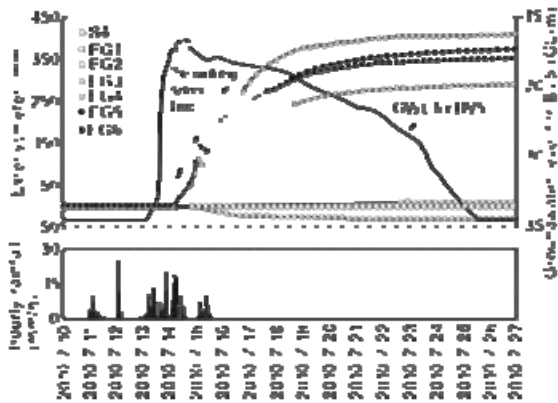
Figure 8 Data of extensometers observed in July 2010
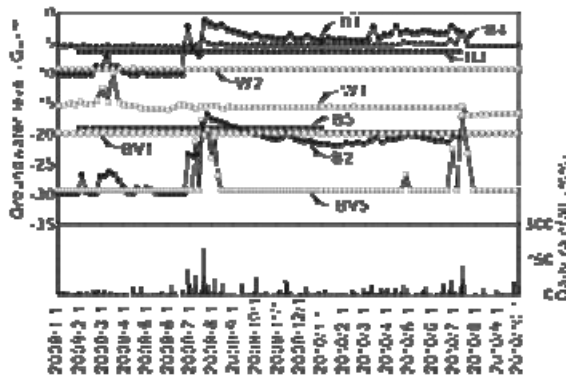
6.1   Rainfall record in 2009

Figure 9 Rainfall record between 2009 – 2010

In 2009, a significant rainfall had been experienced at the same site as shown in Figure 9 with a maximum intensity of 62 mm/hr and cumulative intensity of 289mm over 3 days. However there was no evident of deformation at that time. The evidence indicates that it is difficult to predict the collapse solely by the rainfall forecast. The GWL in B1 in 2009 was 10m BGL compared to 3m BGL in 2010. The potential for slope failure in 2010 was therefore higher. The general tendency over the period 2009 to 2010 was for the GWL to be above normal.

6.2   Collapse behavior in 2011

Deformation of the slope was observed in 2011 due to the smaller rainfall shown in Figure 10. The rainfall in 2011 started on 6/27 and continued intermittently to 7/17. For 21 days, 4 major daily rainfall events were recorded; 60mm on 6/27, 40mm on 7/1, 30mm on 7/4 and 50mm on 7/8. The extensometer begun to act on 7/1 before the GWL for BV5 elevated on 7/3. From this date, the deformation increased gradually and accelerated on 7/7, rising with the rapid increase in the GWL. During the ground water level rise and descent, the displacement of the C-3 block was recorded. The maximum displacement rate appeared during the water level rise while in 2010 it was during water level descent. This implies that the

timing of the warning official announcement would be earlier more for the next heavy rainfall.
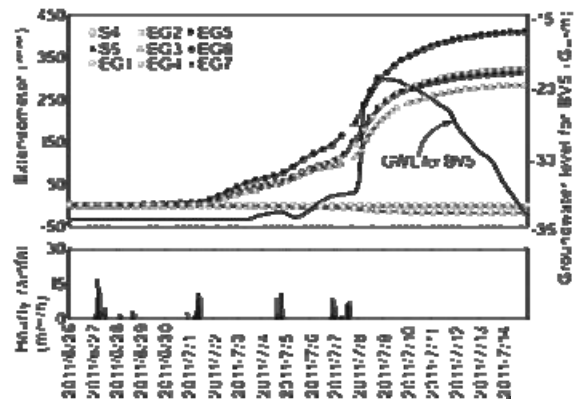

Figure 10 Data of extensometers observed at July in 2011

7   CONCLUSIONS

The paper focused on the evidence of collapse behavior for a slope due to heavy rain in 2010. In the past the site had experienced several collapses. An experimental research was performed to understand the deformation behavior of sand subjected to cyclic loading of pore water pressure using plane strain compression apparatus. Then the observed data on the collapsed slope in 2009-2011 was explained. Finally the lessons from the data were discussed.
1) The experimental test results showed that cyclic loading of pore water pressure never lead to any larger deformation and failure except the first loading. The rigid-perfectly plastic type behavior was observed for the sand specimen subjected to the cyclic changes in pore water pressure.
2) In 2009, a significant rainfall fell at the same site. However, there was no evidence of deformation at that time. This indicated that it was difficult to predict the collapse by the rainfall forecast only and a monitoring system is needed to predict any deformation.
3) The collapse behavior started at the surface layer of the toe part of the slope and then the movement of the major slip block correlated with the rise of ground water level behind the block. Therefore it is important to monitor the ground water level at the appropriate points to understand the collapse behavior.

8   ACKNOWLEDGEMENTS

9   REFERENCES

Ohtsuka S. and Miyata Y. 2001. Failure mechanism of clay in pore water pressure loading test. Landslide 37(4), 10-17 (in Japanese).
Orense R., Farooq K. and Towhata I. 2004. Deformation behavior of sandy slopes during rainwater infiltration. Soils and Foundations 44(2), 15-30.

Future evolution of slope stability analysis created by SPH method

Évolution future de l'analyse de stabilité des pentes créé par la méthode SPH

Nonoyama H.
Nagoya University, Japan

Yashima A., Moriguchi S.
Gifu University, Japan

ABSTRACT: In this paper, the SPH (Smoothed Particle Hydrodynamics) method is applied to slope stability problems. This method can handle large deformation problems because it is based on the free mesh system. In addition, the constitutive models of geomaterials can be used directly. First, a simulation of a simple shear test is carried out to validate the SPH method. Then, slope stability analysis considering countermeasures is carried out. The numerical results are compared with results of the safety factors calculated by the Fellenius method. Based on the obtained results, the effectiveness of the SPH method for slope stability analysis is discussed.

RÉSUMÉ : Dans cet article, la méthode SPH (hydrodynamique des particules lissées) est appliquée à des problèmes de stabilité des pentes. La méthode peut traiter des problèmes de grandes déformations parce qu'elle est basée sur le système de maillage libre. En outre, les modèles de comportement des géomatériaux peuvent être utilisés directement. Dans un premier temps, une simulation d'essai de cisaillement simple a été réalisée afin de valider la méthode SPH. Ensuite, une analyse de stabilité des pentes considérant des contre-mesures a été réalisée. Les résultats numériques ont été comparés avec les résultats des facteurs de sécurité calculés par la méthode Fellenius. Sur la base des résultats obtenus, l'efficacité de la méthode SPH pour l'analyse de la stabilité des pentes a été discutée.

KEYWORDS: slope stability analysis, meshfree method, constitutive model

1 INTRODUCTION

In terms of the slope stability problems, design of structures and evaluation of countermeasures are carried out using a safety factor of slope obtained from circular slippage calculations at the practical level. In this approach, the safety factor of the slope is easily obtained from equilibrium of force. However, it is not possible to take into account of the deformation of slope. If it is possible to predict the deformation of slope, more detailed design of structures and evaluation of countermeasures can be facilitated. A lot of deformation analyses using the Finite Element Method (FEM) with developed constitutive models have been reported. It is, however, still difficult to solve large deformation problems using the FEM due to the distortion of the mesh. On the other hand, to solve such problems, various numerical approaches have been proposed, such as a modeling based on the computational fluid dynamics (CFD) and the discrete modeling (Cundall and Strack 1979). In the method based on CFD, it is not necessary to pay attention to mesh distortion, because the mesh is fixed in space. However, soils are assumed to be a kind of non-Newtonian fluids (Moriguchi 2005). Thus this modeling is an effective tool for flow problems, but is difficult to apply to static deformation problems. In addition, it is difficult to use constitutive models based on solid mechanics, because they cannot easily handle the history information of soils during deformation. The discrete modeling uses an assembly of discrete elements, and is inappropriate for dealing with constitutive models based on a continuum approximation.

Against these backgrounds, the purpose of this research is to express the large deformation behavior of geomaterials in the framework of continuum mechanics. The smoothed particle hydrodynamics (SPH) method, proposed by Lucy (1977) and Gingold and Monaghan (1977), is based on a mesh-free Lagrangian scheme, and is one of the effective numerical methods. The method can solve large deformation problems without mesh distortion. Moreover, it can handle the governing equations and existing constitutive models for geomaterials, since it is based on a continuum approximation. The method has already been used to solve many types of geotechnical problems, and a number of interesting achievements have been published (e.g., Maeda et al. 2004, Bui 2007). From these achievements, it is shown that the SPH is applicable to geotechnical problems. However, as far as the introduction of the constitutive models of geomaterial into the SPH method, detailed discussions have not been carried out.

In this paper, the SPH method was applied to slope stability problems. In order to validate the method, a simulation of the simple shear test for elasto-plastic materials is carried out. Then, a slope stability analysis considering countermeasures is carried out. The numerical results are compared with the results of the Fellenius method. Based on the obtained results, the effectiveness of the SPH method for slope stability analysis is discussed.

2 NUMERICAL METHOD

2.1 *Basic theory of SPH method*

In the SPH method, an object is expressed as an assembly of particles. If the motions of the particles are solved individually, the deformation behavior of the continuum cannot be represented by this technique. In order to treat an object as a continuum, a unique interpolation theory is used. This interpolation theory includes two key approximations: a kernel approximation and a particle approximation. The first step is a kernel approximation of the field functions. The kernel approximations are based on neighboring particles β located at points x^β within the support domain $\kappa^d h$ of a smoothing function W for a reference particle α located at point x^α, as shown in Fig. 1. In the first step of the interpolation, we define a smoothed

physical quantity $\langle f(x^\alpha)\rangle$ for the physical quantity $f(x^\alpha)$ at the reference particle α as follows:

$$\left\langle f\left(x^\alpha\right)\right\rangle = \int_\Omega f\left(x^\beta\right)W\left(r,h\right)dx^\beta \tag{1}$$

where $r = |x^\alpha - x^\beta|$, h is the radius of the influence domain, and Ω is the volume of the integral that contains x^α and x^β.

In the second step of the interpolation, the physical quantity $\langle f(x^\alpha)\rangle$ for the reference particle α is expressed as the summation of the distribution of the assumed physical quantities $f(x^\beta)$ for each particle. Thus, the physical quantity can be expressed in terms of N discrete points:

$$\left\langle f\left(x^\alpha\right)\right\rangle = \sum_\beta^N \frac{m^\beta}{\rho^\beta}f\left(x^\beta\right)W^{\alpha\beta} \tag{2}$$

where m^β is the mass, and ρ^β is the density of neighboring particles β. N is the numbers of neighboring particles in the support domain, and $W^{\alpha\beta}$ is the smoothing function that expressed the contribution from the neighboring particles β to the reference particle α. In this study, Cubic spline function (Swegle 1994) is used as the smoothing function. Equation (2) is a formula for evaluating a physical quantity via the SPH method. It is also possible to approximate the spatial gradient of a physical quantity in a similar way, using the spatial derivative of the smoothing function. The spatial derivative of Eq. (2) can be written as

$$\frac{\partial\left\langle f\left(x^\alpha\right)\right\rangle}{\partial x_i} = \sum_\beta^N \frac{m^\beta}{\rho^\beta}f\left(x^\beta\right)\frac{\partial W^{\alpha\beta}}{\partial x_i} \tag{3}$$

Based on the two-step interpolation procedure, it is possible to calculate any physical quantity and its special derivative of a physical quantity.
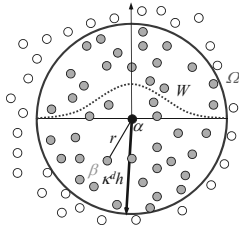

Figure 1. An image of basic concept of SPH method

2.2 *SPH method based on the solid mechanics*

The governing equations used in this study are based on solid mechanics. The equation of continuity and the equation of motion can be defined as follows,

$$\frac{d\rho}{dt} = -\rho\frac{\partial u_i}{\partial x_i} \tag{4}$$

$$\frac{du_i}{dt} = \frac{1}{\rho}\frac{\partial\sigma_{ij}}{\partial x_j} + F_i \tag{5}$$

where u_i is the velocity vector, ρ is the density, σ_{ij} is the stress tensor and F_i is the external force vector. Applying the SPH interpolation theories, the equations are expressed as follows:

$$\frac{d\rho^\alpha}{dt} = -\sum_\beta^N m^\beta\left(u_i^\beta - u_i^\alpha\right)\frac{\partial W^{\alpha\beta}}{\partial x_i} \tag{6}$$

$$\frac{du_i^\alpha}{dt} = \sum_\beta^N m^\beta\left(\frac{\sigma_{ij}^\alpha}{\left(\rho^\alpha\right)^2} + \frac{\sigma_{ij}^\beta}{\left(\rho^\beta\right)^2} + C_{ij}^{\alpha\beta}\right)\frac{\partial W^{\alpha\beta}}{\partial x_j} + F_i^\alpha \tag{7}$$

where C_{ij} is the summation of the artificial viscosity term (Monaghan and Gingold 1983) and the artificial stress term (Monaghan 2000; Gray et al. 2001). In order to introduce the artificial viscosity and the artificial stress, the numerical instability and the tensile instability are decreased (Swegle et al. 1995). Tensile instability, specifically the instability of the solution for tension deformation, is one of the problems with the SPH method for solid mechanics. In this study, the Drucker-Prager model (Drucker and Prager 1952) and the Super-subloading Yield Surface Modified Cam-clay model (Asaoka et al. 2000; 2002) are used in the deformation analysis of geomaterial to validate potential of the SPH method.

3 SIMULATION OF SIMPLE SHEAR TEST

In the validations of the SPH method for solid mechanics, a simulation of simple shear test under plane strain condition is carried out using Drucker-Prager model and Super-subloading Yield Surface Modified Cam-clay model. Calculated stress strain relation and stress paths are compared with the theoretical solution at the center of specimen. Figure 2 illustrates the numerical model used in the simulation. As the figure indicates, the specimen is a square object (10 cm by 10 cm). In the SPH method, numerical instabilities and errors tend to arise due to lack of calculation points. Therefore, a virtual area surrounded the specimen was used in this simulation. The solid line denotes the initial configuration of the specimen, and the dashed line denotes the configuration after deformation. In the simulation, the virtual area is forcibly deformed with a constant displacement to represent simple shear conditions, and the deformation of the specimen is calculated. Since a virtual area surrounded the specimen, only the scheme is employed in this validation. The parameters used in this simulation are summarized in Tables 1. As Table 1 indicates, seven different cases are considered in this simulation. In Cases 1, cohesive frictional material is used. In Cases 2 and 3, parameters of typical clay under two different values of the initial mean stress and initial overconsolidation ratio are used. In Cases 4 to 7, parameters of typical sand under three different values of the initial mean stress and degree of structure are utilized.
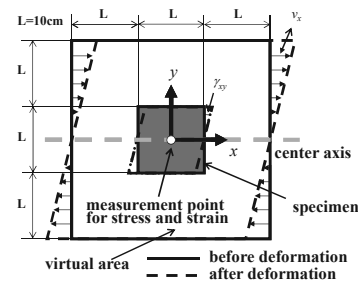

Figure 2. Numerical model

Figures 3 to 5 shows calculated stress-strain relation and stress paths at the center of the specimen. The theoretical solutions are also described in these figures for comparison. The solid line denotes the theoretical solutions, and plotted points indicate the obtained results. Based on the comparison, the results from the SPH scheme are in good agreement with the theoretical solution. Also, by introducing the Super-subloading Yield Surface Modified Cam-clay model (Asaoka et al. 2000; 2002) into the method, the softening with plastic compression behavior of structured soil and rewinding behavior of overconsolidated clay (Fig. 4) are expressed. Also, the softening behaviors with plastic compression of medium-dense sand and subsequent hardening behavior with plastic expansion (Fig. 5)

are expressed. It is summarized that the high performance elasto-plastic constitutive model can be introduced into the SPH method. Also, it is possible to simulate the various state of geomaterial, such as the clay and sand, using the SPH method.

Table 1. Material parameters

(a)Drucker-Prager model

Case		1
Young's modulus	E [kPa]	1000.0
Poisson's ratio	v	0.33
cohesion	c [kPa]	50.0
internal friction angle	ϕ [deg]	30.0
initial mean stress	p_0[kPa]	98.0

(b) Super-subloading Yield Surface Modified Cam-clay model

Case		2	3	4	5	6	7
＜elasto-plastic parameters＞							
compression index	λ	0.200		0.052			
swelling index	κ	0.050		0.010			
critical state constant	M	1.40		1.0			
NCL intercept	N	2.20		1.98			
Poisson's ratio	v			0.3			
＜evolution parameters＞							
degradation index of overconsolidation	m	3.0		0.06			
degradation index of structure	a	0.5		2.2			
degradation index of structure	$b=c$			1.0			
＜initial value＞							
initial degree of overconsolidation	$1/R_0$	5.01	1.16	20.0			
initial degree of structure	$1/R_0^*$	5.0		1.40	10.0	23.6	39.0
initial specific volume	v_0	2.20		1.95			
initial mean stress	p_0[kPa]	98.1	294.3	20.0	98.1	196.2	294.3

(a)stress-strain relation   (b)stress paths
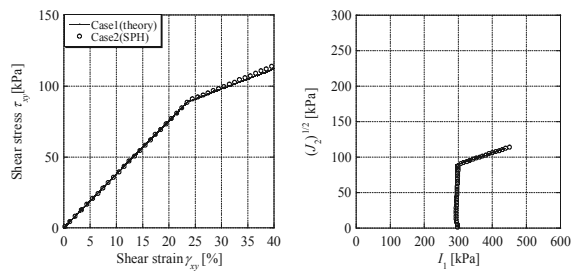
Figure 3. Drucker-Prager model (Case 1)

(a)stress-strain relation   (b)stress paths
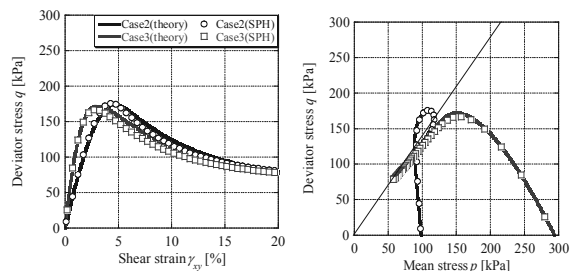
Figure 4. Super-subloading Yield Surface Modified Cam-clay model (Cases 2 and 3)

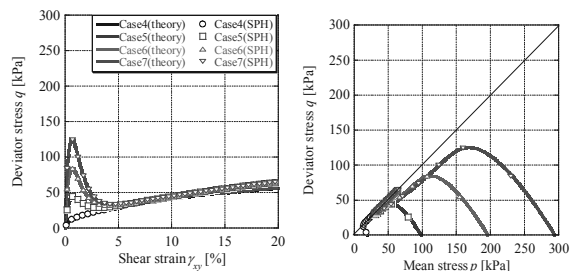(a)stress-strain relation   (b)stress paths

Figure 5. Super-subloading Yield Surface Modified Cam-clay model (Cases 4 to 7)

4 SLOPE STABILITY ANALYSIS CONSIDERING COUNTERMEASURES

A slope stability analysis considering countermeasures is carried out, using the Drucker-Prager model. Two types of countermeasures, such as top soil removal work and counterweight fill, are considered into these simulations. The numerical results are compared with results obtained using the safety factors calculated by the Fellenius method. Figure 6 illustrates the numerical models in Cases 1 to 8. The slope angle is 45 degrees and the model ground is cohesive. Also, as the figure shows, the displacements at the top of the slope are checked. The parameters used in this simulation are listed in Table 2. For the boundary conditions, the horizontal direction at the side wall of the slope was fixed, and the vertical direction is free. The horizontal and vertical directions at the bottom of the embankment are fixed. Fixed boundary particles are used to describe the walls. In order to take into account the effect of surface compaction, the internal friction angle of the counterweight fill material is set to 30 degrees. The effect of pore water pressure is not taken into account. The isotropic stress corresponding to static earth pressure is used as the initial stress.
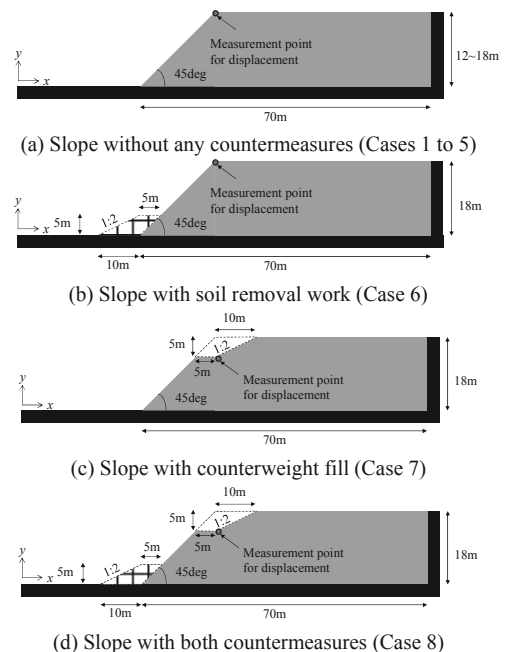

(a) Slope without any countermeasures (Cases 1 to 5)

(b) Slope with soil removal work (Case 6)

(c) Slope with counterweight fill (Case 7)

(d) Slope with both countermeasures (Case 8)

Figure 6. Numerical models.

Table 2. Material parameters.

Young's modulus	E [MPa]	100.0
Poisson's ratio	v	0.30
cohesion	ϕ [deg]	0.0
internal friction angle	c [kPa]	50
unit weight	γ [kN/m³]	19.6

Table 3. Safety factors obtained from the Fellenius method for each case.

Case	Countermeasures	Height of slope H[m]	safety factor Fs
1		12	1.24
2		14	1.01
3	Without any countermeasures	15	0.91
4		16	0.86
5			0.75
6	Soil removal work	18	0.87
7	Counterweight fill		0.90
8	Both countermeasures		1.02

The safety factors obtained from the Fellenius method are listed in Table 3. As Table 3 indicates, the safety factors rise according to the order of case without any countermeasures,

case with soil removal work, case with counterweight fill, and case with both soil removal work and counterweight fill.

The distributions of accumulation of the maximum shear strain are shown in Fig. 7. As explained in above, boundary particles are used for the wall, but are not shown in these figures. Figure 8 shows the relationship between the safety factor and the value obtained by dividing the displacement δ at the top of the slope by the height of the slope H. When the safety factor is larger than 1.0(Cases 1 and 2), shear strain does not appear in the figures. However, when the safety factor is less than 1.0(Cases 3 to 5), a distribution of circular shear strain can be seen. When the safety factor is close to 0.9, shear strain is observed but still large deformation cannot be observed. In particular, a crack forms at the crown of the slope, and block slippage is confirmed in the cases with the lowest safety factors. In the case without any countermeasures (Case 5), the shear strain is conspicuous and the slope is largely deformed. On the other hand, in the cases with countermeasures (Cases 6 to 8), the shear strain does not become more prominent and the displacements can be controlled as the safety factor increased. Thus, similar tendencies are observed in the results from the SPH method and the Fellenius method. In addition, while conventional circular slippage calculations are used to estimate the occurrence of rigid block slippage, the SPH method can estimate not only the stability, but also the effects of deformation. In Cases 3 and 7, the slope is not deformed, although the safety factor is less than 1.0. On the boundary between stable and unstable states, we consider that the slope is stabilized due to the redistribution of stress following an initial small deformation. The SPH method can estimate deformation and stability simultaneously. Moreover, it is capable of continuously predicting the deformation, even in a large deformation region. In other words, the SPH method can predict the entire deformation process of a geomaterial. Therefore, one may conclude that a variety of useful information about slope stability problems can be obtained via the SPH method.
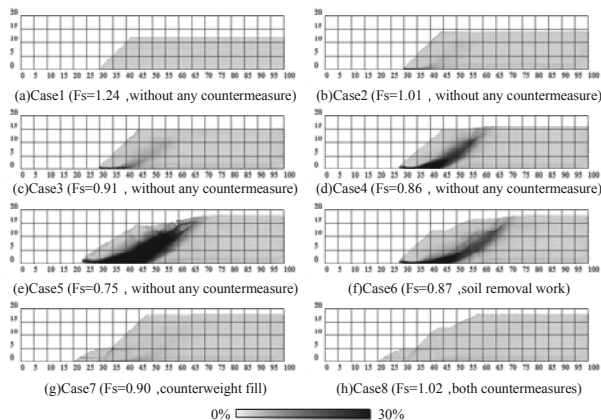

(a)Case1 (Fs=1.24 ,without any countermeasure)
(b)Case2 (Fs=1.01 , without any countermeasure)
(c)Case3 (Fs=0.91 , without any countermeasure)
(d)Case4 (Fs=0.86 , without any countermeasure)
(e)Case5 (Fs=0.75 , without any countermeasure)
(f)Case6 (Fs=0.87 ,soil removal work)
(g)Case7 (Fs=0.90 ,counterweight fill)
(h)Case8 (Fs=1.02 ,both countermeasures)

0%　　　　　　30%

Figure 7. Distributions of accumulation of the maximum shear strain
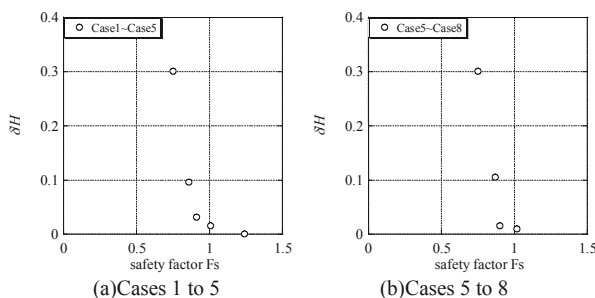

(a)Cases 1 to 5　　　　　(b)Cases 5 to 8

Figure 8. Relationship between safety factor and displacement at the top of slope.

5 CONCLUSION

In this study, introducing the constitutive model into the SPH method, deformation analyses of geomaterials were carried out. Firstly, in order to validate the method, the simulation of simple shear test of elasto-plastic material was simulated using two kinds of constitutive models of geomaterials. The numerical results were compared with the theoretical solutions. Then, a slope stability analysis considering countermeasures was carried out. The conclusions can be summarized as follows:

- The simulation of a simple shear test demonstrated that the SPH method could calculate the appropriate stress state of geomaterials using high performance elasto-plastic constitutive models.
- The SPH method was applied to slope stability analysis. The results indicated that the method was able to express the same safety factor tendencies obtained from the conventional circular slippage calculations. At the same time, the SPH method can simultaneously estimate both the deformation and stability. From the results of a slope stability analysis considering countermeasures, it can be inferred that the SPH method was capable of predicting the deformation and stability of slopes even in complex situations, such as simulations that include countermeasures.
- From a series of the numerical results, the SPH method was found to be applicable to slope stability analysis. Also, the SPH method has the potential to describe the deformation of geomaterials from the initial state to subsequent large deformations.

6 REFERENCES

Asaoka A. et al. 2000. Superloading yield surface concept for highly structured soil behavior, *Soils and Foundations*, 40 (2), 99-110.

Asaoka A. et al. 2002. An elasto-plastic description of two distinct volume change mechanisms of soils, *Soils and Foundations*, 42 (5), 47-57.

Bui, H.H. 2007. Lagrangian mesh-free particle method (SPH) for large deformation and post-failure of geomaterial using elasto-plastic constitutive models, *Ph.D. Dissertation of Ritsumeikan University*, Japan.

Cudall P.A. and Strack O.D.L. 1979. A discrete numerical model for granular assemblies, *Geotechnique*, 29 (1), 47-65.

Drucker D.C. and Prager W. 1952. Soil mechanics and plastic analysis for limit design, *Quart. Appl. Math.*, 10 (2), 157-165.

Gingold R.A. and Monaghan J.J. 1977. Smoothed particle hydrodynamics: theory and application to non-spherical stars, *Monthly Notices Roy. Astron. Soc.*, 181, 375-389.

Gray J.P. et al. 2001. SPH elastic dynamics, *Comput. Methods Appl. Mech. Engrg.*, 190, 6641-6662.

Lucy L.B. 1977. A numerical approach to the testing of the fission hypothesis, *Astron. J.*, 82, 1023-1024.

Maeda K. and Sakai M. 2004. Development of seepage failure analysis procedure of granular ground with Smoothed Particle Hydrodynamics (SPH) method, *J. Appl. Mech.*, JSCE, 7, 775-786 (in Japanese).

Monaghan J.J. and Gingold R.A. 1983. Shock simulation by the particle method SPH, *J. Comput. Phys.*, 52, 374-389.

Monaghan J.J. 2000. SPH without a tensile instability, *J. Comput. Phys.*, 159, 290-311.

Moriguchi S. 2005. CIP-based numerical analysis for large deformation of geomaterials, *Ph.D. Dissertation of Gifu University*, Japan.

Swegle J.W. et al. 1994. An analysis of smoothed particle hydrodynamics, *SAND93-2513*, *Sandia National Laboratories*, *Albuquerque, NM*.

Swegle J.W. et al. 1995. Smoothed particle hydrodynamics stability analysis, *J. Comput. Phys.*, 116(1), 123-134.

Slope stability along a new road "Drisht –Drisht castle"

Stabilité de pente le long de la nouvelle route "Drisht-Drisht castle"

Paçi E., Cullufi H., Dervishaj A.
Polytechnic University of Tirana, Albania

ABSTRACT: Some slopes along the new road from the village Drisht center to the medieval castle entrance are located in a very disturbed tectonic zone. Due to overthrust geological processes the rock quality are extremely poor. In surface there are different active slides that due to water circulations especially during seismic events are very unstable and slide towards road pavements or cause side channel and culvert fills.

This article describes the numerical calculation concerning frequent normal conditions during construction and use of road and accidental condition during seismic events. Based in these calculations design solution are given. The calculations will be controlled by a back analysis algorithm. We have decided the upper and lower boundaries for the main results and we have made a sensitivity analysis that will show the influence of each parameter to the predicted results. So during maintenance time with same site tests results we can correct numerical parameters used in the model and predict long time behavior of the slope. In this manner we can also correct the future rehabilitation measures (if necessary) for the above mention road slope and other road slopes in similar conditions.

RÉSUMÉ : Certaines pentes le long de la nouvelle route allant du centre du village de Drisht à l'entrée du château médiéval sont situées dans une zone tectonique très perturbée. En raison de différent processus géologiques, la qualité de la roche est extrêmement médiocre. En surface, il existe différents glissements actifs qui, en raison de circulations d'eau lors d'événements sismiques, sont très instables et glissent vers chaussées et remplissent le canal longitudinal.

Cet article présente un calcul numérique (en conditions fréquentes – normales) pendant la construction et l'utilisation de la route. Les conditions accidentelles correspondant à des événements sismiques sont aussi traitées. Sur les bases des calculs effectués, des solutions techniques sont proposées. Les calculs sont contrôlés par un algorithme de "back analysis". Nous avons décidé les limites supérieure et inférieure pour les principaux résultats et nous avons fait une analyse de sensibilité qui montre l'influence de chaque paramètre. Ainsi, pendant le temps d'entretien du site, nous pouvons déterminer les paramètres numériques à utiliser dans le modèle pour prédire le comportement de la pente à long terme. Nous pouvons aussi proposer des mesures de réhabilitation futures (si nécessaire) pour la pente.

KEYWORDS: Slope stability, seismic events, weathering.

1 INTRODUCTION

The new road links the center of the village with a very famous medival castle. It pass through a mauntainous area and need a lot of structures such as retaining walls, culverts, small bridges etc. The last part of the roads pass in a very steep slope where a year after the construction ware seen local slope failures.

Figure 1. Photo of local slope failures

The road width is 6m with 0.5 shoulders and a longitudional concrete paved channel on the side of the mauntain. The road body is partly in filling and partly in cutting. The zone is one of the wetest zone in Albania with a average rainfall of 1750mm/year. Due to lack of budget during the construction phase for finishing all the engineering measures and maintanence problems during exploitation phase local slope slides have occured after a period of 3 years.

1.1 *Geological and geotechnical aspects*

The road to Drisht castle pass through a very disturbed tectonic zone. The study area takes part in subzone Cukali which, in the west and northwest is overthrust from the Albanian Alps zone , and in the southeast area is overthrust from Mirdita zone. Slope of the right side of the road represented by mainly constrained dark color old clays. Inside the clay mass can be meet compact sandstone layers bodies with dimensions up to 1 m in length, and up to 30 cm thickness and sandstone pieces measuring 5 to 10 cm with rounded shape and often alienated. These deposits are turbidits with a clayey - sandy cementation. They are too weak and are divided into small pieces. The above mention formation can be classified as very heterogonous flysch. Within the clay mass at the bottom of the slope (on the right side of the road) can be meet limestones olistolite size 5 to 10 meters above which are placed massive limestone rocks of Triassic geologic time.
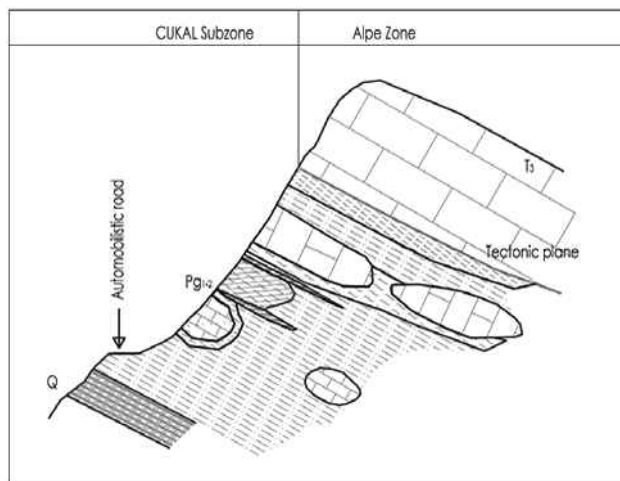
Figure 2. Schematic representation of the geological aspects of the slope

1.1.1 *Geotechnical parameters*

As given above we have identified two main type of terrain. The limestone rock formations with very good mechanical characteristics and flysch formations that are very weak rocks to soils.

These last rocks are described as rocks with relatively low strength and high deformability. They can be easily eroded by water, have a plastic behavior and poor stability on the slopes. Volume weight ranges from 2.2 - 2.6 g/cm^3, porosity up to 35%, elasticity module $2 * 10^3 - 10^4$ daN/cm^2, compression strength 5 - 25 daN/cm^2, intact rock cohesion 20 100 kPa, internal friction angle <15 °.

Based upon the lab test and empirical evaluation the main geotechnical parameters for unweathered formations used in the design are as follows

Table 1. Geotechnical main parameters

Layer	gs	c	F
Flysch/Clay	23	20-100	15
Limestone	26	400	45

2 MODELING OF THE SLOPE

2.1 *FE 2D model*

The slope stability analysis is made with finite element software Plaxis. The geometry and the layers are given in figure 3. For the calculation of sliding slopes should be distinguish the existing slides as well as those caused by changes in loading, reduction of parameters so first time slides. In finite element numerical calculations for the new slide slopes can not predefined a critical surface along its length the strength mobilized parameters progressively softened. The problem must pass in two stages, initially determining a critical sliding plan (if any) and then to give the soil strength mobilized parameters of this plan the residual parameters.

Through the first model we can determine the stability of the slope for a long time while the second model we can define the engineering measures (walls, piles, anchored wires, nails, etc.) and make the their design.
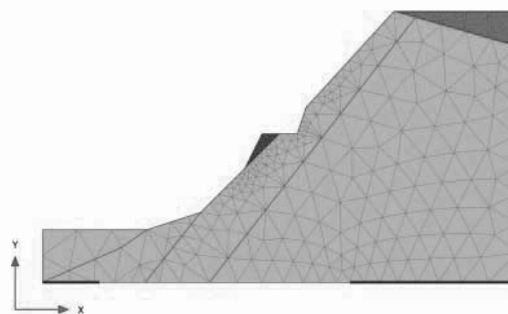

Figure 3. FE model of the slope

The soil is modeled as elasto-plastic material with yield criterion of Mohr-Coulomb. Advanced models with softening behavior would be more appropriate, but for lack of data (as well as the impossibility of accurate assessment of softening process) in our case can not be used. Weathering processes have been taken into account by dividing a surface layer in which the strength parameters gradually increase in depth until intact rock/soil values. In each analysis we took into account the initial natural stages as well as the following stages during the construction and the final stage during exploitation.

Influence of time, the accumulation of deformation, creep, brittle behavior that manifest same old overconsolidated clays, the formation of shear bands, influence of existing fissures, change of resistant parameters along the extent of the critical sliding surface, etc. in our model can not be taken in consideration. However, this modeling by taking the average parameters gives us practical results for the controls of the slope stability and dimensioning of retaining structures in the final limit state of the slope.

The fillings for road widening are reinforced with geogrids. Slope nailed wire mesh, anchors are simulated by applying a surface pressure perpendicular to the slope. The value of the pressure is taken such that the safety coefficient of the second model after application of this pressure to be 1.25. Plaxis program allows a sensivity analysis to see the influence of each parameter to the stability of the slope.

2.2 *Water influence*

The zone is one of the wetest zone in Albania with a average rainfall of 1750mm/year. It is well known that the rainfall precipitation degrade the soil properties due to progressive weathering. The weathered soil material has filled the longitudional channel blocking the dewatering. The water infiltrate through existing fissures reducing significantly the soil parameters. The flysch/old clay formation have been separated into two soil layers. Upper surface layer that has been weakened as a result of rain water infiltrations and bottom layer of the terrain representing the intact formation. We haven't used an underground water level and thus a seepage calculation because in this type of formation we can not speak for a real water level. The water influence is taken into account only between the reduction of surface layer parameters and increase of the thickness of this layer at the end of the excavated slope, toe of the slope. For the surface layer geotechnical parameters that are used are the residual parameters c_r, F_r.

2.3 *Seismic input*

One of the reasons of slope instabilities are seismic events. So for the long term stability in the seismic zones is necessary to do also slope seismic loads analysis. Seismic input can be considered from time history of acceleration. These time

histories can be produced artificially or taken from records. In every case the accelerograms must be compatible with the acceleration spectra required by the codes.

For seismological and geotechnical applications real accelerograms are preferred because they are more realistic for frequency content, number of cycles, correct correlation between the vertical and horizontal components of ground motion and for the energy content in relation to the seismogenic parameters. In our case the site is near the zone of a seismic source that can generate earthquakes so we need to consider also near fault influence. However, in order to use a real accelerogram in near-fault conditions it is required for the time histories to include directivity effects and fling step, in other words they should refer to real, near-field earthquakes. So just for comparing the results we have also generated an artificial accelerogram taking account the near source effects.

Considering that we have been interested for the design of slope retaining structures the chosen accelerogram according to EC8 spectra is multiply by $2*1.4/1.146\approx 2.45$ for being compatible with PGA taken from PSH analysis for $T_R\approx 475$ years. The ground motion parameters are given below:
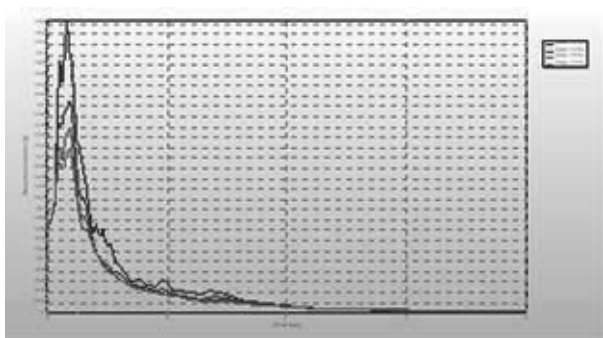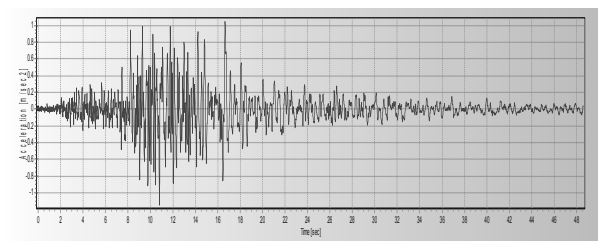

Figure 4. Acceleration response spectras

Figure 5. Time history of acceleration

PGA : 1.146m/sec2 in t=10.790sec
PGV : 0.082m/sec   in t=16.590sec
PGD: 0.020m   in t=47.880sec
Vmax / Amax: 0.071sec. Predominant Period (Tp): 0.300sec

2.4   *Results*

From the analysis is seen that local instabilities occur before global instabilities. To overcome this problem the filling reinforcement with geogrids have been activated from the first stage of excavation before defining the critical sliding surface. In figure 6 are given the displacement of the road body fillings.
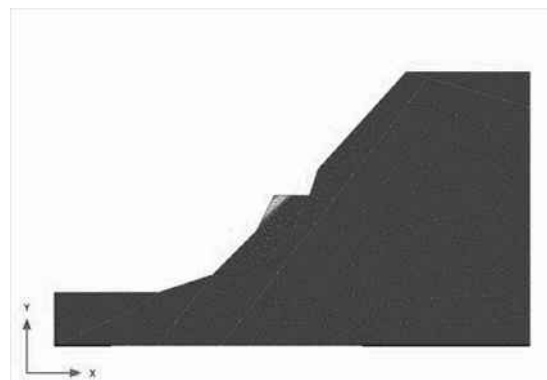

Figure 6. Local displacement

After that stage of local stabilization is done the global stability analysis. From analysis of the displacement and displacement incrementations we receive critical sliding surface shape and position as shown in Figure 7.
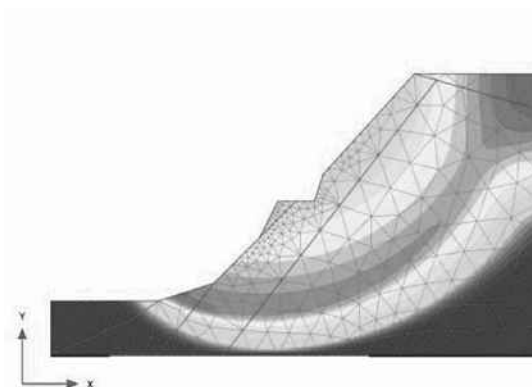

Figure 7. Total displacement

To simulate the critical sliding surface the "interface" element is activated with residual mechanical characteristics, c_r=5kPa, $F_r = 10^o$

Since in site are not observed existing deep slides that affect the global stability of the slope conditioning the preexisting sliding surfaces the value of cohesion is not taken zero, thus improving also the numerical calculations The displacement rate effect on residual strength parameters especially for seismic loading aren't taken in consideration.

In the case of application of a seismic load the safety coefficient for the second model decrease and wire anchored mesh of the slope should be strengthened, although for this case the coefficient of security can be taken close to 1. By sensitivity analysis of the parameters the cohesion changes are within small limits and their small changes doesn't affect the stability of the slope. The friction angle changes from peak values in those residual gives the greatest impact. These assessments we think correspond with the real monitored cases referred in literature. Since in the site is not implemented the wire anchored mesh the monitoring of weathering processes of slope materials in the future will give us the opportunity to correct resistance parameters values taken in the first analysis and reanalyze the slope stability.

3   CONCLUSIONS

Although the lack of data and the inability of finite element software with elasto-plastic modeling with Mohr-Coulomb yield criteria or softening criteria, to take into account the

numerous elements that affect the stability of slopes in soft rock / old clay the simulation of processes by means of two modeling even in the case of application of simple models of yield criteria gives practical good results for first time slides ultimate stage or when we have a reactivation of an existing surface of non-brutal slide. This modeling does not provide intermediate data for the developed process, giving the possibility to correct in time the analysis parameters, and provide in time appropriate engineering measures. In any case when it will be used it will be referred only to the final phase with residual parameters.

4   ACKNOWLEDGEMENTS

5   REFERENCES

A.Anagnostopoulos 2011. The stability of natural cut slopes in stiff clays. Symposium of Landslide and Geoenvironment. Tirana,

A.Federico and A.Murianni 2011, Empirical approaches to temporal prediction of slope failure. Symposium of Landslide and Geoenvironment. Tirana,

Plaxis Reference Manual

Landslides induced by the interaction of an earthquake and subsequent rainfall. A spatial and temporal model

Glissements de terrain induits par l'interaction d'un tremblement de terre suivi de précipitations. Un modèle spatio-temporel

Quan Luna B., Vangelsten B.V., Liu Z.Q., Eidsvig U., Nadim F.
Norwegian Geotechnical Institute (NGI) / International Centre for Geohazards (ICG), Norway

ABSTRACT: The consideration of multiple hazards and their interaction to achieve risk reduction is a necessity since many regions are prone to different types of threats. However, this is neither simple and straightforward nor commonly undertaken at present since different natural hazards are usually analyzed individually and managed separately. A common example of this is the alteration of the density and locations of rainfall-induced landslides after an earthquake due to the extensive disturbance of surface strata. That implies an influence of the earthquake on the soil structure that alters the disposition towards landslides. Taking this into consideration, a model was developed that could give a rough spatial and temporal prediction of expected change in landslide hazard in an area following an earthquake. The model is able to describe the reduced impact of earthquakes with distance from epicentre as well as how the soil gradually regains its strength with time. These reductions are then applied to an equilibrium stability analysis in order to compute new Factors of Safety. Although analysis schemes can be proposed and software tools can be provided to facilitate many steps, a well-conceived and reflective approach to multi-hazard settings is still essential.

RÉSUMÉ : Etant donné que différentes régions sont sujettes à différent types de menace, l'étude de multiples facteurs de risque et de leur interaction est nécessaire afin de réduire le risque. Ce genre d'études est néanmoins rarement entrepris de nos jours puisque chaque risque naturel est usuellement analysé et traité séparément. Un exemple courant est l'évolution de la densité et de la localisation des glissements de terrain induits par des précipitations suite à un tremblement de terre en raison de l'importante perturbation des couches superficielles. Cela implique que l'influence des tremblements de terre sur la structure du sous-sol modifie la prédisposition aux glissements de terrain. Compte de tenu de cela, un modèle de prédiction spatio-temporelle de la variation du risque de glissement de terrain dans une région donnée suite à un tremblement de terre a été développé. Le modèle est capable de décrire la diminution de l'impact des tremblements de terre en fonction de la distance à l'épicentre ainsi que la manière dont le sous-sol retrouve sa résistance initiale. Ces diminutions sont ensuite appliquées à une analyse de stabilité de façon à calculer de nouveaux facteurs de sécurité. Bien que des programmes d'analyses puissent être proposés et que des logiciels peuvent être fournis afin de faciliter de nombreuses étapes, une approche réfléchie et bien conçue des environnements à dangers multiples reste indispensable.

1 INTRODUCTION

A multi-hazard analysis refers to the implementation of methodologies and approaches aimed at assessing and mapping the potential occurrence of different types of natural hazards in a given area. Analytical methods and mapping have to take into account the characteristics of the single hazardous events as well as their mutual interactions and interrelations (Delmonaco et al. 2006). The existence of relations between natural hazards and the potentially resulting consequences is an issue of increasing importance in multi-hazard studies (Kappes et al. 2010). The specific methods to deal with related hazards are as diverse as the terms and the phenomena falling into this category. However, a general approach can be applied where the investigation of the individual chain of one hazard triggering the next is performed (so-called cascading events).

Evidently, performing multi-hazard risk analysis is not a simple operation. Apart from the data requirements and time-consuming conduction of single-hazard risk studies that require know-how from different disciplines, many further aspects have to be considered. One important source of difficulty is the contrast in hazard characteristics. Hazards differ with respect to their properties such as time of onset, duration, physical properties and extent. As a result, the modelling approaches adjusted to the hazard specifics also contrast strongly (Bovolo et al 2009).

2 MODEL DESCRIPTION

The proposed model aims to compute and estimate the associated alteration in the landslide hazard following an earthquake event. The model describes the reduced impact of earthquakes with distance from epicentre as well as how the soil gradually regains its strength with time. This was achieved by analyzing the collected data on how seismic activity influences the critical rainfall intensity and duration needed to trigger landslides in the area impacted by the earthquake. Based on the gathered information the modelling objective was met by constructing three sub-models: A) Use empirical data to construct a sub-model linking rainfall threshold reduction as function of time after earthquake impact; B) Use empirical data to construct a sub-model linking rainfall threshold reduction as function of distance from epicentre and earthquake magnitude, C) Use an analytical hydrological model to link rainfall threshold reduction to changes in soil shear strength.

Sub-models A and B together form an empirical model for rainfall threshold reduction as a function of magnitude, distance and time after the earthquake. The model is based on the following assumptions:

- The effect of earthquake on the rainfall threshold reduction decays with distance from and time after the earthquake.
- The maximum rainfall threshold reduction (i.e. rainfall threshold reduction immediately after and at epicenter) is assumed to be a function of earthquake magnitude only.

- The temporal and spatial effects are independent and thus the spatial and temporal variations are treated separately in two different functions and multiplied to find the actual rainfall threshold reduction.
- The earthquake effect is included into the spatial model. The temporal model is a normalized model representing the remaining threshold reduction as a function of time after the earthquake.

According to the assumptions above, the threshold reduction for a given point in time and space is a product of the spatial model and the temporal model (Eq. 1):

$$\text{Threshold reduction } (X, T, M) = f_{spatial}(X, M) \cdot f_t(T) \qquad \text{Eq.(1)}$$

In this model, X is the distance to the epicenter, T is the time after the earthquake and M is the earthquake magnitude. The purpose of the model is to relate the post-earthquake rainfall threshold to the pre-earthquake threshold using the derived threshold reduction function (Eq. 2):

$$\text{Post-earthquake threshold} = (1 - \text{Threshold reduction}(X, T, M)) \cdot \text{Pre-earthquake threshold} \qquad \text{Eq.(2)}$$

The rainfall threshold changes referred to in the model is the numerical value of the mean rainfall intensity for a duration of one hour, i.e. α in Eq. 3 below:

$$I = \alpha D^\beta \qquad \text{Eq.(3)}$$

In this equation, I is the mean rainfall threshold intensity, D is the rainfall duration in hours and β is the slope of the threshold curve in log-log space.

2.1 *Rainfall threshold reduction as function of time*

Shou et al. (2011) modelled the effect of earthquake on the rainfall threshold reduction by an exponentially decaying function with time. The model parameter could be transferred to cumulative precipitation by using the annual mean precipitation. In the proposed model, the variations caused by other relevant parameters, such as slope angle and actual precipitation, are not treated explicitly; but model uncertainty is added to account for such variations. Shou et al. (2011) provided some data on the temporal effect of the Chi-Chi earthquake. No such data exist for the Wenchuan earthquake. From the available data it appears that the temporal behavior is site-dependent. However, Shou et al. (2011) used a model representing the average of three sites in Taiwan. Model uncertainty was introduced by two curves representing uncertainty bands. The uncertainty bands represent deviations of ±50% from the average curve in a semi-log coordinate system.

Figure 1 shows the variation of the normalized rainfall threshold reduction with time for three different locations in Taiwan together with the average curve and uncertainty bands. The figure illustrates the long-term effects after the Chi-chi earthquake.
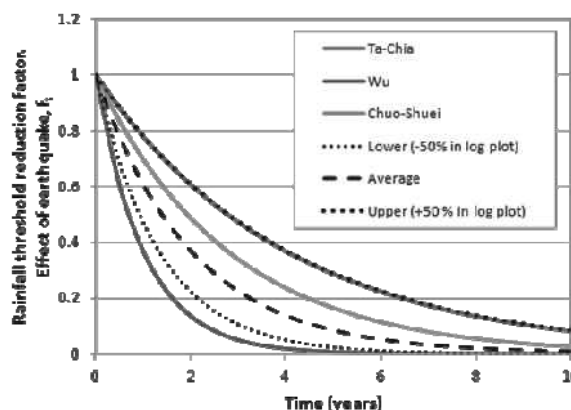

Fig. 1 Remaining rainfall threshold reduction (i.e. rainfall threshold reduction factor) as a function of time for three locations in Taiwan (colored curves) as well as an average curve and curves representing model uncertainty (black curves).

2.2 *Rainfall threshold reduction as function of distance and earthquake magnitude*

The rainfall threshold reduction as a function of earthquake magnitude and distance from the epicenter is based on the following relations and assumptions:

- For the spatial variation, the effect of earthquake on the rainfall threshold reduction is assumed to decay exponentially with distance from the epicenter/fault. This assumption is based on observations after the Chi-Chi earthquake by Khazai & Sitar (2003).
- The maximum "influence radius" of an earthquake is a function of the magnitude. The function described by Keefer (1984) is applied. This function describes the maximum distance from epicenter for seismically induced landslides as a function of earthquake magnitude. It was further assumed that at for a distance equal to the influence distance of the earthquake, the rainfall threshold reduction was 1/100 of the rainfall threshold reduction at distance 0.
- The model for maximum rainfall threshold reduction as a function of magnitude is assumed to increase with increasing magnitude.

Based on the above mentioned relations, a conceptual model for rainfall threshold reduction as a function of earthquake magnitude and distance from epicenter may be established as illustrated in Figure 2.
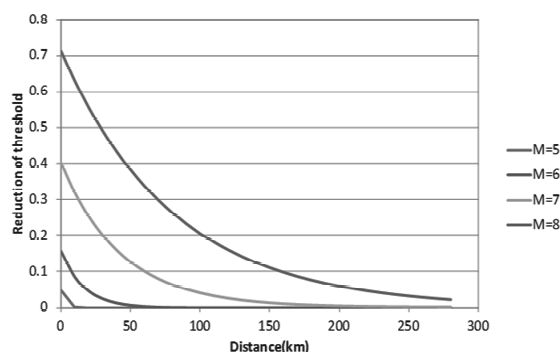

Fig. 2 Reduction of rainfall threshold caused by earthquake as a function of magnitude and distance

2.3 *Linking rainfall threshold reduction and reduction of soil shear strength*

Post-earthquake soil strengths may be lower than pre-earthquake (static) strengths for zones that are susceptible to

strength loss. As time passes, the progression of soil self-healing will result in increased shear strength compared to shortly after the earthquake. Temporal changes of soil properties are known to have an effect on the rainfall thresholds required to trigger landslides (Tang et al. 2009). Due to the decreased soil strength, landslide-triggering rainfall thresholds decrease compared with their pre-earthquake values (Lin et al. 2004).

A proposed methodology is presented for estimating temporal changes in soil strength related to landslide-triggering rainfall thresholds after an earthquake over a wide area (a few square kilometers). This methodology is based on response analysis with a deterministic, spatially distributed model that combines a 1-D transient infiltration model with a safety-factor analysis for calculating rainfall threshold.

After an earthquake, an abundance of loose landslide debris can be present on the hillslopes. The potential failure surface typically lies at or near the contact between the relatively permeable colluvium and the relatively impermeable underlying bedrock. The thickness of the soil cover is small compared with the length of slope, thus the infinite slope stability model can be performed to evaluate slope stability. Limit equilibrium conditions are reached at a certain depth when the mobilized shear stress (a function of soil unit weight, failure surface depth and slope angle) equals the soil shear strength, given by the Mohr-Coulomb failure criterion (Eq. 4):

$$\frac{\tan \phi'}{\tan \alpha} + \frac{c' - \gamma_w \psi \tan \phi'}{\gamma_s d_b \sin \alpha \cos \alpha} = 1 \qquad \text{Eq.(4)}$$

where c' and φ are the effective cohesion and friction angle of the soil, d_b is the depth of the failure surface, α is the slope angle, γ_s is the soil unit weight γ_w, is the specific weight of water, and ψ is the pressure head at the failure surface.

The limiting value of the pressure head which leads a slope with given geometrical characteristics and soil properties to limit equilibrium conditions can be calculated from Equation 5 as:

$$\psi_{\lim} = \frac{c'}{\gamma_w \tan \phi'} + \frac{\gamma_s}{\gamma_w} d_b \cos^2 \alpha \left(1 - \frac{\tan \alpha}{\tan \phi'}\right) \qquad \text{Eq.(5)}$$

For a saturated soil cover, the evolution of the pressure head with time and depth inside the slope is governed by the following one-dimensional conservation equation (Eq. 6) (Iverson 2000):

$$\frac{\partial \psi}{\partial t} = D \frac{\partial^2 \psi}{\partial Z^2} \qquad \text{Eq.(6)}$$

where Z is the depth of the point considered with respect to an horizontal reference plane; $D = D_0/\cos^2 \alpha$ and D_0 is the hydraulic diffusivity of the soil.

Two factors, fs and fi, which are respectively reduction factors of soil shear strength and critical rainfall intensity, are now introduced. It is assumed that the effective cohesion and tangent of effective internal friction angle have the same reduction factor fs. The reduction factor of critical rainfall intensity is calculated by dividing the reduced rainfall intensity $I_{reducrit}$ due to soil shear strength reduction by the original critical rainfall intensity I_{critic} (Eq. 7):

$$f_I = \frac{I_{Reducrit}}{I_{crit}} \qquad \text{Eq.(7)}$$

For sandy soil, where the cohesion is zero, i.e. c = 0, an approximation solution is given by Eq. 8:

$$f_I = \frac{\dfrac{\gamma_s}{\gamma_w} d_b \left(1 - \dfrac{\tan \alpha}{f_S \tan \phi'}\right) - (d_b - d_w)}{\dfrac{\gamma_s}{\gamma_w} d_b \left(1 - \dfrac{\tan \alpha}{\tan \phi'}\right) - (d_b - d_w)} \qquad \text{Eq.(8)}$$

3 RESULTS

3.1 *Study area: MATRIX virtual region*

The case presented below is used to demonstrate the capabilities of the model in terms of hazard assessment. It is not a validation of the performance of the model. The case partly makes use of artificial data (including the digital elevation model) and partly typical engineering values (as for the soil parameters and rainfall intensity). A digital elevation model (DEM) has been developed for demonstration of the landslide hazard model (Fig. 3)
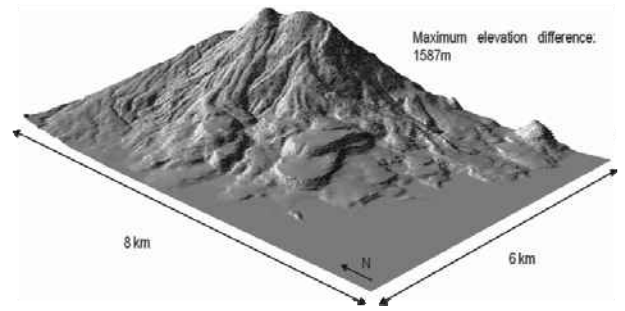

Fig. 3   3D representation of digital elevation model (DEM) for the case study region.

3.2 *Reduction factor for critical rainfall intensity*

Figure 4 shows the results of the reduction factor inside the virtual region for a sandy soil where the earthquake event has a magnitude of 6.98 with a fault length of 3.08 km. The time span after the earthquake is assumed to be 45 days.
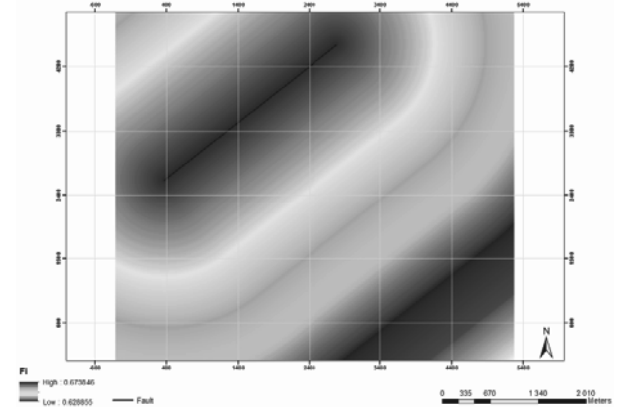

Fig. 4 Rainfall threshold reduction factor *(fi)* as a function of time, magnitude and distance to the fault.

The temporal model represents the remaining threshold reduction as a function of time after the earthquake. The remaining threshold reduction is represented by a normalized function with values between 0 and 1. Value 1 corresponds to the maximum rainfall threshold reduction (i.e. the rainfall threshold reduction immediately after the earthquake) and value 0 corresponds to no remaining rainfall threshold reduction (i.e. after long time, when the occurrence of the earthquake has no effect on the rainfall threshold.) The effect from the earthquake on the rainfall threshold reduction is included in the spatial model.

3.3 *Reduction factor of the soil shear strength*

A quantitative assessment of the relationships between different factors (i.e. slope angle, failure depth and water table depth) and reduction factor of soil shear strength due to earthquake was performed. Figure 5 shows the areal distribution of the reduction factor of the soil shear strength considering a rainfall intensity of 120 mm a day. The bedrock is assumed to be much less permeable than the soil cover. Soil depth varies from 4 to 7 m depending on the type of soil and topographic characteristics inside the virtual region.
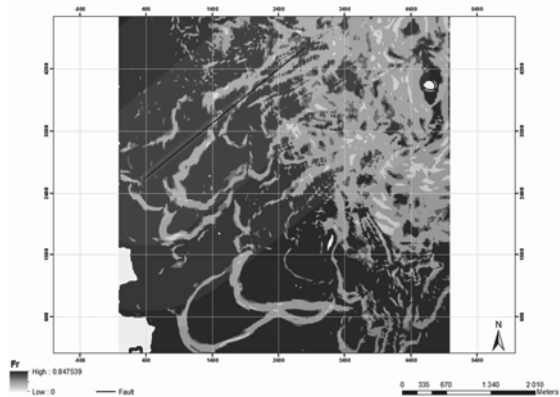
Fig. 5 Spatial distribution of the soil shear strength reduction factor *(fr)*.

3.4 *Slope stability assessment including the reduction factors*

A two dimensional equilibrium stability analysis based on the infinite slope model was carried out in order to compute the new factors of safety that included the reduction factors. The mean values of the logarithmic distributions functions of the input parameters were applied in the analyses. A constant porosity of 42% and an evapotranspiration of 5 mm/day were selected throughout the area. Five different friction angles were used for the different soil types: 30, 32, 34, 36, 38°. Figure 6 shows the results of the stability analysis considering the reduction of the soil strength after an earthquake.
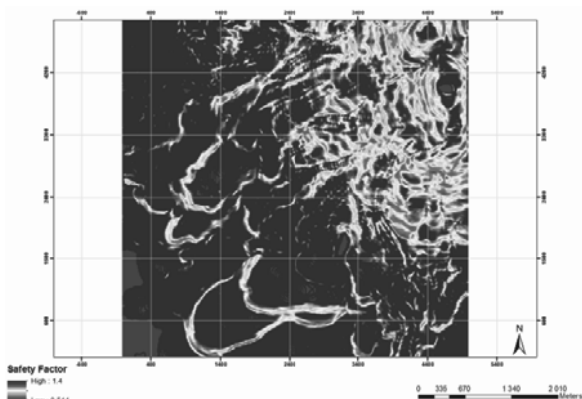

Fig. 6 Stability analysis considering the loss of strength of soil due to the perturbations caused by a magnitude 6.98 earthquake.

4 CONCLUSIONS

A natural system is not just the sum of its components but is the result of many interacting parts. Hence, a multi-hazard assessment should address evolving characteristics in space and time. These characteristics can, for analysis purposes, be analyzed as the alteration of the susceptibility and the triggering mechanism. A multi-hazard assessment offers the advantage to consider a slightly larger part of the overall system. The major challenge is to identify the relationships among the interacting factors and establish the respective links.

For this reason, a model that includes the reduction of the soil strength parameters induced by the strong motion of an earthquake was developed and implemented. A virtual case study was performed to assess the behavior of the model and its parameters. This was achieved by calculating two reduction factors that represented the reduction of rainfall threshold in space and time, and the reduction of the soil strength due to prevailing conditions.

There are still some limitations regarding the model and further validation needs to be done. A thorough calibration of the reduction factors should be done locally and the possibility of using real events that are well documented should be considered. However, despite its limitations, the model provides a practical approach to assess the prospective outcomes of future hazards and their interactions. Thus the model contributes to increasing the knowledge required for the protection of the people at risk and their assets.

5 ACKNOWLEDGEMENTS

6 REFERENCES

Bovolo, C. I., Abele, S. J., Bathurst, J. C., Caballero, D., Ciglan, M., Eftichidis, G., Simo, B. 2009. A distributed framework for multi-risk assessment of natural hazards used to model the e_ects of forest _re on hydrology and sediment yield. *Computers & Geosciences* 35(5): 924 - 945.

Delmonaco, G., Margottini, C., Spizzichino, D. 2006. ARMONIA methodology for multi-risk assessment and the harmonisation of different natural risk maps. *Deliverable 3.1.1, ARMONIA*

Iverson, R. M. 2000. Landslide triggering by rain infiltration. *Water Resources Research*, 36(7), 1897-1910.

Kappes, M., Keiler, M., Glade, T. 2010. From single- to multi-hazard risk analyses: a concept addressing emerging challenges. In Malet, J.-P., Glade, T. & Casagli, N. (Eds.), *Mountain Risks: Bringing Science to Society*. Proceedings of the International Conference, Florence. CERG Editions, Strasbourg, 351-356.

Keefer, D. K. 1984. Landslides caused by earthquakes. *Geological Society of America Bulletin*, v 95, pp. 406 – 421.

Khazai, B., Sitar, N. 2003. Evaluation of factors controlling earthquake-induced landslides caused by Chi-Chi earthquake and comparison with the Northridge and Loma Prieta events. *Engineering Geology*, 71, pp. 79 - 95.

Lin, C.W., Shieh, C. L., Yuan, B. D., Shieh, Y. C., Liu, S. H., and Lee, S. Y. 2004. Impact of Chi-Chi earthquake on the occurrence of landslides and debris flows: example from the Chenyulan River watershed, Nantou, Taiwan. *Engineering Geology*, 71, 49-61

Shou, K. J., Hong, C.Y., Wu, C.C., Hsu, H. Y., Fei, L. Y., Lee, J. F., Wei, C. Y. 2011. Spatial and temporal analysis of landslides in Central Taiwan after 1999 Chi-Chi earthquake. *Engineering Geology,* 123, pp. 122 – 128.

Tang, C., Zhu, J., Li, W. L. 2009. Rainfall-triggered debris flows following the Wenchuan earthquake. *Bulletin of Engineering Geology and the Environment,* 68, 187-194.

Analyse des glissements de terrains en région urbanisée

Analysis of landslides in urban regions

Rahhal M.E.
Université Saint Joseph, Beyrouth, Liban

Hajal M.
Université Libanaise, Beyrouth, Liban

Seoud J.P.
GSC Consultants, Beyrouth, Liban

Rafie E.
STS Consultants, Beyrouth, Liban

RÉSUMÉ: Des glissements de terrains importants ont eu lieu au pays du cèdre. La topographie montagneuse du Liban, la présence des aquifères et les fouilles réalisées pour les travaux de construction sont à l'origine du risque élevé de glissements de terrains. Un objectif principal visé par cette étude est de comprendre les facteurs causant ces instabilités. Deux études de cas bien documentés sont analysées. Les glissements ont lieu dans des formations argileuses à l'interface au-dessus de formations plus rigides composées de marne argileuse ou de roche calcaire. On observe aussi les glissements dans des alternances de banc calcaire fracturé et couche d'argile intercalée. Des conclusions intéressantes sur le comportement des sols à la rupture sont avancées. Les résultats escomptés devront compléter une cartographie éventuelle des cas de glissement à travers le Liban.

ABSTRACT: Important landslides took place in the land of cedar. Lebanon's mountainous topography, the presence of aquifers and excavations for construction are at the origin of the high risk of landslides. A main objective of this study is to understand the factors causing these instabilities. Two well-documented case studies are analyzed. Landslides occur in clay formations at the interface over more rigid formations composed of clayey marl or limestone. There are also landslides in alternating fractured limestone bench and intercalated clay layer. Interesting conclusions on the behavior of soil at failure are proposed. The expected results should help in achieving a possible landslide cases mapping throughout Lebanon.

KEYWORDS: landslide, marly clay, shale

MOTS-CLÉS: glissement de terrains, argile marneuse, schiste argileux

1 INTRODUCTION

Le Liban a connu ces dernières années des hivers avec des pluies particulièrement abondantes. Ces intempéries sont à l'origine de plusieurs cas d'instabilité des terrains surtout en régions montagneuses parfois très proches du littoral densément habité. La densité moyenne de la population libanaise est de 450 habitants par km^2, ce chiffre étant beaucoup plus élevé sur la côte méditerranéenne et diminuant en altitude. L'urbanisation couvre donc aujourd'hui une grande superficie du pays du cèdre. En janvier 2013, la tempête qui a frappé le pays a laissé des dégâts énormes avec des glissements menaçant des habitations dans plusieurs régions. Mais l'activité humaine due à l'urbanisation se manifestant par les fouilles réalisées pour les travaux de construction vient aussi se conjuguer aux facteurs naturels déclenchant les glissements.

La répartition spatiale des mouvements relève de la topographie et de la géologie (Carrara et al. 1995). Leur occurrence est très marquée par les variations climatiques mais peut aussi être liée à des secousses sismiques ou encore être induite par les activités humaines. Le glissement est défini par le déplacement de terrains meubles ou rocheux et peut être identifié par un état d'activité (Cruden et Couture 2011). Selon la géométrie de la surface de rupture, deux types principaux de glissements sont distingués: d'abord, le glissement plan où la ligne de rupture suit généralement une couche mince ayant de mauvaises caractéristiques mécaniques et sur laquelle s'exerce souvent l'action de l'eau (couche savon). Ensuite, le glissement plutôt rotationnel où la surface de glissement est plus ou moins circulaire; ce mouvement étant caractérisé par l'existence d'une zone de départ (Abramson et al. 2002). Le passage de l'état de stabilité à l'état d'instabilité (Dikau et al. 1996) relève de causes nombreuses: externes (l'érosion, les séismes, les surcharges d'un ouvrage); et internes (l'augmentation de la pression interstitielle, l'altération d'une roche). Souvent aussi, les causes sont conjuguées. Les matériaux affectés sont très variés (Fletcher et al. 2002), mais globalement la présence d'argile en forte proportion est toujours un élément défavorable. Au Liban, le rôle de l'eau est reconnu comme le facteur déclenchant des glissements en l'absence du facteur tectonique. Il y a aussi les excavations réalisées qui deviennent un facteur déstabilisant. Beaucoup de techniques ont été développées afin de minimiser l'impact des glissements de terrains (Popescu 2002). Une analyse des facteurs causant les instabilités de pentes au Liban a été réalisée (Rahhal et al. 2003). Un travail de cartographie des mouvements de terrains a aussi été entrepris (Rahhal et al. 2004). Enfin, des études probabilistes sont aussi conduites dans le but de comprendre la sensibilité des paramètres géotechniques dans l'évaluation de la stabilité des pentes. (Rahhal and Abou Rached 2005; Rahhal 2006; Benarroch et al. 2011).

Cet article présente une analyse étoffée de deux glissements, survenus au nord de Beyrouth dans deux régions densément peuplées. La compréhension du comportement des sols est une étape fondamentale lors de l'analyse d'un glissement de terrain.

2 CAS DU GLISSEMENT DE ESSFIRÉ

2.1 *Localisation et contexte*

Essfiré est une bourgade au nord du Liban, d'altitude moyenne 1100 mètres. Elle est située à 120 km de la ville de Beyrouth. En mars 1998, le sol à Essfiré a glissé, suite à la fonte de la neige accumulée. Ce glissement montré dans la Figure 1 sera l'objet de cette étude. La région a déjà connu dans son

histoire plusieurs glissements depuis les années soixante. La zone glissée a 70m de largeur, et 835m de longueur. Le profil de la pente a été tracé entre les cotes 960 et 1170 mètres. La pente à la cote 960m a un angle de 18°, elle commence à s'atténuer peu à peu, pour atteindre 12° au milieu du glissement, et arrive enfin à 10° au sommet, aux alentours de la cote 1170m.

Figure 1. Vue globale du glissement dans le centre de la bourgade Essfiré. Le mouvement entre les maisons est indiqué par la flèche.

2.2   Données géotechniques

Pour pouvoir identifier les différentes couches de sol constituant la région glissée, une analyse détaillée des forages réalisés s'avère être indispensable. Le profil du sol qui a glissé peut être représenté par 3 couches principales: une première couche en surface constituée d'une argile sableuse avec du gravier; une seconde couche en profondeur formée d'une argile marneuse; et enfin, une troisième couche constituant le substratum rocheux. Les propriétés géotechniques minimales et maximales des deux couches argileuses sont présentées dans le Tableau 1.

Tableau 1. Plage de valeurs pour les propriétés des couches d'argile sableuse et d'argile marneuse.

Propriété	Argile sableuse	Argile marneuse
Limite de liquidité (%)	30-52	21-67
Limite de plasticité (%)	12-24	7-35
Pourcentage de fines (%)	31-96	42-83
Pourcentage d'argile (%)	9-42	9-52

La couche superficielle du sol est formée principalement d'une argile sableuse d'épaisseur variable allant de 1 à 13m. Les essais de cisaillement direct réalisés permettent d'attribuer à cette couche d'argile sableuse les valeurs moyennes de cohésion et d'angle de frottement suivantes: $c = 20$ kN/m² et $\phi = 22°$. Par ailleurs sa perméabilité mesurée est $k= 8\times10^{-5}$ cm/s. En dessous de la couche d'argile sableuse, se trouve une couche d'argile marneuse d'épaisseur variant entre 1.5 m et 8 m. Les essais de cisaillement direct réalisés sur cette argile marneuse donnent les valeurs moyennes de cohésion et d'angle de frottement suivantes: $c = 46$ kN/m² et $\phi = 18.5°$. Une perméabilité représentative de cette couche d'argile marneuse est donnée par $k= 7\times10^{-6}$ cm/s. L'indice de plasticité de 22 % laisse supposer un taux et un potentiel de gonflement pour cette argile marneuse assez élevés. En cas de saturation de cette argile, elle pourrait gonfler considérablement, et sa cohésion risquerait de diminuer. Cette couche d'argile jouerait donc en cas de saturation, le rôle d'une couche savon. Sachant que pendant la période des forages, aucune nappe n'a été détectée, cela laisserait supposer que ces valeurs sont «à sec». Enfin, le substratum rocheux a été

trouvé à des profondeurs variant entre 5 m et 17m. Ce rocher est moyennement fracturé et fissuré, et ses fractures sont remplies d'argile. Sous l'effet des pluies et des infiltrations d'eau dans le sol, la saturation d'argile comblant les fissures entraînerait leur gonflement, ce qui exercerait une importante pression latérale dans le rocher, et augmenterait le risque de détachement du rocher de l'argile qui est en dessus.

2.3   Calcul et analyse de la stabilité

Une analyse du profil de sol obtenu laisserait présager les causes éventuelles qui ont déclenché le glissement. La couche d'argile marneuse, en cas de saturation pourrait très bien jouer le rôle de couche savon pour cette pente. Le glissement s'étant produit au mois de mars, la fonte des neiges a un rôle à jouer dans la saturation du sol. La nature gonflante de cette argile et son grand potentiel d'effondrement renforcent la théorie de la couche savon; ce qui nous laisse deviner une surface de rupture potentielle qui se trouverait au niveau de l'argile marneuse. Ceci valide l'existence d'un glissement plan dû à une couche saturée aux faibles propriétés mécaniques qui glisserait sur une discontinuité. Le problème serait donc à priori un problème d'eau. Ayant considéré la saturation de la couche d'argile marneuse comme étant la cause du glissement, il a été décidé de répartir le profil en 3 couches: une première couche d'argile sableuse (couche 1), une deuxième couche d'argile marneuse non saturée (couche 2) qui perd de ses propriétés mécaniques, et enfin une dernière couche qui représente le substratum rocheux (couche 3). L'analyse qui suit va considérer donc deux périodes, selon que la couche d'argile marneuse soit non saturée (période sèche) ou saturée (période humide), pour observer l'évolution du coefficient de sécurité entre ces deux périodes de l'année.

2.3.1   La période sèche

Cette période est la période d'été en principe, où il n'existe pas d'eau dans le sol. Pendant la période d'été, quand les forages ont été réalisés, l'argile marneuse n'a pas de partie saturée. Les propriétés mécaniques à considérer seront celles trouvées lors la réalisation des essais sur des échantillons tirés à partir des forages exécutés. La surface de rupture a été prédéfinie à l'avance. Ainsi durant la période sèche, les coefficients de sécurité obtenus suivant quatre méthodes de calcul (Fellenius, Bishop, Janbu, Morgenstern-Price) sont de l'ordre de 3.

2.3.2   La période humide

Cette période est normalement caractérisée par les mois d'hiver et du début du printemps, où les fortes pluies, et la fonte des neiges ont un effet sur l'approvisionnement du sol en eau, et la saturation de ses couches. Les propriétés mécaniques à observer pour l'argile marneuse saturée en profondeur sont: $\phi_u =0$, et une valeur réduite de la cohésion C_u sera considérée. La saturation de l'argile marneuse entraînant son gonflement et une diminution de ses propriétés cohésives, plusieurs itérations seront effectuées sur cette valeur en la diminuant constamment, afin de trouver la valeur critique de la cohésion qui entraînerait la rupture, et la chute du versant. La surface de rupture a été prédéfinie à l'avance, comme étant parallèle à la discontinuité entre le rocher et le sol. Une variation en diminution de la cohésion donne les valeurs de coefficients de sécurité montrés dans le Figure 2. Les cohésions qui induisent la rupture pour les différentes méthodes de calcul varient entre 23 et 29 kPa. Le coefficient de sécurité diminue presque linéairement avec la cohésion tel que montré dans la Figure 2. D'autre part, en considérant une cohésion de 26 kPa pour l'argile marneuse saturée, l'équilibre des forces pour une même tranche a été analysé, et l'évolution des forces sur cette tranche entre période sèche et période humide a été calculée. L'analyse des résultats montre une diminution moyenne de 33 % de la résistance au cisaillement à l'interface roche/sol dans les conditions humides.
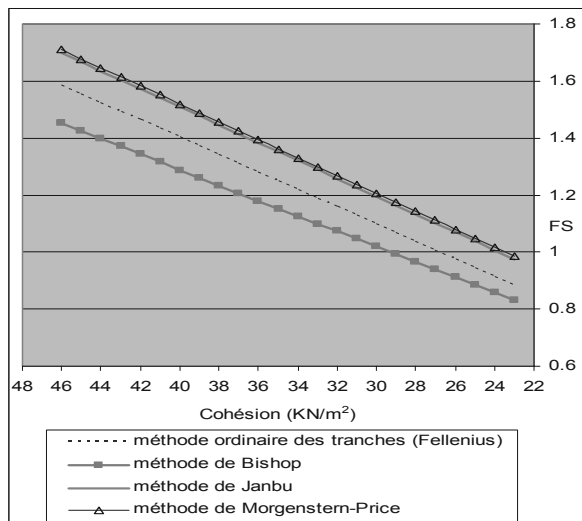
Figure 2. Evolution du coefficient de sécurité en fonction de la cohésion en période humide pour différentes méthodes de calcul.

3   CAS DU GLISSEMENT DE ANTELIAS

3.1   *Localisation et contexte*

Le deuxième glissement de terrain analysé est survenu en Avril et Mai 2006 à Antélias, une ville sur le littoral au nord de Beyrouth, emportant une partie de la route Faouar Antélias-Raboueh (Figure 3 et Figure 4). La synthèse des levées géologiques, des sondages de reconnaissance et des constatations sur le site, permet de schématiser le site comme suit. Dans la partie supérieure du glissement (cote 130m) et le sommet de la fouille Mission La Vie (cote 95m), la surface du sol a une pente de 15° dans la direction Ouest-25°-Sud. Dans sa partie inférieure, la surface se poursuit avec une pente 15° dans la direction Ouest-45°-Sud pour arriver sur un plat artificiel ayant servi d'aire de stockage de déchets à la cote 86m. Dans la zone de glissement, le pendage ne peut être mesuré en surface car le rocher n'y affleure pas, mais des sondages indiquent que le toit du rocher a un pendage de 14° dans la direction Nord-78°-Ouest. Les relevés piézométriques montrent que la zone de glissement est imbibée d'eau; Elle est alimentée par un aquifère et par les égouts défaillants le long de la route.

Figure 3. Route Faouar Antélias-Raboueh coupée par le glissement.

Figure 4. Le glissement de Antélias vers la fouille Mission la Vie. L'ouverture de la fouille serait un facteur déclenchant

3.2   *Données géotechniques*

Dans la zone de glissement, on rencontre de haut en bas 3 couches, à savoir: D'abord, à la surface, une couche d'éboulis et de dépôts quaternaires alluviaux formée de silts argilo-sableux et caillouteux. Cette couche s'étend jusqu'à la surface et a une épaisseur moyenne de 7m. Ensuite, une couche d'argile silteuse fortement surconsolidée (schiste argileux ou shale), de couleur brun chocolat. Son épaisseur est variable entre 0,5 et 4m avec une moyenne de 1,5m. L'épaisseur semble croître en allant vers le Nord. Enfin, le substratum rocheux calcaire, altéré et fissuré. Cette roche est relativement perméable (10 à 20 lugeons) et sert de drain aux argiles qui la surmontent En termes de caractéristiques mécaniques, la couche de surface a un angle de frottement ϕ=25° et une cohésion c= 20 kPa. Cette couche n'intéresse pas le glissement. La deuxième couche (schiste argileux) est responsable du glissement. En effet, dans leur état naturel ces schistes argileux sont très résistants, avec une cohésion de plusieurs centaines de kN/m². Cependant, mis en contact prolongé avec l'eau, ils sont fortement absorbants et leurs propriétés mécaniques se dégradent fortement, jusqu'à provoquer un glissement à leur surface. Deux échantillons de ce schiste argileux ont été testés (essais CU) pour en déduire un angle de frottement ϕ_{cu} et une cohésion C_{cu}. Les résultats sont les suivants: Essai 1 (Ic = indice de consistance= 0,803; ϕ_{cu} = 15° ; C_{cu} = 44 kPa); Essai 2 (Ic = indice de consistance = 0,725; ϕ_{cu} = 17° ; C_{cu} = 46 kPa). Les caractéristiques ci-dessus ne représentent pas en réalité les caractéristiques des schistes argileux lors du glissement et ce, pour deux raisons, à savoir: Premièrement, ϕ_{cu} et C_{cu} représentent les caractéristiques mesurées à court terme; or quand les sols argileux sont soumis à des contraintes de cisaillement pendant un temps assez long, les particules le long de la ligne de glissement potentielle se réorientent progressivement (fluage); il en résulte un affaiblissement des caractéristiques du sol le long de cette ligne et elles tendent vers les "caractéristiques résiduelles" en grande déformation. Ces dernières sont estimées, aux deux tiers des caractéristiques mesurées (IP=17%), soit: ϕ_{rcu}= 2/3 ϕ_{cu} et C_{rcu} = 2/3 C_{cu}. Deuxièmement, si en plus de l'affaiblissement dû au fluage, on permet au schiste argileux fortement absorbant de se saturer d'eau et de gonfler (gonflement 5,6 et 7,8%), il s'affaiblit encore plus pour tendre vers des caractéristiques minimales ϕ_{mcu} et C_{mcu} qui sont essentiellement fonction de l'indice de consistance Ic. Cependant, en surface de la couche de schiste argileux, directement en contact avec l'eau, l'indice de consistance Ic peut atteindre 0,5 formant ainsi une pellicule de quelques centimètres extrêmement affaiblie (couche savon). En appliquant les deux réductions (caractéristiques résiduelles et

caractéristiques minimales) aux deux échantillons, pour obtenir les caractéristiques des schistes argileux le long de la ligne de glissement, nous obtenons: pour l'essai 1 (ϕ_{mcu} = 10° et C_{mcu} = 2,8 kPa) et pour l'essai 2 (ϕ_{mcu} = 11° et C_{mcu} = 4,8 kPa).

Pour une couverture de 7m de sol, de densité 2, la résistance au cisaillement au toit de la couche de schiste argileux (shale) serait de 26,3 à 30,7 kPa. Ces valeurs se recoupent assez bien avec celles dans la littérature pour des argiles raides et shales à long terme, soit une résistance au cisaillement de 20 à 40 kPa.

3.3 *Calcul et analyse de la stabilité*

Une estimation des forces dues à la pression de l'eau dans les fissures montre que celles-ci sont très faibles comparées aux forces actives de gravité qui provoquent le glissement et aux forces passives de cohésion qui le freinent (de l'ordre de 4 à 5%). Ces faibles forces de pression d'eau n'ont d'importance pour le glissement que si les forces actives de gravité et les forces passives de cohésion s'équilibrent à peu de chose près, c'est-à-dire si les forces actives de gravité seules sont très légèrement inférieures aux forces passives de cohésion (période sèche stable) mais en y ajoutant les forces actives de poussée d'eau, elles deviennent légèrement supérieures aux forces de cohésion (fortes précipitations).

Le glissement plan se fait sur le toit des shales, qui dans la direction du glissement (Ouest 13° Sud) faisant un angle de 25° avec la ligne de plus grande pente, a une pente de 12°7. En effet, il ne peut se faire dans les couches de surface (éboulis et dépôts quaternaires) car l'angle de frottement ϕ = 20° est supérieur a la pente 12°7 et il ne peut se faire dans la masse des shales ou au contact shale-rocher car dans ces zones, le schiste argileux a un indice de consistance supérieur à 0,725 donc des caractéristiques résiduelles $\phi_{cu} \geq 10°$ et $C_{cu} \geq 29,3$ kPa entraînant une résistance au glissement supérieure aux forces actives de gravité. Sur le toit des schistes argileux (couche savon), les contraintes de cisaillement dues au poids des sols de surface, sur un élément de pente 12°7, sont en moyenne de 30 kPa.

Pour équilibrer ces forces actives, le toit des schistes argileux devrait avoir en moyenne une résistance au cisaillement de 30 kPa, or les schistes argileux mis en présence d'eau de façon prolongée, atteignent leur état minimal, c'est-à-dire une résistance au cisaillement de 26,3 à 30,7 kPa. Ce calcul montre que les forces actives et passives s'équilibrent sensiblement (le coefficient de sécurité étant très voisin de 1) et que le glissement peut se produire. Si aux forces actives nous ajoutons les faibles forces dues aux pressions d'eau dans les fissures, il devient alors très probable que le glissement s'active comme il a été constaté après de fortes précipitations. En admettant une résistance moyenne au cisaillement égale 28,5 kPa, les coefficients de sécurité sont: Absence de précipitations, F = 28,5/30=0,95; incertitude sur le glissement. Fortes précipitations: poussées de l'eau= 1,8 kPa par mètre carré de glissement: F =28,5/31,8=0,9 ; le glissement est presque certain. Le bilan des forces, présenté ci-dessus, néglige les forces de butée au pied du glissement comme cela est effectivement le cas après ouverture de la fouille Mission La Vie.

La question qui se pose naturellement est de savoir si l'ouverture de la fouille a contribué au glissement, sachant que le sol avait été très affaibli par les écoulements d'eaux usées. Pour y répondre nous avons évalué les forces de butée au pied du glissement, avant ouverture de la fouille. Pour une fouille de 7m de hauteur en moyenne et 30m de long environ, la force de butée est de 50000 kN, soit une contrainte moyenne tangentielle sur le plan de glissement (estime à 10.000m²) de 4,75 kPa. En admettant une résistance moyenne au glissement de 28,5 kPa, l'ensemble des forces passives serait égal à 28,5+4,75 =33,25 kPa, soit une sécurité F =33,25/30= 1,1 ; ce qui signifie que le glissement n'aurait probablement pas eu lieu. Il semblerait donc que l'ouverture de la fouille Mission La Vie ait contribué au glissement bien que faiblement, la raison essentielle étant

l'affaiblissement du sol par les eaux usées. En définitive, nous pouvons affirmer que le glissement est dû à deux causes, l'une majeure et l'autre mineure, à savoir: la cause majeure est due à l'imbibition en surface, et pendant une période prolongée, des schistes argileux qui se situent à 7m sous la surface du sol. Cette imbibition est due aux pertes en continu des égouts vétustes le long de la route Fouar Antélias-Raboueh. Elle réduit très fortement la résistance du sol le ramenant dans un état à la limite du glissement (sécurité F= 1.1). Quant à la cause mineure: le sol étant à la limite du glissement, l'ouverture de la fouille qui enlève la faible butée en pied du glissement (15% des forces résistantes) le fragilise encore plus, rendant le glissement possible à la moindre force active supplémentaire.

4 CONCLUSION

Les deux glissements sont plans: le sol glissé subit une translation, formant un bloc non ou peu fissuré. Le glissement se fait sur le toit de formations argileuses affaiblies par l'eau et sensiblement parallèles au toit du rocher. Pour le deuxième glissement, l'ouverture de la fouille en aval constitue un élément de déclenchement supplémentaire. L'effet néfaste des propriétés mécaniques affaiblies des argiles est expliqué.

5 REFERENCES

Abramson L.W., Lee T.S., Sharma S. and Boyce G.M. 2002. *Slope stability and stabilization methods, Second edition*. John Wiley & Sons, USA.

Benarroch A., Hernandez M.A. and Manzanilla R. 2011. Evaluation of sensitivity of the geotechnical parameters in the analysis of slope stability, *Proceedings of the 64th Canadian Geotechnical Conference*, Toronto, Ontario, Canada, Volume 3: 2633-2639.

Carrara A., Cardinali M., Guzzetti F. and Reichenbach P. 1995. *GIS-based techniques for mapping landslide hazard*. Edited by A. Carrara and F. Guzzetti. Kluwer Academic Publishers, Dordrecht, Netherlands.

Cruden D.M and Couture R. 2011. The working classification of landslides: material matters, *Proceedings of the 64th Canadian Geotechnical Conference*, Toronto, Ontario, Canada, Volume 3: 2540-2546.

Dikau R., Brunsden D., Schrott L. and Ibsen M.L. 1996. *Landslide Recognition: Identification, Movement and Causes*. John Wiley & Sons, England.

Fletcher L., Hungr O. and Evans S.G. 2002. Contrasting failure behavior of two large landslides in clay and silt. *Canadian Geotechnical Journal*, 39(1), 46-62.

Popescu M.E. 2002. Landslide causal factors and landslide remedial options. *Keynote Lecture. Proceedings of the third international conference on landslides, slope stability and safety of infrastructures*, Singapore: 61-81.

Rahhal M.E., Nini R. and Favre J.L. 2003. Analysis of factors causing slope instabilities, *Proceedings of the 56th Canadian Geotechnical Conference*, Winnipeg, Manitoba, Canada, Volume 2: 368-375.

Rahhal M.E., Nini R. and Favre J.L. 2004. Une Approche Simple de la Cartographie du Risque du Glissement de Terrains. *Proceedings of the 57th Canadian Geotechnical Conference*, Québec, Canada, Session 5C: 13-18.

Rahhal M.E. and Abou Rached, Z. 2005. Reliability Analysis of Slope Stability Involving Generalized Slip Surfaces. *Proceedings, 9th International Conference on Structural Safety and Reliability*, ASCE Geo-Institute Risk Assessment and Management Committee, Universita di Roma La Sapienza, Rome, ITALY, Millpress 2005 Eds, pages: 985-992.

Rahhal, M.E., 2006. Geotechnical Understanding of Probabilistic Landslides Appraisal Approaches. *Proceedings 5th International Conference on Computational Stochastic Mechanics*, Rhodes, GREECE, Millpress 2007 Eds, pages: 559-568.

A smart adaptive multivariable search algorithm applied to slope stability in locating the global optima

Un algorithme adaptatif multivariable de recherche d'optimum global appliqué à la stabilité des pentes

Saha A.
Irrigation & Waterways Department, Govt. of West Bengal, Kolkata, India

ABSTRACT: The paper addresses the topic of single objective optimisation of a three dimensional real-world problem and introduces a hybrid technique of an iterative random population search within a geometrically shrinking hypercube and a sort of simplified Design of Experiments (DOE). A 'population' of design variables are generated and augmented with the multivariable objective function, and the design variables pertaining to the local optima are perturbed by a factor (Δk) sequentially in both positive and negative directions to create $2(2^N-1)$ offspring in the neighbourhood of local optima to hopefully produce some better progeny. The 'fittest' perturbed offspring decides a new contracted search interval for the consecutive generation according to a geometric decay rule commensurate with the generation number. A 'simple hill-climbing' strategy in Artificial Intelligence context is followed subsequently and the loop is continued to produce fresh generations of refined offspring till the outcome converges to the global optimum. The method is applied in searching the critical slip-surface of a vulnerable soil-slope and it was revealed that the optimum found by this method is superior to that found by traditional and non-traditional (genetic algorithms) optimization techniques while using much less computational resources.

RÉSUMÉ: L'article traite de l'optimisation à une seule fonction objectif pour un problème réel tridimensionnel et introduit une technique hybride de recherche itérative à partir d'une population aléatoire au sein d'un hyper cube de taille décroissante, selon une méthode simplifiée de plan d'expérience. Une "population" de variables de design est générée, et étendue grâce à la fonction objectif multi variable. Les variables de design correspondant à l'optimum local sont alors perturbées par une facteur (Δk) de manière séquentielle dans les directions à la fois positives et négatives pour créer $2(2^N-1)$ individus de génération suivante dans le voisinage de cet optimum, dans l'espoir de produire une meilleure génération. La génération perturbée la plus satisfaisante selon l'objectif définit un nouvel intervalle de recherche, de taille réduite pour la génération suivante, selon une règle de décroissance géométrique en rapport avec le rang de génération. Une stratégie simple de plus grande pente dans un contexte d'intelligence artificielle est suivie pas à pas et une boucle produit de nouvelles générations améliorées jusqu'à ce que le résultat converge vers l'optimum global, indépendant de la population initiale. La méthode est appliquée à la recherche de la surface de glissement critique d'un sol en pente vulnérable. Il a été constaté que l'optimum trouvé par cette méthode est plus critique que celui donné par les méthodes traditionnelles et non traditionnelles (algorithmes génétiques) et de plus, cette méthode est moins exigeante en terme de capacité de calcul.

KEYWORDS: hybrid technique, random population search, optimization algorithm, slope stability.

1 INTRODUCTION

The stability of slopes has received wide attention due to its practical importance in the design of excavations, embankments, and dams. There are numerous methods available for stability analysis and the majority of analyses performed in practice still use traditional limit equilibrium approaches. By the advent of computers, the use of optimization techniques in locating the critical slip surface has been a major topic for the researchers. Duncan (1996) presented a comprehensive review of both limit equilibrium and finite-element analysis of slopes. Malkawi et al (2001) developed an effective approach for locating the critical circular slip surface based on Monte-Carlo techniques. Non-traditional optimization algorithms simulating processes drawn from nature like genetic algorithm (GA) and simulated annealing (SA) have proved to be efficient in locating the global optima. GA mimics the principles of Darwin's natural selection and survival of the fittest rule, in which an optimum solution evolves through a series of generations of population and has the super ability of global convergence and parallel searching. SA is the stochastic evolution of thermodynamic state of slow cooling of molten metals to achieve a crystalline absolute minimum energy state, where a perpetual decreasing sequence of temperature controls the reproduction rate, which is very efficient in neighborhood search. Li et al (2009), Author (2011) proposed hybrid global search procedures combining GA with SA. While summarizing

the state of the art techniques for evolutionary algorithm (EA) parameter tuning, T. Beielstein (2003) exclaims that "*real world optimization problems allow only a few preliminary experiments to find good EA settings. As the commonly used 'one factor at a time approach' is considered as inefficient and ineffective, we recommend DOE methods*". The present paper introduces a new Soft Computing algorithm- a hybrid technique of an iterative ***random population based search embedded with simulated annealing (SA) features within a geometrically shrinking hypercube coupled with simplified Design of Experiments (DOE)***.

2 APMA-A NOVEL OPTIMIZING TOOL

A smart adaptive population based multivariable function optimization algorithm proposed herein, and referred to as APMA hereinafter, is a simple yet robust optimization procedure basically of heuristic nature. Before plunging into details, a fitness function is defined to maintain uniformity over various problem domains and to map the 'goodness' of the objective function (here FOS) value to a fitness value. The fitness of an individual is calculated as the worst objective function objective function (FOS) value of the whole population subtracted from the individual's objective function value. Hence, this fitness function is computed for the individual as $\mathcal{F}_i$ = max.$\{f(x)_i|_{j=1, 2, ..., n}\} - f(x)_i$. Where; 'n' is the population

size. $f(x)_i$ is the objective function (here FOS of ith individual). The technique is known as windowing as it eliminates the worst individual (FOS)-the probability comes to zero, and stimulates the better ones.

Within the random generated set of population (n) of design multivariable (N-dimensions or feature vectors), $f(x_i, y_i, z_i, ...w_i)$ within wide deterministic search boundaries for each variable, and subsequent objective function evaluations, the minimum is located. With a view to exploit the search space neighbourhood the N-multivariable set $f\left(x_{i_{min}}, y_{i_{min}}, z_{i_{min}}, ...w_{i_{min}}\right)$ creating this minimum is perturbed by a factor (Δk) sequentially in both directions (positive as well as negative directions) $f\left\{\left(x_{i_{min}} \pm \Delta k\right),\left(y_{i_{min}} \pm \Delta k\right),\left(z_{i_{min}} \pm \Delta k\right),..\left(w_{i_{min}} \pm \Delta k\right)\right\}$ to

create $2\sum_{i-1}^{i=N} {}^N C_i = 2\sum_{i=1}^{i=N} \frac{N!}{(i!)(N-i)!} = 2(2^N-1)$ offspring {Where, N!=N.(N-1).(N-2).......3.2.1} in the neighbourhood of the local minimum in an attempt to generate some superior offspring. Hence, for a three variable function (like slope-stability problem) $f\{(x_i),(y_i),(z_i)\}$, a population (of n individuals) are randomly generated and their local minimum $f\left\{\left(x_{i_{min}}\right),\left(y_{i_{min}}\right),\left(z_{i_{min}}\right)\right\}$ located for the first generation. Thereafter, this local minimum is perturbed initially in the positive direction and function evaluations are made at $f\left\{\left(x_{i_{min}}+\Delta k\right),\left(y_{i_{min}}\right),\left(z_{i_{min}}\right)\right\}; f\left\{\left(x_{i_{min}}\right),\left(y_{i_{min}}+\Delta k\right),\left(z_{i_{min}}\right)\right\};$ $f\left\{\left(x_{i_{min}}\right),\left(y_{i_{min}}\right),\left(z_{i_{min}}+\Delta k\right)\right\}; f\left\{\left(x_{i_{min}}+\Delta k\right),\left(y_{i_{min}}+\Delta k\right),\left(z_{i_{min}}\right)\right\};$ $f\left\{\left(x_{i_{min}}\right),\left(y_{i_{min}}+\Delta k\right),\left(z_{i_{min}}+\Delta k\right)\right\}; f\left\{\left(x_{i_{min}}+\Delta k\right),\left(y_{i_{min}}\right),\left(z_{i_{min}}+\Delta k\right)\right\};$ $f\left\{\left(x_{i_{min}}+\Delta k\right),\left(y_{i_{min}}+\Delta k\right),\left(z_{i_{min}}+\Delta k\right)\right\};$

and finally in the negative direction, by changing the sign of Δk in above expressions. Hence, apart from objective function evaluations of all n number of population individuals in each generation, the algorithm requires further function evaluations at $2(2^N-1)$ points around the local minimum of each generation. Now as fresh generations are produced, often different selection pressures of reproduction are needed at successive generations. Hence, the choice of a value of the sequential perturbing factor (Δk) becomes of paramount importance, in a sense that if it is too large it will be adequate in the first phase of the search but not in the final phase and vice versa if it is too small. Further, this Δk is likely to be different for different design variables commensurate with their individual feasible search intervals. As such, the situation calls for some sort of normalization of Δk in initial phase for application in various problem domains, and further it should possess the flexibility of shrinking itself automatically in successive generations according some decay rule in compliance with the selection pressure criteria. In this study, this perturbing parameter is defined as $\Delta k=\kappa.(x_i^U-x_i^L).\Delta_i$, where, κ is a problem specific constant; to be fixed after some initial trials. x_i^U and x_i^L are the upper and lower bounds of a design variable and Δ_i [$=G_i(1-r)^{(Gi-1)}$] is the size reduction parameter, where, G_i is the generation number and 'r' a constant less than unity. As the number of design variables (N-dimensions) increases, more trials are needed for fixing the value of κ. The 'fittest' perturbed offspring $f\left(x^p_{i_{min}}, y^p_{i_{min}}, z^p_{i_{min}}, ...w^p_{i_{min}}\right)$ of the ith generation decides a new contracted search interval for the consecutive generation, wherein the value each design variable corresponding to the fittest perturbed offspring is assigned the central value of the interval. The two new extreme bounds of the fresh search interval is the product of the positive and negative value of this central value and the size reduction parameter, Δ_i. Thus, if the local minimum objective function of the previous generation be

$f\left(x^p_{(i-1)_{min}}, y^p_{(i-1)_{min}}, z^p_{(i-1)_{min}}, ...w^p_{(i-1)_{min}}\right)$, the current (that is, i^{th}) search interval becomes,

$$\left[\begin{array}{l}\left\{x^p_{(i-1)_{min}} \pm G_i(1-r)^{G_i-1} x^p_{(i-1)_{min}}\right\}, \left\{y^p_{(i-1)_{min}} \pm G_i(1-r)^{G_i-1} y^p_{(i-1)_{min}}\right\}, \\ \left\{z^p_{(i-1)_{min}} \pm G_i(1-r)^{G_i-1} z^p_{(i-1)_{min}}\right\}...\left\{w^p_{(i-1)_{min}} \pm G_i(1-r)^{G_i-1} w^p_{(i-1)_{min}}\right\}\end{array}\right].$$

A new population of random variables (of size n) is again generated from *scratch* within the new reduced stochastic search interval and again objective function evaluations are made for each set of new random variables so generated. The generated set replaces the initial one and the loop is continued to produce fresh generations of refined offsprings till the outcome converges to the global optima.

2.1 APMA efficacy checked with benchmark test functions

With a view to examine the performance of the algorithm, APMA is initially applied to some benchmark unconstrained global optimization test functions like Goldstein-Price's function, Hartman's function, Beale's function, Perm's function, Booth's function, Bohachecsky's function (A. Hedar), Six hump camel's back function and Xin-She-Yang's function (X.-S. Yang, 2010) and promising results were obtained. APMA successfully captured all the four optima of the multimodal Himmelblau function (Deb K., 2000): $f(x_1,x_2)=(x_1^2+x_2-11)^2+(x_1+x_2^2-7)^2$, [*the optima being (-2.805, 3.131); (-3.779, -3.283); (3.584, -1.848); (3,2)*] in each and every simulation run while finally converging to the global minimum at *(3,2)* [*The simulation runs has been done with κ=80-90% & r=0.10*]. The method may be regarded as a basic thrust of 'Artificial Intelligence', that is to get the computer to perform tasks fast and automatically. The method is independent of the initial vector and as no specific search direction is used in this method, this random search method is expected to work efficiently in many classes of problems.

3 THE PROBLEM DEFINITION

A problem cited by Spencer (1967) is chosen for analysis. The problem parameters, soil-data and search boundaries are depicted in Fig.1. In the search process, the three independent design variables are the abscissa (CX) and ordinate (CY) of the circle centre and the depth factor (N_d) of the circular failure surface. The base width (B) and height (H) of slope are assumed as 60 meters and 30 meters respectively.
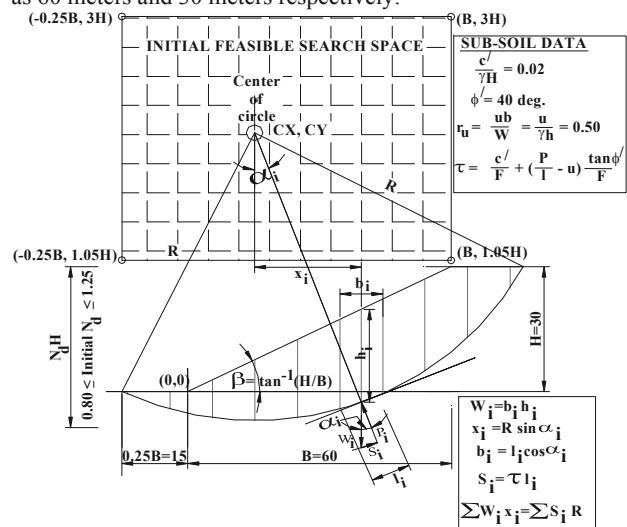

Fig.1. Initial variable bounds of the tri-variable & soil data used in search for critical circle-*The Slope-Stability problem definition*.

The radius R=f{CX, CY, N_dH}. Based on a few trials, the feasible bounds of the design variables, has been identified as: -

$0.25B \leq CX \leq B$, $1.05H \leq CY \leq 3H$, $0.80 \leq N_d \leq 1.25$. In the widely used limit equilibrium methods of slope analysis, the potential slip surface and the sliding mass are divided into segments or slices. The FOS, (F) is related to the total height of the slope H, the effective subsoil parameters c', φ' and γ, the pore pressure ratio r_u ($= u/\gamma h$), the individual slices of width b_i, height h_i and α_i-the inclination of slice on the failure arc with the horizontal, by the following equation (Bishop, 1955):

$$F = \frac{\sum_{i=1}^{n} \left[\left\{ \left(\frac{c'}{\gamma H}\right)\left(\frac{b_i}{H}\right) + \left(\frac{b_i}{H}\right)\left(\frac{h_i}{H}\right)(1 - r_u)\tan\varphi' \right\} \dfrac{\sec\alpha_i}{1 + \tan\alpha_i \tan\varphi'} \right]}{\sum_{i=1}^{n} \left(\frac{b_i}{H}\right)\left(\frac{h_i}{H}\right)\sin\alpha_i} \cdot \frac{1}{F}$$

A modest population size (n) of 20 is adopted. The design variables of the fittest population genre (local $FOS_{min.}$) is perturbed sequentially by a factor Δk in both directions, resulting in $2(2^3-1) =14$ 'offsprings'. ***Initial value of Δk is fixed at 5% of the search interval*** for each variable after some initial trials. Hence, Δk works out to be 3.75 [=.05x{(60.00)-(-15.00)}] for x_i-the abscissa of the slip-circle centre, 3.225 {=.05x(94.50-30.00)} for y_i-the ordinate of the slip-circle centre and 0.0225 {=.05x(1.25-0.80)} for z_i-the depth factor of the slide (refer Fig.2). ***This Δk is further shrinked in successive generations by multiplying it with the size reduction parameter, $\Delta_i = G_i(1-r)^{(Gi-1)}$.*** Again, the objective function evaluations are made for the perturbed individuals and the minimum of these 14 points is located. This local minimum point (offspring) acts as the 'mother' of the next generation, and the corresponding design variables acts as the mean of the search space of next generation.
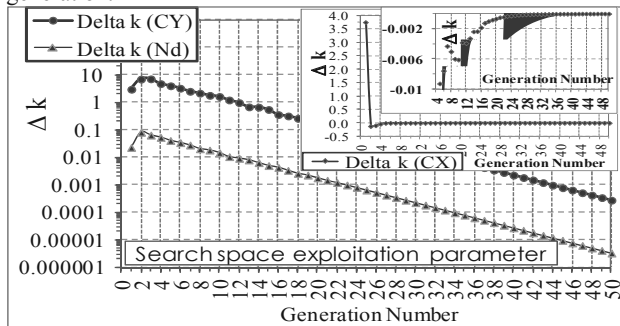
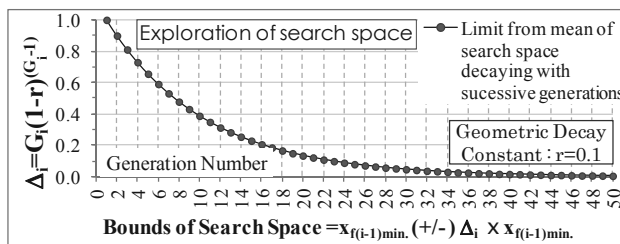Fig.2. Search space exploitation in line with Design of Experiments.

Fig.3. Search space exploration analogous to simulated annealing schedule by contraction of search boundary in successive generations.
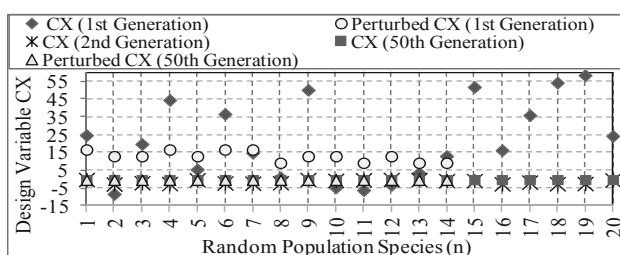

Fig.4. Initial deterministic search space turns heuristic at 2nd Generation- a quick shift towards the best part of search space.
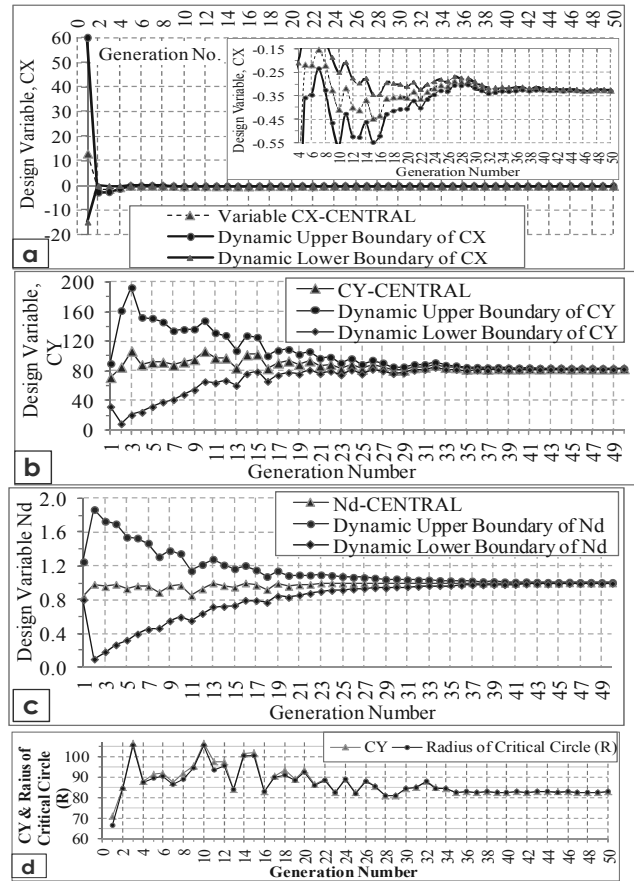

Fig.5. Robust movement of variable bounds along with the central value of tri-variables (CX, CY, N_d) shown in (a), (b), (c) respectively. In (a), a further close-up view from 2nd generation is shown. *From (d) it emerges that $R \approx CY$ for critical circle.*

4 COMPUTER SIMULATION & GRAPHICAL DEPICTION OF THE SMART ADAPTIVE PROCESS

Fig.3 shows how the limit of search boundary shrinks towards the mean (that is, the central value or the best point of the preceding generation) of the search space. Fig.4 shows a typical result of 1st, 2nd and 50th randomly generated population along-with the perturbed population set of 1st and 50th generations. ***It may be noted that initial wide deterministic search space turns heuristic at 2nd generation with a quick shift towards the best part of search space.*** Fig.5(a) to (c) depict the robust movement of variable bounds along with the central value of the three design variables (CX, CY & N_d), illustrating the generate-and-test heuristic search technique that exploit domain-specific knowledge. It emerged that whatever be the initial search bounds specified deterministically, the algorithm adjusts itself to move to the best part of search space in the immediate 2nd generation. It is revealed that the ***bounds of CX are drastically reduced (Fig.5a), and that of CY & N_d are radically expanded (Fig.5b&c) in immediate 2nd generation***, and thereafter the bounds move steadily with successive generations that are guided by the mean of the search space, while maintaining a heuristic character. It emerged that the value of radius of critical circle (R) almost merges with the ordinate (CY) of the critical slip circle (Fig.5d). Fig.6 depicts the change in average fitness, standard deviation and variance of fitness function of population with successive generations. The variance of fitness decreases steadily with increasing generations maintaining its randomness. Fig.7 shows the maximum fitness of each generation vs. search space size reduction parameter in log-log scale. Fig.8 portrays the stochastic movement of Min. FOS in successive generations to converge to global optimum, wherein results of five simulation runs are superimposed. The inherent

stochastic nature of the algorithm showing value convergence with increasing generations is reflected in all the results.
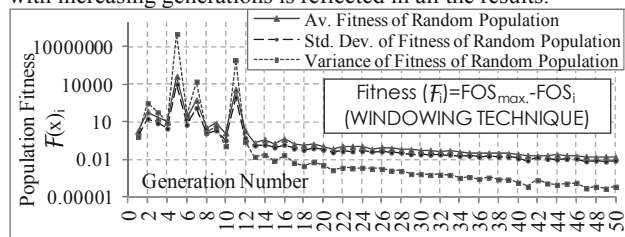

Fig.6. Change in average fitness, standard deviation & variance of population fitness function with successive generations.
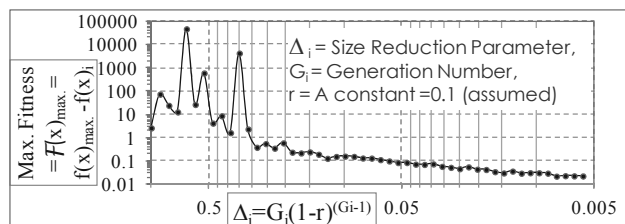

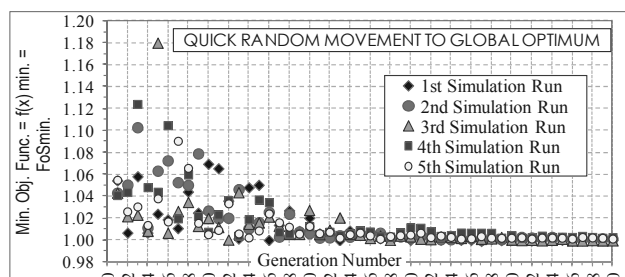Fig.7. Max^m. fitness of each gen. vs. search space size red. parameter.

Fig.8. Stochastic movement of Min. FOS (obj. func.) in successive gens. to converge to global optimum (Results of five simulation runs).
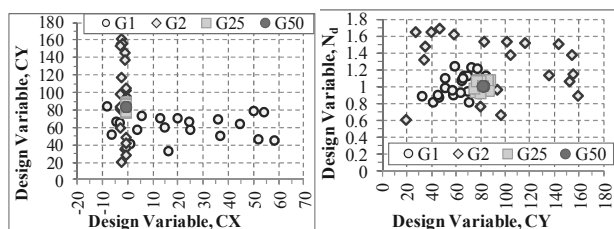

Fig.9. CX vs. CY & CY vs. N_d: The artificial intelligent character depiction. Fast random movement of candidate solutions to best part of the search space with increasing generations.
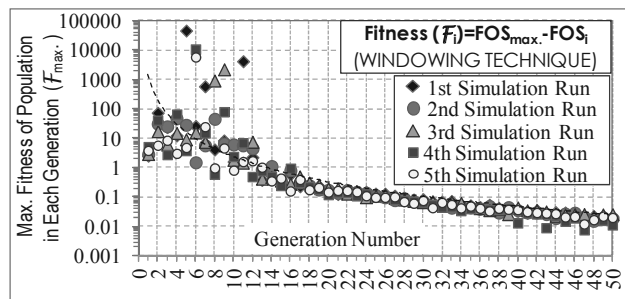
Fig.10. Stochastic decrease of maximum fitness in successive generations (Results of five simulation runs superimposed).

Fig.9 depicts the artificial intelligent character of the algorithm wherein a fast random movement of candidate solutions with increasing generations to best part of the search space is noticed. Fig.10 shows the stochastic decrease of maximum fitness in successive generations in 5 simulation runs. Fig.-11 gives the validation of results against other studies reported in literature.

5 CONCLUSIONS

A global population based search procedure (APMA) is developed and successfully applied to slope-stability problem. It does not require problem specific knowledge in searching the critical slip-surface of a soil-slope and is a heuristic technique based on the 'generate-and-test' strategy. Diverse aspects are presented to demonstrate its efficiency and robustness. The spectrum of application area of APMA is widespread as it is a direct search method where no specific search direction is used and multivariable functions, both continuous and discontinuous can be handled. Function value evaluations at discrete points only enable it to handle non-differentiable functions at ease. The beauty of the process is that, it handles a number of designs in each simulation run. The result of some simulation runs revealed minimum factor of safety obtained by APMA is less than that found by directed grid search, variational method, GA and GA-SA hybrid.
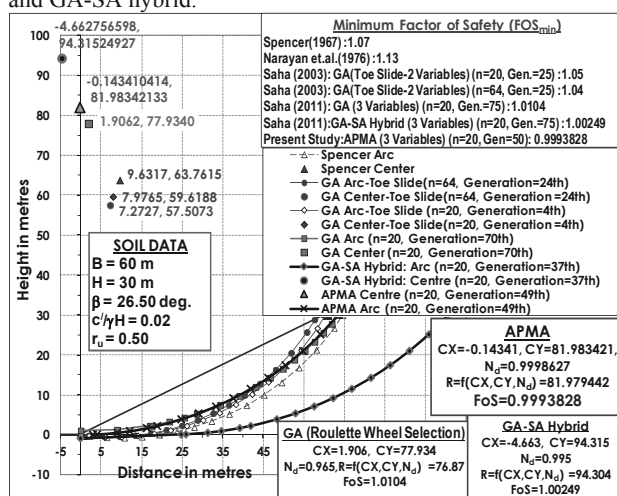

Fig.11. Comparison of results obtained by various methods.

6 REFERENCES

A.Hedar. Test function web pages, *http://www-optima.amp.i.kyoto-u.ac.jp/member/student/hedar/Hedar_files/TestGO_files/Page364.htm*

Bishop A.W. 1955. "The use of slip circles in the stability analysis of slopes", Geotechnique. Vol.-5, 7-17.

Deb Kalyanmoy 2000. *Optimization for Engineering Design, Algorithms and Examples*, Prentice Hall, New Delhi, India.

Duncan J.M. 1996. State of the art: limit equilibrium and finite-element analysis of slopes, Journal of Geotec. Eng.,ASCE, 122(7), 577-596.

Li K.S., Z. Shangguan, H. Duan, Y Liu, M. Luan 2009. Searching for critical failure surface in slope stability analysis by using hybrid genetic algorithm, Geomechanics and Engg., 1(1), 85-96.

Malkawi A.H., Hassan W.F., and Sarma S.K. 2001. Global search method for locating general slip surface using Monte Carlo techniques, Journ. of Geotech. & Geoenv. Engg., 127(8), 688-398.

Narayan C.G.P., Bhatkar V.P. & Ramamurthy T. 1976. Slope stability analysis by variational method, Indian Geotech. J., Vol.- 6, 68-90.

Saha Abhijit 2003. Genetic algorithm based search in slope stability analysis, Proc. of 12th Asian Regional Conference in Soil Mech. & Geotechnical Engg., Singapore, Vol.-I, 981-984.

Saha Abhijit 2011. Genetic algorithm based search coupled with Boltzmann selection in locating the critical surface in slope stability, Proc. of 14th Asian Regional Conference in Soil Mech. & Geotechnical Engg., Hong Kong, Paper No.-115.

T. Beielstein 2003. Tuning evolutionary algorithms/Overview & Comprehensive Introduction. Tech. Report 148/03, Universität Dortmund, Germany.

Spencer E. 1967. A method of analysis of the stability of embankments assuming parallel inter-slice forces, Geotechnique, London, Vol.-17, 11-26.

X.-S. Yang 2010. *Test problems in optimization, in: Engineering Optimization: An Introduction with Metaheuristic Applications (Eds Xin-She Yang)*, John Wiley & Sons.

Soil slope stability of hydropower reservoirs - from geological site investigation to design of mitigation measures

La stabilité des talus de réservoirs hydroélectriques - de l'investigation géologique du site à la conception de mesures d'atténuation

Saurer E., Prager C., Marcher T.
ILF Consulting Engineers, Rum/Innsbruck, Austria

ABSTRACT: Many reservoir slopes are affected by different types of instabilities during the first impoundment, due to reservoir level fluctuations and due to earthquakes. These potential failure processes are caused by complex hydro-mechanically coupled processes, which in most cases cannot be fully assessed during the design stage due to a limited knowledge of the soil behaviour and properties. Thus, for the site selection and the design of power storage plants, especially for the risk assessment and mitigation of potentially unstable soil slopes, a systematic methodology for the selection of the appropriate stability measures is presented. Based on case studies from both engineering projects and literature, a methodological approach and a decision matrix for the design of appropriate mitigation measures depending on the failure mode and size of the potentially instable slope are proposed.

RÉSUMÉ : Un grand nombre de talus à proximité des réservoirs sont affectés par différents types d'instabilités en raison des fluctuations des niveaux de réservoir et en raison de tremblements de terre. Ces procès potentiels de défaillance sont causés par des transformations complexes hydromécaniques, qui dans la plupart des cas, ne peuvent être entièrement évalués au cours de la phase de conception en raison d'une connaissance limitée sur le comportement et des propriétés des sols. Ainsi, pour la sélection des sites et la conception des installations de stockage d'énergie, il est essentiel de tenir compte des expériences antérieures et d'appliquer ces connaissances à la conception de nouvelles installations pour créer une stratégie d'évaluation des risques et d'atténuation. Ici une méthode pour la sélection des mesures de la stabilité appropriées en fonction du mode de défaillance est fournie. Basé sur des études de projets et de la littérature une méthodologie systématique et une matrice de décision pour la conception de mesures d'atténuation appropriées en fonction du mode de défaillance et la taille de la pente potentiellement instables sont proposées.

KEYWORDS: soil slope stabilization, mitigation measures, decision matrix

1 INTRODUCTION AND FRAMEWORK

1.1 *Reservoir slope instabilities (causes, triggers)*

Concerning site selection studies for a water storage reservoir, particular focus has to be placed on the assessment of terrain stability, especially in the dam area but also along the reservoir slopes.

In general, failures are related to changes of stability parameters of natural slopes or artificial cuts. Related to reservoirs, the disturbance may be caused by water level changes (due to first impoundment and/or recurring water level fluctuations during operation) which may cause catastrophic (uncontrollable) slope failures of all sizes. According to Riemer 1995, the causes and triggers of soil displacements include, e.g.
- change of consistency due to saturation (fine soils)
- change of effective stresses (pore pressure)
- groundwater flow (steady and transient flow)
- external erosion, e.g. caused by waves
- internal erosion (suffosion, subrosion)

At the design stage of a reservoir, these processes have to be considered in order to assess the slope stability. Commonly, slope failures are only treated when they affect the serviceability (storage volume loss, operational restrictions, land use along shoreline, water quality) or failure of a reservoir and its surroundings.

1.2 *Slope stability assessment and risk management*

Extensive literature reviews of landslides and reservoirs as well as detailed case studies have been carried out by many authors (e.g. in Riemer 1995). In particular deep-seated rock slides have been monitored and investigated intensively, and monitoring results have been reported over the last decades (Leobacher and Liegler 1998, Tentschert 1998, Jäckli 1996, Watson et al. 2006, Barla et al. 2010).

Moreover, process based investigation methods and monitoring measures have been developed (Keusen 1998, Zangerl et al. 1999, Leobacher and Blauhut 2010).

The issue of slope stability, in particular for dam safety, during rapid drawdown and earthquake loading and has been studied widely (e.g. ICOLD 1980, Casagrande 1937, Sherard 1963, Alonso and Pinyol 2009). Besides the stability assessment,(e.g. according to Casagrande 1937), it is expected that engineers are able to make a statement not only on stability but also on the consequences of potential mass movements.

Following the stability assessment, a risk management plan may be produced. Whereas several research projects on landslide risk management have been undertaken (e.g. ICG 2009 and 2011), only few data concerning slope stability in the vicinity of water reservoirs are publically available..

Here, an overview of a systematic approach to assess the slope stability before and after reservoir impoundment with particular consideration of earthquake and rapid drawdown conditions and a proposal for a customized toolbox for slope stabilization in cohesive and granular soils are provided.

2 SLOPE STABILITY ASSESSMENT

A possible flowchart for the slope stability assessment is provided in Figure 1. The individual steps are described in the subchapters below.

2.1 Site selection

The site selection process for hydropower reservoirs is driven by the need to optimise decision criteria which are initially mainly of an economic nature,.

In the best case, several sites are shortlisted based on economic factors followed by comparisons of options and more detailed feasibility studies including detailed geological and geotechnical investigations and designs.

2.2 Geological and hydrogeological model

A geological and hydrogeological model may be developed using the following investigation techniques (selection):
- geological site mapping, incl. structural geological surveys;
- remote sensing and terrain analyses (e.g. optical images, LiDAR, DEMs);
- hydrogeological field surveys (mapping of springs, surface flow systems incl. discharge measurements, recharge and infiltration characteristics);
- groundwater measurements, tests and monitoring (spring parameters e.g. EC, T and discharge, stage-discharge stream gauges, groundwater elevation gauges, piezometers/hydraulic heads, tracer tests, hydrochemical and isotopic analyses, etc.);
- core drillings with in-situ measurements and tests (e.g. core SPTs, geophysical borehole logs, geotechnical and hydraulic tests, e.g. packer tests, water pressure tests, dilatometer tests) and (un)disturbed rock/soil sampling;
- geophysical surveys (surface and borehole seismics);
- slope monitoring (geodetic surveys, inclinometer measurements and others).

Based on these data, a comprehensive rock mass model may be established, which in turn constitutes the basis for the subsequent steps (see Figure 1).

2.3 Geotechnical model and assessment of actual slope stability

Based on the geological model (incl. results from lab and field tests), characteristic soil parameters and a geotechnical model are defined. "Characteristic" soil properties may be i) obtained from field and lab tests and/or ii) back calculated from the geological model, (taking into account the soil strata and slope inclinations). In the latter case an assumption on earthquake loads which have already been acting on the slope has to be made and included in the back analyses. When using back calculations it is assumed that the slope is in limit equilibrium. Ideally both approaches should be combined.

These calculations yield values for the assessment of the actual slope stability. However, these assessments are commonly based on geological and geotechnical models of limited accuracy due to a limited number of available results from laboratory and field tests. Therefore, the "real" soil parameters are to be verified at the latest at the stage of the first impoundment of a reservoir.

2.4 Assessment of slope stability under changed boundary conditions

The boundary conditions of reservoir slopes may change drastically due to impoundment and rapid drawdown

Therefore the back calculated geotechnical slope model (see above) has to be adapted to these changed boundary conditions and the slope stability has to be reassessed. From this analysis four different scenarios may be obtained (see Figure 1):

In the best case, the slope stability is not affected by the new boundary conditions at all. This is the case when the failure plane is located entirely above the shoreline.

The remaining three cases may be assessed according to i) the size and shape of the potential landslide mass and ii) the acceptance of the consequences of a failure.
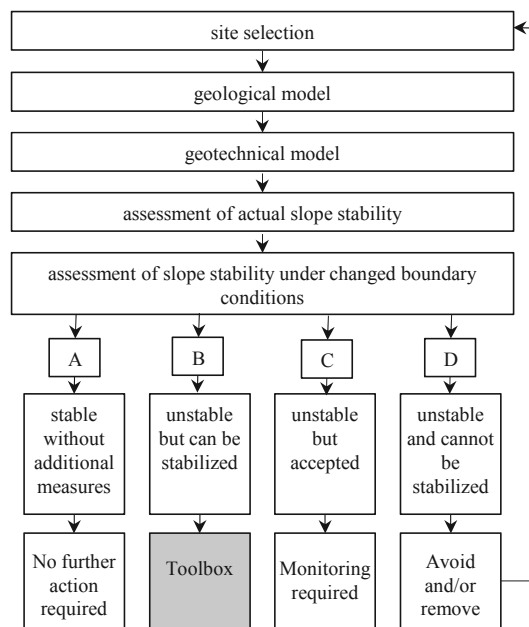

Figure 1: Flow chart for the assessment of slope stability (explanations , see text).

The decision whether a potential slope failure is acceptable depends on various criteria: If the slope stability deteriorates, proof has to be provided that the safety of the dam and its surroundings are not affected. This means that the size and the velocity of potential landslides do not cause critical tsunamis overtopping the dam.

For this proof and the risk assessment, the slope deformation behaviour has to be evaluated according to the types shown in Figure 2. While deformation types 1 and 2 are commonly unproblematic and type 3 requires a sound risk assessment, the stick-slip behaviour of type 4 landslides is much more difficult to predict. Such deformation behaviour requires intensive monitoring and a fundamental knowledge of the soil properties (Barla et al. 2010, Leobacher and Liegler 1998, Zangerl et al. 1999).
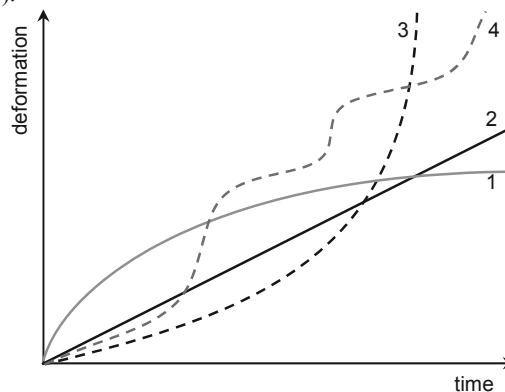

Figure 2: slope kinematics (temporal deformation types): (1) decreasing slope velocity; (2) constant velocity; (3) accelerating and failing slope; (4) episodic accelerated slope (after Keusen 1998)

Planning any mitigation measures depends on the geometry and depth of landslides. Concerning this, the classification of landslide thickness (according to BAFU 2009 and ICG 2011) is shown in Table 1.

Table 1: Landslide categories as a function of the depth of movement (acc. to BAFU, 2009 and ICG 2011).

Category	Depth of movement [m]	
	BAFU 2009	ICG 2011

Superficial	0 -2	< 0.5
Shallow		0.5 - 3
Medium	2 - 10	3 - 8
Deep	> 10	8 - 15
Very deep	> 30	> 15

Depending on the findings from the above mentioned work packages (Ch. 2.1. to 2.4) four possible slope scenarios and respective measures may be differentiated (Figure 1):

- A) stable without additional measures, no further action is required.
- B) unstable due to changed boundary conditions and cannot be stabilized with feasible measures. However, the slope instability may be avoided by flattening the slope by massive earth works.
- C) unstable due to changed boundary conditions but the consequences of the instability do not affect the serviceability of the reservoir and are therefore acceptable and do not affect the serviceability of the facility.
- D) potentially unstable due to changed boundary conditions but can be stabilized with additional stabilization measures: for this case a toolbox is presented in Table 2; depending on the geometry, of the potential slide and its failure mode, the required measures may be chosen.

3 MITIGATION MEASURES

3.1 *Superficial and shallow landslide mitigation measures*

Shallow landslide (i.e. < 3m thick, see table 1) mitigation measures aim to prevent surface erosion and to improve the drainage capacity of the uppermost meters. Appropriate measures comprise, e.g.:

- drainage trenches, to reduce the length of drainage path and hence erosion; they may be lined with geotextiles and combined with drainage tubes;

Figure 3: reservoir slope featuring drainage trenches above the storage level.

- wave protection, to prevent soil from external erosion

Figure 4: Wave protection measure (stone wall) in an impounded reservoir.

- cultivated crib walls;
- geomembranes, along with soil nailing, gabion mattresses and/or blocks as surface erosion protection, especially for fine-grained soils; nails are used primarily to stabilize the geotextile and secondarily to stabilize the soil itself;
- geomembranes, along with flat gabions, as erosion protection measure.

Protection in the vicinity of road cuts above the shoreline comprises gabion walls and soil nailing, used as artificially steepened natural slope measure.

3.2 *Medium to deep seated landslide mitigation measures*

By installing a defined grid of geotextile wrapped stone columns, the shear strength of the soil may increase and the length of the drainage path in the soil can be shortened. Both effects increase the slope stability. Also, by means of local soil substitution with material of higher shear strength and permeability, the stability and erosion protection are improved.

Supporting embankments may be used to prevent erosion and to stabilize deep seated potential slip circles. Such embankments have already been successfully applied to stabilize unstable slopes of operating hydropower facilities.

If subaquatic soil instabilities (i.e. below the reservoir water level) are accepted, which may acceptable if they do not influence the serviceability of the reservoir, but the shore above water level has to be protected, a pile wall at the height of the maximum water level may be installed as a protection measure.

3.3 *Very deep seated landslide mitigation measures*

Very deep seated (i.e. > 15 m thick, see table 1) landslides generally require cost-extensive mitigation and monitoring measures such as drainage drillings and adits (Bonzanigo et al. 2007, Zangerl et al. 2010).

4 COMBINATIONS OF MEASURES

In order to find feasible and appropriate combinations of mitigation measures, Table 2 presents a matrix of scenarios (scenarios 1 to 7).

- Scenario 1 represents possible combinations of protection measures below storage level to prevent superficial mass movements and erosion.
- Scenarios 2 to 7 combine mitigation measures against potential superficial instability with medium to deep seated mass movements. Whereas in scenario 2 flattening of the upper part of the slope reduces the driving force of a potential instability, in scenario 3, the increase of the safety level is obtained by increasing the resisting force at the toe of the slope. Note that for scenario 3 the safety against surface erosion is given when using accordingly graded fill material. In contrast, when combining measures as shown in scenario 4, measures for both failure mechanisms have to be designed individually. This may also be the case for scenario 5.
- The most drastic measure is hence the soil replacement depicted as scenario 6, whereas in scenario 7 the goal is that the safety of the slope above the impoundment level remains, without taking into consideration the stability below the measure.

Table 2: Matrix of combinations. +: appropriate measure/combination. ` inappropriate measure/combination.

1	2	3	4	5	6	7	Scenario	
+	`	`	`	`	`	`	drainage trench	superficial instability
+	`	`	`	`	`	`	wave protection	
+	+	`	+	+	`	`	geomembranes with gabbion mattresses	
+	+	`	+	+	`	`	geomembranes with soil nailing	
+	+	`	+	+	`	`	cultivated protection walls	
`	+	`	`	`	`	`	flatten slope geometry by soil removal	shallow to medium deep seated instability
`	`	+	`	+	`	`	flatten slope geometry by support fill	
`	`	`	+	`	`	`	Deep soil nailing	
`	`	`	`	+	`	`	soil improvement (e.g. vibro replacement)	
`	`	`	`	`	+	`	soil replacement	
`	`	`	`	`	`	+	pile wall	

5 RESIDUAL RISK ASSESSMENT

The residual risk from a potential mass movement has to be analysed independently from mitigation measures. This is due to the fact that the mitigation measures are designed for a certain defined load (e.g. design earthquake). However, remaining residual risks may comprise events larger than the design event and resulting slope instabilities. Thus, also the impacts of such instabilities on both the safety of the dam and reservoir (probability and consequences of overtopping) have to be assessed.

For this both empirical approaches (Fritz et al. 2003, Heller 2007) and numerical models (e,g, Grilli and Watts 2005) may be applied.

6 MONITORING MEASURES

Slope stability behaviour can be monitored a) pointwise, b) linear and c) areally and can be measured in-situ and/or by remote sensing methods (see Sect. 8 References). Point data can be obtained through triangulation, levelling, GPS surveys, wire extensometer, joint- or crackmeter, laser distance meter and water level gauge measurements. Line data may be obtained from inclinometer, extensometer and Trivec measurements and/or from fibre optic sensing techniques. The deformation field of a surface of a landslide can be obtained by photogrammetry, terrestrial or satellite based radar interferometry and terrestrial or airborne laser scanning. A variety of these monitoring methods has already been successfully applied to some well-documented reservoir slopes (e.g. Leobacher and Liegler 1998, Tentschert 1998, Watson 2006, Zangerl et al. 2009, 2010).

7 CONCLUSION

Assessment of slope stability of potential reservoir sites requires interdisciplinary knowhow, comprising intensive field investigations and sound determination of soil characteristics. Data thus obtained enable the assessment of slope stability (due to changed boundary conditions) and the design of appropriate mitigation measures.

For the design phase, possible scenarios of mitigation measures are described and presented in a matrix form. These measures serve as a basis during later design phases and during execution when the stabilization measures are allocated to the appropriate slopes in the reservoir according to the corresponding refined geological model and boundary conditions.

The scenarios 1 to 7 (Table 2) may be applied to different slope conditions (Figure 1: A to D), i.e. areas with acceptable slope stability, areas where near-surface stabilization measures are required, and areas with shallow to deep seated mass movements which have to be stabilized.

On the basis of available geological surface and subsurface data (field survey, geophysics, drillings) representative geological slope cross sections are established in order to illustrate, evaluate and assess the current and future slope stability in the individual regions. These geological sections and geotechnical data are used to for stability calculations.

Due to the repeated water level fluctuations, some areas may experience erosion and landslide processes (landslides, flow processes), especially in areas with large granular or cohesive soil layers. Stability studies including all load cases (including earthquakes) have to be carried out. If the safety calculation without stabilization measures returns an insufficient safety factor, measures required to achieve the required level of safety have to be determined. The goal of constructing mitigation measures is that the slopes for the mentioned load combinations (including earthquake load) remain stable.

For the monitoring of slope stability during the construction and operating phase, instrumental measurements of selected slope areas are required. These include both episodic campaigns and permanent measurements, e.g. geodetic surveys, levelling and inclinometer measurements.

8 REFERENCES

Alsonso E. & Pinyol N. (2009). *Slope stability under rapid drawdown.* 1st Italian Workshop on Landslides11 - 27, Napols

BAFU, 2009: Schutz vor Massenbewegungsgefahren, Technische Richtlinie als Vollzugshilfe, Entwurf 09.09.2009. – Bundesamt für Umwelt BAFU, 90 pp., Bern.

Barla, G., Antolini, F., Barla, M., Mensi, E., Piovano, G. (2010). *Monitoring of the Beauregard landslide (Aosta Valley, Italy) using advanced and conventional techniques.* Engineering Geology, 116, 218-235.

Eberhardt E., Bonzanigo L., Loew S. (2007): *Long-term investigation of a deep-seated creeping landslide in crystalline rock. Part II. Mitigation measures and numerical modelling of deep drainage at Campo Vallemaggia.* Can. Geot. J., 44/10, 1181-1199.

Casagrande, A. (1937). *Seepage through dams.* Contributions to soil mechanics, 1925-1940. Boston Society of Civil Engineers.

Fritz, H. M., Hager, W. H., Minor, H.-E. (2003). Landslide generated impulse waves. Experiments in Fluids 35, 505-532.

Grilli, S. T. & Watts, P. (2005). Tsunami generation by submarine mass failure. I: Modeling, experimental validation and sensitivity analyses. II: Predictive Equations and case studies. J. Waterw. Port Coast. Ocean Eng. 131(6), 283-310. Heller, V. (2007). Landslide generated impulse waves: Prediction of near field characteristics. ETH Diss. No. 17531

ICG (2009) *SafeLand – Living with landslide risk in Europe: Assessment effects of global change, and risk management strategies.* 7th Framework Programme Cooperation Theme 6 Environment, Sub-Activity 6.1.3 Natural Hazards, Deliverable 5.2 Toolbox of landslide mitigation measures, 47 pp.

ICG (2011) *SafeLand – Living with landslide risk in Europe: Assessment effects of global change, and risk management strategies.* 7th Framework Programme Cooperation Theme 6 Environment, Sub-Activity 6.1.3 Natural Hazards, Deliverable 5.1 Compendium of tested and innovative structural, non-structural and risk-transfer mitigation measures for different landslide types, 340 pp.

ICOLD (1980). *Deterioration of dams and reservoirs. Examples and their analysis.* ICOLD, Paris, Balkema, Rotterdam.

Jäckli, H. (1996). *Durch Spiegelschwankungen des Stausees Wägital beeinflusste Kriechbewegungen.* Instabile Hänge und andere risikorelevante natürliche Prozesse. in: Oddson B. (ed.), Instabile Hänge und andere risikorelevante natürliche Prozesse, 219-226, Birkhäuser.

Keusen, H.R. (1998) *Warn- und Überwachungssysteme* (Frühwarndienste). Fan-Forum, Zollikofen, 1-40.

Leobacher, A. Liegler, K. (1998) *Langzeitkontrolle von Massenbewegungen der Staruraumhänge des Speichers Durlaßboden.* Felsbau 16/3, 184-193.

Leobacher, A., Blauhut, A. (2010). Gerlos power station/Gmünd dam – stabilization of a reservori slope (Grasegger slope). Geomechanics and Tunnelling 3, 462-469.

Riemer, W. (1995). *Keynote lecture: Landslides and reservoirs.* in: Bell (ed.), Landslides, pp. 1973-2004, Balkema, Rotterdam.

Sherard, J.L., Woodward, R.J. Gizienski, S.F. & Clevenger, W.A. (1963). *Earth and earth-rock dams.* Wiley&Sons.

Tentschert. E. (1998). Das Langzeitverhalten der Sackungshänge im Speicher Gepatsch (Tirol, Österreich). Felsbau 16/3, 194-200.

Watson, A.D., Martin, C.D., Moore, D.P., Steward, W.G. Lorig, L.J. (2006) *Integration of Geology, Monitoring and Modelling to Assess Rockslide Risk.* Felsbau 24/3, 50-58.

Zangerl C., and others, 2009: Landslide failure and deformation mechanisms, investigation and monitoring methods. - in: Veulliet E. et al (eds.), Sustainable Natural Hazard Management in Alpine Environments, 135-178, Springer.

Zangerl C., Eberhardt E. & Perzlmaier S., 2010: Kinematic behaviour and velocity characteristics of a complex deep-seated crystalline rockslide system in relation to its interaction with a dam reservoir. - Engineering Geology 112/1-4, 53–67.

Landslide stabilization by piles: A case history

Stabilisation des glissements de terrain par des pieux : un cas d'étude

Şengör M.Y.
Yuksel Project Co. Inc., Ankara, Turkey

Ergun M.U., Huvaj N.
Middle East Technical University, Ankara, Turkey

ABSTRACT: During the foundation excavation of an industrial plant in Eskişehir, Turkey, a landslide occurred in the neighbouring slope, and consequently, the excavation had to be stopped. The instability occurred in a natural slope which had an average slope angle of 9-13 degrees. The aerial extent of the slide mass was 400 m by 115 m. The material in the slope was 7 to 20 meter-thick colluvium (slide debris), which constitutes a historic landslide mass, underlain by a gravelly sandy silty clay matrix containing limestone blocks, weathered tuff and tuff. Soil profile and location of the slip surface were determined through a site investigation program including nine boreholes and inclinometers. A back analysis was carried out and shear strength parameters of the slope forming materials were determined. Slope stability analyses were carried out, stabilization alternatives were evaluated and slope stabilization by piled retaining walls was considered as the most feasible alternative. The analyses and design procedure for the piles will be presented together with a summary of existing analyses and design methods for landslide stabilizing piles.

RÉSUMÉ : Pendant les excavation des fondations d'un site industriel à Eskisehir, en Turquie, un glissement de terrain a eu lieu dans un talus voisin, et par conséquent, les travaux ont été arrêtés. L'instabilité s'est produite dans un terrain naturel présentant une pente moyenne de 9 – 13 degrés. Les dimensions en plan du glissement étaient de 400 m par 115 m. Le matériau du glissement était composé de colluvions, sur 7 à 20 m d'épaisseur, qui constituaient une masse de glissement postérieur. Les colluvions reposaient sur une argile graveleuse et sablo-limoneuse contenant des blocs de calcaire, du tuf sain et du tuf altéré. La coupe géotechnique du site et la localisation de la surface de glissement ont été mises en évidence par une campagne d'investigations incluant neuf forages et inclinomètres. Les paramètres de résistance au cisaillement des terrains en place ont été déterminés par une rétro-analyse. Suite aux études de stabilité des pentes et à l'examen des systèmes de renforcement alternatifs, la solution de stabilisation par une paroi en pieux s'est avérée comme la plus judicieuse. Les analyses et la procédure de dimensionnement pour ces pieux vont être présentées en même temps qu'un résumé des analyses et des méthodes de calcul existantes sur la stabilisation des glissements par pieux.

KEYWORDS: landslide, piles, inclinometer.

1 INTRODUCTION AND SOILS AT THE SITE

Instability occurred in a natural slope which had an average slope angle of 9-13 degrees, during excavation works near the toe. The aerial extent of the slide mass was 400 m by 115 m. The construction site was located at the toe of this sliding mass (Figure 1). The slope movement had a NW-SE direction. The material in the slope was 7 to 20 meter-thick colluvium (slide debris), which constitutes a historic landslide mass, underlain by gravelly sandy silty clay layers with limestone blocks, weathered tuff and unweathered tuff at different borehole locations. The colluvium was also composed of pieces of limestone cobbles and blocks in a clayey silty matrix.

It was observed that the slide debris lies on tuff. The pliosen age tuffs are approximately 100 m thick and lies on limestone. In the borehole descriptions the tuff layer at the upper levels are weathered to highly weathered condition and can be considered as a transition between rock and soil and identified as a layer of stiff clay. Samples from this weathered tuff had natural water content 19-43% (high natural water content such as 43% was obtained near the shear surface at about 20 m depth at borehole SK9). Since this material can be considered clay-like, Atterberg limits are determined LL=45-49%, PI=11-28% (for the material near the shear surface LL=49-66% and PI=27-36%), fines content=34-74% and clay-size fraction was 23-57%, and the material can be classified as CL, ML, GC and SC. The natural unit weight of samples were 20-21 kN/m^3. Unconfined compressive strength of this material was 30-240 kPa and UU triaxial tests gave c_u=13-44 kPa and ϕ_u=11-22°. Since the

residual shear strength will be of interest in this reactivated landslide case, direct shear tests were carried out on limited number of undisturbed samples taken from near the shear surface in order to find the residual friction angle. 46 mm diameter specimens were sheared undrained without submerging in water, then sheared continuously and slowly to reach residual condition. From the lab tests it was concluded that the 100 and 250 kPa undrained shear strength for tuffaceous clay and clayey tuff are reasonable values. Drained friction angle of slope debris/colluvium was 15-20 degrees, and tuffaceous clay taken from near the shear surface had 10.2 degrees residual friction angle.

1.1 *Soil Profile and The Mechanism of the Slope Movement*

The sliding mass has grown progressively backward into the slope as multistage rupture surfaces from the toe of the landslide developed. First, the tension crack (scarp) C1 has been observed while excavation works were going on. Then, within about 15 days, there were total of four major tension cracks (visible scarps) (C1 to C4 in Figures 1 and 2) and one meter horizontal and vertical movements have been observed at the ground surface. Fifty days after the start of the first scarp, a small road located at the slope was observed to move 15 m downslope and 4 m in vertical direction.

Nine boreholes are opened at a line of NW-SE direction which is also the direction of the movement and inclinometers are also placed in these boreholes. In all boreholes except SK7, SK8 (at the toe) and SK6; the top layer is slope debris and

below that tuffs sometimes in clayey state and sometimes in harder state are encountered.

2 ANALYSES AND RESULTS

In this section the types of the analyses , the results of the back-analyses of the landslide movement and then the stabilization works will be presented.

2.1 *Back-Analyses and the Shear Strength Parameters*

In all boreholes inclinometer readings were taken, and the depth of the slip has been determined. As it is a fast movement, all inclinometer pipes were sheared by the landslide (except SK-3 and SK-8) shortly after they are placed. These depths were considered as the depth of the slip surface. The cross section of the landslide were prepared according to the borehole data and inclinometer readings and the scarps of the progressive slips. The positions of the slope debris and tuff layers and also the scarps of the progressive failure slides are shown in Figure 2. The shear surface passes mostly through the colluvium material in the upper half of the sliding mass, whereas it passes near the contact between the colluvium and tuff (more within the tuff) in the lower half of the sliding mass. There was no groundwater level, however in stability analysis to be on the safe side some water level is considered.

Figure 1. General layout plan

It was not easy to take samples from the sliding mass near the shear surface, therefore only a limited number of soil samples were tested in the laboratory. Determination of the soil parameters at the sliding surface of a landslide at the limit equilibrium state by the back analyses of the movement is a widely used method. In this method the c and ϕ parameter couples are determined which give a factor of safety value of one at the sliding surface. In the back analyses the cohesion and angle of friction parameter couples for the tuff and the slope debris layers are identified. In this case the number of the unknowns is four. They are decreased progressively using a methodology given below.

At the first stage, the back analyses of sliding surfaces of C3 and C4 were performed. By this way the parameters for the slope debris were determined as c′=5.6 kPa and ϕ′=15.7°, E′=35 MPa are used in the analyses.

At the second stage, calculations for sliding surfaces of C1 and C2 were performed. The above parameters were used for slope debris, and the shear strength parameters for the tuff layers were determined. The parameters for the weathered tuff layer at the sliding level are assessed as c′=0 kPa and ϕ′= 9.2°. But these parameters were not suitable to use for the whole tuff layers. Table 1 summarizes the parameters used in the analyses.

Table 1. Material properties used in analyses

Material	Drained			Undrained	
	c′ (kPa)	ϕ′ (°)	E′ (MPa)	c_u (kPa)	E_u (MPa)
Slope debris	5.6	15.7	35	60-75	20
Weathered tuff (first 3 m)	0	9.2		100	60
Unweathered tuff	20	25	60	250	130

Undrained triaxial compression and consolidated drained direct shear tests were performed on the debris and tuff soil samples from the boreholes which are located between the slope debris and tuff layers. The results of these tests show that the internal friction angle for the slope debris and for the clay soil originated form tuff are 15 to 20° and 10.2° respectively. This findings support the results of the back analyses.

2.2. *Slope Stabilization by Piles*

Piles used in slope stabilization are subject to lateral force caused by the movement of surrounding soil, and they are called "passive piles" (Viggiani 1981; Poulos 1995). One of the major issues in the design of these piles is the magnitude of the force on the pile. Since this is related to the soil movement and soil movement is influenced by the presence of piles, the interaction between the passive piles and the soil is quite complicated. There exists a number of empirical, analytical, and numerical methods available in the literature about the design of piles used in slope stabilization (Brinch Hansen 1961, De Beer 1977, Fukuoka 1977, Ito and Matsui 1977, Sommer 1977, Winter et al. 1983, Popescu 1991, Reese et al. 1992). Some of these methods are pressure or displacement-based and some of them are numerical methods, such as finite element and finite difference (Kourkoulis et al., 2012).

In the pressure or displacement based methods, the pile is modeled as a beam supported by springs at its sides. A single laterally loaded pile is considered, and the ultimate soil-pile resistance is correlated with the undrained shear strength for clays, and with the overburden stress and friction angle for sands. In these methods group effects are taken into account by using reduction factors. Although spring constants are dependent on pile deflection, or the movement of the soil, they are typically assumed constant. In the current study this approach is used.
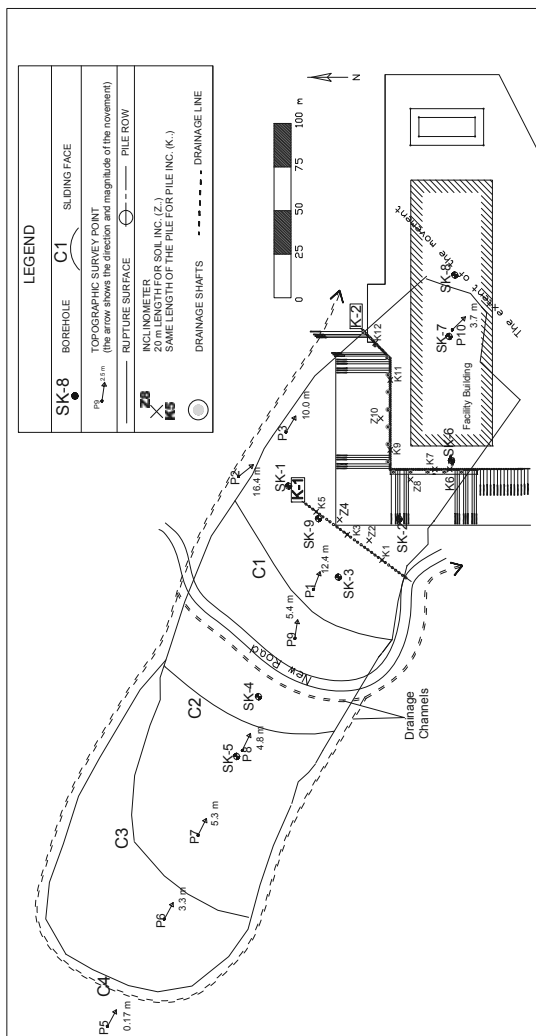
The general design procedure consists of two main steps: Step 1: Provision of the required total lateral force needed to increase the factor of safety of the slope to the desired value (based on analysis of the unreinforced slope). Step 2: Calculation of loading on piles and pile lateral capacity.

In the last few years, 3-dimensional finite-element and finite-difference methods are becoming increasingly popular. Using these methods complex geometries and complicated phenomenon such as soil arching, pile group effects, nonlinearity of soil and pile could be modeled. Use of 3D numerical methods is still not very attractive to practitioner engineers because of the long computational time and learning effort. Kourkoulis et al. (2012) developed a hybrid solution to the problem, combining the benefits of accurate 3D finite element simulation with the simplicity of widely accepted analytical techniques.
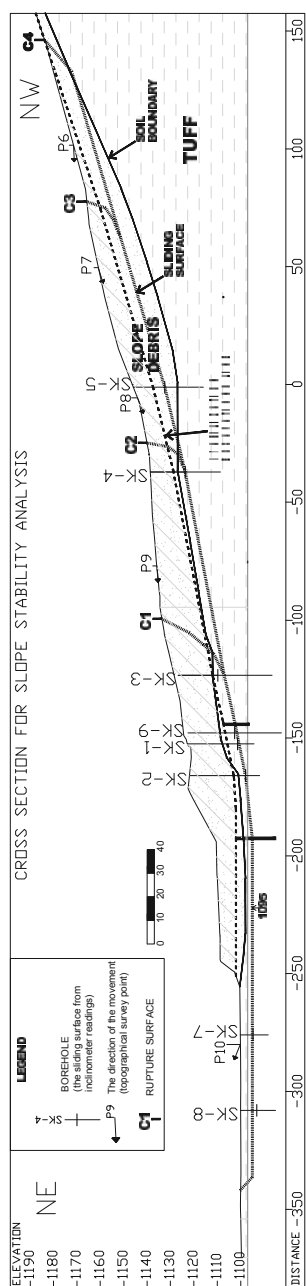
Figure 2. Cross section for the analyses

2.2 *Stabilization Works for Foundation Excavation and Prevention of the Slope Movements*

As a result of the preliminary works it is understood that the diameter of the stabilizing passive piles should be 1.2 m and more than single pile row would be needed. The depth of the sliding mass was 20 m at the centerline. It was not possible to stabilize this amount of soil mass by two rows of piles only. So stabilizing excavations were needed to decrease the amount of sliding mass (about half of the sliding depth was removed-see Figure 2), and then the following piled analyses were performed.

1. Slope Stability (GEOSLOPE 6.02, SLIDE 5.014) / Structural Analyses (SAP 2000, V8.4)

2. Finite Element Method (PLAXIS 2D, V8.6)

In this stabilization program, one row of stabilizing piles are placed at an upper level (Pile Row K1 in Figure 1). The lower row of piles (Pile Row K2 in Figure 1) will also have a function of retaining wall for the facility. To decrease the moment and the displacements of the piles in this second row, permanent ground anchorages were planned at the top beam of the piles.

The most critical issue in the analyses were the excavation works for the foundation of the facility which would be performed after the stabilizing works were completed. Because of the excavations just behind the second row of the piles, the pile displacements and the moments were increasing for both row of piles. This critical concept was best configured in 2D finite element analyses (figure 3).

2.3 *Finite Element and Limit State Analyses*

The place of the two rows of the stabilizing piles is shown in the plan view in Figure 1. In the analyses the construction stages were excavations for stabilization, the construction of the piles and the foundation excavations to the 1095 m elevation just in front of the K2 Pile Row. For the drained analyses of the K1 pile row it was found that the pile head displacement as 18 cm, the shear force as 468 kN/m and the bending moment as 1240 kN.m/m. The same values for the K2 pile row were 10.8 cm, 387 kN/m and 970 kN.m/m, respectively.

The horizontal peak ground acceleration at the construction site was accepted as 0.25g and accordingly the seismic stability of the stabilizing system was also checked. The slope stability analyses of the final stage of the works were repeated for a horizontal seismic ground acceleration of 0.125g.

The cohesive soil exerts a pressure on the piles when it tries to pass between the piles forming a failure mechanism. This pressure being related to the undrained cohesion of the soil and is a limit value to be checked (see Eq. 1). This equation is valid for s≥3d where s is the pile center-to-center spacing and d is the pile diameter. If s<3d there will be a reduction up to a factor of 0.5.

$$p = c_u k D \tag{1}$$

Active and passive lateral earth pressures are represented by spring constants k above and below sliding surface. The k values for this case were 1.30 for the passive side of the lower level (K2) piles and 1.34 and 0.86 for the passive and active side of the upper level (K1) piles. These are lower than the limit values (Ergun, 2000).

3 CONCLUSION

A long landslide which progresses backwards had occurred because of the foundation excavations of an industrial plant which coincided with the toe of a historic landslide. The construction works were stopped, and the landslide was investigated through boreholes. The clayey debris (colluvium) containing limestone cobbles and boulders had slided over

plastic tuffs. Back analyses and the laboratory tests were performed for the determination of the shear strength parameters at the sliding surface. Two rows of stabilizing piles were designed through the sliding mass and the structural analyses and also FE analyses of these piles were performed independently.
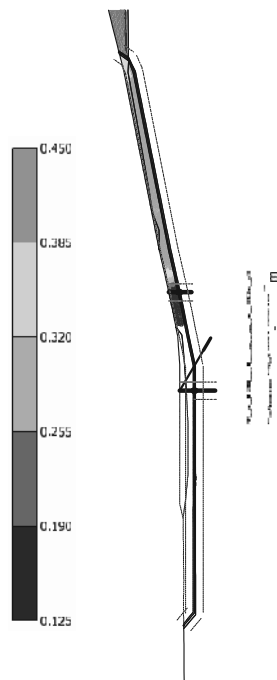

Figure 3. Total displacements plot of FE analysis

10 to 15 m deep excavations were performed for the first stage of the stabilization works. The upper level piles (K1) were 12 m in length and 1.2 m in diameter. Center to center spacing of piles were 2.5 m. The total number of stabilizing piles is 30 covering a longitudinal length of 72 m reaching the South edge of the landslide. The 2nd row of stabilizing piles (K2) was also used as the retaining walls of the facility. The 1.2 m diameter bored reinforced concrete piles are placed with 1.25 m spacing in this row. The pile lengths are 17 m. The total length of the pile row is 137 m in plan view passing over the South edge of the landslide.
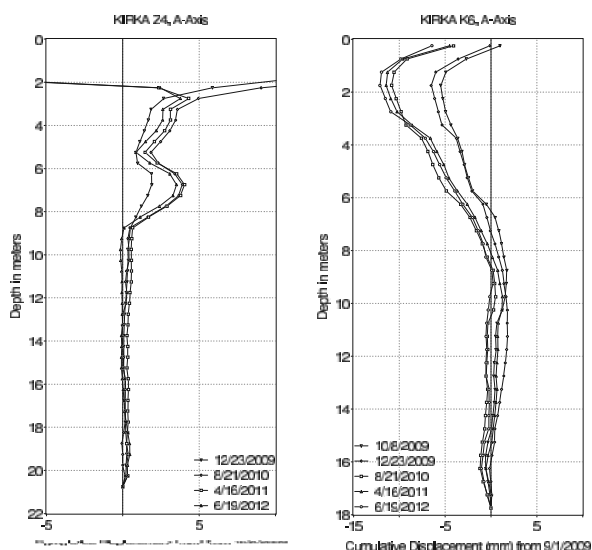
Figure 4. Cumulative displacements (mm) at Z4 (soil) and K6 (pile) inclinometers

The permanent ground anchors were constructed at the head beam of the piles with 1.25 m spacing, 30 to 35 m in length and inclined at 30 and 45 degree to the horizontal.

No drainage system was planned in the sliding mass. Instead surface drainage was implemented as reinforced concrete drainage channels at the edges of the landslide and at the upper levels of the new road. Behind the retaining walls of the construction site 0.60 m diameter vertical drainage shaft between the piles were planned and the collected groundwater was transferred to the water drainage system of the facility.

The deformations of the system are controlled by the 12 inclinometers (8 in the soil, 4 in the piles) at each stage of the construction works. There are no displacements in three years (Figure 4).

4 REFERENCES

Brinch Hansen, J. 1961. The Ultimate Resistance of Rigid Piles against Transversal Forces. *Bulletin of the Danish Geotechnical Institute* (12).

De Beer, E. 1977. Piles Subjected to Static Lateral Loads. Proceedings, 9th I.C.S.M.F.E., Specialty Session 10, Tokyo.

Ergun. M.U. (2000), "Stabilization of Landslides using Piles", Landslides in Research, Theory and Practice, Proceedings of the 8th International Symposium on Landslides, Vol.1, pp:513-518, Cardiff, 2000.

Fukuoka, M., "The Effects of Horizontal Loads on Piles due to Landslides", Proceedings, 9th I.C.S.M.F.E., Specialty Session 10, Tokyo, 1977

Ito, T. and Matsui, T., "The Effects of Piles in a Row on the Slope Stability", Proceedings, 9th I.C.S.M.F.E., Specialty Session 10, Tokyo, 1977

Kourkoulis, R. Gelagoti F., Anastasopoulos I, and Gazetas, G. (2012) Hybrid Method for Analysis and Design of Slope Stabilizing Piles, *Journal of Geotechnical and Geoenvironmental Engineering*, v138(1), pp:1-14.

Popescu, M.E., "Landslide Control by Means of a Row of Piles", Slope Stability Engineering, Thomas Telford, pp: 389-394, London, 1991

Poulos, H. G. (1995). "Design of reinforcing piles to increase slope stability." *Can. Geotech. J.,* 32(5), 808–818.

Reese, L., Wang, S., and Fouse, J. "Use of Shafts in Stabilizing a Slope", Slopes and Embankments-II A.S.C.E., Speciality Session, 1992

Sommer, H., "Creeping Slope in a Stiff Clay", Proceedings, 9th I.C.S.M.F.E., Specialty Session 10, Tokyo, 1977

Viggiani, C., "Ultimate Lateral Load on Piles Used to Stabilize Landslides", Proceedings, 10th I.C.S.M.F.E., Vol.3, pp: 555-560, Stockholm, 1981

Winter, H., Schwarz, W. and Gudehus, G., "Stabilization of Clay Slopes by Piles", Proceedings, 8th European Conference on S.M.F.E., pp: 545-550, Helsinki, 1983

Landslide Susceptibility Mapping Using Bayesian Conditional Probability Model at An Linh Commune, Tuy An District, Phu Yen Province, Vietnam

Élaboration de la carte de risques de glissement de terrain sur la commune de An Linh, district de Tuy An, province de Phu Yen, à l'aide d'un modèle Bayesien de probabilité conditionnelle

Son N.T.
Tuy Hoa Industrial College, Phu Yen Province, Vietnam

Ha P.T.S.
Faculty of Geology and Petroleum Engineering, Ho Chi Minh City University of Technology, Ho Chi Minh City, Vietnam

Son L.M.
flatGEO Consulting Co., Ltd.

ABSTRACT: Landslide phenomenon at An Linh commune, Tuy An district, Phu Yen province is more and more severe year after year. The prediction of a highly landslide susceptibility zone will support the government and local residents to save their properties. In this paper the authors carried out the landslide susceptibility mapping at An Linh commnune using the deterministic approach with knowledge-driven methods and the stochastic approach with data-driven methods. The deterministic approach is conducted using traditional survey, field investigation, geophysical survey… to evaluate not only geotechnical properties of rock and soil materials but also the mechanism of landslide phenomenon in the studied area. The stochastic approach with probability methods is chosen to evaluate the weights of influence factors such as the elevation, aspect, slope angle, distance to roads and distance to drainages, geology and topographical wetness index of the materials. Landslide susceptibility zonation is developed using the model of Bayesian conditional probability with different criteria for weighting factor calculation integrated with GIS analytical tools. Landslide susceptibility maps from different models are validated with the current landslide inventory to select the most reasonable model for the study area.

RÉSUMÉ : Les glissements de terrain sont devenus de plus en plus fréquents sur la commune de An linh, district de Tuy An, province de Phu Yen, au cours des dernìeres années. Les auteurs ont réalisé une carte de risques de glissement de terrain sur la commune An Linh selon une approche déterministe fondée sur une connaissance experte et à l'aide d'une approche stochastique basée sur les données. L'approche déterministe est conduite à partir des méthodes de reconnaissance, d'observation du terrain, de prospection géophysique… afin de quantifier non seulement les propriétés géotechniques du sol et de la roche mais aussi le mécanisme de glissement de terrain dans la région concernée. L'approche stochastique fondée sur les modèles statistiques est choisie pour évaluer le poids de facteurs d'influence comme l'altitude, l'aspect, la pente, la distance aux cours d'eau, la distance aux voies routières, et au drains, les paramètres géologiques, et l'indice de l'humidité des sols. Le zonage des risques de glissement de terrain a été développé en utilisant un modèle de probabilité conditionnelle de Bayes avec différents critères de calcul du poids des variables, en intégrant les outils analytiques de SIG. Les cartes de risques élaborées selon ces modèles ont été validées à l'aide de l' inventaire des glissements actuels afin de choisir le modèle le plus approprie pour ce site.

KEYWORDS: Landslide susceptibility; Bayesian conditional probability; Stochastic model.

1 INTRODUCTION

The study area locates at An Linh commune, Tuy An district, Phu Yen province in the south central coast of Vietnam (see Fig. 1).
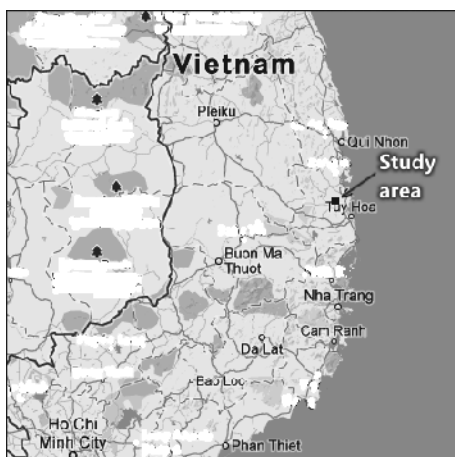

Figure 1. Location of the study area

During the past few years, landslides often occur in the study area after heavy and long rains. This phenomenon damages roads and construction works and results in serious cracks in the residential areas that in turn affect to human lives. Therefore the landslide prediction is an urgent task for scientists to support the government in planning and save human lives of local residents.

1.1 *Geographic characteristics*

An Linh area which has hill and mountain landscape locates on the eastern side of Van Hoa highland whose elevation of $12 \sim 500$m. In that area, hills are rounded and have steep slopes, decorated by narrow valleys which follow along north-south direction. The ground surface which inclines to the north is a bare area with basaltic boulders or cobbles. This topographic landscape is favorite for erosion progress and stimulate landsliding and cracking process.

The study area belongs to the monsoon tropical region with oceanic climate. The annual precipitation is approximate 2000mm. Especially in the rainy season the precipitation can reach $70 \sim 80\%$ the annual precipitation. Furthermore, the precipitation concentrates in a short time – only one or two months at the end of a year.

Water systems strongly develop with Cai river and Ho Lo river in the west and the east respectively. Both rivers form a hydrological network distributed evenly in the study area.

1.2 *Geological characteristics*

A general stratigraphy of the study area composes of following formations:

Table 1. Brief description of geological formations

Formation	Composition
Phong Hanh formation ($\varepsilon - Sph$)	Quartzite of blocky structure, quartz-sericite schist
Mang Yang formation (T_2my)	Boulders, cobbles, sandstone, siltstone and claystone, blocky structure, thick bedding
Kon Tum formation (N_2kt)	Green, dark grey, greenish grey basalt, bubble or porosity structure, fracturing; diatomite, clay with diatomite, basalt with interbedded clay
Dai Nga formation ($N_2 - Q_1dn$)	Greenish grey, dark grey basalt, blocky structure, fracturing
Quaternary formation	Boulders, cobbles, gravel, sand, silt, clay

1.3 *Landslide characteristics*

Landslide occurs mainly at low areas with elevations less than 200m and gentle slopes (slope angles vary from 5° to 20°) in heavily weathered rocks which compose of clay, swelling clay with diatomite… Landscape after sliding forms terraces with many fractures on the ground surface. Landslide exposures usually locate at positions associated with hydrological factors. There are water flows at the toe of slopes in massive landslides. The shear strength of soils within landslide areas is rather low (cohesions vary from 12 to 17kPa, friction angles from 10° to 13°).

1.4 *Landslide causes*

The fieldwork study shows some of causes of landslides in the study area:

- Heavy landslides ususally occur at geological structures which compose of clay, clay with diatomite underlying thin heavily weathered basaltic layers. Soils and rocks at landslide areas are different in permeability, swelling, strength (weak soils overlay hard rocks).

- The erosion process occurs at the toe of slopes and piping develops due to the surface run off and underground water flow.

- Heavy and long rains cause rocks and soils swelling or liquefaction that in turn cause the volume change suddenly.

- Human activities also take part in the landslide trigger: the forest clearance, reservoir and rice field preparation… Those activities result in loosing strength at the toe of slopes.

2 LANDSLIDE SUSCEPTIBILITY MAPPING

2.1 *Theoretical Background*

Nowadays there are two common groups of methods for landslide prediction:

a) Knowledge-driven methods: those methods are based on experiences of experts and rely on empirical relationships.

b) Data-driven methods: those methods analyse collected data and establish models based on the inherent relationship of data. This approach, especially, Bayesian conditional probability method will be applied for the landslide susceptibility mapping in this research. In Bayesian conditional probability method, the likelihood of event D given the presence of factor B can be expressed as the prior probability:

$$P\{D \mid B\} = \frac{P\{D \cap B\}}{P\{B\}} = P\{D\} \frac{P\{B \mid D\}}{P\{B\}} \qquad (1)$$

On the contrary, the unlikelihood of event D given the presence of factor B is the probability:

$$P\{\overline{D} \mid B\} = \frac{P\{\overline{D} \cap B\}}{P\{B\}} = P\{\overline{D}\} \frac{P\{B \mid \overline{D}\}}{P\{B\}} \qquad (2)$$

where

$P\{D \mid B\}$	the likelihood of event D given the presence of factor B
$P\{\overline{D} \mid B\}$	the unlikelihood of event D given the presence of factor B
$P\{B \mid D\}$	the likelihood of factor B given the presence of event D
$P\{B \mid \overline{D}\}$	the likelihood of factor B given the absence of event D
$P\{D \cap B\}$	the probability of the presence of both event D and factor B
$P\{B\}$	the probability of the presence of factor B

If there are more datasets (more B factors) involved in the mapping prediction and those datasets are conditionally independent to each other with respect to a set of landslide occurences, the Bayesian conditional probability of event D is expressed by the following formula:

$$P\{D \mid (B_1 \cap B_2 \cap \ldots \cap B_n)\} = \frac{e^{(\log it\{D\} + \sum W^k)}}{1 + e^{(\log it\{D\} + \sum W^k)}} \qquad (3)$$

where

$$\log it\{D\} = \ln \frac{P\{D\}}{1 - P\{D\}} \qquad (4)$$

$$W^+ = \log \frac{P\{B \mid D\}}{P\{B \mid \overline{D}\}} \qquad (5)$$

$$W^- = \log \frac{P\{\overline{B} \mid D\}}{P\{\overline{B} \mid \overline{D}\}} \qquad (6)$$

W^k: positive weight (W^+) or negative weight (W^-) of factor B depending on the presence or absence of factor B

The total weight of all B factors at each pixel on the prediction map is the sum of W^k, in which W^k will be the positive weight W^+ if the factor B is present or negative weight W^- if B is absent.

The constrast of weight is:

$$C_W = W^+ - W^- \qquad (7)$$

2.2 *Landslide susceptibility mapping*

After the landslide survey at the end of year 2010, 142 landslide occurences are recorded in which 103 positions are used for the landslide susceptibility prediction by Bayesian conditional probability and 39 occurences are used for the validation. The location of 103 landslide occurrences is presented in Fig 2. Black plus symbols on this figure are landslide occurences.

There are seven factors chosen for the calculation of the landslide probability: elevation (DEM), slope direction (ASPECT), slope angle (SLOPE), geology (GEO), distance to road (DTR), distance to drainage (DTD), topographical wetness

index (TWI). Each factor is classified into several classes; the positive and negative weights of each class for each factor are calculated using an open-source software ILWIS (Integrated Land and Water Information System). To each factor, a class trigger for positive or negative weight is chosen at the class whose contrast reaches the highest value (see highlight classes in Table 2).
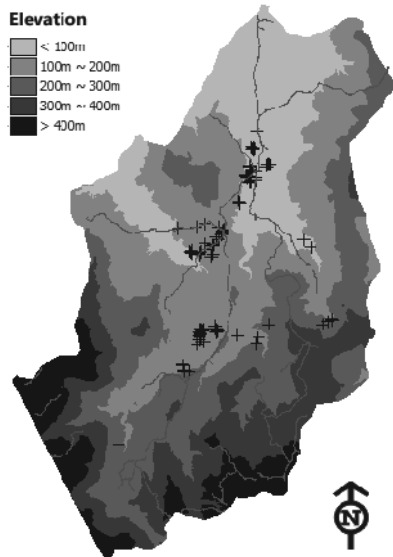

Figure 2. Landslide inventory map for modelling (103 points)

Table 2. Weight values of classes from parameters

Parameter	Value	W⁺	W⁻
DEM	100m ~ 200m	0.620	-0.488
ASPECT	West	0.470	-0.121
SLOPE	0° ~ 10°	0.073	-0.078
GEO	Claystone, sandstone with diatomite	1.009	-1.960
DTR	< 100m	0.758	-0.274
DTD	300m ~ 400m	0.881	-0.180
TWI	4 ~ 6	0.137	-0.077

The flow chart of the procedure for landslide susceptibility mapping by Bayesian conditional probability is shown in Fig. 3.

Weights of seven factor maps are calculated and expressed as weight maps and displayed in Fig. 4 to Fig. 10.

The Bayesian conditional probability map is derived from seven factor maps using the formula (3). However the slicing of this probability map into landslide susceptibility zones is not applicable because the ranges of landslide probability on different probability maps from different methods are totally different. Therefore the probability pattern is sliced into susceptibility zones using the ranking of predicted probability value instead of predicted value itself (Chung and Fabbri, 2003). A pixel of highest probability will be assigned the highest rank and pixel of lowest probability will be the lowest rank. After ranking all pixels within the study area, the landslide zoning could be carried out using predefined threshold values of different zones: high, moderate and low susceptibility.

In the study area, those threshold values are 15%, 25% and 60% for the high, moderate and low susceptibility area respectively. The landslide susceptibility map is presented in Fig. 11.

2.3 *Validation*

The landslide susceptibility map is validated by using 39 heavy landslide occurences (white plus symbols on Fig. 12). Among them there are 31 points classified as high landslide susceptibility (80% accuracy).
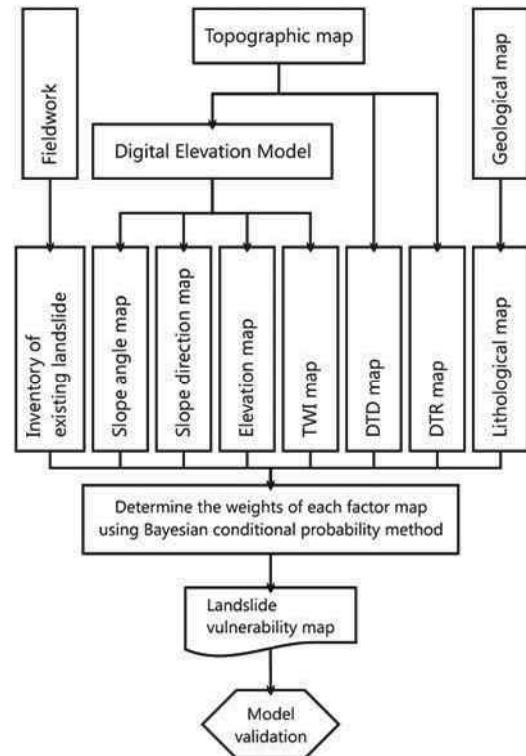
Figure 3. Procedure of landslide susceptibility mapping
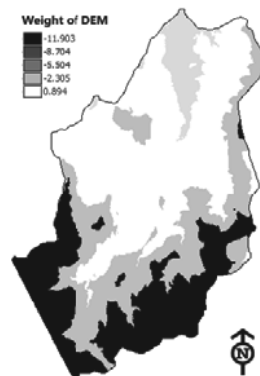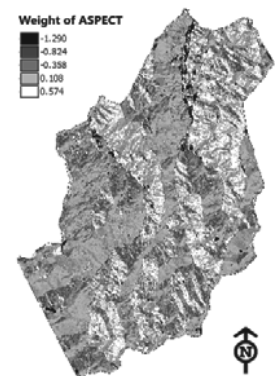

Figure 4. Weight of elevation factor

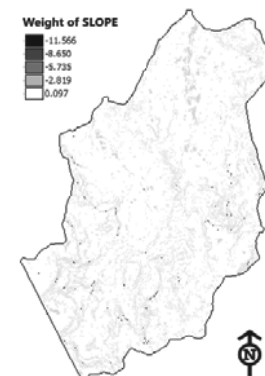Figure 5. Weight of aspect factor

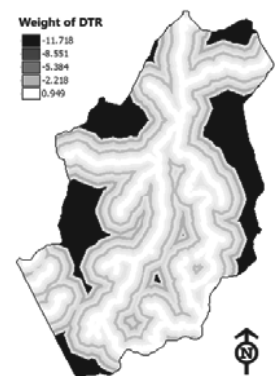Figure 6. Weight of slope angle factor
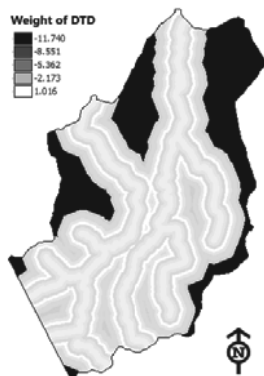

Figure 7. Weight of DTR factor
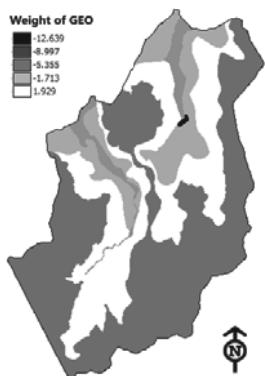
Figure 8. Weight of DTD factor

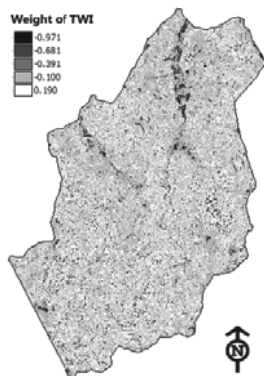Figure 9. Weight of geological factor

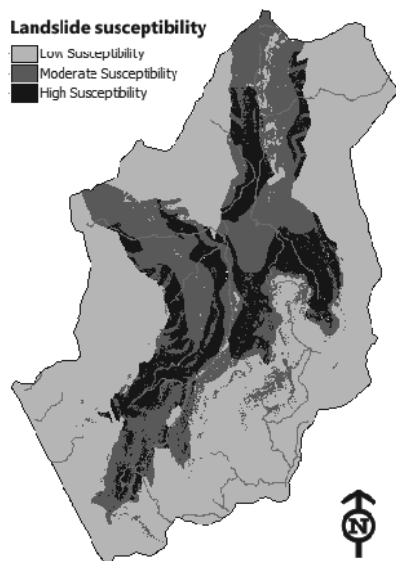Figure 10. Weight of TWI factor

Figure 11. Landslide susceptibility map

3 CONCLUSION

a) The landslide susceptibility map shows that most of landslide occurences concentrate at the areas of low elevation (100~200m), gentle slopes (slope angles vary from 5° to 20°), high TWI values (high water accumulation).

b) Landslides are also triggered due to the road construction. The roadway cuts into the slope faces and reduces the stability of slopes. Landslides occurs near the road construction sites (approximate 100m far from roads).

c) Landslides also distribute along the east-west direction which coincides with the direction of narrow valleys of steep slopes in the study area.

d) The results of Bayesian conditional probability model and the fieldwork survey show that landslides occur usually in soil layers with high proportion of clay and diatomite clayey soils which are heavily weathered.

e) The Bayesian conditional probability model gives the reliable result of landslide susceptibility for the study area. The validation was conducted for 39 heavy landslide positions which show that there are 31 positions (80% accuracy) located in the high landslide susceptibility zone.

f) The reliability of this model could be improved year after year when new landslide occurences are updated annually in the landslide inventory.
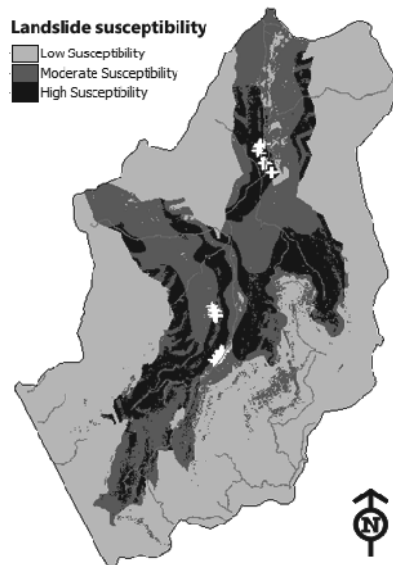

Figure 12. Landslide location for model validation (39 points)

4 REFERENCES

Bonham-Carter G.F. 1994. *Geographic Information Systems for Geoscientists: Modelling with GIS*, Volume 13 (Computer Methods in the Geosciences). Pergamon.

Brett G. Dickson et al. 2006. Mapping the Probability of Large fire Occurrence in Northern Arizona, USA. *Landscape Ecology* (21), 747-761.

Chung C.F. and Fabbri A.G. 1999. Probabilistic Prediction Models for Landslide Hazard Mapping. *Photogram Engineering Remote Sensing* (65), 1389-1400.

Chung C.F. and Fabbri A.G. 2003. Validation of Spatial Prediction Models for Landslide Hazard Mapping. *Natural Hazards* (30), 451-472.

Lee S., J. Choi , K. Min. 2002. Landslide Susceptibility Analysis and Verification Using the Bayesian Probability Model. *Environmental Geology* (43), 120-131.

Raul Romero-Calcerrada et al. 2008. GIS analysis of spatial patterns of human-caused wildfire ignition risk in the SW of Madrid (Central Spain). *Landscape Ecology* (23), 341-354.

Influence of Ground Motion Variability on Seismic Displacement Uncertainty

Influence de la variabilité des mouvements de terrain sur l'incertitude des déplacements en régime sismique

Strenk P.M.
Golder Associates, Inc., Reno, Nevada, USA

Wartman J.
University of Washington, Department of Civil and Environmental Engineering, Seattle, Washington, USA

ABSTRACT: A series of probabilistic seismic displacement analyses were performed to understand how material property variability coupled with systematic changes in the type and complexity of ground motion variability affect the displacement prediction uncertainty of the Newmark rigid-block method.

RÉSUMÉ: Une série d'analyses probabilistes des déplacements en régime sismique ont été effectués pour comprendre comment les variations des propriétés des matériaux couplées avec le type et la complexité des variabilités des mouvements de terrain affectent les incertitudes dans les prédictions de déplacement avec la Méthode des blocs rigides de Newmark.

KEYWORDS: Newmark, displacement, seismic, probabilistic, ground motion, variability, uncertainty, Monte Carlo

1 INTRODUCTION

Seismic slope deformation methods are used to make predictions of earthquake-induced permanent displacements in natural slopes and man-made dams and embankments. The predictive capability of well-established methods such as rigid-block (Newmark 1965) and decoupled (Makdisi and Seed 1978) procedures, however, are often associated with a high-degree of uncertainty which is a consequence of both parametric and modeling sources of variability. Parametric variability describes a method's sensitivity to the range of input parameters (e.g., shear strength, groundwater and earthquake ground motions) and is a function of the number of input parameters as well as the amount of variability in each parameter. Modeling variability is related to how well the method captures the actual physical mechanism of seismic-induced deformation when all input parameters are fully known. Although the majority of deformation-based method available today have a common conceptual origin in the sliding-block model proposed by Newmark (1965), differences in their analytical formulation, procedural structure, underlying assumptions and mathematical or regression functional form can result in different predictive capabilities and sensitivities to parametric variability (Strenk and Wartman 2011).

In seismic slope deformation analyses, parametric variability comes from parameters characterizing the seismic demand (earthquake ground motions) and those characterizing the slope's seismic resistance (represented by the seismic yield coefficient, k_y which is a function of the slope geometry, shear strength and groundwater conditions). In a probabilistic framework, the interplay between these two sources of parametric variability can make evaluating their relative contributions to total displacement uncertainty a difficult task. The main focus of this study is to examine how ground motion variability influences the prediction uncertainty of the Newmark (1965) rigid-block method. To that end, a series of probabilistic seismic slope deformation analyses were performed on an idealized slope for a scenario earthquake event. Displacement uncertainty was quantified for several scenarios designed with increased levels of ground motion variability. Variability in the seismic resistance of the slope was also included. In this approach, realistic levels of variability in both seismic resistance and demand are systematically changed to evaluate their collective effect on displacement prediction uncertainty.

2 PROBABILISTIC DISPLACEMENT ANALYSIS

Performing a rigid-block analysis consists of the following steps: (1) a limit-equilibrium pseudostatic slope stability analysis to compute k_y; and (2) characterization of the earthquake-induced shaking at the site. The seismic yield coefficient represents the minimum acceleration required to initiate down-slope displacement of a slide mass. In the rigid-block method, earthquake shaking is characterized by acceleration time-histories that represent a rock outcropping condition which is consistent with the concept of slide mass rigidity assumed by Newmark (1965). Each of these analyses was implemented in a probabilistic framework using Monte-Carlo simulation. All simulations were performed for 1000 iterations using Latin-Hypercube sampling of the input distributions.

The idealized slope model has a height of 20 m with a slope face inclined at an angle of 18 degrees. The failure surface shown in Figure 1 is intended to represent a first-time, shallow translational landslide. Shear strength of the landslide material (unit weight, $\gamma = 20$ kN/m^3) was assumed to be controlled by the peak friction angle (ϕ'_{peak}) only.
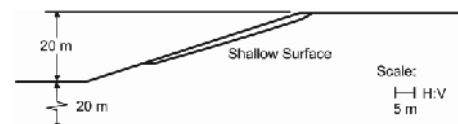

Figure 1. Cross-section of the idealized slope model with a shallow failure surface (maximum thickness of 2 m).

The scenario earthquake used for this analysis is the 1994 Northridge event (moment magnitude, $M_w = 6.7$), in California, USA. The slope was assumed to be located 28 km to the northwest of the epicenter. Based on the assumed site location, acceleration time histories were selected from recording stations that recorded the Northridge event. Four stations were selected: (1) Lake Hughes 12A (LHA); (2) Castaic-Old Ridge Road (ORR); (3) Vasquez Rock Park (VAS); and (4) Newhall-West

Pico Canyon Road (WPI). These time-histories were rotated to their fault-normal/parallel components and only the fault-normal components were used in the analysis.

3 GROUND MOTION VARIABILITY

Shaking experienced at the hypothetical site was characterized using published ground motion prediction equations (GMPE) using a pseudo-probabilistic approach to model variability in the ground motions. In this approach, the Abrahamson and Silva (2008) GMPE was used to obtain a median acceleration response spectrum and the intra-event component of standard deviation (σ) (i.e., single-event variability) for the median prediction. Variability was modeled by varying the number of standard deviations (n_σ) around the median spectrum ($n_\sigma = 0$) as a normally-distributed random variable ranging from $n_\sigma = -3$ to +3. The use of a normal distribution achieves symmetry in the range of n_σ generated while preserving the underlying log-normal distribution of the spectral ordinates. Different target response spectra were obtained by multiplying n_σ by the intra-event standard deviation and adding or subtracting this from the medium spectrum. The median, $\pm 1\sigma$ and $\pm 3\sigma$ spectra are shown in Figure 2; the *PGA* ranges from 0.07 g to 1.15 g with a median value of 0.28 g. A rock outcropping condition was simulated by assuming a shear wave velocity over 30 m (v_{s30}) of 1100 m/s and depth of rock of 0 m (ground surface).
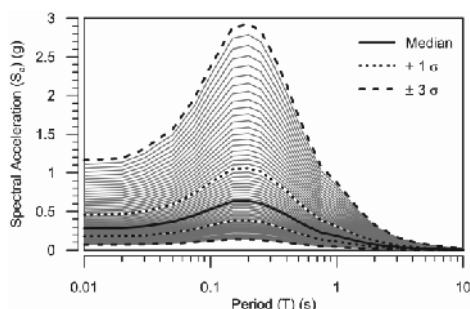

Figure 2. Illustration of the range of acceleration response spectra for the hypothetical site

To understand how ground motion variability affects the displacement uncertainty, the pseudo-probabilistic approach described above was implemented in the seismic displacement analysis in a systematic way by performing multiple probabilistic analyses for four different scenarios. These scenarios were designed to progressively increase in their inherent complexity by introducing different types of ground motion variability to the seismic displacement analysis. The four scenarios evaluated are described below.

No variability – This is a baseline condition with no variability where the ground motion is held at a constant intensity. Each parent motion (LHA, ORR, VAS, WPI) was spectrally-matched to the median target response spectra generating four separate motions each with a *PGA* of 0.28 g. All spectral-matching was performed using a wavelet-based algorithm developed by Mukherjee and Gupta (2002).

Variable intensity – For this scenario, variability in the ground motion intensity is introduced. Using the median spectrally-matched motions from the previous scenario, in this approach, variation in intensity is modeled by simple uniform-scaling to the target $\pm 3\sigma$ *PGA* values generated from the pseudo-probabilistic approach. For each parent motion, a suite of 1000 *PGA*-scaled acceleration time-histories were generated.

Variable intensity and frequency – For this case, additional variability in form of richer ground motion frequency content is combined with the variation of intensity. This form of variability was introduced by considering the variation of spectral acceleration (S_a) with period (T) provided by the full target response spectra. Variability in the frequency content is

modeled in an approximate manner through variation of the spectral shape and bandwidth of the response spectra between the $\pm 3\sigma$ bounds (Figure 2). This additional variability was achieved by spectrally-matching a single parent ground motion to randomly-selected response spectrum between $\pm 3\sigma$ bounds generated from the pseudo-probabilistic approach. For each parent motion, 1000 spectra-compatible acceleration time-histories were generated.

Variable, intensity, frequency and waveform – In this approach, additional variability is introduced by using all four parent ground motions in the spectral-matching process. Since the wavelet-based spectrally-matching algorithm generally maintains the non-stationary characteristics of the parent motions, this scenario provides variability in the core waveforms that are propagated through the displacement analysis. To accomplish this, randomly selected parent motions are paired with randomly selected response spectra (between the $\pm 3\sigma$ bounds generated from the pseudo-probabilistic approach) and spectrally-matched. A total of 1000 spectra-compatible acceleration time-histories were generated that incorporate all four parent ground motions.

4 SEISMIC DISPLACEMENT NON-LINEARITY

While the intended purpose of this study is to examine ground motion variability, Strenk and Wartman (2011) demonstrated that predictive uncertainty of common seismic displacement methods is also a function of a slope's relative degree of stability. In the context of Newmark's sliding block analogy, the stability of a slope with respect to sliding is defined as the ratio of a slope's ability to resist sliding (k_y) over the peak value of the earthquake-induced acceleration (*PGA*) and is referred to as the acceleration ratio (k_y/PGA). For a variety of simplified, equation-based methods and even more complex decoupled methods, a highly-nonlinear relationship exists between the acceleration ratio and displacement (δ); this is illustrated in Figure 3.
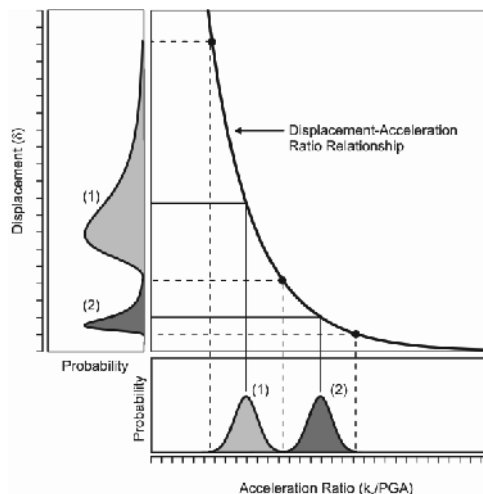

Figure 3. Illustration of the relationship linking the position of the acceleration ratio distribution to displacement prediction uncertainty.

Non-linearity is a consequence of Newmark's modeling decision to approximate the physical mechanism of earthquake-induced displacement after the inherently non-linear dynamic behavior of a sliding-block system. This inherent non-linearity manifests itself through the calculation procedure of "double-integrating" the acceleration time-history in excess of k_y (Newmark 1965) to compute the permanent displacement. In a probabilistic framework, non-linearity was observed to have a strong influence on how parametric variability (in seismic resistance and demand) is propagated through the analysis and can lead to varying degrees of displacement uncertainty (Strenk

and Wartman 2011). This relationship is characterized by a threshold behavior whereby nominal changes in acceleration ratio are greatly amplified into large changes in predicted displacement and hence uncertainty (Figure 3).

In order to capture this, multiple simulations were performed with the purpose of generating three different distributions of k_y targeted to have low, moderate and high median values. To do this, probability distributions of ϕ'_{peak} were systematically varied through the pseudostatic analysis to control the slope's seismic resistance; these distributions are referred to as "low", "moderate" and "high" strength and are illustrated in Figure 4a.
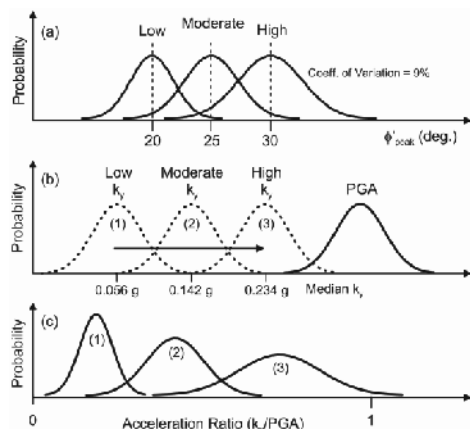
Figure 4. Illustration of the relationship between the k_y and *PGA* distributions and the resulting k_y/PGA distributions. Corresponding distributions of ϕ'_{peak} are shown for the three strength conditions.

By holding the distribution of *PGA* constant and varying the k_y distributions (Figure 4b), sampling of acceleration ratios was targeted to concentrate along different portions of the k_y/PGA scale (Figure 4c). For each ground motion variability scenario, three separate simulations for each strength condition were performed. This approach allowed displacement uncertainty to be quantified along different regions of displacement-acceleration ratio relationship and provided insight into how both method non-linearity and ground motion variability affect the level of prediction uncertainty.

5 DISPLACEMENT ANALYSIS RESULTS

Statistical measures of central tendency and spread were calculated for the displacement data obtained from the Monte-Carlo simulations of the different scenarios of ground motion variability. Overall, the displacement data was observed to be positively skewed as a result of several sources including inherent distributional assumptions (e.g. log-normal GMPE), truncation at prescribed limits (e.g. k_y below zero cannot exist, no k_y/PGA greater than 1) and method non-linearities (Figure 3). Non-parametric statistics based on percentiles that are less sensitive to data asymmetry and were used to describe the data.

For this study, uncertainty in the displacement predictions was assessed using the interquartile range (*IQR*). This parameter represents the range of the middle 50% of the displacement data and is calculated as:

$$IQR = P_{75} - P_{25}$$

where, P_{75} and P_{25} are the 75th and 25th percentiles of the data. Interquartile range data is summarized in Table 1 for the different ground motion variability scenarios and strength conditions.

Table 1. Summary of displacement interquartile range for the different types of ground motion variability and strength conditions

Ground Motion Variability	Displacement IQR (cm)			
No Variability	LHA	ORR	VAS	WPI
Low Strength	8.2	7.5	9.1	9.4
Moderate Strength	0.4	0.5	0.9	0.8
High Strength	0.1	0.1	0.2	0.2
Varied intensity				
Low Strength	14.6	12.9	15.9	16.4
Moderate Strength	2.3	2.0	3.4	3.0
High Strength	0.7	0.7	1.3	1.0
Varied intensity-frequency				
Low Strength	15.3	13.9	17.1	17.5
Moderate Strength	2.6	2.3	3.9	3.5
High Strength	0.8	0.9	1.5	1.3
Varied intensity-frequency-waveform (all 4 motions)				
Low Strength	16.7			
Moderate Strength	3.0			
High Strength	1.0			

6 DISCUSSION

The seismic displacement results presented in Table 1 demonstrate that the combined variability from both ground motions and the soil properties have a marked influence on displacement prediction uncertainty. For the scenarios evaluated, uncertainty is also observed to increase as variability in the intensity, frequency content and waveform are incrementally introduced into the probabilistic seismic displacement analysis.

6.1 *No Variability*

For this scenario, displacement uncertainty is due *entirely* to the variability in the seismic resistance, specifically the k_y distributions. With no variability in the ground motions, the displacement-acceleration ratio relationship (δ-k_y/PGA) plots as a smooth, monotonically-increasing line; the δ-k_y/PGA relationship for the LHA parent motion is shown in Figure 5. At low acceleration ratios, this relationship is highly non-linear which causes parametric variability of k_y to be magnified into large displacement uncertainty (IQR of 8 to 9 cm at the low strength) that progressively reduces as the relative stability of the slope increases (moderate to high strength conditions). This is consistent with the median k_y/PGA that increases from about 0.20, 0.51 and 0.83 for the low, moderate and high strength k_y distributions. For this scenario, the δ-k_y/PGA relationship for the LHA motion is similar to that for the other parent motions which is due to the fact that all four motions were spectrally matched to the same median response spectrum and thus predict a similar response.

6.2 *Varied Intensity*

For this scenario, variability in k_y and intensity of the ground motions contribute to the overall displacement uncertainty. As these are scaled motions, the frequency content is constant in the displacement analysis of each parent motion. The δ-k_y/PGA relationship for the LHA motion is compared to the case of no ground motion variability in Figure 5. Significant scatter is observed in the δ-k_y/PGA relationship and the displacement uncertainty for each parent motion is higher than that for the case of no ground motion variability. By including variability in the shaking intensity, the displacement IQR is observed to increase by a factor of nearly 2 for the low strength condition. The IQR increases by factors of 4 and 5 for the moderate to high strength conditions.
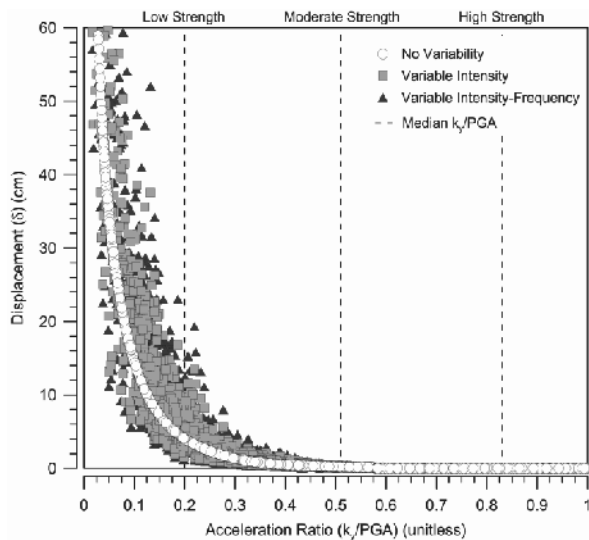
Figure 5. Comparison of the δ-k_y/PGA relationships for the LHA parent motion for the different ground motion variability scenarios

From this it may be inferred that the displacement uncertainty for marginally stable slopes is more sensitive to variability in the site conditions (i.e., input parameters that feed into k_y) while slopes with greater relative stability are more sensitive to ground motion variability. This suggests that for weaker slopes, greater resources and effort should be focused on constraining the variability of the subsurface conditions, whereas for more stable slopes the focus should be on characterizing the earthquake ground motions.

6.3 *Varied Intensity and Frequency*

When additional variability from frequency content is introduced into the analysis, marginal increases in the displacement uncertainty are observed. This is indicated by the slight increase in scatter in the δ-k_y/PGA data shown in Figure 5. For the four parent motions, displacement uncertainty increases by a factor of about 1.2, this is substantially less change than that observed when variability in intensity was introduced into the analysis. This is consistent with research that has demonstrated the efficiency of intensity ground motion parameters (e.g., *PGA*, peak ground velocity, *PGV* and Arias Intensity, I_a) over frequency content parameters for correlating with displacement predictions (Saygili and Rathje 2008).

While the range of response spectra simulated in the analysis (Figure 2) do show variations in their spectra shape, the peak spectral acceleration between the $\pm$ 3σ bounds remains constant at a predominant period (T_p) of about 0.2 s. This characteristic as well as the frequency-smoothing affect that spectral-matching has on the output motions could explain the marginal increase in displacement uncertainty. It is likely that displacement uncertainty would increase had the T_p of the simulated response spectra been allowed to take on a range of values. If, for example, the sub-model for site-conditions (specifically v_{s30}) in the Abrahamson and Silva (2008) GMPE had been modeled as a random variable this would have generated more diverse spectral shapes and hence additional variability in the ground motions. If this technique is implemented in a probabilistic analysis it should be compatible with the underlying assumptions of the method being used. For example, the Newmark (1965) rigid-block model assumes that the slope and slide mass are a non-deformable, rigid body. As such it would be inappropriate to use motions spectrally-matched to a response spectrum for site conditions representative of soft soil as this implies that the slope and slide mass can respond dynamically to the motions. In this case, decoupled-type analyses such as Makdisi and Seed (1978) would be appropriate.

6.4 *Variable Intensity, Frequency and Waveform*

When the intensity, frequency and waveform are varied, the combined affect yields displacement uncertainty that is marginally different from the previous case. Similar to frequency, introducing more diverse waveforms has little effect on the prediction uncertainty. However, it is interesting to note that *IQR* for this scenario is sometimes greater or less than the *IQR* for the individual parent motions. This is related to the wavelet-based spectral-matching process where the parent motion is decomposed, scaled up/down using wavelets and re-assembled such that modified time-history is compatible with the spectrum and non-stationary characteristics of the parent motion are preserved. Thus, even though the response spectra varies between $\pm$ 3σ bounds using only one parent motion yields a suite of spectra-compatible motions that have very similar non-stationary characteristics. This explains the systematic differences between the four parent motions for three previous ground motion variability scenarios. For example, the non-stationary characteristics of the VAS and WPI motions are such that when input into the "double-integration" computation of the rigid-block method, regardless of being scaled or spectrally matched, systematically yield higher median displacements and more prediction uncertainty than motions LHA and ORR. When all four motions are propagated through the displacement analysis, the effects of individual motions are tempered and a more average displacement response is computed. This average response, however, is not necessarily more precise than using a single parent motion.

7 CONCLUSIONS

Systematically increasing ground motion variability (and complexity) in the probabilistic displacement analysis showed a trend of increased displacement uncertainty. For the idealized slope, this trend was consistent across a range of relative stabilities (low, moderate and high). Ground motion variability had its most pronouced affect on displacement uncertainty at low acceleration ratios as a consequence of the non-linear δ-k_y/PGA relationship. Of the four scenarios considered, variability in ground motion intensity alone has the greatest impact on the displacement prediction uncertainty. When additional variation in frequency content and waveform is introduced, only minimal changes in uncertainty are observed. These results suggest that displacement uncertainty may be adequately characterized through simple scaling of ground motion intensity and that the effort required to create variability in both intensity and frequency through spectral-matching may be of limited utility. Also, the use of mutliple parent motions in a displacement analysis can overcome potential biases introduced by individual motions, but may not always lead to more constrained prediction uncertainty.

8 REFERENCES

Abrahamson N.A. and Silva W.J. 2008. Summary of the Abrahamson & Silva NGA ground motion relations. *Earthquake Spectra* 24, 67-97.

Makdisi F. I. and Seed H. B. 1978. Simplified procedure for estimating dam and embankment earthquake-induced deformations. *Journal of Geotechnical Engineering Division* 104(GT7), 849-867.

Mukherjee S. and Gupta V.K. 2002. Wavelet-based generation of spectrum-compatible time-histories. *Soil Dynamics and Earthquake Engineering* 22(9-12), 799-804.

Newmark N.M. 1965. Effects of earthquakes on dams and embankments. *Géotechnique* 15(2), 139-160.

Strenk P.M. and Wartman J. 2011. Uncertainty in seismic slope deformation model predictions. *Engineering Geology* 122(1-2), 61-72.

Saygili G. and Rathje E.M. 2008. Empirical predictive models for earthquake-induced sliding displacements of slopes. *Journal of Geotechnical and Geoenvironmental Engineering* 134(6), 790–803.

A new approach to assess the potential for flow slide in sensitive clays

Une nouvelle approche pour évaluer le potentiel d'écoulement des argiles sensibles

Thakur V., Degago S.A., Oset F., Dolva B.K., Aabøe R.
Geotechnical section, Norwegian Public Roads Administration

ABSTRACT: Sensitive clays could constitute a major threat to nearby infrastructure due to potential flow slides. A key question is if all sensitive clays have the same potential to retrogress to the same extent and the significance of remoulded shear strength (c_{ur}) in flow slides. This paper proposes a new approach to asses the potential for flow slides and in doing so presents a new laboratory test procedure referred to as the quickness test. The test focuses on remoulded behaviour of sensitive clays in terms of a numerical value referred as quickness (Q). Sensitive clay samples were collected from three different landslide locations. The quickness test was used to demonstrate why sensitive clays with $c_{ur} >1$ kPa are not susceptible to flow slides. Based on this study, it is possible to state that a $Q < 15$ % or $c_{ur} > 1$ kPa seems to be the threshold limit above which the extent of the retrogression of a landslide is limited to the initial slide. This criteria has been supported using data available from several Norwegian landslides in sensitive clays.

RÉSUMÉ : Les argiles sensibles pourraient constituer une grave menace pour les infrastructures en raison de coulées potentielles. Une question clé est de savoir si toutes les argiles sensibles ont un potentiel de rétrogression équivalent et de d'estimer l'amplitude de la résistance de cisaillement remaniée (c_{ur}) des les coulées. Cet article propose une nouvelle approche pour évaluer le potentiel de coulées et présente ainsi une nouvelle procédure de laboratoire appelée le test de rapidité. Le test se concentre sur le comportement de l'argile sensible remaniée en termes de valeur numérique dénommée rapidité (Q). Des échantillons d'argiles sensibles ont été recueillis à partir de trois sites différents où il y a eu des glissements de terrain. Le test de rapidité a été utilisé pour démontrer pourquoi les argiles sensibles avec $c_{ur} > 1$ kPa ne sont pas sujettes à des coulées. Sur la base de cette étude, il est possible d'affirmer que $Q < 15$% ou $c_{ur} > 1$ kPa semble être le seuil au-delà duquel l'ampleur de la rétrogression d'un glissement de terrain est limitée à la rupture initiale. Ce critère se base sur des données disponibles à partir de plusieurs glissements de terrain dans les argiles sensibles norvégiens.

KEYWORDS: Flow slide, sensitive clays, quickness, remolded shear strength, landslide.

1 INTRODUCTION

Soft sensitive clays are normally associated with loss of stability as well as substantial ground deformation, which can lead to structural damage and jeopardize the overall stability of an area. It is worth mentioning the statement by Bhishop in 1973 that "*Rotational slips alone may cause damage to services and property, but seldom involve loss of life. It is the subsequent development into a flowslide which has been responsbile in each case where disaster has occured*". In the sensitive clay deposits of Scandinavia and eastern Canada, landslides are particularly destructive, due to the possibility of small landslides initiating a flow slide, which may involve massive soil movements in the order of millions of cubic meters.

For flow slides to occur after an initial slide, it is important that at least the following two criteria are fulfilled (Tavenas et al. 1983):
- The slide debris should be sufficiently remoulded.
- The slide debris should be able to flow out of the slide area if remoulded.

There may be additional factors, such as the topography and the stability of the area behind the initial slide zone. However, if the two criteria mentioned above are not fulfilled, then vast landslides, such as those listed in Table 1, are unlikely to occur. An overview of Norwegian landslides as shown on Table 1 clearly indicates that soft sensitive clays must be handled carefully. However, the term 'sensitive clay' encompasses a wide range of clays depicting significant variations in engineering behaviour such as the remoulded shear strength

(c_{ur}). Therefore, a key question is whether all sensitive clays have the same potential to create flow slide and the significance of c_{ur} for occurrence of flow slide? Answer to this question has a direct relevance in the selection of an appropriate safety level for constructions, measures and in hazard mapping.

A relationship between the c_{ur} and the soil sensitivity (S_t) as well as between c_{ur} and the liquidity index (I_L) has been used to evaluate the potential for flow slides in sensitive clays. Mitchell and Markell (1974) suggest a direct relationship between c_{ur}, S_t and the retrogression distance (L). They suggest that landslides with an $L > 100$ m are observed for $c_{ur} < 1$ kPa. Retrogression was zero for $c_{ur} > 1$ kPa. Leroueil et al. (1983) and Locat and Demers (1988) presents correlations between c_{ur} and I_L. The correlations are $c_{ur} = (I_L-0.21)^{-2}$ and $c_{ur} = 1.46\ I_L^{-2.44}$ respectively. These showed that sentsive clays with $I_L > 1.2$ are susceptible to flow slides. This finding is also supported by the landslide data presented in Table 1. It must be noted that, according to the correlations $I_L> 1.2$ is only possible when c_{ur} is less than 1 kPa. In other words, the findings by Mitchell and Markell (1974), Leroueil et al. (1983), Tavenas et al. (1983) and Locat and Demers (1988) are in line with each other. Based on the landslide data, Lebuis et al (1983) also suggested that $c_{ur} < 1$ kPa may define the threshold limit for occurrence of flow slides.

I_L and c_{ur} based criteria have been widely adopted to study the flow slide potential of sensitive clays, However, the measurement of I_L demands determination of three parameters a priori, i.e. liquid limit (wl), plastic limit (wp) and natural water content (w). Notably the conventional thread-rolling method of

determining *wp* has a significant drawback as it can easily be biased by subjective judgement. Also, c_{ur} is usually measured using the fall-cone test, a point based measurement system, which may not necessarily be representative of a large soil volume.

Keeping this in view this paper proposes a new test procedure, the quickness test, to evaluate the flow slide potential of sensitive clays. In contrast to the convential c_{ur} and I_L based approaches, the quickness test is a soil volume based approach and has an added advantage of qualitative description that provides   provide a better visualisation with respect to understanding of flow slides.

Table 1 Selected large landslides in Norwegian sensitive clays.

No.	Year	Landslide	L_R [m]	c_{ur} [kPa]	S_t [-]	I_L [-]	I_P [%]
1	2012	Byneset	300	0.12	120	3.8	4.8
2	2010	Lyngen	230	0.35	50	1.5	12
3	2009	Kattmarka	300	0.24	63	2.9	8
4	1978	Rissa	1200	0.24	100	2.2	6
5	1974	Baastad	930	0.53	35	1.8	8
6	1967	Hekseberg	230	0.25	100	2.4	4
7	1965	Selnes	700	0.35	100	2.3	7
8	1959	Furre	215	0.2	85	1.3	6
9	1953	Bekkelaget	145	0.2	130	2.4	9
10	1953	Borgen	165	0.7	100	1.2	20
11	1953	Ullensaker	250	0.35	42	1.9	6.7
12	1893	Verdalen	2000	0.2	300	2.2	5

*L_R = Retrogression distance

2   THE QUICKNESS APPROACH

In this section, a simple test known as the quickness test is presented. The quickness test aims to provide the basis for a physical understanding of flow behaviour of fully remoulded sensitive clays using a new type of geotechnical engineering test. Additional description on the test methodology can be referred to Thakur and Degago (2012).
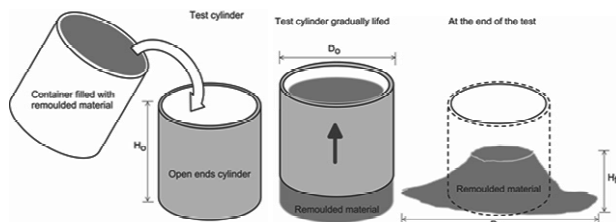
Figure 1. Quickness test procedure (Thakur and Degago, 2012).

2.1   Test procedure

The quickness test is a simple procedure that is performed by filling an open ended cylinder with remoulded sensitive clay, then slowly lifting the cylinder, and finally measuring the deformation (height and lateral spreading) as the material is subjected to flow due to its own weight. The test concept is similar to the slump test for concrete that is used to measure the consistency of freshly mixed concrete. Two different cylinder sizes were used. The dimensions were the diameter (D_o) = 65 mm and height (H_o) = 45 mm for the small cylinder, and D_o = 100 mm and H_o = 120 mm for the large cylinder. The large cylinder has the same size as the cylinder used for the standard proctor tests. Figure 1, taken from Thakur and Degago (2012), shows the concept of the proposed quickness test. The thoroughly remoulded material is placed into the cylinder, levelled off, and allowed to flow outward as the cylinder is slowly lifted upward with minimum disturbance to the sample. The difference in height between the cylinder and the slumped material (H_o-H_f) is measured. The outward flow spread diameter (D_f) is also noted. The quickness (Q) in % is defined as [1- H_f /H_o] × 100.

2.2 The tested material

Quickness tests were performed on several sensitive clay samples taken from three different locations in the central Norway. One of the landslides, Lersbekken, have been studied and presented in Thakur and Degago (2012). In this work a similar approach is presented for two new landslide locations Byneset and Olsøy. These sites have been studied extensively in connection to landslide hazards. Laboratory index properties of the sampled material are presented in Table 2. Liquid limit (w_L), c_{ui} and c_{ur} of the tested material were obtained using the fall-cone method as described by the National Standard NS 8015 in Norway.

Table 2 Properties of the tested materials from three different landslide locations

Properties	Lersbekken	Byneset	Olsøy
Sampling depth (H) [m]	6 – 10	4 – 12	4 – 15
Clay fractions (< 2 μm) [%]	30	30 – 55	50 – 65
Water content (w) [%]	22 – 34	27 – 48	28 – 38
Plasticity index (I_P) [%]	5 – 7	3 – 15	3 – 10
Liquidity index (I_L) [-]	0.7 – 2.0	0.9 – 5.4	0.6 – 3
Undisturbed undrained shear strength (c_{ui}) [kPa]	12 – 58	5.2 – 72	60 – 100
Remoulded undrained shear strength (c_{ur}) [kPa]	0 – 2	0 – 3	0 – 2.1
Sensitivity (S_t) [-]	16 – 29	4 – 400	30 – 100
Over consolidation ratio (OCR) [-]	1.8 – 2.0	1.1 – 3.3	2 – 4

3   TEST RESULTS AND OBSERVATIONS

Quickness tests were performed on more than 60 different samples extracted from Lersbekken, Byneset and Olsøy landslide locations. A series of pictures taken during the quickness test on two Byneset clay samples, with c_{ur} = 0.1 kPa and c_{ur} = 1.0 kPa, are shown in Fig. 2. The figure shows slump and spread observed at selected stages of the tests given as the precent ratio of the height lifted to the cylinder height (H_o).

Previous observations during a quickness test conducted on Lersbekken clay showed that sensitive clays with c_{ur} ≈ 0.5 kPa were not as fluid as they were originally assumed and sensitive clays with 0.5 kPa < c_{ur} < 1.0 kPa were semisolid in nature (Thakur and Degago, 20120). In line with this observations, the Byneset and Olsøy clay samples with c_{ur} < 0.2 kPa, seemed to be more like a soup as reported by Mitchell and Soga (2004). The registered collapse of the remoulded material was negligible when the remoulded sensitive clay had c_{ur} > 1.0 kPa.
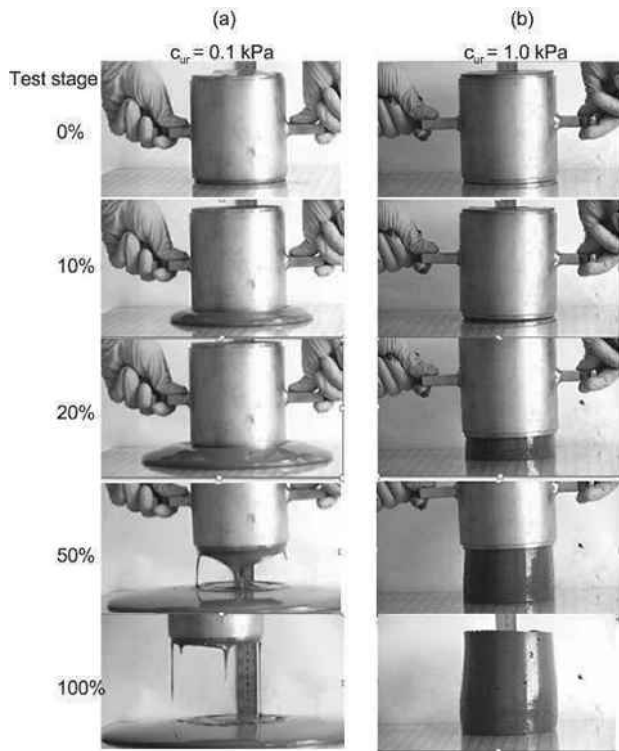
Figure 2. Slump and spread observed from the start to the end of the Quickness tests for remoulded Byneset clays (a) c_{ur} = 0.1 kPa and (b) c_{ur} = 1.0 kPa.

A typical flow and spread behaviour of two remoulded clays from the Olsøy site are presented in Figure 3. The tests on Olsøy clay shows that the remolded material with c_{ur} < 0.2 kPa seemed to be more like a soup, Figure 3(a). As the c_{ur} increases from 0.2 kPa towards 1 kPa, the remolded material increasingly showed less viscous behavior and for a c_{ur} > 1.0 kPa little or no flow is observed, Figure 3(b). This simple test indicates why soft sensitive clays with a c_{ur} > 1 kPa are less likely subjected to a large retrogression or run-out.
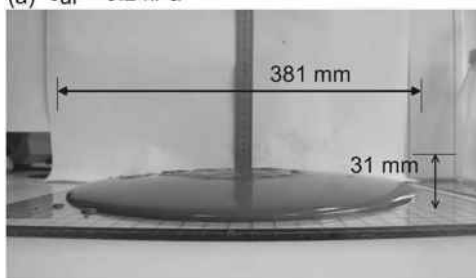
Figure 3. Flow and spread behaviour of the two remoulded Olsøy clays having (a) c_{ur} = 0.2 kPa and (b) c_{ur} = 1.2 kPa.
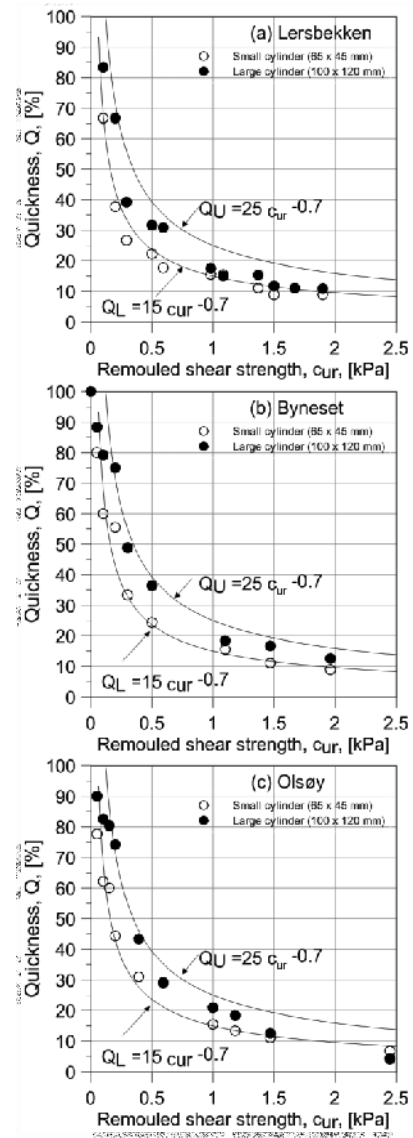
Figure 4. Q versus c_{ur} values registered on soil samples taken from a) Lersbekken b) Byneset and c) Olsøy landslide locations.
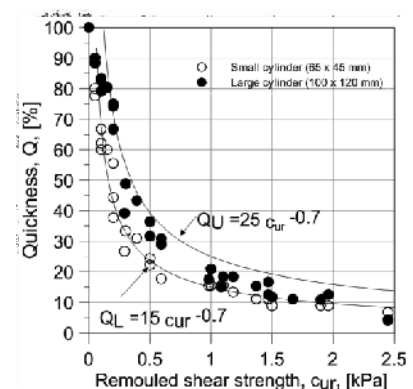
Figure 5. Compilation of Q versus c_{ur} values registered on soil samples taken from the three landslide locations.

Apparently, the flow behaviour of the Lersbekken, Byneset and Olsøy clay is identical. Figure 4 presents Q versus c_{ur} for various sets of tests on the Lersbekken, Byneset and Olsøy clays performed with two different cylinder sizes, 100 mm x 120 mm, 65 mm x 45 mm. For the major area of interest, i.e. clay samples with c_{ur} > 1.0 kPa, material flow was not registered irrespective of the size of the test cylinders. Accordingly, this

study recommends using a cylinder size 100 mm x 120 mm and proposes some correlations based on this cylinder size because this cylinder size is readily available in connection with the standard proctor test. The Figures presents the lower and the upper bound Q values observed for various c_{ur} of the tested material. A combined plot is shown in Figure 5 where all the data from the three landslide locations are plotted together.

Thakur and Degago (2012) suggests considering the lower bound quickness in evaluating flow slide potentials since it provides a conservative estimate. It can be noticed from the quickness test results (Figure 4 and 5) that all Lersbekken, Byneset and Olsøy materials have nearly identical responses and the lower bound $Q = 15$ % corresponds to $c_{ur} = 1$ kPa for all the three sensitive clays.

4   SUITABILITY OF QUICKNESS TEST

Suitability of quickness value (Q) as compared to remoulded shear strength (c_{ur}) in relation to assessment of flow behaviour of materials is briefly discussed.

Fluidity of sensitive clays is difficult to interpret by small numerical values of c_{ur} because a seemingly small change could imply significant alteration in flow behaviour of clay. For example, a significant change in the flow behaviour of the sensitive clay from the Lersbekken site is observed for a small variation of c_{ur}, i.e. from 0.5 to 0.2 kPa. In this case, the significant behavioural change is reflected by the quickness test visually as well as numerically Q varies from 32% to 67% (Thakur and Degago, 2012). The quickness test amplifies the small range of c_{ur}, i.e. from 0 to 2.0 kPa, to a larger scale, 0 to 100%. Quickness test therefore gives a better visualisation of the flow behaviour of sensitive clays where small c_{ur} values have large implications in regards to understanding the potential for retrogressive landslides.
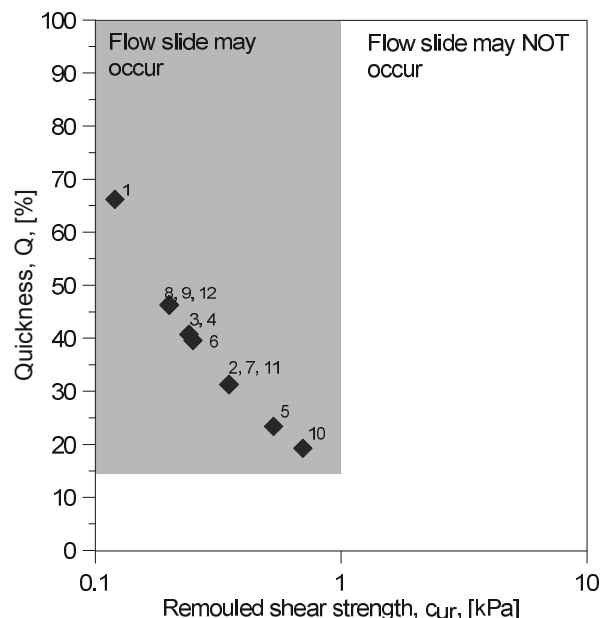

Figure 6. Estimated Q values for Norwegian landslides given in Table 1 and quickness based criteria for occurrence of flow slides.

In general, both c_{ur} and Q principally explains the same soil characteristic through different test approaches. The fall-cone test is a point specific method calibrated against the undrained shear strength of soil under undisturbed and remoulded state; whereas, the quickness test gives a value that is representative of the volume of the material tested. In contrast to the fall-cone test, the quickness test has an added advantage of qualitative

description that can provide a better visualization with respect to understanding flow slide (Thakur and Degago, 2012).

5   ASSESMENT OF FLOW SLIDE POTENTIALS

Significance of quickness test is illustrated in relation to assessment of potential for flow slides using the Norwegian landslides given in Table 1. In doing so the Q values for each landslides is estimated based on the corresponding c_{ur} values and using a lower bound correlation shown in Figure 5 ($Q = 15$ $c_{ur}^{-0.7}$). The estimated Q values of the Norwegian landslides are shown in Figure 6 where the numbers corresponds to the landslide numbers as listed in Table 1.

Based on the quickness test results and the data from the Norwegian landslides, two distinct regions are shown in the Figure 6. These regions depict the potential for occurrence of flow slides based on Q values. Accordingly, large flow slides are less likely to occur when $Q < 15$ % (or $c_{ur} > 1$ kPa) and in this case the slide will be limited to an initial slide only. However, for $Q > 15$ % (or $c_{ur} < 1$ kPa), a flow slide is possible. Based on the retrogression length (L_R) of the Norwegian landslides studied in this work, 15 % < Q < 25 % (or 0.5 kPa < c_{ur} < 1 kPa) mostly corresponds to a flow slide with L_R < 250 m while $Q > 25$ % (or $c_{ur} < 0.5$ kPa) corresponds to a flow slide with $L_R > 250$ m. Effort is being made to establish a correlation between L_R and Q using several landslide data, however at this stage no specific recommendation is made.

6   CONCLUSIONS

This paper presents a new laboratory procedure that focuses on remoulded behaviour of sensitive clays in terms of a numerical value referred to as quickness (Q). The quickness test was used to demonstrate why sensitive clays with $c_{ur} > 1.0$ kPa are not susceptible to flow. This particular study shows that a $Q < 15$% or $c_{ur} > 1.0$ kPa seems to be the threshold limit where the extent of the retrogression of a landslide is limited to the initial slide.

7   ACKNOWLEDGEMENT

8   REFERENCES

Lebuis J., Robert J.-M. and Rissmann P. 1983. "Regional mapping of landslide hazard in Quebec", In Proceedings of the Symposiumn Slopes on Soft Clays, SGI Report 17, 205–262.

Leroueil S., Tavenas F. and Le Bihan J.P. 1983. "Propriétés caracteristiqués des argiles de I'est du Canada", Canadian Geotechnical Journal 20,681–705.

Locat J. and Demers D. 1988. "Viscosity, yield stress, remolded strength, and liquidity index relationships for sensitive clays", Canadian Geotechnical Journal 25,799–806.

Mitchell R. J. and Markell A. R. 1974. "Flow slides in sensitive soils. Canad. Geotech. J. 11 (1), 11–31.

Tavenas F., Flon P., Lerouil S. and Lebuis J. 1983. "Remolding energy and risk of slide retrogression in sensitive clays", Proc. Symp. Slopes on Soft Clays, Linkoping, Swedish Geotechnical Institute (SGI) Report 17, 423 – 454.

Thakur V. and Degago S.A. 2012. "Quickness of sensitive clays", Géotechnique Letters 2 (3), 87-95.

Landslide risk assessment in the Göta river valley: effect of climate changes

L'évaluation des risques de glissement de terrain dans la vallée de la rivière Göta : effet des changements climatiques

Tremblay M., Svahn V., Lundström K.
Swedish Geotechnical Institute, Linköping and Gothenburg, Sweden

ABSTRACT: The predicted effects of the ongoing climate change such as increased precipitation and longer dry periods are expected to result in an increased frequency of landslides in Sweden. In order to meet this challenge, the Swedish Government commissioned the Swedish Geotechnical Institute (SGI) to investigate and assess the landslide risk in the Göta river valley, which is one of the Swedish valleys with the highest landslide frequency and where consequences of a landslide could be severe due to the number of large industrial sites as well as residential areas and infrastructure. A mapping of the landslide risk considering both present conditions and the effects of a future climate change has been performed. The investigation shows that climate change will increase the risk of landslides in the valley. However, it also shows that high level of risk is already estimated in many areas which can be affected even in today's climate.

RÉSUMÉ : Les effets prévus du changement climatique en cours, comme l'augmentation des précipitations et des périodes sèches plus longues devraient se traduire par une augmentation de la fréquence des glissements de terrain en Suède. Afin de relever ce défi, le gouvernement suédois a chargé l'Institut suédois de géotechnique (SGI) d'étudier et d'évaluer le risque de glissement de terrain dans la vallée de la rivière Göta, qui est une zone à haute fréquence de glissement de terrain et une zone particulièrement vulnérable en raison du nombre de grands sites industriels ainsi que des zones résidentielles et des infrastructures. Une étude des risques de glissement de terrain considérant à la fois les conditions actuelles et les effets d'un changement climatique à venir a été effectuée. L'étude montre que le changement climatique augmente les risques de glissements de terrain dans la vallée, mais elle montre aussi que le niveau de risque est déjà élevé dans de nombreuses parties de la vallée, même dans le climat actuel.

KEYWORDS: lanslides, risk assessment, climatic changes, mapping.

1 INTRODUCTION

The Göta river valley is situated in the southwest of Sweden and runs from Lake Vänern in the north to Gothenburg in the south, Figure 1. It is one of the areas in Sweden which is most frequently affected by landslides. Each year, several landslides of various size and character occur in this region. The landslides are generally small and shallow, however, a number of large landslides have occurred during the past century, some of them with human casualties and extensive property damages (e.g. Alén et al. 2000; Hultén et al. 2007). One reason for the high frequency of landslides in the Göta river valley is its geological history. The deep clay layers were formed during and after the latest glaciation period and in some parts reach a thickness up to 100 meters. The Göta river has overtime cut deep into the clay, forming the prerequisites for landslides. As the clays were mainly deposited in a marine environment, quick clay is therefore widespread in the area. The total length of the river is about 100 km.

The valley has a long history of human activities resulting in settlements, industries, shipping and harbours. Roads and railroads of national importance follow the river bank for kilometres, and environmentally hazardous activities and contaminated sites are common. More than 100,000 people live in the valley and the river is also the fresh water source for about 700,000 people. Due to the relatively high exploitation of the area, the consequences of a landslide in the Göta river valley can therefore be very severe.

The Göta river has suffered from many landslides over the years that have been documented. Parts of the most populated areas in the valley have earlier been investigated for mapping the risk of landslides, but in order to predict the effect of climate changes, the Swedish Government has commissioned the Swedish Geotechnical Institute to investigate and map landslide risks in the whole valley.

Figure 1. Location of the Göta river

2 METHODOLOGY OF RISK MAPPING

The concept of risk used in these investigations refers to a combination of the *probability* that an event might happen in a given area and the *consequence* of this event occurring.

Risk is defined as a combination of these two parameters:
Risk = Probability x Consequence

A landslide risk analysis thus includes three separate parts:
- the estimation of the probability for a landslide to occur,
- the determination of the consequences of such a landslide,
- the combination of these two factors resulting in a risk map.

Landslide probability is based on the calculation of the safety factor using conventional stability analysis. By studying the uncertainties in a number of parameters used in the calculation of the safety factor in a given area, the probability of a failure occurring in this area is estimated. The probability is therefore directly dependent on the safety factor and the variation in different parameters such as slope geometry, shear strength and density of the soil, etc. The probability of landslide occurrence is divided into five probability classes from "negligible probability of landslide" (probability class S1) to "substantial probability of landslide" (probability class S5).

The impact of a landslide in an area, i.e. damage to life, property and environment, is also defined in five consequence classes, from "minor damages" (consequence class K1) to "catastrophic damages" (consequence class K5). The assessment of the consequences of a landslide takes into account the damage that a possible landslide would cause. Extent of the damage is assumed to be in proportion to how the land is used for dwelling, industries, infrastructure and other facilities and activities. Of course, the size of the landslide is important for the assessment of the consequences, both on land and in the river, and it is affected by the presence of quick clay in the area as well as the topography of the slope. In earlier investigations, the consequences were described following a scale with incremental effects, but in the present project the financial aspects have been added on the impact assessment in order to more systematically compare the consequences of landslides in different areas, affecting different functions in the society.

The combination of landslide probability classes and landslide consequence classes results in an expression of the risk of landslide. Landslide risk class is expressed as a pair of numbers that reflects the consequences of a landslide (K) and its probability to happen (S). A total of 25 risk classes may be obtained from the risk matrix, see Figure 2, and they are clustered into three risk levels (low, medium, high) in order to simplify the risk mapping. The different levels of risk of landslides involve different requirements for geotechnical actions including the need of detailed stability investigations and eventually protective measures.

Figure 2. Risk matrix used in the present investigation.

The landslide risk map is obtained by overlaying the probability map and the consequence map and combining them into risk levels. The results of the risk analysis is finally presented in colored maps representing the three risk levels (low, medium and high) as shown in Figure 3. Areas with no landslide risk, e.g. areas with visible bedrock, are omitted from the risk map.
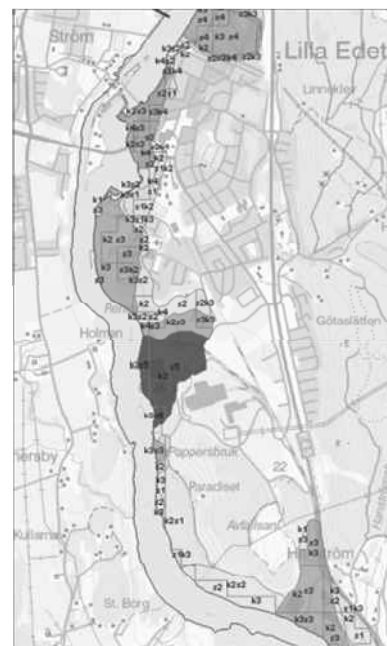

Figure 3. Principle of landslide risk mapping: probability map and consequence map are combined into a risk map.

3 EFFECTS OF CLIMATE CHANGE

Climate change is generally expected to result in increased frequency of natural disasters. In order to limit the damages and meet the new threat that a changing climate will mean for society, it is necessary to work both proactively to identify risks and to protect exposed areas by improving the quality of planning with regard to the new situation. SGI has for several years and on several occasions drawn attention to the geotechnical impacts of climate change. The analysis was summarized in an action plan for climate adaptation work and reported in various publications including the report "Geotechnical conditions for an increased flow of lake Vänern to the Göta River", SGI Varia 565 (Hultén et al, 2006).

Expected climate change in the Göta river valley over the coming 100 years includes gradually increase of yearly mean temperature and precipitation, see Figure 4 and 5, resulting in a higher mean water level in the river. The climate change will also result in an increase in most intensive rainfall events, an increased number of high and low discharges from the Lake Vänern due to increased inflow during autumn/winter and decreased inflow during spring/summer, and finally increased 100-year flows in Göta river tributaries (Bergström et al., 2011).
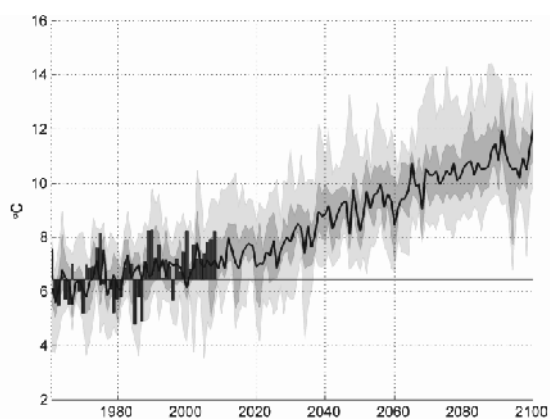

Figure 4. Calculated increase in temperature in the Göta river valley, based on 16 climate scenarios. The historical observations are shown as bars. The dark shaded area shows the 25-75 percentiles and the light shaded area the maximum and minimum values. The black line is the median value (after Bergström et al, 2011).
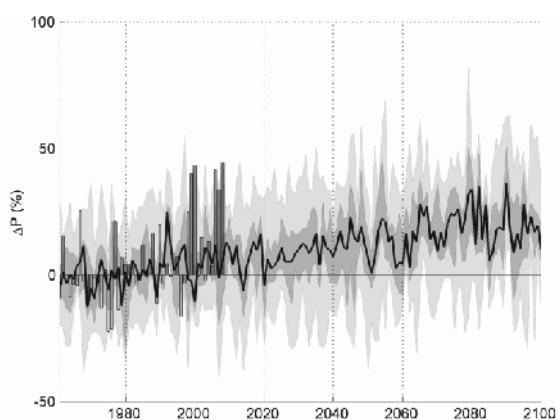

Figure 5. Calculated increase in precipitation in the Göta river valley, based on 16 climate scenarios. The historical observations are shown as bars. The dark shaded area shows the 25-75 percentiles and the light shaded area the maximum and minimum values. The black line is the median value (after Bergström et al, 2011).

A closer study of the results from the different climate scenarios which were performed in the present investigation

shows a significant increase in precipitation during the autumn/winter period, which means that the amount of water coming to the Göta river through discharge from the lake Vänern will increase, increasing the risk of erosion and the risk of landslides along the river.

The forecast produced by the different climate scenarios also shows reduced quantities of water during the drier spring/summer periods in the Vänern basin. This means that a lower water level is expected in the Göta river during these periods and thus an increased risk of landslides due to the decreased stabilizing effect of the water in the river. However, the water level in the Göta river is controlled by the presence of electric power plants along the river and is regulated by court statements and different agreements between the electricity producers and the authorities. Therefore, only minor changes of the highest or lowest water levels are expected to occur due to climate change. However, the mean water flow will increase over longer period, causing erosion along the river.

Studies of the changes in groundwater levels have shown that the expected variations are about 0,5 m in the area which means a minor effect on the total stability (see Blied and Persson, 2011).

An extensive study of the impact on the erosion process has also been conducted in this project. The results show that a number of river sections will be affected by the increase of flow in the valley resulting in an increase of erosion (see Rydell et al., 2011).

4 WORK DONE IN CURRENT INVESTIGATION

4.1 *Stability conditions*

To improve the basis for stability calculations, a detailed topographical model of the area has been set up. The model includes topography from a laser scanning on land and a multibeam scanning of the topography of the river bottom.

Existing studies, surveys, maps, charts and other relevant material were collected from various stakeholders and analyzed. Inventory was also made regarding the older material from a stability study in 1962, and other SGI investigations.

To get an overview of ongoing work and a reasonable amount of stability studies, the river valley has been divided into 10 different areas. For all of these areas, a number of sections were chosen and studied using traditional methods to estimate the stability conditions in the current situation. Thereafter, the impact of climate change on the stability was assessed and quantified. A total of 240 sections along the river have been studied including over 2500 field investigation tests and laboratory testing on about 4000 soil samples.

Erosion of the Göta River is a very important factor associated with increased risk of landslides. Cooperation with universities, government agencies and other appropriate bodies was established early in the project in order to plan the study and investigation work necessary for the implementation of the mandate.

Mapping of quick clay areas has also been a major topic studied in this project since it is a primordial parameter needed for a better prediction of the size of expected landslides. Improved investigation methods have been tested and implemented in the project.

4.2 *Consequences of landslides*

In order to perform a complete risk analysis, elements that may be affected by a possible landslide have been analyzed and taken into account. Among the major elements included in the study are human life, residential properties and infrastructures as well as contaminated soils. Extensive work has been performed for inventory, compilation and report of the selected

elements for impact assessment (see Andersson-Sköld et al, 2011).

4.3 *Data processing and databases*

Information, data and results from different studies must be organized in an orderly manner to allow for quick access to all materials. For this purpose, a GIS database was built up to simplify data processing and to enable work with the large amount of information acquired during the project.

5 R&D IN CURRENT INVESTIGATION

The investigation included a comprehensive risk analysis to be performed in a rather large area with many factors to be taken into account. The methodology chosen for the investigation using a risk matrix was developed and used in previous landslide analysis.

The commission stipulates that the investigation is expected to result in a complete risk analysis along the Göta river together with a general increase of knowledge regarding landslide analysis and risk mapping. A number of working studies were therefore initiated to study and improve different methods used in this kind of analysis. The Research and Development efforts have mainly been concentrated on mapping of input parameters, understanding of the erosion process, the estimation of probability of landslide and new routines for assessment and presentation of impact of landslides in different areas.

The assignment, which in addition to studying the current situation should also take into account increased flow and runoff conditions in the river valley, asked for a study of the climate changes at a regional level.

The research and development linked to the commission was mainly needs-driven and provided direct assistance in the investigation. Research on mapping and handling of quick clay is an example of efforts which provided valuable knowledge for the investigation. A method based on field measurements has been improved and implemented in the project for classification and mapping of sensitive and quick clays.

Efforts have also been made to try to understand and predict the impact of climate changes on prevailing groundwater conditions. These changes are expected to affect both the mean value of the groundwater level and its variations in time.

Even though it has been the object of a number of earlier analysis and studies, the ongoing erosion in the Göta river valley is still incompletely known. Better knowledge has been acquired and improved models have been developed for both the bottom erosion and erosion of the slopes at the waterline. Analysis and measurements of erosion and sediment transport coordinated with the determination of bathymetric and topographic conditions have been performed in this project. The R&D-work has also included studies of boat related erosion and the use of advanced numerical models.

6 RESULTS AND REPORTING

The results of the project are presented in two different forms:
- a series of 34 reports in which the results from the different R&D groups are presented including study of groundwater, erosion, methodology of probability analysis, methodology for estimation of consequences, mapping of quick clay, etc.

- a final report in three parts including general discussions and recommendations, a complete presentation of the methods used in the investigation and finally risk maps covering the whole valley, see Swedish Geotechnical Institute (2012) or SGI's website: www.swedgeo.se.

As expected, the investigation shows that climate changes will increase the risk of landslides in the Göta river valley. However, it also shows that high level of risk is already estimated in many areas which can be affected even in today's climate. Both the risk for landslide in the present climate conditions and the effect of the climate change in form of new estimation of risk in the future are presented in the final report.

The investigation also leads to a general presentation of protective and preventive measures which could be taken in different parts of the valley. Examples of practical measures that have to be considered are excavations, backfills, soil reinforcement and erosion protection. Besides a rough estimation of the costs of protective measures, the report also includes recommendations regarding different monitoring activities which should be regularly performed along the river.

7 REFERENCES

Alén, C., Bengtsson, P.-E., Berggren, B., Johansson, L. & Johansson, Å. (2000). Skredriskanalys i Göta älvdalen – Metodbeskrivning. (In Swedish). Swedish Geotechnical Institute, Report 58, Linköping.

Andersson-Sköld, Y. (2011). Metod för inventering och värdering av konsekvenser till följd av skred i Göta älvdalen samt Metodik konsekvensbedömning - Känslighetsanalys, klassindelning och applicering av metodik i hela utredningsområdet. (In Swedish). Swedish Geotechnical Institute, Göta älvutredningen delrapport 12 & 13, Linköping.

Bergström, S., Andreasson, J., Losjö, K., Stensen, B. & Wern, L. (2011) Hydrologiska och meteorologiska förhållanden i Göta älvdalen. (In Swedish). Swedish Geotechnical Institute, Göta älvutredningen delrapport 27, Linköping.

Blied, L. och Persson, H. (2011). Bedömd förändring av maximala grundvattennivåer i Göta älvdalen till följd av förändrat klimat. (In Swedish). Swedish Geotechnical Institute, Göta älvutredningen delrapport 9, Linköping.

Hultén, C., Andersson-Sköld, Y., Ottosson, E., Edstam, T. & Johansson, Å. (2007). Case studies of landslide risk due to climate change in Sweden, International geotechnical conference on climate change and landslides, Ventnor, Isle of Wight. Proceedings 2007, pp 149-157.

Hultén, C., Edstam, T., Arvidsson, O. & Nilsson, G. (2006). Geotechnical conditions for increased drainage from Lake Vänern to River Göta. (In Swedish). Swedish Geotechnical Institute, SGI Varia 565, Linköping.

Rydell, B., Persson, H., Blied, L. & Rankka, W. (2011). Erosionsförhållanden i Göta älv. (In Swedish). Swedish Geotechnical Institute, Göta älvutredningen delrapport 1, Linköping.

Swedish Geotechnical Institute (2012). Landslide risk in the Göta river valley in a changing climate. Final Report Part 1-3, Swedish Geotechnical Institute, Linköping.

Deformation and water seepage observed in a natural slope during failure process by artificial heavy rainfall

Déformation du sol et infiltration d'eau observes le long d'une pente naturelle pendant le processus de glissement du a de fortes pluies artificielles

Uchimura T., Gizachew G.
Department of Civil Engineering, University of Tokyo, Tokyo, Japan

Wang L., Nishie S., Seko I.
Chuo Kaihatsu Corporation, Tokyo, Japan

ABSTRACT: Monitoring and early warning is one of the most effective ways toward reduction of disasters induced by landslides due to heavy rainfall. The authors has developed a simple and low-cost early warning system which measures tilting angles on the surface and/or in the ground of a slope, as well as volumetric water contents in the ground. Unlike conventional sensing devices, measurement with tilt sensors is simple and easy, but the translation of the obtained data of tilting angle is still under consideration. The authors conducted an artificial rainfall test on a natural slope of weathered and loose andesite deposit in order to observe its prefailure behaviours. The tilt angles and volumetric water contents were measured during the deformation and failure process. The tilt sensors showed tilting rates between 0.1 and 0.5 degree / hour before failure. In addition, there was a unique relation between the deformation and the water content, which is independent of the time history of the artificial rainfall. Simple shear tests were also conducted to observe the prefailure deformation of an unsaturated soil. These observations will give us ideas on the warning criteria for slope failure based on monitoring of tilting angle and water contents.

RÉSUMÉ : Donner l'alerte au plus tôt est sûrement la solution efficace pour réduire l'ampleur des désastres induits par les glissements de terrain dus à des chutes massives de pluie. Un système d'alerte simple et à bas-coût qui mesure les angles d'inclinaison de la surface du sol et/ou dans la terre, ainsi que le volume d'eau absorbé est proposé. Contrairement aux appareils conventionnels, la mesure avec les sondes de l'inclinaison est simple et facile, mais la traduction des données obtenues est encore à l'étude. Un test de chute de pluie artificielle sur une pente naturelle d'andésite durcie et dégagée pour observer les comportements des pré-fractures a été réalisé. L'orientation de l'inclinaison ainsi que le volume d'eau ont été mesurés pendant la déformation de la surface. Les sondes ont révélé des pentes comprises entre 0,1 et 0,5 degré/heure avant glissement. De plus, une relation unique indépendante de la durée de la chute de pluie artificielle est établie entre la déformation du sol et le contenu d'eau. Des tests de cisaillement ont aussi été effectués pour observer la déformation des pré-fractures d'un sol non saturé. Ces observations nous donnent des informations sur les critères d'alerte pour prévenir un glissement de terrain.

KEYWORDS: landslide, slope failure, monitoring, early warning.

1 INTRODUCTION

There is a long history in prevention and mitigation of rainfall and/or scouring-induced landslides. Mechanical counter measures to prevent slope failure, like retaining walls and ground anchors, have been widely used. However, they are expensive and it is not realistic to apply such mechanical measures for all of these slopes with potential risk, because most of landslide occurs in small scale, but a large number of slopes. Therefore, careful monitoring of slope behaviors and consequent early warning is reasonable as alternatives.

The authors have proposed and developed an early warning system for slope failures, as one of feasible countermeasures (Figure 1) (Uchimura, et. al. 2010 & 2011a). The system consists of minimum number of low-cost sensors on a slope, and the data is transmitted through wireless network. Thus, the system is low-cost and simple so that the residents in risk areas can handle it to protect themselves from slope disasters.

There are several publications which report incremental deformation of slopes before failure due to heavy rainfall (Ochiai, et. al. 2004, Orense, et. al. 2003 & 2004). These behaviors can be used as criteria of early warning for slopes disasters. Extensometers and borehole inclinometers are conventional and widely used devices to detect such displacements of slopes. But, these devices require high skills and equipments for installation and operation, resulting in a respectable cost.

Therefore, the proposed early warning system uses tilt sensors to detect abnormal deformation of slopes as shown in

Figure 1. The surface tilt sensor is installed with a rod inserted into the slope surface for a depth of 0.5 or more. It has a MEMS tilt meter (nominal resolution = 0.04 mm/m) to measures the tilting angle in the surface layer of the slope. The obtained tilt angle is equivalent to shear deformation of the surface layer, which can be translated to the surface displacement if the tip of rod reaches the intact base layer.
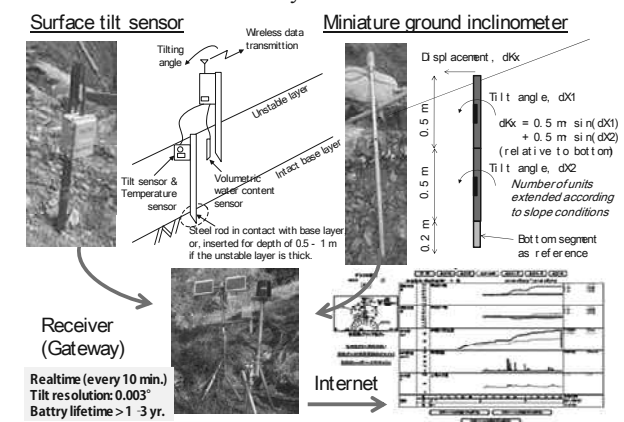

Figure 1. Tilt sensor units and wireless monitoring system

The miniature ground inclinometer consists of stainless steel pipe segments with a length of 50cm or 1m and outer diameter of 25 mm. The segments are connected to each other by a

2273

flexible mechanism, so that the device moves together with the ground displacement. A sensor unit covered by a small aluminum cylindrical case is installed in each segment. The sensor unit contains the MEMS tilt meter and a geomagnetic sensor (digital compass, nominal resolution = 0.5 deg) to detect the direction of unit. Each unit also contains a microcontroller chip, which control the sensors, and transfer the control commands and the obtained data to the next units by serial interfaces. A significant advantage of this device is that it can be installed quickly into the slope ground being blown with a hammer, as its diameter is as small as 25 mm. Besides, it can be installed into a deeper layer of slopes (3-5 m) by connecting the segments as many as needed.

Unlike conventional sensing devices, such as borehole inclinometer and extensometer which measures displacements of slope, measurement with tilt sensors is simple and easy. However, the translation of the obtained data of tilting angle is still under consideration. It is because there are few case histories of early warning with tilt sensors compared to those with conventional sensors. Therefore, it is essential to observe the behaviors of tilt angles in prefailure stages of slopes.

2 SLOPE FAILURE TESTS BY ARTIFICIAL RAINFALL

An artificial rainfall test was conducted on a natural slope of weathered and loose (N_d <10 for 10 cm of penetration by portable dynamic cone penetration tests) andesite deposit in order to observe its prefailure behaviour. The site is located on an unstable slope in Taziping, Sichuan Province, China. Figure 2 shows the cross-section and photo of the site together with the instruments. The slope angle is around 18 degrees, and its lower end was excavated for a depth of 1.4 m with an angle of 40 degrees. The deposit contains some big rocks with diameter of 300 mm or more. The particle size distribution of component finer than 100 mm is show in Figure 2. It is a sandy material containing some gravel and fine particles.

Figure 2 also shows surface tilt sensors (T50-1, T50-2, T200, and T300), and miniature ground inclinometer (K50 and K150). The number in the notation of each sensor represents the distance from the bottom end of slope in cm. Each rod of the surface tilt sensors was inserted into the ground by 75 cm. Each miniature ground inclinometer consists of 2 segments with a length of 500 mm.
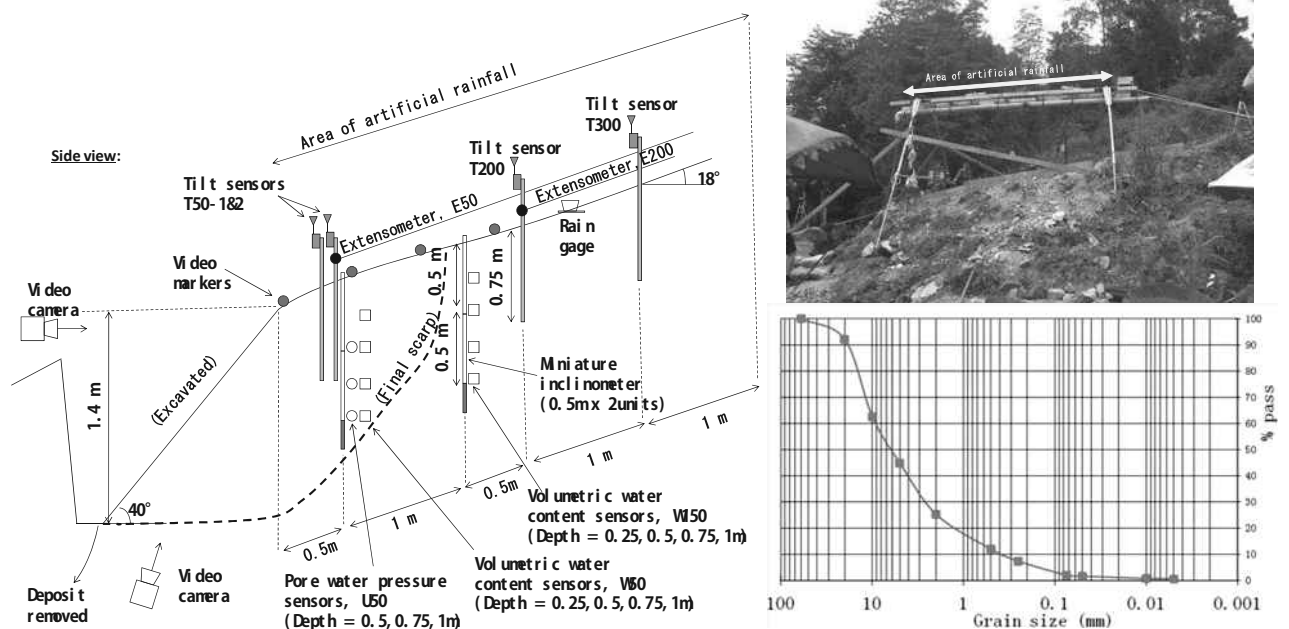

Figure 2. Cross-section, photo, and particle size distribution (finer part than 100 mm) of the site for the artificial rainfall test.
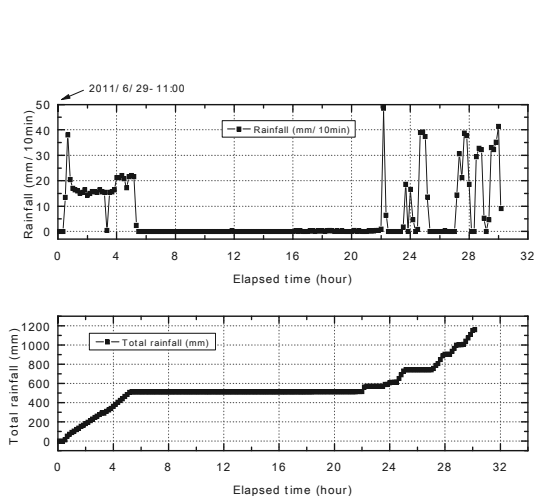

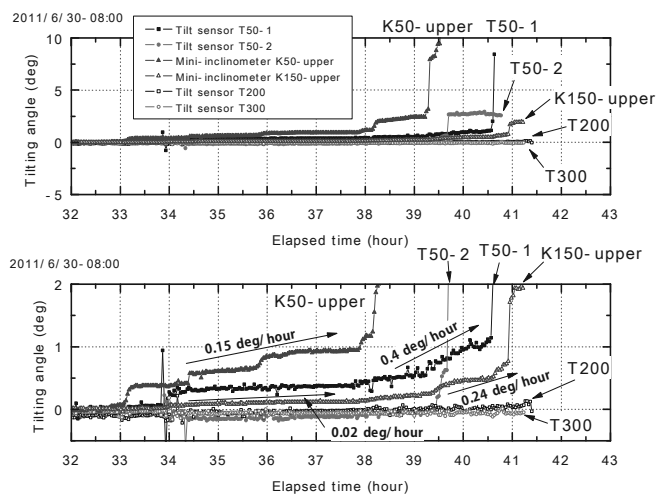Figure 3. Records of the artificial rainfall.

Figure 4. Tilting angles on the slope.

Artificial heavy rainfall was given as shown in Figure 3. The rainfall intensity fluctuated due to restriction of water supply, but around 500 mm of total of rain was applied in the first day, and 700 mm was given in the second day.

Major deformation was observed in the second day, and the slope failed progressively from the bottom with scarp angle of 40 to 50 degrees. The final shape of scarp is shown with thick broken line in Figure 2.

Figure 4 shows the changes in tilting angles detected by the tilt sensors due to the rainfall in the second day. Tilt angles of the upper segment are shown for the miniature ground inclinometers. The nearer to the bottom of slope, the more tilting angles are observed. The tilting rate for each sensor is between 0.1 and 0.5 degree / hour before failure. It is also remarkable that K150-upper, 150 cm apart from the bottom of slope, started to tilt slowly in the early stage, when the failure was observed only at the bottom scarp. This suggests that the sensor detected slight effects of the failure event at some distance of the sensor position. This behaviour is not visible to human eyes because its tilting rate was only 0.02 degree / hour.

Figure 5 shows the behaviours of the tilting angle of the upper unit of the miniature inclinometer, K50, at 50 cm from the bottom of slope. This represents the average shear deformation of the soil layer between depth of 0 and 50 cm. Besides, Figure 5 also shows the volumetric water content at a depth of 50cm at a position of 50 cm from the bottom of slope. The volumetric water content repeated to increase and decrease corresponding to the intermissive rainfall and drainage stages.

Figure 6 plots the tilting angle versus the volumetric water contents of Figure 5. This represents relationships between the shear deformation and water content. The deformation increased when the water content was high corresponding to rainfall, although some additional deformation was also recorded due to removal of soil which dropped and deposited in front of the bottom of slope.

A unique relation between the deformation and the water content can be drawn as an envelope of the plot, as indicated in Figure 6, which is independent of the time history of the artificial rainfall. Similar behaviours was be also observed in laboratory model tests on slip surface of unsaturated soil under constant shear stress and cyclic water infiltration/drainage processes (Uchimura et. al. 2011b).

3 SIMPLE SHEAR TESTS ON SLIP SURFACE

A series of simple shear tests were conducted on unsaturated sandy soil specimens to observe their prefailure behaviors more precisely. Figure 7 shows the arrangement of the testing device. Edosaki Sand (D_{max} = 2 mm, D_{50} = 0.23 mm, fine content = 6 %, Gs = 2.665, e_{max} = 1.685, e_{min} = 0.578) was compacted into a disc shape with a diameter of 60 mm and a height of 20 mm, and a relative density of Dr = 70 % with initial volumetric water content of 7 %. The specimen is surrounded by a stacked layers made of Teflon, which has low friction coefficient, to reduce the effect of friction. The specimen was loaded with 60 kPa of vertical confining pressure. And then, 15, 24, 30 kPa of constant shear stress was applied, which corresponds to 0.25, 0.4 and 0.5 of stress ratio, respectively. These three stress ratio simulate the stress state on the slip surface for gentle, medium, and steep slopes. Then, water was injected into the specimen from the top and bottom surface through ceramic discs with a constant injection rate of 310 ml/hr, which corresponds to a rainfall intensity 110 mm/hr fall on the top area of the specimen.

Figure 8 shows the obtained volumetric water contents and shear strain during the water infiltration process. It seems that there are three patterns of deformation and failure processes. In the case with stress ratio of 0.25 (gentle slope), the shear deformation increases with water infiltration, but it converged to a limited value not showing failure. On the other hand, in the case of steep slope with stress ratio of 0.5, the strain started to increase with a similar rate to that in the case of gentle slope, but it suddenly yielded at incremental volumetric water content of around 7 % and shear strain of around 1.7 %, followed by a quick deformation with high strain rate.
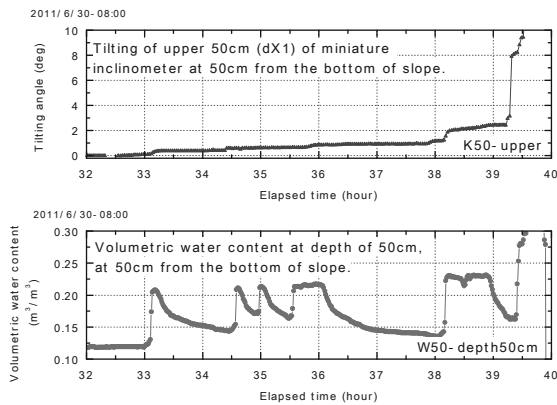

Figure 7 Equipments for direct shear tests.

Figure 5 Time histories of tilting angles and volumetric water contents at 50 cm from the bottom of slope.

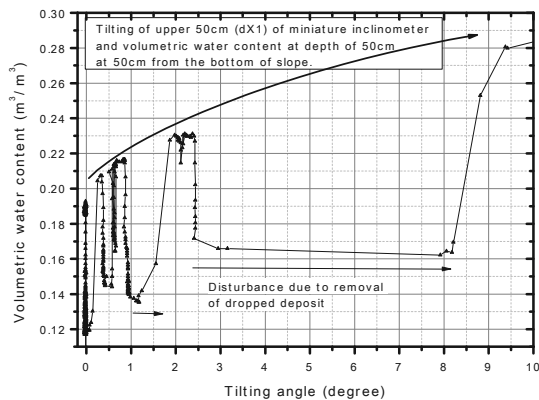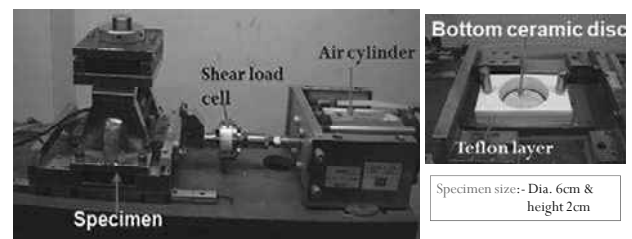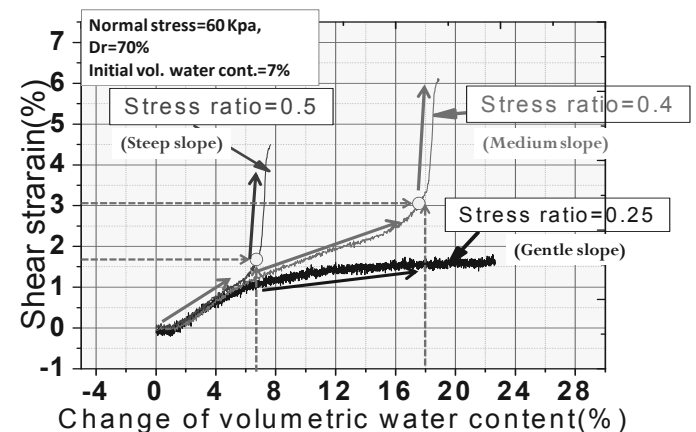Figure 6 Tilting angles versus volumetric water contents at 50 cm from the bottom of slope.

Figure 8 Shear strain versus volumetric water content under 3 values of constant stress ratio.

The behavior in the case of medium slope with stress ratio of 0.4 was more complicated. The strain started to increase with a similar rate to those in the other cases, but it slowed down when the change of volumetric water content was between around 7 % and 18 %. And then, it yielded, followed by a quick deformation with high strain rate.

The reason for the slowing down of strain rate observed in the case of medium slope could be explained with the behaviors of suction. The authors developed a miniature suction sensor to measure the suction in the specimen (Figure 9). A tiny metal pipe (ϕ1.5 mm x 4 mm) with small hole is wrapped with a micro-porous membrane. One end of the pipe is connected to a water pressure transducer via a plastic tube, while the other end is closed. The membrane allows water to pass through, but prevent air to pass by capillary effect. Thus, the pipe with the membrane works just like a miniature ceramic cup. Properties of a similar membrane are studied by Nishimura et. al. (2011). Due to its small size, the miniature suction sensor can be installed with minimum disturbance to deformation and water seepage in the specimen as seen in Figure 9.

Figure 10 shows relationships between the suction and the change of volumetric water content measured in another specimen during water infiltration process. The suction decreases with fast rate until the change of volumetric water content reaches around 4.5 %. Then, the decreasing rate of suction slowed down.
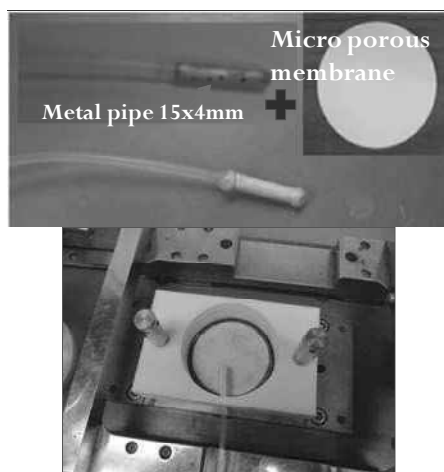

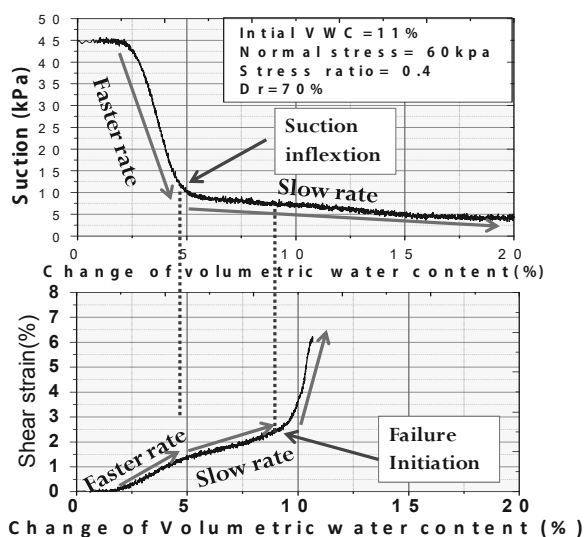Figure 9 Miniature suction sensor with microporous membrane.

Figure 10 Relations among volumetric water content, suction, and shear strain.

The strain rate of the specimen also slowed down at the same change of volumetric water content. Thus, this behavior can be

explained with the suction-water characteristics curve (SWCC) of the soil. Finally, the specimen yielded at higher change of volumetric water content, corresponding to lower suction.

This observation suggests that a tentative slowing down of slope deformation does not always mean stabilization of slope.

4 CONCLUSIONS

A slope failure test with an artificial rainfall was conducted on a natural slope. The tilt sensors installed into the slope showed tilting rates between 0.1 and 0.5 degree / hour. These values of tilting rate could be used as criteria of early warning for slope disasters.

The deformation proceeded when the water content was high corresponding to rainfall, while it is less progressive when the water content is low. Similar behaviours were also observed in model test in laboratory, where an unsaturated soil layer was sheared under constant shear stress with cyclic water infiltration and drainage. It seems that there is a unique relation between the deformation and the water content, which is independent of the time history of the artificial rainfall. These results suggest a possibility of conbined monitoring of tilting angle and water contents for more precise comprehension of the status of slopes.

The results of direct shear tests on unsaturated soil under constant shear stress and constant water injection rate suggest that there are three patterns of deformation and failure processes corresponding to the slope angle. In a case of medium slope, the strain rate may slow down due to the SWCC of the soil even though water is injected with a constant rate. However, it does not always mean that the slope is getting stable.

5 ACKNOWLEDGEMENTS

6 REFERENCES

Ochiai, H., Okada, Y., Furuya, G., Okura, Y., Matsui, T., Sammori, T., Terajima, T., and Sassa, K. (2004): A fluidized landslide on a natural slope by artificial rainfall, *Landslides*, Vol. 1, No. 3, pp. 211-219.

Orense R.P., Towhata I., and Farooq K. (2003): Investigation of failure of sandy slopes caused by heavy rainfall, *Proc. Int. Conf. on Fast Slope Movement-Prediction and Prevention for Risk Mitigation (FSM2003)* , Sorrento.

Orense R.P., Farooq K., and Towhata I. (2004): Deformation behavior of sandy slopes during rainwater infiltration. *Soils and Foundations* 44(2):15-30.

Uchimura, T., Towhata, I., Trinh, T. L. A., Fukuda, J., Bautista, C. J. B., Wang, L., Seko, I., Uchida, T., Matsuoka, A., Ito, Y., Onda, Y., Iwagami, S., Kim, M. S., and Sakai, N. (2010): "Simple monitoring method for precaution of landslides watching tilting and water contents on slopes surface", *Landslides*, (Published online: 17 October 2009)

Uchimura, T., Wang, L., Qiao, J.-P., and Towhata, I. (2011a). Miniature ground inclinometer for slope monitoring, *Proc. of The 14th Asian Regional Conference on Soil Mechanics and Geotechnical Engineering*, ATC3 Session.

Uchimura, T., Suzuki, D., and Seo, H.-K. (2011b): Combined monitoring of water content and displacement for slope instability, *Proc. of 4th Japan-Korea Geotechnical Workshop*, Kobe, pp. 67-72.

Nishimura, T., Koseki, J., Fredlund, D.G., and Rahardjo, H. (2011): Microporous Membrane Technology for Measurement of Soil-Water Characteristic Curve, *Geotechnical Testing Journal*, Vol. 35, No. 1, Paper ID GTJ103670.

Study on field detection and monitoring of slope instability by measuring tilting motion on the slope surface

Détection et surveillance in situ des phénomènes d'instabilités de pente par mesure locale des mouvements de surface

Wang L., Nishie S., Seko I.
Chuo Kaihatsu Corporation, Tokyo, Japan

Uchimura T.
University of Tokyo, Japan

ABSTRACT: Monitoring and early warning is one of the most effective methods toward reduction of disasters induced by landslides and slope instabilities, but the traditional methods such as multiple borehole inclinometers or extensometer are expensive and unsuitable to zoning monitoring. To overcome the above weaknesses, a simple and low-cost early warning system was developed for slope failure and landslide (Uchimura et al. 2009). The developed tilt sensor is easy to install and it can monitor slope deformation by means of a tilting MEMS module angle which embedded in the sensor, and transfers real time data via wireless network. The warning system with its developed equipments has been deployed in several actual slopes for validation of field performance in Japan and China. In this paper, the authors will show that the developed system and sensor can successfully detect the situation of slope and landslide, and issue useful information that allows residents to avoid slope failure or landslide disasters. Based on the results of field case studies, the developed low-cost sensor unit and real-time warning system are considered particularly effective against rainfall-induced slope failure or landslides and its general use is recommended.

RÉSUMÉ : Une surveillance constante associée à un dispositif rapide d'avertissement est une solution efficace pour lutter contre les désastres et les pertes humaines liés aux glissements de terrain ou aux ruptures de pentes. Cependant, les équipements traditionnels tels que les inclinomètres ou extensomètres installés par forage sont généralement d'un coût prohibitif et sont peu adaptés à une surveillance plus généralisée du territoire. Un nouveau système plus flexible et de coût plus réduit a été proposé par Uchimura et al. (2009). Il incorpore des micro-inclinomètres de type MEMS faciles d'installation qui permettent d'estimer les mouvements de surface. Les données peuvent être transmises en temps réel via réseau sans fil. Ce système a été déployé sur plusieurs sites en Chine et au Japon. A partir des données recoltées sur ces sites, il est démontré que ce système est efficace et fiable dans l'estimation et la détection précoce des glissements de terrain, et qu'il permet d'obtenir des renseignements cruciaux pour prévenir leur poursuite ou pour réduire les dégâts occassionés.

KEYWORDS: landslide, slope failure, monitoring, early warning.

1 INTRODUCTION.

Typical measures to prevent slope failure are retaining walls and ground anchors which improve safety factor against failure. These measures have been widely used everywhere in the world and its effectiveness has been confirmed. However, the traditional methods take a lot of cost, as a result that a limited application can be used only for large scale slopes. In fact, most of landslide occurs at small scale slopes, but with a large number. It is not realistic to apply mechanical reinforcement measures for these slopes with potential risk.

Rainfall-induced slope failures are one kind of the most destructive natural hazards. Many slope failures have been observed to occur during or immediately after rainfall. For a wide range slope safety monitoring, a problem in the first was that the equipments were high-cost; this is a problem that

Figure 1. Wireless tilt sensor unit with water content sensor.

disaster prevention measures was difficult for implementation into developing countries. The cost issues should be overcome for a purpose of widespread use; another is that a simple and effective real-time monitoring becomes necessary.

The authors have proposed an early warning system for sediment disasters, as one of more feasible countermeasures for small-scale slope failures. The system measures minimum number of items by using the developed smart sensor units; the measured data is transferred through wireless network. Thus, the system is low-cost and simple enough so that the residents in risk areas can handle it to protect themselves from slope disasters (Uchimura et al. 2009).

2 A LOW-COST AND SIMPLE WARNING SYSTEM.

A simple and low-cost early warning sensor unit was developed that only two parameters of the volumetric water content of soil and the inclination of slope or landslide were focused, and its applicability and effectiveness were tested on model slopes under artificial heavy rainfall (Uchimura et al. 2009). The senor unit works with batteries, and transfers real time data via wireless network, and installation is simple and easily to control so that non-expert residents in risk area can handle it by themselves, even in developing countries. Figure 1 shows the basic concept of the wireless monitoring unit using for early warning system.

2.1 RF (Radio Frequency) wireless data transmit method

Figure 2 shows the outline of wireless monitoring and early warning system for slope failure. The system is designed to be wireless, that is, each unit works autonomously with
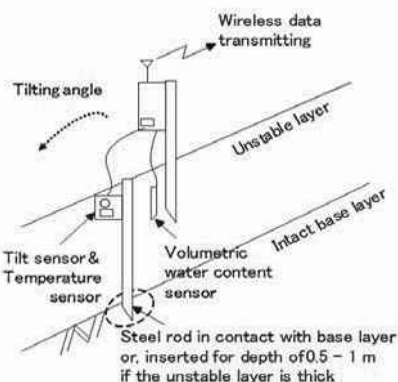
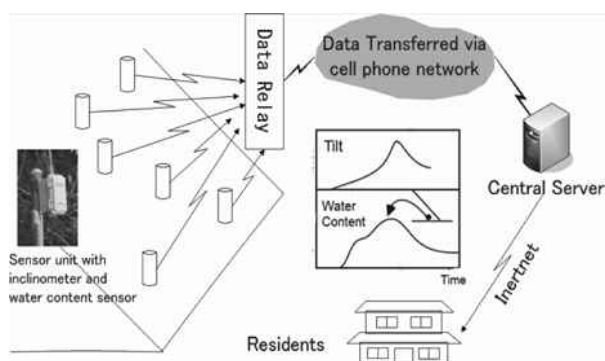microcomputer with independent power supply by batteries or

Figure 2.Outline of wireless monitoring units and early warning system for slope failure.

solar cells. Radio modems operated in the 429 MHz ISM band for Japan, 434 MHz ISM band for E.U. counties and China.

The sensor units measure the condition of the slope periodically every 10 minutes for example. The data is transferred to a gateway unit, which is also placed near the slope, by using low power radio communication modules. The data transmitting distance is 300-600 meters under typical conditions in the field. The gateway unit collects the data from all the sensor units, and sends them to a data server on internet through a mobile phone network. Thus, the data can be browsed anywhere and anytime on web site. The data is processed by the server, and any abnormal phenomena of the slope can be detected and used for a precaution of failure, and then issue an evacuation warning.

2.2 MEMS inclinometer technology embedded to sensor unit

The proposed system measures the inclination on the slope surface and the volumetric water content in the slope. A MEMS tilt module (nominal resolution = 0.04 mm/m = 0.0025 degree) is embedded in each sensor unit. The tilt module is a 3D-MEMS-based dual axis inclinometer that provides sensor unit grade performance for leveling applications. The measuring axes of the sensing elements are parallel to the mounting plane and orthogonal to each other. Low temperature dependency, high resolution, power-saving and low noise, together a with robust sensing element design, if we keep on leveling installation, this MEMS type inclinometer is ideal choice for slope failure sensors.

2.3 Saving power designed based on 16-bit ultra-low-power MCU

In order to reach the purpose of a low-cost and simple warning system, the choice of CPU controller become very important. 16-bit Ultra-Low-Power MCU with ultralow power consumption being very suitable to no commercial power supply region was selected.

A long-term sensor unit power consumption test (not include Micro SD) was started on July 7, 2008, the interval time of data sampling and transmit was 10 minutes. 4 cells alkaline batteries were installed in the test senor unit. Figure 3 shows the relation of battery voltage and elapsed time, the test unit has been worked for 3.5 years.

3 FIELD VALIDATION FOR SIMPLE SLOPE MONITORING AND LANDSLIDE IN JAPAN AND CHINA.

3.1 A case of detection on Three Gorge Dam landslide failure in China

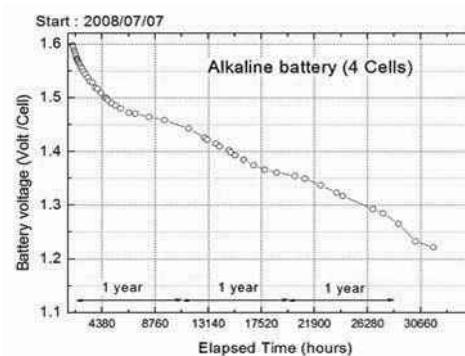Prototype of the developed monitoring system has been established on a side slope of Three Gorge Dam region, the

Figure 3. Sensor unit long-term power consumption test.

world largest dam in China, since 2008. The site named Sai-Wan-Ba is located on the right side of the dam lake, near Wenzhou Ward, 80 km eastward from Chongqing City (Figure 4). Several landslide blocks were found by geological investigations.

The time histories of the tilting angles in X-axis and Y-axis, the volumetric water content at a depth of 30 cm on the ground surface, and the record of precipitation are shown in Figure 5 and Figure 6 respectively.

A consecutive movement of a sliding block shown in Figure 5 was observed for a long period. A quick movement of tilt sensor was detected at a heavy rainfall event on June 6-7. 2009; a large scale of landslide disaster nearby observation point 2
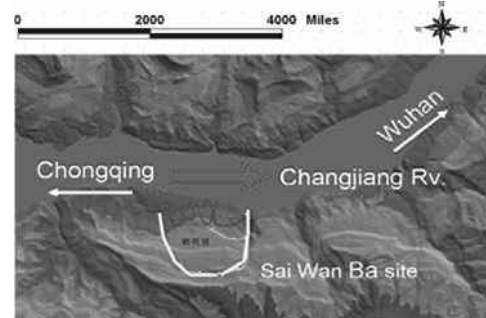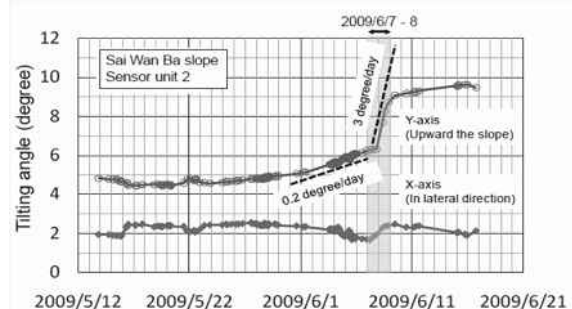

Figure 4. Location of Sai Wan Ba landslide site.

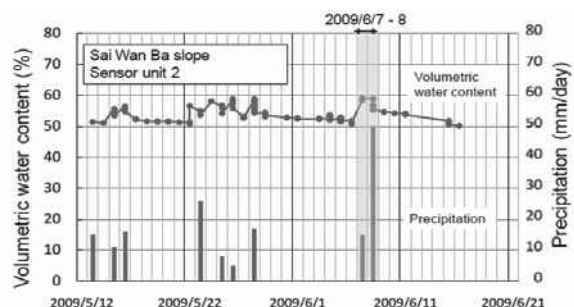Figure 5. Time history of tilting angle & precipitation by sensor unit 2.

Figure 6. Time history of volumetric water content & precipitation by sensor unit 2.

was happened on 8 June shown in Figure 7, and this landslide disaster caused the slope of observation point 2 inclined gradually at the same time. As a result, there was almost two day for taking refuge before the landslide happened.

Figure 7. New landslide on June 7, 2009.

1.1 *Monitoring of a slope failure site for secondary disaster prevention in Japan*

Another field detection result of a slope failure site along a national road in Kyushu of Japan is shown in Figure 8. This slope consists of strongly weathered granite, and it was failed due to a heavy rainfall in July of 2009. The slope was excavated to have a gradient of 45 degrees for disaster relief work, and was monitored with three sensor units. Heavy rainfall caused a second failure, and a local part of slope including the sensor unit fallen down. Figure 9 shows the records of tilt sensor of the unit, in directions toward and laterals to the slope, respectively. Specially, the tilting in Y-axis (lateral direction) showed
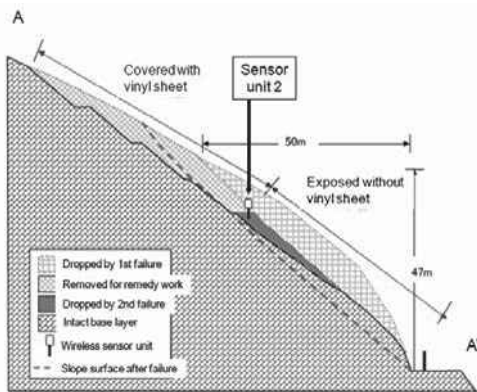

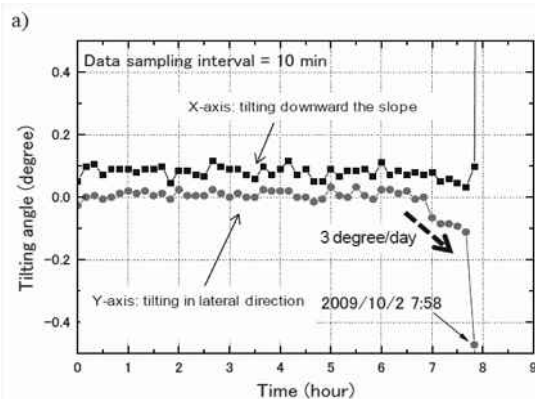Figure 8. Sketch of failed slope along highway

Figure 9. Tilt angle change just before the second failure.

extraordinary behaviors 50 minutes before the second failure.

Its tilting rate was around 3 degrees per day (0.12 degrees per hour). As this second failure took place adjacent to the location of the sensor unit 2, the behaviors of the slope before and after the failure was detected by the monitoring system. The site manager got aware of the extraordinary behaviors of the data from sensor unit 2, and he stopped the disaster relief work and the road service to avoid large loss successfully.

1.2 *Field evaluation for developed tilt sensors to traditional extensometers based on in-site measuring*

Another in-site measurement results were showed in Figure 10 to Figure 11a-e, a heavy rainfall on July 2011 caused a slope failure alone local national road in Kyushu of Japan.

For the road earthwork construction, an emergency monitoring system using multiple borehole inclinometers, extensometers, tilt sensors and rain gauge has been set up at
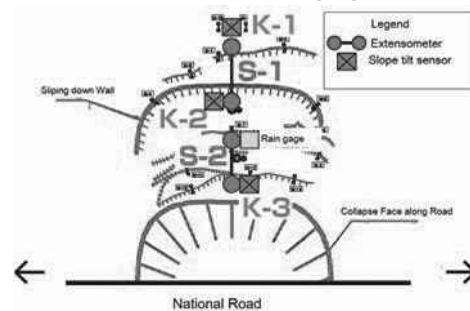

Figure 10. A field site of failed slope along national road in Japan
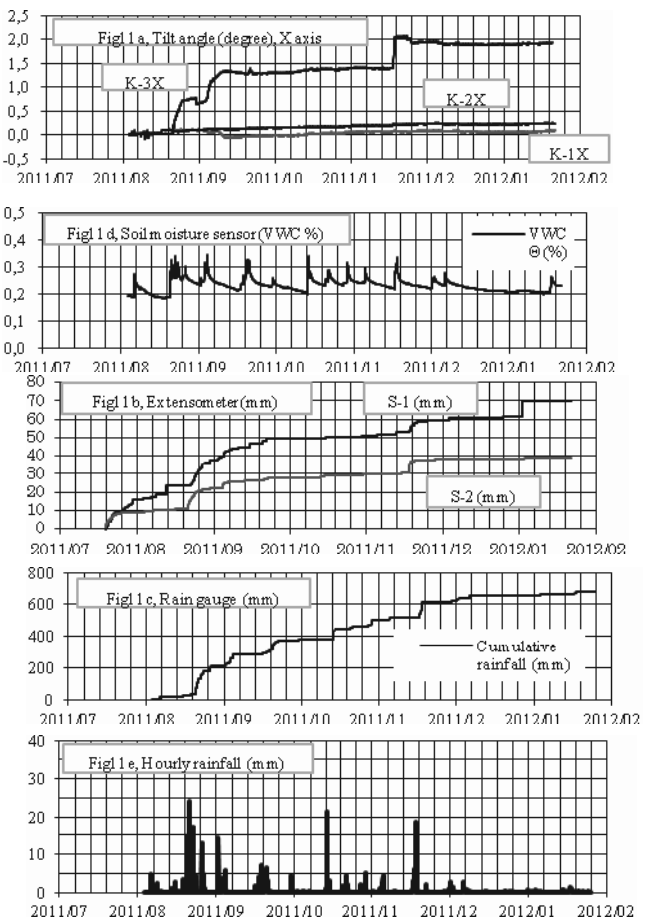

Figure 11, Time histories vs. measuring values.

slope failure site. For validating developed tilt sensor with field extensometers data, the three tilt sensors were installed nearby

fixed pole of extensometers moving point shown in Figure 10. In this field site, other 4 boring surveys have been carried out and multiple borehole inclinometers were installed, two of the tilt sensors (K-2, 3) were just set up nearby the survey boring holes. According to the result of boring survey, a landslide slip surface, which depth was 17m, was found shown in Figure 12.

Figure 10a-b show the time histories of tilt sensor inclination alone extensometer wire direction (tilt sensor x axis) and the extensometer movement(S-1, S-2), Figure 10c shows the result of cumulative rainfall value by rain gauge. Figure 10d shows the result of volume water content by ECH2O water content
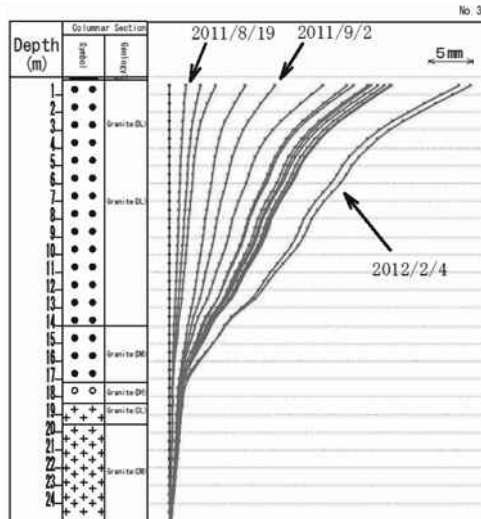

Figure 12. The result of multiple borehole inclinometers.

sensor.

The normal case, the fix pole of tilt sensor was inserted into earth of slope surface at the depth of 1.0 meter, so that the inclination of tilt sensor means average movement of the slope surface. The inclinations of tilt sensors especially tilt sensor K-3, and movement of extensometers were increased with rainfall and showed a strong correlation each other based on the results of Figure 10a-e.

Figure 13 shows the relation of slope movement (mm) by extensometer(S-1) vs. inclination (degree) by tilt sensor (K-3). Based on the result, the almost linear relationship between extensometer and tilt sensor was obtained except for the storms period of August, October and November, 2011.
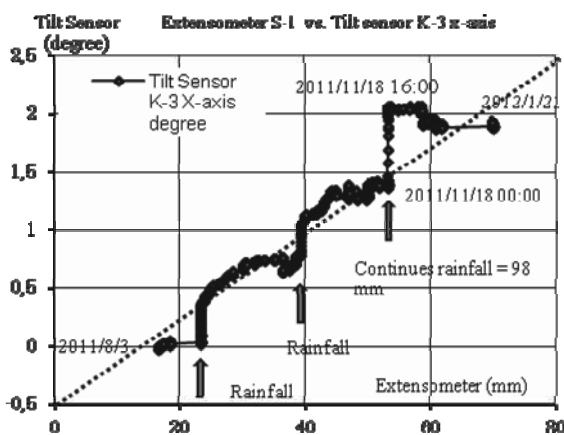

Figure 13. The relation of slope movement vs. tilt angle.

Another important result is that between heavy rainfall start and landslide initiation, the value of extensometer seems no any change but the tilt sensor inclination has reacted quickly, for example, the heavy rainfall on 18 November 2011, that hourly rainfall reached 20mm and continues rainfall reached 96mm, run continuously for 16 hours, during this period, the inclination of tilt sensor was increased but the value of extensometer

showed no any change (Figure 13). The tilt sensor measures a local change of slope surface, and the extensometer measures a whole movement of slope failure or landslide. The failure of slope starts from local and enlarges to whole area usually, so that this result should be considered as an important slope pre-failure phenomenon, which can let warning system to issue useful information to residents to avoid slope failure or landslide disaster in advance.

2 CONCLUSION

Based on above case histories and field validation result, a low-cost and simple monitoring method of measuring tilting motion on these slope surface is effective and proposed for precaution of rainfall-induced slope failure and landslides; The tilt sensor unit with MEMS inclinometer module and wireless module is very save power and installed easily. At a side slope of Three Gorge Dam in China, consecutive movement of a sliding block was observed for a long period.

A quick movement was detected at a heavy rainfall event, in which a tilting rate of about 3 degrees per day was continued for 2 days. This event includes a slope failure and significant displacement in a wide area including the position of the sensor unit.

At a slope failure site along a national road in Japan, the slope surface showed abnormal tilting behaviors 30 to 50 minutes before failure. The tilting rate was around 3 degrees per day, although it continued for only 50 minutes before failure. Such behaviors could be used as a signal for early warning.

Furthermore, between heavy rainfall and landslide initiation, the tilt sensor inclination has reacted quickly than extensometer value; it can be considered that the tilt sensor unit is effective tool for early warning system.

3 ACKNOWLEDGEMENTS

4 REFERENCES

Orense R.P., Towhata I., Farooq, K. 2003. Investigation of failure of sandy slopes caused by heavy rainfall. *Proc. Int. Conf. on Fast Slope Movement-Prediction and Prevention for Risk Mitigation (FSM2003)*, Sorrento.

Towhata,I., Uchimura,T. and Gallage,C.P.K. 2005. On early detection and warning against rainfall-induced landslide. *Proc. of The First General Assembly and The Fourth Session of Board of Representatives of the International Consortium on Landslides (ICL)*. Washington D.C., Springer, pp.133-139.

Uchimura, T., Towhata, I., Wang, L. and Seko, I. 2008. Simple and Low-Cost Wireless Monitoring Units for Slope Failure. *Proc. of the First World Landslide Forum, International Consortium on Landslides (ICL)*. Tokyo, pp. 611-614.

Uchimura, T., Towhata, I., Wang, L. and Seko, I. 2009. Development of Low-cost Early Warning System of Slope Instability for Civilian Use. *Proc. of 17th ISSMGE*. Alexandria, Vol. 3, pp.1897-1900.

Uchimura, T., Wang, L., Qiao, J.P., and Towhata, I. 2011. Miniature ground inclinometer for slope monitoring. *Proc. of the 14th Asian Regional Conference on Soil Mechanics and Geotechnical Engineering*, Hongkong.

The physical vulnerability of roads to debris flow

La vulnérabilité physique des routes aux coulées de boue

Winter M.G., Smith J.T.
Transport Research Laboratory (TRL), Edinburgh, United Kingdom

Fotopoulou S., Pitilakis K.
Aristotle University of Thessaloniki,Thessaloniki, Greece

Mavrouli O., Corominas J.
Technical University of Catalona, Barcelona, Spain

Agyroudis S.
Aristotle University of Thessaloniki,Thessaloniki, Greece

ABSTRACT: The physical vulnerability of roads to debris flow is expressed through fragility functions that relate flow volume to damage probabilities. Fragility relations are essential components of quantitative risk assessments (QRA) and allow for the estimation of risk within a consequence-based framework. This paper describes fragility curves produced in order to provide the conditional probability for a road to be in, or to exceed, a certain damage state for a given debris flow volume. Preliminary assessments were undertaken by means of a detailed questionnaire. Fragility curves have been defined for three damage states for high speed (reported herein) and for low speed roads (to be reported later) in order to cover the typical characteristics of roads vulnerable to debris flow. The probability of any given damage state being met or exceeded by a debris flow of a given volume ($10m^3$ to $100,000m^3$) was derived from the mean of the responses received. The development of the fragility curves is described and data issues discussed.

RÉSUMÉ : La vulnérabilité physique des routes aux coulées de boue s'exprime à travers des fonctions de fragilité qui mettent en rapport le débit volumique et les probabilités de dommages. Les relations de fragilité sont des composantes essentielles des évaluations quantitatives de risques (QRA) et permettent d'estimer le risque au sein d'un cadre basé sur les conséquences. Cet article décrit les courbes de fragilité produites afin d'indiquer la probabilité conditionnelle qu'une route se trouve, ou dépasse, un certain état d'endommagement pour un débit volumique donné de boue. Des évaluations préliminaires ont été réalisées au moyen d'un questionnaire détaillé. Des courbes de fragilité ont été définies pour les trois états d'endommagement pour les routes à grande vitesse (présentées dans ce document) et pour les routes à petite vitesse (qui feront l'objet d'un rapport ultérieur) afin de couvrir les caractéristiques typiques des routes vulnérables au coulées de boue. La probabilité d'atteinte ou de dépassement d'un état d'endommagement donné en présence d'une coulée de boue d'un volume donné ($10m^3$ à $100\ 000m^3$) a été dérivée de la moyenne des réponses reçues. L'élaboration des courbes de fragilité est décrite et les problématiques liées aux données sont abordées.

KEYWORDS: Landslides, debris flows, hazard, risk, probability, fragility, QRA.

1 INTRODUCTION

Fragility curves are a graphical means of describing the physical vulnerability of elements at risk to a given hazard. They give the conditional probability of a particular element at risk to be in, or to exceed, a certain damage state as a result of a hazard of a particular type or intensity (Mavrouli & Corominas 2010). Fragility relationships are essential components of quantitative risk assessments (QRA) as they allow for the estimation of risk within a consequence-based framework.

For the purposes of this work the element at risk is a road and the hazard is debris flow. Damage probabilities have been assigned for specific debris flow volumes; these should not be confused witht he probability of event occurence. Fragility curves have been produced which indicate the probability of a debris flow of a given volume exceeding each of three damage states. To the best of the Authors' knowledge this is the first time that fragility curves have been developed for the effects of debris flow on roads. Fragility relationships are widely adopted in seismic 'expected loss' and risk assessments, being a valuable tool to explicitly assess the vulnerability of structures to earthquake hazard (Pitilakis et al. 2006).

While several possible approaches were available, including analytical and empirical ones, for the development of fragility curves, it was decided that expert engineering judgement should be used due to a lack of a comprehensive empirical dataset as well as the complex nature of the problem.

This paper describes the questionnaire sent to experts globally to collect data for the fragility curve development. It also describes the analysis and interpretation of the data collected, and its validation using real world examples.

2 METHODOLOGY

2.1 Road characterisation

Many different classifications of roads could be considered, covering numerous key factors such as construction type, stiffness, and traffic speed. However, in order to reduce the questionnaire to a reasonable size some simplification was needed. Primarily it was decided that, for the purposes of this exercise, all roads could be considered to be relatively stiff and brittle (the low strain stiffness of even an unbound pavement is such that it is likely to behave in a stiff, brittle manner). In order to further simplify the analysis roads have been divided into low and high speed roads, characterized as follows:
•   High speed: speed limit between 80 and 110km/h and one or more running lane in each direction, most likely in conjunction with a hardstrip or hard shoulder.
•   Local (or low speed) roads: speed limit typically <50km/h on a single-carriageway (one lane for each traffic direction) or single-track. This category is intended to encompass both paved (bituminous, unreinforced or reinforced concrete) and unpaved constructions.

The gap between the speed limits of the two classes of road, reflects the transition between local roads and high speed roads, which is by no means geographically consistent. This reflects reality – in some countries and regions certain road geometries are more closely aligned with the definition of local roads and

in others they are more closely aligned with the definition of high speed roads. The results reported here are for high speed roads.

2.2 Damage states

Representative damage states associated with the consequences of a debris flow of a given volume intersecting a road were defined. The damage states considered in the questionnaire are defined in Table 1 and range from the type of damage that is unlikely to significantly affect the passage of vehicles, at least on high speed roads, to that which causes longer term damage and restrictions to the speed and/or passage of traffic.

Respondents to the survey were requested to use their expert judgement to assess the probability of each damage state being exceeded (Table 2) for a given event size. Respondents were asked to use the qualitative descriptors 'Highly Improbable' and 'Extremely Likely' with caution, and only where an extensive, high quality dataset supports the classification.

Table 1. Damage state definition.

Damage State	High Speed Roads
P1 (Limited damage)	Encroachment limited to verge/hardstrip
P2 (Serious damage)	Blockage of hardstrip and one running lane
P3 (Destroyed)	Complete blockage of carriageway and/or repairable damage to surfacing

Table 2. Description of probabilities.

Qualitative Descriptor	Description	Value for Analysis
Highly improbable	Damage state almost certainly not exceeded, but cannot be ruled out	0.000001
Improbable (remote)	Damage state only exceeded in exceptional circumstances	0.00001
Very unlikely	Damage state will only be exceeded in very unusual circumstances	0.0001
Unlikely	Damage state may be exceeded, but would not be expected to occur under normal circumstances	0.001
Likely	Damage state expected to be exceeded under normal circumstances	0.01
Very likely	Damage state expected to be exceeded	0.1
Extremely likely	Damage state is almost certainly exceeded	1.0

3 RESULTS

The questionnaire was sent to 176 experts; 47 responses (27%) were received from 17 countries: UK (34%), Greece (23%), other European countries (26%), Asia (4%), Australasia (4%), North America (4%) and the Middle East (2%). The respondents' backgrounds were Academia (32%), the Commercial Sector (51%) and Government Bodies (17%).

4 ANALYSIS

4.1 Preliminary fragility curves

It is a relatively straightforward matter to construct preliminary fragility curves from the average of the probability responses at each volume, at each damage state and for both high speed roads and local roads as illustrated in Figure 1. These curves have the basic attributes of typical fragility curves. In broad terms these curves and the data that underpin pass the sense test. The curves generally show that landslides of a given volume are associated with higher probabilities of exceeding a certain damage state when they affect local roads than when they affect high speed roads, as would be expected. In addition, the curves for high speed roads generally show little effect at small landslide volumes, below a few hundred cubic metres.

It is noticeable that the mean probabilities do not reach unity for any of the curves. This implies that the damage states as defined can never be met or exceeded with complete certainty. However, this is an inevitable function of using the average of the responses, as the maximum possible response coincides with the desired termination point of each curve (a volume at which exceeding the given damage state is inevitable and the probability is unity). Further stages of analysis were undertaken to interrogate and better understand the data.
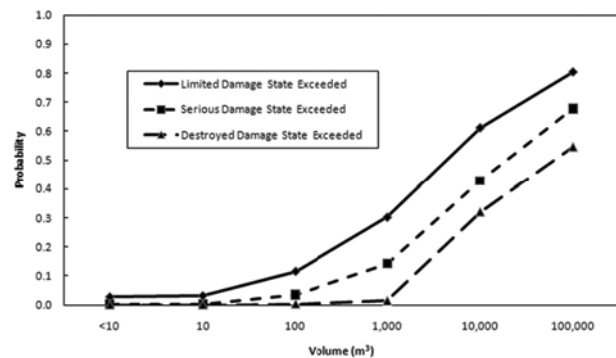

Figure 1. Preliminary fragility curves for high speed roads.

4.2 Curve fitting

Standard Excel™ curves were fitted (third order polynomial for Limited Damage and fourth for Severe Damage and Destroyed states). This gave better separation of the individual curves than is shown in Figure 1, and there was greater contrast between the results for high speed and local roads (Pitilakis & Fotopoulou 2011). This technique allows a degree of extrapolation of the data to higher volumes/probabilities. However, over application of such extrapolation tends to distort the curves at lower volumes.

4.3 Manual extrapolation

The data presented in Figure 1 may be manually extrapolated by a further logarithmic cycle by visually judging the appropriate value of probability at 1,000,000m^3 in order to maintain the broad appearance and trend of the curves. It is noticeable that, even when the volume is increased to 1,000,000 m^3 in this way none of the fragility curves reach unity; only that for Limited Damage for local roads reaches a value of around 0.95.

4.4 Weighting the data

Clearly the experience of the respondents is a critical metric in terms of understanding, evaluating, analysing and interpreting these data. The respondents were asked to assess their experience on a scale of zero (no experience) to 10 (extensive experience). The scores of this self-assessment weight towards the higher end of the range, as might be expected from a sample of respondents who were selected for their known expertise in this area. It thus seems potentially appropriate to place a greater confidence in the responses received from those who reported that their level of experience was higher than the average and a number of approaches is possible.

Firstly, a weighting approach may be taken. However, care is needed to ensure that the sample is weighted rather than the individual responses; otherwise bias will be introduced into the results. (Weighting the individual responses will, depending upon the precise approach taken, either increase or decrease the individual probabilities contained within the questionnaires for those with higher expertise and the converse for those with lower levels of expertise. There is no logical justification for such a change and this should therefore be avoided.) Weighting the sample may be done as follows

$$p = \frac{\sum_{i=1}^{n} p_i E_i}{\sum_{i=1}^{n} E_i}$$

(1)

where p = weighted mean probability of a particular damage state being exceeded; p_i = the individual responses of the probability of a particular damage state being exceeded; E_i = the individual responses in terms of self-assessed experience; and n = the number of responses.

However, there does remain a question as to what a weighted average means and statistical advice (Sexton, pers. comm.) indicates that the results should be treated with a degree of caution.

This yields fragility curves with lower probabilities of given damage states being exceeded by a given event volume than those derived from the full data set (Figure 2). This may indicate that either those with less experience overestimate, or those with greater expertise underestimate, potential damages.

The second approach involves rejecting the data from those respondents reporting less experience, leaving only that from those who assessed themselves as more experienced in this area. Statistical advice (Sexton, Pers. Comm.) indicates that approximately only scores from the upper 25% of the available range should be examined. This implies that the analysis should be undertaken for those judging their experience level as eight or above (33% of respondents). However, plotting the data led to a rather confused picture and to the conclusion that the 16 responses corresponding to the 33% of respondents reporting their experience level to be eight or above were insufficient to present a coherent picture. As for the weighting approach the resulting fragility curves yield lower probabilities of given damage states being exceeded by a given volume of event than those derived from the full data set.
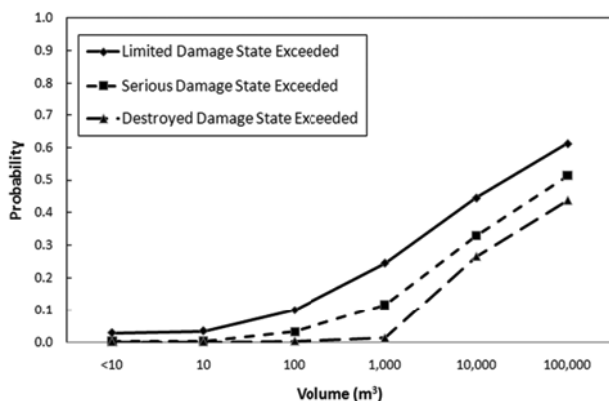

Figure 2. Weighted fragility curves: top, local roads; bottom, high speed roads.

5 INTERPRETATION

The curves illustrated in Figure 1 do not stretch between zero and unity. Even when manually extrapolated to a landslide volume of 1,000,000m³ the curves do not reach unity as would be expected if they had been derived from by modelling in which such an outcome would have been constrained.

Using the current approach it is inevitable that the mean probability of each damage state being reached or exceeded is less than unity unless all of the respondents return such a value. This then begs the question of how to account for such an inevitable, and seemingly contradictory, facet of the results. It is straightforward to 'force' the curves to reach to unity by a ratio approach (the forced probability at any value of landslide volume, $p_{if} = p_i \cdot [1/p_n]$ where p_i is the mean probability and p_n is the mean probability at the maximum landslide volume).

In order to determine whether such an approach can be justified one must examine the more detailed responses of the respondents to the questionnaire and in particular the responses

of those where a probability of unity was assigned to the combinations of landslide volume and damage state. These data illustrate, as might be anticipated, that the number of responses assigning a probability of unity increases markedly with landslide volume while decreasing with increased damage state severity. Most importantly, for high landslide volumes, the majority of respondents give unity for the likelihood of a given damage state being reached or exceeded, lending justification to 'forcing' the curves to reach unity.

As discussed, the preliminary fragility curves of Figure 1 can be forced to unity, and manually extrapolated to the next order of magnitude in terms of landslide volume (i.e. 1,000,000m³). The next logical step is to combine these two actions as illustrated in Figure 3. The curves illustrated therein conform to the 's'-shape generally perceived as being the correct form for fragility curves. Notwithstanding this, one would normally expect that the curves for different damage states would reach unity at different landslide volumes; that they do not is a function of the type of analysis undertaken and it seems reasonable, as none of the curves reach unity, to force them all to such a level at the highest volume considered.

Geographical variations and variations potentially caused by respondents' backgrounds (Academic, the Commercial Sector, and Governments) were investigated. It was concluded that the datasets were generally too small to draw definitive conclusions albeit that the data appeared to suggest that:

- Responses for the UK exhibited slightly higher probabilities for larger landslide volumes compared to those for the 'Rest of the World'.
- The responses for Academia exhibited slightly higher probabilities for larger landslide volumes compared to those for the Commercial Sector.
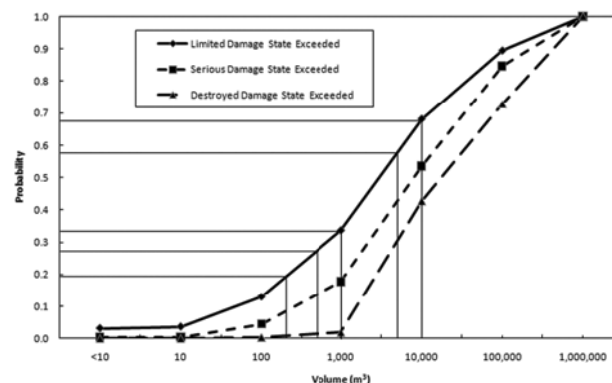

Figure 3. Fragility curves for high speed roads 'forced' to unity and manually extrapolated to the next order of magnitude of debris flow volume. Lines for Limited Damage at 200, 500, 1,000, 5,000 and 10,000m³ are also shown.

6 VALIDATION

The comments received from respondents generally supported the use of curves of the form illustrated in Figure 3 and events from Scotland in the UK and the Republic of Korea are considered here. Figure 4 illustrates hypothetically-shaped curves in which the numbers given relate to a 5,000m³ event on a high speed road (Figure 3). The probabilities (p) of the damage being equal to or greater than a given level are:

- Damage greater than or equal to 'Limited', $p = 0.6$.
- Damage greater than or equal to 'Serious', $p = 0.4$.
- Damage greater than or equal to 'Destroyed', $p = 0.3$.

The discrete, or conditional, damage state probabilities (i.e. the probabilities of the occurrence of a given damage state) are estimated from the probabilities given above:

- Probability of no damage = 1.0 - 0.6 = 0.4.
- Probability of 'Limited' damage = 0.6 – 0.4 = 0.2.
- Probability of 'Serious' damage = 0.4 – 0.3 = 0.1.
- Probability of 'Destroyed' damage state = 0.3.

Note that the conditional probability of the 'Destroyed' damage state is always equal to the probability of that state being exceeded. Vulnerability assessment using fragility curves is, of course, probabilistic in nature and the models used in their construction – in this case based upon expert judgment – have inherent uncertainties. Accordingly, the validation examples are not expected to precisely predict the observed damages.
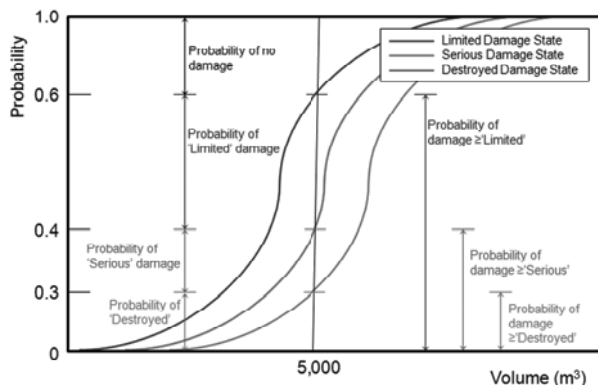

Figure 4. Hypothetical fragility curves: the numbers relate to a 5,000m³ event on a high speed road (see Figure 3) and show conditional probabilities and those of a given event exceeding a damage state.

6.1 A85 Glen Ogle, Scotland

In August 2004 two debris flow events occurred at Glen Ogle blocking the A85 strategic road, culverts and other drainage features, and necessitated a full repair to the road pavement, safety barriers and parapets. Some 20 vehicles were trapped by the events and 57 people were airlifted to safety; one vehicle was swept away in the latter stages of the event (Winter et al. 2005, 2006, 2009). The smaller southerly and larger northerly events were estimated to have deposited around 3,200m³ and 8,500m³ in their respective debris lobes having been triggered by smaller translational slides of around 285m³ and 280m³ (Milne et al. 2009). These figures are believed to exclude material deposited on the road and it seems reasonable therefore to round these figures up to around 5,000m³ and 10,000m³. This illustrates the uncertainty when dealing with debris flow volumes between the amount mobilised and that deposited at road level.

Figure 4 shows how these event volumes plot on the fragility curves. For the smaller (5,000m³) event the conditional probabilities for no damage, 'Limited', 'Serious and 'Destroyed' damage states are 0.4, 0.2 (0.6), 0.1 (0.4) and 0.3 (0.3) (the probabilities of the damage states being met or exceeded are given in parentheses); for the larger (10,000m³) event the conditional probabilities are around 0.3, 0.15 (0.7), 0.15 (0.55) and 0.4 (0.4). Certainly the damage caused by the larger event would have been described as 'Destroyed' using the scheme considered here and the probability of this state being 0.4 seems to be broadly in line with observations in its immediate aftermath, affecting a road length of around 200m. Similarly the damage caused by the smaller event, although significantly less in terms of physical damage to the infrastructure, would also be classified as 'Destroyed' and this seems to broadly reflective the probability of 0.3 (Figure 4).

6.2 Chuncheon National Highway, Republic of Korea

Debris flows of around 500m³ to 1,000m³ were evident at the Chuncheon National Highway Tunnel Portals (Lee & Winter, 2010). For an event of this volume (1,000m³) the conditional probabilities of the damage states no damage, 'Limited', 'Serious', and 'Destroyed' are 0.7, 0.1 (0.3), 0.18 (0.2), and 0.02 (0.02) (Figure 4).

Only very minor damage was incurred and this reflects the small volumes and the combined conditional probabilities of 0.8 for no damage and of the 'Limited' damage. The road was not open at the time of the event and there is every possibility of both further and larger events that have the potential to meet or exceed higher damage states.

7 CONCLUSIONS

A survey of experts was conducted to develop of preliminary fragility curves for the effects of debris flows on roads.

Included in the questionnaire was the opportunity for the respondents to make 'free text' responses to defined questions. Their responses have been used, in part, to determine the form of analysis. Consequently the proposed fragility curves have been extrapolated to include events one order of magnitude greater than the largest considered in the questionnaire. In addition, this form of determining fragility curves renders it almost impossible for the probabilities to range from zero to unity; according the proposed fragility curves have been stretched to ensure such a spread.

The derived fragility curves have been compared to known events in Scotland (UK) and the Republic of Korea. In general the curves tend to give results that might be deemed 'sensible' with probabilities of around 0.3 to 0.8 being suggested for the known damage states. Exceptions to this occur when detailed site characteristics introduce complexities that are not, and could not be, accounted for in the analysis.

Notwithstanding this, the method of data acquisition and the perceived interpretations of the questionnaire for this first approach raise some interesting issues that will be explored in a later paper. Continued efforts are needed, potentially including the use of modelled and empirical data.

8 ACKNOWLEDGEMENTS

9 REFERENCES

Lee, S.-G. & Winter, M.G. 2010. The effects of debris flow in the Republic of Korea and some issues for successful management and mitigation. In A.L. Williams, G.M. Pinches, C.Y. Chin, T.M. McMorran & C.I. Massey (eds.), *Geologically Active: Proceedings, 11th IAEG Congress*, 1243-1250. London: CRC Press.

Mavrouli, O. & Corominas, J. 2010. Rockfall vulnerability assessment for reinforced concrete buildings, *Natural Hazards and Earth System Sciences* 10, 2055-2066.

Milne, F. D., Werritty, A., Davies, M. C. R. & Browne, M. J. 2009. "A recent debris flow event and implications for hazard management", Quarterly Journal of Engineering Geology and Hydrogeology 42, 51-60.

Pitilakis, K., Alexoudi, M., Argyroudis, S., Monge, O. & Martin, C. 2006. Earthquake risk assessment of lifelines. *Bulletin of Earthquake Engineering* **4**, 365-390.

Pitilakis. K. & Fotopoulou, S. (Eds.) 2011. Physical vulnerability of elements at risk to landslides: methodology for evaluation, fragility curves and damage states for buildings and lifelines. SafeLand Deliverable 2.5. (www.safeland-fp7.eu.)

Winter, M. G., Macgregor. F. & Shackman, L. (Eds.) 2005. Scottish Road Network Landslides Study, 119p. Trunk Roads: Network Management Division Published Report Series. Edinburgh: The Scottish Executive.

Winter, M. G., Heald, A. P., Parsons, J. A., Macgregor, F. & Shackman, L. 2006. Scottish debris flow events of August 2004, Quarterly Journal of Engineering Geology and Hydrogeology 39, 73-78.

Winter, M.G., Macgregor, F. & Shackman, L. (Eds.) 2009. *Scottish road network landslides study: implementation*: 278p. Transport Scotland Published Report Series. Edinburgh: Transport Scotland.

Inspection and Capacity Assessment of Anchored Slopes

Inspection et évaluation des capacités des pentes renforcées par ancrage

Yeh H.n-S., Wang C.-S., Wei C.-Y.
Taiwan Area National Freeway Bureau, MOTC

Lee S.-M., Ho T.-Y., Hsiao C.-A., Tsai L.-S.
CECI Engineering Consultants, Inc., Taiwan

ABSTRACT: In Taiwan, anchors were first used in the Techi Dam for slope protection in 1970s. Since then, anchors were often used for stabilizing slopes in the construction of roads or communities. Lots of anchor experience of engineering practices have been accumulated in the past 40 years, however, it still remains some problems to be solved. In particular, after the failure of anchored slope at station 3.1K of Highway No. 3 in 2010, the function of existing anchors and the safety of anchored slopes have raised lots of concern. This paper introduces examining items, methods and processes of functional inspection of existing anchors. Also, results of 16 functional inspection of existing anchors in western Taiwan are presented. It is expected that the concepts and suggestions described in this article would be helpful for an engineer in gaining the ability of the analysis of slopes so that the more effective design can be developed for such a problem in the future.

RÉSUMÉ : A Taiwan, les renforcements par ancrages ont d'abord été utilisé dans le barrage Techi pour la protection des talus dans les années 1970. Depuis lors, les ancrages étaient souvent utilisés pour la stabilisation des pentes dans la construction de routes. Beaucoup d'expérience dans les pratiques d'ingénierie d'ancrages a été accumulées au cours des 40 dernières années. Cependant, il reste encore quelques problèmes à résoudre. En particulier, après la rupture d'une pente ancrée à la station 3.1k de la route n°3 en 2010, l'efficacité des ancrages existants et la sécurité des talus ancrées ont soulevé beaucoup d'inquiétude. Cet article présente l'examen des ancrages, des méthodes et des processus de contrôle du fonctionnement des ancrages existants. En outre, les résultats d'inspection de 16 talus renforcés par ancrages existants dans l'ouest de Taiwan sont présentés. Il est prévu que les concepts et les suggestions décrits dans cet article soit utilisable par un ingénieur via l'acquisition d'outils d'analyse des pentes de sorte qu'une conception plus efficace puisse être développé à l'avenir.

KEYWORDS: Landslides, anchor, lift-off test, anchor inspection, maintenance and management.

1 INTRODUCTION

Taiwan's area is approximately 3,600,000 hectare, and of it moderately flat area comprises about 26% while sloped and forested land make up the remaining 74%. Therefore Taiwan is mostly mountainous with lesser plains topography, though in the recent decade with the economic growth and the pursuit of comfort and ease of transportation, the trend of developing public infrastructure such as roadways and public facilities is moving toward hillsides and slopes.

Ground anchoring usage over steep slope has its certain advantages. Ground anchoring technique originated since the 1970s in Taiwan. Since 1988, Northern Taiwan Second Highway construction had begun, as its alignment laid predominantly among mountainous ranges and slopes, this type of method had proved itself to be an effective technique under such natural constraints and coupled with rapid economic growth, many new projects had begun to adopt this method in many sloped terrain community developments. Until today, ground anchorage technique has proven to be a reliable method and have been widely used, as well as the design and field installation has vastly improved since its earlier days. However, there are still many ground anchoring failure instances in recent years, one of which is the quite high profiled case of the 1997 Xizhi Lincoln Mansions disaster and 2010 National Highway No. 3 at 3.1k accident. Both failure cases are considered ground anchoring accidents and attributed to parallel landslide as the cause.

According to Briaud et al.(1998), Bruce and Wolfhope (2007), Liao et al. (2011), Ho et al.(2011), Jeng et al.(2011) and various domestic and foreign ground anchoring case studies, failure instances involved most commonly pre-stressed losses.

The main cause of that include 1) free section of tendon(unbounded tendon) rusted and cracked, 2) ground anchoring wedges rusted or had sub-standard quality, 3) Installation did not conform to the specification, as the steel tendon had not gone far enough into the earth, 4) change of terrain layer, and 5) ground cave in at bottom of the bearing plate.

After the National Highway No. 3 incident involving ground anchoring failure, see Figure 1, a complete study had done on ground anchor inspection and assessment. Even so, the findings of the study were routine and not consistent among the investigators. This article will introduce and explain the currently most adopted ground anchoring inspection, procedure, and assessment. In addition, this article will propose a new way of ground anchoring assessment, in hoping to establish a standardized quantitative analysis procedure for professional reference.

Figure 1. National Highway No. 3 at 3.1k accident

2 INSPECTION ITEMS AND PROCEDURE

Ground anchoring inspection and assessment is aimed to analyze and understand the performance of existing anchors and the impact to the site and its surrounding.

2.1 *Inspection items*

Currently there are some initial inspection items including: exterior inspection, anchor head inspection, endoscopy inspection and Lift-off test, the four major itemswill be explained in detail later.

2.2 *Inspection procedure*

Inspection procedure is as indicated in Figure 2. First gather basic data from all sloped terrains for ground anchor index, then remove all outgrowth on the slope, and check the entire ground anchors for outside appearance, pressure bearing integrity and water seepage status. According to the gathered data and inspection results, select the most typical anchor in characteristics of all achors, remove the concrete casing to examine the anchor head and steel tendon closely, and record findings. After examining the anchor, use the findings to select partial ground anchors for endoscopy inspection to exam steel tendon corrosion and proceed with Lift-off Test, in order to understand the existing ground anchor Residual load(Tr). Lastly, based on sloped terrain basic data and findings of various test results, evaluate in totality the ground anchors current capacity. If ground anchor capacities no longer meet the requirement of original specifications or there are other anomalies present which render the anchors inappropriate for continuing usage, then a proposal is required to improve or remediate the situation, including refurbishment, remedy, reinforcement or reconstruction as required.
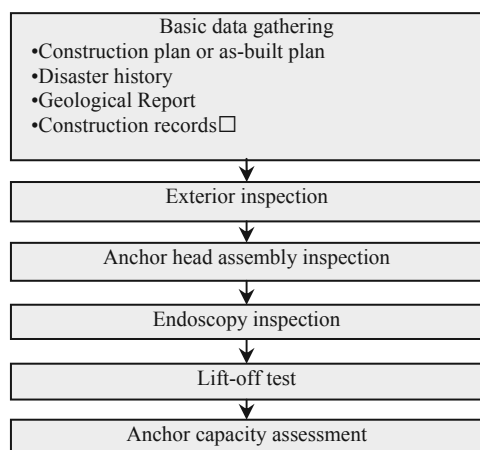
```
┌─────────────────────────────────────┐
│ Basic data gathering                 │
│ •Construction plan or as-built plan  │
│ •Disaster history                    │
│ •Geological Report                   │
│ •Construction records□               │
└─────────────────────────────────────┘
                   ↓
┌─────────────────────────────────────┐
│ Exterior inspection                  │
└─────────────────────────────────────┘
                   ↓
┌─────────────────────────────────────┐
│ Anchor head assembly inspection      │
└─────────────────────────────────────┘
                   ↓
┌─────────────────────────────────────┐
│ Endoscopy inspection                 │
└─────────────────────────────────────┘
                   ↓
┌─────────────────────────────────────┐
│ Lift-off test                        │
└─────────────────────────────────────┘
                   ↓
┌─────────────────────────────────────┐
│ Anchor capacity assessment           │
└─────────────────────────────────────┘
```

Figure 2. Ground anchor capacity assessment flowchart

3 CAPACITY INSPECTION METHOD

Various inspection category results can be used to provide as the basis for evaluating the capacity of anchors, summary of each categories is as follows:

3.1 *Exterior inspection*

Prior to knocking off the ground anchor concrete protected seats, obtain as-built drawings to mark off each and every anchors with numeric identifications. Visually inspect, investigate and record all anchor protected seats and load bearing structure system conditions. Visual inspection should emphasize on 1) anchor head protected seat hammer knocking test and the quality of sound whether solid or hollow, 2) visually inspect exterior of anchor protected seat for any damages, 3) between anchor head and load bearing structure,

look for any sign of separation, rotation, or even detachment, 4) Whether subsoil below shows sign of cave-in for the load bearing structure and 5) anchor head proximity has sign of efflorescence or ground water seepage, and all visual inspection should be carefully documented.

3.2 *Anchor head assembly inspection*

Anchor head assembly includes locking mechanism(wedges and screw head), load bearing plate and angle plate, as such parts tend to have anomalies. When inspecting anchor head assembly, carefully select a representative anchor head, after the removal of concrete protected seat, visually inspect the corrosive state of the anchor heads. After removal of anchor head protected seat the following category of items need to be recorded: load bearing plate dimension, angle plate dimension, load bearing plate angle, anchor head dimension, steel tendon style and remaining length data.

   At this stage visual inspection should emphasize on 1) anchor head wedges and steel tendon corrosion, 2) anchor head assembly and water seepage condition and 3) steel tendon interior shortening, and all inspection should be recorded in detail.

3.3 *Endoscopy inspection*

Endoscopy can be used to inspect the backside of anchor head and free section of steel tendon, to determine whether the steel tendon is corroded, broken or free section has water inside. Entire inspection process should be video recorded to allow further inspection and study back in the lab. The equipment used is as shown in Figure 3.

   Besides inspecting steel tendon status, this stage should measure the steel tendon length of free section. The measuring technique is to use a stainless steel rod to insert into the anchor free section portion until the rod can not be inserted further, as Figure 4 indicated. Then record the length of the rod which was inserted, as such length can be taken as the exposed section length.

   Endoscopy inspection should emphasis on 1)steel tendon corrosion level, 2)steel threads loosened condition, 3) free-section concrete condition, 4) any concrete casting pipes and 5) interior moisture level or any water seepage, all inspection processes should be done carefully and in detail.

3.4 *Lift-off test*

After locking in load bearing of ground anchors, it's possible that due to creep at the bond end, wedges not properly function which would reduce or increase the loading capacities. To measure the change of loading capacities after lock-in, typical lift-off test is conducted, as shown in Figure 5. Lift-off test is aimed at finding the remaining load capacity of anchor(Tr), and the reason being when tensile load is greater than the anchor remaining capacty, anchor will demonstrate obvious displacement increase, from which can be taken to evaluate the remaining capacity of ground anchors, as shown in a standard test curve in Figure 6. Ground anchor residual load(Tr) divided by ground anchor original designed load capacity (Tw) is the remaining load capacity ratio.

Figure 3. Equipment installation and operation

4 GROUND ANCHOR CAPACITY ASSESSMENT PROCEDURE AND CASE STUDY

For the purpose of quantitative assessment on the ground anchor capacities, and with regard to the ground anchors performance on the sloping terrain application is the goal of this procedure. Based on the inspection and assessment items, this article shall introduce a new set of ground anchor capacity assessment procedure, in hoping to establish a standardized way to quantitatively evaluate and assess ground anchoring. Such procedure shall comprised of exterior inspection, anchor head inspection, endoscopy inspection and lift-off test. The findings based on Table 1 distribution is point based. The total score will then be carried to Table 2 to evaluate (β) and classification. Sloped terrain performance and ground anchoring total capacity shall be classified based on Table 2 standards. Ground anchoring total performance assessment classified as A or B grade, respectively, will be given corresponding effective rehabilitation to ensure the full and reliable capacity of the ground anchors.
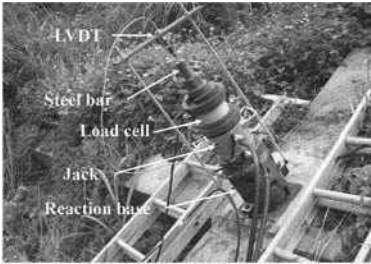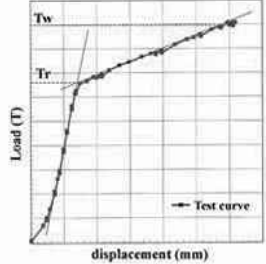
Figure 4. Free section exposed portion length investigation	Figure 5. Lift-off test installation	Figure 6. Lift-off test curve diagram

Table 1. Score of anchor capacity assessment

item	scoring	Content of inspection	Weight	subtotal
Exterior inspection	10	Buckled or detached.	0	
		Greater than 2mm separation from bearing plate or water corrosion is severe.	0.25	
		Anchor head protected seat and bearing plate separation is less than 2mm.	0.50	
		Anchor head protected seat surrounded by water seepage, efflorescence or anchor seat outside is slightly damaged or water corrosive level is moderate.	0.75	
		No observable anomalies or water quality is normal.	1.0	
Anchor head assembly inspection	15	Assembly came apart(clamp became loosened, steel tendon shrinkage or broken)	0	
		Anchor head surface appeared rusted and cracked, spread over 50% of the surface, steel tendon section is deformed due to corrosion.	0.25	
		Anchor head surface appeared rusted and cracked, but spread less than 50% of the surface.	0.50	
		Slightly corroded or water seepage. Anchor head appeared rusted, but the depth of the rust is quite thin, not measurable or lesser than 0.1mm.	0.75	
		No corrosion or water seepage is present.	1.0	
Endoscopy inspection	30	Steel tendon broken or steel threads became loosened and completely rusted.	0	
		Steel tendon appeared dark brownish, the surface already appeared corral-like or lumpy or rusted surface spread over 90%.	0.15	
		Steel tendon appeared dark brownish, the surface is rough, but not appearing corral-like or lumpy or rusted surface is between 50~90%.	0.45	
		Steel tendon appeared light brownish, but the surface is smooth and shining or rusted surface is between 10~50%.	0.75	
		No anomaly presence or rusted surface is below 10%.	1.0	
lift-off test	45	Detached, steel tendon broken or Tr=0.	0	
		Tr>1.2Tw or Tr≦0.2Tw	0.33	
		0.2Tw<Tr≦0.5Tw	0.67	
		0.5Tw<Tr≦0.8Tw	0.75	
		0.8Tw<Tr≦1.2Tw	1.0	
Single ground anchor capacity assessment(β)				
Total score of anchor capacity assessment(α)				

Remark: 1. If any of the items in categories 1,2,3,4 assessed a score of 0, such ground anchor shall be deemed as defective, and the total score of the anchor shall be zero.

2. When a sloped terrain of which 1/3 of the ground anchors inspected has reach over 90% rusted surface under the examination of endoscopy, but the lift-off test revealed remaining capacity falls into the range 0.8Tw<Tr≦1.2Tw, additional investigations in the field and test data is recommended to determine whether the slope may have a tendency to slide.

Table 2. Ground anchor assessment classifications

Individual capacity assessment		Total capacity assessment	
β	class	α	class
0	X. Defective		
β☐30	A. Worst	α☐30	A. Worst
30<β☐55	B. Unacceptable	30<α☐55	B. Unacceptable
55<β☐80	C. Acceptable	55<α☐80	C. Acceptable
80<β	D. Normal	80<α	D. Normal

Ground anchor inspection items will be measured with apparatus, which is the best and most direct way to understand the existing conditions of the anchors and remaining bearing capacities. These values usually will be referred to while performing sloping reinforcing analysis. Of course the anchor capacity cannot and should not base solely on the lift-off test result. There are other factors such as ground condition below the anchors for possible cave-ins, steel tendon or anchor head surface appeared rusted and cracked. When a sloped terrain of which 1/3 of the ground anchors inspected has reach over 90% rusted surface under the examination of endoscopy, but the lift-off test revealed remaining capacity falls into the range $0.8Tw<Tr☐1.2Tw$. Such conditions should be cross referenced with other data like field observations and inspections and evaluate in totality whether the slope has a tendency to slide. This article brings forth various anchor evaluations by which will address the possible different scenarios that might be overlooked otherwise. In order to validate the practicality of Table 1, this article takes 16 slopes and conduct a simulating calculation for them. The results are as shown in Table 3 and 4. The results and classifications are consistent, thus prove the validity of this assessment procedure and its practicality.

Table 3. Case study of Single ground anchor capacity assessment

No. of anchors	S4-1	S4-2	S4-3	S4-4	S4-5
Exterior inspection	7.5	7.5	7.5	7.5	7.5
Anchor head assembly inspection	11.25	11.25	11.25	11.25	11.25
Endoscopy inspection	22.5	30	22.5	30	30
Lift-off test	33.75	45	33.75	45	45
β	75.0	93.8	75.0	93.8	93.8
α	86.3				
Class of lift-off test	C	D	C	D	D
Class of β	C	D	C	D	D
Class of α	D				

5 CONCLUSION

Based on collected statistical data, 90% ground anchor failure are resulted at the anchor head proximity and free section part of the steel tendon. This article had gathered data which initially showed free section was not completely filled with concrete for nearly 85% of the ground anchors being examined, therefore making it the most prevalent shortcoming. To avoid anchors becoming defective which leads to disaster, anti-corrosive remedy should be done promptly.

This article only took 16 areas of sloping terrain to gather data on ground anchors for inspection and assessment as explained previously. This evaluation procedure demonstrates that the four categories assessment: inspecting the exterior aspect of the anchor, the anchor head examination, endoscopy inspection and lift-off tests is a logical process in finding

shortcomings. In the future it is bound to have additional data available added to and revised upon, and would become a valuable systematic way for the engineering industry to adopt widely across.

Table 4. Case study of anchored slope capacity assessment

Slope No.	lift-off test			Total capacity	
	Amounts	Tr(%)	Class	Scoring	Class
S1	6	88.2	D	83.9	D
S2	5	77.8	C	55.3	C
S3	6	35.6	B	38.9	B
S4	5	88.2	D	86.3	D
S5	5	65.5	C	77.2	C
S6	4	35.6	B	54.2	B
S7	3	52.9	C	60.2	C
S8	3	70.2	C	63.6	C
S9	4	43.3	B	62.9	C
S10	3	85.1	D	87.9	D
S11	3	108.6	D	74.7	C
S12	8	69.5	C	64.8	C
S13	7	71.2	C	61.6	C
S14	5	55.6	C	62.0	C
S15	8	53.5	C	68.4	C
S16	7	47.7	B	52.9	B

6 REFERENCES

Briaud J.L., Powers W.F. and Weatherby D.E. 1998. Should grouted anchors should have short tendon bond length. Journal of Geotechnical and Geoenvironmental Engineering 124(2), ASCE, New York.

Bruce D.A. and Wolfhope J. 2007. Rock anchors for north American dams: the national research program bibliography an database. Institution of Civil Engineers, Ground Anchorages and Achored Structures in Service, London, England, U.K., 481-491.

Liao H.J. and Cheng S.H. 2011. Failure cases of anchors and anchored slopes in Taiwan", Proc. of the 5th Cross-strait Conference on Structural and Geotechnical Engineering, Hong Kong.

Ho T.Y., Hsiao C.A. and Tsai L.S. 2011. Present situations and improvement suggestions of existing anchors in Taiwan. Sino-Geotechnics 130, 43-54.

Jeng C.J., Chen Y.C., Chen R., Yang P.J. and Lin Y.C. 2011. Discussion and recommendation on performance influence of current permanent ground anchor factors through case study. Sino-Geotechnics 130, 19-30.

Liao J.T., Wu T.H., Chen C.W. and Lu C.H. 2011. Discussion on Establishment of prestressed ground anchor maintenance and management system. Sino-Geotechnics 130, 79-90.

2011 Seoul Debris Flow and Risk Analysis

Coulée de boue à Séoul en 2011 et analyse des risques

Yune C.-Y., Kim G., Lee S.W., Paik J.
Department of Civil Engineering, Gangneung-Wonju National University

ABSTRACT: A series of debris flow events occurred around 8:00 to 8:50 a.m. on July27, 2011 in the Umyeon Mountain area located in central Seoul, Korea. Umyeon Mountain is a relatively small one with a height of 250m and slopes with the average angle of around 15°. Due to the debris flows with runout distances ranging from 300m to 1,000m, 16 people were killed and more than 150 houses had been damaged in the area. In this work, we seek to understand the physical characteristics of the initiation and propagation behavior of debris flows from field investigation in the area and the analysis of rainfall data collected by AWS (Automatic Weather Stations) rain gauges. Field investigation shows that about 33 debris flows occurred in the Umyeon Mountain area and most of these debris flows were initiated from small slope failures induced by high-intensity rains. The application of landslide hazard map which has been recently developed by taking slope angle and direction, strength of soil, hazard record, rainfall condition and plantation into account demonstrates its good performance to highlight areas that are vulnerable of heavy-rainfall-induced slope failure and the resulting debris flow disasters.

RÉSUMÉ : Une série de coulées de boue s'est produite vers 8h00 ~ 8h50 le 27 Juillet 2011 dans la région du mont Umyeon situé dans le centre de Séoul, en Corée. La montagne Umyeon est relativement petite avec une hauteur de 250m et des pentes à angle moyen d'environ 15°. En raison de ces coulées de boue sur une distance allant de 300 à 1000m, 16 personnes ont été tuées et plus de 150 maisons ont été endommagées dans la région. Dans cette étude, nous chercherons à comprendre les caractéristiques physiques de l'initiation et du la développement de la propagation des coulées de boue à partir d'une enquête sur place dans la zone concernée et de l'analyse des informations de précipitations recueillies par les pluviomètres de l'AWS (« Automatic Weather Stations », Station météorologique automatique). L'enquête sur place montre que près de 33 coulées de boue ont eu lieu dans la région du mont Umyeon et la plupart de ces coulées de boue ont pris naissance à partir de petites ruptures de pente provoquées par des pluies très intenses. L'application de la carte des risques de glissement de terrain qui a été récemment mise au point en prenant en compte l'angle et la direction des pentes, la résistance du sol, l'historique des désordres, les conditions des précipitations et des plantations démontre sa bonne performance pour mettre en évidence les zones qui sont vulnérables à des ruptures de pente provoquées par de fortes pluies et des catastrophes résultant de ces coulées de boue.

KEYWORDS: debris flows, field investigation, rainfall, hazard map

1 INTRODUCTION

Most of the debris flow hazard has been concentrated during the rainy season from June to August in Korea. In 2011, there were Typhoon Meari (22 June to 27 June), Typhoon Muifa (28 July to 9 August) and the seasonal rain front that stayed in the middle part of the Korean peninsula. They poured much more rainfall compared to the average value, and eventually led to debris flows around the country (Yune and Jun, 2011). A series of debris flow events occurred around 8:00 to 8:50 a.m. on July27, 2011 in the Umyeon Mountain area located in southern part of Seoul, Korea.

Debris flows which generally contain more than 50% of granular materials larger than sand particles flow fast (Johnson and Rahn, 1970; Hutchinson, 1988). Because of their fast movement, it is very hard to take refuge, even though people recognize beforehand the outbreak of the debris flow. Between 8:00 to 8:50 a.m. on July 27, 2011, many debris flows occurred simultaneously at Umyeon Mountain in Seoul where there had been a previous debris flow event in 2010 caused by Typhoon Kompasu. Because the mountain is located at the center of a dense residential area in Seoul, the hazard had a great impact on the society compared to debris flows that occur in rural areas, and it led to careful scrutiny of the hazard area and the causes of debris flows.

In this research, a site survey on the debris flow at Umyeon Mountain was carried out to analyze the causes of the event, and rainfall records were also collected to investigate the triggering characteristics of the rain. In addition, risk analysis based on the hazard map of the landslide and debris flow was performed.

2 2011 SEOUL DEBRIS FLOW

2.1. Overview of Umyeon Mountain

Located in southern part of Seoul (Fig. 1) with the height of 312.6 m above the sea level, Umyeon Mountain includes lots of eco-friendly facilities, such as natural ecological park and mineral spring which can be easily accessed by local residents. It has a main ridge formed from the northeast to the southwest, including several valleys perpendicular to the main ridge. Most of the mountain consists of highly-weathered banded gneiss with subordinate granitic gneiss. Directions in ENE- and NW to NNW-striking faults are predominant with strike- or normal-slip sense. The groundwater level in the basin seems high because six mineral springs are located side by side at the altitude of 220 to 250 meters on the slope. Field observation of Son et al. (2012) also showed that groundwater level at locations where debris flows initiated reaches to the surface so that surface runoff occurs at the continuous rainfall condition of more than 250 mm, even if there is no significant antecedent rainfall. In

2010, regional intensive rainfall following Typhoon Kompasu caused a few landslides, and some of them developed as debris flows at the northern valleys in Umyeon Mountain (Fig. 2). However, the damage in 2010 was not great compared with the debris flow hazard in 2011.
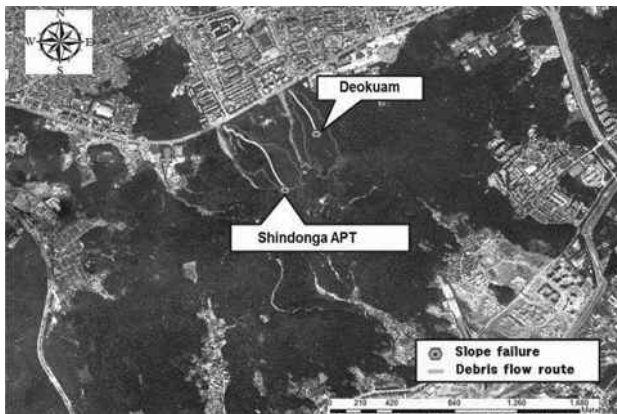

Figure 1. Location of Umyeon Mountain

Figure 2. Locations of Slope Failures and Debris Flows around Umyeon Mountain in 2010

2.2. Field Survey

Field survey was performed to get data, such as longitude/latitude and topographical/geotechnical characteristics in places where debris flows were initiated, transported, and accumulated using a portable GPS, a laser ranger, and a clinometer. Based on the data from field survey, coordinates regarding initiation zones and debris flow routes were indicated on an aerial photograph around Umyeon Mountain as shown in Fig. 3. In this figure, the initiation slope failures are marked by blue dots, and debris flow routes are marked by yellow lines. Orange dots and green dots are also the initiation slope failure at the boundary and inside of air force base at the summit of the mountain, respectively. Most of the debris flows were initiated by slope failure and flowed down the valley. It was determined that they occurred simultaneously in the whole Umyeon Mountain area. The total number of slope failure that initiated debris flow was about 150. Based on the outlet in which the debris flows accumulated, the number of debris flows was about 33.

When we classified debris flows by direction, it was found that many of the slope failures occurred on the southern slope but many of the debris flows occurred on the northern slope. The debris flows moving towards the south were channelized debris flows which flowed down the valley and merged together. On the other hand, debris flows on the northern slope were hillslope debris flows which moved rapidly without being confined in an established channel. Therefore, the northern

slope has fewer initiation zones but more debris flows compared to the southern slope.

The field survey result showed that the average moving distance of debris flows in Umyeon Mountain was about 615m, ranging from 95 to 1,584m. Also, the average gradient of initiation slopes was about 27 degrees, ranging from 11 to 37 degrees. The initiation volume of the slope failure was measured from 73 to 4,000 m^3.

Figure 3. Locations of Slope Failures and Debris Flows around Umyeon Mountain in 2011

2.3. Rainfall Conditions

Korea Meteorological Administration (KMA) reported that the torrential heavy rain which triggered landslides at Umyeon Mountain in 2011 was due to unstable atmospheric conditions mainly determined by cold and dry air from inland China along with the hot and humid air masses from the strong Southwestern wind alongside the Western North Pacific subtropical high (Fig. 4).

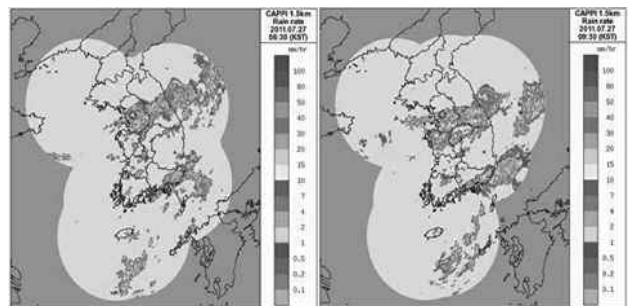(a) 6:30 a.m. 27 July 2011   (b) 9:30 a.m. 27 July 2011
Figure 4. Spatial patterns of rainfall in Korea peninsula by KMA

There are two automatic weather stations (AWSs) operated by KMA near Umyeon Mountain as shown in Fig. 5. Namhyeon and Seocho stations are located at west and northeast part of Umyeon Mountain, respectively. Rainfall records from Namhyeon and Seocho stations were analyzed as daily and cumulative rainfall for 2 months as shown in Fig. 6. The cumulative rainfall for 2 months before debris flow event was 1,489.5mm and 1,105.0 mm at Namhyeon and Seocho station, respectively. Those values were comparable to the average annual rainfall in Seoul (1,450.5 mm). A significant amount of rainfall (681.5 mm at Seocho station) was concentrated during the period from 21 June to 18 July which was 10 to 36 days before the occurrence of the debris flows. Then there was no rainfall up to 4 days before the debris flow event and 88.5 mm of rainfall was recorded 1 to 3 days before debris flow. On the day of the debris flows, 359 mm and 281 mm of rainfall at Namhyeon and Seocho station were recorded. Unlike neighboringGwanak Mountain, which is primarily

composed of granite, the geological structure of Umyeon Mountain is made up of gneiss. Therefore, the prolonged rainfall one month prior to the debris flow event might have caused saturation of the ground and made it more vulnerable to collapse. Average return period of rainfall for the duration of one hour and more was about 120 and 20 year for the Namhyeon and Seocho stations, respectively.

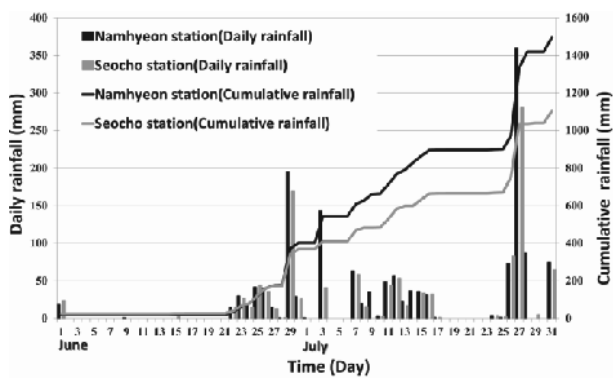Figure 5. Locations of automatic weather stations around Umyeon Mountain

Figure 6. Locations of automatic weather stations around Umyeon Mountain

3 RISK ANALYSIS

3.1 *Landslide susceptibility assessment*

There are two general approaches for landslide susceptibility assessment. The first approach is based on a physical mechanism and the second is based on a statistical method. In this work, statistical model developed in Gangneung-Wonju national university was used (Lee et. al., 2012). This model can directly yields the probability of landslide because the equation of the model was derived from logistic regression. The landslide susceptibility map is created by using GIS data which includes geomorphological characteristics, soil properties, rainfall, vegetation, and forest fire history. Figure 7 shows the landslide susceptibility map which was made with 329 mm of accumulated rainfall for 3 days, and the field survey result which included the initial slope failure and flow path of the debris flows was overlayed. As shown in figure 7, most of the slope failures were occurred in highly susceptible regions for landslide.
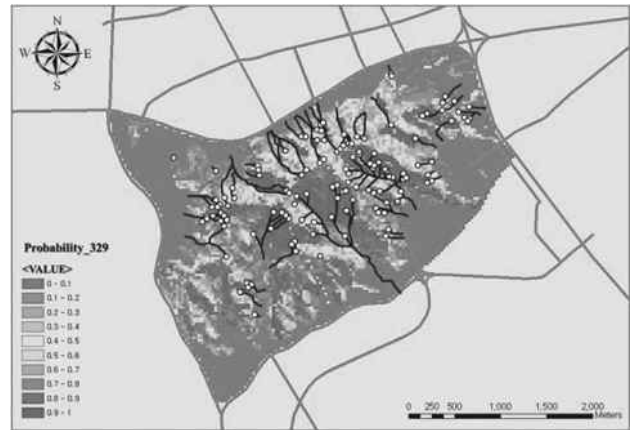

Figure 7. Landslide susceptibility map with field survey results

3.2 *Debris flow risk assessment*

A methodology for the evaluation of debris flow risk in a watershed incorporated with GIS was proposed in this work. This model predicts the debris flow hazard risk on any given watershed. The model was developed using statistical analysis of debris flow hazard data in Korea from 2005 to 2011. These data was obtained from field surveys, disaster reports on national roads of Korea, aerial photos, and digital maps. Each set of data in the database includes geomorphologic factors influencing debris flow size, rainfall information, bedrock types, and run out distance of the debris. Figure 8 shows flow chart of the methodology.
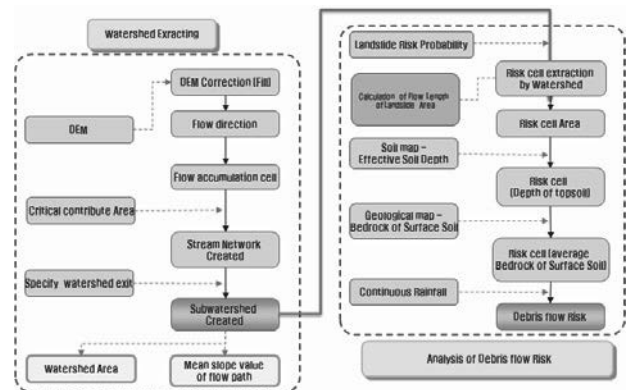

Figure 8. Flow chart of the debris flow risk assessment

Debris flow hazard probability is calculated by equation (1).

$$\text{Debris flow hazard probability} = \qquad (1)$$

where Logit(p) = -5.4 -1.3E-5×(area indicating landslide probability higher than 50%×depth of surface soil) +0.005× (amount of continuous rainfall) +4.522×(bedrock type) +2.1E-8×(mean slope of flow path-area of watershed). Table 1 shows the data and data acquisition method used in the model.

Based on the analysis of DEM (Digital Elevation Map) of Umyeon Mountain, 31 watersheds can be generated as shown in Figure 9. The probability of debris flow hazard for individual watershed in Umyeon Mountain is summarized in Table 2. As shown in Table 2, most of the watershed where debris flow took place showed high probability for the debris flow hazard except one watershed (Seonbawi) where debris flow hazard did not occur. Unlike the other watersheds, the bedrock of Seonbawi watershed was granite and the bedrock condition might be one of the important factor in the occurrence of debris flow. These results confirmed the applicability of the developed risk assessment model for the landslide and debris flow hazard.

Table 1. Data of the debris flow hazard occurrence

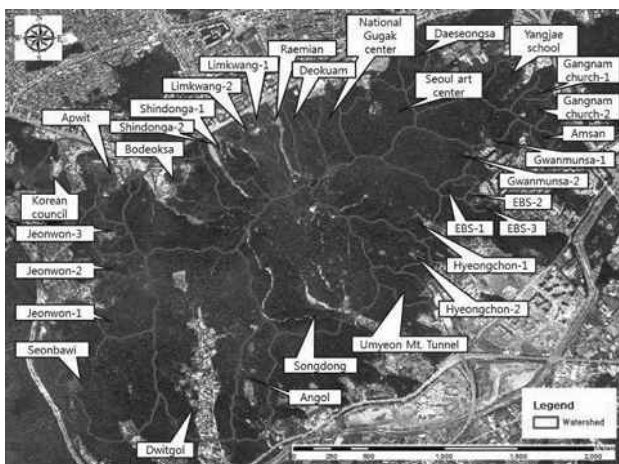| Dataset	Data acquisition
Potential landslide area ()	Landslide susceptibility map
Depth of top soil (m)	Soil classification map
Possible sediment area ()	Field survey, DEM
Mean slope gradient of flow path(°)	Field survey, DEM
Watershed area()	GIS tool, DEM
Rainfall(mm)	AWS
Bedrock type	Geological map
Mean flow distance(m)	GIS tool, DEM

Figure 9. Watersheds in Umyeon Mountain

Table 2. The probability of debris flow hazard for individual watershed

Watershed	Prob.	Watershed	Prob.
Raemian	84%	EBS-1	77%
Limkwang-1	72%	EBS-2	70%
Limkwang-2	76%	EBS-3	71%
Shindonga-1	87%	Gwanmunsa-1	96%
Shindonga-2	87%	Gwanmunsa-2	97%
Hyeongchon-1	99%	Amsan	73%
Hyeongchon-2	92%	Gangnam church-1	71%
Jeonwon-1	94%	Gangnam church-2	79%
Jeonwon-2	80%	Yangjae school	84%
Jeonwon-3	75%	Daeseongsa	79%
Bodeoksa	99%	Seoul art center	96%
Apwit	69%	National gugak center	87%
Korean Council	73%	Dwitgol	99%
Songdong	99%	Angol	90%
Umyeon Mt. tunnel	83%	Seonbawi	17%
Deokuam	85%		

4 CONCLUSIONS

A series of debris flow events occurred around 8:00 to 8:50 a.m. on July 27, 2011 in the Umyeon Mountain area located in Seoul, Korea. Field survey on the debris flow at Umyeon Mountain was carried out to understand the comprehensive situation of the hazard. The field survey result showed that debris flows occurred all around Umyeon Mountain and the average moving distance of debris flows was about 615m, ranging from 95 to 1,584m. Also, the average gradient of initiation slopes was about 27 degrees, ranging from 11 to 37 degrees. The initiation volume of the slope failure was measured from 73 to 4,000 m^3.

In addition, risk analysis based on the hazard map of the landslide and debris flow was performed. Risk assessment of the landslide hazard showed the most of the slope failures were occurred in highly susceptible regions for landslide. And debris flow risk assessment also showed that the most of the watershed experienced debris flow hazard showed high probability of debris flow occurrence. And these results confirmed the applicability of the developed risk assessment model for the landslide and debris flow hazard.

5 ACKNOWLEGEMENT

6 REFERENCES

Hutchinson, J. 1988. Morphological and geotechnical parameters of landslides in relation to geology and hydrogelogy, 5th. Int. Symp. on Landslides 1, 3-35.

Johnson, A.M. and Rahn, P. 1970. Mobilization of debris flows, Z. Geomorphology 9, 168-186.

Lee, S.-W., Kim, G.-H., Yune, C.-Y., Ryu, H.-J., and Hong, S.-J. 2012. Development of Landslide-Risk Prediction Model thorough Database Construction, Journal of Korea Geotechnical Society 28(4) 23-33. (in Korean)

Son, S.-H., Choi, B. and Paik, J. 2012. Characteristics of rainfall and groundwater table in a small forested watershed of Mt. Umyeon, Proceedings of 38th Korea Society of Civil Engineering Conference and Civil Expo 2012, Chonnam National University, Korea, October 24-26

Yune, C.-Y. and Jun, K.J. 2011. National investigation on the landslides and debris flows in 2011, Korea, River and Road in Mountain Area, Vol. 4, Special publication, 15-19.

Proceedings of the 18ᵗʰ International Conference on Soil Mechanics and Geotechnical Engineering

CHALLENGES AND INNOVATIONS IN GEOTECHNICS

Actes du 18ᵉ Congrès International de Mécanique des sols et de Géotechnique

DÉFIS ET INNOVATIONS EN GÉOTECHNIQUE

The 18ᵗʰ International Conference on Soil Mechanics and Geotechnical Engineering (Paris 2013) was devoted to "Challenges and Innovations in Geotechnics". The call for abstracts was based on a large series of themes covering most aspects of Geotechnical Engineering and around 800 abstracts were received from the Member Societies. According to the ISSMGE new vision for strengthening the role of the Technical Committees, the papers were distributed to the corresponding Technical Committees, which then selected the General Reporters, the Invited Speakers and the Poster presentations. The involvement of TCs (which could also propose Workshop Sessions on an independent basis) was enthusiastic and successful, which probably explains the success of the Conference with more that 1500 delegates.

The four volumes of the Proceedings contain the Terzaghi Oration, the Honour lectures, the Special lectures followed by the papers presented according to the relevant TC and introduced by the TC General Report. All volumes, together with late papers, will also be made available online free of charge. These volumes will provide a state of the art and serve as an essential reference for practitioners, academics and researchers involved in Soil Mechanics and Geotechnical Engineering.

Le 18ᵉ Congrès International de Mécanique des sols et de Géotechnique (Paris 2013) a été dédié aux « Défis et Innovations en Géotechnique ». L'appel à résumé était ouvert sur un large éventail de thèmes couvrant la plupart des aspects de la Géotechnique ; les Sociétés Membres ont sélectionné environ 800 résumés. En cohérence avec le souhait de la Société Internationale (SIMSG) de renforcer le rôle des Comités Techniques (CTs), les contributions ont été transmises aux CTs correspondants, en charge de choisir les Rapporteurs Généraux, les Orateurs Invités et les Présentations sur Posters. L'implication des CTs, qui pouvaient en outre proposer des sessions d'Atelier à leur convenance, a été enthousiaste et fructueuse ; ceci explique probablement le succès du Congrès avec plus de 1500 délégués.

Les quatre volumes des Actes contiennent l'Allocution Terzaghi, les Conférences Honorifiques, les Conférences Spéciales, suivies des contributions, réunies par CT, et précédées du Rapport Général du CT correspondant. L'ensemble, accompagné des contributions complémentaires, sera mis en ligne sur le Web, en accès libre. Ces volumes constituent un état de l'art et serviront de référence essentielle pour les praticiens, les enseignants et les chercheurs en Mécanique des Sols et en Géotechnique.

Paris 2013